Condensed Matter and Interphases
Kondensirovannye sredy i mezhfaznye granitsy

Peer-reviewed scientific journal
Published since January 1999
Periodicity: Quarterly
Volume 26, No. 4, 2024

Full-text version is available in the Russian language on the website: https://journals.vsu.ru/kcmf

Condensed Matter and Interphases (Kondensirovannye Sredy i Mezhfaznye Granitsy) publishes articles in Russian and English dedicated to key issues of condensed matter and physicochemical processes at interfaces and in volumes.

The mission of the journal is to provide open access to the results of original research (theoretical and experimental) at the intersection of contemporary condensed matter physics and chemistry, material science and nanoindustry, solid state chemistry, inorganic chemistry, and physical chemistry, and to share scientific data in the **following sections**: atomic, electron, and cluster structure of solids, liquids, and interphase boundaries; phase equilibria and defect formation processes; structure and physical and chemical properties of interphases; laser thermochemistry and photostimulated processes on solid surfaces; physics and chemistry of surface, thin films and heterostructures; kinetics and mechanism of formation of film structures; electrophysical processes in interphase boundaries; chemistry of surface phenomena in sorbents; devices and new research methods.

The journal accepts for publication: reviews, original articles, short communications by leading Russian scientists, foreign researchers, lecturers, postgraduate and undergraduate students.

FOUNDER AND PUBLISHER:
Voronezh State University

The journal is registered by the Russian Federal Service for Supervision of Communications, Information Technology and Mass Media, Certificate of Registration ПИ № ФС77-78771 date 20.07.2020

The journal is included in the List of peer reviewed scientific journals published by the Higher Attestation Commission in which major research results from the dissertations of Candidates of Sciences (PhD) and Doctor of Science (DSc) degrees are to be published. Scientific specialties of dissertations and their respective branches of science are as follows: 1.4.1. – Inorganic Chemistry (Chemical sciences); 1.4.4. – Physical Chemistry (Chemical sciences); 1.4.6. – Electrochemistry (Chemical sciences); 1.4.15. – Solid State Chemistry (Chemical sciences); 1.3.8. – Condensed Matter Physics (Physical sciences).

The journal is indexed and archived in: Russian Scientific Index Citations, Scopus, Chemical Abstract, EBSCO, DOAJ, CrossRef

Editorial Board and Publisher Office:
1 Universitetskaya pl., Voronezh 394018
Phone: +7 (432) 2208445
https://journals.vsu.ru/kcmf
E-mail: kcmf@main.vsu.ru

CONTENTS

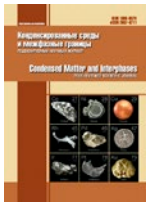

ISSN 1606-867X (Print)
ISSN 2687-0711 (Online)
Condensed Matter and Interphases
Kondensirovannye Sredy i Mezhfaznye Granitsy
https://journals.vsu.ru/kcmf/

Review

Review article
https://doi.org/10.17308/kcmf.2024.26/12367

Complex copper-based chalcogenides: a review of phase equilibria and thermodynamic properties

M. B. Babanly[1,2]✉, L. F. Mashadiyeva[1], S. Z. Imamaliyeva[1], D. M. Babanly[1,3], D. B. Tagiyev[1], Yu. A. Yusibov[4]

[1]*Institute of Catalysis and Inorganic Chemistry, 113 H. Javid av., Baku AZ-1143, Azerbaijan*

[2]*Baku State University, 23 Z. Khalilov st., Baku AZ-1148, Azerbaijan*

[3]*French-Azerbaijani University 183 Nizami st., Baku AZ-1010, Azerbaijan*

[4]*Ganja State University, 187 H. Aliyev av., Ganja AZ-2000, Azerbaijan*

Abstract

Complex copper-based chalcogenides are among the most important functional materials in modern engineering and technology due to their diverse physical and physicochemical properties, environmental safety and availability. The development of new similar materials and the improvement of the applied characteristics of known compounds is largely associated with the use of approaches based on the physicochemical analysis and, in particular, the "composition-structure-property" relationship.

This review summarizes the available data on phase equilibria in ternary systems Cu-Tl(B^{IV}, B^{V})-X (B^{IV}-Si, Ge, Sn; B^{V}-As, Sb, Bi; X-S, Se, Te) and the thermodynamic properties of their intermediate phases. Similar data are also considered for more complex systems forming solid solutions of various types of substitution based on known ternary copper chalcogenides. A significant part of the presented sets of mutually consistent data on phase equilibria and thermodynamic properties of the considered systems was obtained by our group over the past 10-15 years. Although these data cover only a small part of the systems described above, they provide great possibilities for manipulation of composition and structure, including entropic engineering strategies. The authors consider it extremely important to further develop fundamental research on phase equilibria and thermodynamic properties of complex copper chalcogenides and use their results widely in selecting alloy compositions for physical measurements.

Keywords: Environmentally friendly materials, Complex copper chalcogenides, Phase diagram, Solid solutions, Thermodynamic properties

Funding: The study was supported by the Azerbaijan Science Foundation - Grant No. AEF-MCG-2022-1(42)-12/10/4-M-10.

For citation: Babanly M. B., Mashadiyeva L. F., Imamaliyeva S. Z., Babanly D. M., Tagiyev D. B., Yusibov Yu. A. Complex copper-based chalcogenides: a review of phase equilibria and thermodynamic properties. *Condensed Matter and Interphases*. 2024;26(4): 579–619. https://doi.org/10.17308/kcmf.2024.26/12367

Для цитирования: Бабанлы М. Б., Машадиева Л. Ф., Имамалиева С. З., Бабанлы Д. М., Тагиев Д. Б., Юсибов Ю. А. Сложные халькогениды на основе меди: обзор по фазовым равновесиям и термодинамическим свойствам. *Конденсированные среды и межфазные границы*. 2024;26(4), 579–619. https://doi.org/10.17308/kcmf.2024.26/12367

✉ Mahammad B. Babanly, e-mail: babanlymb@gmail.com

1. Introduction

Metal chalcogenides are currently used or considered promising for use in various areas of modern high technologies as semiconductor, thermoelectric, photoelectric, optical, magnetic and other materials due to their diverse physical and physicochemical properties [1–9]. The discovery of a new quantum state of matter, a topological insulator, at the beginning of our century [10], provided new impetus to research of physics, chemistry and materials science of chalcogenides. It turned out that many-layered chalcogenides have the properties of a topological insulator [11–17], and some of them combine the properties of a topological insulator and a magnet [18–21] and are extremely promising for a variety of applications, including spintronics, quantum memory and information processing devices, security systems, and medicine [13, 14].

In recent decades, copper-based chalcogenides have also attracted attention from researchers as environmentally friendly, safe, and affordable functional materials [5–9, 22–30]. Many of these compounds, along with unique electronic properties, have high ionic conductivity and can be used as solid-state electrodes, selective membranes, sensors, etc. Synthetic analogues of natural copper chalcogenide minerals should be especially noted among the intensively studied similar materials [31–37]. These compounds are very attractive as mixed ion-electron conductors, thermoelectrics, photovoltaics, photocatalysts, and optical materials.

In addition, according to several recent studies, some copper-based chalcogenides are promising for use in medicine [22, 38–40]. It should also be noted that many copper chalcogenides exist in nature as minerals and are of great interest to the geochemistry of the Earth [41, 42].

Analysis of data from many studies [22, 34–37] on complex copper chalcogenides demonstrated that their functional properties can be significantly improved by manipulating the structure and composition, including the concept of entropy engineering. The latter implies thermodynamic stabilization of phases with favorable applied characteristics by increasing the complexity of the composition and structural disorder [35].

The solution to the most important problems of materials science, especially in the so-called alloy systems, which include chalcogenides, is mainly associated with the use of physicochemical analysis [43, 44]. At the initial stage of development of new materials, the application of this method involves obtaining reliable data on phase equilibria in the corresponding systems, which allows not only the identification of new compounds or phases of variable composition but also the establishment of their nature of formation, thermal stability, primary crystallization and homogeneity regions, the presence of phase transitions, etc. [14, 37, 45–47]. The combination of these data forms the basis for the development of methods for the synthesis and growth of crystals with specified composition and properties.

The use of physicochemical analysis is also very effective for the design of known materials and the optimization of their properties. It is based on the well-known relationship "composition-structure-property". For the optimization of the functional indicators of certain compounds of stoichiometric composition, it is important to establish the nature of the physicochemical interaction in complex systems that include such compounds - structural or formula analogues, since the formation of various types of solid solutions (cationic, anionic and both types simultaneously) of substitution can be expected [14, 37, 48]. This allows the control of properties by varying structure and composition.

Optimization of the indicated technological parameters and many other processes requires their deeper thermodynamic analysis and the implementation of appropriate thermodynamic calculations. The efficiency of such calculations is directly related to the reliability and accuracy of data on the thermodynamic properties of substances involved in the considered processes [47, 49].

Hence, the wide application of physicochemical analysis for solving problems of materials science of chalcogenides, in particular, conducting comprehensive studies of phase equilibria and thermodynamic properties of the corresponding systems is important. Some aspects of such complex studies were considered by us in several studies [47, 50, 51]. Due to the widespread application of this approach in the study of

complex copper-based chalcogenide systems discussed in this review, we will only note that the basis of the approach is the use of the EMF method in a complex of experimental methods for studying phase equilibria. The EMF method, being one of the most accurate equilibrium methods of chemical thermodynamics, allows combining studies of phase equilibria and thermodynamic properties. We have used this approach since the beginning of the 1980s for the investigation of ternary thallium-containing chalcogenide systems [51–55], and in subsequent years also for other systems [50, 56–59].

The purpose of this review was to demonstrate the importance of the physicochemical analysis method and, in particular, the development of studies on phase equilibria and thermodynamic properties of multicomponent copper-based chalcogenide systems for the elaboration of scientific foundations for obtaining new complex phases with controlled composition, structure and properties.

The three sections of the review present the results of a study of phase equilibria in ternary and quaternary systems composed of copper chalcogenides and p^1–p^3-elements. At the beginning of each section, a general description is provided, crystallographic data of the most characteristic compounds of the corresponding class are shown, and a brief overview of their functional properties is presented. After, data on phase equilibria in the considered ternary and quaternary systems and fundamental thermodynamic characteristics of intermediate phases are presented and discussed.

2. Copper-thallium chalcogenides and phases based on them

The most characteristic copper chalcogenides with p^1-elements are compounds of the chalcopyrite type with the general formula $CuB^{III}X_2$ (B^{III}-Al, Ga, In, Tl; X-S, Se, Te) [1, 22]. At the same time, thallium and copper form a series of chalcogenides (see subsection 2.1), in which thallium is present in a more characteristic oxidation state (1+): CuTlX, Cu_3TlX_2, Cu_9TlX_5 and others. The $CuTlS_2$ and CuTlS crystal structures are shown in Fig. 2.1 and crystallographic data of copper-thallium chalcogenides are presented in Table 2.1.

The crystal structure of the CuTlS was established in [60] by powder and single-crystal X-ray diffraction methods. It has been shown that it crystallizes in the tetragonal syngony in the PbFCl structural type. The layers of Cu_2S_2, formed by CuS_4 tetrahedra with common edges, placed between double foils of Tl atoms. The Cu atoms are located inside the layers at the centers of tetrahedra, and Tl atoms are located in square two-dimensional networks and determine the *a* parameter. Each Tl atom is located in a pyramid cup and is bonded to four sulfur atoms at the base.

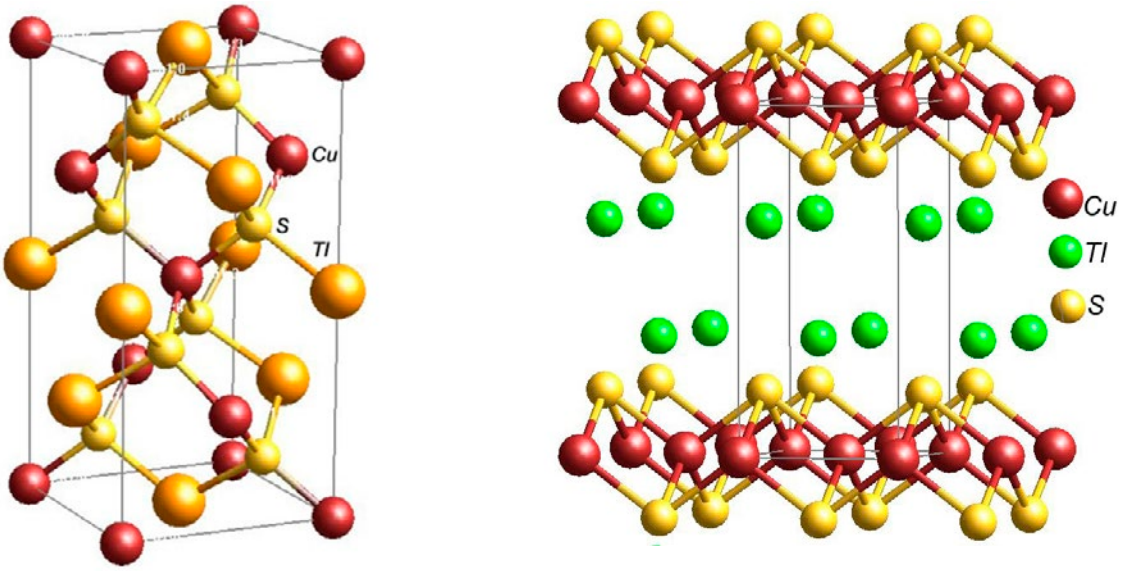

Fig. 2.1. Crystal structures of $CuTlS_2$ and CuTlS

Table 2.1. Crystallographic parameters of the copper-thallium chalcogenides

Compound	Crystal system, sp. gr. and lattice parameters, nm	Ref.
$CuTlS_2$	Tetragonal, I$\bar{4}$2d, *a* = 0.5576, *c* = 1.1256	[94]
CuTlS	Tetragonal, *P4/nmm*, *a* = 0.3922(2), *c* = 0.8123(6)	[60]
	Tetragonal, *P4/mmm, a* = 0.3912, *c* = 0.8164	[94]
Cu_3TlS_2	Monoclinic, C2/*m, a* = 1.463, *b* = 0.3863, *c* = 0.8298, β = 111.72°	[89]
Cu_7TlS_4	Tetragonal, *I4/m, a* = 1.01792(18), *c* = 0.38567(9)	[90]
$CuTlSe_2$	Tetragonal, I$\bar{4}$2d, *a* = 0.583, *c* = 1.162	[100]
CuTlSe	Tetragonal, *P4/nmm*, *a* = 0.4087(6), *c* = 0.8195(19)	[100]
Cu_3TlSe_2	Monoclinic, C2/*m, a* = 1.52128, *b* = 0.40115, *c* = 0.83944, β = 111.7°	[88]
Cu_2TlSe_2	Tetragonal, *I4/mmm*, *a* = 0.380, *c* = 1.377	[100]
Cu_7TlSe_4	Tetragonal, *I4/m, a* = 1.04453(18), *c* = 0.39735(8)	[90]
$CuTl_4Te_3$	Tetragonal, *I4/mcm*, *a* = 0.8929(1), *c* = 1.2603(1)	[106]
Cu_2TlTe_2	Tetragonal, *I4/mmm*, *a* = 0.4001, *c* = 1.4208	[100]
Cu_3TlTe_2	Tetragonal, $P4_2/nnm$, *a* = 0.8427(4), *c* = 1.4492(6)	[105]

Copper chalcogenides with elements of the gallium subgroup, as well as solid solutions and doped phases based on them, are excellent materials [22] for photovoltaic [62–70], optoelectronic [71–73], and thermoelectric [70, 75–80] devices, as well as luminescent materials [81–83].

The use of these materials as solar energy absorbers is because the width of their band gap correlates well with the maximum photon power density in the sunlight spectrum and at the same time demonstrates long-term stability and resistance to radiation [22, 84]. Several studies proposed changing the bulk or surface composition by sulphidization [65, 67, 68], regulation the ratios of constituent atoms, adding alloying components [61, 63, 66], and other strategies [22] to increase their efficiency. It should be noted that sulphidization of the Cu(Ga, In)Se_2 layers led to the record efficiency (23.35%) of the solar cell [85]. Thin-film solar cells based on Cu(Ga, In)Se_2 are also considered promising for generating electricity at space stations [86].

Copper chalcogenides with p^1-elements with a wide range of band gap energies and unique optical properties are very promising for use in optoelectronic and light-emitting devices [22, 72, 73]. The authors of [81] reported the development of quantum dot LEDs exhibiting red color with a narrow emission peak by controlling the copper content in Cu(GaIn)S_2 phases.

Copper-thallium selenides and tellurides are of interest as thermoelectric materials with abnormally low thermal conductivity [22, 75, 76, 80, 87].

The main reasons for the relatively low efficiency of photovoltaic and thermoelectric systems based on copper-gallium chalcogenides (indium, thallium) and the proposed optimization methods for obtaining their nanocrystals with specified characteristics are discussed in reviews [22, 66].

2.1. Phase equilibria in the Cu-Tl-X systems

The results of studies on phase equilibria in the indicated systems carried out before the beginning of the 90s of the last century are summarized in [91]. The results of the most important works of the indicated period, as well as the research performed in subsequent years by our group, are presented and discussed below.

The Cu-Tl-S system. The quasi-binary section of the Cu_2S-Tl_2S system was studied almost simultaneously by two groups of authors [92, 93]. According to [92] (Fig. 2.2), three ternary compounds are formed in the system: Cu_9TlS_5, Cu_3TlS_2, and CuTlS. The first two melt with decomposition by peritectic reactions at 706 and 693 K, respectively, and the last one melts congruently at 689 K. The phase diagram constructed in [93] reflects two congruently melting compounds CuTlS and $Cu_8Tl_2S_5$. Later, in the study [94], crystallographic data for the $CuTlS_2$ and CuTlS compounds are presented (Table 2.1). The phase diagram presented in [92]

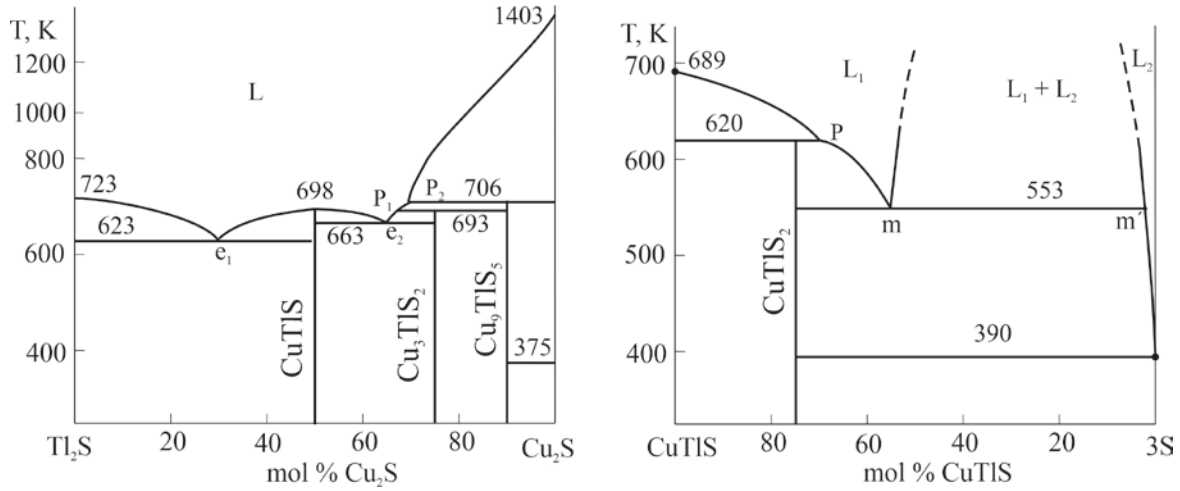

Fig. 2.2. Phase diagrams of the quasi-binary systems Cu_2S-Tl_2S and CuTlS-S

was confirmed by the authors of [95]. The CuTlS-S and CuTlS-Tl sections are also quasi-binary. The first is characterized by the formation of the compound $CuTlS_2$ with incongruent melting at 620 K [96] (Fig. 2.2), and the second is designated by the presence of a wide immiscibility region and degenerate eutectic [97].

The study [98] presents a complete *T-x-y* diagram of the Cu-Tl-S system, including a diagram of solid-phase equilibria at 300 K and a projection of the liquidus surface (Fig. 2.3). As can be seen, the system is characterized by the presence of four ternary compounds of practically constant composition. The liquidus surface consists of 10 primary crystallization fields, including four ternary compounds. A characteristic feature of the system is the presence of three wide immiscibility regions of two liquid phases and a region of immiscibility of three liquid phases.

The Cu-Tl-Se system. Quasi-binary section Cu_2Se-Tl_2Se (Fig. 2.4) of this system is characterized by the formation of ternary compounds CuTlSe, $Cu_7Tl_3Se_5$, Cu_3TlSe_2, $Cu_8Tl_2Se_5$ and Cu_9TlSe_5 [99]. According to [91], the CuTlSe-TlSe, CuTlSe-Tl, and CuTlSe-Se sections are also quasi-binary. The first one forms a phase diagram of a simple eutectic type, the second one forms a phase diagram of a monotectic type, and the third one is characterized by the formation of a ternary compound $CuTlSe_2$ that melts incongruently at 550 K (Fig. 2.4)

The literature contains information on the synthesis and crystal structure of about ten copper selenides with thallium [91, 100]. However, a complete picture of phase equilibria in the Cu-Tl-Se system has not been obtained yet. A fragment of the solid-phase equilibrium diagram, constructed by us based on the data of studies [91, 102] is shown in Fig.2.5 and a projection of the liquidus surface of the Cu-Cu_2Se-Tl_2Se-Tl subsystem is shown in Fig. 2.6. This projection, the corresponding sulfide projection, is characterized by the presence of wide double and triple immiscibility regions and is congruently triangulated into three elementary triangles.

The Cu-Tl-Te system. Phase equilibria in this system have been studied for the Cu_2Te-Tl_2Te_3 section [103, 104]. This section is not quasi-binary due to the incongruent melting of Tl_2Te_3, but is stable below the solidus and is characterized by the formation of the ternary compounds $CuTlTe_2$ and Cu_3TlTe_3 with incongruent melting at 573 and 673 K, respectively. According to [95, 101], the Cu_2Te-Tl_2Te section, unlike similar sulfide and selenide systems, is non-quasi-binary and unstable in the subsolidus. It is characterized by the formation of the ternary compounds Cu_9TlTe_5 and Cu_3TlTe_2 with incongruent melting.

There is also information about copper-thallium tellurides with Cu_2TlTe_2 and $CuTl_4Te_3$ compositions [91, 100, 105, 106] (Table 2.1).

In studies [104, 107] a fragment of the diagram of solid-phase equilibria of Cu-Tl-Te at 300 K was presented (Fig. 2.5), which reflects all of the above-mentioned ternary compounds.

2.2. Thermodynamic properties of copper-thallium chalcogenides

The thermodynamic properties of copper-thallium chalcogenides were investigated in

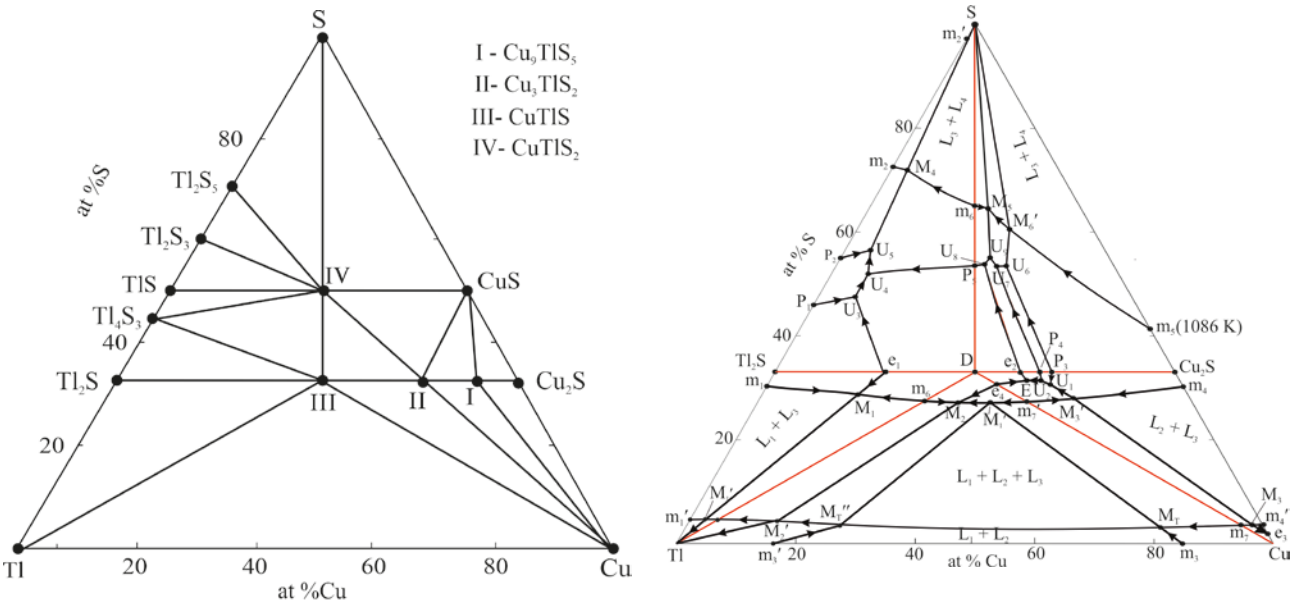

Fig. 2.3. Solid-phase equilibrium diagram at 300 K and liquidus surface projection of the Cu-Tl-S system. Red lines are quasi-binary sections

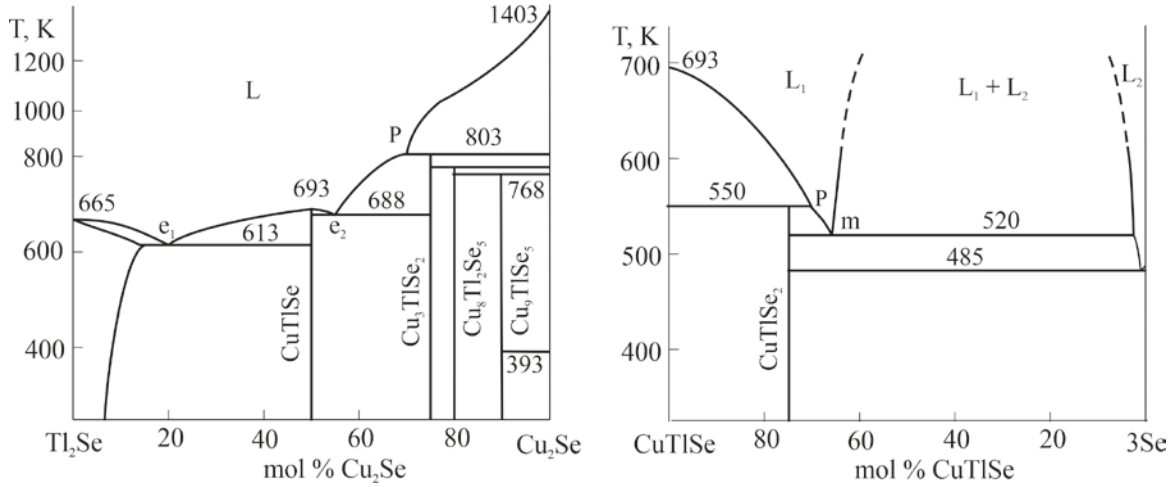

Fig. 2.4. Phase diagrams of the quasi-binary systems Cu_2Se-Tl_2Se and CuTlSe-Se

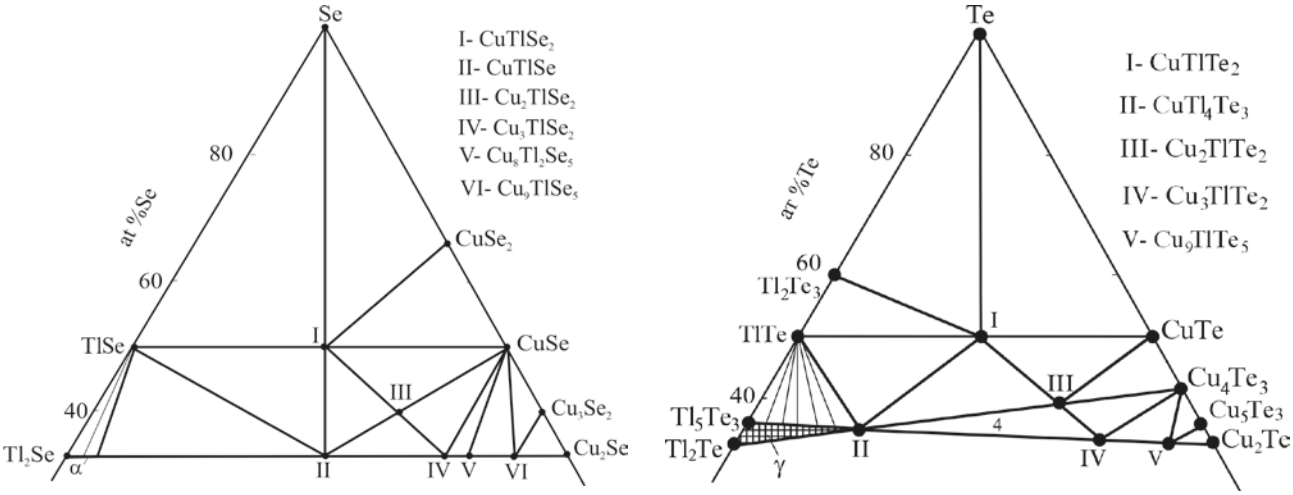

Fig. 2.5. Solid-phase equilibria diagrams of the Cu-Tl-Se and Cu-Tl-Te systems at 300 K

several studies [91, 98, 101, 104, 107-109] using the electromotive force (EMF) method. In these studies, the EMFs of two types of concentration circuits were measured:

(–) Tl (s.) | liquid + Tl^+ | (Tl in alloy) (s.) (+) (2.1)
electrolyte

(–) Cu (s.) | $Cu_4RbCl_3I_2$ (s.) | (Cu in alloy) (s.) (+)(2.2)

in a wide range of temperatures, starting from room temperature. The methods for compiling chains of (2.1) and (2.2) types, conducting experiments and processing their results are described in detail in [51, 109, 110]. It should be noted that various modifications of the EMF method with liquid [61-59, 109-115] and solid electrolytes [50, 51, 113, 116-120] are successfully used to study the thermodynamic properties and phase equilibria of various inorganic systems.

The results of thermodynamic studies of copper-thallium chalcogenides by measuring the EMF of type (2.1) concentration cells are shown in [98, 107, 109]. Later, in [101, 104, 108], a thermodynamic study of the indicated systems was carried out by measuring the EMF of type (2.2) concentration cells relative to a copper electrode. It should be noted that the thermodynamic data obtained in the above two series of studies are independent: they used the results of measurements of the EMF of concentration cells of various types, and based on these data, partial thermodynamic functions of different components (thallium or copper) which characterize completely different potential-forming reactions of the studied systems were calculated.

The obtained two series of data of standard integral thermodynamic functions of copper-thallium chalcogenides are shown in Table 2.2.

As can be seen from Table 2.2 the values of the standard thermodynamic functions for the formation of ternary compounds, obtained by two modifications of the EMF method, are generally in satisfactory agreement with each other. This confirms both the reversibility of types (2.1) and

Table 2.2. Standard integral thermodynamic functions of the copper-thallium chalcogenides

Compound	$-\Delta_f G^0$ (298 K)	$-\Delta_f H^0$ (298 K)	S^0_{298} J·K^{-1}·mol^{-1}	Ref.
	kJ·mol^{-1}			
$CuTlS_2$	91.5±0.5 94.3±0.7	98.6±4.0 93.6±1.4	172.7±2.8	[51, 98] [108]
CuTlS	84.1±1.5 90.3±0.7	82.1±4.9 88.3±2.1	132.4±6.2	[51, 98] [108]
Cu_3TlS_2	152.7±1.8 163.8±2.6	145.8±12.3 159.2±9.8	251.8±5.8	[51, 98] [108]
Cu_9TlS_5	354.6±4.5 373.8±3.9	339.7±30.8 371.8±21.4	529.0±19.0	[51, 98] [108]
$CuTlSe_2$	96.3±0.2 96.5±0.6	97.9±1.0 97.2±1.3	176.1±5.1	[101] [51]
CuTlSe	84.5±0.2 84.2±1.3	81.4±0.9 80.5±3.9	149.9±2.8	[101] [51]
Cu_2TlSe_2	119.1±0.3	118.6±1.5	216.2±6.8	[101]
Cu_3TlSe_2	150.8±3.7	150.7±9.8		[51]
Cu_9TlSe_5	333.6±10.1	350.5±28.6		[51]
$CuTlTe_2$	75.1±0.4	72.6±1.3	208±4	[104]
Cu_2TlTe_2	99.2±0.5 94.8±0.9	94.3±2.1 92±7	249±6 237±3	[104] [107]
Cu_3TlTe_2	122.0±0.6 117.1±1.2	115.2±2.7 117±5	288±8 263±4	[104] [107]
Cu_9TlTe_5	264.3±2.6 244.0±2.4	253.8±9.8 2431±14	637±15 621±7	[104] [107]
$CuTl_4Te_3$	201.4±1.4	203.8±2.6	433±9	[104]

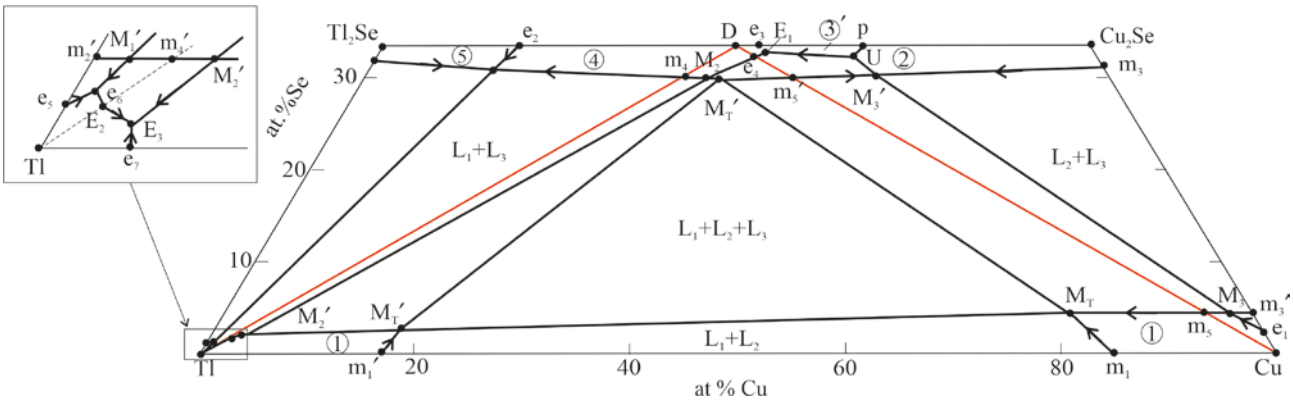

Fig. 2.6. Liquidus surface projection of the Cu-Cu_2Se-Tl_2Se-Tl subsystem. Red lines are quasi-binary sections

(2.2) concentration cells and the reliability of the thermodynamic data used in the calculations for binary copper and thallium chalcogenides.

2.3. Complex systems based on CuTlX compounds

The results of the study of phase equilibria in quasi-binary systems composed of the CuTlX compounds and their silver-containing analogues, as well as in mutual AgTlS+CuTlSe↔AgTlSe+CuTlS and quasi-ternary systems CuTlS-CuTlSe-AgTlTe were presented in [121-124]. It has been shown that the CuTlS-CuTlSe system was characterized by the formation of a continuous series of solid solutions [121], while systems of the CuTlX-AgTlX type [122–124] were characterized by limited mutual solubility of the components and eutectic equilibrium (Fig. 2.7).

The new phase of variable composition with a wide homogeneity region was identified in the CuTlS-AgTlS system [122]. According to the data [123, 124], wide homogeneity regions of

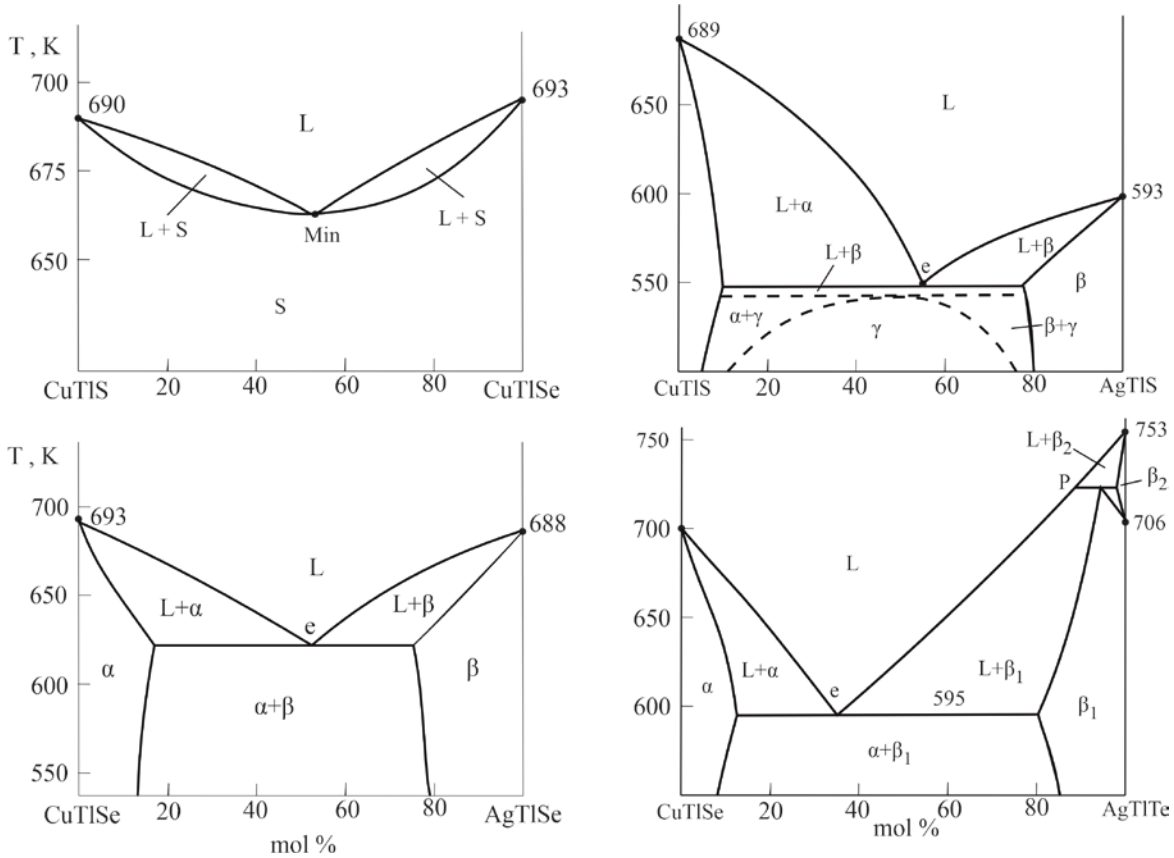

Fig. 2.7. *T-x* diagrams of some quasi-binary systems based on CuTlX compounds

solid solutions with simultaneous Cu ↔ Ag and chalcogen substitutions were revealed in the above-mentioned mutual and quasi-ternary systems.

3. Copper chalcogenides with Si, Ge, Sn

Triple compounds of Cu-B^{IV}-X (B^{IV} - Si, Ge, Sn; X – S, Se, Te) systems tend to crystallize in a large number of phases and structural forms, resulting in different functional properties and application possibilities [22]. In silicon- and germanium-containing systems (sections 3.1 and 3.2), the compounds of $Cu_2B^{IV}X_3$ and $Cu_8B^{IV}X_6$ types are the most characteristic and studied. The first group of compounds can be considered as synthetic analogues of the mineral mohite (Cu_2SnS_3), and the compounds of the second group are synthetic analogues of the mineral argyrodite (Ag_8GeS_6). The Cu-Sn-S system (section 3.3) is characterized by the formation of several ternary compounds with various compositions and structures. The crystal structures of some copper-tin sulfides are shown in Fig. 3.1, and crystallographic data of copper chalcogenides with p^2-elements are presented in Table 3.1.

The compounds of $Cu_2B^{IV}X_3$ type have various structural forms, such as cubic sphalerite-like (sp. gr. $F\bar{4}3m$), monoclinic sphalerite superstructure; orthorhombic structure (sp. gr. *Im*2) and a hexagonal structure of the wurtzite type (sp. gr. *P*63/*mc*) (Fig. 3.1). In the orthorhombic phase, the cations are ordered in a way that all cation positions in each plane are occupied by the same element and follow an ordered sequence of two planes with Cu cations and one plane with Ge cations. In contrast, in the cubic structure of zinc-blende, the Cu and Ge cations are randomly distributed over the cationic sites with filling factors of 2/3 and 1/3 for Cu and Ge, respectively [22, 115].

All compounds of the argyrodite family have a tetrahedral close-packed structure containing weakly bound cations A^+ [35, 36]. Cations B^{4+} tetrahedrally coordinated by 4 anions and form polyanions $[BX_4]^{8-x}$. These polyanions, along with the X^{2-} anions, form a rigid framework with vacancies for A^+ cations (Fig. 3.2). A characteristic feature of compounds of the argyrodite family is the presence of polymorphic phase transitions at

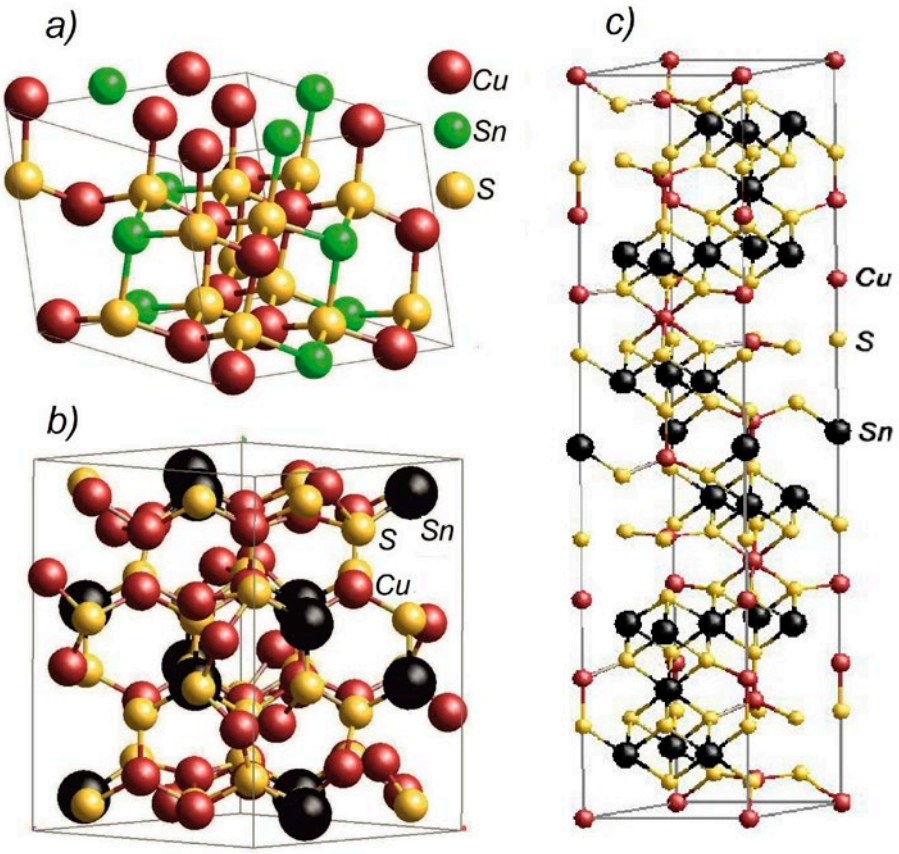

Fig. 3.1. Crystal structures of copper-tin sulfides: monoclinic Cu_2SnS_3 (a), orthorhombic Cu_4SnS_4 (b) and hexagonal $Cu_4Sn_7S_{16}$ (c)

relatively low temperatures (≤ 530 K) [37]. Low-temperature modifications have various ordered low-symmetry structures, which are described in detail in the literature [35–37]. They contain cations A^+ arranged in a specific order in certain positions. As a result of the distortion of the rigid anionic framework of the crystal lattice, a transition of low-temperature modifications into high-temperature disordered modifications occurs. Despite the relative diversity of the crystal structures of the low-temperature phases, all high-temperature argyrodites have a highly symmetrical cubic structure with sp. gr. *F*-43*m* (Table 3.1). Disordered high-temperature cubic

Table 3.1. Crystallographic parameters of ternary compounds of the Cu-B^{IV}-X systems

Compound	Crystal system, sp. gr. and lattice parameters, nm	Ref.
Cu_2SiS_3	Monoclinic, *C*1*c*1, *a* = 0.6332, *b* = 1.123, *c* = 0.6273, β = 107.49°	[159]
HT-Cu_8SiS_6	Cubic, *F*-43*m*, *a* = 0.976	[37]
RT-Cu_8SiS_6	Orthorhombic, $Pmn2_1$, *a* = 0.70445 (3), *b* = 0.69661(3), *c* = 0.98699 (5)	[37]
Cu_2SiSe_3	Monoclinic, *C*1*c*1, *a* = 0.6669(1), *b* = 1.1797(1), *c* = 0.6633(1), β = 107.67°	[159]
HT-Cu_8SiSe_6	Cubic, *F*-43*m*, *a* = 0.1017	[37]
Cu_2SiTe_3	Cubic, *F*-43*m*, *a* = 0.593	[160]
Cu_2GeS_3	Monoclinic, *C*1*c*1, *a* = 0.6449, *b* = 1.1319, *c* = 0.6428, β = 108.37	[125]
Cu_8GeS_6 HT	Cubic, *F*-43*m*, *a* = 0.99567	[37]
RT-Cu_8GeS_6	Orthorhombic, $Pmn2_1$, *a* = 0.70445, *b* = 0.69661, *c* = 0.98699	[37]
HT-Cu_2GeSe_3	Orthorhombic, *Imm*2, *a* = 1.1878, *b* = 0.3941, *c* = 0.5485	[168]
RT-Cu_2GeSe_3	Monoclinic, *Cm*, *a* = 0/6772, *b* = 0/3956, *c* = 0/3958, β = 125/83°	[164]
HT-Cu_8GeSe_6	Cubic, *F*-43*m*, *a* = 1.1020	[168]
IT-Cu_8GeSe_6	Hexagonal, $P6_3mc$, *a* = 0.7280, *c* = 1.167	[165]
RT-Cu_8GeSe_6	Hexagonal, $P6_3mcm$, *a* = 1.26438, *c* = 1.17570	[168]
Cu_2SnS_3	Monoclinic, *Cc* , *a* = 0.6653, *b* = 1.1537, *c* = 0.6665 β = 109.39°	[179]
Cu_4SnS_4	Orthorhombic, *Pnma*, *a* = 1.3558, *b* = 0.7681, *c* = 0.6412	[178]
$Cu_4Sn_7S_{16}$	Hexagonal, R-*3m*, *a* = 0.7372, *c* = 3.601	[180]
$Cu_4Sn_{15}S_{32}$	Cubic, *F*-43*m*, *a* = 1.0393	[182]
HT-Cu_2SnSe_3	Cubic, K(F), *a* = 0.56878	[183]
RT-Cu_2SnSe_3	Monoclinic, *Cc*, *a* = 0.65936, *b* = 1.21593, *c* = 0.66084, β = 108.56°	[183]
Cu_2SnTe_3	Cubic, *F*-43*m*, *a* = 0.60490	[189]

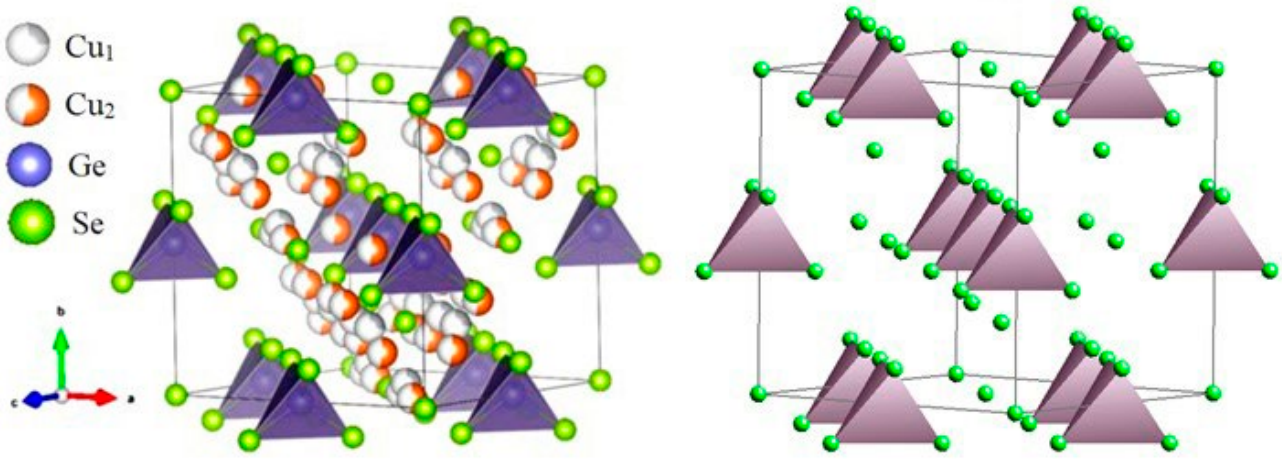

a b

Fig. 3.2. Crystal lattice of HT-Cu_8GeSe_6 (a) and anionic framework without Cu^+ ions (b)

phases are the aristotype of this structural family, and various low-temperature partially or completely ordered phases are the hettotype [37].

The schematic crystal structure of HT-Cu_8GeSe_6 and its anionic sublattice are shown in Fig. 3.2. In a unit cell containing 4 formula units, there are 32 Cu^+ cations statistically distributed in 2 crystallographic positions with a multiplicity of 24 (Cu1) and 48 (Cu2). The number of Cu^+ cations is more than twice lower than these cationic positions, therefore in HT-Cu_8GeSe_6 and other isostructural high-temperature phases, they are disordered and mobile as in a liquid.

Compounds of the mohite family, especially Cu_2SnSe_3, Cu_2GeSe_3, and alloys based on them have attracted considerable research interest as environmentally friendly and affordable thermoelectric materials [126–136]. It was shown that Cu_2SnSe_3 doped with various elements [126–134], as well as composites based on it [130–132], demonstrate good thermoelectric properties. The improvement of thermoelectric properties of Cu_2GeSe_3 doped with various elements [133–135], as well as solid solutions based on it [136], was achieved.

Studies have shown that compounds of the $Cu_2B^{IV}X_3$ type are also very promising for use as photovoltaic and optoelectronic materials [22, 34, 137–144]. The photoelectric and optical properties of the Cu_2SnS_3 and alloys based on it have been studied in more detail [139–142]. Reviews [22, 137] cover numerous studies on the synthesis, structural transformation, morphological engineering and band gap energy rearrangement of Cu–Sn–S (Se) nanoparticle systems and discuss the prospects for the development of solar cells based on them. They also highlight other photovoltaic applications such as photoelectrocatalytic hydrogen production and degradation of Cu–Sn–S (Se) nanoparticle dyes, etc.

According to the authors of another review [138], the ternary compound Cu_2SnS_3, consisting of non-toxic and readily available elements, is the most preferred photovoltaic material for solar cell applications due to its optimal structural and optical properties.

Copper-containing argyrodites are also of great interest as efficient ionic conductors, thermoelectric, photoelectric, and nonlinear optical materials [35–37]. These compounds, which are typical superionic semiconductors with two independent structural units (rigid anionic framework and weakly bound Cu^+ cations), can serve as very good base compounds for the development of high-performance thermoelectric materials by separate tuning of the electrical and thermal properties [35]. It should be noted that only a small part of the research on thermoelectric argyrodites is devoted to the study of stoichiometric compounds [35, 145, 146]. Most of the studies are focused on obtaining nano- and single crystals, thin films, polycrystals with a high density of complex phases and composite materials based on them [35, 147–149]. For the improvement of thermoelectric properties, researchers often complicate the composition by substituting analogous atoms, adding doping impurities, or creating a deficit of individual elements in the stoichiometric composition [37].

In [150] the production of thin-film layers of Cu_8SiS_6 and Cu_8SiSe_6 for optoelectronic applications was reported. The authors [151] noted that the replacement of Ag with Cu in isostructural compounds of the argyrodite family causes a clear increase in the generation of secondary harmonics. This result opens up the possibility of synthesizing high-quality infrared nonlinear optical materials based on them.

3.1. Phase equilibria in Cu-Si-X systems

The Cu-Si-S system was studied based on the quasi-binary section Cu_2S-SiS_2 [152–154]. The *T-x* diagram of this section in the composition range 0-50 mol. % SiS_2 was constructed in [152]. The formation of Cu_8SiS_6 congruently melting at 1468 K was demonstrated. In the study [153] this section was investigated in the entire composition range and two ternary compounds Cu_8SiS_6 and Cu_2SiS_3 were identified. It was found that the first melts congruently at 1473 K, and the second melts with decomposition according to the peritectic reaction at 1173 K. The latest version of the phase diagram of this system was presented by the authors [154]. According to their data, Cu_8SiS_6 and Cu_2SiS_3 compounds melt congruently at 1459 and 925 K. The *T-x* diagram constructed by us based on the data of [153, 154], taking into account the melting temperatures and polymorphic transitions of compounds specified in [155] is presented in Fig. 3.3.

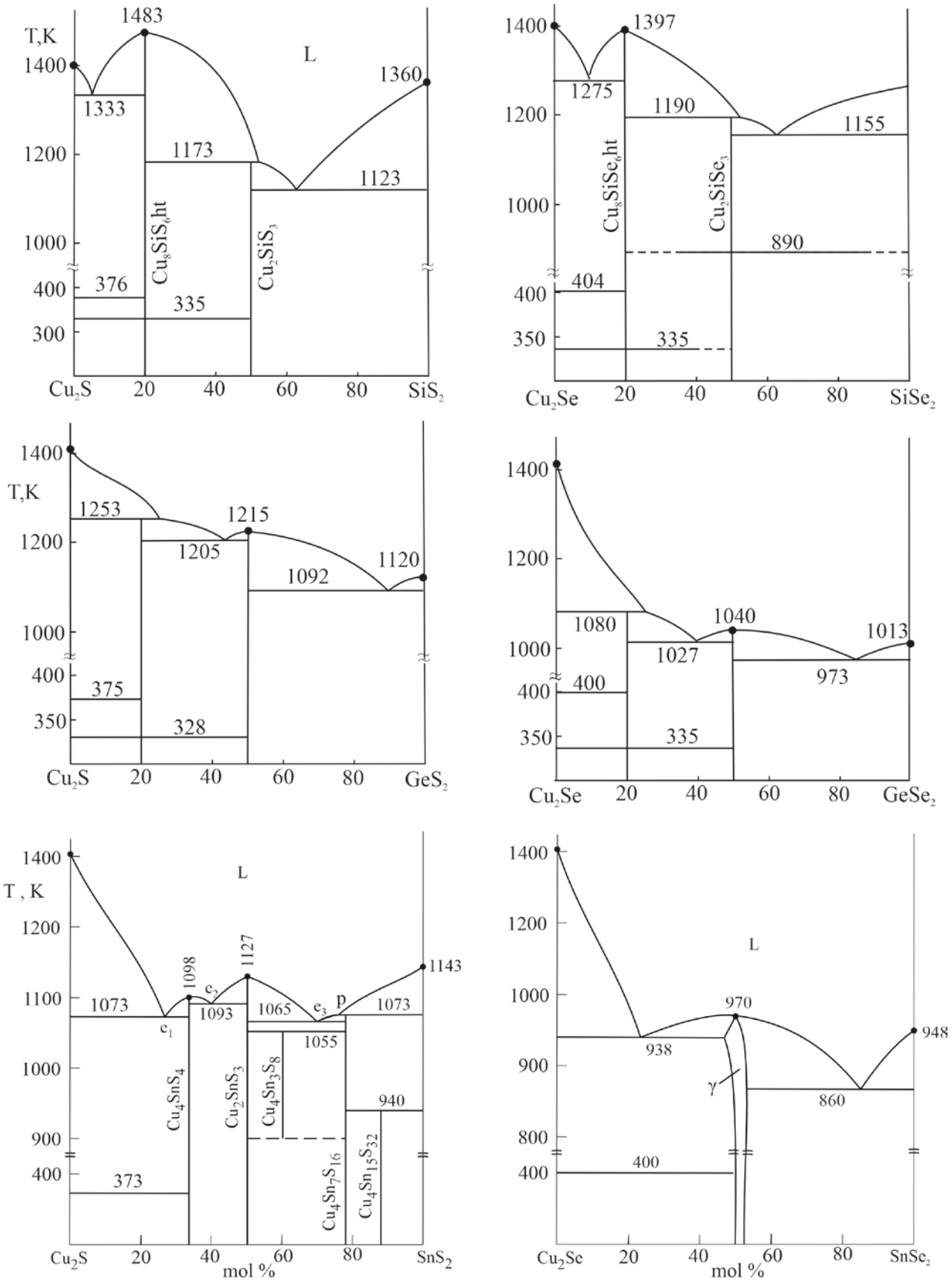

Fig. 3.3. Phase diagrams of quasi-binary systems Cu_2X-$B^{IV}X_2$

The Cu-Si-Se system also was studied only based on the quasi-binary section Cu_2Se-$SiSe_2$. In the study [156] ternary compounds Cu_8SiSe_6 and Cu_2SiSe_3, which melt congruently at 1380 K and incongruently at 1190 K and undergo polymorphic transformations at 335 and 890 K, respectively, were identified. Data [156] for the Cu_2Se-Cu_8SiSe_6 subsystem were confirmed in [157] (Fig. 3.3).

The Cu-Si-Te system. The complete *T-x-y* diagram of this system was constructed by the authors [158]. It has been shown that it is characterized by the formation of one ternary compound Cu_2SiTe_3, melting with decomposition according to a peritectic reaction.

Crystallographic data of copper-silicon chalcogenides [37, 159, 160] are shown in Table 3.1.

3.2. Phase equilibria in Cu-Ge-X systems

The Cu-Ge-S system. Quasi-binary section Cu_2S-GeS_2 of this system has been investigated in several studies [91, 161–164]. According to [161], ternary compounds Cu_8GeS_6 and Cu_2GeS_3 with incongruent melting at 1253 and 1213 K are formed in it. The Cu_8GeS_6 undergoes a polymorphic transformation at 328 K. The author [162] presented a new, more precise version of the *T-x* diagrams of this system (Fig. 3.3), which differs from the data [161] only in that the Cu_2GeS_3 compound melts congruently at 1215 K and forms eutectics with Cu_8GeS_6 and GeS_2.

In the study [164], an isothermal section of the phase diagram of the Cu-Ge-S system at 800 K was constructed, which reflected both of the above-mentioned ternary compounds. In [91] a diagram of solid-phase equilibria at 300 K (Fig. 3.4) and a schematic projection of the liquidus surface were presented. The latter reflects the primary crystallization fields of 11 phases, including ternary compounds Cu_8GeS_6 and Cu_2GeS_3.

The Cu-Ge-Se system. According to [165], the nature of phase equilibria of the Cu_2Se-$GeSe_2$ section is similar to the corresponding sulfide system: ternary compounds Cu_8GeSe_6 and Cu_2GeSe_3 melt incongruently at 1080 K and 1037 K. The phase diagram presented in [166] confirms the existence of the Cu_2GeSe_3 compound with congruent melting at 1033 K, and the Cu_8GeSe_6 compound represented as Cu_6GeSe_5. Later, the system was re-studied in the composition range of 15-60 mol. % $GeSe_2$ [167]. It was shown that the congruent melting temperature of Cu_2GeSe_3 is equal to 1053 K, and Cu_8GeSe_6 melts incongruently at 1083 K. In the review article [168], preference was given to the data of the study [167]. These data were later confirmed in [169] (Fig. 3.4).

The Cu-Ge-Te system was investigated in many studies [91, 170-172]. It was shown that the Cu_2Te-GeTe [170, 171] and Cu_2Te-Cu_3Ge [172] sections are almost quasi-binary. The first one belongs to the eutectic type, and the second one is characterized by the presence of monotectic and degenerate eutectic equilibria. The first version of the complete *T-x-y* diagrams of the Cu-Ge-Te system was constructed in [170]. The Cu_2GeTe_3 compound previously indicated in some studies was not reflected in this diagram [91]. In the second version of the phase diagram presented in [171], this error was corrected. This compound has been shown to form via a peritectic reaction at 773 K. It was also shown that, in contrast to the data [170], there were two immiscibility regions in the system, with one of them arising in the center of the concentration triangle. Finally, the third version of the phase diagram of the system was presented in [91, 172]. It basically confirmed the data of [171] but significantly differed greatly from it by the extent of the fields of primary crystallization of phases and the presence of one wide immiscibility region.

3.3. Phase equilibria in Cu-Sn-X systems

The Cu-Sn-S system. Some polythermal sections of this system were studied in 1974 [174]. It was shown that the Cu_2S-SnS and Cu_2S-SnS_2 sections are quasi-binary. The first one is of the eutectic type, and 4 intermediate phases are formed in the second one: Cu_4SnS_4, Cu_2SnS_3, $Cu_4Sn_3S_6$, and $Cu_2Sn_4S_9$. In a later published study ternary compounds Cu_4SnS_4, Cu_2SnS_3, and $Cu_4Sn_7S_{16}$ have been identified in the Cu_2S-SnS_2 system [175]. The same results were obtained by the authors [176]. Later the Cu_2S-SnS_2 section was re-studied in [177] and a phase diagram reflecting copper-tin sulfides Cu_4SnS_4, Cu_2SnS_3, $Cu_4Sn_3S_6$, and $Cu_2Sn_3S_7$ was presented. Structural studies [175-181] confirmed the existence of Cu_4SnS_4, Cu_2SnS_3, and $Cu_4Sn_7S_{16}$ compounds. We have not found crystallographic data for the other two compounds mentioned above. At the same time, the authors of [182] reported the synthesis of

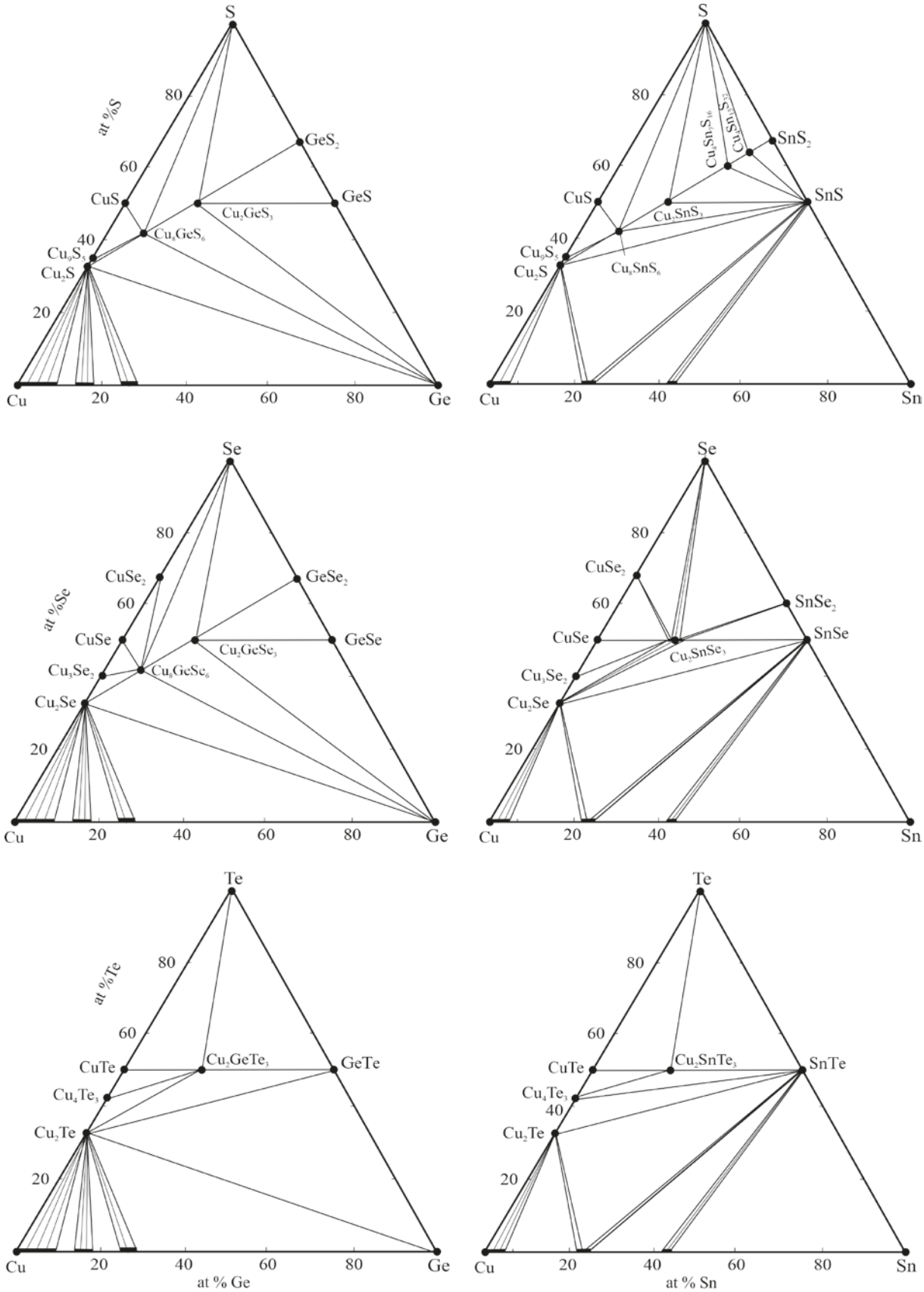

Fig. 3.4. Solid-phase equilibria diagrams of Cu-Ge-X and Cu-Sn-X systems at 300 K

the $Cu_4Sn_{15}S_{32}$ compound with a cubic structure, close in composition to $Cu_2Sn_4S_9$ indicated in [174] and also with a cubic structure. Taking into account the above data, we have constructed a phase diagram of the Cu_2S-SnS_2 system (Fig. 3.3), reflecting five triple compounds. Probably, this system requires further investigation. A diagram of solid-phase equilibria of the Cu-Sn-S system, constructed by us considering the data of these studies, is presented in Fig. 3.4 [175–178].

The Cu-Sn-Se system. The results of the study on this system are summarized in [91, 183]. The only ternary compound of this system is Cu_2SnSe_3, formed on the quasi-binary section of Cu_2Se-$SnSe_2$, it melts congruently at 963 K and crystallizes in a cubic structure [184] (Fig. 3.3). Another quasi-binary Cu_2Se-SnSe section of this system belongs to the eutectic type [184]. A repeated study of the indicated sections [185] led to results similar to those reported in [184]. The results of [185] demonstrated that Cu_2SnSe_3-Se and Cu_2SnSe_3sections, which also belong to the eutectic type are quasi-binary. In [186] a projection of the liquidus surface and some polythermal sections of the Cu-Sn-Se system were presented. The authors [91] pointed out some shortcomings of the study [186] and presented a second version of the projection of the liquidus surface. According to [91], the system has two wide immiscibility regions and associated invariant synthetic and three monotectic equilibria. The solid-phase equilibria diagram of the Cu-Sn-Se system, constructed in [91], is shown in Fig. 3.4. As can be seen, the Cu_2SnSe_3 compound has a noticeable homogeneity region in the stable CuSe-SnSe cross section (g-phase) and forms connodes with all phases in the composition range of Cu_2Se-SnSe-Se.

The Cu-Sn-Te system. The studies [187, 188] present a complete *T-x-y* diagram of this system, characterized by the presence of one ternary compound Cu_2SnTe_3 composition. It has a cubic structure and melts incongruently at 680 K. Later in [91] a version slightly different from the data in [187, 188] of the liquidus surface projection was presented. The isothermal section of the phase diagram at 300 K according to data from [91, 187, 188] is shown in Fig. 3.4. A detailed overview of the system is provided in [189].

3.4. Thermodynamic properties of ternary compounds of Cu-B^{IV}-X systems

The thermodynamic properties of copper-silicon are practically unstudied. There are studies [155, 190] where the thermodynamic functions of phase transitions of the Cu_8SiS_6 and Cu_8SiSe_6 compounds were determined using differential scanning calorimetry (DSC).

The standard thermodynamic functions of copper-germanium chalcogenides were determined by measuring the EMF of concentration cells of type (2.2) [50, 51, 191–194].

The authors planned experiments on the Cu-Ge-S and Cu-Ge-Se systems [191] based on the fact that Cu_8GeS_6 and Cu_8GeSe_6 compounds have polymorphic transitions in the temperature range of EMF measurements. Experiments have shown that the temperature dependences of the EMF for electrode alloys containing Cu_8GeS_6 and Cu_8GeSe_6 compounds are two straight lines with a breakpoint at the temperature of their polymorphic transformation. From the EMF measurement data, partial molar functions of copper were calculated for two modifications of the indicated compounds, which were used to calculate the thermodynamic functions of formation (Table 3.2) and polymorphic transitions (Table 3.3).

The thermodynamic properties of copper-tin chalcogenides have been studied by the EMF method with a solid electrolyte [50, 51, 196], and the Cu_2SnSe_3 compounds were studied also using a classic version of the EMF method with a liquid electrolyte [51] (Table 3.3). As can be seen, the thermodynamic functions of Cu_2SnSe_3, obtained by two modifications of the EDS method, agree well with each other. It was also evident that the numerical values of the thermodynamic functions of copper-tin sulfides according to [196] were significantly lower than the data of [50, 51]. Data for the $Cu_2Sn_4S_9$ and Cu_4SnS_4 compounds [196] were lower than even the sum of the corresponding values for Cu_2S and SnS_2, which is thermodynamically impossible. A similar situation was also observed for the Cu_2GeSe_3 and Cu_8GeSe_6 compounds [193]. In our opinion, this was due to the incorrect formulation of potential-forming reactions by the authors [193, 196]. The results of a new calorimetric study of the Cu_2SnS_3 [197] were also in good agreement with the data obtained by the EDS method [193] (Table 3.2).

Table 3.2. Standard integral thermodynamic functions of ternary compounds of the Cu-B^{IV}-X systems

Phase	$-\Delta_f G^0$	$-\Delta_f H^0$	S^0 J·K^{-1}·mol^{-1}	Ref.
	kJ·mol^{-1}			
Cu_2GeS_3	211.3±2.4	213.7±2,3	190.3±5.5	[194]
RT-Cu_8GeS_6	438.9±2.5	425.9±4.2	536.3±13.1	[191]
HT-Cu_8GeS_6	*445.3±3.1	420.8±5.6	552.1±15.8	[191]
Cu_2GeSe_3	176.8±3.1	173.9±3.1	233.3±5.1	[192]
	80.7±1.5	86.7±6.9	-	[193]
RT- Cu_8GeSe_6	341.1±3.3	327.4±4,5	596.7±11.6	[191]
	105.1±1.9	114.5±9.2	143±2	[193]
HT- Cu_8GeSe_6	*348.1±3.7	315.6±5.0	632.3±12.5	[191]
$Cu_2Sn_4S_9$	659.9±4.3	650.9±29.7	560.3±74.7	[50, 51]
	165.4±1.5	141.6±6.3	639.8±18.3	[196]
Cu_2SnS_3	239.6±1.5	242.6±12.0	196.3±21.9	[50, 51]
	169.3±1.3	150.0±5.5	278.6±15.7	[196]
		263.79 ± 2.28		[197]
Cu_4SnS_4	316.4±2.4	327.7±18.8	266.5±28.2	[50, 51]
	261.3±2.4	220.8±9.4	414.4±20	[196]
Cu_2SnSe_3	189.5±2.6	187.5±4.8	251.6±5.0	[50, 195]
	198.4±0.6	198.5±2.9	237±5	[51]
Cu_2SnTe_3	117.7±1.4	116.2±2.4	264±6	[50, 51]

***Note:** data related to 400 K is marked with an asterisk

Table 3.3. Temperatures and thermodynamic functions of phase transitions of some ternary compounds of the Cu-B^{IV}-X systems

Compound	T_{melt}	$\Delta H_{phase\ trans}$, kJ·mol^{-1}	$\Delta S_{phase\ trans}$, J·mol^{-1}·K^{-1}	Method, Ref.
Cu_8GeS_6	328	5.1±2.4	15.5±7.5	EMF, [191]
	330	15.5±0.6	47.1±1.9	DSC, [155]
Cu_8GeSe_6	335	11.9±2.8	35.5±8.4	EMF, [191]
	330	11.2±0.5	34.0±1.4	DSC, [190]
Cu_8SiS_6	336	14.9±0.6	44.2±1.8	DSC, [155]
Cu_8SiSe_6	325	14.7±0.6	45.3±1.8	DSC, [190]

The values of heat and entropies for polymorphic transitions of $Cu_8B^{IV}X_6$ compounds, obtained by both methods, except for Cu_8GeS_6, are in good agreement as can be seen in Table 3.3. The relatively high errors in the data obtained by the EMF method were because in this method the partial enthalpy and entropy are calculated indirectly from the temperature dependence coefficient of the EMF [51, 110].

3.5. Phase equilibria in quaternary systems consisting of copper chalcogenides and p^2-elements

The concentration planes $2Cu_2X + B^{IV}X' \leftrightarrow 2Cu_2X' + (B^{IV})'X_2$ **(I),** $Cu_2X–B^{IV}X_2–(B^{IV})'X_2$ **(II)** и Cu_2X-Ag_2X-$B^{IV}X_2$ **(III)**, (where B^{IV} and $(B^{IV})'$ – Si, Ge, Sn; X and X′ – S, Se, Te) of the corresponding quaternary systems are of greatest interest for the search for solid solutions with different types of substitution based on ternary compounds of Cu-B^{IV}-X systems. In the last decade we have studied some systems of the indicated types (Cu_2Se-$GeSe_2$-$SnSe_2$ [198], Cu_2S-Cu_8SiS_6-Cu_8GeS_6 [155], Cu_2Se-Cu_8SiSe_6-Cu_8GeSe_6 [157], $2Cu_2S+GeSe_2 \leftrightarrow 2Cu_2Se+GeS_2$ [199, 200], Cu_2S-Ag_2S-GeS_2 [37] and Cu_2Se-Ag_2Se-$GeSe_2$ [37]), as well as individual polythermal sections [201–205], composed of ternary compounds-analogues of the $A^I_8B^{IV}X_6$ and $A^I_2B^{IV}X_3$ types. The isothermal sections of the phase diagrams of these systems at room temperature are shown in Fig. 3.5, and the sections based on $Cu_8B^{IV}X_6$ compounds are presented in Fig. 3.6, sections based on $Cu_2B^{IV}X_3$ are shown in Fig. 3.7. These diagrams

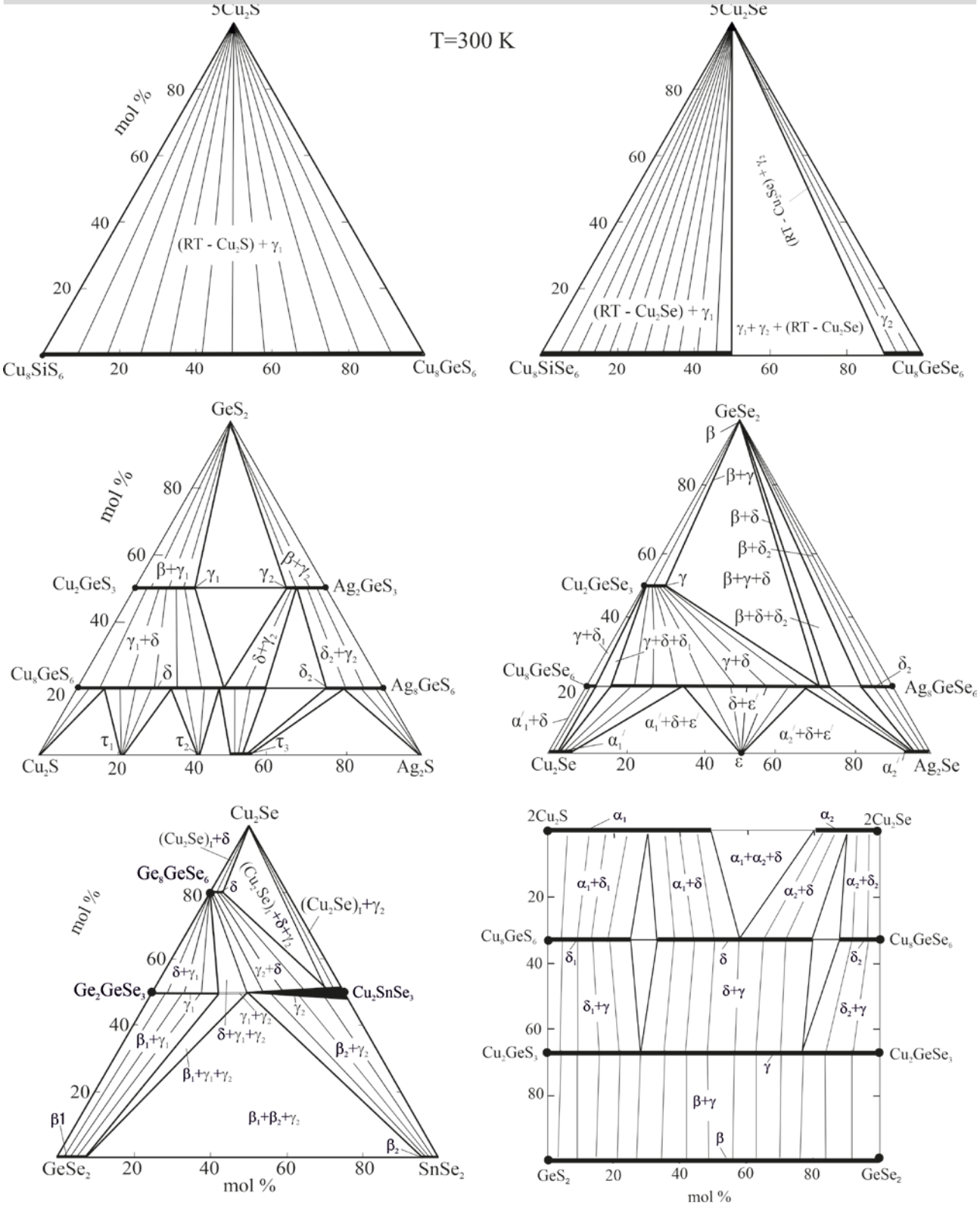

Fig. 3.5. Solid-phase equilibria diagrams at 300 K of some quaternary systems formed by copper chalcogenides and p2-elements

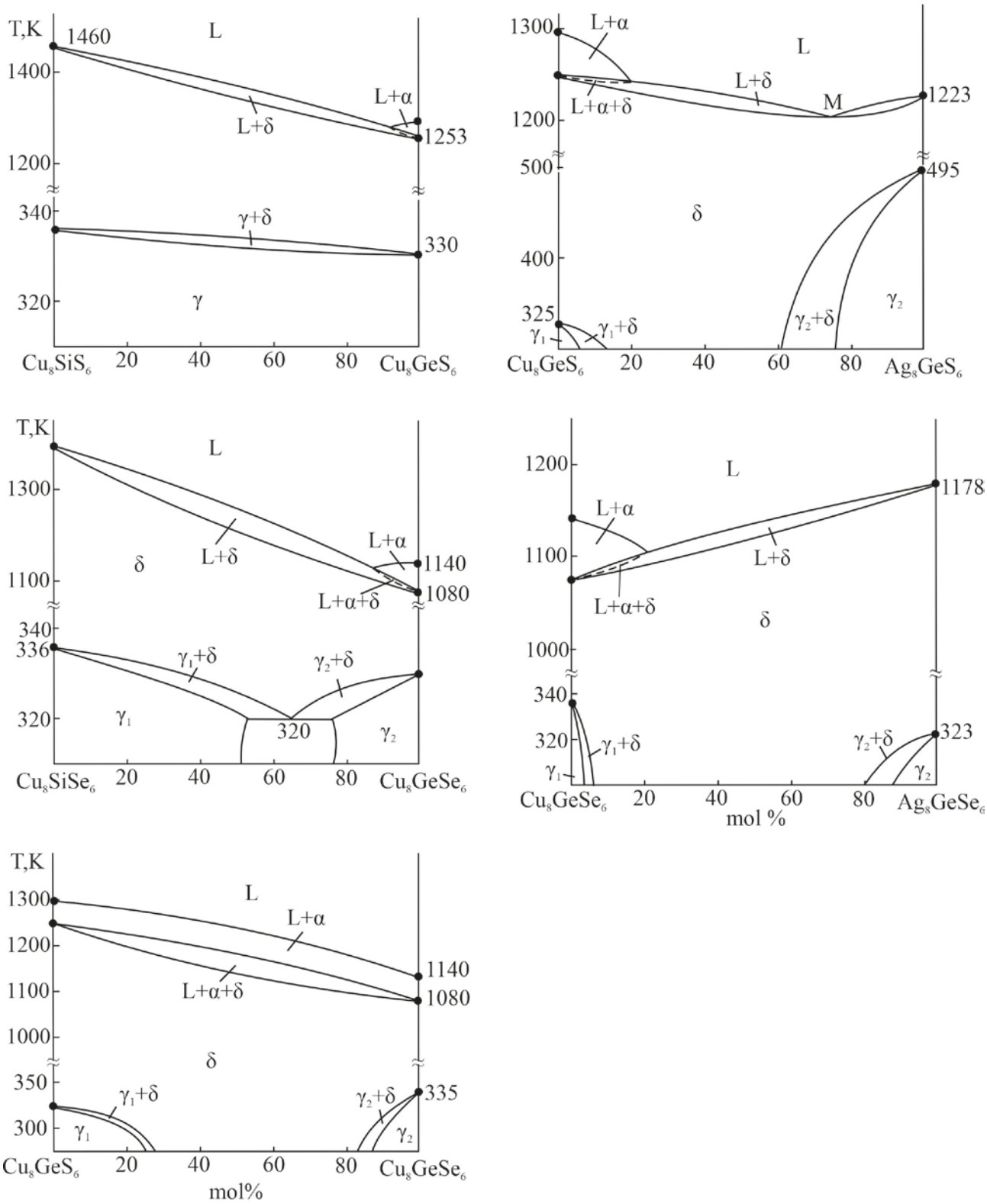

Fig. 3.6. *T-x* diagrams of some systems composed of compounds of the Cu_8GeX_6 type

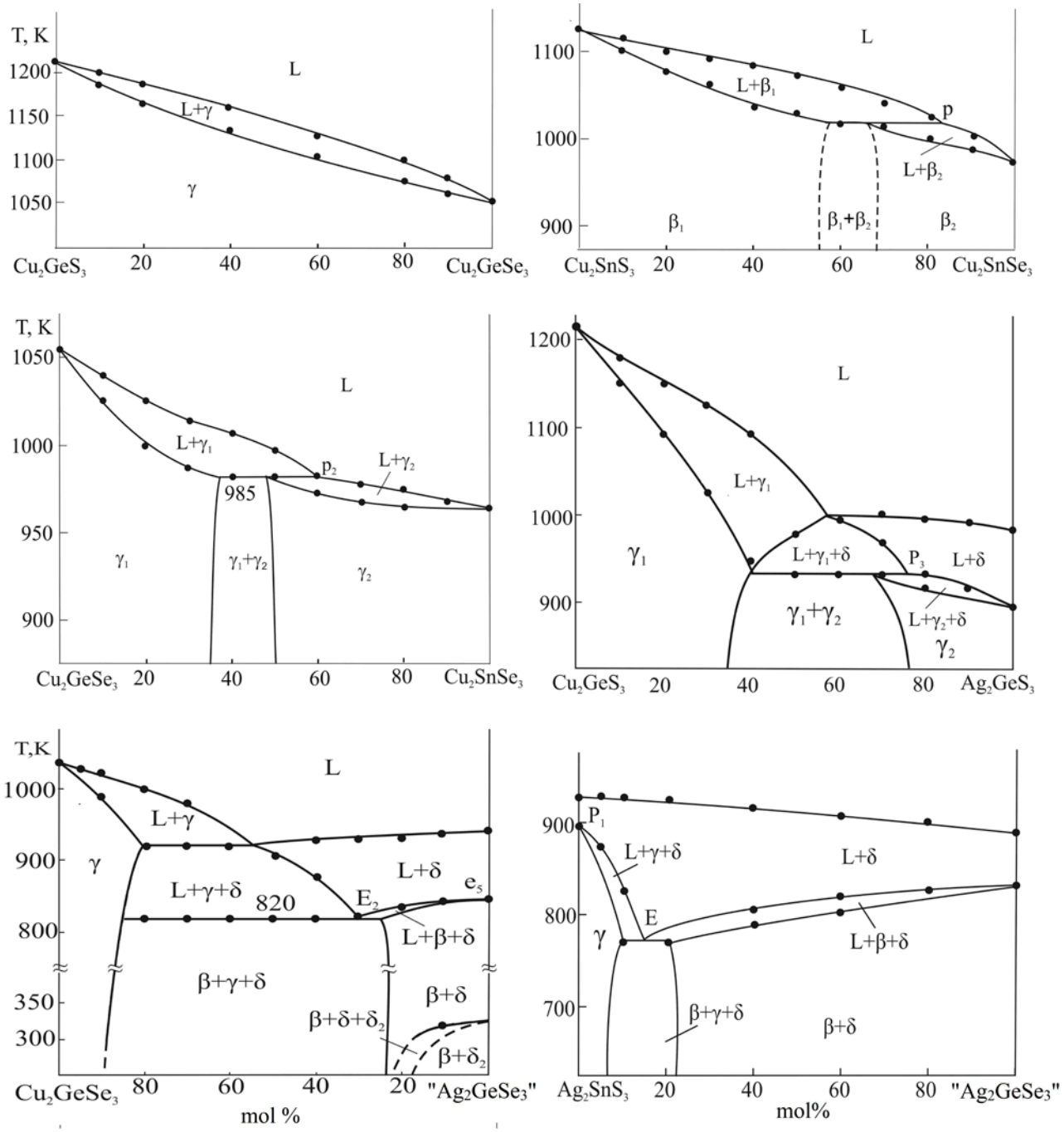

Fig. 3.7. *T-x* diagrams of some systems composed of compounds of the $Cu_2B^{IV}X_3$ type

demonstrate the formation of unlimited or broad solid solutions based on ternary compounds of both types. Several studies [200–205] present the results of a comprehensive study of phase equilibria and thermodynamic properties of the above and some similar systems.

$2Cu_2X + B^{IV}X' \leftrightarrow 2Cu_2X'$ systems. Out of the systems of this type, only the reciprocal system $2Cu_2S+GeSe_2 \leftrightarrow 2Cu_2Se+GeS_2$ has been fully studied [199, 200]). The system is characterized by the formation of continuous or wide regions of chalcogen-substituted solid solutions based on Cu_8GeX_6 and $Cu_2B^{IV}X_3$ compounds (Figs. 3.6–3.8). In the Cu_8GeS_6-Cu_8GeSe_6 system, this is accompanied by a decrease in the temperatures of polymorphic transitions of the original ternary compounds and stabilization of their high-temperature cubic modifications at room temperature and below.

The projection of the liquidus surface of the $2Cu_2S+GeSe_2 \leftrightarrow 2Cu_2Se+GeS_2$ system is shown in Fig. 3.8. It can be used for growing crystals of solid solutions based on ternary compounds by directional crystallization from solution-melts in a wide range of compositions.

Cu_2X–$B^{IV}X_2$–$(B^{IV})'X_2$ systems. The *T-X* Cu section diagrams of the Cu_8SiS_6-Cu_8GeS_6 [155] and Cu_8SiSe_6-Cu_8GeSe_6 [157] sections are shown in Fig. 3.6. As can be seen, both systems are partially quasi-binary and are characterized by the formation of continuous series of solid solutions between high-temperature cubic modifications of the original ternary compounds. However, they significantly differ by the nature of phase

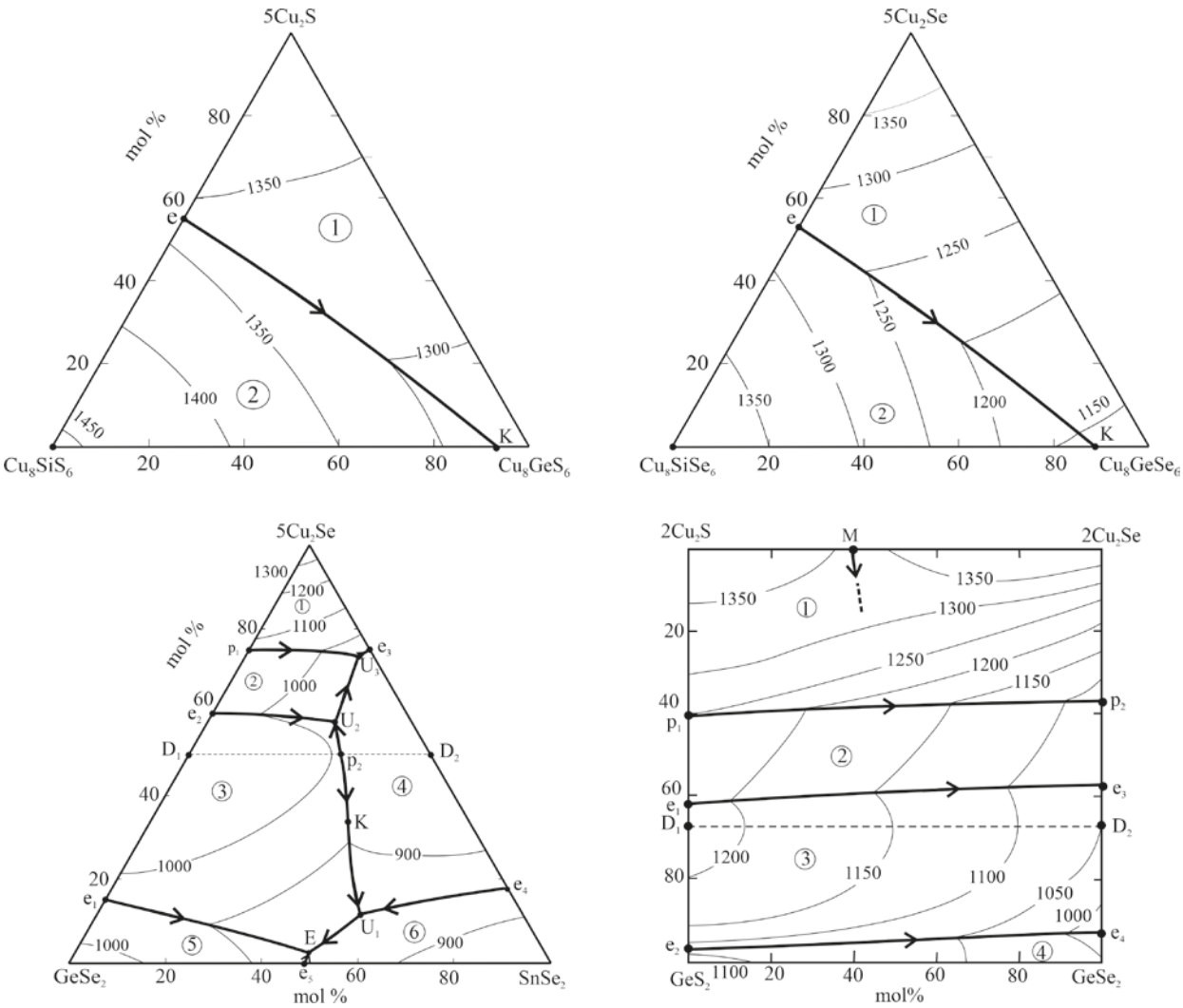

Fig. 3.8. Projections of liquidus surfaces of some quaternary systems composed of copper chalcogenides and p^2-elements

equilibria in the subsolidus region. In the sulfide system, a continuous series of solid solutions are also formed between RT modifications of the initial isostructural compounds, crystallizing in an orthorhombic lattice with sp. gr. $Pna2_1$ or $Pmn2_1$ (Table 3.1). In the Cu_8SiSe_6-Cu_8GeSe_6 system based on RT modifications of the initial compounds, limited regions of solid solutions are formed (g_1- and g_2-phase), and eutectoid equilibrium is established at a temperature of (320 K).

A projection of the liquidus surface was constructed for the Cu_2Se-$GeSe_2$-$SnSe_2$ system [198], and for two systems of this type, their fragments Cu_2S-Cu_8SiS_6-Cu_8GeS_6 [155] and Cu_2Se-Cu_8SiSe_6-Cu_8GeSe_6 [157] were constructed (Fig. 3.8). In the indicated studies, various isothermal and vertical sections of phase diagrams of the considered systems were also constructed.

Cu_2X-Ag_2X-$B^{IV}X_2$ systems. There are data on two vertical sections of phase diagrams: Cu_8GeS_6-Ag_8GeS_6 [204] and Cu_8GeSe_6-Ag_8GeSe_6 [203] (Fig. 3.6). They are characterized by a decrease in phase transition temperatures and a significant expansion of homogeneity regions of d-phases with a cubic structure down to room temperature and below. Both systems are partially quasi-binary, with the HT-$Cu_{2-x}Ag_xS(Se)$ phases primarily crystallizing from melts near incongruently melting copper argyrodites, which based on composition are outside the *T-x* planes of these sections.

Summarizing the above data in this section, it should be noted that the quasi-binary Cu_2X-$B^{IV}X_2$ sections, on which compounds of the $Cu_2B^{IV}X_3$ and $Cu_8B^{IV}X_6$ types were formed have been studied in detail in all Cu-B^{IV}-X systems (Fig. 3.3). Out of then, only the Cu_2S-SnS_2 section is characterized by more complex interactions. At least five triple compounds are formed on it. At the same time, the complete *T-x-y* diagrams are known only for the Cu-Si-Te, Cu-Ge-Te, Cu-Sn-Se, and Cu Sn-Te systems with relatively simple interactions of components. It should also be noted that the thermodynamic properties of most copper-germanium and copper-tin chalcogenides have been studied by the EMF method and mutually consistent sets of standard integral thermodynamic functions have been obtained for them. The studies devoted to the investigation of several quaternary systems composed of copper chalcogenides and p^2-elements are important from the point of view of optimizing the functional properties of $Cu_2B^{IV}X_3$ and $Cu_8B^{IV}X_6$ compounds.

4. Copper chalcogenides with elements of the arsenic subgroup

Ternary Cu-As(Sb, Bi)-chalcogen systems have long been the focus of close attention of researchers for two reasons. Firstly, in these systems, especially in sulfide systems, many crystalline phases with different structural forms are formed [22], which leads to different functional properties and potential applications. According to data from numerous studies [22, 206–236], ternary compounds of these systems are valuable environmentally friendly functional materials with photoelectric, optical, thermoelectric, and other properties. Secondly, many ternary compounds of these systems occur in nature as minerals: enargite and lucionite Cu_3AsS_4; tennantite $Cu_{12}As_4S_{13}$, tetrahedrite $Cu_{12}Sb_4S_{13}$; chalcostibite $CuSbS_2$; synergite $Cu_6As_4S_9$; lautite CuAsS, etc. They are of great interest to mineralogy and geochemistry and provide valuable information about the physical conditions on Earth at the time of their formation [41, 42].

The crystal structures of some of the above minerals are shown in Figure 4.1. The compound $CuSbS_2$ crystallizes in the orthorhombic system (sp. gr. *Pnma*) and has a layered structure consisting of SbS_2 and CuS_3 chains along the axis *b*, formed by the interlocking of square pyramids of Sb and tetrahedral units of CuS_4. These two infinite chains are linked together and create layers that are perpendicular to the axis *c*. The distance between them (2.051 Å) allows intercalation of small atoms, ions or molecules [22]. Tetrahedrite $Cu_{12}Sb_4S_{13}$ has a cubic sphalerite-like structure (sp. gr. $I\bar{4}3m$). Six of the 12 Cu atoms occupy trigonal planar 12e sites, and the rest are distributed among tetrahedral 12d sites. Four of the six tetrahedral positions are occupied by Cu^+, and the other two positions are occupied by Cu ions^{2+} [22]. At the same time, the trigonal planar positions are occupied exclusively by Cu^+ ions. The Sb atoms also occupy a tetrahedral position but are bonded to only three S atoms, resulting in a void in the structure and an unshared pair of electrons, as in Cu_3SbS_3. The combination of factors such as a large number of atoms in the

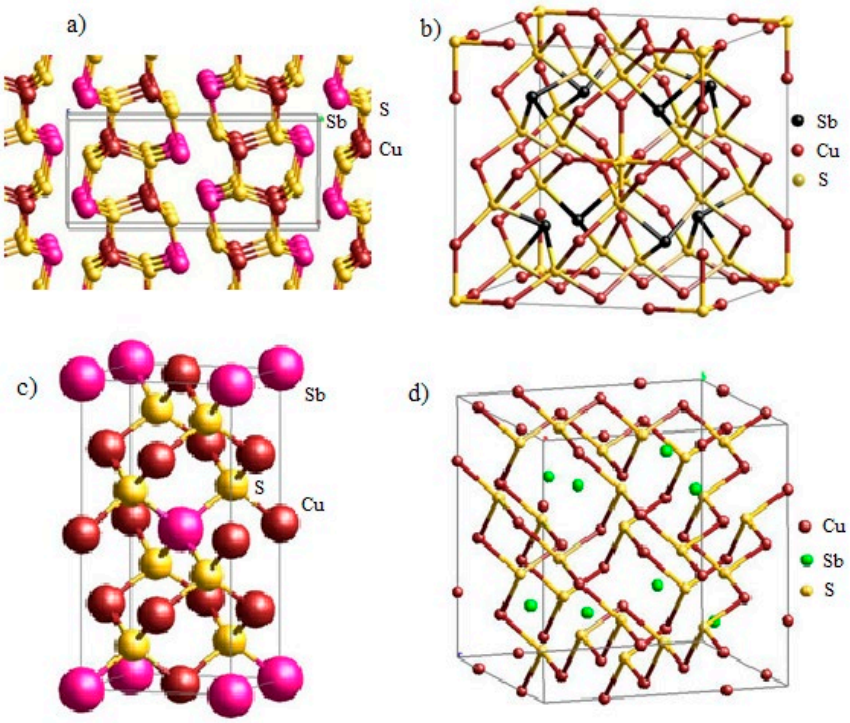

Fig. 4.1. Crystal structures of copper-antimony sulfides: orthorhombic $CuSbS_2$ (a), cubic $Cu_{12}Sb_4S_{13}$ (b), tetragonal Cu_3SbS_4 (c) and orthorhombic Cu_3SbS_3 (d)

unit cell, high anharmonicity and low-energy vibrations of the Cu atom outside the trigonal planar unit [CuS_3] lead to abnormally low thermal conductivity of this material, which is important for thermoelectrics.

Crystallographic data of the most characteristic ternary compounds of the Cu-B^V-X systems are presented in Table 4.1.

Copper-arsenic and copper-antimony sulfides and complex phases based on them [206–212] are considered promising candidates for use as absorbers of *p*-type in solar cells due to the wide availability and environmental safety of raw materials, suitable band gap width and high absorption coefficient. The favorable band gap width of these phases indicates the prospect of their application also as wide-band gap semiconductors in third-generation photovoltaic devices. The largest number of studies [213–221] are devoted to chalcostibite $CuSbS_2$, which is considered a substitute material for $CuInS_2$ due to its similar optical properties and the additional advantage of its higher abundance in the Earth and lower cost of antimony compared to indium.

In a recently published review [222], the Cu_3BiS_3 compound is characterized as a sustainable and cost-effective photovoltaic material.

Synthetic analogues of many chalcogenide minerals of copper with arsenic and antimony [223-228], as well as solutions and composite materials based on them [228-231], possessing low thermal conductivity and an anisotropic crystalline structure, have promising thermoelectric properties. Thus, in the review [228] it was noted that by 2015, for some natural and alloyed tetrahedrite materials, zT values of about ~1.0 at ~723 K had been achieved, which is comparable to conventional thermoelectric *p*-type materials. In recent years, there has been increased interest in copper-bismuth chalcogenides as thermoelectric materials with very low thermal conductivity [232–235].

The authors [236] proposed a new concept for increasing the stability and efficiency of copper thermoelectrics by obtaining composites of the “copper chalcogenide-copper tetrahedrite” type. According to the authors, the proposed solution allows the successful blocking of excessive copper migration and stabilization of the composition and properties of the material during subsequent thermal cycles.

It should also be noted that, according to several studies, copper-bismuth chalcogenides, in particular $CuBiS_2$, exhibit good photothermal

Table 4.1. Crystallographic parameters of the ternary compounds of Cu-B^{V}-S(Se) systems

Compound	Crystal system, sp. gr. and lattice parameters, nm	Ref.
Cu_3AsS_4	Rhombic, *Pmn*2$_1$, *a* = 7.399, *b* = 6.428, *c* = 6.145	[238]
$Cu_{12}As_4S_{13}$	Cubic, *I*-43*m, a* = 1.0168	[239]
$Cu_6As_4S_9$	Triclinic, *a* = 9.064, *b* = 9.830, *c* = 9.078, α = 90°, β = 109°30, γ = 107°48	[240]
CuAsS	Rhombic, *Pnma, a* = 11.356, *b* = 3.754, *c* = 5.453	[237]
$Cu_4As_2S_5$	Monoclinic, *C*12/*m*1, *a* = 10.35,*b* = 14.65, *c* = 33.34, β = 96°	[238]
HT-Cu_3AsSe_4	Cubic, *Fm*3*m, a* = 0.5535	[251]
RT-Cu_3AsSe_4	Tetragonal, *I*-42*m, a* = 5.53, *c* = 10.83	[251]
$CuAsSe_2$	Monoclinic, *a* = 5.117, *b* = 12.293, *c* = 9.464, β = 98.546°	[248]
$Cu_4As_2Se_5$	Rhombohedral, *R*3, *a* = 14.0401, *c* = 9.6021	[248]
Cu_3AsSe_3	Cubic, *Pm*-3*m, a* = 5.758	[250]
$Cu_7As_6Se_{13}$	Hexagonal, *R*3, *a* = 14.025, *c* = 9.61, γ = 120	[250]
$CuSbS_2$	Orthorhombic, *Pnma*; *a* = 6.018(1), *b* = 3.7958(6), *c* = 14.495(7)	[264]
RT-Cu_3SbS_3	Monoclinic, *P21/c*; *a* = 7.808(1), *b* = 10.233(2), *c* = 13.268(2), β = 90.31(1)°	[266]
HT-Cu_3SbS_3	Rhombic, *Pnma*; *a*=7.828(3), *b* = 10.276(4), *c* = 6.604(3)	[266]
Cu_3SbS_4	Tetragonal, *I*$\bar{4}$2*m* ; *a* = 5.391(1), *c* = 10.764(1)	[267]
$Cu_{12}Sb_4S_{13}$	Cubic, *I*–43*m, a* = 10.308(1)	[265]
$Cu_{14}Sb_4S_{13}$	Cubic, *I*–43*m*, *a* = 10.448(1)	[261]
HT-Cu_3SbSe_4	Tetragonal, *I*$\bar{4}$2*m*, *a* = 0.5631, *c*= 1.1230	[272]
RT-Cu_3SbSe_4	Cubic, *Fm*3*m, a* = 0.5637	[100]
HT-Cu_3SbSe_3	Cubic, *F*$\bar{4}$3*m, a* = 0.560	[100]
RT-Cu_3SbSe_3	Orthorhombic, *Pnma, a* = 0.79668, *b* = 1.06587, *c* = 0.68207	[273]
$CuSbSe_2$	Orthorhombic, *Pnma, a* = 0.640, *b* = 0.395, *c* = 1.533	[100]
$CuSb_3Se_5$	Monoclinic, *C2/m*; *a* = 1.36499, *b* = 0.40711, *c* = 1.49215, β = 9 0.31°	[274]
Cu_3BiS_3	Orthorhombic, *P*2$_1$2$_1$2$_1$, *a* = 0.7723, *b* = 1.0395, *c* = 0.6715	[100]
$CuBiS_2$	Orthorhombic, *Pnma, a* = 0.6134(1), *b* = 0. 39111(8), *c* = 1.4548(8),	[264]
$CuBi_3S_5$	Monoclinic, *c*2*m*, *a* = 13.221, *b* =4.023, *c* = 14.077Å	[281]
$CuBi_5S_8$	Monoclinic, *C2/m*; *a* = 1.3214, *b* = 0.4025, *c* = 1.4087, β = 115.6°	[100]
HT-Cu_3BiSe_3	Cubic, *F*$\bar{4}$3*m, a* = 0.5865	[277]
RT-Cu_3BiSe_3	Monoclinic, *a* = 1.366, *b* = 0.417, *c* = 1.486, α = 119.1°	[100]
$CuBiSe_2$	Cubic, *Fm*3*m, a* = 0.569	[100]
$CuBi_3Se_5$	Triclinic, *P*1, *a* = 0.4168, *b* = 0.7182, *c* = 1.3388, α = 85.4°, β = 81.3°, γ = 73°	[278]

properties and anticancer effect [22, 38]. Due to the high X-ray attenuation coefficient, these compounds can visualize computed tomography [39].

4.1. Phase equilibria in Cu-As-X systems

The Cu-As-S system. Numerous studies on phase equilibria and the properties of ternary phases in the Cu–As–S system covering the period up to the beginning of the 90s of the last century are summarized in [91, 237]. It was shown that the available data on the Cu_2S-As_2S_3 section of phase diagrams are contradictory and differ from each other both in the number and composition of ternary compounds, and in the temperatures and nature of their melting. In particular, in [241] it was shown that this system is quasi-binary and is characterized by the formation of Cu_5AsS_4, Cu_3AsS_3, $Cu_{12}As_4S_{13}$, $Cu_4As_2S_5$, and $Cu_6As_4S_9$ ternary compounds. The authors of [237], taking into account data from several studies, presented a slightly different version of

the phase diagram from [238], according to which there are 3 ternary compounds in the system: $Cu_{12}As_4S_{13}$, $Cu_4As_2S_5$, and $Cu_6As_4S_9$. It should be noted that the $Cu_{12}As_4S_{13}$ phase by composition is outside the plane of this section, which could question the data [237] on its quasi-binary nature. In [242], a new review of the literature on the Cu–As–S system was presented and a critical assessment and thermodynamic modelling of the phase diagram were carried out.

The studies [243–246] published by our group presented the results of a comprehensive study of phase equilibria and thermodynamic properties of the Cu-As-S system. The solid-phase equilibrium diagram (Fig. 4.3) reflects Cu_3AsS_4, $Cu_{12}As_4S_{13}$, $Cu_6As_4S_9$ and CuAsS ternary compounds, which are synthetic analogues of known minerals. According to [246], in contrast to previously proposed versions of the phase diagram, the Cu_2S- As_2S_3 section is only partially quasi-binary (Fig. 4.2). This is because below the solidus in the composition range 0-40 mol. % of As_2S_3 this section passes through three-phase Cu_2S+II+IV and II+III+IV fields (Fig. 4.3). In [246] a detailed comparative analysis of the results obtained by authors on this section with literary data was carried out.

The liquidus of this system (Fig. 4.4) consists of 14 primary crystallization fields of phases, two of which (CuS and S) degenerate at the sulfur corner of the concentration triangle. This part of the phase diagram is shown schematically in an enlarged form. The system is characterized by the presence of two wide immiscibility regions formed by the penetration of the corresponding regions of the Cu-S boundary system into the depth of the concentration triangle. Another immiscibility region, originating from the binary system As-S is shown in Fig. 4.4. However, the boundaries of this region are not precisely established and are marked with dotted lines.

The Cu-As-Se system. Phase equilibria in this system are studied using the quasi-binary Cu_2Se-As_2Se_3 section [247–250]. The data from these studies significantly differ from each other. According to [247], a Cu_3AsSe_3 compound is formed in the system by a peritectic reaction at 773, the homogeneity region of which extends from 66.7 to 82 mol. % Cu_2Se. The $CuAsSe_2$ compound stable in the temperature range of 550-720 K is formed as the result of peritectic interaction of Cu_3AsSe_3 with the melt. In [247] the $Cu_6As_4Se_9$ compound, previously indicated in [249] was not confirmed. The second version of the phase diagram of the Cu_2Se-As_2Se_3 system was constructed by the authors [248]. The existence of ternary compounds Cu_3AsSe_3, $Cu_4As_2Se_5$, $CuAsSe_2$ has been demonstrated. The first compound exists in the temperature range of 700–770 K, and the second and third compounds melt with decomposition according to the peritectic reaction at 746 and 683 K. Another variant of the *T-x* diagrams of this system was presented in [250]. Only one ternary compound $CuAsSe_2$, melting incongruently at 725 K is reflected in this diagram.

According to [249], the Cu_2Se-As, Cu_3AsSe_4-As_2Se_3, Cu_2Se-Cu_3As, and Cu_3AsSe_4- Se sections are also practically quasi-binary. The first two belong to the eutectic type, and the subsequent ones are characterized by the presence of monotectic and eutectic equilibria.

In [250] a projection of the liquidus surface of the Cu-As-Se system is presented, on which two ternary compounds Cu_3AsSe_4 and $CuAsSe_2$ are shown. Two immiscibility regions emanating from the Cu-Se binary system were identified. The study also shows the presence of a wide glass formation region in the system, adjacent to the As-Se binary system.

According to [251] the Cu_3AsSe_4 compound melts incongruently at 773 K and undergoes a phase transition at 715 K. The low-temperature modification has a tetragonal structure, and the high-temperature modification has a cubic structure.

The studies [252-254] present the results of the research on phase equilibria and thermodynamic properties of the Cu-As-Se system. It has been established that it is characterized by the presence of five triple compounds: Cu_3AsSe_3, $CuAsSe_2$, $Cu_7As_6Se_9$, Cu_3AsSe_4, and CuAsSe (Fig. 4.3). Out of them, only the first two compounds are located on the quasi-binary Cu_2Se-As_2Se_3 section (Fig. 4.2). The projection of the liquidus surface constructed by us taking into account the data from [252–254] is shown in Fig. 4.4. It reflects primary crystallization fields of all the above copper-arsenic selenides. A complex interaction of components was observed in the Cu_2Se-As_2Se_3-

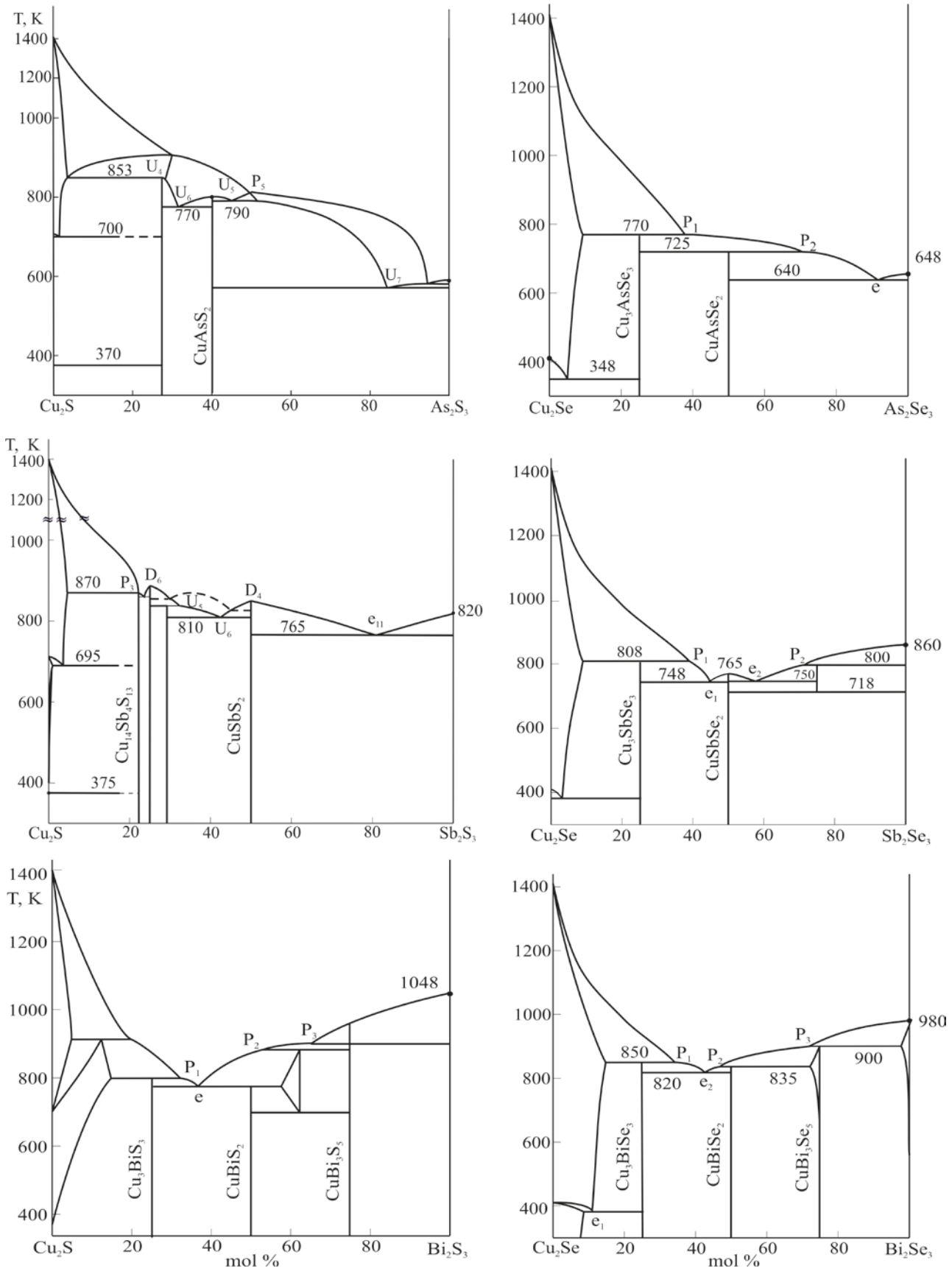

Fig. 4.2. Phase diagrams of the Cu_2X-$B^V{}_2X_3$ systems

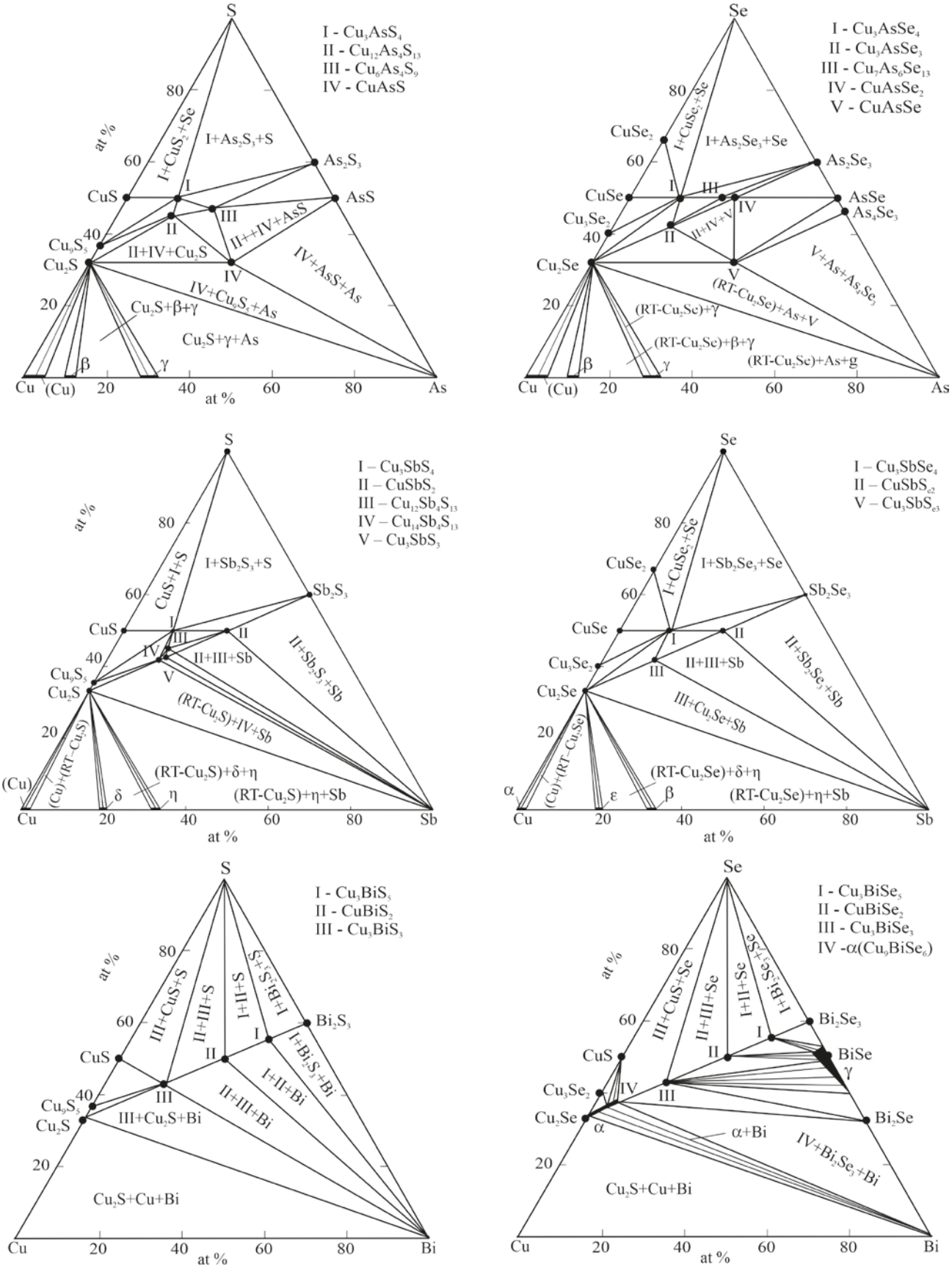

Fig. 4.3. Solid-phase equilibria diagrams of the Cu-B^{V}-X systems at 300 K

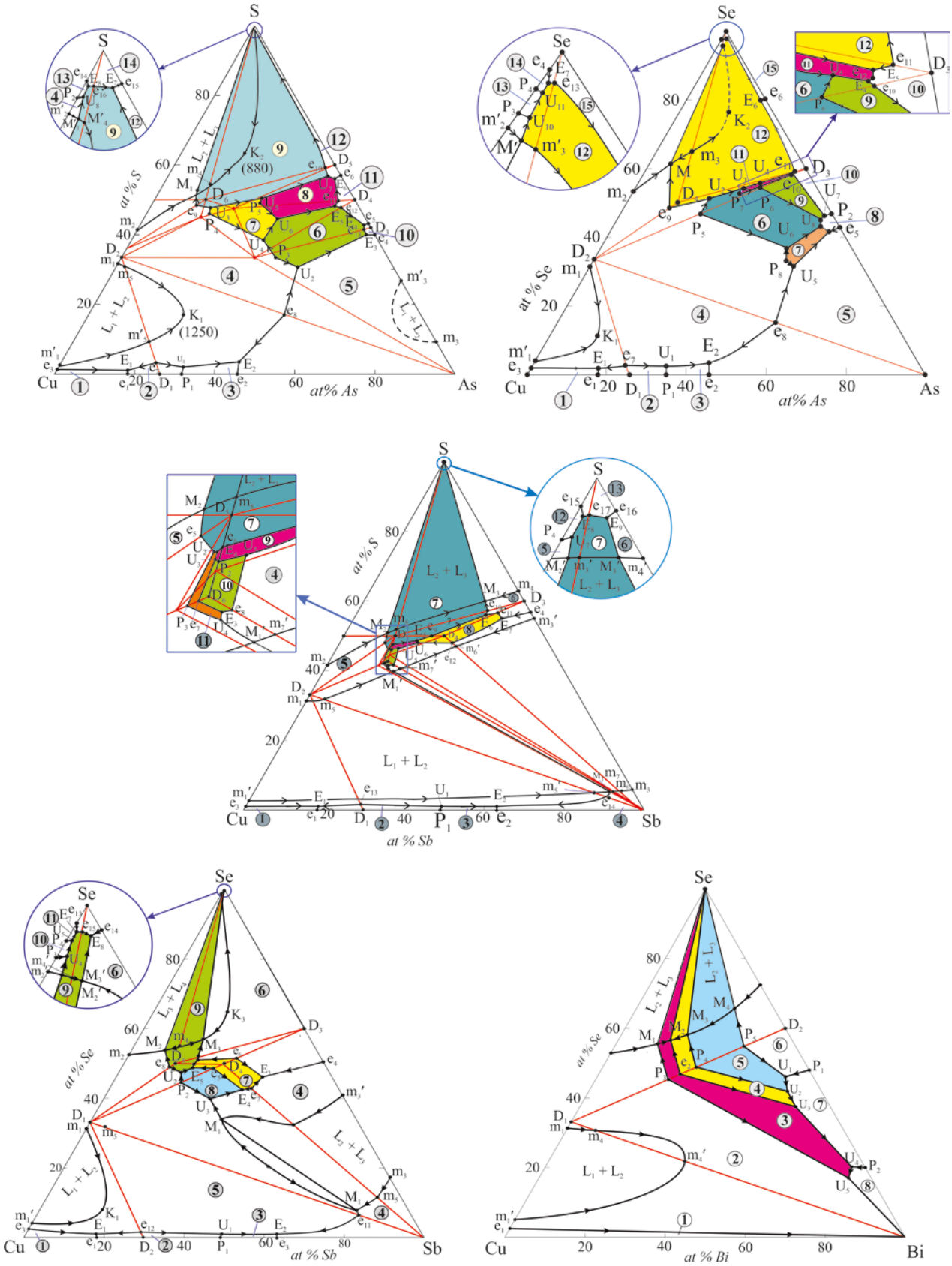

Fig. 4.4. Projections of liquidus surfaces of the Cu-B^{V}-X systems. The colored areas are the fields of primary crystallization of ternary compounds

Cu_3AsSe_4 subsystem, this region of the diagram was described in detail in [254].

The Cu-As-Te system. According to available data [91], ternary compounds are not formed in this system.

4.2. Phase equilibria in Cu-Sb-X systems

The Cu-Sb-S system. The studies of phase equilibria in the Cu-Sb-S system began at the beginning of the last century. The results of numerous studies in different years were summarized in the monograph [91] and studies [256, 257].

We will discuss some studies devoted to the Cu_2S-Sb_2S_3 section. Thus, the authors [258] showed that this section is quasi-binary and forms ternary compounds Cu_3SbS_3 and $CuSbS_2$. According to the data [259] on this section there is only one $CuSbS_2$ compound with congruent melting at 825 K. A detailed re-examination [260] showed that a complex interaction occurs in the vicinity of Cu_3SbS_3, involving the decomposition of this compound below 400 K and the formation of three different phases.

In a recently published study [257], the Cu–S–Sb system was studied using the CALPHAD method and a new version of the *T-x* diagram of the Cu_2S-Sb_2S_3 section, significantly different from previous studies was presented.

The complete *T-x-y* diagram, including various polythermal sections and an isothermal section at 300 K (Fig. 4.3), as well as a projection of the liquidus surface (Fig. 4.4), was shown in studies [261, 262]. According to [261], at room temperature, ternary compounds Cu_3SbS_4, $Cu_{12}Sb_4S_{13}$, $Cu_{14}Sb_4S_{13}$, Cu_3SbS_3, and $CuSbS_2$ exist in the system (Fig. 4.3).

According to [262], the liquidus surface of this system consists of 13 primary crystallization fields of phases. The crystallization fields of CuS and S degenerate at the sulfur corner of the concentration triangle. This part of the phase diagram is shown schematically in an enlarged form. A characteristic feature of the Cu-Sb-S system is two wide immiscibility regions. These regions have the appearance of wide continuous stripes between the immiscibility regions of the boundary binary Cu-S and Sb-S systems and occupy ~ 90% of the total area of the concentration triangle. Some curves of monovariant equilibria intersect the immiscibility regions and are transformed into four-phase monotectic equilibria (M_1 – M_1', M_2 – M_2' and M_3 – M_3' conjugate points in Fig. 4.4).

It should be noted that the complex nature of phase equilibria in a narrow region of compositions, is highlighted by a rectangle and presented in an enlarged form. In [262] data on the coordinates of invariant equilibria on *T-x-y* diagram of the system were presented and a detailed comparative analysis with data from previous studies was carried out. According to this study, the Cu_2S-Sb_2S_3 section (Fig. 4.2) is partially quasi-binary. In the region ⩾50 mol. % Sb_2S_3 the results coincide with the data of studies [258–260], according to which this part of the system is quasi-binary and belongs to the eutectic type. The region ⩽ 25 mol % Sb_2S_3 is also quasi-binary. This part of the phase diagram is characterized by the formation of $Cu_{14}Sb_4S_{13}$ and Cu_3SbS_3 compounds. However, in the intermediate range of compositions (25–50 mol. % Sb_2S_3), the Cu_2S-Sb_2S_3 section is not quasi-binary. The X-ray analysis data presented in [262] convincingly demonstrate the presence of a connode connection between the tetrahedrite $Cu_{12}Sb_4S_{13}$ phase, which according to the composition is located outside this section, with elemental antimony. This leads to the formation of three-phase regions of Cu_3SbS_3+$Cu_{12}Sb_4S_{13}$+Sb and $Cu_{12}Sb_4S_{13}$+$CuSbS_2$+Sb in the specified composition range.

The Cu-Sb-Se system. The quasi-binary Cu_2Se-Sb_2Se_3 section was investigated in studies [91, 259, 268–270]. According to [259], one compound of the $CuSbSe_2$ composition was formed in the system. The phase diagram was refined near this compound in [256]. The $CuSbSe_2$ and Cu_3SbSe_3 ternary compounds are shown on the phase diagram presented in [91]. In a recently published study [270], in addition to these compounds, a compound with the $CuSb_3Se_5$ composition, which exists in a narrow temperature range of 720-800 K, was discovered (Fig. 4.2).

The diagram of solid-phase equilibria at 300 K is shown in Fig. 4.3, and a projection of the liquidus surface, which reflects three ternary compounds $CuSbSe_2$, Cu_3SbSe_3, and Cu_3SbSe_4 is presented in Fig. 4.4. In a recently published study [271], the Cu-Sb-Se system was modelled

using the CALPHAD method and a projection of the liquidus surface was presented.

The Cu-Sb-Te system. According to [91], ternary compounds are not formed in this system. The compound of composition $CuSbTe_2$, indicated in some early studies, was not subsequently confirmed.

4.3. Phase equilibria in Cu-Bi-X systems

The Cu-Bi-S system. Phase equilibria in this system have been studied for more than 100 years. The results of these studies are summarized in [91, 256]. Their results have been shown to differ significantly. The *T-x* diagram constructed by us based on the data [275] is shown in Fig. 4.2. According to this diagram, Cu_3BiS_3, $CuBiS_2$, and $CuBi_3S_5$ sulfides are formed in the system. All of them melt with decomposition according to the peritectic reaction. The Cu_2S-Bi section is also quasi-binary, characterized by the presence of monotectic and degenerate eutectic equilibria [276]. According to the solid-state equilibrium diagram [91], three copper-bismuth sulfides exist at room temperature: $CuBi_3S_5$, $CuBiS_2$, and Cu_3BiS_3 (Fig. 4.3).

The Cu-Bi-Se system. According to [276] the Cu_2Se-Bi section is quasi-binary and forms a phase diagram with monotectic and degenerate eutectic equilibria for Bi.

The first version of the *T-x* diagram of the Cu_2Se-Bi_2Se_3 quasi-binary section is presented in [277]. It is shown that it belongs to the eutectic type with limited mutual solubility of the components. The ordering occurs in the region of Cu_2Se-based solid solutions at 25 mol. % Bi_2Se_3 (Cu_3BiSe_3). According to [277] the Cu_3BiSe_3 phase crystallizes in the cubic syngony (superstructure close to the CaF_2 type). According to the data [100], the Cu_3BiSe_3 compound has a monoclinic structure.

The literature also contains information on the synthesis and crystal structure of ternary compounds $CuBiSe_2$ and $CuBi_3Se_5$ (Table 4.1). The first compound crystallizes in a cubic lattice, while the second has a triclinic structure.

The study [279] summarizes all available results on phase equilibria in the Cu-Bi-Se system and presents a complete picture of phase equilibria, including a series of polythermal sections, an isothermal section at room temperature (Fig. 4.3) and a projection of the liquidus surface (Fig. 4.4). In this system, as in the sulfur-containing one, three ternary compounds $CuBi_3Se_5$, $CuBiSe_2$, and Cu_3BiSe_3 melting incongruently (Fig. 4.2) are formed. The study also presents a new version of the phase diagram of the quasi-binary Cu_2Se-Bi_2Se_3 section. The formation of the three above-mentioned ternary compounds melting by the peritectic reaction at 900 K ($CuBi_3Se_5$), 835 K ($CuBiSe_2$), and 850 K (Cu_3BiSe_3) was confirmed. It has also been established that the Cu_3BiSe_3 compound is outside the homogeneity region of Cu_2Se, which has a maximum length of ~17 mol. % Bi_2Se_3 at 850 K.

The Cu-Bi-Te system. According to available data [91], ternary compounds are not formed in this system.

4.4. Thermodynamic properties of copper chalcogenides with p^3-elements

The standard integral thermodynamic functions of copper-arsenic sulfides and selenides are determined by measuring the EMF of concentration cells of type (2.2) with a solid electrolyte [245, 246] (Table 4.2). These data sets for Cu_3AsS_4, $Cu_6As_4S_9$, and CuAsS compounds were significantly (up to 20%) lower than those shown in [280] and were closer to the data of [283, 284]. Unfortunately, the thermodynamic data [280-284] were presented without errors, which complicates the assessment of their reliability. We believe that the data in [280] were significantly overestimated.

Data on the standard integral thermodynamic functions of copper-antimony and copper-bismuth chalcogenides are shown in Table 4.2. For almost all of these compounds, complete mutually consistent sets of thermodynamic quantities were obtained using the EMF method with Cu^+ conductive electrolyte. Thermodynamic functions of $CuSbS_2$, Cu_3SbS_3, and $CuSbS_2$ determined by the EMF method [261, 285] except D_fG^0(298 K) for the latter compound are in good agreement with calorimetric data [263, 286].

Thus, mutually consistent sets of data on phase equilibria and thermodynamic properties are available for ternary Cu-B^V-S(Se) systems, and for five systems complete *T-x-y* diagrams were constructed and the primary crystallization fields of ternary phases were determined.

Table 4.2. Standard thermodynamic functions of formation and standard entropies of ternary phases of the Cu-BV-S(Se) systems

Compound	$-\Delta_f G^0$ (298 K)	$-\Delta_f H^0$ (298 K)	S^0_{298} J·K^{-1}·mol^{-1}	Ref.
	kJ·mol^{-1}			
Cu_3AsS_4	179.2±0.6	172.2±2.6	278±8	[245, 246]
	211.6	215.7	276.6	[283]
	230.4	224.0	285.0	[281]
		179.0	256.4	[282]
			277.2	[284]
$Cu_6As_4S_9$	445.3±1.6	434.6±7.5	668±22	[245, 246]
	517.8	505.1	673.0	[280]
$Cu_{12}As_4S_{13}$	701.8±2.5	673.7±10.7	1050±13	[245, 246]
CuAsS	69.5±0.3	64.1±1.7	109±5	[245, 246]
	76.2	76.5	100.0	[280]
Cu_3AsSe_4	147.3±0.5	146.3±1.5	307±13	[253]
$Cu_7As_6Se_9$	441.8±2.3	446.1±11.7	970±27	[284]
$CuAsSe_2$	66.6±0.4	67.3±2.0	150.9±6.2	[255]
	99.5±4.8	97.9±5.1	158±5	[285]
Cu_3AsSe_3	141.8±0.5	140.0±2.0	258.5±5.6	[285]
CuAsSe	55.1±0.3	55.6±2.0	109.5±4.7	[285]
Cu_3SbS_4	254.7 ± 2.3	247.8 ± 2.3	295.6 ± 7.0	[261]
$CuSbS_2$	128.5 ± 2.2	126.9 ± 2.4	147.5 ± 3.8	[261]
	*132.7±4.2	130.8±4.4	-	[263]
	130.6±6.0	131.7±5.2	-	[286]
$Cu_{12}Sb_4S_{13}$	958.7 ± 9.6	929.7 ± 11.2	1092.0 ± 29.0	[261]
Cu_3SbS_3	226.4 ± 2.3	219.0 ± 2.6	265.5 ± 7.2	[261]
	*221.6±6.0	215.0±6.2	-	[286]
$Cu_{14}Sb_4S_{13}$	971.7 ± 9.8	984.8 ± 11.9	1018.0 ± 33.0	[261]
Cu_3SbSe_4	191.6±2.5	178.6±5.4	358.18	[285]
$CuSbSe_2$	101.4±1.8	98.5±2.2	173±8	[285]
	77.3±1.3	104.8±1.7	-	[286]
Cu_3SbSe_3	175.6±2.5	164.0±5.3	311±15	[286]
$CuBiS_2$	138.6±4.0	138.2±2.9	156±12	[50]
Cu_3BiS_3	213.0±4.4	209.9±5.2	264±21	[50]
$CuBi_3S_5$	248.7±1.9	248.6±5.8	421.9±7.8	[50]
$CuBiSe_2$	107.6±0.8	105.9±2.51	189.8±2.4	[279]
Cu_3BiSe_3	162.5±1.2	155.9±5.7	315.0±8.5	[279]
Cu_9BiSe_6	324.8±3.5	313.1±18.6	659±28	[279]

Note: - our calculation from calorimetric data [286]

5. Conclusions

Thus, the above-presented results of numerous studies demonstrate significant successes in the development of environmentally friendly and affordable functional materials based on copper chalcogenides with p^1-p^3-elements. The analysis shows that the improvement and optimization of the functional properties of these materials is largely associated with targeted research on the variation of their composition and structure.

This review summarizes the studies of phase equilibria in ternary systems Cu-Tl(B^{IV}, B^{V})-X (B^{IV} – Si, Ge, Sn; B^{V} – As, Sb, Bi; X – S, Se, Te) and some concentration planes and sections of quaternary systems that form various types of substitutional solid solutions based on ternary

compounds of the described systems. Even though the studied phase diagrams cover only a small part of such systems, they contain valuable information that offers great opportunities for scientifically based manipulation of composition and structure, including the concept of entropy engineering. Here we also present data on the fundamental thermodynamic properties of ternary compounds of the considered systems. Most of these data were obtained using the EMF method, which allowed to ensure not only the consistency of $\Delta_f G^0$, $\Delta_f H^0$, and S^0 functions, but also the mutual consistency of these values with phase diagrams.

At the same time, it should be noted that in studies of the physical properties of complex copper chalcogenides, phase diagrams and thermodynamic data were not used fully when selecting sample compositions and synthesis conditions. We believe that addressing this gap and further development of research on phase equilibria and thermodynamic properties of similar and more complex systems are important. This would allow us to obtain complex copper-based chalcogenides, thermodynamically stable over wide ranges of compositions and temperatures, including high-entropy phases with good applied characteristics.

Author contributions

Babanly M. B. – idea, text writing, scientific editing of the text; Mashadieva L. F., Imamalieva S. Z. and Babanly D. M – search and analysis of literary data, text writing, preparation of figures and tables; Tagiev D. B and Yusibov Yu. A. – processing of literature data and editing of the text.

Conflict of interests

The authors declare that they have no known competing financial interests or personal relationships that could have influenced the work reported in this paper.

References

1. *Physical-chemical properties of semiconductor substances**. Reference-book. A. V. Novoselova, V. B. Lazarev (eds.). Moscow: Nauka Publ., 1976. 339 p. (In Russ.)

2. Abrikosov N. Kh., Bankina V. F., Poretskaya L. V., Skudnova E. V., Chizhevskaya S. N. *Semiconductor chalcogenides and their base alloys**. Moscow: Nauka Publ., 1974. 220 p. (In Russ.)

3. Aven M., Prener J. S. *Physics and chemistry of II-VI compounds*. North-Holland Publishing Co; First Edition. 1967. 844 p.

4. Lazarev V. B., Berul S. I., Salov A. V. *Ternary semiconductor compounds in A^I-B^V-C^{VI} systems**. Moscow: Nauka Publ.; 1982. 150 p. (In Russ.)

5. Ahluwalia G. K. (ed.). *Applications of chalcogenides: S, Se, and Te*. Springer, 2016. 461p.

6. Woodrow P. *Chalcogenides: advances in research and applications*. New York: Nova Science Publishers, 2018. 111 p.

7. Scheer R., Schock H. W. *Chalcogenide photovoltaics: physics, technologies, and thin film devices*. Weinheim: Wiley-VCH, 2011. 384 p.

8. Alonso-Vante N. *Chalcogenide materials for energy conversion: pathways to oxygen and hydrogen reactions*. New York: Springer; 2018. 234 p. https://doi.org/10.1007/978-3-319-89612-0

9. Khan M. M. *Chalcogenide-based nanomaterials as photocatalysts*. Amsterdam: Elsevier, 2021. 376 p.

10. Hasan M. Z., Kane C. L. *Colloquium: topological insulators*. *Reviews of Modern Physics*. 2010;82: 3045–3067. https://doi.org/10.1103/RevModPhys.82.3045

11. Hagmann A. J. Chalcogenide topological insulators. In: *Chalcogenide from 3D to 2D and beyond*. Woodhead Publishing Series in Electronic and Optical Materials, 2020. p. 305–337. https://doi.org/10.1016/b978-0-08-102687-8.00015-4

12. Flammini R., Colonna S., Hogan C., ... Ronci F. Evidence of β-antimonene at the Sb/Bi_2Se_3 interface. *Nanotechnology*. 2018;29(6): 065704. https://doi.org/10.1088/1361-6528/aaa2c4

13. Tian W.,Yu W.,Shi J., Wang Y. The property, preparation and application of topological insulators: a review. *Material*. 2017;10(7): 814. https://doi.org/10.3390/ma10070814

14. Babanly M. B., Chulkov E. V., Aliev Z. S., Shevel'kov A. V., Amiraslanov I. R. Phase diagrams in materials science of topological insulators based on metal chalkogenides, *Russian Journal of Inorganic Chemistry*. 2017;62(13): 1703–1729. https://doi.org/10.1134/S0036023617130034

15. Pacile D., Eremeev S. V., Caputo M., ... Papagno M. Deep insight into the electronic structure of ternary topological insulators: A comparative study of $PbBi_4Te_7$ and $PbBi_6Te_{10}$. *Physica Status Solidi (RRL)*. 2018;12(12): 1800341-8. https://doi.org/10.1002/pssr.201800341

16. Nurmamat M., Okamoto K., Zhu S., ... Kimura A. Topologically non-trivial phase-change compound $GeSb_2Te_4$. *ACS Nano*. 2020;14(7): 9059–9065. https://doi.org/10.1021/acsnano.0c04145

17. Shvets I. A., Klimovskikh I. I., Aliev Z. S., ... Chulkov E. V. Impact of stoichiometry and disorder on the electronic structure of the $PbBi_2Te_{4-x}Se_x$ topological insulator. *Physical Review B*. 2017;96: 235124–235127. https://doi.org/10.1103/PhysRevB.96.235124

18. Otrokov M. M., Klimovskikh I. I., Bentmann H. ... Chulkov E. V. Prediction and observation of an antiferromagnetic topological insulator. *Nature*. 2019;576: 416–422. https://doi.org/10.1038/s41586-019-1840-9

19. Jahangirli Z. A., Alizade E. H., Aliev Z. S., ... Chulkov E. V. Electronic structure and dielectric function of Mn-Bi-Te layered compounds. *Journal of Vacuum Science and*

Technology B. 2019;37: 062910. https://doi.org/10.1116/1.5122702

20. Eremeev S. V., Rusinov I. P., Koroteev Yu. M., ... Chulkov E. V. Topological magnetic materials of the $(MnSb_2Te_4)\cdot(Sb_2Te_3)_n$ van der Waals compounds family. *The Journal of Physical Chemistry Letters*. 2021;12(17): 4268–4277. https://doi.org/10.1021/acs.jpclett.1c00875

21. Garnica M., Otrokov M. M., Casado Aguilar P., ... Miranda R. Native point defects and their implications for the Dirac point gap at $MnBi_2Te_4$(0001). *npj Quantum Materials*. 2022;7: 7. https://doi.org/10.1038/s41535-021-00414-6

22. Coughlan C., Ibanez M., Dobrozhan O., Singh A., Cabot A., Ryan K. M. Compound copper chalcogenide nanocrystals. *Chemical Reviews*. 2017;117(9): 5865–6109. https://doi.org/10.1021/acs.chemrev.6b00376

23. Xing C., Lei Y., Liu M., Wu S., He W. Environment-friendly Cu-based thin film solar cells: materials, devices and charge carrier dynamics. *Physical Chemistry Chemical Physics*. 2021;23: 16469–16487. https://doi.org/10.1039/D1CP02067F

24. Fu H. Environmentally friendly and earth-abundant colloidal chalcogenide nanocrystals for photovoltaic applications. *Journal of Materials Chemistry C*. 2018;6: 414–445. https://doi.org/10.1039/C7TC04952H

25. Kumar M., Meena B., Subramanyam P., Suryakala D., Subrahmanyam C. Emerging copper-based semiconducting materials for photocathodic applications in solar driven water splitting. *Catalysts*. 2022;12(10): 1198. https://doi.org/10.3390/catal12101198

26. Akhil S., Balakrishna R. G. $CuBiSe_2$ quantum dots as ecofriendly photosensitizers for solar cells. *ACS Sustainable Chemistry and Engineering Journal*. 2022;10(39): 13176–13184. https://doi.org/10.1021/acssuschemeng.2c04333

27. Deng T., Wei T. R., Song Q., ... Chen L. Thermoelectric properties of *n*-type $Cu_4Sn_7S_{16}$-based compounds. *RSC Advances*. 2019;9: 7826. https://doi.org/10.1039/c9ra00077a

28. Choudhury A., Mohapatra S., Asl H. Y., ... Petricek V. New insights into the structure, chemistry, and properties of Cu_4SnS_4. *Journal of Solid State Chemistry*. 2017;253: 192–201. http://dx.doi.org/10.1016/j.jssc.2017.05.033

29. Ivanchenko M., Jing H. Smart design of noble metal–copper chalcogenide dual plasmonic heteronanoarchitectures for emerging applications: progress and prospects. *Chemistry of Materials*. 2023;35(12): 4598–4620. https://doi.org/10.1021/acs.chemmater.3c00346

30. Zhou N., Zhao H., Li X., ...Tong X. Activating earth-abundant element-based colloidal copper chalcogenide quantum dots for photodetector and optoelectronic synapse applications. *ACS Materials Letters*. 2023;*5*(4): 1209–1218. https://doi.org/10.1021/acsmaterialslett.3c00035

31. Polevik A. O., Sobolev A. V., Glazkova I. S., ... Shevelkov A. V. Interplay between Fe(II) and Fe(III) and its impact on thermoelectric pProperties of iron-substituted colusites $Cu_{26-x}Fe_xV_2Sn_6S_{32}$. *Compounds*. 2023;3: 348–364. https://doi.org/10.3390/compounds3020027

32. Polevik A. O., Efimova A. S., Sobolev A. V., ... Shevelkov A. V. Atomic distribution, electron transfer, and charge compensation in artificial iron-bearing colusites $Cu_{26-x}Fe_xTa_{2-\gamma}Sn_6S_{32}$. *Journal of Alloys and Compounds*. 2024;976: 173280. https://doi.org/10.1016/j.jallcom.2023.173280

33. Nasonova D. I., Sobolev A. V., Presniakov I. A., Presniakov I. A., Andreeva K. D., Shevelkov A. V. Position and oxidation state of tin in Sn-bearing tetrahedrites $Cu_{12-x}Sn_xSb_4S_{13}$. *Journal of Alloys and Compounds*. 2019;778: 774–778. https://doi.org/10.1016/j.jallcom.2018.11.168

34. Reddy V. R. M., Pallavolu M. R., Guddeti P. R., ... Park C. Review on Cu_2SnS_3, Cu_3SnS_4, and Cu_4SnS_4 thin films and their photovoltaic performance. *Journal of Industrial and Engineering Chemistry*. 2019;76: 39–74. https://doi.org/10.1016/j.jiec.2019.03.035

35. Lin S., Li W., Pei Y. Thermally insulative thermoelectric argyrodites. *Materials Today*. 2021;48: 198–213. https://doi.org/10.1016/j.mattod.2021.01.007

36. Nilges T., Pfitzner A. A structural differentiation of quaternary copper argyrodites: structure – property relations of high temperature ion conductors, *Zeitschrift für Kristallographie - Crystalline Materials*. 2005; 220(2-3): 281–294. https://doi.org/10.1524/zkri.220.2.281.59142

37. Babanly M. B., Yusibov Y. A., Imamaliyeva S. Z., Babanly D. M., Alverdiyev I. J. Phase diagrams in the development of the argyrodite family compounds and solid solutions based on them. *Journal of Phase Equilibria and Diffusion*. 2024;45: 228–255. https://doi.org/10.1007/s11669-024-01088-w

38. Wu X., Liu K., Wang R., Yang G., Lin J., Liu X. Multifunctional $CuBiS_2$ nanoparticles for computed tomography guided photothermal therapy in preventing arterial restenosis after endovascular treatment. *Frontiers in Bioengineering and Biotechnology*. 2020; 8: 585631. https://doi.org/10.3389/fbioe.2020.585631

39. Askari N., Askari M. B. Apoptosis-inducing and image-guided photothermal properties of smart nano $CuBiS_2$. *Materials Research Express*. 2019;6: 065404. https://doi.org/10.1088/2053-1591/ab0c3e

40. Zhou M., Tian M., Li C. Copper-based nanomaterials for cancer imaging and therapy. *Bioconjugate Chemistry*. 2016;27(5): 1188-99. https://doi.org/10.1021/acs.bioconjchem.6b00156

41. Mindat.org: *Open database of minerals, rocks, meteorites and the localities they come from*. Available at: http://www.mindat.org

42. Filippou D., Germain P., Grammatikopoulos T. Recovery of metal values from copper—arsenic minerals and other related resources. *Mineral Processing and Extractive Metallurgy Review*. 2007;28: 247–298. https://doi.org/10.1080/08827500601013009

43. Afinogenov Yu. P., Goncharov E. G., Semenova G. V., Zlomanov V. P. *Physicochemical analysis of multicomponent systems*[*]. Moscow: MFTIB Publ.; 2006. 332 p. (In Russ.)

44. Lazarev V. B., Shevchenko V. I., Marenkin S. F. Some problems of physics, chemistry and materials science of new semiconductors. In: *Physical methods for studying inorganic materials*. Moscow: Nauka Publ.; 1981. p.19–34. (In Russ.)

45. West D. R. F. *Ternary phase diagrams in materials science*. Boca Raton: CRC Press; 2013. 3rd edition. p. 240. https://doi.org/10.1201/9781003077213

46. Saka H. *Introduction to phase diagrams in materials science and engineering*. London: World Scientific Publishing Company; 2020. pp.188. https://doi.org/10.1142/11368

47. Babanly M. B., Mashadiyeva L. F., Babanly D. M., Imamaliyeva S. Z., Taghiyev D.B., Yusibov Y.A. Some issues of complex investigation of the phase equilibria and

thermodynamic properties of the ternary chalcogenide systems by the EMF method. *Russian Journal of Inorganic Chemistry*. 2019;64(13): 1649–1671. https://doi.org/10.1134/S0036023619130035

48. Imamaliyeva S. Z. Phase diagrams in the development of thallium-ree tellurides with Tl_5Te_3 structure and multicomponent phases based on them overview. *Condensed Matter and Interphases*. 2018;20(3): 332–347. https://doi.org/10.17308/kcmf.2018.20/570

49. Babanly M. B., Mashadiyeva L. F., Imamaliyeva S. Z., Tagiev D. B., Babanly D. M., Yusibov Yu. A. Thermodynamic properties of complex copper chalcogenides. Review. *Chemical Problems*. 2024;3: 243–280. https://doi.org/10.32737/2221-8688-2024-3-243-280

50. Babanly M. B., Yusibov Yu. A., Babanly N. B. The EMF method with solid-state electrolyte in the thermodynamic investigation of ternary copper and silver chalcogenides. In: *Electromotive force and measurement in several systems*. S. Kara (ed.). Intechweb.Org. 2011. p. 57–78. https://doi.org/10.5772/28934

51. Babanly M. B., Yusibov Yu. A. *Electrochemical methods in thermodynamics of inorganic systems*. Baku: ELM Publ.; 2011. 306 p. (In Russ.)

52. Babanly M. B, Akhmadyar A., Kuliev A. Thermodynamic properties of intermediate phases in Tl-Sb(Bi)-Te systems. *Russian Journal of Physical Chemistry*. 1985;59(3): 335–336.

53. Yusibov Y. A., Babanly M. B., Gasanov R. F. Thermodynamic properties and solid phase equilibrium of Tl-Ga-Te system*. *Inorganic Materials*. 1991;27(7): 1402–1406. (In Russ.)

54. Babanly M. B., Kuliev A. A. Phase equilibria and thermodynamic properties in the system Ag-Tl-Te*. *Russian Journal of Inorganic Chemistry*. 1982;27(6); 1538–1546. (In Russ.)

55. Babanly M. B., Muradova G. V., Ilyasly T. M., Babanly D. M. Solid-phase equilibria and thermodynamic properties of the Tl_2Se-As_2Se_3-Se system. *Russian Journal of Inorganic Chemistry*. 2012;57: 270–273. https://doi.org/10.1134/S0036023612020039

56. Aliev Z. S., Babanly M.B. Solid-state equilibria and thermodynamic properties of compounds in the Bi-Te-I system. *Inorganic Materials*. 2008;44(10): 1076–1080. https://doi.org/10.1134/S0020168508100099

57. Jafarov Y. I., Ismaylova S. A., Aliev Z. S., Imamaliyeva S. Z., Yusibov Y. A., Babanly M. B. Experimental study of the phase diagram and thermodynamic properties of the Tl-Sb-S system. *CALPHAD*. 2016;55: 231–237. https://doi.org/10.1016/j.calphad.2016.09.007

58. Babanly D.M., Aliev Z.S., Jafarli F.Y., Babanly M.B. Phase equilibria in the Tl-TlCl-Te system and thermodynamic properties of the compound Tl_5Te_2Cl. *Russian Journal of Inorganic Chemistry*. 2011;56: 442–449. https://doi.org/10.1134/S0036023611030065

59. Seidzade A. E., Orujlu E. N., Babanly D. M., Imamaliyeva S. Z., Babanly M. B. Solid-phase equilibria in the SnTe–Sb_2Te_3–Te system and the thermodynamic properties of the tin–antimony tellurides. *Russian Journal of Inorganic Chemistry*. 2022;67(5): 683–690. https://doi.org/10.1134/S003602362205014X

60. Aliev Z. S., Zúñiga F. J., Koroteev Y. M., ... Chulkov E. V. Insight on a novel layered semiconductors: CuTlS and CuTlSe. *Journal of Solid State Chemistry*. 2016;242: 1–7. https://doi.org/10.1016/j.jssc.2016.05.036

61. Vijayan K., Thirumalaisamy L., Vijayachamundeeswari S. P., Sivaperuman K., Ahsan N., Okada Y. A novel approach for designing a sub-bandgap in $CuGa(S,Te)_2$ thin films assisted with numerical simulation of solar cell devices for photovoltaic application. *ACS Omega*. 2023;8(25): 22414–22427. https://doi.org/10.1021/acsomega.2c08196

62. Vijayan K., Vijayachamundeeswari S. P. Scrutinizing the effect of substrate temperature and enhancing the multifunctional attributes of spray deposited copper gallium sulfide ($CuGaS_2$) thin films. *Phase Transitions*. 2023;96(8): 607–619. https://doi.org/10.1080/01411594.2023.2238110

63. Maeda T., Nakanishi R., Yanagita M., Wada T. Control of electronic structure in $Cu(In, Ga)(S, Se)_2$ for high-efficiency solar cells. *Japanese Journal of Applied Physics*. 2020;59: SGGF12. https://doi.org/10.35848/1347-4065/ab69e0

64. Shukla S., Sood M., Adeleye D., ... Siebentritt S. Over 15% efficient wide-band-gap $Cu(In,Ga)S_2$ solar cell: suppressing bulk and interface recombination through composition engineering. *Joule*. 2021;5(7): 1816–1831. https://doi.org/10.1016/j.joule.2021.05.004

65. Yang Y., Xiong X., Han J. Modification of surface and interface of copper indium gallium selenide thin films with sulfurization. *Emerging Materials Research*. 2022;11(3): 325–330. https://doi.org/10.1680/jemmr.21.00171

66. Stanbery B. J., Abou-Ras D., Yamada A., Mansfield L. CIGS photovoltaics: reviewing an evolving paradigm. *Journal of Physics D: Applied Physics*. 2021;55(17): 173001. https://doi.org/10.1088/1361-6463/ac4363

67. Li W., Song Q., Zhao C., ... Yang C. Toward high-efficiency $Cu(In,Ga)(S,Se)_2$ solar cells by a simultaneous selenization and sulfurization rapid thermal process. *ACS Applied Energy Materials Journal*. 2021;4(12): 14546–14553. https://doi.org/10.1021/acsaem.1c03198

68. Khavari F., Keller J., Larsen J. K., Sopiha K. V., Törndahl T., Edoff M. Comparison of sulfur incorporation into $CuInSe_2$ and $CuGaSe_2$ thin-film solar absorbers. *Physica Status Solidi A*. 2020;217(22). https://doi.org/10.1002/pssa.202000415

69. Wang Y., Yang Y., Wang L., ... Guo Z. Design, photoelectric properties and electron transition mechanism of Cr doped p-$CuGaS_2$ compound based on intermediate band effect. *Materials Today Physics*. 2021;21: 100545. https://doi.org/10.1016/j.mtphys.2021.100545

70. Fan F.J., Liang Wu L., Yu S.-H. Energetic I-III-VI_2 and I_2-II-IV-VI4 nanocrystals: synthesis, photovoltaic and thermoelectric applications. *Energy Environmental Science*. 2014;7: 190-208. https://doi.org/10.1039/C3EE41437J

71. Torimoto T., Kameyama T., Uematsu T., Kuwabata S. Controlling optical properties and electronic energy structure of I–III–VI semiconductor quantum dots for improving their photofunctions. *Journal of Photochemistry and Photobiology C: Photochemistry Reviews*. 2023;54: 100569. https://doi.org/10.1016/j.jphotochemrev.2022.100569

72. Gullu H. H., Isik M., Gasanly N. M. Structural and optical properties of thermally evaporated Cu-Ga-S (CGS) thin films. *Physica B: Condensed Matter*. 2018;547: 92–96. https://doi.org/10.1016/j.physb.2018.08.015

73. Soni A., Gupta V., Arora C. M., Dashora A., Ahuja B. L. Electronic structure and optical properties of $CuGaS_2$ and

$CuInS_2$ solar cell materials. *Solar Energy*. 2010;84(8): 1481–1489. https://doi.org/10.1016/j.solener.2010.05.010

74. Candeias M. B., Fernandes T. V., Falcão B. P., ... Leitão J. P. Cu(In,Ga)Se_2-based solar cells for space applications: proton irradiation and annealing recovery. *Journal of Materials Science*. 2023;58: 16385–16401. https://doi.org/10.1007/s10853-023-09033-x

75. Plata J. J., Posligua V., Márquez A. M., Sanz J. F., Grau-Crespo R. Charting the lattice thermal conductivities of I–III–VI_2 chalcopyrite semiconductors. *Chemistry of Materials Journal*. 2022;34(6): 2833–2841. https://doi.org/10.1021/acs.chemmater.2c00336

76. Djelid K., Seddik T., Merabiha O., ... Bin Omran S. Effects of alloying chalcopyrite $CuTlSe_2$ with Na on the electronic structure and thermoelectric coefficients: DFT investigation. *The European Physical Journal Plus*. 2022;137: 1347. https://doi.org/10.1140/epjp/s13360-022-03577-8

77. Gudelli V. K., Kanchana V., Vaitheeswaran G., Svane A., Christensen N. E. Thermoelectric properties of chalcopyrite type $CuGaTe_2$ and chalcostibite $CuSbS_2$. *Journal of Applied Physics*. 2013;114: 1223707-8. https://doi.org/10.1063/1.4842095

78. Plirdpring T., Kurosaki K., Kosuga A., ... Yamanaka S. Chalcopyrite $CuGaTe_2$: a high-efficiency bulk thermoelectric material. *Advanced Materials*. 2012;24(127): 3622–3626. https://doi.org/10.1002/adma.201200732

79. Kurosaki K., Goto K., Kosuga A., Yamanaka S. Thermoelectric and thermophysical characteristics of Cu_2Te-Tl_2Te pseudo binary system. *Materials Transactions*. 2006;47(6): 1432-1435. https://doi.org/10.2320/matertrans.47.1432

80. Matsumoto H., Kurosaki K., Muta H., Yamanaka S. Thermoelectric properties of $TlCu_3Te_2$ and $TlCu_2Te_2$. *Journal of Electronic Materials*. 2009;38: 1350–1353. https://doi.org/10.1007/s11664-009-0664-z

81. Jiang C., Tozawa M., Akiyoshi K.,... Torimoto T. Development of Cu–In–Ga–S quantum dots with a narrow emission peak for red electroluminescence. *The Journal of Chemical Physics*. 2023;158: 164708. https://doi.org/10.1063/5.0144271

82. Kim Y.-K., Ahn S.-H., Chung K., Cho Y.-S., Choi C.-J. The photoluminescence of $CuInS_2$ nanocrystals: Effect of non-stoichiometry and surface modification. *Journal of Materials Chemistry*. 2012;22: 1516–1520. https://doi.org/10.1039/c1jm13170b

83. Isik M., Gasanly N.M., Gasanova L. G., Mahammadov A. Z. Thermoluminescence study in $Cu_3Ga_5S_9$ single crystals: application of heating rate and T_m-T_{stop} methods. *Journal of Luminescence*. 2018;199: 334–338. https://doi.org/10.1016/j.jlumin.2018.03.076

84. Kim J.-H., Han H., Kim M. K., ... Lim J. A. Solution-processed near-infrared Cu(In,Ga)(S,Se)$_2$ photodetectors with enhanced chalcopyrite crystallization and bandgap grading structure via potassium incorporation. *Science Reports*. 2021;11: 7820. https://doi.org/10.1038/s41598-021-87359-9

85. Nakamura M., Yamaguchi K., Kimoto Y., Yasaki Y., Kato T., Sugimoto H. Cd-free Cu(In,Ga)(Se,S)$_2$ thin-film solar cell with record efficiency of 23.35%. *IEEE Journal of Photovoltaics*. 2019;9(6): 1863–1867. https://doi.org/10.1109/JPHOTOV.2019.2937218

86. Clarke D., Breguel R. Analysis of thermodynamic properties of Cu(In,Ga)Se_2 thin-film solar cells for viable space application. *PAM Review: Energy Science and Technology*. 2018;5: 131–149. https://doi.org/10.5130/pamr.v5i0.1501

87. Shevelkov A. V. Chemical aspects of the design of thermoelectric materials, *Russian Chemical Reviews*. 2008;77: 1–19. https://doi.org/10.1070/rc2008v077n01abeh003746

88. Berger R., Eriksson L. Crystal structure, refinement of monoclinic $TlCu_3Se_2$. *Journal of Less-Common Metals*. 1990;61: 101–108. https://doi.org/10.1016/0022-5088(90)90318-e

89. Klepp K. O., Yvon K. Thallium dithiotricuprate (I). *Acta Crystallographica Section B Structural Crystallography and Crystal Chemistry*. 1980;36: 2389–2391. https://doi.org/10.1107/s0567740880008795

90. Norén L., Larsson K., Delaplane R. G., Berger R. Size or polarisability effects? A comparative study of $TlCu_7S_4$ and $TlCu_7Se_4$. *Journal of Alloys and Compounds*. 2001;314: 114–123. https://doi.org/10.1016/S0925-8388(00)01202-0

91. Babanly M. B., Yusibov Y. A., Abishev V. T. *Ternary chalcogenides based on copper and silve*[*] Baku: BSU Publ.; 1993. 342 p. (In Russ.)

92. Abishev V. T., Babanly M. B., Kuliyev A. A. Phase equilibria in the $T_{l2}S$–$C_{u2}S$ system. *ChemChemTech [Izv. Vyssh. Uchebn. Zaved. Khim. Khim. Tekhnol.]*. 1978;21(5): 630–632.

93. Mammadov M. I., Alizade M. Z., Zamanov S. K., Aliyev O. M. Study of the phase diagram of the Tl_2S-Cu_2S system[*]. *Russian Journal of Inorganic Chemistry*. 1978;14(8): 1527–1529. (In Russ.)

94. Gardes B., Brun G., Raymond A., Tedenac J. C. Trois phases ternaire Cu-Tl-S. *Materials Research Bulletin*. 1979;14(7): 943–946. https://doi.org/10.1016/0025-5408(79)90161-2

95. Sobbott E. Das system Tl_2S-Cu_2S. *Monatshefte Chemie*. 1994;115(12): 1397–1400. https://doi.org/10.1007/BF00816337

96. Babanly M. B., Un L. T., Kuliev A. A. System Tl_2S–CuTlS–S[*]. *Russian Journal of Inorganic Chemistry*. 1985;30(4): 1047–1050. (In Russ.)

97. Babanly M.B., Un L.T., Kuliev A.A. System Tl–Tl_2S–CuTlS–Cu[*]. *Russian Journal of Inorganic Chemistry*.1985;30(4): 1043–1046. (In Russ.)

98. Babanly M. B., Un L. T., Kuliev A. A. System Cu-Tl-S[*]. *Russian Journal of Inorganic Chemistry*. 1986;32(7): 1837–1844. (In Russ.)

99. Abishov V. T., Babanly M. B., Kuliev A. A. Phase equilibria in the Cu_2Se-Tl_2Se system[*]. *Inorganic Materials*. 1979;15(11): 1926. (In Russ.)

100. Voroshilov Yu. V., Evstigneeva T. L., Nekrasov I. Ya. *Crystal chemical tables of ternary chalcogenides*[*]. Moscow: Nauka Publ.; 1989. 224 p. (In Russ.)

101. Babanly N. B. Thermodynamic properties of some ternary phases of the Cu-Tl-Se system. *Inorganic Materials*. 2011;47: 1306–1310. https://doi.org/10.1134/S0020168511120016

102. Babanly N. B. Phase diagram of the Tl-Tl_2Se-Cu_2Se-Cu system. *Journal of Qafqaz University-Chemistry*. 2015;5(1): 43–50.

103. Kovaleva I. S., Kranchevich K. S., Nikolskaya G. F. Section of Cu_2Te–Tl_2Te_3 in the Cu–Tl–Te system.[*] *Inorganic Materials*. 1971;7(5): 865–867. (In Russ.)

104. Babanly N. B., Salimov Z. E., Akhmedov M. M., Babanly M. B. Thermodynamic study of the Cu–Tl–Te system by the EMF method with solid electrolyte $Cu_4RbCl_3I_2$. *Russian Journal of Electrochemistry*. 2012;48: 68–73. https://doi.org/10.1134/S1023193512010041

105. Kleep K. O. Darstellung und Kristallostructur von $TlCu_3Te_2$: ein Tellurocuprat mit aufgefuelltem $CuAl_2$-typ. *Journal of the Less-Common Metals*. 1987;127: 79–89. https://doi.org/10.1016/0022-5088(87)90194-9

106. Bradtmöller S., Böttcher P. Crystal structure of copper tetrathallium trutelluride $CuTl_4Te_3$. *Zeitschrift für Kristallographie*. 1994;209: 97. https://doi.org/10.1524/zkri.1994.209.1.97

107. Babanly M. B., Salimov Z. E., Babanly N. B., Imamaliyeva S. Z.Thermodynamic properties of copper thallium tellurides. *Inorganic Materials*. 2011;47: 361–364. https://doi.org/10.1134/S0020168511040030

108. Babanly N. B., Aliev Z. S., Yusibov Yu. A., Babanly M. B. A thermodynamic study of Cu—Tl-S system by EMF method with $Cu_4RbCl_3I_2$ solid electrolyte. *Russian Journal of Electrochemistry*. 2010;46: 354–358. https://doi.org/10.1134/S1023193510030146

109. Babanly M. B., Yusibov Y. A., Abishov V. T. *Method of electromotive forces in the thermodynamics of complex semiconductor substances*[*]. Baku: BSU Publ.; 1992. 327 p. (In Russ.)

110. Morachevsky A. G., Voronin G. F., Heiderich V. A., Kutsenok I. B. *Electrochemical methods of research in the thermodynamics of metallic systems*[*]. Moscow: ICC "Akademkniga" Publ.; 2003. 334 p. (In Russ.)

111. Aliev Z. S., Musayeva S. S. Imamaliyeva S. Z., Babanlı M. B. Thermodynamic study of antimony chalcoiodides by EMF method with an ionic liquid. *Journal of Thermal Analysis and Calorimetry*. 2018;133(2): 1115–1120. https://doi.org/10.1007/s10973-017-6812-4

112. Osadchii E. G., Korepanov Y. I., Zhdanov N. N. A multichannel electrochemical cell with glycerin-based liquid electrolyte. *Instruments and Experimental Techniques*. 2016;59: 302–304. https://doi.org/10.1134/S0020441216010255

113. Voronin M. V., Osadchii E. G. Determination of thermodynamic properties of silver selenide by the galvanic cell method with solid and liquid electrolytes. *Russian Journal of Electrochemistry*. 2011;47: 420–426. https://doi.org/10.1134/S1023193511040203

114. Orujlu E. N., Babanly D. M., Alakbarova T. M., Orujov N. I., Babanly M. B. Study of the solid-phase equilibria in the GeTe-Bi_2Te_3-Te system and thermodynamic properties of GeTe-rich germanium bismuth tellurides. *The Journal of Chemical Thermodynamics*. 2024;196: 107323. https://doi.org/10.1016/j.jct.2024.107323

115. Aliyev F. R., Orujlu E. N., Mashadiyeva L. F., Dashdiyeva G. B., Babanly D. M. Solid – phase equilibria and thermodynamic properties of the Sb-Te-S system. *Physics and Chemistry of Solid State*. 2024;25(1): 26–34. https://doi.org/10.15330/pcss.25.1.26-34

116. Moroz M., Tesfaye F., Demchenko P., ... Hupa L. Phase equilibria and thermodynamic properties of selected compounds in the Ag-Ga-Te-AgBr system. *Journal of Phase Equilibria and Diffusion*. 2024;45: 447–458. https://doi.org/10.1007/s11669-024-01095-x

117. Moroz M., Tesfaye F., Demchenko P., ... Gladyshevskii R. Synthesis, thermodynamic properties, and structural characteristics of multicomponent compounds in the Ag–Ni–Sn–S System. *JOM*. 2023;75: 2016–2025. https://doi.org/10.1007/s11837-023-05784-9

118. Moroz M. V., Demchenko P. Y., Tesfaye F... Reshetnyak O. V. Thermodynamic properties of selected compounds of the Ag–In–Se system determined by the electromotive force method. *Physics and Chemistry of Solid State*. 2022;23(3): 575–581. https://doi.org/10.15330/pcss.23.3.575-581

119. Babanly N. B., Orujlu E. N., Imamaliyeva S. Z., Yusibov Y. A., Babanly M. B. Thermodynamic investigation of silver-thallium tellurides by EMF method with solid electrolyte Ag_4RbI_5. *The Journal of Chemical Thermodynamics*. 2019;128: 78–86. https://doi.org/10.1016/j.jct.2018.08.012

120. Amiraslanova A. J., Mammadova A. T., Imamaliyeva S. Z., Alverdiyev I. J., Yusibov Yu. A., Babanly M. B. Thermodynamic investigation of Ag_8GeTe_6 and $Ag_8GeTe_{6-x}Se_x$ solid solutions by the emf method with a solid Ag^+ conducting electrolyte. *Russian Journal of Electrochemistry*. 2023;12: 834–842. https://doi.org/10.31857/s0424857023120034

121. Babanly M. B., Abishov V. T., Kuliev A. A. Crystal lattice of Cu(Ag)TlX compounds and phase equilibria in Cu(Ag)TlS-Cu(Ag)TlSe systems. *ChemChemTech [Izv. Vyssh. Uchebn. Zaved. Khim. Khim. Tekhnol.]*. 1981;24(8): 931–934.

122. Babanly M. B., Lee Tai Un, Kuliev A. A. Phase equilibria in CuTlS(Se)-AgTlS(Se) systems[*]. *Inorganic Materials*. 1985;21(10): 1649–1652. (In Russ.)

123. Lee Tai Un, Babanly M. B., Kuliev A. A. System AgTlS+CuTlSe«AgTlSe+CuTlS[*]. *Russian Journal of Inorganic Chemistry*. 1985;30(9): 2353–2355. (In Russ.)

124. Babanly M. B., Lee Tai Un, Kuliev A. A. Study of phase equilibria in the CuTlS-CuTlSe-AgTlTe system. *ChemChemTech [Izv. Vyssh. Uchebn. Zaved. Khim. Khim. Tekhnol.]*. 1986;29(2): 112–113.

125. Chalbaud L. M., Delgado G. D., Delgado J. M., Mora A. E., Sagredo V. Synthesis and single-crystal structural study of Cu_2GeS_3. *Materials Research Bulletin*. 1997;32(10): 1371–1376. https://doi.org/10.1016/S0025-5408(97)00115-3

126. Li Y., Cao T., Liu G., ... Zhou M. Enhanced thermoelectric properties of Cu_2SnSe_3 by (Ag, In)-Co-doping. *Advanced Functional Materials*. 2016;26: 6025–6032. https://doi.org/10.1002/adfm.201601486

127. Ma R. L., Liu G., Li Y., ... Li L. Thermoelectric properties of S and Te-doped Cu_2SnSe_3 prepared by combustion synthesis. *Journal of Asian Ceramic Societies*. 2018;1: 13–19. https://doi.org/10.1080/21870764.2018.1439609

128. Prasad S., Rao A., Gahtori B., ... Kuo Y.-K. The low and high temperature thermoelectric properties of Sb doped Cu_2SnSe_3. *Materials Research Bulletin*. 2016;83: 160–166. https://doi.org/10.1016/j.materresbull.2016.06.002

129. Ding M., Bai C., Lang Y., ...Almutairi Z. Enhanced thermoelectric performance of Cu_2SnSe_3 by synergic effects via cobalt-doping. *Journal of Alloys and Compounds*. 2024;988: 174272. https://doi.org/10.1016/j.jallcom.2024.174272

130. Ma R. L., Liu G., Li J., ... Li L. Effect of secondary phases on thermoelectric properties of Cu_2SnSe_3. *Ceramics International*. 2017;43(9): 7002–7010. https://doi.org/10.1016/j.ceramint.2017.02.126

131. Siyar M., Siyar M., Cho J. Y., ... Parker C. Thermoelectric properties of Cu_2SnSe_3-SnS. *Journal of Composite Materials*. 2019;12(13): 2040–2043. https://doi.org/10.3390/ma12132040

132. Zhao D., Wang X., Wu D. Enhanced thermoelectric properties of graphene, Cu_2SnSe_3 composites. *Crystals*. 2017;7: 71. https://doi.org/10.3390/cryst7030071

133. Yang J., Lu B., Song R., ...Qiao G.. Realizing enhanced thermoelectric properties in Cu_2GeSe_3 via a synergistic effect of In and Ag dual-doping. *Journal of the European Ceramic Society*. 2022;42(1): 169–174. https://doi.org/10.1016/j.jeurceramsoc.2021.10.009

134. Yang J., Song R., Zhao L., ...Qiao G. Magnetic Ni doping induced high power factor of Cu_2GeSe_3-based bulk materials. *Journal of the European Ceramic Society*. 2021;41(6): 3473–3479. https://doi.org/10.1016/j.jeurceramsoc.2020.12.037

135. Wang R., Li A., Huang T., ... Wang G. Enhanced thermoelectric performance in Cu_2GeSe_3 via (Ag, Ga)-co-doping on cation sites. *Journal of Alloys and Compounds*. 2018;769: 218–225. https://doi.org/10.1016/j.jallcom.2018.07.318

136. Jacob S., Delatouche B., Péré D., Jacob A., Chmielowski R. Insights into the thermoelectric properties of the Cu_2Ge $(S_{1-x}Se_x)_3$ solid solutions. *Materials Today*. 2017;4: 12349–12359. https://doi.org/10.1016/j.matpr.2017.10.003

137. Pejjai B., Reddy V. R. M., Gedi S., Park C. Review on earth-abundant and environmentally benign Cu–Sn–X(X = S, Se) nanoparticles by chemical synthesis for sustainable solar energy conversion. *Journal of Industrial and Engineering Chemistry*. 2018;60: 19–52. https://doi.org/10.1016/j.jiec.2017.09.033

138. Lokhande A. C., Chalapathy R. B. V., He M., Joo E. Development of Cu_2SnS_3 (CTS) thin film solar cells by physical techniques: A status review. *Solar Energy Materials and Solar Cells*. 2016;153: 4–107. https://doi.org/10.1016/j.solmat.2016.04.003

139. Chantana J., Chantana J., Uegaki H., Minemoto T. Influence of Na in Cu_2SnS_3 film on its physical properties and photovoltaic performances. *Thin Solid Films*. 2017;636: 431-437. https://doi.org/10.1016/j.tsf.2017.06.044

140. Chaudhari J. J., Joshi U. S. Fabrication of high quality Cu_2SnS_3 thin film solar cell with 1.12% power conversion efficiency obtain by low cost environment friendly sol-gel technique. *Materials Research Express*. 2018;5: 036203. https://doi.org/10.1088/2053-1591/aab20e

141. De Wild J., Babbe F., Robert E. V. C. Silver-doped Cu_2SnS_3 absorber layers for solar cells application. *IEEE Journal of Photovoltaics*. 2018;8: 299–304. https://doi.org/10.1109/JPHOTOV.2017.2764496

142. Oliva F., Arqués L., Acebo L. Characterization of Cu_2SnS_3 polymorphism and its impact on optoelectronic properties. *Journal of Materials Chemistry A*. 2017;5: 23863–23871. https://doi.org/10.1039/C7TA08705E

143. Zaki M. Y., Sava F., Simandan I. D., ... Galca A. C. Cu_2SnSe_3 phase formation from different metallic and binary chalcogenides stacks using magnetron sputtering. *Materials Science in Semiconductor Processing*. 2023;153: 107195. https://doi.org/10.1016/j.mssp.2022.107195

144. Pallavolu M. R., Banerjee A. N., Minnam Reddy V. R., Joo S. W., Barai H. R., Park C. Status review on the Cu_2SnSe_3 (CTSe) thin films for photovoltaic applications. *Solar Energy*. 2020;208: 1001–1030. https://doi.org/10.1016/j.solener.2020.07.095

145. Yang C., Luo Y., Xia Y., ... Cui J. Improved thermoelectric performance of *p*-type argyrodite Cu_8GeSe_6 via the simultaneous engineering of the electronic and phonon transports. *ACS Applied Materials and Interfaces Journal*. 2022;14: 16330–16337. https://doi.org/10.1021/acsami.2c02625

146. Zong P., Li Y., Negishi R., Li Z., Zhang C., Wan C. Thermoelectric performance of Cu_8SiS_6 with high electronic band degeneracy. *ACS Applied Electronic Materials Journal*. 2023;6(5): 2832–2838. https://doi.org/10.1021/acsaelm.3c00423

147. Schwarzmüller S., Souchay D., Günther D., ... Oeckler O. Argyrodite-type $Cu_8GeSe_{6-x}Te_x$ ($0 \leqslant x \leqslant 2$): temperature-dependent crystal structure and thermoelectric properties. *Zeitschrift für anorganische und allgemeine Chemie*. 2018;664: 1915–1922. https://doi.org/10.1002/zaac.201800453

148. Fan Y., Wang G., Wang R., ... Zhou X.-Y. Enhanced thermoelectric properties of *p*-type argyrodites Cu_8GeS_6 through Cu vacancy. *Journal of Alloys and Compounds*. 2020;822: 153665. https://doi.org/10.1016/j.jallcom.2020.153665

149. Jiang B., Qiu P., Eikeland E., ... Chen L. Cu_8GeSe_6-based thermoelectric materials with an argyrodite structure. *Journal of Materials Chemistry C*. 2017;5: 943–952. https://doi.org/10.1039/C6TC05068A

150. Brammertz G., Vermang B., ElAnzeery H., Sahayaraj S., Ranjbar S., Meuris M., Poortmans J. Fabrication and characterization of ternary Cu_8SiS_6 and Cu_8SiSe_6 thin film layers for optoelectronic applications. *Thin Solid Films*. 2016;616: 649–654. https://doi.org/10.1016/j.tsf.2016.09.049

151. Gao L., Lee M.-H., Zhang J. Metal-cation substitutions induced the enhancement of second harmonic generation in A8BS6 (A = Cu, and Ag; B = Si, Ge, and Sn). *New Journal of Chemistry*. 2019;43: 3719–3724. https://doi.org/10.1039/C8NJ06270F

152. Cambi L., Monselise G. G. *Gazzetta Chimica Italiana*. 1936;66: 696-700. Quoted from [153]

153. Venkatraman M., Blachnik R., Schlieper A. The phase diagrams of M_2X-SiX_2 (M is Cu, Ag; X is S, Se). *Thermochimica Acta*. 1995;249: 13–20. https://doi.org/10.1016/0040-6031(95)90666-5

154. Olekseyuk I. D., Piskach L. V., Zhbankov O. Y., Parasyuk O. V., Kogut Y. M., Phase diagrams of the quasi-binary systems Cu_2S–SiS_2 and Cu_2SiS_3–PbS and the crystal structure of the new quaternary compound Cu_2PbSiS_4. *Journal of Alloys and Compounds*. 2005;399(1-2): 149–154. https://doi.org/10.1016/j.jallcom.2005.03.086

155. Bayramova U. R., Babanly K. N., Ahmadov E. I., Mashadiyeva L. F., Babanly M. B. Phase equilibria in the Cu_2S-Cu_8SiS_6-Cu_8GeS_6 system and thermodynamic functions of phase transitions of the $Cu_8Si_{(1-x)}Ge_xS_6$ argyrodite phases. *Journal of Phase Equilibria and Diffusion*. 2023;44: 509–519. https://doi.org/10.1007/s11669-023-01054-y

156. Shpak O., Kogut Y., Fedorchuk A., Piskach L., Parasyuk O. The Cu_2Se–PbSe–$SiSe_2$ system and the crystal structure of $CuPb_{1.5}SiSe_4$. *Lesia Ukrainka Eastern European National University Scientific Bulletin. Series: Chemical Sciences*. 2014;21(298): 39–47.

157. Bayramova U. R., Babanly K. N., Mashadiyeva M. F., Yusibov Yu. A., Babanly M. B. Phase equilibria in the Cu_2Se-Cu_8SiSe_6-Cu_8GeSe_6 system. *Russian Journal of Inorganic Chemistry*. 2023;68(11): 16714–1625. https://doi.org/10.1134/s0036023623602027

158. Dogguy M., Rivet J., Flahaut J. Description du systeme ternaire Cu-Si-Te. *Journal of the Less Common Metals*. 1979;63(2): 129–145. https://doi.org/10.1016/0022-5088(79)90238-8

159. Chen X. A., Vada H., Sato A., Nozaki H. Synthesis, structure and electronic properties of Cu_2SiQ_3 (Q = S, Se). *Journal of Alloys and Compounds*. 1999;290(1-2): 91–96. https://doi.org/10.1016/s0925-8388(99)00208-x

160. Rivet J., Flahaut J., Laurelle P. Sur un groupe de composes ternaires a structure teraedrique. *Comptes Rendus Hebdomadaires des Seances de l Academie des Sciences*. 1963;257: 161–164.

161. Khanafer M., Rivet J., Flahaut J. Etude du système Cu_2S-GeS_2, Surstructure du composé Cu_2GeS_3. Transition de phase de Cu_8GeS_6. *Bulletin de la Société Chimique de France*. 1973;3: 859–862. (In French.)

162. Alverdiyev I. J. Refinement of the phase diagram of the Cu_2S-GeS_2 system. *Chemical Problems*. 2019;3(17): 423–428. https://doi.org/10.32737/2221-8688-2019-3-423-428

163. Chang Y. A., Neumann J. P., Choudary U. V. *Phase diagrams and thermodynamic properties of ternary copper-sulfur-metal systems*. Washington: International Copper Research Association; 1979. 191 p.

164. Lychmanyuk O. S., Gulay L. D., Olekseyuk I. D., Stępień-Damm J., Daszkiewicz M., Pietraszko A. Investigation of the Ho_2X_3-Cu_2X-ZX_2 (X = S, Se; Z = Si, Ge) systems. *Polish Journal of Chemistry*. 2008;81(3): 353–367.

165. Carcaly C., Chezeau N., Rivet J., Flahaut J. Description of the systeme $GeSe_2$-Cu_2Se. *Bulletin de la Société Chimique de France*. 1973;1(4): 1191–1195. (In French)

166. Rogacheva E. I., Melikhova N., Panasenko N. M. A Study of the system Cu_2Se-$GeSe_2$. *Inorganic Materials**. 1975;11(5): 719–722. (In Russ.)

167. Piskach L. V., Parasyuk O. V., Romanyuk Ya. E. The phase equilibria in the quasi-binary Cu_2GeS_3/Se_3/–CdS/Se/ systems. *Journal of Alloys and Compounds*. 2000;299(1-2): 227–231 https://doi.org/10.1016/S0925-8388(99)00797-5

168. Tomashik V. N. *Cu-Ge-Se (Copper–Germanium–Selenium)*. G. Effenberg, S. Ilyenko (eds.). Springer Materials – the Landolt-Börnstein database. 2006;11(1). p. 288–299.

169. Alverdiyev I. J. Refinement of the phase diagram of the Cu_2Se-GeSe system. *Chemical Problems*. 2019;17(3): 423–428. https://doi.org/10.32737/2221-8688-2019-3-423-42

170. Abrikosov N. Kh., Bankina V. F., Sokolova I. F. Cu-Ge-Te system*. *Inorganic Materials*. 1973;9(1): 129–131. (In Russ.)

171. Dogguy M., Carcaly C., J. Rivet, Flahaut J. Description du systeme ternaire Cu-Ge-Te. *Journal of the Less Common Metals*. 1977;51(2): 181–199. https://doi.org/10.1016/0022-5088(77)90081-9

172. Yusibov Yu. A., Abyshov V. T., Nabiyev B. A., Babanly M. B. Cu-Cu_2Te-Cu_3Ge system*. *Inorganic Materials*. 1991;27(11): 2282–2284. (In Russ.)

173. Olekseyuk I. D., Piskach L. V., Susa L. V. The Cu_2GeTe_3-CdTe system and the structure of compound $Cu_2CdGeTe_4$. *Russian Journal of Inorganic Chemistry*. 1996;41: 1356–1358.

174. Khanafer W., Rivet J., Flahaut J. Etude du ternaire Cu–Sn–S. Diagrammes d'equilibre des systémes Cu_2S–SnS, Cu_2S–Sn_2S_3 et Cu_2S–SnS_2. Etude cristallographique des composés Cu_4SnS_4, Cu_2SnS_3, $Cu_2Sn_4S_9$, et $Cu_4Sn_3S_8$. *Bulletin de la Société Chimique de France*. 1974;12: 267–276. (In French)

175. Moh G. H. Tin-containing mineral systems. Part II: Phase relations and mineral assemblage in the Cu–Fe–Zn–S system. *Chemie Der Erde*. 1975;34: 1–61.

176. Chang Y. A., Neuman J. P., Choudary U. V. Phase diagrams and thermodynamic properties of ternary copper-sulfur- metal systems: Cu-S-Sn. In: *Phase diagrams. Thermodynamic properties ternary copper- sulfur- metal systems*. 1979;7: 159–170.

177. Fiechter S., Martinez M., Schmidt G., Henrion W., Tomm Y. Phase relations and optical properties of semiconducting ternary sulfides in the system Cu–Sn–S. *Journal of Physics and Chemistry of Solids*. 2003;64(9-10): 1859–1862. https://doi.org/10.1016/S0022-3697(03)00172-0

178. Jaulmes S., Rivet J., Laruelle P. Cuivre–etain–soufre Cu_4SnS_4. *Acta Crystallographica Section B Structural Crystallography and Crystal Chemistry*. 1977;33: 540–542. https://doi.org/10.1107/s0567740877004002

179. Onoda M., Chen X., Sato A., Wada H. Crystal structure and twinning of monoclinic Cu_2SnS_3. *Materials Research Bulletin*. 2000;35: 1563–1570. https://doi.org/10.1016/S0025-5408(00)00347-0

180. Chen X., Wada H., Sato A., Mieno M. Synthesis, electrical conductivity, and crystal structure of $Cu_4Sn_7S_{16}$ and structure refinement of Cu_2SnS_3. *Journal of Solid State Chemistry*. 1998;139: 144–151. https://doi.org/10.1006/JSSC.1998.7822

181. Jemetio J. P. F., Zhou P., Kleinke H. Crystal structure, electronic structure and thermoelectric properties of $Cu_4Sn_7S_{16}$. *Journal of Alloys and Compounds*. 2006;417: 55–59. https://doi.org/10.1016/j.jallcom.2005.09.030

182. Jaulmes S., Julien Pouzol M, Rivet J., Jumas J. C., Maurin M. Structure cristalline du sulfure de cuivre et detain $CuSn_{3.75}S_8$. *Acta Crystallographica Section B Structural Crystallography and Crystal Chemistry*. 1982; B38(1): 51–54. https://doi.org/10.1107/s0567740882002027

183. Tomashik V., Lebrun N., Perrot P. *Copper-selenium-tin*. In: *Landolt–Börnstein New Series. Group IV: physical chemistry, vol. 11, ternary alloy systems. Subvolum C. Non-ferrous metal systems. Pt. 1. Selected semiconductor systems*. Verlag, Berlin, Heidelberg: Springer; 2006. p. 361–373. https://doi.org/10.1007/10915981_26

184. Rivet J., Laruelle P., Flahaut J. Phase diagrams of the SnSe-Cu_2Se and $SnSe_2$-Cu_2Se systems. Order-disorder phenomena and thermoconductivity of Cu_2SnSe_3 compound. *Bulletin de la Société Chimique de France*. 1970;(5): 1667–1670.

185. Berger L. I., Kotina E. K. Phase diagrams of the Cu_2Se-$SnSe_2$, Cu_2SnSe_3-SnSe and Cu_2Se-SnSe systems. *Inorganic Materials*. 1973;9(3): 330–322.

186. Berger L. I., Kotina E. G., Oboznenko Yu. V., Obodovskaya A. E. Cross sections of the system Cu-Sn-Se. *Inorganic Materials*. 1973;9(2): 203–207.

187. Carcaly C., Rivet J., Flahaut J. Description du système ternaire Cu-Sn-Te. *Journal of the Less Common*

Metals. 1975;41(1): 1–18. https://doi.org/10.1016/0022-5088(75)90089-2

188. Carcaly C., Rivet J., Flahaut J. Commentaires sur le système Cu-Sn-Te. *Journal of the Less Common Metals*. 1977;51(1): 165–171. https://doi.org/10.1016/0022-5088(77)90184-9

189. Tomashik V., Lebrun N. Copper-tin-tellurium. In: *Landolt–Börnstein New Series. Group IV: physical chemistry, vol. 11, ternary alloy aystems. Subvolum C. Non-ferrous metal systems. Pt. 1. Selected semiconductor systems*. Verlag, Berlin, Heidelberg: Springer; 2006. pp. 374–386. https://doi.org/10.1007/10915981_27

190. Bayramova U. R., Ahmadov E. I., Babanly D. M., Mashadiyeva L. F., Babanly M. B. Calorimetric study of phase transition of Cu_8GeSe_6 and comparison with other argyrodite family compounds. *Chemical Problems*. 2023;4(21): 396–403. https://doi.org/10.32737/2221-8688-2023-4-396-403

191. Alverdiyev I. J., Imamaliyeva S. Z., Akhmedov E. I., Yusibov Yu. A., Babanly M. B. Thermodynamic properties of some ternary compounds of the argyrodite family. *Azerbaijan Chemical Journal*. 2023;4: 21–30. https://doi.org/10.32737/0005-2531-2023-4-21-30

192. Yusibov Yu. A., Aliyeva Z. M., Babanly M. B. Thermodynamic properties of the Cu_2GeSe_3 compound. *Azerbaijan Chemical Journal*. 2023;1: 108–114. https://doi.org/10.32737/0005-2531-2023-1-108-114

193. Abbasov A. S., Aliyeva N. A., Aliyev I. Ya., Asadov Y. G., Askerova A. A. Thermodynamic properties of the Cu_2GeSe_3 and Cu_8GeSe_6. *Report of the Academy of Sciences of the Azerbaijan SSR*. 1987;42(12): 27–28.

194. Alverdiev I. J., Abbasova V. A., Yusibov Yu. A., Tagiev D. B., Babanly M. B. Thermodynamic study of Cu_2GeS_3 and $Cu_{2-x}Ag_xGeS_3$ solid solutions by the EMF method with a $Cu_4RbCl_3I_2$ solid electrolyte. *Russian Journal of Electrochemistry*. 2018;54(2): 153–158. https://doi.org/10.1134/s1023193518020027

195. Alverdiyev I. J. Thermodynamic study of Cu_2SnSe_3 by EMF method with solid electrolyte Cu_4RbCl_3I. *Azerbaijan Journal of Physics*. 2019; XXV(3): 29-33.

196. Mustafayev F. M., Abbasov A. S., Aliyev I. Ya. Thermodynamic investigation of the Cu_2S-SnS_2. *Report of the Academy of Sciences of the Azerbaijan SSR*. 1987;43(1): 51–54. (In Russ.)

197. Stolyarova T. A., Brichkina E. A., Osadchii E. G. Standard enthalpy of Cu_2SnS_3 (mohite) formation from sulfides. *Russian Journal of Inorganic Chemistry*. 2020;65: 636–639. https://doi.org/10.1134/S003602362005023X

198. Mashadieva L. F., Alieva Z. M., Mirzoeva R. Dzh., Yusibov Yu. A., Shevel'kov A. V., Babanly M. B. Phase equilibria in the Cu_2Se–$GeSe_2$–$SnSe_2$ system. *Russian Journal of Inorganic Chemistry*. 2022;67(5): 670–682. https://doi.org/10.1134/S0036023622050126

199. Bagheri S. M., Alverdiyev I. J., Aliev Z. S., Yusibov Y. A., Babanly M. B. Phase relationships in the $1.5GeS_2$+Cu_2GeSe_3«$1.5GeSe_2$ +Cu_2GeS_3 reciprocal system. *Journal of Alloys and Compounds*. 2015;625: 131–137. https://doi.org/10.1016/j.jallcom.2014.11.118

200. Alverdiyev I. J., Aliev Z. S., Bagheri S. M., Mashadiyeva L. F., Yusibov Y. A., Babanly M. B. Study of the $2Cu_2S$+$GeSe_2$↔Cu_2Se+GeS_2 reciprocal system and thermodynamic properties of the $Cu_8GeS_{6-x}Se_x$ solid solutions. *Journal of Alloys and Compounds*. 2017;691: 255–262. https://doi.org/10.1016/j.jallcom.2016.08.251

201. Amiraslanova A. J., Mammadova A. T., Alverdiyev I. J., Yusibov Yu. A., Babanly M. B. $Ag_8GeS_6(Se_6)$ – Ag_8GeTe_6 systems: phase relations, synthesis, and characterization of solid solutions. *Azerbaijan Chemical Journal*. 2023;1: 22–29. https://doi.org/10.32737/0005-2531-2023-1-22-29

202. Alverdiev I. J., Bagheri S. M., Aliyeva Z. M., Yusibov Yu. A., Babanly M. B. Phase equilibria in the Ag_2Se–$GeSe_2$–$SnSe_2$ system and thermodynamic properties of $Ag_8Ge_{1-x}Sn_xSe_6$ solid solutions. *Inorganic Materials*. 2017;53(8): 786–796. https://doi.org/10.1134/S0020168517080027

203. Abbasova V. A., Alverdiyev I. J., Mashadiyeva L. F., Yusibov Y. A., Babanly M. B. Phase relations in the Cu_8GeSe_6-Ag_8GeSe_6 system and some properties of solid solutions. *Azerbaijan Chemical Journal*. 2017;1: 30–33.

204. Abbasova V. A., Alverdiyev I. J., Rahimoglu E., Mirzoyeva R. J., Babanly M. B. Phase relations in the Cu_8GeS_6-Ag_8GeS_6 system and some properties of solid solutions. *Azerbaijan Chemical Journal*. 2017;2: 25–29.

205. Alverdiev I. J., Abbasova V. A., Yusibov Yu. A., Babanly M. B. Thermodynamic properties of the Cu_8GeS_6-Ag_8GeS_6 solid solutions. *Condensed Matter and Interphases*. 2017;19(1): 22–26. (In Russ., abstract in Eng.). https://doi.org/10.17308/kcmf.2017.19/172

206. Centeno P., Alexandre M., Neves F., ... Mendes M. J. Copper-arsenic-sulfide thin-films from local raw materials deposited via RF co-sputtering for photovoltaics. *Nanomaterials*. 2022;12(19): 3268. https://doi.org/10.3390/nano12193268

207. McClary S. A., Taheri M. M., Blach D. D., ... Agrawal R. Nanosecond carrier lifetimes in solution-processed enargite (Cu_3AsS_4) thin films. *Applied Physics Letters*. 2020;117(16): 162102. https://doi.org/10.1063/5.0023246

208. Studenyak I. P, Molnar Z. R., Makauz I. I. Deposition and optical absorption studies of Cu–As–S thin films. *Semiconductor Physics, Quantum Electronics and Optoelectronics*. 2018;21(2): 167–172. https://doi.org/10.15407/spqeo21.02.167

209. Wallace S. K., Svane K. L., Huhn W. P., ... Walsh A. Candidate photoferroic absorber materials for thin-film solar cells from naturally occurring minerals: enargite, stephanite, and bournonite. *Sustainable Energy and Fuels*. 2017;1(6): 1339–1350. https://doi.org/10.1039/C7SE00277G

210. Wallace S. K., Butler K. T., Hinuma Y., Walsh A. Finding a junction partner for candidate solar cell absorbers enargite and bournonite from electronic band and lattice matching. *Journal of Applied Physics*. 2019;125(5): 055703. https://doi.org/10.1063/1.5079485

211. Ballow R. B., Miskin K. K., Abu-Omar M. M. Synthesis and characterization of $Cu_3(Sb_{1-x}As_x)S_4$ semiconducting nanocrystal alloys with tunable properties for optoelectronic device applications. *Chemistry of Materials Journal*. 2017;29(2): 573–578. https://doi.org/10.1021/acs.chemmater.6b03850

212. Alqahtani T., Khan M. D., Lewis D. J., Zhong X. L., O'Brien P. Scalable synthesis of Cu–Sb–S phases from reactive melts of metal xanthates and effect of cationic manipulation on structural and optical properties. *Scientific*

Reports. 2021;11(1): 1–17. https://doi.org/10.1038/s41598-020-80951-5

213. Ornelas-Acosta R. E., Shaji S., Avellaneda D., Castillo G. A., Das Roy T. K., Krishnan B. Thin films of copper antimony sulfide: A photovoltaic absorber material. *Materials Research Bulletin.* 2015;61: 215–225. https://doi.org/10.1016/j.materresbull.2014.10.027

214. Vinayakumar V., Shaji S., Avellaneda D., Aguilar-Martínez J. A., Krishnan B. Copper antimony sulfide thin films for visible to near infrared photodetector applications. *RSC Advances*. 2018;8: 31055–31065. https://doi.org/10.1039/C8RA05662E

215. Van Embden J., Mendes J. O., Jasieniak J. J., Chesman A. S. R., Della Gaspera E. Solution-processed $CuSbS_2$ thin films and superstrate solar cells with CdS/In_2S_3 buffer layers. *ACS Applied Energy Materials Journal*. 2020;3(8): 7885–7895. https://doi.org/10.1021/acsaem.0c01296

216. Chalapathi U., Bhaskar P. U., Sangaraju S., Al-Asbahi B. A., Park S.-H. $CuSbS_2$ thin films and solar cells produced from Cu/Sb/Cu stacks via sulfurization. *Heliyon*. 2024;10(6): e27504. https://doi.org/10.1016/j.heliyon.2024.e27504

217. Zhang M., Wang C., Chen C., Tang J. Recent progress in the research on using $CuSbS_2$ and its derivative $CuPbSbS_3$ as absorbers in case of photovoltaic devices. *Front. Optoelectron*. 2021;14(4): 450–458. https://doi.org/10.1007/s12200-020-1024-0

218. Riha S. C., Koegel A. A., Emery J. D., Pellin M. J., Martinson A. B. F. Low-temperature atomic layer deposition of $CuSbS_2$ for thin-film photovoltaics. *ACS Applied Materials and Interfaces Journal*. 2017;9(5): 4667–4673. https://doi.org/10.1021/acsami.6b13033

219. Chalapathi U., Poornaprakash B., Ahn C. H., Park S.-H. Two-stage processed $CuSbS_2$ thin films for photovoltaics: effect of Cu/Sb ratio. *Ceramics International*. 2018;44(12): 14844–14849. https://doi.org/10.1016/j.ceramint.2018.05.117

220. Banu S., Ahn S. J., Ahn S. K., Yoon K., Cho A. Fabrication and characterization of cost-efficient $CuSbS_2$ thin film solar cells using hybrid inks. *Solar Energy Materials and Solar Cells*. 2016;151: 14–23. https://doi.org/10.1016/j.solmat.2016.02.013

221. Raju N. P., Lahiri S., Thangavel R. Electronic and optical properties of $CuSbS_2$ monolayer as a direct band gap semiconductor for optoelectronics. *AIP Conference Proceedings*. 2021;2352(1): 020001. https://doi.org/10.1063/5.0052990

222. Libório M. S., Queiroz J. C. A, Sivasankar S. M., Costa T. H. C., Cunha A. F., Amorim C. O. A review of Cu_3BiS_3 thin films: a sustainable and cost-effective photovoltaic material. *Crystals*. 2024;14(6): 524. https://doi.org/10.3390/cryst14060524

223. Nasonova D. I., Verchenko V. Yu., Tsirlin A. A., Shevelkov A. V. Low-temperature structure and thermoelectric properties of pristine synthetic tetrahedrite $Cu_{12}Sb_4S_{13}$. *Chemistry of Materials*. 2016;28(18): 6621–6627. https://doi.org/10.1021/acs.chemmater.6b02720

224. Hathwar V. R., Nakamura A., Kasai H., ... Nishibori E. Low-temperature structural phase transitions in thermoelectric tetrahedrite, $Cu_{12}Sb_4S_{13}$, and Tennantite, $Cu_{12}As_4S_{13}$. *Crystal Growth and Design Journal*. 2019;19(7): 3979–3988. https://doi.org/10.1021/acs.cgd.9b00385

225. Yaroslavzev A. A., Kuznetsov A. N., Dudka A. P., Mironov A. V., Buga S. G., Denisov V. V. Laves polyhedra in synthetic tennantite, $Cu_{12}As_4S_{13}$, and its lattice dynamics. *Journal of Solid State Chemistry*. 2021;297: 122061. https://doi.org/10.1016/j.jssc.2021.122061

226. Tanishita T., Suekuni K., Nishiate H., Lee C.-H., Ohtaki M. A strategy for boosting thermoelectric performance of famatinite Cu_3SbS_4. *Physical Chemistry Chemical Physics*. 2020;22(4): 2081–2086. https://doi.org/10.1039/c9cp06233e

227. Du B., Zhang R., Chen K., Mahajan A., Reece M. J. The impact of lone-pair electrons on the lattice thermal conductivity of the thermoelectric compound $CuSbS_2$. *Journal of Materials Chemistry A*. 2017;5(7): 3249–3259. https://doi.org/10.1039/C6TA10420G

228. Chetty R., Bali A., Mallik R. C. Tetrahedrites as thermoelectric materials: an overview. *Journal of Materials Chemistry C*. 2015;3(48): 12364–12378. https://doi.org/10.1039/c5tc02537k

229. Suekuni K., Takabatake T. Research update: Cu–S based synthetic minerals as efficient thermoelectric materials at medium temperatures. *ACS Applied Materials and Interfaces Journal*. 2016;4(10): 104503–104513. https://doi.org/10.1063/1.4955398

230. Levinsky P., Candolfi C., Dauscher A., Tobola J., Hejtmánek J., Lenoir B. Thermoelectric properties of the tetrahedrite–tennantite solid solutions $Cu_{12}Sb_{4-x}As_xS_{13}$ and $Cu_{10}Co_2Sb_{4-y}As_yS_{13}$ ($0 \leqslant x, y \leqslant 4$). *Physical Chemistry Chemical Physics*. 2019;21(8): 4547–4555. https://doi.org/10.1039/C9CP00213H

231. Powell A. V. Recent developments in Earth-abundant copper-sulfide thermoelectric materials. *Journal of Applied Physics*. 2019;126(10): 100901. https://doi.org/10.1063/1.5119345

232. Hobbis D., Wang H., Martin J., Nolas G. S. Thermal properties of the very low thermal conductivity ternary chalcogenide $Cu_4Bi_4M_9$ (M = S, Se). *Physica Status Solidi (RRL) – Rapid Research Letters*. 2020;14(8). https://doi.org/10.1002/pssr.202000166

233. Ye Z., Peng W., Wang F., ... Wang J. Quasi-layered crystal structure coupled with point defects leading to ultralow lattice thermal conductivity in *n*-type $Cu_{2.83}Bi_{10}Se_{16}$. *ACS Applied Energy Materials*. 2021;4(10): 11325–11335. https://doi.org/10.1021/acsaem.1c02154

234. Bhui A., Dutta M., Mukherjee M., ... Biswas K. Ultralow thermal conductivity in Earth-abundant $Cu_{1.6}Bi_{4.8}S_8$: anharmonic rattling of interstitial Cu. *Chemistry of Materials*. 2021;33(8): 2993–3001. https://doi.org/10.1021/acs.chemmater.1c00659

235. Aishwarya K., Maruthasalamoorthy S., Thenmozhi R., ... Navamathavan R. Enhanced seebeck coefficient of Cu-Bi-S heterogeneous composite synthesized via solvothermal method. *ECS Journal of Solid State Science and Technology*. 2023;12(12): 123005. https://doi.org/10.1149/2162-8777/ad13b1

236. Mikuła A., Mars K., Nieroda P., Rutkowski P. Copper chalcogenide–copper tetrahedrite composites—a new concept for stable thermoelectric materials based on the chalcogenide system. *Materials*. 2021;14(10): 2635. https://doi.org/10.3390/ma14102635

237. Rikel M., Harmelin M., Prince A. Arsenic-copper-sulfur system. In: *Ternary alloys*. Petzow G., Effenberg G., Aldinger F. (eds.). Weinheim: VGH; 1994;11: 109–127.

238. Pfitzner A., Bernert T. The system Cu_3AsS_4-Cu_3SbS_4 and investigations on normal tetrahedral structures. *Zeitschrift für Kristallographie - Crystalline Materials*. 2004;219(1): 20–26. https://doi.org/10.1524/zkri.219.1.20.25398

239. Maske S., Skinner B. J. Studies of the sulfosalts of copper: I. phases and phase relations in the system Cu-As-S. *Economic Geology*. 1971;66: 901–918. https://doi.org/10.2113/gsecongeo.66.6.901

240. Makovicky E., Skinner B. J. Studies of the sulfosalts of copper: IV. Structure and twinning of sinnerite, $Cu_6As_4S_9$. *American Mineralogist*. 1975;60: 998–1012.

241. Kurz G., Blachnik R. New aspects of the system Cu-As-S. *Journal of the Less Common Metals*. 1989;155: 1–8. https://doi.org/10.1016/0022-5088(89)90441-4

242. Prostakova V., Shishin D., Jak E. Thermodynamic optimization of the Cu–As–S system. *Calphad*. 2021;72: 102247. https://doi.org/10.1016/j.calphad.2020.102247

243. Gasanova Z. T., Mashadieva L. F., Yusibov Y. A., Babanly M. B. Phase equilibria in the Cu_2S–Cu_3AsS_4–S system. *Russian Journal of Inorganic Chemistry*. 2017;62(5): 591–597. https://doi.org/10.1134/S0036023617050126

244. Gasanova Z. T., Aliev Z. S., Yusibov Y. A., Babanly M. B. Phase equilibria in the Cu-Cu_2S-As system. *Russian Journal of Inorganic Chemistry*. 2012;57(8): 1158–1162. https://doi.org/10.1134/s0036023612050075

245. Babanly M. B., Gasanova Z. T., Mashadieva L. F., Zlomanov V. P., Yusibov Y. A. Thermodynamic study of the Cu-As-S system by EMF measurements with $Cu_4RbCl_3I_2$ as a solid electrolyte. *Inorganic Materials*. 2012;48(3): 225–228. https://doi.org/10.1134/s0020168512020021

246. Mashadiyeva L. F., Babanly D. M., Hasanova Z. T., Yusibov Yu. A., Babanly M. B. Phase relations in the Cu-As-S system and thermodynamic properties of copper-arsenic sulfides. *Journal of Phase Equilibria and Diffusion*. 2024. (In press.)

247. Khvorostenko A. S., Kirilenko V. V., Popov B. I. Phase diagram of the As_2Se_3–Cu_2Se system*. *Inorganic Materials*. 1972;8(1): 73–79. (In Russ.)

248. Blachnik R., Kurz G. Compounds in the system Cu_2Se-As_2Se_3. *Journal of Solid State Chemistry*. 1984;55(2): 218–224. https://doi.org/10.1016/0022-4596(84)90267-6

249. Gambi L, Elli M. La chimica et I'industria. 1968;50: 94–98.

250. Cohen K., Rivet J., Dugue J. J. Description of the Cu – As – Se ternary system. *Journal of Alloys and Compounds*. 1995;224(2): 316–329. https://doi.org/10.1016/0925-8388(95)01534-5

251. Blachnik R., Gather B. Enthalpies of melting of some ternary ABX_2-compounds. *Zeitschrift fuer Naturforschung*. 1972;327: 1417–1413. https://doi.org/10.1515/znb-1972-1129

252. Mashadieva L. F., Gasanova Z. T., Yusibov Yu. A., Babanly M. B. Phase equilibria in the Cu–Cu_2Se–As system. *Russian Journal of Inorganic Chemistry*. 2017;62(5): 598–603. https://doi.org/10.1134/S0036023617050151

253. Mashadieva L. F., Gasanova Z. T., Yusibov Yu. A., Babanly M. B. Phase Equilibria in the Cu_2Se–Cu_3AsSe_4–Se system and thermodynamic properties of Cu_3AsSe_4. *Inorganic Materials*. 2018;54(1): 8–16. https://doi.org/10.1134/S0020168518010090

254. Mashadiyeva L. F., Hasanova Z. T., Yusibov Yu. A., Babanly M. B. Phase equilibria in the Cu_2Se–Cu_3AsSe_4–As_2Se_3 system. *Azerbaijan Chemical Journal*. 2024;3: 83–93. https://doi.org/10.32737/0005-2531-2024-3-83-93

255. Hasanova Z. T. Thermodynamic study of the $CuAsSe_2$ compound by EMF method with solid electrolyte. *New Materials, Compounds and Applications*. 2021;5(3): 205–211. Available at: http://jomardpublishing.com/UploadFiles/Files/journals/NMCA/V5N3/Hasanova.pdf

256. Peccerillo E., Durose K. Copper–antimony and copper–bismuth chalcogenides —Research opportunities and review for solar photovoltaics. *MRS Energy and Sustainability*. 2018;5: 1–56. https://doi.org/10.1557/mre.2018.10

257. Cui J., Zhang Y., Hao X., Liu X., Shen Y. Thermodynamic calculation of S–Sb system and Cu–S–Sb system. *Calphad*. 2021;75: 102362. https://doi.org/10.1016/j.calphad.2021.102362

258. Cambi L., Elli M. Processi idrotermali, sintesi di solfosali da ossidi di metalli e metalloidi, nota II—Cuprosolfoantimoniti. *La Chimica el'Industria,* 1965;47: 136–147.

259. Kuliev R. A., Krestovnikov A. N., Glazov V. M. Synthesis and thermodynamic properties of alloys of the Cu_2S-Sb_2S_3 system. *Russian Journal of Physical Chemistry*. 1969;43(12): 3063–3066.

260. Ilyasheva N. A. Study of the Cu_2S-Sb_2S_3 system at 320–400 °C*. *Inorganic Materials*. 1963;9(10): 1677–1679. (In Russ.)

261. Mashadiyeva L. F., Mammadli P. R., Babanly D. M., Ashirov G. M., Shevelkov A. V., Yusibov Y. A. Solid-phase equilibrium in the Cu-Sb-S ternary system and thermodynamic properties of ternary phases. *JOM*. 2021;73(5): 1522-1530. https://doi.org/10.1007/s11837-021-04624-y

262. Mashadiyeva L. F., Babanly D. M., Poladova A. N., Yusibov Y. A., Babanly M. B. Liquidus surface and phase relations in the Cu-Sb-S system. In: *Properties and Uses of Antimony*. David J. Jenkins (ed.). *Nova Science Publishers*. 2022: 45-72. https://doi.org/10.52305/OJKB5395

263. Bryndzia L. T., Kleppa O. J. High-temperature reaction calorimetry of solid and liquid phases in part of the quasi-binary system Cu_2S-Sb_2S_3. *American Mineralogist*. 1988;73(7-8): 707–713.

264. Kyono A., Kimata M. Crystal structures of chalcostibite ($CuSbS_2$) and emplectite ($CuBiS_2$): Structural relationship of stereochemical activity between chalcostibite and emplectite. *American Mineralogist*. 2005;90(1): 162–165 https://doi.org/10.2138/am.2005.1585

265. Lemoine P., Bourgès C., Barbier T., Nassif V., Cordier S., Guilmeau E. High temperature neutron powder diffraction study of the $Cu_{12}Sb_4S_{13}$ and $Cu_4Sn_7S_{16}$ phases. *Journal of Solid State Chemistry*. 2017;247: 83–89. https://doi.org/10.1016/j.jssc.2017.01.003

266. Pfitzner A. Cu_3SbS_3: Zur Kristallstruktur und Polymorphie. *Zeitschrift für anorganische und allgemeine Chemie*., 1994;620: 1992–1997. https://doi.org/10.1002/zaac.19946201126

267. Pfitzner A., Reiser S. Refinement of the crystal structures of Cu_3PS_4 and Cu_3SbS_4 and a comment on normal tetrahedral structures. *Zeitschrift für Kristallographie*. 2002;217(2): 51–54. https://doi.org/10.1524/zkri.217.2.51.20632

268. Golovey M. I., Tkachenko V. I., Rigan M. Yu., Stasyuk N. P. State diagram of the Cu_2Se-Sb_2Se_3 system in the region of existence of the $CuSbSe_2$ compound*. *Inorganic Materials*. 1990;26(5): 933–934. (In Russ)

269. Scott W, Conch J. R. Phase diagram and properties of Cu_3SbSe_4 and other $A_3^{I}B^{V}C_4^{VI}$ compounds. *Materials Research Bulletin*. 1973;8(10): 1257–1267. https://doi.org/10.1016/0025-5408(73)90164-5

270. Shtykova M. A., Molokeev M. S., Zakharov B. A., ... Andreev O. V. Structure and properties of phases in the $Cu_{2-x}Se$-Sb_2Se_3 system. The $Cu_{2-x}Se$-Sb_2Se_3 phase diagram. *Journal of Alloys and Compounds*. 2022;906: 164384. https://doi.org/10.1016/j.jallcom.2022.164384

271. Liu R., Wang J., Cui D. Thermodynamic modeling of the Cu-Sb-Se system. *Journal of Phase Equilibria and Diffusion*. 2023;44: 687–703. https://doi.org/10.1007/s11669-023-01074-8

272. Pfitzner A. Crystal structure of tricopper tetraselenoantimonate (V), Cu_3SbSe_4 *Zeitschrift für Kristallographie – Crystalline Materials*. 1994;209: 685. https://doi.org/10.1524/zkri.1994.209.8.685

273. Chorba O., Filep M., Pogodin A., Malakhovska T., Sabov M. Crystals growth and refinement of the Cu_3SbSe_3 crystal structure. *Ukrainian Chemistry Journal*. 2022; 88(9): 25–33. https://doi.org/10.33609/2708-129X.88.09.2022.25-33

274. Schwarzmüller S., Amsler M., Goedecker S., Huppertz H. 4p-pavonite-type $Cu_{1.8}Sb_{5.4}Se_9$: a one-dimensional copper ion conductor. *SSRN*. 2024. https://doi.org/10.2139/ssrn.4852905

275. Buhlman B. Untersuchungen im System Bi_2S_3-Cu_2S und geologische Schlussfolgerungen. *Neues Jahrbuch für Mineralogie, Monatshefte*. 1971: 137–141.

276. Gather B., Blachnik R. Temperature-composition diagrams in the Cu_2(VIb)-(Vb) sections of the ternary Cu-(Vb)-(VIb) systems (Vb = As, Sb, Bi, VIb = S, Se, Te). *Journal of the Less Common Metals*. 1976;48(2): 205–212. https://doi.org/10.1016/0022-5088(76)90003-5

277. Golovey M. I., Voroshilov Yu. V., Potoriy M. V. Study of Cu (Ag, Tl)-B^{V}-Se systems. *ChemChemTech [Izv. Vyssh. Uchebn. Zaved. Khim. Khim. Tekhnol.]*. 1985;28(1): 7–11.

278. Liautard B., Garcia J. C., Brun G., Tedenac J. C., Maurin M. Crystal structure of $Cu_{(1+3x)}Bi_{(5-x)}X_8$ (X = S,Se) alloys. *European Journal of Solid State and Inorganic Chemistry*. 1990;27: 819–830. https://doi.org/10.1002/chin.199108005

279. Babanly N. B., Yusibov Yu. A., Aliyev Z. S., Babanly M. B. Phase equilibria in the system Cu-Bi-Se and thermodynamic properties of selenobismuthides of copper. *Russian Journal of Inorganic Chemistry*. 2010;55(9): 1471–1481. https://doi.org/10.1134/S0036023610090238

280. Prostakova V., Shishin D., Jak E. Thermodynamic optimization of the Cu–As–S system. *Calphad*. 2021;72: 102247. https://doi.org/10.1016/j.calphad.2020.102247

281. Sugaki A., Kitakaze A., Hayashi K. Synthesis of minerals in the Cu-Fe-Bi-S system under hydrothermal condition and their phase relations. *Bulletin de Minéralogie*. 1981;104: 484-495. https://doi.org/10.3406/bulmi.1981.7499

282. Filippou D., Germain P., Grammatikopoulos T. Recovery of metal values from copper—arsenic minerals and other related resources. *Mineral Processing and Extractive Metallurgy Review*. 2007;28: 247–298. https://doi.org/10.1080/08827500601013009

283. Zikanova T. A., Muldagalieva R. A., Kuzgibekova Kh., Isabaev S. M. Heat capacity and thermodynamic functions of copper orthoarsenate. *High Temperatu*. 2000;38(3): 492–493. https://doi.org/10.1007/bf02756014

284. Skinner B. J., Luce F. D., Makovicky E. Studies of the sulfosalts of copper: III Phases and phase relations in the system Cu-Sb-S. *Economic Geology*. 1972;67: 924–938. https://doi.org/10.2113/GSECONGEO.67.7.924

285. Babanly N. B., Yusibov Y. A., Mirzoyeva R. J., Shykhiyev Yu. M., Babanly M. B. $Cu_4RbCl_3I_2$ solid superionic conductor in thermodynamic study of three-component copper chalcogenides. *Russian Journal of Electrochemistry*. 2009;45(4): 405–410. https://doi.org/10.1134/s1023193509040089

286. Tkachenko V. I., Regan M. Yu., Voroshilov Yu. V., Golovey M. I. In: *Abstracts of reports. IV All-Union. Council on chemistry and technology of chalcogens and chalcogenides**. Karaganda; 1980. p. 200. (In Russ.)

**Translated by author of the article*

Information about the authors

Mahammad B. Babanly, DSc in Chemistry, Professor, Associate Member of the Azerbaijan National Academy of Sciences, Deputy-director of the Institute of Catalysis and Inorganic Chemistry (Baku, Azerbaijan).
https://orcid.org/0000-0001-5962-3710
babanlymb@gmail.com

Leyla F. Mashadieva, PhD in Chemistry, Senior Scientific Fellow of Institute of Catalysis and Inorganic Chemistry (Baku, Azerbaijan).
https://orcid.org/0000-0003-2357-6195
leylafm76@gmail.com

Samira Z. Imamaliyeva, DSc in Chemistry, Assistance Professor, Institute of Catalysis and Inorganic Chemistry (Baku, Azerbaijan).
https://orcid.org/0000-0001-8193-2122
samira9597a@gmail.com

Dunya M. Babanly, DSc in Chemistry, Assistance Professor, French-Azerbaijani University (Baku, Azerbaijan).
https://orcid.org/0000-0002-8330-7854
dunya.babanly@ufaz.az

Dilgam B. Taghiyev, Academician of the Azerbaijan National Academy of Sciences, Director of the Institute of Catalysis and Inorganic Chemistry (Baku, Azerbaijan).
https://orcid.org/0000-0002-8312-2980
dtagiyev@rambler.ru

Yusif A. Yusibov, DSc in Chemistry, Professor, Rector of the Ganja State University (Ganja, Azerbaijan).
https://orcid.org/0000-0003-4081-6170
yusifyusibov1951@gmail.com

Received 03.06.2024; approved after reviewing 21.06.2024; accepted for publication 16.09.2024; published online 25.12.2024.

Translated by Valentina Mittova

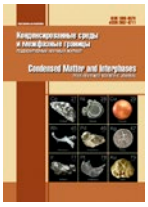

ISSN 1606-867X (Print)
ISSN 2687-0711 (Online)
Condensed Matter and Interphases
Kondensirovannye Sredy i Mezhfaznye Granitsy
https://journals.vsu.ru/kcmf/

Review

Review article
https://doi.org/10.17308/kcmf.2024.26/12384

Functional borates and their high-pressure polymorphic modifications. Review

T. B. Bekker[1,2]✉, A. V. Davydov[1,2], N. E. Sagatov[1,2]

[1]*V. S. Sobolev Institute of Geology and Mineralogy of the Siberian Branch of the Russian Academy of Sciences, 3 Ac. Koptyuga ave., Novosibirsk 630090, Russian Federation*

[2]*Novosibirsk State University*
1 Pirogova st., Novosibirsk 630090, Russian Federation

Abstract

The article presents the results of many years of studies of the growth of a low-temperature modification of barium borate β-BaB_2O_4 (*R*3*c*) crystals in the Na, Ba, B // O, F quaternary reciprocal system. Barium borate β-BaB_2O_4 is the most important nonlinear optical crystal of the UV spectrum. The key factor determining the quality of crystals is the choice of an optimal solvent. The article presents phase diagrams and the results of the growth of β-BaB_2O_4 crystals in several subsystems of the studied quaternary reciprocal system. Using atomistic modeling, we predicted and then experimentally obtained new high-pressure modifications: γ-BaB_2O_4 ($P2_1/n$), whose structure includes edge-sharing tetrahedra, and d-BaB_2O_4 with assumed symmetry $Pa\bar{3}$. In our study, we also focused on a solid solution with an "antizeolite" structure, which also crystallizes in the Na, Ba, B // O, F system.

Keywords: Low-temperature modification of barium metaborate, Quaternary reciprocal system, High-temperature solution growth, Borates with "antizeolite" structure

Funding: The study was supported by the Russian Science Foundation grant No. 24-19-00252, https://rscf.ru/project/24-19-00252/

For citation: Bekker T. B., Davydov A. V., Sagatov N. E. Functional borates and their high-pressure polymorphic modifications. Review. *Condensed Matter and Interphases*. 2024;26(4): 620–632. https://doi.org/10.17308/kcmf.2024.26/12384

Для цитирования: Беккер Т. Б., Давыдов А. В., Сагатов Н. Е. Функциональные бораты и их высокобарические полиморфные модификации. Обзор. *Конденсированные среды и межфазные границы*. 2024;26(4): 620–632. https://doi.org/10.17308/kcmf.2024.26/12384

✉ Tatyana B. Bekker, e-mail: bekker@igm.nsc.ru, t.b.bekker@gmail.com

1. Introduction

Modifications of barium metaborate, α-BaB_2O_4 ($R\bar{3}c$) and β-BaB_2O_4 ($R3c$), are important materials with birefringent and nonlinear optical properties in the UV and visible spectra respectively. Low-temperature non-centrosymmetric modification β-BaB_2O_4 is widely used for the generation of the fourth and fifth harmonics of $Y_3Al_5O_{12}$:Nd^{3+} lasers (266 and 213 nm respectively), and as optical parametric generators and amplifiers [1–4]. β-BaB_2O_4 crystals are characterized by a wide transparency range (from 185 to 2500 nm), high nonlinear optical susceptibility (d_{22} (1064 nm) = 2.2 pm/V, d_{22} = 5.7d_{36} (KDP), an acceptable birefringence value (Δn = 0.113 (1064 nm)), a low light dispersion in the range from 204 to 1500 nm, and good physical and chemical properties [5].

The melting point of the high-temperature modification α-BaB_2O_4 is 1100 °C. Due to the α-β phase transition at a temperature of 925 °C the main method of growing β-BaB_2O_4 crystals is the high-temperature solution growth method, which ensures crystallization before the phase transition temperature is reached. The key factor determining the actual structure and optical quality of crystals is the choice of an optimal solvent. Earlier we suggested combining the main solvents used for the growth of β-BaB_2O_4 crystals, namely Na_2O [6] and components of the BaO–Na_2O–B_2O_3 ternary system [7–9], NaF [10–13] and BaF_2 [14, 15, 16], into a single quaternary reciprocal system Na, Ba, B // O, F [1, 17, 18]. Composition diagrams of quaternary reciprocal systems containing six salts A, B, C // X, Y are presented as a trigonal prism according to Jänecke [19]. A polytope of the Na, Ba, B // O, F system is shown in Fig. 1. The compositions of individual phases are presented in Table 1. Presented below are the results of the growth of β-BaB_2O_4 crystals performed using six solvents and the results of the synthesis of two new polymorphic modifications of BaB_2O_4 at high temperatures and pressures.

The Na, Ba, B // O, F system also includes a composition range of the solid solution of borates with an "antizeolite" structure. The structure of the solution is based on the $\{Ba_{12}(BO_3)_6\}^{6+}$ framework with channels along the *c* axis built of barium cubes and anticubes. The general formula of the solid solution in *this system* can be presented as $\{Ba_{12}(BO_3)_6\}[(F_2)_x(BO_3)_{1-x}][(F_4)_x(NaF_4)_y(BO_3)_{1-x-y}]$, where $x + y \leqslant 1$, and $[(F_2)_x(BO_3)_{1-x}]^{3-}$ and $[(F_4)_x(NaF_4)_y(BO_3)_{1-x-y}]^{3-}$ – are anionic groups in the barium anticubes and cubes, respectively. Fig. 1 shows a crosshatched triangle whose vertices contain experimentally determined phases: $Ba_3(BO_3)_2$, $\{Ba_{12}(BO_3)_6\}[BO_3][BO_3]$, x = 0, y = 0 [23], $Ba_3(BO_3)_{1.8}F_{0.6}$, $\{Ba_{12}(BO_3)_6\}[(F_2)_{0.4}(BO_3)_{0.6}][(F_4)_{0.4}(BO_3)_{0.6}]$, x = 0.4, y = 0 [24] and $NaBa_{12}(BO_3)_7F_4$, $\{Ba_{12}(BO_3)_6\}[BO_3][NaF_4]$, x = 0, y = 1 [22]. The $NaBa_{12}(BO_3)_7F_4$ phase was first described in [25] as having a centrosymmetric *I*4/*mcm* structure.

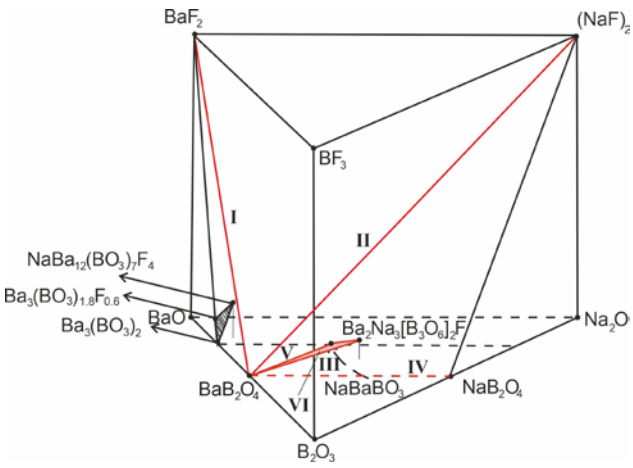

Fig. 1. Polytope of the quaternary reciprocal system Na, Ba, B // O, F. Subsystems used for growing β-BaB_2O_4 crystals: I BaB_2O_4–BaF_2, II BaB_2O_4 – $(NaF)_2$, III BaB_2O_4 – $Ba_2Na_3[B_3O_6]_2F$, IV BaB_2O_4 – $(NaBO_2)_2$, V BaB_2O_4 – 30 $NaBaBO_3$, VI 70BaB_2O_4 – $NaBaBO_3$ – $Ba_2Na_3[B_3O_6]_2F$

Table 1. Compositions of individual phases of the quaternary reciprocal system Na, Ba, B // O, F

Chemical formula	Compositions, mol %				Syngony, sp. gr., Z	Reference
	BaO	Na_2O	B_2O_3	BaF_2		
$NaBaBO_3$	50	25	25	–	Monoclinic, *C*2/*m*, 4	[20]
$Ba_2Na_3[B_3O_6]_2F$	23.1	23.1	46.1	7.7	Hexagonal, $P6_3/m$, 2	[21]
$NaBa_{12}(BO_3)_7F_4$	62.5	3.1	21.9	12.5	Tetragonal, $P4_2bc$, 4	[22]

However, this was not confirmed by the results of our X-ray structural analysis [22]. In this article we briefly describe the conditions for the growth of the $NaBa_{12}(BO_3)_7F_4$ phase and analyze the stability of the $Ba_3(BO_3)_{1.8}F_{0.6}$ phase at high temperatures and pressures.

2. Experimental research methods

2.1. High-temperature solution growth of β-BaB_2O_4 and NaBa12(BO3)7F4 crystals

β-BaB_2O_4 crystals were grown from high-temperature solutions in a top seed solution growth (TSSG) furnace. The compositions of the used high-temperature solutions I–VI are given in Table 2.

The starting materials were commercially available extra pure reagents $BaCO_3$, Na_2CO_3, H_3BO_3, NaF, and BaF_2. The initial batch weighing about 2 kg, whose composition corresponded to those presented in Table 2, was prepared by means of solid-phase synthesis and then melted in a platinum crucible (standard diameter of 80 and 100 mm). After determining the equilibrium temperature, a crystal seed was placed in contact with the top surface of the high-temperature solution; the seed was oriented along the optical axis and had a cross-section of 5×5 mm^2. The crystals were grown by constantly revolving the seed at a speed of 1 r/min. The cooling and pulling rates varied from 0.4 to 2 °C/day and from 0.5 to 0.1 mm/day respectively. In order to use the solution multiple times, β-BaB_2O_4 was added after each growth cycle obtained by means of solid-phase synthesis from metaboric acid HBO_2 and barium carbonate $BaCO_3$. The weight of the added β-BaB_2O_4 corresponded to the weight of the grown crystals.

$NaBa_{12}(BO_3)_7F_4$ crystals were grown from 38 mol % BaO, 36 mol % BaF_2, 13 mol % B_2O_3, and 13 mol % Na_2O compositions; the starting materials were the same commercially available reagents as used for the growth of β-BaB_2O_4 crystals. After the solid-phase synthesis, the batch (300 g) was melted in a platinum crucible (diameter 60 mm). To grow the crystals, a crystal seed was used oriented along the [001] axis with constant pulling (0.3 mm/day) and revolving (1 r/min). The weight of the grown crystal was about 30 g.

2.2. Synthesis at high temperatures and pressures

Based on the ab initio calculations, we predicted the existence of two high-pressure polymorphic modifications of BaB_2O_4, which we denoted as γ-BaB_2O_4 and δ-BaB_2O_4. These modifications are stable under pressures above 0.9 GPa and 6.1 GPa respectively [14]. According to the calculations, δ-BaB_2O_4 is isostructural to CaB_2O_4 – $Pa\bar{3}$ [15].

We synthesized the new high-pressure modification γ-BaB_2O_4 using a Discoverer-1500 multi-anvil hydraulic press of the DIE type at a pressure of 3 GPa and a temperature of 900 °C [26]. The experiment lasted 24 hours. The anvils were 26 mm cubes of tungsten carbide. The medium of pressure transmission was semi-sintered ceramics ZrO_2 in the shape of an octahedron with the edge of 20.5 mm. Conducting another experiment at a pressing force of 6 GPa, which is the maximum pressure for the hydraulic press used, and a temperature of 900 °C for 48 hours, we also obtained the phase γ-BaB_2O_4. In both experiments the initial samples were

Table 2. Characteristics of high-temperature solutions used for growing β-BaB_2O_4 crystals

№	Compositions (mol %)	Na (wt. %)	ΔT_{theor} (°C)	K_{theor} / K_{exp} (g/(kg·°C))	Reference
I	54.5 BaB_2O_4 – 45.5 BaF_2	–	165	1.58 / 1.05,0.72	[18, 39]
II	79.9 BaB_2O_4 – 20.1 $(NaF)_2$ 60 BaB_2O_4 – 20 $Ba_2Na_3[B_3O_6]_2F$ – 20 BaF_2	**4.75**	125	3.63 / 2.76,2.02	[13]
III	60 BaB_2O_4 – 40 $Ba_2Na_3[B_3O_6]_2F$	**7.22**	100	3.09 / 2.85,2.39	[39, 30]
IV	70 BaB_2O_4 – 30 $(NaBO_2)_2$	**7.05**	94	3.83 / 3.22,3.20	[34, 35]
V	70 BaB_2O_4 – 30 $NaBaBO_3$	**3.11**	115	2.49 / 1.89,1.60	[40]
VI	70BaB_2O_4 – 22.5$NaBaBO_3$ – 7.5$Ba_2Na_3[B_3O_6]_2F$	**4.09**	120	2.80 / 2.2,2.03	[18, 39]

polycrystalline β-BaB_2O_4 obtained by means of solid-phase synthesis.

Up to the present moment, the fourth modification δ-BaB_2O_4 has only been obtained as a product of decomposition of barium-sodium metaborate $Ba_2Na_3(B_3O_6)_2F$ in an experiment conducted at a pressure of 6 GPa and a temperature of 900 °C for 64 hours [27]. The initial sample was a grounded $Ba_2Na_3(B_3O_6)_2F$ crystal.

The stability of the $Ba_3(BO_3)_{1.8}F_{0.6}$ phase was analyzed at 3 GPa and 1000 °C for 5 hours. The initial sample was a grounded $Ba_3(BO_3)_{1.8}F_{0.6}$ crystal.

During all the experiments, polycrystalline samples were put into holes in graphite cassettes. The diameter of the holes was 0.9 mm and the depth was 1.1 mm. Each sample was covered with an individual graphite lid. The temperature gradient between the low-temperature (LT) and high-temperature (HT) regions of the samples at 900 °C was about 5°C. The design of the high-pressure cell was detailed in [28].

2.3. Analytical research methods

The samples synthesized at high temperatures and pressures were filled with epoxy resin and polished. Due to the small size of the synthesized samples, whose crystals are usually no bigger than tens of micrometers, the main analysis method was scanning electron microscopy (MIRA 3 LMU, Tescan Orsay Holding) using an INCA 450 energy-dispersive microanalysis system with a large area EDS X-Max-80 Silicon Drift Detector.

Raman spectroscopy was also used to determine the composition and the polymorphic modification of each phase. Raman spectra were registered using a Horiba Jobin Yvon LabRAM HR800 spectrometer with a 1024-pixel LN/CCD detector. The wavelength of the Nd-YAG laser was 532 nm. Raman spectra were measured in the backscattering geometry using an Olympus BX41 microscope. The spectral resolution was ~2.0 cm^{-1}. The microscope with an Olympus 100× lens, WD = 0.37 mm with a numerical aperture for the visible spectrum had a focal diameter of ~2 μm. The power of laser radiation was 0.5 mW to prevent the heating of the sample.

The study was conducted using the equipment of the Centre for Collective Use of Scientific Equipment of the Institute of Geology and Mineralogy of the Siberian Branch of the Russian Academy of Sciences.

3. Results and discussion

3.1. Growth of β-BaB_2O_4 and $NaBa_{12}(BO_3)_7F_4$ crystals

Presented below is a brief description of the six systems used for the growth of β-BaB_2O_4 crystals (Table 2). Besides the compositions of the initial high-temperature solutions, Table 2 presents some additional characteristics, namely the concentration of sodium in the initial high-temperature solution, theoretical crystallization intervals (ΔT_{theor}), and theoretical and experimental yield coefficients (K_{theor} / K_{exp}). Theoretical crystallization interval (ΔT_{theor}) is a temperature range corresponding to the region of primary crystallization of β-BaB_2O_4 in the system. The theoretical yield coefficient (K_{theor}) is the difference (in grams) in the concentration of BaB_2O_4 in 1 kg of the high-temperature solution in the compositions limiting the region of primary crystallization of β-BaB_2O_4 divided by the theoretical crystallization interval. Therefore, the yield coefficient is measured in g/(kg×°C). Both parameters (the theoretical crystallization interval and the theoretical yield coefficient) are determined based on the phase diagram of the system. The experimental yield coefficient is determined as the weight of the grown crystal divided by the weight of the initial high-temperature solution and by the crystallization interval specific for each experiment.

I BaB_2O_4 – BaF_2. The melting point of BaF_2 is 1353 °C. The coordinates of the eutectic points are 41 mol % BaB_2O_4, 59 mol % BaF_2, 760 °C [18], the theoretical yield coefficient is 1.58 g/(kg×°C). A significant difference between the experimental and theoretical yield coefficients, as well as the drop of the experimental coefficient from 1.05 to 0.72 g/(kg×°C) in three consequent experiments can be explained by a rapid pyrohydrolysis of barium fluoride. During the third consequent experiment, co-crystallization of phases β-BaB_2O_4 and $Ba_5B_4O_{11}$ took place, which can be described by the following reactions:

$$BaF_2 + H_2O \rightarrow BaO + 2HF\uparrow \quad (1)$$

$$2BaB_2O_4 + 2BaO \rightarrow Ba_5B_4O_{11}. \quad (2)$$

II BaB_2O_4 – $(NaF)_2$. The study determined that the BaB_2O_4 – $(NaF)_2$ system is not chemically stable, which is completely different from the results obtained in [10]. A chemical reaction occurs between BaB_2O_4 and NaF [13, 29], which results in the formation of barium-sodium borate fluoride $Ba_2Na_3[B_3O_6]_2F$ ($P6_3/m$) [21], available for the study of phase equilibria in the system. The second product of the chemical reaction is barium fluoride:

$$79.9\ BaB_2O_4 + 20.1\ (NaF)_2 \rightarrow$$
$$\rightarrow 13.4\ Ba_2Na_3[B_3O_6]_2F + 13.4\ BaF_2 + 39.7\ BaB_2O_4 \quad (3)$$

$$66.7\ BaB_2O_4 + 33.3\ (NaF)_2 \rightarrow$$
$$\rightarrow 22.2\ Ba_2Na_3[B_3O_6]_2F + 22.2\ BaF_2 \quad (4)$$

Thus, the initial composition 79.9 mol % BaB_2O_4, 20.1 mol % $(NaF)_2$ transforms into a composition 20 mol % $Ba_2Na_3[B_3O_6]_2F$, 20 mol % BaF_2, 60 mol % BaB_2O_4 during the solid-phase synthesis at 720 °C, which is demonstrated in Table 2. The region of primary crystallization of β-BaB_2O_4 in the system is limited by the composition 66.7 mol % BaB_2O_4, 33.3 mol % $(NaF)_2$, when BaB_2O_4 and $(NaF)_2$ react completely according to (4), which results in the formation of $Ba_2Na_3[B_3O_6]_2F$ and BaF_2 (Fig. 2a). This composition was used to grow a $Ba_2Na_3[B_3O_6]_2F$ crystal [13], whose image is given in the insert to Fig. 2a. We should note that the composition of $Ba_2Na_3[B_3O_6]_2F$ is not on the BaB_2O_4 – $(NaF)_2$ section. It belongs to the Na, Ba // BO_2, F ternary reciprocal system, which was detailed in [29].

The crystallization interval of β-BaB_2O_4 is 125 °C. The drop in the experimental yield coefficient from 2.76 to 2.02 g/(kg×°C) in three consequent experiments can be accounted for by the pyrohydrolysis of barium fluoride formed in the system. An image of the β-BaB_2O_4 crystal grown in the system is presented in the insert to Fig. 2a.

III BaB_2O_4 – $Ba_2Na_3[B_3O_6]_2F$. The $Ba_2Na_3[B_3O_6]_2F$ compound melts congruently at 835 °C. The coordinates of the eutectic points of the system are 85 mol % $Ba_2Na_3[B_3O_6]_2F$, 15 mol % BaB_2O_4, 810 °C [30]. The system is characterized by a relatively high theoretical yield coefficient of 3.09 g/(kg×°C). The experimental yield coefficient in three consequent cycles changed from 2.85 to 2.39 g/(kg×°C). The phase diagram and an image of the crystal grown in the system are presented in Fig. 2b.

IV BaB_2O_4 – $(NaBO_2)_2$. The melting point of $NaBO_2$ is 997 °C. The coordinates of the eutectic points of the system are 44 mol % $(NaBO_2)_2$, 56 mol % BaB_2O_4, 831 °C [31]. The crystallization interval of β-BaB_2O_4 is 94 °C and the theoretical yield coefficient is 3.83 g/(kg×°C). The system is

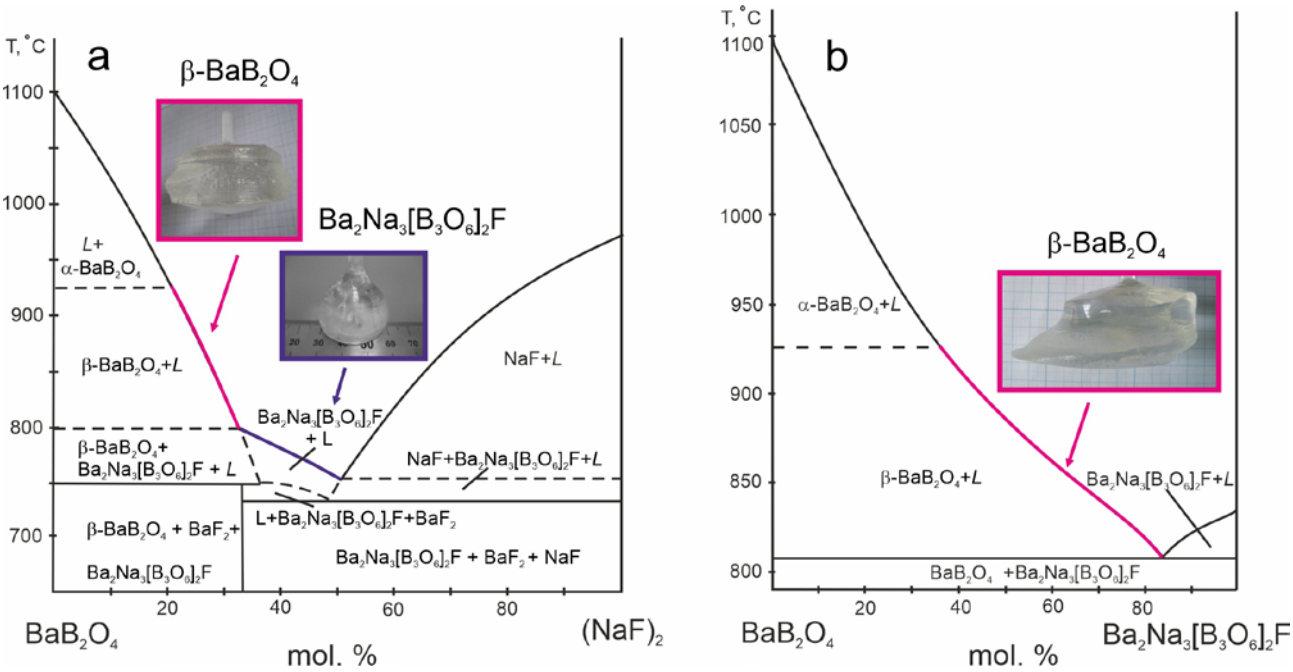

Fig. 2. Phase diagrams of the BaB_2O_4 - $(NaF)_2$ (a) and BaB_2O_4 - $Ba_2Na_3[B_3O_6]_2F$ (b) systems and photographs of crystals grown in these systems

characterized by the highest experimental yield coefficient of 3.22 g/(kg×°C).

V BaB_2O_4 – $NaBaBO_3$. The $NaBaBO_3$ (*C*2/*m*) compound [20] melts congruently at 1270 °C. It was determined that the BaB_2O_4–$NaBaBO_3$ system is quasi-binary only in the solid state, i.e. at temperatures below 760 °C, and crosses the region of primary crystallization of $Ba_5B_4O_{11}$ [32] and $NaBa_4(BO_3)_3$ [33]. The crystallization interval corresponding to the region of primary crystallization of β-BaB_2O_4 (Fig. 3) is 115 °C and the theoretical yield coefficient is 2.49 g/(kg×°C). The experimental yield coefficient varies in the range of 1.89÷1.60 g/(kg×°C).

VI BaB_2O_4 – $NaBaBO_3$ – $Ba_2Na_3[B_3O_6]_2F$. The composition used for the growth of β-BaB_2O_4 in this ternary system is 70 mol % BaB_2O_4, 22.5 mol % $NaBaBO_3$, and 7.5 $Ba_2Na_3[B_3O_6]_2F$ mol %. The crystallization interval of β-BaB_2O_4 is 120 °C and the theoretical yield coefficient is 2.80 g/(kg×°C). The experimental yield coefficient is 2.20 g/(kg×°C).

One of the key characteristics determining the possibility of using optical elements based on β-BaB_2O_4 crystals in laser systems is the absence of scattering, when laser radiation passes through a crystal. We assume that the formation of scattering centers in β-BaB_2O_4 crystals is associated with the introduction of sodium impurities. The concentration of sodium in the initial high-temperature solution is presented in Table 2. Inductively coupled plasma atomic emission spectroscopy demonstrated that the concentration of sodium in crystals is lower by at least three orders of magnitude [34, 35]. Sodium ions can be incorporated both into barium positions and into interstitial sites [36–38].

Despite the rapid pyrohydrolysis and a drop in the yield coefficient, crystals grown in system I did not scatter the laser beam. During long-term storage, the crystals were split by cleavage, which can be a result of thermoelastic relaxation. Crystals grown in systems II and III (the concentration of Na in the initial solutions was 4.75 wt. % and 7.22 wt. % respectively) appeared to be of good quality. However, they demonstrated laser beam scattering in the entire volume. Crystals obtained in system IV (7.05 wt. % Na) contained solid-phase inclusions of up to 200 μm; the regions without inclusions also

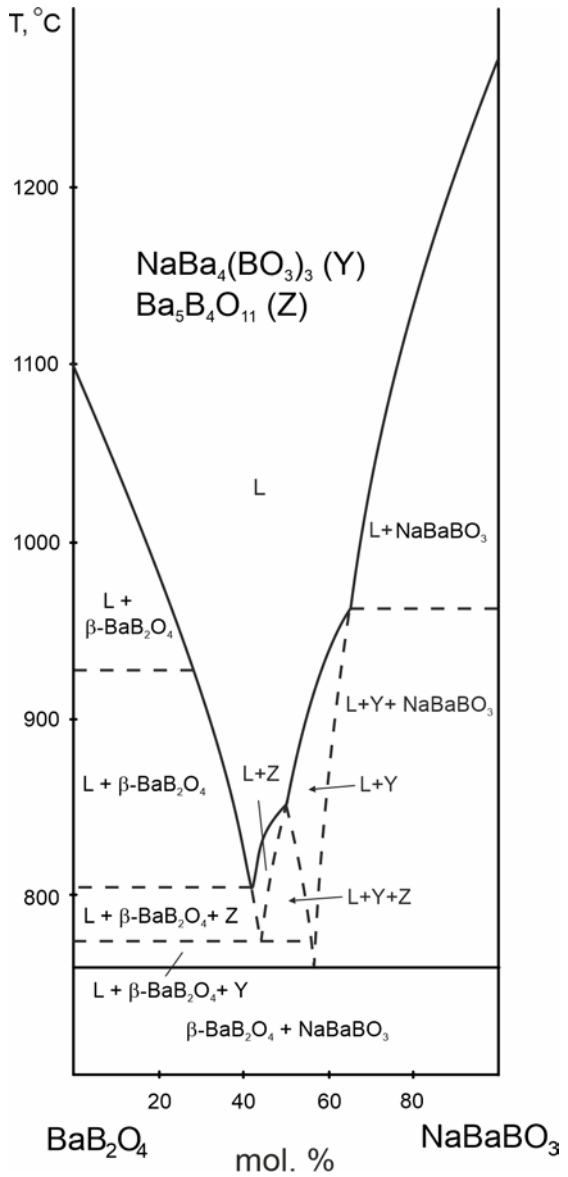

Fig. 3. Phase diagram of the BaB_2O_4 - $NaBaBO_3$ system

demonstrated laser scattering. Crystals grown in system V (3.11 wt. % Na) did not scatter laser beams, which was confirmed be a few dozen experiments. The disadvantages of the system are a low yield coefficient and a loss of stability of the crystallization front at a certain point resulting in cellular growth. The crystals of system VI (4.09 wt. % Na) were also characterized by a high optical quality and a higher experimental yield coefficient than the crystals of system V. We should note that in the consequent experiments with system VI the yield coefficient changed insignificantly, which can be explained by the absence of free barium fluoride susceptible to

pyrohydrolysis in the initial composition. At the same time, the presence of borate fluoride $Ba_2Na_3[B_3O_6]_2F$ apparently helps to reduce the viscosity of the high-temperature solution.

Fig. 4 demonstrates an image of the $NaBa_{12}(BO_3)_7F_4$ crystal, the end member of the solid solution with an "antizeolite" structure grown in the Na, Ba, B // O, F system. The crystal presented in Fig.4 is dark crimson. Another formally colorless group of compounds that were first classified as "antizeolites", are compounds of the meionite group $Ca_{12}Al_{14}O_{33}$ [41-44]. The color of the $NaBa_{12}(BO_3)_7F_4$ crystals grown in the Na, Ba, B // O, F system is determined by the concentration of intrinsic defects and depends on the composition of the initial high-temperature solution [45]. The crystals are characterized by *linear dichroism*, i.e. different light absorption depending on the orientation of the light-wave vector, which makes it possible to use them as polarizers in optical systems [46]. It was also determined that depending on the composition of the initial high-temperature solution, the dielectric permeability of the $NaBa_{12}(BO_3)_7F_4$ crystals changes by an order of magnitude and becomes unusually high for borate crystals (319(5)) [47].

Fig. 4. Photograph of a crystal $NaBa_{12}(BO_3)_7F_4$ ($P4_2bc$), 28×28×11 mm, grown in the system Na, Ba, B // O, F from a composition of 38 mol % BaO, 13 mol % Na_2O, 13 mol % Ba_2O_3, 36 mol % BaF_2

3.2. Synthesis at high temperatures and pressures

As an initial sample in our experiment we used polycrystalline β-BaB_2O_4 obtained by means of solid-phase synthesis. At 3 GPa and 900 °C we obtained a BaB_2O_4 single crystal of about 350 μm, which could further be used for X-ray diffraction analysis (Fig. 5a). Letter L in Fig. 5a denotes the region of partial melting (quenched melt). The obtained crystal is a *new high-pressure modification* of γ-BaB_2O_4, which is crystallized in the centrosymmetric space group $P2_1/n$, a = 4.6392(4) Å, b = 10.2532(14) Å, c = 7.066(1) Å, β = 91.363(10)°, Z = 4. The structure was added to the CCDC database, No. 2106970. A unique feature of the structure is the presence of the $[B_2O_6]$ group consisting of edge-sharing tetrahedra. The

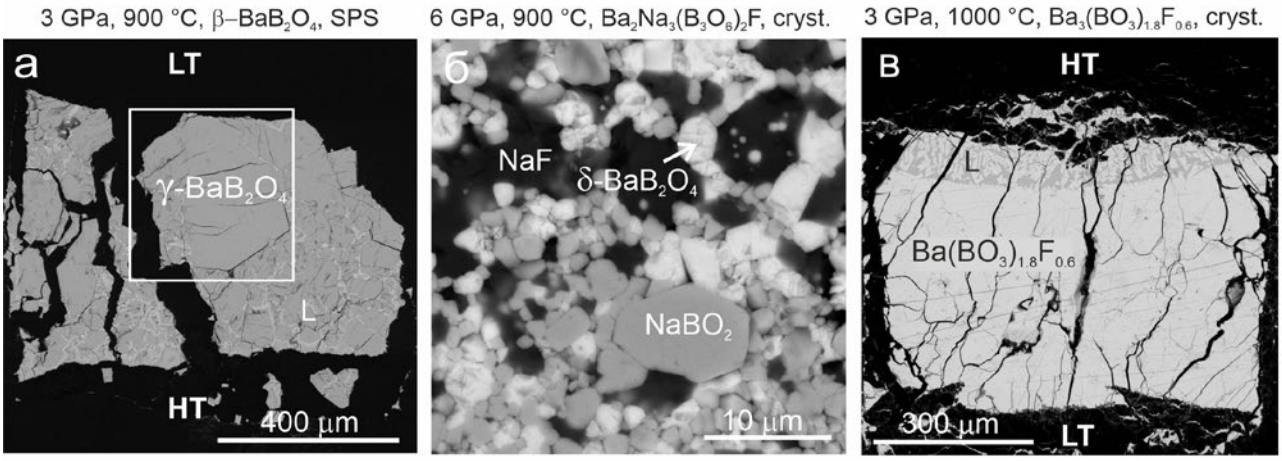

Fig. 5. Backscattered electron image of synthesis products under high pressure and temperature conditions: (a) synthesis at 3 GPa, 900 °C, initial sample – β-BaB_2O_4, obtained by solid-phase synthesis (SPS); (b) synthesis at 6 GPa, 900 °C, the initial sample is a ground crystal of $Ba_2Na_3[B_3O_6]_2F$; (c) synthesis at 3 GPa, 1000 °C, the initial sample is a ground crystal of $Ba_3(BO_3)_{1.8}F_{0.6}$. L – quenched melt, LT and HT – low and high temperature zones of the sample, respectively

metaborate ring disappears from the γ-BaB_2O_4 and two $_\infty[B_4O_4O_{8/2}]$ double endless chains appear along the *a* axis built of $[B_2O_6]$ groups connected by two $[BO_3]$ triangles. The γ-BaB_2O_4 phase is characterized by the shortest distance between the boron atoms of the edge-sharing tetrahedra, 1.984 Å, with the corresponding angles of 95.5° and 105.5° [24,48].

Edge-sharing tetrahedra were first discovered in 2002 in the $Dy_4B_6O_{15}$ compound synthesized at 8 GPa and 1000 °C by a group of researchers headed by professor Huppertz [49]. The discovery of edge-sharing tetrahedra led to the revision of one of the main rules of crystal chemistry of borates: it used to be considered that polymerization in borates takes place only at the vertices [50]. At the moment, there are a limited number of known structural types of borates with edge-sharing tetrahedra synthesized at high pressures by Prof. Huppertz's group [51, 52], as well as $KZnB_3O_6$ [53], $Li_4Na_2CsB_7O_{14}$ [54], $BaZnB_4O_8$ [55], and other compounds synthesized at atmospheric pressure. The theory of crystal chemistry of hard boron-oxygen groups formed by edge-sharing tetrahedra is only starting to develop, so there is little information yet about the properties of such compounds [56]. Thus, [54] states that $Li_4Na_2CsB_7O_{14}$ demonstrates an uncharacteristic anisotropy of a thermal expansion, $BaZnB_4O_8$ is characterized by both high birefringence $\Delta n = 0.14$ at a wavelength of 589.3 nm and a large band gap [55], while the $BaZnB_4O_8$: Tb^{3+}, Eu^{3+} phosphor based on it demonstrates outstanding thermal stability (90.2 % at 423 K) [57].

Based on the calculations, the fourth modification δ-BaB_2O_4 with the proposed structure $Pa\bar{3}$ isostructural to CaB_2O_4-$Pa\bar{3}$ [15], is stable under pressure above 6.1 GPa. In order to obtain δ-BaB_2O_4 crystals we conducted an experiment at a pressure of 6 GPa, which is the maximum pressure for the Discoverer-1500 multi-anvil hydraulic press of the DIE type. The initial samples were both β-BaB_2O_4 samples obtained by means of solid-phase synthesis and grounded crystals. The Raman spectra of the synthesized BaB_2O_4 crystals were identical to the spectra of γ-BaB_2O_4. However, we still managed to experimentally confirm the existence of the fourth modification δ-BaB_2O_4 when studying compound $Ba_2Na_3(B_3O_6)_2F$. When grounded $Ba_2Na_3(B_3O_6)_2F$ crystals were used as an initial sample at 6 GPa and 900 °C, the synthesized sample contained phases BaB_2O_4, $NaBO_2$, and NaF (Fig. 5b), which were identified by means of energy dispersive X-ray spectroscopy and Raman spectroscopy. At the same time, the $Ba_2Na_3(B_3O_6)_2F$ phase completely disappeared [27]. The small size of the formed crystals made it impossible to conduct X-ray diffraction studies. The results of the analysis of the synthesized BaB_2O_4 phase by means of Raman spectroscopy are presented in section 3.3.

For the first time we conducted experiments in order to study the stability of borates with an "antizeolite" structure under high pressures. When grounded $Ba_3(BO_3)_{1.8}F_{0.6}$ crystals were used as the initial sample at 3 GPa and 1000 °C, we obtained a single-phase sample of a similar composition, which had a region of partial melting (quenched melt) (Fig. 5c). The study determined that the compositions of the initial and synthesized samples were close, while their Raman spectra differed, which makes it possible to assume the presence of a phase transition that requires further research.

3.3. Raman spectra of polymorphic modifications of BaB_2O_4

Fig. 6 shows the Raman spectra of the four known polymorphic modifications of BaB_2O_4. The basis of the α-BaB_2O_4 ($R\bar{3}c$) [58] and β-BaB_2O_4 ($R3c$) structure [59] is a *metaborate* ring $[B_3O_6]^{3-}$, built of three triangles sharing a common vertex $[BO_3]$. The most intense vibration in the Raman spectra for metaborates traditionally corresponds to the so-called breathing mode of the metaborate ring, whose location practically does not depend on the composition of the compound. Thus, for α-BaB_2O_4 the vibration is registered at 634 cm^{-1} (Fig. 6a), for β-BaB_2O_4 – at 637 cm^{-1} (Fig. 6b), for $Ba_2Na_3[B_3O_6]_2F$ - at 628 cm^{-1} [27], and for $NaBO_2$ ($R\bar{3}c$) at 626 cm^{-1} [60].

The spectrum of β-BaB_2O_4 (Fig. 6b) is in good agreement with the previous studies, namely with [61], which describes out-of-plane modes at 58, 73, 99, 124, 172, and 197 cm^{-1}, and in-plane modes at 598, 620, 770, 788, 1499, 1526, and 1541 cm^{-1} of the metaborate ring $[B_3O_6]^{3-}$. In [62], the most intense peaks at 390, 498, and 620 cm^{-1} in the spectra of β-BaB_2O_4 at temperatures from 300 to

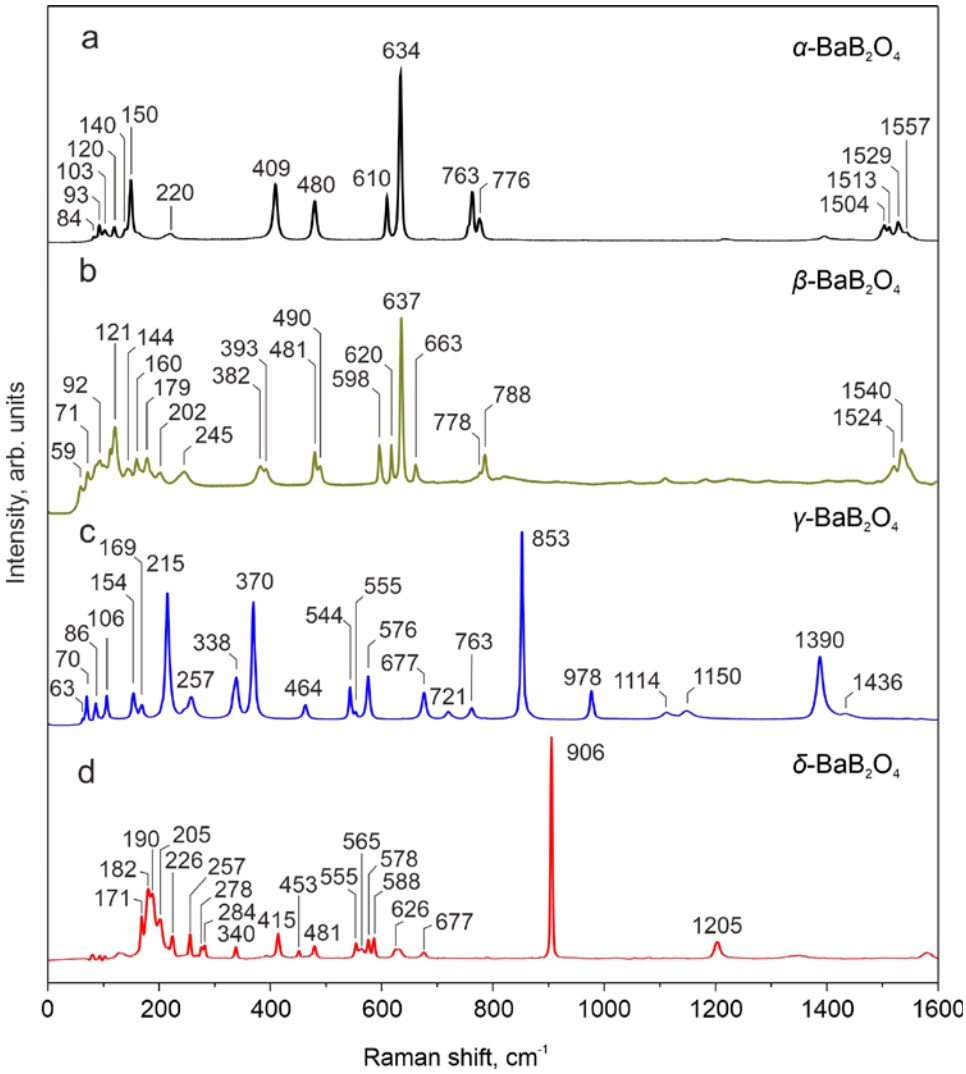

Fig. 6. Raman spectra of four polymorphs of BaB_2O_4

1100 K are attributed to the in-plane deformation vibrations of $[B_3O_6]^{3-}$; at higher temperatures the peaks monotonously move towards the region of lower frequencies.

The structure of γ-BaB_2O_4 ($P2_1/n$) includes double endless chains built of edge-sharing tetrahedra connected by $[BO_3]$-triangles [26]. Experimental and numerical studies of the Raman spectra demonstrated that the most intense band at 853 cm^{-1} corresponds to the breathing mode of the $^{(4)}$B–O–$^{(4)}$B–O ring formed by two edge-sharing tetrahedra. Bands at 1436, 1390, 1150, and 1114 cm^{-1} correspond to stretching modes $^{(3)}$B–O. Bands in the range of 770–300 cm^{-1} are a combination of libration and deformation modes of groups $[BO_3]$ and $[BO_4]$, and bands below 300 nm – are combined out-of-plane libration and translation modes $[BO_3]$ of barium atoms and triangles. A more detailed study of the analyzed Raman spectra is presented in [26]. An analysis of the previous studies led us to a conclusion that the location and the intensity of the vibration corresponding to the breathing mode of the $^{(4)}$B–O–$^{(4)}$B–O ring significantly depend on the structure of the boron-oxygen anionic complex *in general*. Thus, for $KZnB_3O_6$ the most intense vibration is registered at 723 cm^{-1} [52], and for HP-KB_3O_5 – at 760 cm^{-1} [51].

As we have mentioned earlier, we could not conduct X-ray diffraction studies of δ-BaB_2O_4 single crystals due to their small size. According to *ab initio* calculations, modification δ-BaB_2O_4 is

isostructural to CaB_2O_4-$Pa\bar{3}$ [15]. We can assume that the most intense vibration at 906 cm^{-1} is explained by the stretching vibrations of the $[BO_4]$ tetrahedron.

Numerical methods demonstrated that in the series $\alpha \rightarrow \beta \rightarrow \gamma \rightarrow \delta$ the band gap gradually increases (6.315 → 6.468 → 7.045 → 7.340 eV respectively). We should note that the calculated band gaps for the α- and β-BaB_2O_4 modifications are in good agreement with the experimental ones. The calculated *PT* phase diagram of BaB_2O_4 is presented in [48].

4. Conclusions

Based on the numerous studies of phase equilibria in the Na, Ba, B // O, F quaternary reciprocal system conducted in order to optimize the composition of the solvent used for the growth of β-BaB_2O_4 crystals, we can conclude that crystals of reproducibly good optical quality can be obtained when using compounds of systems BaB_2O_4 –$NaBaBO_3$ and BaB_2O_4 – $NaBaBO_3$ – $Ba_2Na_3[B_3O_6]_2F$. Using a Discoverer-1500 multi-anvil hydraulic press of the DIE type at high temperatures and pressures we synthesized two new polymorphic modifications: γ-BaB_2O_4 with a $P2_1/n$ structure (CCDC, № 2106970) and δ-BaB_2O_4 with a proposed structure $Pa\bar{3}$. A unique feature of the γ-BaB_2O_4 structure is the presence of the $[B_2O_6]$ group consisting of edge-sharing tetrahedra. Both modifications were analyzed using the Raman light scattering method.

The Na, Ba, B // O, F system also includes the region of compositions of the solid solution with an "antizeolite" structure. The composition of the solution in the system can be presented as $\{Ba_{12}(BO_3)_6\}[(F_2)_x(BO_3)_{1-x}][(F_4)_x(NaF_4)_y(BO_3)_{1-x-y}]$, where $x+y \leqslant 1$. Phases $Ba_3(BO_3)_2$, $Ba_3(BO_3)_{1.8}F_{0.6}$, and $NaBa_{12}(BO_3)_7F_4$ were experimentally determined. The crystals have dichroic properties that depend on the composition of the initial high-temperature solution; the dielectric permeability of $NaBa_{12}(BO_3)_7F_4$ is unusually high for borate crystals (319(5)). Raman spectroscopy determined that under high pressures $Ba_3(BO_3)_{1.8}F_{0.6}$ undergoes a phase transition, whose nature requires further research.

Author contributions

T. B. Bekker – idea, writing of the article, scientific editing of the text, experimental studies, head of the project; A. V. Davydov – experimental studies, project executor; N. E. Sagatov – numerical and experimental studies.

Conflict of interests

The authors declare that they have no known competing financial interests or personal relationships that could have influenced the work reported in this paper.

References

1. Chen C., Wu B., Jiang A., You G. A new-type ultraviolet SHG crystal – β-BaB_2O_4. *Materials Science, Physics Science in China Series B.* 1985;28: 235–243. https://doi.org/10.1360/yb1985-28-3-235

2. Perlov D., Livneh S., Czechowicz P., Goldgirsh A., Loiacono D. Progress in growth of large β-BaB_2O_4 single crystals. *Crystal Research and Technology.* 2011;46: 651–654. https://doi.org/10.1002/crat.201100208

3. Mutailipu M., Poeppelmeier K. R., Pan S. Borates: A rich source for optical materials. *Chemical Reviews.* 2021;121: 1130–1202. https://doi.org/10.1021/acs.chemrev.0c00796

4. Fedorov P. P., Kokh A. E., Kononova N. G., Barium borate beta-BaB_2O_4 as a material for nonlinear optics. *Russian Chemical Reviews* 2002;71(8): 651–671. https://doi.org/10.1070/RC2002v071n08ABEH000716

5. Chen C., Sasaki T., Li R., … Kaneda Y. *Nonlinear optical borate crystals, principles and applications*. Wiley-VCH Verlag GmbH & Co. KGaA; 2012. 387 p. https://doi.org/10.1002/9783527646388

6. Feigelson R. S., Raymakers R. J., Route R. K. Solution growth of barium metaborate crystals by top seeding. *Journal of Crystal Growth.* 1989;97: 352–366. https://doi.org/10.1016/0022-0248(89)90217-0

7. Nikolov V., Peshev P. On the growth of β-BaB_2O_4 (BBO) single crystals from hightemperature solutions: I. Study of solvents of the BaO–Na_2O–B_2O_3 system. *Journal of Solid State Chemistry.* 1992;96: 48–52. https://doi.org/10.1016/S0022-4596(05)80295-6

8. Tang D.Y., Zeng W. R., Zhao Q. L. A study on growth of β-BaB_2O_4 crystals. *Journal of Crystal Growth.* 1992;123: 445–450. https://doi.org/10.1016/0022-0248(92)90605-I

9. Fedorov P. P., Kokh A. E., Kononova N. G., Bekker T. B. Investigation of phase equilibria and growth of BBO (β-BaB_2O_4) in BaO-B_2O_3-Na_2O ternary system. *Journal of Crystal Growth.* 2008;310: 1943–1949. https://doi.org/10.1016/j.jcrysgro.2007.11.119

10. Roth M., Perlov D. Growth of barium borate crystals from sodium fluoride solutions, *Journal of Crystal Growth.* 1996;169: 734–740. https://doi.org/10.1016/S0022-0248(96)00450-2

11. Chen W., Jiang A., Wang G. Growth of high-quality and large-sized β-BaB_2O_4 crystal. *Journal of Crystal Growth.* 2003;256: 383–386. https://doi.org/10.1016/S0022-0248(03)01358-7

12. Perlov D., Livneh S., Czechowicz P., Goldgirsh A., Loiacono D. Progress in growth of large β-BaB_2O_4 single crystals. *Crystal Research and Technology*. 2011;46: 651–654. https://doi.org/10.1002/crat.201100208

13. Bekker T. B., Kokh A. E., Kononova N. G., Fedorov P. P., Kuznetsov S. V. Crystal growth and phase equilibria in the BaB_2O_4–NaF system. *Crystal Growth and Design*. 2009;9: 4060–4063. https://doi.org/10.1021/cg9002675

14. Sagatov N. E., Bekker T. B., Podborodnikov I. V., Litasov K. D. First-principles investigation of pressure-induced structural transformations of barium borates in the BaO–B_2O_3–BaF_2 system in the range of 0–10 GPa. *Computational Materials Science*. 2021;199: 110735. https://doi.org/10.1016/j.commatsci.2021.110735

15. Marezio M., Remeika J. P., Dernier P. D. The crystal structure of the high-pressure phase CaB_2O_4 (IV), and polymorphism in CaB_2O_4. *Acta Crystallographica B*. 1969;25: 965–970. https://doi.org/10.1107/S0567740869003256

16. Bekker T. B., Fedorov P. P., Kokh A. E. Phase formation in the BaB2O4 -BaF2 system. *Crystallogr. Rep*. 2012;57(4): 574–578. https://doi.org/10.1134/S1063774512040025

17. Jiang A., Cheng F., Lin Q., Cheng G., Zheng Y. Flux growth of large single crystals of low temperature phase barium metaborate. *Journal of Crystal Growth*. 1986;79: 963–969. https://doi.org/10.1016/0022-0248(86)90579-8

18. Bekker T. B., Kokh A. E., Fedorov P. P. Phase equilibria and beta-BaB_2O_4 crystal growth in the BaB_2O_4-BaF_2 system. *CrystEngComm*. 2011;13: 3822–3826. https://doi.org/10.1039/C1CE05071K

19. Jänecke E. Über reziproke Salzpaare und doppelt-ternäre Salzmischungen, *Zeitschrift für Physikalische Chemie*. 1913;82: 1–34. https://doi.org/10.1515/zpch-1913-8202

20. Tu J. -M. Keszler D. A. $BaNaBO_3$. *Acta Crystallographica*.1995;51(10): 1962–1964. https://doi.org/10.1107/s010827019400750x

21. Kokh A.E., Kononova N.G., Bekker T. B., Fedorov P.P., Nigmatulina E.A., Ivanova A.G. An investigation of the growth of β-BaB_2O_4 crystals in the BaB_2O_4-NaF system and new fluoroborate $Ba_2Na_3[B_3O_6]_2F$. *Crystallogr. Rep*. 2009;54(1): 146–151. https://doi.org/10.1134/S1063774509010258

22. Bekker T. B., Rashchenko S. V., Solntsev V. P., ... Kuznetsov A. B. Growth and optical properties of $Li_xNa_{1-x}Ba_{12}(BO_3)_7F_4$ fluoride borates with 'anti-zeolite' structure. *Inorganic Chemistry*. 2017;56(9): 5411–5419. https://doi.org/10.1021/acs.inorgchem.7b00520

23. Bekker T. B., Rashchenko S. V, Seryotkin Y. V., Kokh A. E., Davydov A. V., Fedorov P. P. BaO–B_2O_3 system and its mysterious member $Ba_3B_2O_6$. *Journal of the American Ceramic Society*. 2018;101(1): 450–457. https://doi.org/10.1111/jace.15194

24. Rashchenko S. V., Bekker T. B., Bakakin V. V., Seryotkin Y. V., Simonova E. A., Goryainov S. V. New fluoride borate with 'anti-zeolite' structure: A possible link to $Ba_3(BO_3)_2$. *Journal of Alloys and Compounds*. 2017;694: 1196–1200. https://doi.org/10.1016/j.jallcom.2016.10.119

25. Zhao J., Li R. K. Two new barium borate fluorides ABa_{12} $(BO_3)_7F_4$ (A= Li and Na). *Inorganic Chemistry*. 2014;53(5): 2501-2505. https://doi.org/10.1021/ic4025525

26. Bekker T. B., Podborodnikov I. V., Sagatov N. E., ... Litasov K. D. γ-BaB_2O_4: high-pressure high-temperature polymorph of barium borate with edge-sharing BO_4 tetrahedra. *Inorganic Chemistry*. 2022;61(4): 2340–2350. https://doi.org/10.1021/acs.inorgchem.1c03760

27. Sagatov N. E., Bekker T. B., Vinogradova Y. G., Davydov A. V., Podborodnikov I. V., Litasov K. D. Experimental and ab initio study of $Ba_2Na_3(B_3O_6)_2F$ stability in the pressure range of 0–10 GPa. *International Journal of Minerals, Metallurgy and Materials*. 2023;30(9): 1846–1854. https://doi.org/10.1007/s12613-023-2647-0

28. Shatskiy A., Sharygin I. S., Gavryushkin P. N., ... Ohtani E. The system K_2CO_3-$MgCO_3$ at 6 GPa and 900-1450 °C. *American Mineralogist*. 2013;98(8-9): 1593–1603. https://doi.org/10.2138/am.2013.4407

29. Bekker, T. B., Fedorov, P. P. New type of ternary reciprocal system: Na,Ba|BO_2,F system. *Russian Journal of Inorganic Chemistry*. 2014;59: 1507–1511. https://doi.org/10.1134/S0036023614120055

30. Bekker T. B., Fedorov P. P., Kokh A. E. The ternary reciprocal system Na, Ba // BO_2, F. *Crystal Growth and Design*. 2012;12(1): 129–134. https://doi.org/10.1021/cg2008705

31. Huang Q. -Z., Liang J. K. The crystal growth of barium borate low temperature phase and the study of phase diagrams of related systems. *Acta Physica Sinica* 1981;30: 559. (In Chinese). https://doi.org/10.7498/aps.30.559

32 Furmanova, N. G., Maksimov, B. A., Molchanov, V. N., Kokh A. E., Kononova N. G., Fedorov P. P. Crystal structure of the new barium borate $Ba_5(BO_3)_2(B_2O_5)$. *Crystallography Reports*. 2006;51: 219–224. https://doi.org/10.1134/S1063774506020076

33. Kokh A. E., Kononova N. G., Bekker T. B., ... Kargin Yu. F. New sodium barium orthoborate $NaBa_4(BO_3)_3$. *Russian Journal of Inorganic Chemistry*. 2004;49(7): 984–988.

34. Bekker T. B. *Phase formation and crystal growth in the quaternary reciprocal system Na, Ba, B // O, F*. Dissertation of Dr. Geol.-miner. Sci. Novosibirsk: 2015. 279 p. https://www.dissercat.com/content/fazoobrazovanie-i-rost-kristallov-v-chetvernoi-vzaimnoi-sisteme-na-ba-b-o-f

35. Bekker T. B., Fedorov P. P., Kokh A. E. Phase formation and crystal growth in the quaternary reciprocal system Na, Ba, B // O, F. Novosibirsk: Siberian Branch of the Russian Academy of Sciences Publ. 2016. 217 p. (In Russ.). Available at: https://www.rfbr.ru/library/books/2416/

36. Carrillo Romo F., Goutaudier C., Guyot Y., Cohen-Adad M. Th., Boulon G., Lebbou K., Yoshikawa A., Fukuda T. Yb^{3+}-doped $Ba_2NaNb_5O_{15}$ (BNN) growth, characterization and spectroscopy. *Optical Materials*. 2001;16: 199–206. https://doi.org/10.1016/S0925-3467(00)00078-1

37. Hong W., Perlov D., Halliburton L. E. Electron paramagnetic resonance study of Ag^0 atoms and Ag^{2+} ions in β-BaB_2O_4 nonlinear optical crystals. *Journal of Physics D: Applied Physics*. 2003;36: 2605–2611. https://doi.org/10.1088/0022-3727/36/21/002

38. Hong W., Halliburton L. E., Perlov D., Stevens K. T., Route R. K., Feigelson R. S. Observation of paramagnetic point defects in BBO (β-BaB_2O_4) crystals. *Optical Materials*. 2004;26(4): 437–441. https://doi.org/10.1016/j.optmat.2003.08.012

39. Bekker T. B., Kokh A. E., Fedorov P. P., Stonoga S. Yu. Phase equilibria and growth of β-BaB_2O_4 crystals in the BaB_2O_4-$Ba_2Na_3[B_3O_6]_2F$ system. *Crystallography Reports*. 2012;57(2): 327–331. https://doi.org/10.1134/s1063774512020022]

40. Fedorov P. P., Kokh A. E., Kononova N. G., Bekker T. B. Investigation of phase equilibria and growth of BBO (β-BaB_2O_4) in BaO-B_2O_3-Na_2O ternary system. *Journal of Crystal Growth*. 2008;310(7-9): 1943–1949. https://doi.org/10.1016/j.jcrysgro.2007.11.119

41. Palacios L., Cabeza, A., Bruque S., García-Granda S., Aranda M. A. Structure and electrons in mayenite electrides. *Inorganic Chemistry*. 2008;47(7): 2661–2667. https://doi.org/10.1021/ic7021193

42. Kim S. W., Hosono H. Synthesis and properties of 12CaO·7Al_2O_3 electride: review of single crystal and thin film growth. *Philosophical Magazine*. 2012;92(19-21): 2596-2628. https://doi.org/10.1080/14786435.2012.685770

43. Zhang X., Feng Q., Zhao J., ... Lu Q. Sr-doping enhanced electrical transport and thermionic emission of single crystal 12CaO·7Al_2O_3 electride. *Current Applied Physics*. 2020;20(1): 96–101. https://doi.org/10.1016/j.cap.2019.10.008

44. Li R., Zhang X., Xiao Y., Liu Y. One-step preparation and electrical transport characteristics of single-crystal $Ca_{24}Al_{28}O_{66}$ electrides. *Journal of Electronic Materials*. 2020;49: 7308–7315. https://doi.org/10.1007/s11664-020-08469-0

45. Bekker T. B., Solntsev V. P., Rashchenko S. V., ... Park S.-H. Nature of color of the borates with the 'anti-zeolite' structure. *Inorganic Chemistry*. 2018;57(5); 2744–2751. https://doi.org/10.1021/acs.inorgchem.7b03134

46. Bekker T. B., Solntsev V. P., Eliseev A. P., ... Kuznetsov A. B. *Dichroic material – fluoride borate with an "anti-zeolite" structure**. Russian Federation Patent RF: No. 2689596. Publ. 05.28.2019, bull. No. 16. (In Russ.)]

47. Bekker T. B., Khamoyan A. G., Davydov A. V., Vedenyapin V. N., Yelisseyev A. P., Vishnevskiy A. V. $NaBa_{12}(BO_3)_7F_4$ (NBBF) dichroic crystals: optical properties and dielectric permittivity. *Dalton Transactions*. 2024; 53(29): 12215-12222. https://doi.org/10.1039/d4dt01380h

48. Bekker T. B., Davydov A. V., Sagatov N. E. Comparative characteristics of various solvents of the Na, Ba, B//O, F system for the growth of β-BaB_2O_4 crystals and PT-diagram of BaB_2O_4 polymorphs. *Journal of Crystal Growth*. 2022;599: 126895. https://doi.org/10.1016/j.jcrysgro.2022.126895

49. Huppertz H., von der Eltz B. Multianvil high-pressure synthesis of $Dy_4B_6O_{15}$: the first oxoborate with edge-sharing BO_4 tetrahedra. *Journal of the American Chemical Society*. 2002;124(32): 9376-9377. https://doi.org/10.1021/ja017691z

50. Grice J. D., Burns P. C., Hawthorne F. C. Borate minerals. II. A hierarchy of structures based upon the borate fundamental building block. *The Canadian Mineralogist*. 1999;37(3): 731–762.

51. Knyrim J. S., Roessner F., Jakob S., ... Huppertz H. Formation of edge-sharing BO_4 tetrahedra in the high-pressure borate HP-NiB_2O_4. *Angewandte Chemie International Edition*. 2007;46(47): 9097–9100. https://doi.org/10.1002/anie.200703399

52. Neumair S. C., Vanicek S., Kaindl R., ... Huppertz H. HP-KB_3O_5 highlights the structural diversity of borates: corner-sharing BO_3/BO_4 groups in combination with edge-sharing BO_4 tetrahedra. *European Journal of Inorganic Chemistry*. 2011;27: 4147–4152. https://doi.org/10.1002/ejic.201100618

53. Jin S., Cai G., Wang W., He M., Wang S., Chen X. Stable oxoborate with edge-sharing BO_4 tetrahedra synthesized under ambient pressure. *Angewandte Chemie International Edition*. 2010;122(29): 5087–5090. https://doi.org/10.1002/ange.200907075

54. Mutailipu M., Zhang M., Li H., ... Pan S. $Li_4Na_2CsB_7O_{14}$: a new edge-sharing $[BO_4]_5$–tetrahedra containing borate with high anisotropic thermal expansion. *Chemical Communications*. 2019;55(9): 1295–1298. https://doi.org/10.1039/c8cc09422e

55. Han J., Liu K., Chen L., ... Mutailipu M. Finding a deep-UV borate $BaZnB_4O_8$ with edge-sharing $[BO_4]$ tetrahedra and strong optical anisotropy. *Chemistry – A European Journal*. 023;9(6): 202203000. https://doi.org/10.1002/chem.202203000

56. Li J. J., Chen W. F., Lan Y. Z., Cheng J. W. Recent progress in crystalline borates with edge-sharing BO_4 tetrahedra. *Molecules*. 2023;28(13): 5068. https://doi.org/10.3390/molecules28135068

57. Liu N., Kong J., Wang Z., Wang Y. Color-tunability and energy transfer of a highly thermal-stable $BaZnB_4O_8$: Tb^{3+}/Eu^{3+} phosphor for single-component w-LEDs. *Journal of Molecular Structure*. 2024;1311: 138441. https://doi.org/10.1016/j.molstruc.2024.138441

58. Mighell A. D., Perloff A., Block S. The crystal structure of the high temperature form of barium borate, BaO·B_2O_3. *Acta Crystallographica*. 1966;20: 819–823. https://doi.org/10.1107/S0365110X66001920

59. Bubnova R., Volkov S., Albert B., Filatov S. Borates – crystal structures of prospective nonlinear optical materials: high anisotropy of the thermal expansion caused by anharmonic atomic vibrations. *Crystals*. 2017;7(3): 93. https://doi.org/10.3390/cryst7030093

60. Voronko Yu. K., Sobol A. A., Shukshin V. E. Structure of boron-oxygen fragments of metaborates of alkali and alkaline earth metals in crystalline, molten and glassy states. *Inorganic materials*. 2012:48(7); 837. (In Russ.). Available at: https://www.elibrary.ru/item.asp?id=17745523

61. Lu J. Q., Lan G. X., Li B., Yang Y. Y., Wang H. F., Bai C. W. Raman scattering study of the single crystal β-BaB_2O_4 under high pressure. *Journal of Physics and Chemistry of Solids*. 1988;49(5): 519–527. https://doi.org/10.1016/0022-3697(88)90063-7

62. Liu S., Zhang G., Wan S., ... Wu Y. High-temperature Raman spectroscopy of microstructure around the growing β-BaB_2O_4 crystal in the BaO–B_2O_3–Na_2O system. *Journal of Applied Crystallography*. 2014;47(2): 739-744. https://doi.org/10.1107/S160057671400377X

**Translated by author of the article*

Information about the authors

Tatyana B. Bekker, Dr. Sci. (Geol.-Mineral.) Leading Researcher, Sobolev Institute of Geology and Mineralogy, Siberian Branch of Russian Academy of Sciences, (Novosibirsk, Russian Federation), Senior Research Worker of Novosibirsk State University (Novosibirsk, Russian Federation).
https://orcid.org/0000-0003-3100-5210
bekker@igm.nsc.ru, t.b.bekker@gmail.com

Nursultan E. Sagatov, Cand. Sci. (Phys.- Math.), Researcher Fellow, Sobolev Institute of Geology and Mineralogy, Siberian Branch of Russian Academy of Sciences, (Novosibirsk, Russian Federation), Novosibirsk State University (Novosibirsk, Russian Federation).
https://orcid.org/0000-0001-5158-3523
sagatovnye@igm.nsc.ru

Aleksey V. Davydov, Researcher, Sobolev Institute of Geology and Mineralogy, Siberian Branch of Russian Academy of Sciences, (Novosibirsk, Russian Federation), Novosibirsk State University (Novosibirsk, Russian Federation).
https://orcid.org/0000-0003-2770-3331
adavidov@igm.nsc.ru, a.davydov1@nsu.ru

Received 01.07.2024; approved after reviewing 08.07.2024; accepted for publication 16.09.2024; published online 25.12.2024.

Translated by Yulia Dymant

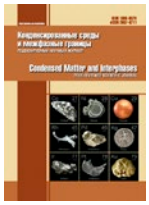

ISSN 1606-867X (Print)
ISSN 2687-0711 (Online)
Condensed Matter and Interphases
Kondensirovannye Sredy i Mezhfaznye Granitsy
https://journals.vsu.ru/kcmf/

Review

Review article
https://doi.org/10.17308/kcmf.2024.26/12396

Nonstoichiometry of refractory inorganic compounds with a volatile component determined by new methods of physicochemical analysis. Review

I. G. Vasilyeva

Nikolaev Institute of Inorganic Chemistry of Siberian Branch Russian Academy of Sciences
3 Lavrent'ev ave., Novosibirsk 630090, Russian Federation

Abstract

The nonstoichiometry of refractory compounds with a volatile component is based on solid-phase and heterophase processes. At the same time, measurements of the parameters of these high-temperature phase transformations are often inaccurate. The inaccuracy results from the instability of the equipment as well as the behavior of themselves samples. To overcome these limitations, we developed three new methods of physicochemical analysis, which were then used in a comprehensive approach to the study of nonstoichiometry and the chemical composition of defective phases at the macro and micro levels. We refer to are high-speed thermal analysis, static tensimetric membrane technique, and stoichiographic differential dissolution method. The methods were used to measure temperatures up to 2400 °C, pressure up to 10 atm, and the degree of nonstoichiometry up to 10^{-4} mol. %.

The review demonstrates the effectiveness of the proposed methodology applied to refractory compounds LnS, Ln_2S_3 (Ln = P3M), $Yb(Ln)_{14}MnSb_{11}$, $ZrGeO_4$, Zr_3GeO_8, MgO, and Mg(Ru)O, as well as highly volatile REM polychalcogenides and $ZnMo(W)O_4$, presented in the form of powders, large crystals, ceramics, and films. For each of the studied substances, fundamental knowledge was gained regarding their spatial-temporal evolution responsible for the occurrence and the degree of nonstoichiometry. The data was obtained by studying *T-x* and *p-T* diagrams and by using of the stoichiographic method to determine the phase purity, microstructural inclusions, and spatial chemical inhomogeneity of individual phases at a micro level.

The obtained new quantitative thermodynamic and physicochemical data regarding the nonstoichiometry of the studied compounds was used as a basis for the choice of the composition and the design of the crystallization process, sintering and chemical deposition of thin films to realize a directed synthesis of materials with the desired properties. The review was initiated by Professor Magomed Babanly, DSc in Chemistry, Associate Member of the Russian Academy of Sciences, and editor of the special issue of the journal *Condensed Matter and Interphases* dedicated to physicochemical analysis in material science.

Keywords: Refractory chemically unstable compounds, Physicochemical analysis, Phase diagrams, nonstoichiometry

Funding: The research was carried out with the financial support of the Ministry of Science and Higher Education of the Russian Federation under the Government Order by Nikolaev Institute of Inorganic Chemistry of the Siberian Branch of the Russian Academy of Sciences (agreement No. 21031700315-2).

For citation: Vasilyeva I. G. Nonstoichiometry of refractory inorganic compounds with a volatile component determined by new methods of physicochemical analysis. Review. *Condensed Matter and Interphases*. 2024;26(4): 633–645. https://doi.org/10.17308/kcmf.2024.26/12396

Для цитирования: Васильева И. Г. Нестехиометрия тугоплавких неорганических соединений с летучим компонентом через призму оригинальных методов физико-химического анализа. Обзор. *Конденсированные среды и межфазные границы*. 2024;26(4): 633–645. https://doi.org/10.17308/kcmf.2024.26/12396

✉ I. G. Vasilyeva, e-mail: kamars@niic.nsc.ru

1. Introduction

Nonstoichiometry plays a special role in inorganic material science since it solves practically important problem of controllability of the material characteristics. Current theoretical approaches to the nonstoichiometry of complex compounds do not allow an a priori prediction of its nature and scale in the temperature and pressure coordinates. Therefore, it is important to experimentally determine any dependences regarding the formation, structure, and properties of nonstoichiometric phases. Physicochemical analysis methods combined with a dynamic approach are predominantly used to study the equilibria that involve phases of variable composition. These methods help to discover new facts and dependences and play a crucial role in the development of new theories and synthesis of new compounds and materials with desired properties. Investigation of the nonstoichiometry of refractory chemically unstable compounds with active volatile components requires particular attention. Therefore, we developed a system of unique methods of thermal [1–2], tensimetric [3], and stoichiographic analysis [4–5], which helps to determine the key thermodynamic parameters of a system with the same accuracy and ensure the reliability of phase pictures.

Earlier we demonstrated a high effectiveness of these methods by providing a detailed characteristic of large single crystals of $AgGaS_2$, $AgGaGeS_4$, $ZnGeP_2$, and $LiMX_2$ (M = In, Ga; X = S, Se, Te) which contained volatile and chemically active components [6]. In that particular study we focused on the nonstoichiometry and the mechanisms of formation of intrinsic point and extended defects and their connection with optical properties. The degree of nonstoichiometry is presented by T-x and $p_{volatile}$-T-x diagrams, which served as a basis for the growth of the said crystals with an optical quality that would meet the requirements to materials used in nonlinear optics.

This review presents new data regarding high-temperature phase transformations of refractory sulfides and complex antimonides of rare earth metals (REM), as well as oxide compounds of systems Zn-Ge-O, Zn-Mo(W)-O, and MgO-ZrO_2, where even a small loss in volatile component significantly effects the structural state and functional properties. These compounds have different thermal stability and different scale of nonstoichiometry. Their phase transformations are susceptible to a large number of interferences including reactions with oxygen, which often distorts the results of the commonly used analysis methods. The review demonstrates that the use of effective methods and procedures specific for each system bring physicochemical experiments at a principally new level and develop a deeper understanding of the nature of nonstoichiometry of the studied compounds.

2. High-speed thermal analysis method (HSTA) [1–2]

The method is used in an atmosphere of a helium buffer at temperatures ranging from 500 to 2500 °C and pressures of up to 10 atm. It proved to be an innovative method both for studying the nonstoichiometry of REM antimonides and oxide compounds of Zn-Ge-O and Zn-Mo(W)-O, and for determining the conditions regulating the formation of their functional properties. Refractory sulfides of REM, LnS, and Ln_2S_3 are both promising high-temperature thermoelectrics and magnetic and optical materials. They are synthesized in the form of large crystals by means of melt crystallization and in the form of dense non-porous ceramics by means of electropulse sintering and dynamic hot pressing. The synthesis methods are based on p_s-T-x diagrams and the methodological variability of the HSTA approach, which helps to accurately determine the thermodynamic parameters (Fig. 1). The $p_{He} \gg p_S$ based methodology is used to reliably measure the liquidus and solidus temperatures and thus ensure the accuracy of the topology of the T-x diagram (Fig. 1a). The $p_{He} = p_S$ based methodology is used to measure the temperature at the boiling poin and to obtain an equilibrium p-T diagram of the dissociation process (Fig. 1b). The $p_{He} \ll p_S$ based methodology helps to obtain data regarding the nature and degree of nonstoichiometry, its initial and intermediate stages, and the kinetics of the transformations (Fig. 1c). The heating process is registered in several ways: automated recording of the heating curves $dU/d\tau$ (a derivative of the thermal emission along time), visual observation of the heated sample, and analytical data regarding the amount

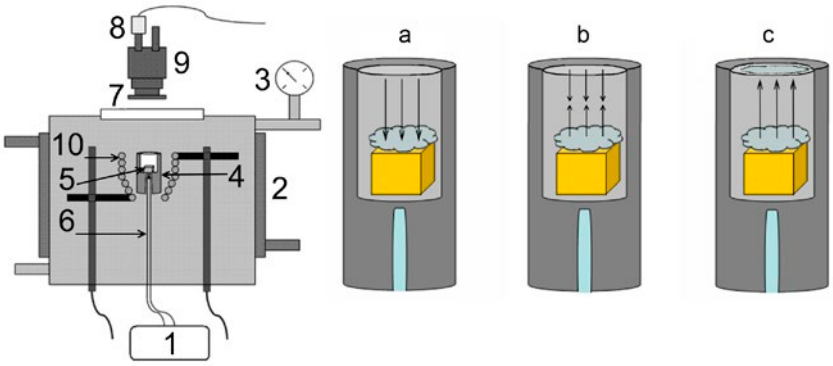

Fig. 1. Block synopsis setup and procedures used in the experiments. Setup: *1* – temperature control block, *2* – chamber; *3* – manometer, *4* – Mo holder, *5* – sample, *6* – thermocouple, *7* – quartz window, *8* – IR photodiode, *9* – microscope, *10* – tungsten heater. Procedures from the left to the right: (a) full preservation of composition, (b) equality of vapor pressures between sample and helium, (c) free evaporation with the vapor condensate formation

of the volatile component distributed between the condensate (on the sight glass of the crucible) and the solid residue. The crucible was calibrated with regard to the melting points of Au (1100 °C), Co (1493 °C), Pt (1772 °C), Rh (1963 °C), and Al_2O_3 (2050 °C) and the pressure of decomposition of GaAs crystals, with p = 1.0 atm at 1610 °C. The measurement accuracy of the melting points was 1 % and the measurement accuracy of the pressure was 5 %.

The experimental data regarding the La-S system is presented as p_S-T and T-x diagrams. The topology of the latter is also typical for the Nd-Sm systems (Fig. 2). The values T_{melt} = 2130 K and p_s = 2.3 atm are the operating parameters of the growth of large stoichiometric La_2S_3 crystals, and T_{press} = 1510 K and p_s = 0.016 atm resulted in the formation of stoichiometric ceramics of the La_2S_3, β and γ polymorphs with a good optical quality [7-9]. For HoS and GdS monosulfides, HSTA was effectively used to obtain the liquidus line in the temperature range of 2400–2700 K and sulfur compositions of 47–53 at. %, and to determine the homogeneity regions of both monosulfides, which had practically no oxygen dissolved in the sulfide matrix. The obtained data was used for the sintering process to obtain dense non-porous ceramics of monosulfides. HSTA was also used to detect small amounts of impurity oxide phases of REM. This helped us to synthesize oxygen-free ceramics when sintering powder mixtures Ho_2S_3+Ho and Gd_2S_3+GdH_2 using the electropulse technology [10–11].

Complex antimonides $A_{14-x}Me_xMnSb_{11}$, A = Yb, Eu, x = La-Lu (except for Eu and Ce) are known to be Zintl phases and promising high-

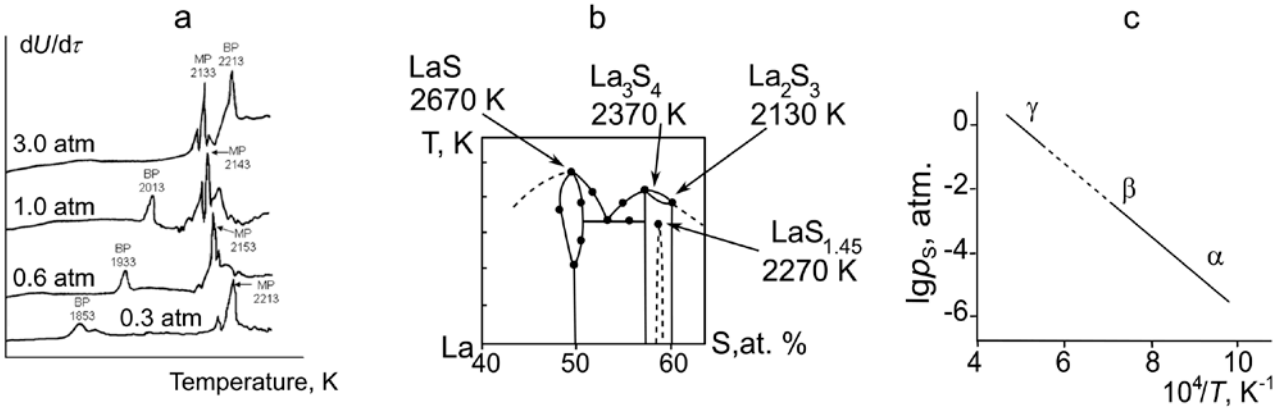

Fig. 2. Physicochemical study of the La–S system (a) heating curves of La_2S_3 with melting (MP) and boiling (BP) peaks in a function of the helium pressure; (b) top of T-x diagram of the condensed state of the La–S system; (c) p-T dependence for α, β and γ forms of La_2S_3

temperature thermoelectrics. The limitations of the physicochemical methods of analysis of these compounds were obvious due to the high melting points and the reactive nature of the melts. Reliable data regarding the phase state of the Eu-Mn-Sb system were obtained by HSTA and the *T-x* diagram of the Eu-Sb system with the data about the thermodynamic and thermochemical stability of binary antimonides presented in Fig. 3a. The thermodynamic data regarding the stable phases facilitated further synthesis of the desired ternary compound $Eu_{14}MnSb_{11}$ in the single-phase state by means of a direct reaction of Eu_4Sb_3 and $EuSb_2$ with manganese [12]. Diagrams of $Yb(Eu)Sb_2$-Mn and $Yb(Eu)_4Sb_3$-Mn were topologically identical with the Eu diagram tending to move towards higher temperatures. They were also used for the synthesis of single-phase ternary $Ln_{14}MnSb_{11}$ crystals according to the Ln_4Sb_3+Mn reaction and based on the similarity of the thermochemical parameters of phases Ln_4Sb_3 and Mn [13].

HSTA also contributed to the problem of enhancing the thermal stability of $Yb_{14}MnSb_{11}$ [14–15]. Long-term use of stoichiometric ceramics in aerospace vacuum at a temperature of 1000 °C is hindered by a high sublimation rate. By partially replacing ytterbium with other REM, the volatility of which was 5–10 orders of magnitude lower, well-shaped crystals were obtained from a $Yb_{14-x}Ln_xMn_6Sn_{86}$ solution melt with an excess of tin as a solvent. The limiting solubility of Ln cations, having various dimensions, was determined, as well as the specifics of their ordered distribution between three possible structural positions of Yb ions in the lattice of the ternary antimonide (Fig. 4a) [14]. This approach provided rising of the thermodynamic data (melting point) of 40 °C and lowering of thermochemical parameters (the mass loss) by 15 times of the doped samples, that are explained by the strengthening of the ionic bond in the lattice and lower mobility of the volatile ytterbium cation (Fig. 4b). With an idea to reduce the sublimation rate of $Yb_{14}MnSb_{11}$ by

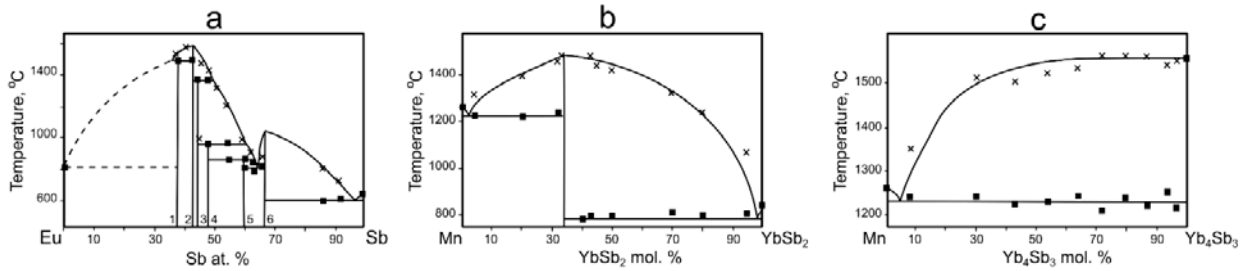

Fig. 3. a) *T-x* diagram of condensed state system Eu - Sb with the phases Eu_5Sb_3 – *1*, Eu_4Sb_3 – *2*, Eu_5Sb_4 – *3*, $Eu_{11}Sb_{10}$ – *4*, Eu_2Sb_3 – *5*, $EuSb_2$ – 6; (b) *T-x* diagram of the condensed state system Mn-$YbSb_2$; (c) *T-x* diagram of the condensed system Mn-Yb_4Sb_3

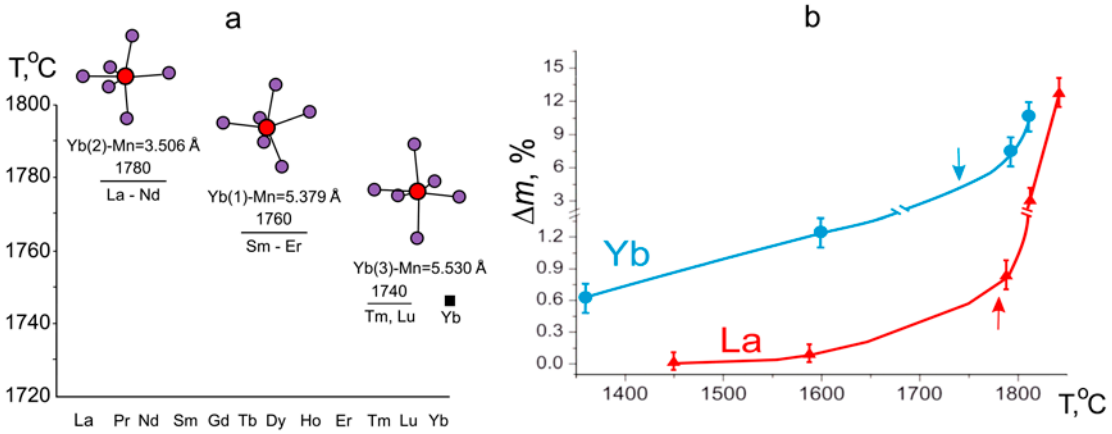

Fig. 4. Thermodynamic and thermochemical stabilities of the $Yb_{13.6}Ln_{0.4}MnSb_{11}$ phases: (a) T_{melt} as a function of the Ln distribution in the Yb (*1*), Yb (*2*), Yb (*3*) crystallographic positions; (b) mass loss of the $Yb_{14}MnSb_{11}$ (Yb), $Yb_{13.6}La_{0.4}MnSb_{11}$ (La) samples at temperatures before and after melting (marked by arrows)

creating a protective layer on the surface made of mixed Yb+Ln oxides, HSTA ensured reliable phase interpretation of complex products forming this layer [15]. This result was largely based on the analysis of the *T-x* diagrams of the system already been studied by us.

The nonstoichiometry of $ZnGeO_4$ and Zn_3GeO_8 is explained by an increased mobility of anionic lattice fragments responsible for the incongruent sublimation of these phases. To obtain reliable data regarding the thermochemical reactions and phase transformations of the samples heated to 2300 °C, all HSTA procedures were used: 1) quick and slow heating; 2) visual observation; 3) control of the distribution of the volatile GeO_2 between vapor and solid residue; 4) registration of the temperature of vapor condensation on the sight glass. New data regarding the nonstoichiometry of germanates was obtained, namely the existence of the initial small-scale stage of the GeO_2 loss resulting in the formation of subtraction solid solutions, and the final stage of the formation of the disordered ZrO_2 with 1–2 mol. % of GeO_2 (Fig. 5a). The suggested approach also proved the absence of the direct transition $ZrGeO_4 \rightarrow Zr_3GeO_8$ [16]. The findings regarding the nonstoichiometry and defectiveness of germanates contributed to the understanding of the mechanism of formation of active intermediate defects responsible for the sintering of initial powders (Fig. 5b), since this state is very important for formation of high-temperature non-porous ceramics.

The functional effectiveness of cryogenic scintillation detectors is ensured by a complete stoichiometry of large $ZnMo(W)O_4$ crystals obtained using the low-temperature-gradient Czochralski technique in a system semi-open to air. According to the *T-x* diagram of the $ZnO-MoO_3$ system, the $ZnMoO_4$ phase is linear. However, two negative factors, namely the peritectic melting of the phase and the incongruent evaporation of MoO_3, significantly affect the quality of the grown crystals. In [17], a number of highly precise measurements of the composition, density, and structural parameters were performed to determine the scale of nonstoichiometry of the grown $ZnMoO_4$ crystals with an excess of ZnO of 0.6 mol. %. The nonstoichiometry is described by oxygen vacancies and random distribution of zinc atoms among the possible molybdenum positions (antistructure disordering) and in interstitial sites. HSTA and the differential dissolution methods were used to determine the main sources of the MoO_3 loss. These methods allowed for precision diagnostics of the products during every stage of crystal growth in a semi-open in air system. The first stage of the solid-phase synthesis of the mixture of ZnO and MoO_3 powders at 650 °C demonstrated spatial inhomogeneity of seeds with the formation of a stable surface layer supersaturated with MoO_3 (Fig. 6a). The surface oxide sublimates actively during homogenization at 1010 °C and the crystallization occurs from a nonstoichiometric melt. Another source of the MoO_3 loss is the overheating of the melt resulting in dissociation of the molybdate anion to oxide and oxygen, which changes the composition of the melt (Fig. 6c). When WO_3 was added to a nonstoichiometric molybdate, the liquidus and solidus lines shifted significantly towards lower

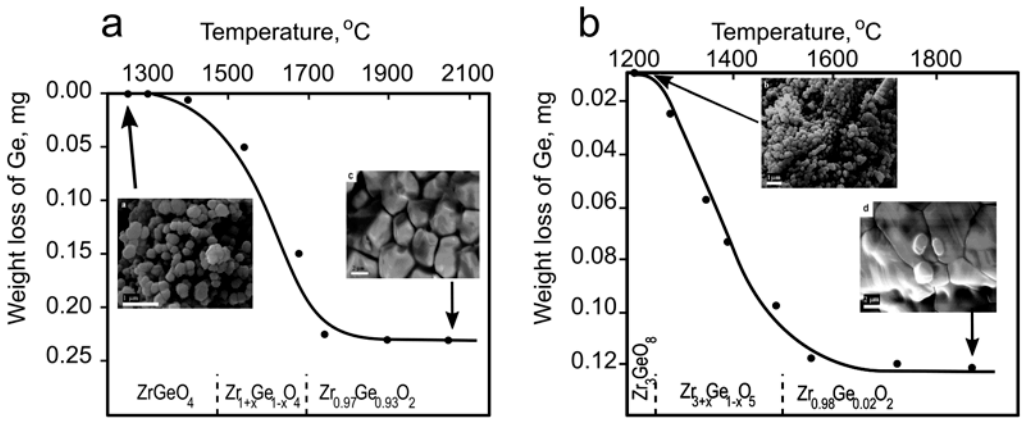

Fig. 5. High-temperature transformations of the $ZrGeO_4$ (a) and Zr_3GeO_8(b) phases. Dependence of compositions from temperature (dashed lines); inserts - morphology of the initial and final samples

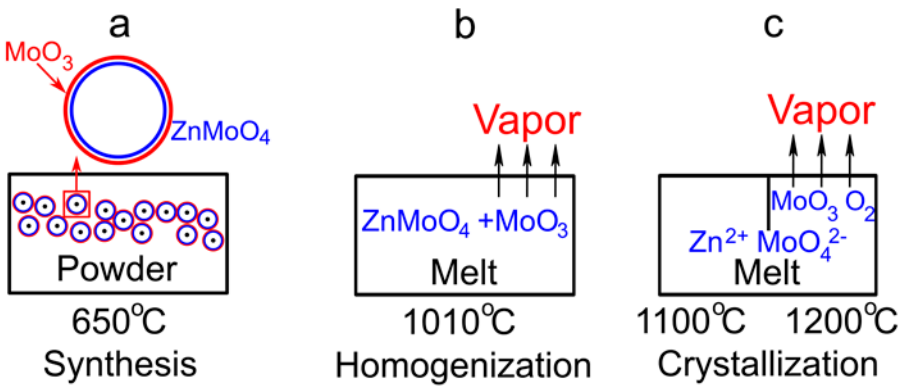

Fig. 6. Sources of formation and loss of the volatile MoO_3component of loss in a semi-open system: (a) during synthesis, (b) during homogenization, (c) during crystallization

temperatures. This kind of minimization of the negative effect of the peritectic melting enhances the quality of large $ZnMo(W)O_4$ crystals.

3. Static tensimetric membrane technique (STM) [3]

This method (Fig. 7a) used at temperatures of 300–1220 K and pressures of 0.01–2 atm thermodynamically determines the existence of nonstoichiometry by means of precise scanning of the composition of the initial sample in the temperature function (Fig. 7c) and can

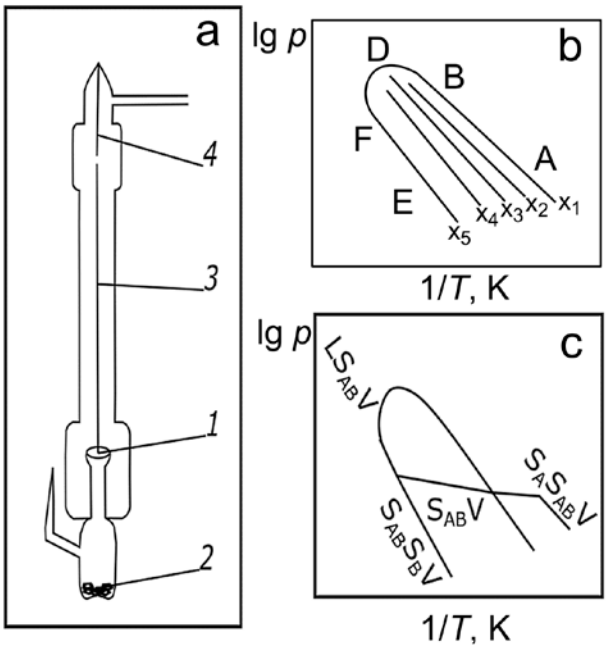

Fig. 7. Possibilities of the tensimetric static method (a) null gauge: plane membrane (*1*), sample (*2*), movable rod (*3*), fixed rod (*4*); (b) *p-T* dependences for the phases with constant compositions x_1-x_5; (c) *p-T* dependence of the AB phase with the homogeneity range

differentiate between several related compounds with very close, but various, compositions (Fig. 7 b). It is this method that played a key role in the understanding of the nature of the nonstoichiometry of REM dichalcogenides with volatile chalcogens.

After their classification based on the structural motif with a general chemical formula $(LnR)_2^+(R_2)^{2-}$ (Ln = REM, R = S, Se) and a unique chemical bond [18], dichalcogenides attracted a lot of attention as quasi-two-dimensional layered materials. A double corrugated cationic layer with a NaCl-type structure is combined with a planar anionic layer built of covalently bonded chalcogen dimers in a lattice with a ZrSSi-type structure. With the loss of chalcogen in the anionic layer, vacancies and isolated ions R^{2-} are added to the dimers R_2^{2-}, from which a superstructure forms with a different electron spectrum [19]. However, it proved to be exceptionally difficult to determine the actual scale of nonstoichiometry and the actual structure of REM polychalcogenides. The problem took over 20 years to be solved.

An analysis of the *p-T-x* diagrams of the LnR_2-$LnR_{1.5}$ (Ln = P3M, R = S, Se) systems is based on the dissociation process of the higher polychalcogenide and the reliability of the final data depends heavily on the quality of the initial sample. When finely dispersed chalcogen-absorbing powders of higher polychalcogenides are studied by the gravimetric method, chemical analysis, and powder diffraction, they were identified as phases of variable composition with a wide homogeneity region from LnR_{2+x} to $LnR_{1.70}$ [19–21]. More advanced techniques, namely the STM method and full-field X-ray structure

analysis, were used when crystals were obtained by means of the CVD method and crystallization from flux. Crystals with a size of ~ 1 mm grown under different pressures of chalcogen vapor had different shapes, colors, and macroscopic structural imperfections. Only a few 0.01–0.03 mm crystals could be tested by X-ray structure analysis, whereas in the membranes always the multicomponent mixture of these crystals was placed. The experimental p_S-T-x diagram of the NdS_2-$NdS_{1.50}$ system with four vertical lines of three-phase equilibria S_1S_2V (two solid phases and vapor) divided by horizontal lines of two-phase equilibria S_2V, demonstrates the existence of three intermediate and linear phases $NdS_{1.900}$, $NdS_{1.875}$, and $NdS_{1.857}$ having non-numeric indices (Fig. 8). Their dissociation kinetics takes 5–10 days, and the backwards kinetics takes 30-40 days, which is explained by the formation of any new superstructures in the anionic layer. These compositions normalized to stoichiometric to be phases $Nd_{10}S_{19}$, Nd_8S_{15}, and Nd_7S_{13} with the general formula Nd_nS_{2n-1}, which reflects defectiveness of the anionic layer and its complex inner arrangement.

We should note that lines 2 and 3 do not have any experimental points in the upper parts. This is a direct indication of the impurity nature of phases $NdS_{1.875}$ and $NdS_{1.857}$ located outside or inside the initial disulfide crystals put in the membrane. The fact that the imperfection of most crystals is caused by the mosaic structure and/or fine-scale twinning is supported also by a microscope experiment [22]. Our fractionation of the initial $SmS_{1.9}$ and PrS_2 crystals based on their identical size, shape, and the type of the Raman spectrum was ineffective, because the phase heterogeneity of initial higher crystals was vivid in their p_S-T-x diagrams [23–24], and twin nature of most $SmS_{1.9}$ and PrS_2 crystals was revealed by the structural diagnostics [25–26]. Thus, the realty of phase heterogeneity of the initial crystals of higher polysulfides grown from solution-melts in a wide range of temperatures and pressures of sulfur vapor was confirmed thermodynamically and structurally.

The overview of the thermodynamic, structural, and physical properties of these polysulfide crystals is presented in [27–29]. Taking into account the dependence of the structure formation of

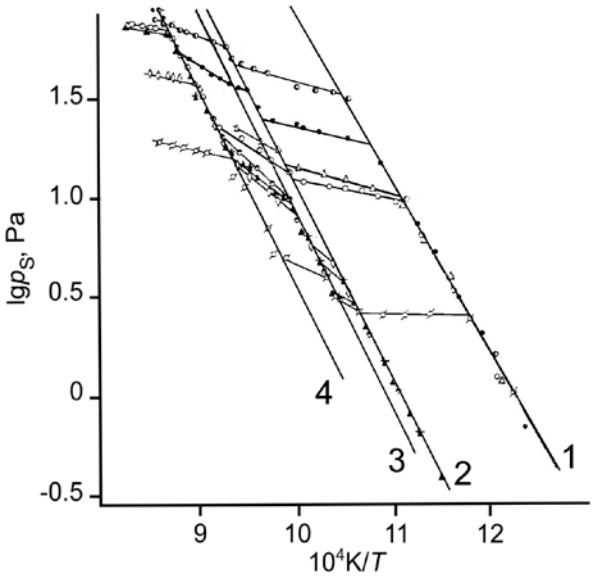

Fig. 8. Experimental *Ps-T-x* diagram of the NdS_2-$NdS_{1.5}$ system with different *m/V* (the sample mass / volume of membrane) ratios and monovariant lines *1-4*

intermediate phases on both the thermodynamics (considering also the molecular composition of vapor) and the dissociation kinetics, the STM procedures were elaborated in order to grow larger single-phase and structurally qualitative crystals of higher polysulfides. The adequacy and reliability of the thermodynamic data regarding the composition of the intermediate phase achieved by following operations: expanding the pressure range up to 2 atm and the temperature range up to 1000 °C, decreasing the temperature step to 15 °C, and increasing the exposure time until the composition remains constant at a level of 0.005 at. %. The growing of 4–5 mm crystals from iodide melts and their fractionation based on the shape, density, and spatial chemical homogeneity, ensured the desired quality of the products. The microburette method was used to determine the density of each individual crystal and differential dissolution was applied to control constancy of the atomic Ln/S ratio in time of complete dissolution of the individual crystal. Both methods proved to be effective for the diagnostics of phase and chemical homogeneity of crystals of each from several fractions in which crystals differed in composition and density. With the fraction of homogeneous initial crystals, diagrams of systems $DyS_{1.85}$-$DyS_{1.5}$ [30] and LaS_2-$LaS_{1.5}$ [31-32] reflected actual phase state (Fig. 9) with a smaller number

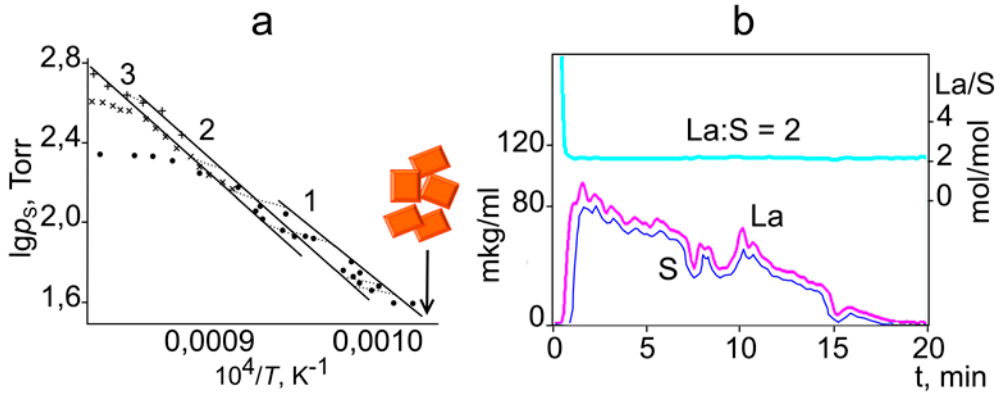

Fig. 9. (a) Experimental *Ps-T-x* diagram of the LaS_2-$LaS_{1.5}$ system for highly homogeneous crystals, monovariant lines (*1–3*) of linear phases LaS_2, $LaS_{1.9}$ and $LaS_{1.76}$; (b) kinetic curves differential dissolution of the homogeneous LaS_2 crystal with stochigram

of coexisting in equilibrium phases than diagrams of non-fractionated crystals. The new type of the diagrams has helped to elucidate the non-equilibrium nature of phases $LaS_{1.96}$, $LaS_{1.87}$, $DyS_{1.81}$, and $DyS_{1.78}$ registered on the previous diagrams. The commonness of occurrence of phase non-equilibrium of polysulfide phases is considered into details in [33].

The homogeneity and microstructural perfection of the $La_{10}S_{19}$ and Dy_8S_{15} crystals ensured the reliability of the quantitative crystal-chemical data relative to the filling factors of all the sulfur positions in the planar anionic layer. For the $La_{10}S_{19}$ phase with 10% of defects, a 10-fold superstructure regarding to structure of the initial ZrSSi subcell was found. For the Dy_8S_{15} with 12.5% of defects, it was already a 24-fold superstructure. Both structures are completely ordered and have geometric proportionality of cationic and anionic layers [31, 34]. The reliability of the chemical and structural data and trustiness of the phase states of the studied systems resulted in classification of Ln polysulfide phases located in the range of 63.7–66.7 at. % of sulfur. The typical phases were LnS_2 (for the La-Nd systems), $LnS_{1.9}$ (for La-Sm), $LnS_{1.85}$ (for Gd-Er), and $LnS_{1.75}$ (for La-Nd). Due to the absence of perfect crystals, phases $LaS_{1.93}$, $DyS_{1.836}$, $HoS_{1.863}$, $DyS_{1.77}$, $NdS_{1.85}$, $SmS_{1.76}$, and $PrS_{1.84}$ with the great structural diversity demonstrate a clear tendency towards disordering of the anionic layer, which could not be realized because of the limited kinetics. Phases $LnS_{2-\delta}$ c $\delta > 0.15$ are characterized by incommensurately modulated structures [26, 35]; the variety of orientations of vacancies, dimers and individual sulfur atoms is considered in [36], where all the studied crystals were twins. In this regard, the authors also believe in correctness of another disordering model, presented as a domain structure of crystals with the domains coherently or incoherently intergrowing with the matrix. Numerous data obtained by the differential dissolution method, which was highly sensitive to the various composition domains located within an individual crystal, confirms the likelihood of the latter model. The pseudomerism masking the actual symmetry of the crystal and the small-scale intergrowing of impurity phases with the matrix are also in good agreement with the results of differential dissolution. Pseudomerism, which is typical for polychalcogenides, is the main source of uncertainty regarding their structural data.

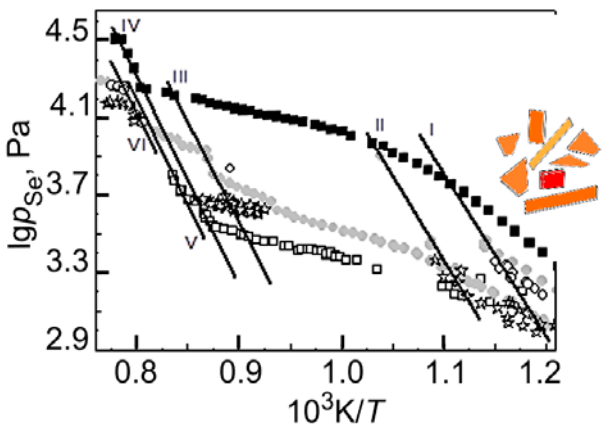

Fig. 10. Experimental p_{Se}-*T*-*x* diagram of the $SmSe_{1.9}$-$SmSe_{1.5}$ system with heterogeneous crystals, monovariant lines *I-YI*, linear intermediate phases $SmSe_{1.875}$, $SmSe_{1.85}$, $SmSe_{1.80}$, $SmSe_{1.75}$, $SmSe_{1.67}$

The thermodynamics of phase transformations in polyselenide diagrams of systems $PrSe_2$-$PrSe_{1.5}$, $GdSe_{1.875}$-$GdSe_{1.5}$, and $SmSe_{1.9}$-$SmSe_{1.5}$ is studied in a different way [37–40]. These experiments were performed with smaller nonfractionated crystals of the initial higher polyselenides and the diagrams of these systems are characterized by a non-reproducible variety of intermediate phases. The diagram of the $SmSe_{1.9}$-$SmSe_{1.5}$ system includes five intermediate phases of closely resembling compositions: $SmSe_{1.90}$, $SmSe_{1.875}$, $SmSe_{1.85}$, $SmSe_{1.80}$, $SmSe_{1.75}$, and $SmSe_{1.67}$ (Fig. 10), most of which, according to the diagram's topology, have a nonequilibrium impurity nature and do not fall into the existing classification of the equilibrium phases of Ln polychalcogenides. The formation of these nonstoichiometric phases complicates the uncontrollable process of the di- and polymerization of selenium in the gas phase during the synthesis, which kinetically hinders the ordering the anionic layer. Nevertheless, such metastable phases continue to attract attention, since the lattice incommensurability of cation-anionic layers is associated with the formation of charge density waves and a good combination of optical, magnetic, and semiconductor properties of the phases [38–39]. In this regard, the conducted physicochemical study significantly contributes to the understanding of the nonstoichiometry of polychalcogenides and the corresponding equilibrium and nonequilibrium structural solid-phase transformations.

4. Stoichiographic differential dissolution method (DD) [4–5]

The effectiveness of the DD method as a key physicochemical tool was especially obvious when analyzing the nonstoichiometry of low-dispersive and amorphous compounds [41–42], as well as thin films with a clear tendency towards spatial inhomogeneity [43–45]. In the DD experiment, the consequent dissolution of phases was performed in a solvent flow with a growing concentration. Based on the analysis of 50–200 portions of the solution, kinetic curves of dissolution of the elements and their stoichiograms are constructed, which after mathematical processing generate data on the number of phases, their composition, and the degree of spatial homogeneity of each individual phase. The effectiveness of the method was demonstrated in [5] and in this review, several special cases are also considered. The color homogeneity of the $[Na_2S]\times Ce_2S_3$ solid solution ensures its popularity as a next generation red pigment. Using the DD method, we determined the phase purity of the powders obtained by solid-phase synthesis at the micro level, as well as the uniformity of the distribution of Na_2S within the grains through fixing invariability the atomic Na/Ce ratio during dissolution of the pigment (Fig. 11). Observed supersaturation of the grain surface with a mobile component Na_2S (that is typical for solid-phase synthesis) resulted in deviation from the standard color value, and

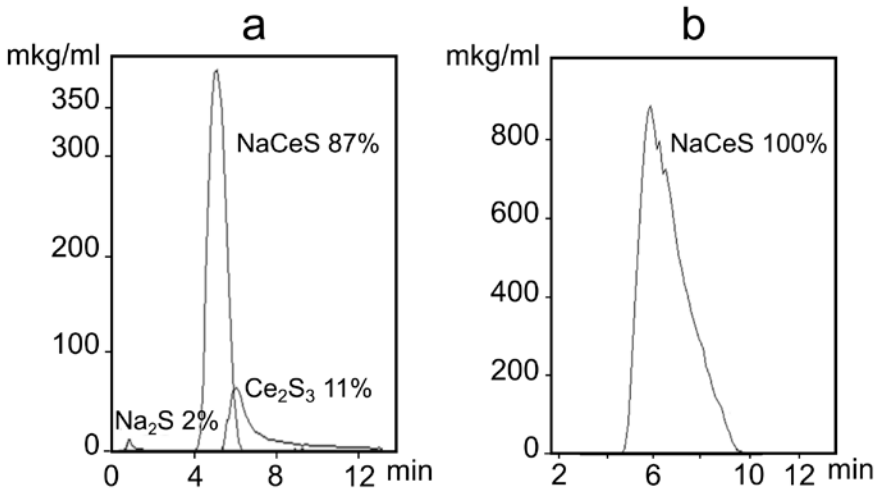

Fig. 11. (a) The phase and chemical composition of the heterogeneous and homogeneous (b) solid solution $Na_2S{\cdot}Ce_2S_3$ according to data of differential dissolution method

only a phase-chemically homogeneous product, giving one peak on the dissolution curves of Na-Ce-S, reflected the quality of pigments with desired color homogeneity [42]. For the $YBa_2Cu_3O_7$ films with a thickness of 0.05-1.0 μm, of vital importance was the data obtained by the DD method regarding the nature and amounts of impurity phases ⩽ 1 wt% and especially their distribution in the film, as well as the determination of sputtering conditions leading to the impurity-free state of the films. The data allowed us to obtain single-crystal specifically oriented films with the best superconducting characteristics of the transition temperature and the current density at that moment [5, 43]. The DD method was used to perform an analysis of the microphase structure of 300 nm films of the ZnS-EuS system. It revealed a very narrow homogeneity region on the level of the $Zn_{0.998}Eu_{0.002}S$ solid solution, which was by an order of magnitude lower than that determined using other trditional methods. This was an important difference, because the appearance of EuS in the form of an impurity phase significantly changed the desired semiconductor properties of the films [44]. MgO thin films are used as effective emitters, and the functional properties are specified to the surface oxygen nonstoichiometry, which is expected to be 10^{-4} at. % at an equilibrium partial pressure of oxygen $p_{O_2} = 10^{-9}–10^{-8}$ Torr. The DD method was successfully in determining of the scale of nonstoichiometry and the conditions favorable for it. It was determined that highly emissive 110 nm MgO films also demonstrated a high chemical activity, due to the formation of a surface layer with oxygen defects. This activity was revealed by dissolving the oxide in hot water. The quantitative data regarding the film dissolution as well as the procedure of creating the required equilibrium partial pressure of oxygen during the film deposition are shown in Fig. 12. We can see that the equilibrium pressure occurs locally in a thin subsurface stationary gas layer due to a heavy dilution of the medium by the release of gaseous products of decomposition of the metal-organic precursor. Heterogeneous equilibrium MgO-O_2 is established according to the reaction $2O_O^X \rightarrow O_{2vapor}$ + Vö + 2e, which is alternative to the traditional defect formation process: $Mg_{vapor} \rightarrow Mg_{Mg}^x$ + Vö + 2e. The new method of controlling the composition of the oxide phase with oxygen defects does not require highest vacuum or radiation generating surface oxygen vacancies. It is quite simple and is often used in the MOCVD processes [45].

In searching for new materials and structures for emissivity coatings, the greatest attention was paid to pairwise mixed oxides MgO with ZrO_2, RuO_2, or CeO_2, obtained in the form of films by means of MOCVD. However, the nature of the measured emission signal and the emission mechanism were not clear due to the amorphous state of the mixed films. Since a diffraction analysis was here useless, the DD method performed a detailed diagnostics of the phase and chemical state of the films of the

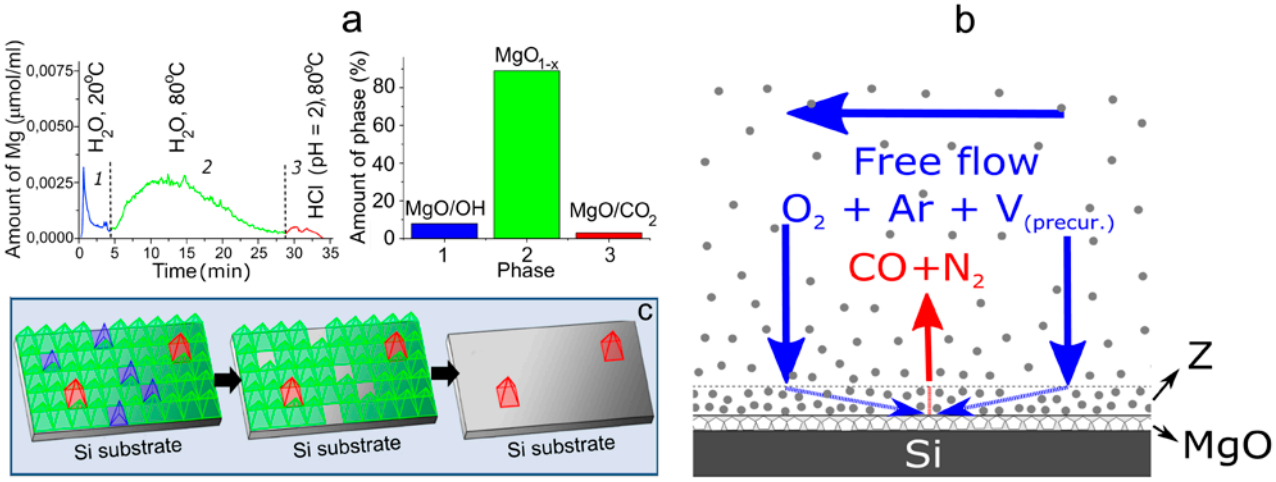

Fig. 12. (a) Kinetic curves of dissolution and phase composition of MgO film; the formation of (b) the gas-near-surface stationary layer Z with $p_{O2} = 10^{-9}$ torr

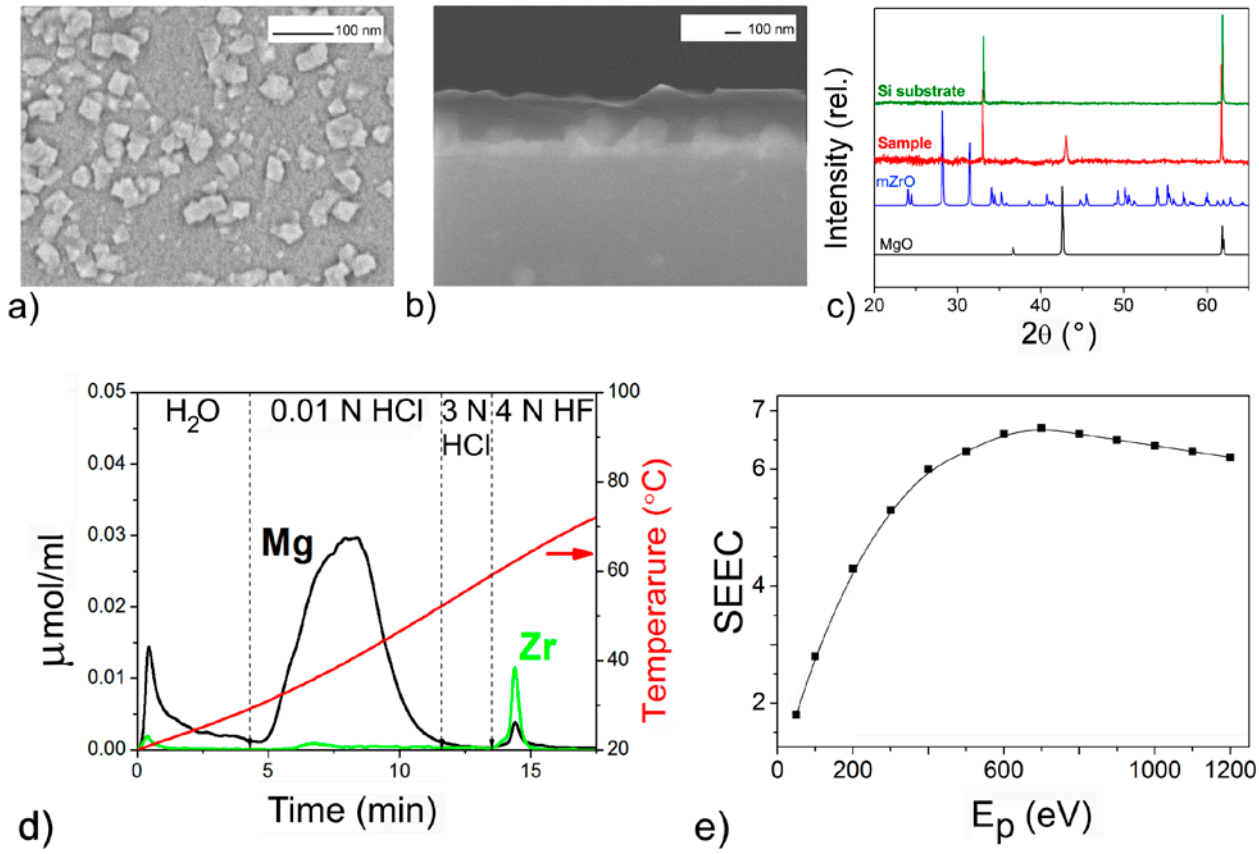

Fig. 13. Characterization of film with the MgO/ZrO_2 = 11/1 composition (a, b) scanning electron microscopy, (c) X-ray diffraction, (d) differential dissolution, (e) coefficient of secondary emission

MgO and ZrO_2 mixture (Fig. 13). It demonstrated that a high chemical activity of both phases, different for MgO and RuO_2, is explained by the oxygen nonstoichiometry of their surfaces resulting from the conditions of film deposition. The active state enabled the oxides to interact and form small fractions of mixed phases based on both oxides Fig. 13. However, the functional properties of the film are determined by its basis, i.e. MgO phase, rather than the mixed impurity phases. In the presented cases, the DD method is the only method that can determine both the phase and chemical state of each from the oxide forms in mixed heterophase films. It facilitates an in-depth understanding of the chemistry and structure of the films and their connection with the functional properties.

5. Conclusions

The review studies the chemistry of promising materials whose compounds melt in the temperature range of 1300–2700 K, but sublimate incongruently, namely LnS, Ln_3S_4, Ln_2S_3, $Yb(Ln)_{14}MnSb_{11}$, $ZrGeO_4$, Zr_3GeO_8, $ZnMo(W)O_4$, $LnS(Se)_2$, and $LnS(Se)_{1.85}$ (Ln – a rare earth element). Due to the specifics of the synthesis of these compounds and their solid-phase and heterophase nature, new physicochemical methods were used to obtain data regarding the nature and dynamics of their transformations. These methods are high-speed high-temperature thermal analysis, static tensimetric membrane technique, and stoichiographic differential dissolution. A combination of the diagnostics methods specific for each compound made it possible to reliably determine the thermodynamic and thermochemical properties of the compounds, as well as the nature of their hightemperature transformations from the initial state to the final product with desired properties. The review demonstrated the importance of accurate *T-x* and *p-T* diagrams of LnS, Ln_2S_3, and $Yb(Ln)_{14}MnSb_{11}$ for the identification of wide and very narrow (up to 10^{-4} at. %) homogeneity regions of the phases.

New data was obtained regarding the lattice mobility of the volatile components of phases $ZrGeO_4$, Zr_3GeO_8, and $ZnMo(W)O_4$ and disordered defective structures of the nonstoichiometric phases of polychalcogenides. The purpose was to review promising methods and approaches to the study of physicochemical systems of various nature and complexity.

Author contributions

I. G. Vasilieva – methodology development, research concept, conducting research, text writing and editing, final conclusions.

Conflict of interests

The author declares that she has no known competing financial interests or personal relationships that could have influenced the work reported in this paper.

References

1. Gibner Ja. I., Vasilyeva I .G. Device for determining the temperatures for phase formations. Patent SU: No. 1806358. Publ. 9.10.1992.

2. Gibner Ja. I., Vasilyeva I. G. Rapid heating in high-temperature thermomicroscopic analysis. *Journal of Thermal Analysis and Calorimetry*. 1998;53: 151–160. https://doi.org/10.1023/a:1010115620439

3. Gibner Ja. I., Vasilyeva I. G. Modified tensimetric set up for the vapor pressure testing*. *Industrial Laboratory*. 1990;56:(7) 45–47. (In Russ.)

4. Malakhov V. V., Vasilyeva I. G. Stoichiography and chemical methods of phase analysis of multielement multiphase compounds and materials. *Russian Chemical Reviews*. 2008;77(4): 370–392. https://doi.org/10.1070/RC2008v077n04ABEH003737

5. Malakhov V. V., Vasilyeva I. G. *Stoichiography: evolution of solid-phase reactions. New principles of research, preparation and characterization of functional materials (book)*. Novosibirsk: Siberian Branch of Russian Academy of Sciences; 2023. 251 c. (In Russ.)

6. Vasilyeva I. G., Nikolaev R. E. Non-stoichiometry and point native defects in non-oxide nonlinear optical large single crystals: advantages and problems. *CrEngComm*. 2019;21: 5890–5897. https://doi.org/10.1039/c9ce01148j

7. Vasilyeva I. G. Nikolaev R. E. High-temperature solid–vapor and liquid–vapor transitions in binary and ternary chalcogenides La_2S_3, MoS_2, Mo_2S_3 and $LiInSe_2$. *Journal of Alloys and Compounds*. 2008;452: 89–93. https://doi.org/10.1016/j.jallcom.2007.01.175

8. Nikolaev R. E. Vasilyeva I. G. Vapor pressure determination for solid and liquid La_2S_3 using boiling points. *Inorganic Materials*. 2008;44(12): 1367–1371. https://doi.org/10.1134/s0020168508120194

9. Gorbunova L. G., Gibner Ja. I., Vasilyeva I. G. The phase diagram of the Nd-S system in the 50-50 at. % S area. *Russian Journal of Inorganic Chemistry*. 1983;29: 222–225.

10. Bien T. N., Hirai S., Vasilyeva I., Nikolaev R., Sekine C., Atsunori K Study of non-stoichiometric GdS_x ($0.68 \leqslant x \leqslant 1.2$) processed by reaction sintering. *Journal of Alloys and Compounds*. 2020;831: 15469. https://doi.org/10.1016/j.jallcom.2020.154691

11. Bien T. N., Hirai S., Vasilyeva I., ... Kawamura Y. Composition and microstructure of holmium monosulfide compacts processed by reaction sintering. *Journal of Alloys and Compounds*. 2021;859: 157872. https://doi.org/10.1016/j.jallcom.2020.157872

12. Abdusalyamova M., Vasilyeva I. The phase equilibrium and intermediate phases in the Eu – Sb system. *Journal of Solid State Chemistry*. 2011;184: 2751–2755. https://doi.org/10.1016/j.jssc.2011.08.018

13. Abdusalyamova M. N., Vasilyeva I. G., Kauzlarich S. The phase equilibrium in Yb-Mn-Sb and Eu-Mn-Sb systems. *SOP Transactions on Physical Chemistry*. 2015;2: 1–9. https://doi.org/10.15764/pche.2015.01001

14. Vasilyeva I. G., Nikolaev R. E., Abdusalyamova M., Kauzlarich S. Thermochemistry study and improved thermal stability of $Yb_{14}MnSb$ alloyed by Ln^{3+} (La-Lu). *Journal of Materials Chemistry C*. 2016;4: 3342–3348. https://doi.org/10.1039/c6tc00178e

15. Vasilyeva I. G., Abdusalyamova M. N., Makhudov F., Eshov B., Kauzlarich S. Thermal air-oxidezed coating on $Yb_{14-x}RE_xMnSb_{11}$ ceramics. The role of rare earth dopants. *Journal of Thermal Analysis and Calorimetry*. 2019;136: 541–549. https://doi.org/10.1007/s10973-018-7659-z

16. Utkin A., Baklanova N., Vasilyeva I. High temperature behavior of zirconium germinates. *Journal of Solid State Chemistry*. 2013;201: 256–261. https://doi.org/10.1016/j.jssc.2013.03.010

17. Vasilyeva I. G., Nikolaev R. E., Nasonov S. G., Kurchev A. V., Shlegel V. N. Peculiarities of the crystallization process and growth of pure nonstoichiometric $ZnMoO_4$ single crystals and those doped with WO_3. *CrystEngComm*. 2019;21: 5890-5897. https://doi.org/10.1039/c9ce01148j

18. Flahauth J., Guittard M., Patrie M. Polysulfides of rare earth metals. *Bulletin de la Société Chimique de France*. 1959;10-12: 1917–1920.

19. Yarembash E. I., Eliseev A. A. *Chalcogenides of rare earth elements*. Moscow: Nauka Publ., 1975, 258 p. (In Russ.)

20. Loginova E. M., Grisik A. A., Ponomarev N. M., Eliseev A. A. The phase *P-T-x* diagram of the La-S system in the La_2S_3-LaS_2 area. Inorganic Materials. 1975;11: 749–751. (In Russ.)

21. Eliseev A. A., Grizik A. A. *Rare earth semiconductors*. Leningrad: Nauka Publ.; 1977. p. 146-177. (In Russ.)

22. Gorbunova L. G., Vasilyeva I. G. Stepped dissociation of the Pr-disulfide*. *Izvestija SO AN SSSR. Serija himicheskih nauk*. 1986;5: 77-81. (In Russ.)

23. Vasilyeva I. G., Belyaeva E. I. Thermodynamic study of the SmS_2-$SmS_{1.5}$ system. *Journal of Solid State Chemistry*. 1999;142: 261–265. https://doi.org/10.1006/jssc.1998.7802

24. Vasilyeva I. G., Belaya S. V. Sulfur nonstoichiometry of PrS_2: a series of new sulfur-deficient phases. *Journal of Solid State Chemistry*. 1999;146: 211–216. https://doi.org/10.1006/jssc.1999.8335

25. Tamazyan R., Arnold H., Molchanov V., Kusmicheva G., Vasilyeva I. The crystal structure and twinning of rare disulfide PrS_2. *Zeitschrift für Kristallographie – Crystalline*

Materials. 2000;215: 272–277. https://doi.org/10.1524/zkri.2000.215.5.272

26. Tamazyan R., Arnold H., Molchanov V., Kusmicheva G., Vasilyeva I. The crystal structure and twinning of $SmS_{1.9}$. *Zeitschrift für Kristallographie – Crystalline Materials*. 2000;215: 346–351. https://doi.org/10.1524/zkri.2000.215.6.346

27. Vasilyeva I. G. Polysulfides. In: *Handbook on the physics and chemistry of rare earths*. K. Gschneider, I. Eyring (eds.). 2001;32: 567–609. https://doi.org/10.1016/s0168-1273(01)32008-1

28. Podberezskaya N., Magarill C., Pervuchina N., Vasilyeva I., Borisov S. Crystallochemical aspects of the structural similarity of rare earth polychalcogenides LnX_{2-x} (x = 0–0.25) *Journal of Structural Chemistry*. 1996; 37: 936–985. https://doi.org/10.1007/bf02439082

29. *Podberezskaya N. V., Pervukhina N. V., Belaya S. V., Vasilieva I. G., Borisov S. V.* Crystal structures of two new holmium polysulfides in the series of rare-earth polychalcogenides. *Journal of Structural Chemistry*. 2001;42(4): 617–627. https://doi.org/10.1023/a:1013198027339

30. Vasilyeva I., Shilkina T., Podberezskaya N., Naumov D. Tensimetric and structural study of dysprosium polysulfides. *Russian Journal of Inorganic Chemistry*. 1999;44(2): 153–156. Available at: https://www.elibrary.ru/item.asp?id=13328511

31. Vasilyeva I., Podberezskaya N., Naumov D., Pervukhina N., Ikorskii V., Borisov S. Growth and structure of lanthanium polysulfide crystals. *Journal of Structural Chemistry*. 2003;44: 154–162. https://doi.org/10.1023/a:1024949418041

32. Vasilyeva I. G., Nikolaev R. E. The La_2S_3-LaS_2 system: thermodynamic and kinetic study. *Journal of Solid State Chemistry*. 2010;183: 1747–1751. https://doi.org/10.1016/j.jssc.2010.05.026

33. Vasilyeva I. G. Phase equilibrium and p_s-T-X-diagrams of the systems Ln_2S_3-LnS_2 (Ln = La, Pr, Nd, Sm-Er). *Russian Journal of Physical Chemistry.* 2006;80: 2068–2073. https://doi.org/10.1134/s003602440611029x

34. Podberezskaya N., Naumov N., Vasilyeva I., Pervuchina N., Magarill C., Borisov S. Structure of dysprosium polysulfide $DyS_{1.83}$(Dy_6S_{11}). according to X-ray diffraction analysis *Journal of Structural Chemistry*. 1998;39: 872-884. https://doi.org/10.1007/bf02903544

35. Graf Ch., Vasilyeva I., Doert Th. Six new rare earth polysulfide compounds with ZrSSi superstructure: $LnS_{1.85(2)}$ (Ln = Y, Gd – Er). Technische Universität Dresden: *Gemainsame Jahrestagung* der Deutschen Gesellschaft fur Kristallographie und der Deutschen fur Kristallzuchtung, Universitat Bremen, 5–9 Marz, 2007.

36. Doert Th., Graf Ch., Vasilyeva I., Schnelle W. Structural frustration and occupational disorder: the rare earth metal polysulfides $Tb_8S_{14.8}$, $Dy_8S_{14.8}$, $Ho_8S_{14.8}$, $Y_8S_{14.8}$. *Inorganic Chemistry*. 2012;51: 282–289. https://doi.org/10.1021/ic201639f

37. Zelenina L., Chusova T., Vasilyeva I. Thermodynamic investigation of the phase formation processes in the systems $LnSe_2$–$LnSe_{1.5}$ (Ln = La, Ce, Pr, Nd). *The Journal of Chemical Thermodynamics*. 2013;57: 101–107. https://doi.org/10.1016/j.jct.2012.08.005

38. Doert Th., Graf Ch., Schmidt P., Vasilyeva I., Simon P., Carrillo-Cabrera W. The $PrSe_2$-$PrSe_{1.5}$ system: studies of the phase relationships and the modulated crystal structure of $PrSe_{1.85}$. *Journal of Solid State Chemistry.* 2007;180: 496-509. https://doi.org/10.1016/j.jssc.2006.10.030

39. Chusova T. P., Zelenina L. N., Vasilyeva I. G., Graf Ch., Doert Th. Thermodynamic study of the system $PrSe_2$-$PrSe_{1.5}$ and $GdSe_{1.875}$-$GdSe_{1.50}$. *Journal of Alloys and Compounds*. 2008;452: 94–98. https://doi.org/10.1016/j.jallcom.2006.12.162

40. Zelenina L. N., Chusova T. P., Vasilyeva I. G. Thermodynamic properties of Sm-and Gd-polyselenides. *The Journal of Chemical Thermodynamics*. 2015;90: 122–128. https://doi.org/10.1016/j.jct.2015.06.031

41. Vasilyeva I. G., Logvinenko V. A. Contribution of chemical methods in the study of nanostructures of ultrafine and amorphous materials. *Solid State Phenomena.* 2016;257: 237–240. https://doi.org/10.4028/www.scientific.net/ssp.257.237

42. Vasilyeva I., Ayupov B., Vlasov A., Malakhov V., Macaudiere P., Maestro P. Color and chemical heterogeneities of γ-[Na]-Ce_2S_3 solid solutions. *Journal of Alloys and Compounds*. 1998;268: 72–77. https://doi.org/10.1016/s0925-8388(97)00580-x

43. Vasilyeva I. G., Malakhov V. V., Vlasov A. A., Predtechensky M. R. New method of microphase and chemical analysis as applied to the YBaCuO thin films. *Thin Films*. 1997;292: 85–90. https://doi.org/10.1016/s0040-6090(96)08945-6

44. Vasilyeva I., Ivanova E., Vlasov A., Malakhov V. Phase composition of mixed ZnS-EuS thin films grown by metal organic chemical vapor deposition. *Materials Research Bulletin*. 2003;38: 409–415. https://doi.org/10.1016/s0025-5408(02)01070-x

45. Vasilyeva I. G., Vikulova E. S., Pochtar A. A., Morozova N. B., Igumenov I. K. Invisible surface oxygen vacancies in a thin MgO film: impacts on the chemical activity and secondary electron emission. *Inorganic Chemistry*. 2020;59: 17999–18009. https://doi.org/10.1021/acs.inorgchem.0c02351

46. Vasilyeva I. G., Vikulova E.S., Pochtar A. A., Morozova N. B. Mixed films based on MgO for secondary electron emission application general trends and MOCVD Prospects. *Coating*. 2021;11: 176–194. https://doi.org/10.3390/coatings11020176

** Translated by author of the article*

Information about the author

Inga G. Vasilyeva, Dr. Sci. (Chem.), Leading Research Fellow of Nikolaev Institute of Inorganic Chemistry Siberian Branch of RAS (NIIC SB RAS) (Novosibirsk, Russian Federation).

https://orcid.org/0000-0003-4045-9820
kamars@niic.nsc.ru

Received 21.06.2024; approved after reviewing 01.07.2024; accepted for publication 16.09.2024; published online 16.09.2024;

Translated by Yulia Dymant

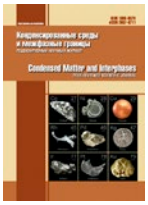

ISSN 1606-867X (Print)
ISSN 2687-0711 (Online)
Condensed Matter and Interphases
Kondensirovannye Sredy i Mezhfaznye Granitsy
https://journals.vsu.ru/kcmf/

Review

Review article
https://doi.org/10.17308/kcmf.2024.26/12398

Phases with layered (AB) and "defective" (A_2B_3) structures in A^{III}–B^{VI} systems
Part 1. Structural uniqueness and properties of bulk samples and films. Review

A. Yu. Zavrazhnov[1]✉, N. Yu. Brezhnev[2], I. N. Nekrylov[1], A. V. Kosyakov[1], V. F. Kostryukov[1]

[1]*Voronezh State University,*
1 Universitetskaya pl., Voronezh 394018, Russian Federation

[2]*Voronezh State Agricultural University,*
1 Michurin st., Voronezh 394087, Russian Federation

Abstract

The review analyses and, where possible, reconciles data on two large groups of inorganic substances that are very unusual in terms of structure and properties, designated as $A^{III}B^{VI}$ compounds. The structures and properties of typical compounds of these systems: $A_1^{III}B_1^{VI}$ and $A_2^{III}B_3^{VI}$ were considered. The relationship between the structure and the nature of the chemical bond and the organization of stoichiometric vacancies in crystal lattices is described in detail. The genesis of structures was analyzed for various modifications of $A_2^{III}B_3^{VI}$ sesqui-chalcogenides. The transformations of these compounds into each other were also considered in relation with the ordering/disordering processes of stoichiometric vacancies. The possibilities of forming nanolayer structures, tubulenes, and intercalates were demonstrated for $A_1^{III}B_1^{VI}$ layered compounds. The prospects for the application of both nanolayer coatings and bulk single crystals of $A_1^{III}B_1^{VI}$ and $A_2^{III}B_3^{VI}$ phases were analyzed. The presented review is based on the analysis of both literary data and the results of the studies of the authors and some other researchers of Voronezh State University.

Keywords: Gallium chalcogenides, Indium chalcogenides, Stoichiometric vacancies, Polymorphism, Vacancy ordering, Epitaxy, Layered structure

For citation: Zavrazhnov A. Y., Brezhnev N. Y., Nekrylov I. N., Kosyakov A. V., Kostryukov V. F. Phases with layered (AB) and "defective" (A_2B_3) structures in AIII- BVI systems. Part 1. Structural uniqueness and properties of bulk samples and films. Review. *Condensed Matter and Interphases*. 2024;26(4): 646–665. https://doi.org/10.17308/kcmf.2024.26/12398

Для цитирования: Завражнов А. Ю., Брежнев Н. Ю., Некрылов И. Н., Косяков А. В., Кострюков В. Ф. Фазы со слоистыми (AB) и «дефектными» (A_2B_3) структурами в системах A^{III} – B^{VI}. Часть 1. Структурное своеобразие и свойства объемных образцов и пленок. Обзор. *Конденсированные среды и межфазные границы*. 2024;26(4): 646–665. https://doi.org/10.17308/kcmf.2024.26/12398

✉ Alexander Y. Zavrazhnov, e-mail: alzavr08@rambler.ru

1. Introduction

This article is devoted to the description of two large groups of inorganic substances, which are very unusual in terms of their structures and properties, designated as $A^{III}B^{VI}$ compounds. The aim of the study was to summarize, analyze, and, if possible, reconcile data on the structures of $A_1^{III}B_1^{VI}$ monochalcogenides and $A_2^{III}B_3^{VI}$ sesqui-chalcogenides, their hierarchies (parent – daughter structures) and transformations into each other. It should be note that A^{III} tellurides are mentioned here only in general terms, and thallium chalcogenides are not described at all due to the specific nature of the compounds involving heavy *sp*-elements (primarily, the 6th period of the Periodic Table).

Almost all A^{III}–B^{VI} binary systems provide a huge number of different structures (up to two dozen according to [1]). However, the greatest interest of researchers and practitioners is associated with the structural features of solid phases and, consequently, with the specific properties of these substances. Among the huge variety of compositions of compounds, realized for each of these chalcogenide systems, two typical approximate stoichiometries stand out: $A_1^{III}B_1^{VI}$ (monochalcogenides) and $A_2^{III}B_3^{VI}$ (sesqui-chalcogenides). It should be noted that there are large structural differences both *between* two separated groups, and *inside* each of these groups. However, all mono- and sesqui-chalcogenides of Al, Ga, and In have a common unifying feature: all these structures are composed only on (almost) tetrahedral fragments. Such a structure of non-molecular substances is not unusual: as is known that $A^{I}B^{VII}$, $A^{II}B^{VI}$, and $A^{III}B^{V}$ compounds form structures such as sphalerite, wurtzite, and their derivatives, in which each atom is tetrahedrally bound to four neighboring atoms. For the listed compounds, chemical bonds are composed of *s*- and *p-valence* states; they consist of eight electrons for the pair of atoms A and B. However, in A^{III} – B^{VI} systems, pairs of atoms have nine valence electrons. For $A^{III}B^{VI}$ compounds this imbalance in the number of electrons results in structures containing atomic-scale voids that are surrounded by non-separated even-electron orbitals [1]. Let us consider the consequences of this fact for the formation of a variety of structures of the $A_1^{III}B_1^{VI}$ and $A_2^{III}B_3^{VI}$ types, starting with the last group (i.e., with the sesqui-chalcogenides).

2. $A_2^{III}B_3^{VI}$ compounds: general structural features of solids *sesqui*-chalcogenides

The calculation of valence electron concentration (*VEC*) [2, 3] for compounds of stoichiometry, $A_2^{III}B_3^{VI}$ allows sphalerite-like, wurtzite-like, and also derivative structures with CN = 4 (*VEC* = 4.8)* to be formed for these compounds.

Indeed, compounds with such a structure are characteristic of sesqui-chalcogenides of aluminum, gallium, and indium. However, the peculiarities of the above-mentioned electronic imbalance lead to the fact that the $A_2^{III}B_3^{VI}$ phases stand out from other solid substances by containing *stoichiometric vacancies* as structural units (Fig. 1).

* The VEC value is calculated as $VEC = \frac{n_{\bar{e}(A)}n_A + n_{\bar{e}(B)}n_B}{n_A + n_B}$, ,

where n_A and n_B are the number of atoms A^{III} and B^{VI} in the formula unit of the compound, and $n_{\bar{e}(A)}$ and $n_{\bar{e}(B)}$ are the total number of *s*- and *p*-valence electrons supplied by single atoms of A^{III} and B^{VI} respectively.

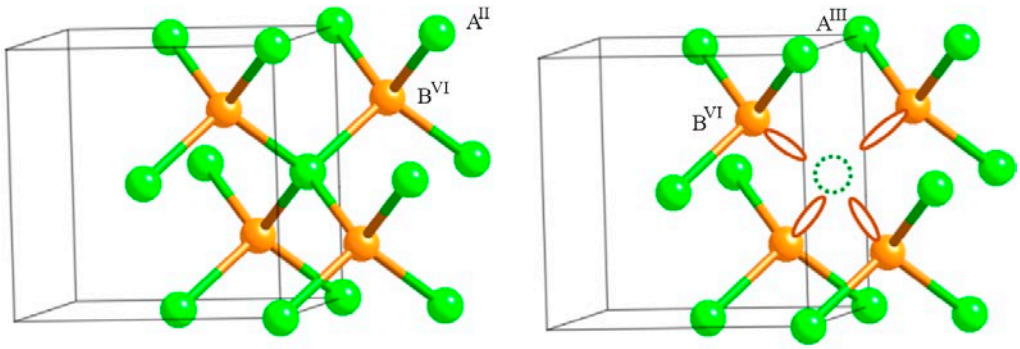

Fig. 1. A fragment of the ideal zinc-blende (sphalerite) structure (left) and a fragment of the sphalerite-like "defective" chalcogenide structure with a stoichiometric vacancy (right). The circle in the form of a dotted line is a stoichiometric vacancy, the ellipses stand for the lone electron pairs of chalcogen atoms directed toward the vacancy

The stoichiometric vacancies occur when disorder takes place in any sublattice (or several at once), arising due to the discrepancy between the stoichiometry and the structural type. As a result, the filling of certain positions in the sublattice by atoms is incomplete, and the unfilled positions are called *stoichiometric vacancies*. Their concentration can be enormous – up to tens of mol. % [2, 4] (p. 105). For the discussed chalcogenides it is about 33 mol. %. This value follows from the fact that the wurtzite or sphalerite-like structure implies a ratio of the number of A atoms to the number of B atoms of 1:1. However, the requirement of 2:3 stoichiometry forces $^1/_3$ of the positions in the cation sublattice to be vacant. Thus, a more appropriate notation for these compounds corresponds to the formula $A^{III}_{\frac{2}{3}}(v_A)_{\frac{1}{3}}B^{VI}$.

If we consider the chemical bond in these compounds to be a covalent pair-electron bond, then the appearance of stoichiometric vacancies can be explained by the fact that chalcogen atoms can form a bond with only three atoms of the cation-forming agent A^{III}, and instead of the fourth bond, such an atom has an orbital with an unshared electron pair, for which there is no suitable vacant orbital. In this case, the A^{III} atoms have all four bonds with chalcogen atoms in the direction of the tetrahedron vertices. It should be noted that such a consideration is not entirely applicable to *indium sulfides*, for which the contribution of the ionic component of the chemical bond is higher.

It should be emphasized that stoichiometric vacancies are structural elements and for this reason, they cannot be fully associated with classical point defects, such as thermal vacancies. Nevertheless, the term "*defective structures*" is used in the literature; the structures of "defective" sphalerite ("defective" wurtzite, "defective" spinel) are also discussed. In some cases, stoichiometric vacancies can order with the formation of a number of their own individual phases of close stoichiometry with a slight distortion of sphalerite-like or wurtzite-like structures.

The terms highlighted here in italics were first introduced in Russian-language scientific literature in 1954 after the studies of N. A. Goryunova [2], [5] and B. F. Ormont [4], and later were developed in the research of the scientific groups of L. S. Palatnik and V. M. Koshkin [6–11]. In the English and French literature, the consideration of special types of vacancies and "defective" structures began in 1949 in studies of Hahn and Klinger [12] and was taken up by Suchet [13].

The discussed compounds allow for obtaining promising materials with the most unusual and diverse characteristics, of which we will consider the most specific ones. First of all, we note that the low coordination numbers and the position of the phase-forming elements in the Periodic Table imply the presence of semiconductor properties for all $A^{III}_2B^{VI}_3$. Moreover, stoichiometric vacancies allow these properties to be maintained practically unchanged even with high concentrations of impurities [14] and with high levels of radiation [8]. Filling of stoichiometric vacancies with atoms of *d*-elements allows isolating these atoms from each other. As a result, for example, in the case of chromium-doped Ga_2Se_3, high ferromagnetic characteristics are already found at room temperature [15]. Lithium atoms can fill these internal voids in $(In_xGa_{1-x})_2Se_3$ nanowires, which is used to create new types of ordered vacancy/lithium atom superlattices and thus obtain lithium-ion storage devices, photovoltaic materials, and phase memory devices [16]. By ideology, the incorporation of lithium atoms is similar to the intercalation of a layered material; however, in the considered sesqui-chalcogenides, the lithium atoms are located on spirals, not on planes. Indium sesqui-chalcogenides, which have a layered structure were demonstrated to be a very promising as photocatalysts for light-induced water splitting [17].

Initial interest in $A^{III}_2B^{VI}_3$ materials, in particular to Ga_2Se_3, arose during the search for ways to create $A^{II}B^{VI}$ heterostructures on $A^{III}B^{V}$ based on the idea of using defective "diamond-like" structures as interlayers. The latter had to match the identically symmetrically oriented single-crystal surfaces of substances with noticeably different lattice parameters. However, this interest quickly faded for a long time, since it was discovered that the impairment of interphase boundaries during the initial stages of the formation of ZnSe-on-GaAs type heterostructures is a serious obstacle [18, 19]. It was later revealed that Ga_2Se_3 on GaAs

itself is a potentially useful material, especially in the form of thin epitaxial film. The Ga_2Se_3 coatings can passivate various oriented surfaces (primarily (001)) of gallium arsenide [20], which has great potential for the use of GaAs taking onto account problems of creating insulating or other functional layers in this important semiconductor. Such layers are needed, first of all, for the creation of optoelectronic devices that use the band gap of gallium arsenide, which is suitable for sunlight [21].

Improvements in molecular beam epitaxy technology in recent years allowed to circumvent the aforementioned problem of interphase boundary impairment when using sesqui-chalcogenides as "interlayer" materials in the formation of $A^{III}B^{V}$ – Si or $A^{II}B^{VI}$ – $A^{III}B^{V}$ type heterostructures [1]. The close correspondence of the lattice parameter of sphalerite-like Ga_2Se_3 to the parameters of Si, GaP, and ZnS substrates facilitate its use in heterostructures. In particular, close lattice matching (0.1%) and minimal interdiffusion at the well-formed Ga_2Se_3/Si interface make such a heterostructure promising for use in electronics. This is due to the fact that the band gap width in epitaxial films of gallium sesqui-chalcogenides is located in a convenient range for visible optoelectronics [22]. In particular, it was proposed to use *n*-alloyed $Ga_2(S_xSe_{1-x})_3$, solid solution deposited on *p*-Si heterojunctions, for solar cells [23]. Among Russian specialists working on obtaining heterostructures using gallium and indium sesqui-chalcogenides as "interlayer" substances or functional coatings when creating heterostructures on $A^{III}B^{V}$ group semiconductors, the scientific group of the authors of the studies [24–27] should be mentioned.

3. "Defective" structure $A_2^{III}B_3^{VI}$ variants: their hierarchy and relationship

Let us consider in more detail the structures of "defective" phases based on wurtzite and sphalerite, paying special attention to the relationship between these structures and the ordering of stoichiometric vacancies. For many compounds in $A_2^{III}B_3^{VI}$ systems, there is a large variety of structures of "defective" various polymorphic phases close to the exact A_2B_3 composition. For some of these compounds, deviations from the ideal composition towards A^{III} component are possible. All $A_2^{III}B_3^{VI}$ structures, except for some modifications of In_2S_3, are composed on almost tetrahedral fragments: A^{III} (Al, Ga, In) atoms, are surrounded by four chalcogen atoms, and the chalcogen atoms, in turn, are surrounded by A^{III} atoms and stoichiometric vacancies. Most of the discussed "defective" structures can be divided into two groups: the so-called "parent" and "daughter" structures. The parent structures are crystals with a fairly high symmetry, these are modifications of the sphalerite or wurtzite type. Structural vacancies in the cation sublattices of these phases are distributed in a disordered manner. Due to the partial or complete ordering of stoichiometric vacancies, such structures can be transformed. In this case, "daughter" structures emerge. For the considered sulfides and selenides, the symmetry of the crystal lattice decreases with ordering. The space group of the crystal also changes. For some $A_2^{III}B_3^{VI}$ modifications, several daughter phases are found (Ga_2S_3, In_2Se_3). This is because the ordering of stoichiometric vacancies can occur in different ways. Daughter modifications with completely ordered structural vacancies are located on the phase diagrams in lower temperature regions, they have narrow homogeneity regions and almost ideally correspond to the A_2B_3 stoichiometry [28–30].

Highly symmetric sphalerite-like structures with disordered stoichiometric vacancies have been found for several metal A^{III} chalcogen systems (γ-Ga_2S_3, α-Ga_2Se_3, α-Ga_2Te_3, α-In_2Te_3). The space group $F\bar{4}3m$ corresponds to such structures, like classical sphalerite ZnS. Due to the deficiency of metal cations, their crystallographic formula is written as $A^{III}(4c)_{2/3}v(4c)_{1/3}B^{VI}(4a)$. The positions of the cation-forming component are 4c ($\bar{4}3m$) (1/4, 1/4, 1/4) occupied by about $^2/_3$. The remaining approximately $^1/_3$ of the positions are not occupied, and these vacant positions are distributed in the cation sublattice in a stochastic manner. Positions 4*a* (43*m*) (0, 0, 0) in the anion sublattice are completely occupied by chalcogen atoms [31] (Fig. 2).

By analogy with zinc sulfide and other substances with "diamond-like" structures, the elementary (almost) tetrahedral "building blocks" of $A_2^{III}B_3^{VI}$ compounds can also fit into wurtzite-type structures (space group $P6_3mc$).

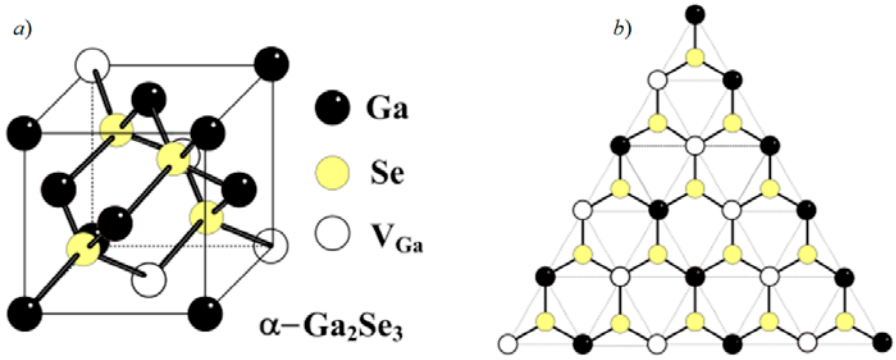

Fig. 2. "Defective" sphalerite-like structure for cubic α-Ga_2Se_3 (a) and the {111} plane in this structure (b) [31].

Like sphalerite-like phases, they contain about $^1/_3$ disordered vacancies in the cation sublattice. The crystal chemical formula of such phases is written as $Me(2b_1)_{2/3}v(2b_1)_{1/3}Ch(2b_2)$, where Wyckoff positions 2*b* (3*m*) (1/3, 2/3, z) are characterized by coordinates: $z_1 = 0$, $z_2 = 3/8$. [12, 30].

Such disordered high-temperature phases can be considered parent phases in relation to "daughter" superstructures. For example, the α-Ga_2S_3 crystal lattice with space group (SG) $P6_1$ was described as a superstructure derived from disordered wurtzite-like β-Ga_2S_3. Similar superstructures are also characteristic of α-Al_2S_3 [32, 33]. In this case, the transformation of the parent phase of "defective" wurtzite into a daughter superstructure occurs with a three-layer ordering of chalcogen vacancies along the [001] axis. According to [28], during such a rearrangement, three crystallographically nonequivalent cationic positions arise, which are completely or partially filled by the A^{III} atoms. Positions of type (1) are almost completely filled: the filling factor is close to 1, and there are practically no vacancies. The cationic positions of type (2) are occupied with a factor of 0.67 and in this respect the occupancy is close to that of all cationic sites in the parent structure of defective "wurtzite". Finally, positions of type (3) are occupied with a factor of 0.35.

This ordering of vacancies requires a change in symmetry from the $P6_3mc$ group to the $P6_1$ subgroup and another choice of the elementary cell with new lattice parameters:

$a_{P6_1} \approx \sqrt{3}a_{P6_3mc}$; $c_{P6_1} \approx 3c_{P6_3mc}$ (Fig. 3). It is important to emphasize that in the resulting daughter structures, each cation position continues to be filled stochastically and, in this sense, we can only discuss quasi-ordering of the structure, in contrast to other types of ordering of stoichiometric vacancies. It should be noted that despite the formation of superstructures with SG $P6_1$, the corresponding phases can be stable only at high (> 900 °C) temperatures. In addition, they have noticeable deviations from the ideal stoichiometric composition [34]. According to these properties, daughter phases with this type of ordering are closer to the parent "defective" structures of wurtzite and sphalerite than to other daughter structures with completely ordered stoichiometric vacancies.

Another type of reorganization of stoichiometric vacancies in the wurtzite-like modification $A_2^{III}B_3^{VI}$ leads to the formation of the second type of daughter phases. In this case, the ordering of vacancies occurs along the vector

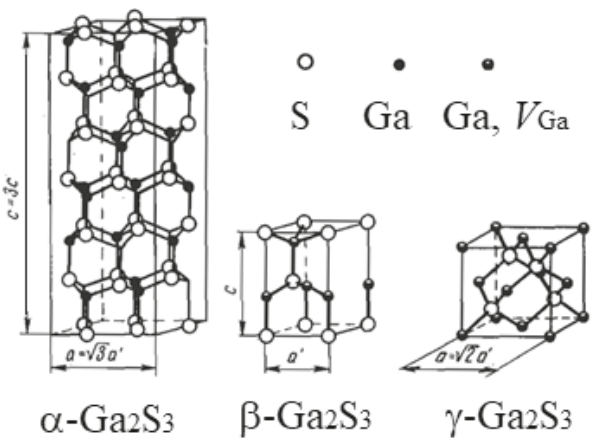

Fig. 3. Structures of some gallium sesquisulfide modifications (present on the phase diagram at high-temperatures, *T* > 878 °C). From left to right: superstructure of the $P6_1$ type, wurtzite-type defect and sphalerite-type defect structure [28]

[110] of the wurtzite parent lattice and leads to the formation of a monoclinic lattice (space group *Cc*). This structure can already be called ordered due to the presence of entire rows of vacancies in the gallium sublattice (Fig. 4) [31]. The formation of such monoclinic modifications occurs in Ga–S systems (α′-Ga_2S_3), Al – Se (α-Al_2Se_3), as well as in telluride systems. In this case, the ordering also leads to a reduction in symmetry, to a *Cc* subgroup of $P6_3mc$ group and the formation of two cationic and three anionic sublattices of the 4*a* (1) *xyz* family.

The variants for ordering stoichiometric vacancies in wurtzite-like structures do not end there. Several variants of the formation of daughter phases are realized for *indium* sesqui-selenide.

Parental wurtzite-like modification for In_2Se_3, described in [35], is most likely always metastable. Among the phases that can be represented on the *T*-*x*-diagram of the In – Se system, the high-temperature δ-In_2Se_3 structure is closest to this (SG $P6_3mc$). Despite the complete correspondence of this SG to the wurtzite crystal lattice, δ-In_2Se_3, is a superstructure and does not belong to the "true" structural type of wurtzite, since for the latter the ratio of the lattice parameters (*c* to *a*) should be equal to ~1.6 [36]. In our studies, we obtained the following values: *a* = 4.025(1) Å, *c* = 19.265(1) Å [37], which are comparable with the results of [38]: *a* = 4.00 Å, *c* = 6.41 Å. These data indicate a multiple (~3 times) increase in the parameter *c* (4.025×1.6×3 = 19.32 Å) compared to the idealized (by parameter *a*) parent wurtzite structure. The latter may be evidence of the ordering of vacancies, which *in this case* occurs *without a change* of the space group.

The lower temperature modification in comparison with δ-In_2Se_3 is g-In_2Se_3 and it is typical for a $A_2^{III}B_3^{VI}$ semiconductor compound structure with ordered stoichiometric vacancies. According to our research data, the γ-In_2Se_3 polymorphic modification has a hexagonal structure with a space group of $P6_1$ ($P6_5$), (*a* = 7.133 Å, *c* = 19.58 Å) [37]. This is consistent with the results of other researchers [38, 39] – including those who used transmission electron microscopy methods [40, 41]. In [42] it was shown that in the γ-In_2Se_3 phase, structural vacancies are aligned along one of the screw axes, and the proportion of vacancies in the cation sublattice, as in most other $A_2^{III}B_3^{VI}$"defective" semiconductors, is ~ $^1/_3$ of the number of cationic positions. The "defective" crystal structure of γ-In_2Se_3 is shown in Figs. 5 and Fig. 6d.

There are also other modifications for indium sesqui-selenides and sesqui-sulfides which taking into account the definition given at the beginning of this review are no longer entirely correctly classified as "defective" structures with stoichiometric vacancies. In these phases, the ordering of vacancies leads to their grouping into separate planes. As a result, the chemical bonds between the layers

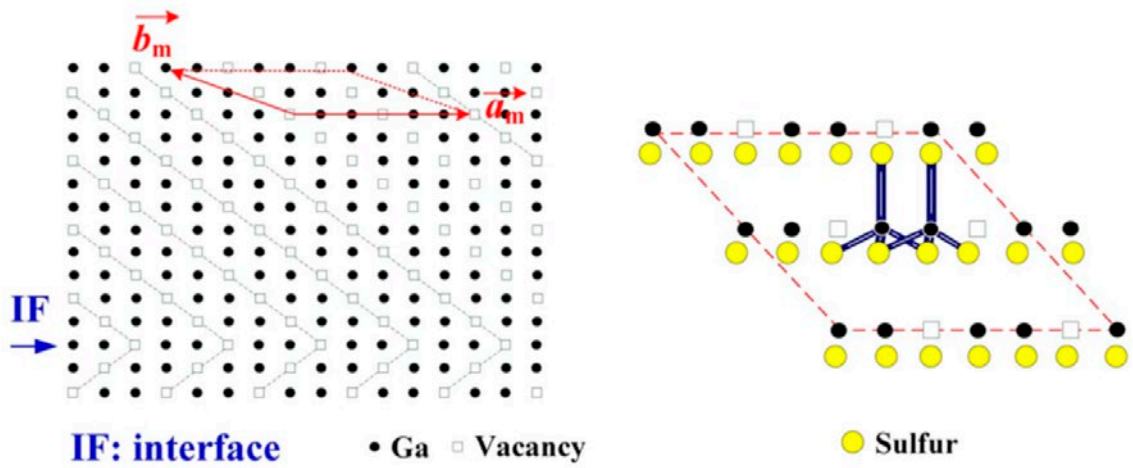

Fig. 4. Fragment of the monoclinic a-Ga_2S_3 structure with an image of stoichiometric vacancies in the Ga-sublattice. The right part of the figure shows the coordination scheme of gallium atoms with an image of chemical bonds close to sp^3-hybrid [31]

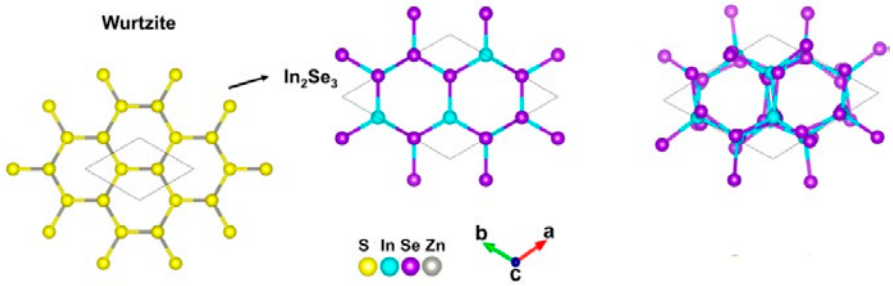

Fig. 5. Relationship between the wurtzite structure (left) with the wurtzite-like idealized structure of In_2Se_3 (center) and the real structure of γ-In_2Se_3 (right)

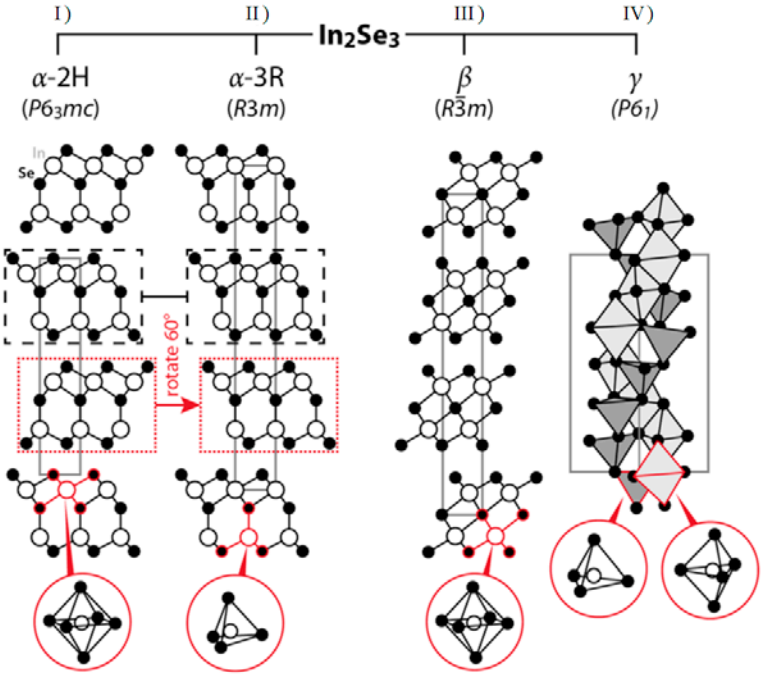

Fig. 6. Structures of In_2Se_3: 2H-α-In_2Se_3 (I), 3R-α-In_2Se_3 (II), β-In_2Se_3 (III) и γ-In_2Se_3 (IV)

are broken and the resulting structures turn out to be typically *layered* and similar in properties to $A_1^{III}B_1^{VI}$ *mono*chalcogenides. In particular, such modifications enter into intercalation reactions, they can easily be exfoliated (splitting into the thinnest layers), etc. In some studies, for example, in [1, 43], the structures under consideration continue to be classified as "defect-vacancy" structures, taking into account that individual layers are formed precisely by the ordering of vacancies. However, it should be noted that with this approach the definitions *compounds with stoichiometric vacancies* and "*defective*" *phases* will require correction.

The following relatively low-temperature modifications are classified as *layered* forms of indium sesqui-selenide: 2H-α-In_2Se_3, 3R-α-In_2Se_3 and β-In_2Se_3 [44]. The lowest temperature 2H-α-In_2Se_3 form (exists when t < –125 °C) belongs to the space group $P6_3mc$ with cell parameters a = 4.025 Å, c = 19.235 Å [45]. The 3R-α-In_2Se_3 trigonal modification is stable at room temperature and belongs to the space group $R3m$ with the parameters a =4.052 Å, c = 28.765 Å. Structures of both a-phases are shown in Fig. 6A and Fig. 6b. For the 3R polytype, the characteristic sequence of layers is ABCABC, for 2H it is ABAB. In both cases, individual layers are composed of five-layer stacks in which Se–In–Se–In–Se chains can be traced.

The β-In_2Se_3 "medium temperature" phase is characterized by a space group $R\bar{3}m$ with lattice parameters a = 4.05 Å, c = 29.41 Å. The main difference of this phase (Fig. 6c) from 3R-α-In_2Se_3

in that selenium atoms occupy octahedral positions instead of tetrahedral ones for α-In_2Se_3 (if we consider these structures as formed by indium atoms with dense hexagonal packing).

It should also be noted that the formation of buffer layers on diamond-like (cubic $F\bar{4}3m$ or hexagonal $P6_3mc$) structures can lead to the formation of coatings with both a layered structure (in the case of In_2Se_3), as well as non-layered films with "defective" structures of sphalerite or wurtzite (in the case of Ga_2Se_3, Fig. 7) [43], due to the different organization of stoichiometric vacancies.

Finally, another existing type of sesqui-chalcogenide with stoichiometric vacancies is fundamentally different from all the above types, since it corresponds to a different ideal stoichiometry: A_3B_4 instead of A_2B_3. These include structures with a high proportion of ionic bonds, which have a spinel crystal lattice [46]. The most famous, and probably the only representative of this type among the chalcogenides of group III metals, are the $In_{3-x}S_4$ phases.

In most literary sources this phase is written as α-In_2S_3, which, in our opinion, is not entirely

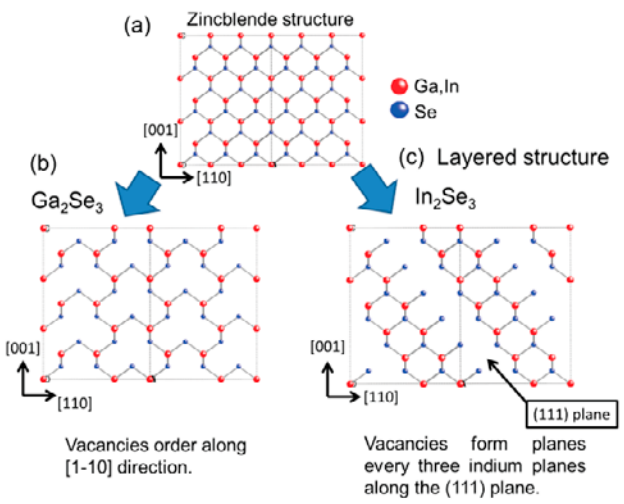

Fig. 7. Mutual relationships between certain surfaces of the following structures: a) – sphalerite, b) – "defective" gallium sesquiselenide with ordering of vacancies (without formation of a layered structure and with) and c) – "defective" indium sesquiselenide (with formation of a layered structure) [43]. Left: vacancies are ordered along the [1$\bar{1}$0]; direction; right: stoichiometric vacancies form planes, grouping every three planes formed by indium atoms, which are located along the (1 1 1) plane

correct. The In_2S_3 formula is explained by the fact that, according to stoichiometry, this phase is closer to sesqui-sulfide (58.5 – 59.5 mol. % S) according to our studies [47, 48]. The $In_{3-x}S_4$ phase (a-In_2S_3) has a *cubic* crystal lattice of inverse spinel (SG $Fd\bar{3}m$, a = 10.724 Å [46, 49–51]), in which there is a deficit of indium atoms compared to the ideal stoichiometry of In_3S_4 (~ 57.1 mol. % S). This modification exists in the "medium temperature" range (according to our data [49] – from 418 to 752 °C, which correlates well with [52]). It is easily hardened and can be isolated at room temperature. According to the latest source, the formula of this compound is most correctly written as $[In_{2/3}(v)_{1/3}]^{tetr}[In_2]^{oct}S_4$, where the symbols "*tetra*" and "*oct*" denote positions in the tetrahedral and octahedral voids of the spinel packing, the framework of which is formed by sulfur atoms; vacancies are designated by the "v" symbol. The given formula follows from the assumption (approximation) that in classical spinels there are charge states of metal M^{2+} and M^{3+}; in the case of indium, taking into account the peculiarities of its classical chemistry, we should discuss the In^{+1} and In^{+3} states. Then the formula $[In_{2/3}(v)_{1/3}]^{tetr}[In_2]^{oct}S_4$ corresponds to the stoichiometry of $In_{2.67}S_4$ = In_2S_3. If the charge states of In^{+2} are allowed, then the given formula will be close to the typical spinel composition M_3S_4. Experimental data, as we already noted, show an intermediate situation between the two stoichiometries. It should be noted that vacancies in cubic form are distributed stochastically among positions (primarily tetrahedral).

On the contrary, in the low-temperature form β-In_2S_3 there is an ordering of vacancies (Fig. 8), and the structure with a decrease in symmetry turns into a tetragonal one (SG $I4_1/amd$; a = 7.61 Å, c = 32.24 Å). This phase exists on the phase *Tx*-diagram up to 418 °C and is easily released during annealing of any other modification of indium sesqui-sulfide below the specified temperature [49]. For the two compounds mentioned, the cubic structure $In_{3-x}S_4$ (α-In_2S_3) can be considered maternal, and the ordered β-In_2S_3 structure is a daughter structure.

In conclusion in this review of defective indium sesqui-sulfides, we will consider the third, most high-temperature and controversial modification in terms of structure, which is γ-In_2S_3. According

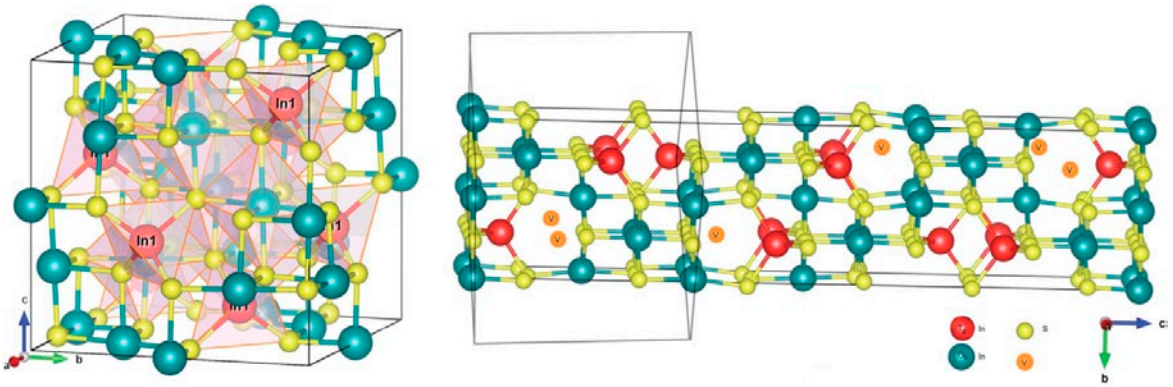

Fig. 8. Structures of In_2S_3: spinel-like, with a more correct formula $In_{3-x}S_4$ (left), tetragonal In_2S_3 (left) [56]

to [52] the structure of this trigonal (SG $R\bar{3}m1$) phase is not spinel-like and is probably close to β-modifications of sesqui-*selenide* indium – i.e., it is layered and formed from a wurtzite "defective" structure due to such an ordering of vacancies that they form separate planes that open separate five-layer packets S–In–S–In–S [53, 54]. This conclusion is not supported by the authors of recent publications [55] and [56], who insist that γ-modifications belongs to the structural type of defective Th_3P_4. In the latter, the cation-forming atoms stochastically occupy only octahedral voids with a filling factor of ~89%. The difficulty of unambiguous interpretation of the structure γ-In_2S_3 is because the pure phase is not quenched, and the authors [56] isolated it by the rapid cooling of a sample deliberately contaminated with vanadium and titanium impurities.

4. $A_1^{III}B_1^{VI}$ compounds: general structural features of solids *mono*chalcogenides

Monochalcogenides typically provide layered structures in which individual four-layer B^{VI}–A^{III}–A^{III}–B^{VI} packets are bound to each other only by weak van der Waals forces (Fig. 9) [1]. The exception is to some extent is α-InS* [49, 57–59].

These compounds are often referred to by technologists as "van der Waals materials." Their ability to exist in isolation as individual B–A–A–B layers opens up prospects for their use in emerging two-dimensional electronics [60].

In $A^{III}B^{VI}$ layered compounds each four-layer stack is composed of two planes containing B^{VI} chalcogen atoms. Layers consisting of such atoms are located on both sides of two adjacent intra-packet planes; in the latter, there are atoms of group III elements bound with each other (and with B^{VI} atoms) (Fig. 9). The basic building block is formed by stacking four hexagonal monoatomic sheets in the sequence B–A–A–B with trigonal prismatic symmetry. Different stacking and/or 180° rotation of these covalently linked layers results in the formation of several polytypes, some of which exhibit inversion symmetry. This fact indicates that, for example, depending on the presence or absence of such symmetry, the linear and nonlinear

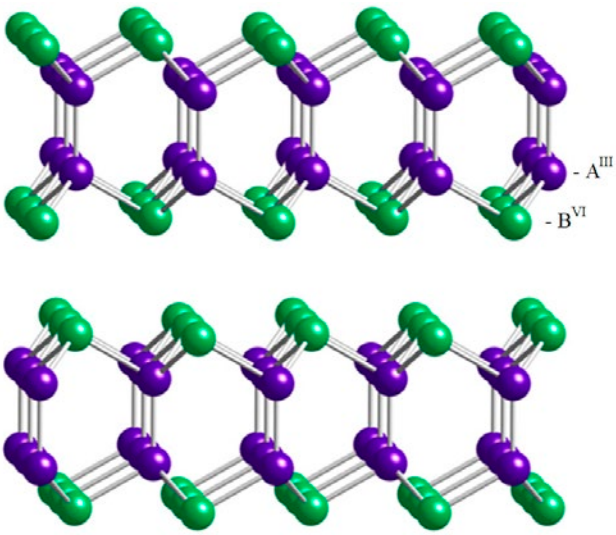

Fig. 9. Fragment of the layered monochalcogenide $A^{III}B^{VI}$ – structure [1]

* At the same time, there is no reliable information about the bulk structures of aluminium monochalcogenides, although the structure of epitaxial films of nanoscale thickness turned out to be close to the structures of other typical layered monochalcogenides. There is also no reliable structural data on the high-temperature form of β-InS, which exists in very narrow (slightly more than 10 °C) temperature range.

optical properties of layered $A^{III}B^{VI}$ will depend on the resulting polytype [61].

The B–A–A–B sequence in quasi-two-dimensional $A^{III}B^{VI}$ layered semiconductors leads to an unusual combination of different types of chemical bonds, which in turn provides non-trivial electronic states [1]. Interlayer bonding is achieved through weak van der Waals interactions with strong intralayer interactions. The covalent homodesmic bond "cation–cation" is non-polar, while the heterodesmic bond "cation–anion" has a partially ionic character [59]. In all three substances, the valence electrons are strongly localized around the B^{VI} atoms, and two A^{III} atoms are bound almost exclusively by a s-bond formed by *s*-electrons. With an increase in the proportion of ionicity from GaSe (0.66) to GaS (0.74) and to InSe (0.80), the ionic nature of the A^{III}–B^{VI} bond obviously increases and the electron density shifts towards to B^{VI} atoms. Moreover, if the gallium atom is replaced by indium or selenium is replaced by sulfur, then the atomic *s*-states of atom A^{III} become less separated in energy from the *p*-states of B^{VI}. The latter is reflected in the delocalization of the bond charge A^{III}-A^{III} and a weakening of the central bond with increasing bond length. A further increase in ionicity leads to the fact that the low-temperature modification a-InS is structurally unique among $A_1^{III}B_1^{VI}$ compounds, since it ceases to be a fully layered 2D structure. In α-InS, it is still possible to distinguish individual S–In–In–S packets, but they are no longer isolated from each other: with a long and weak In–In bond, one packet creeps and wedges into another. As a result, sulfur atoms belonging to one package bond with indium atoms from the neighboring package. In this way, a 3D orthorhombic structure is formed (Fig. 10), in which there are no layers bound only by van der Waals forces [59].

An increase in the size of chalcogen atoms also leads to a change in structure. Thus, layered 2D-structure consisting of loosely coupled four-layer stacks is retained during the GaS → GaSe → GaTe transition. However, for α-GaTe layers, instead of being flat become corrugated (Fig. 11), and the structure changes from hexagonal (2H and 4H polytypes) or rhombohedral (3R polytypes) to monoclinic [62, 63]. At the same time, there is always a metastable modification b-GaTe with a package arrangement identical to gallium monoselenide (Fig. 9) [63].

5. Intercalation reactions in $A_1^{III}B_1^{VI}$ layered crystals (and α- and β-In_2Se_3)

Taking into account the described structural features of aluminum, gallium, and indium monochalcogenides, these substances should be characterized by intercalation reactions i.e.

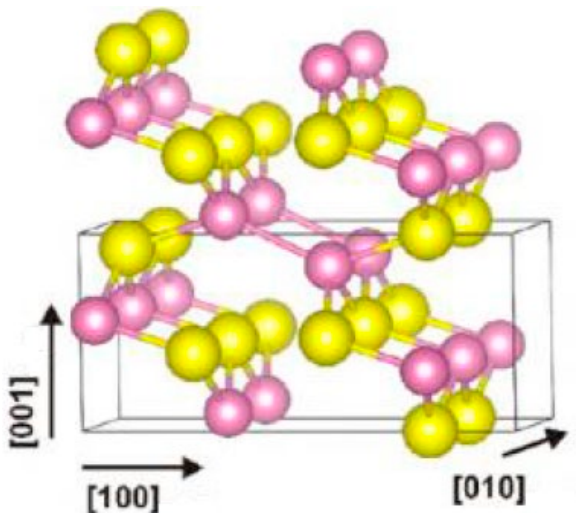

Fig. 10. Fragment of α-InS structure (orthorhombic LT-modification)

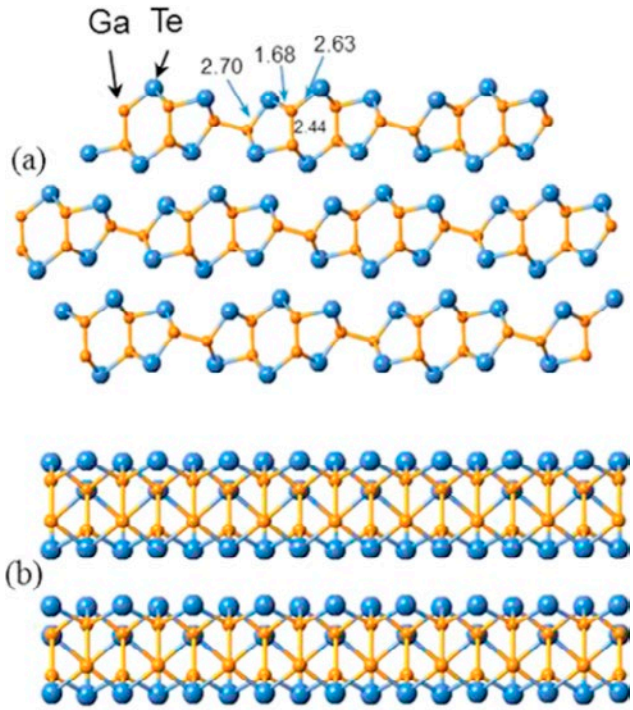

Fig. 11. Frontal (a) and side view (b) of the structure and the layers arrangement in the α-GaTe 3D-structure

interactions associated with the entry of atoms (molecules, ions) into the space between weakly bound 2D layers or 1D chains, as well as the introduction of atoms into atomic-level channels. It should be remembered that the ordering of stoichiometric vacancies is characteristic of $A_2^{III}B_3^{VI}$ sesqui-chalcogenides and can also lead to the formation of structures such as low and medium temperature forms of indium selenide (α-2H- and β-In_2Se_3) with very weakly connected individual layers. As a result, both for the last phase and for almost all $A_1^{III}B_1^{VI}$ monochalcogenides, there are numerous publications on intercalation reactions and on the production of interlayer insertion products – intercalates (reviews [64, 65]).

The peak of interest in such objects and attempts at their practical use occurred in the 90s and 2000s at the turn of the 20th and 21st centuries. In particular, the authors of [64] reported on a project to reduce background radiation in the territory of the Chernobyl Nuclear Power Plant by applying monocrystalline GaSe plates to the internal walls of the damaged power unit and other structures: it was assumed that atoms of iodine isotopes and other radioactive elements in the air would spontaneously be introduced into the layered structure of gallium monoselenide. However, numerous difficulties in the study and the reproducibility of obtaining intercalates of $A^{III}B^{VI}$ compounds led to a decline in interest in these objects.

The guest (implanted) particles included both the smallest particles, individual atoms (ions) of alkali, alkaline earth, rare earth elements, and some other elements, as well as whole molecules with predominantly expressed basic (according to Lewis) properties, from ammonia to pyridine or anthracene, as well as relatively large ions that enter the structure during the processing of A^{III} monochalcogenides by solutions and melts of nitrites and nitrates [64, 65]. Most often, direct interaction of the crystal with the substance-source of guest atoms (incorporation upon contact with the gas or liquid phase) or electrochemical reactions involving solutions (melts) in which monochalcogenides were electrodes were used for the synthesis of such intercalates. One of the authors of this study investigated the interlayer incorporation that occurs during the treatment of single-crystal GaSe and InSe with concentrated nitric acid, solutions of some nitrates, nitrogen tetroxide [66, 67], as well as pyridine and anthracene [68].

It should be noted that we were unable to carry out any intercalation reactions involving gallium monosulphide. In the literature, data on this issue are also extremely scarce. In existing studies, for example in [69], the exfoliation of GaS via the stage of formation of an intermediate intercalated compound was described. However, this stage preceding exfoliation is not analyzed in any way. The reason for the difficulties with interlayer implantation in GaS is probably the too small size of the sulfur atoms lining the interlayer spaces between the packets [1].

Intercalation is most clearly manifested during diffraction structural studies. It is recorded by the shift towards small angles of such reflexes, which are associated with an increase in the distances between planes connected by Van der Waals forces. In some cases, the increase in distances in the direction perpendicular to the layers is observed even visually as an anisotropic "swelling" of the crystal during its intercalation [67–70]. However, small-sized embedded atoms (especially of those *d*-elements as Cu or Pd) seem to pull together the adjacent packages and then the corresponding interplanar distances hardly change or even decrease [71].

In our studies [72, 73] the possibility of autointercalation (with selenium) is considered as being the reason for the significant expansion and displacement (up to 0.6–0.8 mol. %) of the homogeneity region of gallium monoselenide towards selenium in a relatively narrow temperature range close to the congruent melting temperature of GaSe. The hypothesis about the relationship between the specific type of homogeneity region of this phase and autointercalation, the interlayer introduction of atoms of one of the phase-forming components, is described in more detail when examining the phase diagram of the Ga–Se system.

In publications on the study of intercalates, noticeable differences in the electrophysical, optical, catalytic, and other properties of intercalated semiconductors compared to the original substances are almost always noted. In a number of cases, these properties are described as very promising for materials

science. In particular, it was shown in [67] that the introduction of palladium(II) nitrate (from aqueous solutions) into GaSe followed by a reduction of the intercalated product led to the production of a material with pronounced catalytic properties typical for matrices activated by palladium.

However, there are several unresolved problems to this day, which have led to a hopefully temporary decrease of interest in the interlayer introduction into of $A^{III}B^{VI}$ compounds into bulk crystals. In our opinion, the main unresolved problem is the uneven progress of introduction. It is often unclear what part of the crystal and what areas within it were affected by interlayer incorporation. It is well known that guest particles often do not fill every van der Waals gap, they are incorporated through a certain *n*-number of layers (in this case, the formation of an intercalate of the *n*-stage is discussed). However, for the considered structures, a different case most likely occurs: intercalation occurs stochastically, and the number of layers affected by the incorporation may not exceed several percent of their total number (as shown, for example, in the course of studies using a zero-manometer in [68]). In addition, in the bulk $A^{III}B^{VI}$ crystal, probably, there are adjacent layers with a large number of defects (superstoichiometric atoms, layers of another polytype (another phase) with the thickness of several atomic layers, etc.). It is assumed that intercalation occurs *only* into such interlayer regions without affecting the bulk of the crystal. At the same time, in almost all studies on this topic (for example, those described in the review paper [64]), neither the composition of the obtained substance nor the uniformity of the distribution of the guest impurity throughout the volume of the crystal is reported.

The next problem is that intercalation is often destructive: guest molecules or ions actively interact with the substance into which they have been incorporated, changing themselves and altering the structure of the host. In particular, the analysis of the product of GaSe treatment with nitric acid, carried out by one of the authors of this study, revealed Ga–OH, Se–OH, Se=O fragments associated with the initial selenide matrix [66, 67]. Probably, the same destructive processes occur when GaSe (InSe) is treated with nitrite and nitrate melts [64]. These reactions show an analogy with the oxidative incorporation of acids such as $HClO_3$, HNO_3, $HMnO_4$, etc., into graphite, when the incorporated substance partially oxidizes the layers "from the inside", producing carboxyl, ketone, hydroxyl and other groups covalently bonded to the damaged graphite layers ([66, 74]. Fig. 12).

Unfortunately, the possibility of "internal corrosion" of an intercalated layered crystal is often not considered at all, although it can lead to both irreproducibility and degradation of the material properties. Local changes at the atomic level are especially possible for *electrolytic* method of incorporation since the layered structure can include solvent molecules and other foreign impurities active in terms of further oxidation-reduction interactions.

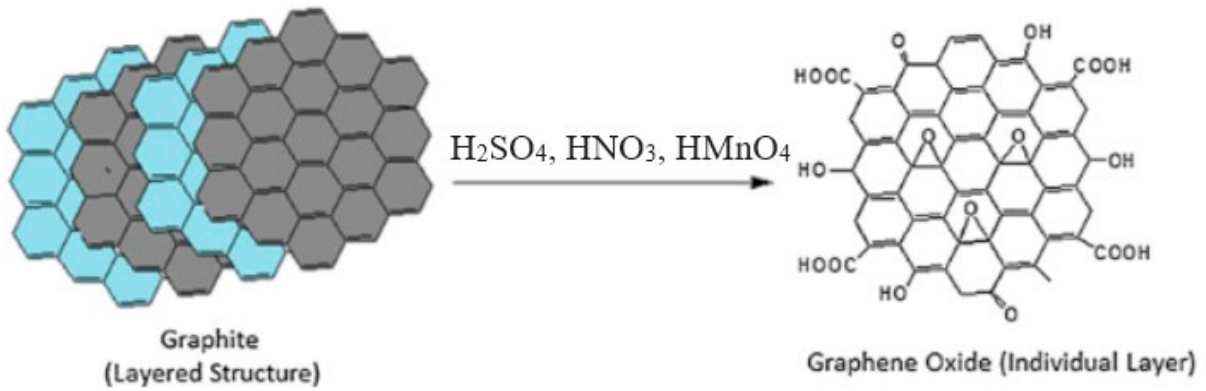

Fig. 12. Changes in the structure of graphite when exposed to acidic oxidizers (HNO_3, $HClO_3$, $HMnO_4$, etc. in strongly acidic solutions) with the formation of damaged graphene layers with hydroxyl, carboxyl, ketone and epoxy-like groups [74]

Despite the slowdown in progress in the ideas and application of intercalation of $A^{III}B^{VI}$ for the design of promising semiconductor and nonlinear optical materials, attempts are currently ongoing to use interlayer incorporation to create new chemical current sources (CCS) [75] (p. 136), combining nanolayers of different layered substances (for example, In_2Se_3 and MoS_2), obtained after intercalation (with lithium) and subsequent spontaneous cleavage (exfoliation) of the intercalate into graphene-like nanoplatelets [76]. In addition, the method of obtaining roquesite-like materials (of Cu(Ag) Ga(In)Se_2 type) when intercalating the matrix of monochalcogenide A^{III} with copper with subsequent stimulated (for example, thermally) restructuring of the intercalate seems to be original [71].

6. Nanostructures based on $A^{III}B^{VI}$ monochalcogenides

The similarity of monochalcogenides to graphite and similar layered substances such as black phosphorus does not end with intercalation reactions. The $A^{III}B^{VI}$ monochalcogenides and adjacent layered modifications of sesquichalcogenide In_2Se_3 can exist in the form of nanolayer graphene-like thin-layer fragments, forming nanoribbons and nanotubes (tubulenes).

Nanolayered graphene-like monochalcogenides of gallium and indium

The unique properties of nanolayered (ideally single-layered) layered substances make them promising for a wide range of applications [77–79]. Containing a small number of layers, (nano)monocrystalline gallium and indium chalcogenides are obtained in different ways, among which the simplest option consists of breaking the monocrystal into layers for example, by stretching a polymer tape such as Scotch tape glued on both sides in opposite directions, predominates. The breaking procedure is repeated many times until the layer remaining on the tape becomes dark grey (after going through stages of obtaining intensely colored due to interference thicker layers). As a result, after removing the adhesive organic polymer, fragments of monochalcogenide layers up to 300 nm thick are obtained [60].

Among other methods, a variant where the splitting (exfoliation) of a bulk single crystal into individual plates is carried out during the electrolysis of a solution using a single crystal of a layered substance as a cathode draws attention. Solutions of alkali metal salts (mainly lithium; usually in the form of $LiClO_4$ [80]) are usually used as electrolytes in water or in ionic organic solvents. Intercalated chalcogenide is obtained by this method. Then a salt of an organic nitrogenous base (most often tetrabutylammonium salt) is added to the solution and electrolysis continues. The huge cations entering between the layers finally break these layers, which are then released in the form of a suspension [81]. It should be noted that when electrolytic exfoliation was carried out, the fact of intermediate formation of intercalate was not always proven. Moreover, the indicated method allowed to obtain nanolayer fragments of even indium monosulphide (a-InS), in which individual layers are bound by a chemical (ionic-covalent) bond [82].

Among the properties of a suspension of individual nano-sized fragments of phases of different layered crystals, the ability of these fragments to self-assemble into a kind of three-dimensional heterostructure should be highlighted. This includes, in particular, a heterostructure "self-assembled" from individual alternating nanolayer fragments of indium selenide and molybdenum disulfide [75].

Among the chalcogenide "true" 2D structures, monolayer gallium monosulphide (*mono*-2D-GaS) was recently investigated and studied [79, 83]. Materials based on *mono*-2D-GaS have proven promising for use in hydrogen evolution reactions [84], as well as in the creation of promising lithium-ion batteries [85], nonlinear optics materials [86], photodetectors [87], and gas sensors [88]. The tetra atomic in thickness (single S–Ga–Ga–S packet) monolayer GaS is a semiconductor with a wide band gap of ~3.33 eV, which is ~0.8 eV larger than for a bulk GaS single crystal [89].

Nanotubes (tubulenes) from indium and gallium monochalcogenides layers

Nanotubes, the closest analogues of carbon nanotubes, are the most studied for gallium monoselenide. The first studies on such

nanotubes appeared, probably, in the 90s. The first publications reported only the results of quantum chemical calculations confirming the possibility of the appearance of such structures. In particular, in [90] an image of a predicted fragment of such a GaSe nanotube is given (Fig. 13). Now such tubulenes have been obtained not only for GaSe, but also for GaS. For the synthesis of both sulfide and selenide nanotubes, a long-term (72 h) interaction of gallium acetylacetonate with chalcogen in an organic solvent (dodecylamine, hexadecylamine) at elevated temperature (200 °C) was used [91].

In [92], spontaneous twisting of some nanolayer fragments of InSe obtained during ultrasonic exfoliation of bulk indium monoselenide samples in isopropanol was noted. The resulting nanotubes had a diameter of less than 1 nm.

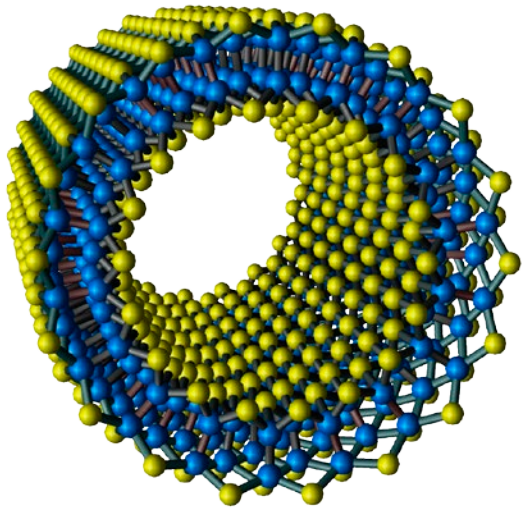

Fig. 13. GaSe nanotube Structure [90]

7. Some aspects of application of single-crystal layered monochalcogenides $A^{III}B^{VI}$ as new promising materials for nonlinear optics

Layered bulk $A^{III}B^{VI}$ crystals exhibit strong optical and electrical anisotropy [93, 94] and high nonlinear optical coefficients in the infrared range [95], which makes them candidates for materials for the generation of second-harmonic radiation (primarily IR lasers) [96–100]. This interest led to extensive work in the 1970s and 1980s on the production of GaSe and InSe bulk single crystals. Many optical and electrical properties of these substances have also been studied in detail [101]. Among the gallium monochalcogenides, gallium monoselenide has the greatest practical significance. Air-stable layered red-ruby single crystals of gallium monoselenide are somewhat similar to colored mica, but heavier (density of 5.03 g/cm^3) and softer (microhardness of 30 kg/mm^2) [14].

Gallium monoselenide is a high-resistance semiconductor with low electron and hole concentrations and low carrier mobility values. Due to low carrier concentrations and low mobility values, this material was long considered an unpromising indirect-gap *p*-type, regardless of the method of production and doping (the transition energy between the valence band and the conduction band is 2.03 eV with a difference in energy between the direct and indirect transitions in GaSe of 0.025 eV) [101].

However, in the last decade, the attitude towards GaSe has changed fundamentally, which is associated with its use in nonlinear optics [78, 98, 101–103]. Currently, various optical systems are being developed on gallium monoselenide, which are used for:

• the generation of second-harmonic radiation of CO_2 laser or similar types of coherent radiation generators (doubling the output frequency when exciting the crystal with short-pulse radiation in the wavelength range from 6.3 to 12 μm); the output signal is stable for many hours with conversion efficiency up to 36%;

• the conversion of frequency of radiation of CO_2 laser into the high-energy region up to the visible region or near IR range (the so-called "up-conversion" [102]);

• the generation of sum frequencies in the mid-IR region;

• the generation of difference frequencies in the mid-IR region from 5.5 to 18 μm;

• creation of radiation-resistant photodiodes designed for the visible and near IR spectral range in the spectral range of 0.6–1.1 μm (for night vision devices) [104];

• the creation of solid-state laser systems based on parametric generation of light using pumping of various types of lasers (for example, those based on Nd-doped yttrium aluminum garnet). A special case of the latter systems are

devices for generating terahertz frequencies with $\nu = 10^{11}–10^{12}$ Hz) [98,105].

We will discuss the last possibility of practical use of materials based on GaSe single crystals in more detail. It is known that electromagnetic waves have a length l = 100-1000 μm (these correspond to the vibration frequencies $\nu = 3{\cdot}10^{12}$ 10^{11} Hz), and occupy an intermediate region between the long-wave infrared and ultra-high-frequency radio ranges. These waves, called terahertz waves, are of considerable interest for a variety of applications, including biology, medicine, and archaeology. Similarly to X-rays, terahertz radiation has high penetrating power, but, unlike the former, does not pose a danger to living organisms or ancient objects. However, until recently, the terahertz range remains one of the technically poorly equipped parts of the spectrum.

The situation has only fundamentally changed in the last decade with the development of various materials, including those constructed from In and Ga monochalcogenides [1], [101, 105, 106]. In particular, a compact terahertz source capable of producing radiation in the range between 56.8 and 1618 microns (from 0.18 to 5.27 THz) was created based on GaSe crystals [107, 108]. In [108] it was noted that the key advantages of such a DFG are an extremely wide tuning range, high stability, small size, and high peak power. Moreover, according to [107], in terms of the accuracy of tuning the wave range, no other terahertz sources can compete with a GaSe-based device.

The production of other layered gallium monochalcogenides as materials for nonlinear optics is also under development. For example, gallium monosulphide (lemon-yellow, mica-like crystals; indirect-gap semiconductor of *n*-type with E_z =2.5 eV) has good photoconductivity in the ultraviolet part of the spectrum [86, 109]. The indium monosulphide (dark brown crystals; semiconductor of *n*-type with several approximate levels; E_z = 1.9 eV) [110] and gallium monotelluride [111, 112] are also promising as photoconductive materials.

8. Conclusions

Unfortunately, the practical use of $A_2^{III}B_3^{VI}$ chalcogenides with various "defective" structures depends, first, on the problem of reproducible synthesis of each of the many modifications considered here. For bulk samples, this problem is primarily because for many binary systems, it has not yet been possible to obtain a consistent idea of the location of the discussed intermediate compounds on the corresponding phase diagrams. In addition to regulating the phase composition, i.e. the structural affiliation of the resulting compound, a problem of the next level is added, associated with the need to regulate the composition within the homogeneity region of a specific phase for a finer "tuning" of the properties of the resulting substance. The latter task is also relevant for film coatings that are parts of the formed heterostructures.

In relation to $A_2^{III}B_3^{VI}$ monochalcogenides the regulation of the polytypic affiliation of the obtained layered single crystals is important (which is a special, but more complex case of the problem of regulation of the phase composition). Thus, the question about the relationship between the main characteristics of the device with the non-stoichiometric composition of the crystal and its belonging to a certain polytype has never been raised in any of the cited studies on the use of monoselenide or related layered monochalcogenides for generators of various long-wave radiation. At the same time, in many studies (for example, in [97]) it was noted that it is impossible to obtain reproducible characteristics of the output radiation without high-quality control of the composition of materials. Approaches to these questions will be considered in the second part of our review.

Contribution of the authors

The authors contributed equally to this article.

Conflict of interests

The authors declare that they have no known competing financial interests or personal relationships that could have influenced the work reported in this paper.

References

1. Olmstead M. A., Ohuchi F. S. Group III selenides: controlling dimensionality, structure, and properties using through defects and heteroepitaxial growth. *Journal of Vacuum Science and Technology A: Vacuum, Surfaces, and Films*. 2021;A39: 020801. https://doi.org/10.1116/6.0000598

2. Goryunova N. A. *Complex diamond-like semiconductors**. Moscow: Sovetskoe Radio Publ.; 1968. 268 p. (In Russ.)

3. Parthé E. *Elements of inorganic structural chemistry*. CH-1213: Petit-Lancy, Switzerland; 1996. 230 p.

4. Ormont B. F. *Introduction to physical chemistry and crystal chemistry of semiconductors*[*]: Textbook. V. M. Glazov (ed.). 3rd ed., corrected and enlarged. Moscow: Vysshaya Shkola Publ.; 1982. 528 p. (In Russ.)

5. Goryunova N. A. Some issues of crystal chemistry of compounds with zinc blende structure[*]. *Izvestiya Akademii nauk SSSR. Fizika.* 1957 21(1): 120. (In Russ.)

6. Atroschenko L. V., Zhuze V. P., Koshkin V. M., Ovechkina E. E., Palatnik L. S. The property of chemical inertness of metal impurities in semiconductors with stoichiometric vacancies[*]. *Byulleten' izobretenii i otkrytii SSSR*. 1981;41: 1. (In Russ.)

7. Palatnik L. S., Komnik Yu. F., Koshkin V. M. Crystal chemistry of compounds with tetrahedral coordination of atoms[*]. *Kristallografiya*. 1952;7(4):563–567. (In Russ.)

8. Koshkin V. M., Volovichev I. N., Gurevich Yu. G., Galchinetsky L. P., Rarenko I. M. Materials and devices with a giant radiation resource[*]. *Materials of scintillation technology: Institute of Single Crystals*. 2006: 5–60. (In Russ.)

9. Palatnik L. S., Rogacheva E. I. Equilibrium diagrams and structure of some semiconductor alloys $A_2^{I}C^{VI}$–$B_2^{III}C_3^{VI}$[*] *Soviet Physics Doklady*. 1967;174(1): 80. (In Russ.)

10. Palatnik L. S., Koshkin V. M., Komnik Yu. F. *Chemical bonding in semiconductors and solids*[*]. Moscow: Nauka i Tekhnika Publ.; 1965. 301 p. (In Russ.)

11. Atroshchenko L. V., Galchinetsky L. V., Koshkin V. M., Palatnik L. S. *Deviations from stoichiometry and solubility of impurities in semiconductors with stoichiometric vacancies. Chemical bonding in semiconductors and thermodynamics*[*]. Minsk: Nauka i Tekhnika Publ.; 1966. 261 p. (In Russ.)

12. Hahn H., Klingler W. Über die Kristallstrukturen von Ga_2S_3, Ga_2Se_3 und Ga_2Te_3. Z. *Zeitschrift für anorganische Chemie*. 1949;259(1-4): 110–119. https://doi.org/10.1002/zaac.19492590111

13. Suchet J. P. *Chimie physique des semiconducteurs*. Dunod, France. 1962. 361 p.

14. Madelung O. III_2–VI_3 compounds. *Semiconductors Data Handbook*. Springer, Berlin. 2004:275–288. https://doi.org/10.1007/978-3-642-18865-7

15. Yitamben E. N., Lovejoy T. C., Pakhomov A. B., Heald S. M., Negusse E. Correlation between morphology, chemical environment, and ferromagnetism in the intrinsic-vacancy dilute magnetic semiconductor Cr-doped Ga_2Se_3/Si(001). *Physical Review B*. 2011;83: 045203. https://doi.org/10.1103/PhysRevB.83.045203

16. Peng H., Zhang X. F., Twesten R. D., Cui Y. Vacancy ordering and lithium insertion in III_2VI_3 nanowires. *Nano Research*. 2009;2: 327-335. https://doi.org/10.1007/s12274-009-9030-y

17. Zhao P., Ma Y., Lv X., Li M., Huang B. Two-dimensional III_2-VI_3 materials: promising photocatalysts for overall water splitting under infrared light spectrum. *Nano Energy*. 2018;51: 533. https://doi.org/10.1016/j.nanoen.2018.07.010

18. Krost A., Richter W., Zahn D. R. T. Chemical reaction at the ZnSe/GaAs interface detected by Raman spectroscopy. *Applied Physics Letters*. 1990;57: 1981. https://doi.org/10.1063/1.104149

19. Wright A. C., Williams J. O. Detection of compound formation at the ZnSe/GaAs interface using high resolution transmission electron microscopy (HRTEM). *Journal of Crystal Growth*. 1991;99: 114. https://doi.org/10.1016/0022-0248(91)90684-W

20. Takatani S., Nakano A., Ogata K., Kikawa T. Structure of chalcogen-stabilized GaAs interface. *MRS Proceedings*. 1992;31: L458. https://doi.org/10.1557/PROC-281-677

21. Guler I., Isik M., Gasanly N. M., Gasanova L. G. Structural and optical properties of Ga_2Se_3 crystals by spectroscopic ellipsometry. *Journal of Electronic Materials*. 2019;48: 2418. https://doi.org/10.1007/s11664-019-07000-4

22. Morley S., Emde M., Zahn D. R. T., ... Poole I. B. Optical spectroscopy of epitaxial Ga_2Se_3 layers from the far infrared to the ultraviolet. *Journal of Applied Physics*. 1996;79: 3196–3199. https://doi.org/10.1063/1.361264

23. El-Rahman K. F. Charge conduction mechanisms and photovoltaic properties of n-(Ga_2S_3 – Ga_2Se_3)/p-Si heterojunctions. *The European Physical Journal Applied Physics*. 2007;37(2): 143–147. https://doi.org/10.1051/epjap:2007004

24. Kuzubov S. V., Kotov G. I., Synorov, Yu. V. Gallium vacancy ordering in Ga_2Se_3 thin layers on Si(100), Si(111), and Si(123) substrates. *Crystallography Reports*. 2017;62(5): 768–772. https://doi.org/10.1134/s1063774517050121

25. Budanov A. V., Vlasov Y. N., Kotov G. I., Rudnev E. V., Mikhailyuk E. A. Deep levels in Ga_2Se_3/GaP (111) heterostructures. *Chalcogenide Letters*. 2018;15(8): 425–428. Available at: https://chalcogen.ro/425_BudanovAV.pdf

26. Budanov A. V., Vlasov Yu. N., Kotov G. I., Burtsev A. A., Rudnev E. V. Photosensitivity of In_2Se_3/InAs heterostructures[*]. In: *Actual problems in micro- and nanoelectronics*. Interuniversity collection of scientific papers: Voronezh-2022. 2022: 24–30. (In Russ.). Available at: https://catalog.inforeg.ru/Inet/GetEzineByID/33862

27. Bezryadin N. N., Kotov G. I., Kubuzov S. V., Vlasov Yu. N. Surface phase of Ga_2Se_3 on GaP (111). *Condensed Matter and Interfaces*. 2013;15: (4): 382–386. (In Russ., abstract in Eng.). Available at: https://elibrary.ru/item.asp?id=20931229

28. Pardo M., Tomas A., Guittard M. Polymorphisme de Ga_2S_3 et diagramme de phase Ga – S. *Materials Research Bulletin*. 1987;22(12): 1677–1684. https://doi.org/10.1016/0025-5408(87)90011-0

29. Pardo M., Guittard M., Chilouet A., Tomas A. Diagramme de phases gallium – soufre et etudes structurales des phases solides. *Journal of Solid State Chemistry*. 1993;102(2): 423–433. https://doi.org/10.1006/jssc.1993.1054

30. Volkov V. V., Sidey V. I., Naumov A. V., ... Zavrazhnov A. Yu. Structural identification and stabilization of the new high-temperature phases in A(III) – B(VI) systems (A = Ga, In, B = S, Se). Part 1: High-temperature phases in the Ga – S system. *Journal of Alloys and Compounds*. 2022;899: 163264. https://doi.org/10.1016/j.jallcom.2021.163264

31. Ho C. H. Ga_2Se_3 defect semiconductors: the study of direct band edge and optical properties. *ACS Omega*. 2020;29(5): 18527–18534. https://doi.org/10.1021/acsomega.0c02623

32. Shi C., Yang B., Hu B., Du1 Y., Yao S. Thermodynamic description of the Al–X (X = S, Se, Te) systems. *Journal of Phase Equilibria and Diffusion*. 2019;40: 392–402. https://doi.org/10.1007/s11669-019-00733-z

33. Chen G., Drennan Z. G., Zou J. Indium selenides: structural characteristics, synthesis and their thermoelectric performances. *Small*. 2014;14(10): 2747–2765. https://doi.org/10.1002/smll.201400104

34. Brezhnev N. Y., Dorokhin M. V., Zavrazhnov A. Y., Kolyshkin N. A., Nekrylov I. N., Trushin V. N. High-temperature gallium sesquisulfides and a fragment of the *T-x* diagram of the Ga – S system with these phases. *Condensed Matter and Interphases*. 2024;26(2):225–237. https://doi.org/10.17308/kcmf.2024.26/11936

35. Likforman A., Fourcroy P.-H., Guittard M., Flahaut J., Poirier R., Szydlo N. Transitions de la forme de haute température α de In_2Se_3, de part et d'autre de la température ambiante. *Journal of Solid State Chemistry*. 1980;33(1): 91–97. https://doi.org/10.1016/0022-4596(80)90551-4

36. Davydov S. Yu., Kobyakov I. B. Dependence of elastic constants of zinc sulfide on the phase composition of wurtzite/sphalerite*. *Soviet Physics: Thechnical Physics*. 1983;53(2): 377–379. (In Russ.). Available at: https://www.mathnet.ru/php/archive.phtml?wshow=paper&jrnid=jtf&paperid=2201&option_lang=rus

37. Brezhnev N. Yu. Ga-S and In-Se systems: crystal structure of intermediate phases and *T-x* diagrams*. Cand. chem. sci. diss. Voronezh, 2023. 189 p. Available at: https://rusneb.ru/catalog/000199_000009_012131968/

38. Lutz D, Fischer M., Baldus H.-P., Blachnik R. Zur polymorphie des In_2Se_3. *Journal of the Less Common Metals*. 1988;143: 83–92. https://doi.org/10.1016/0022-5088(88)90033-1

39. Pfitzner A., Lutz H. D. Redetermination of the crystal structure of γ-In_2Se_3 by twin crystal X-ray method. *Journal of Solid State Chemistry*. 1996;124: 305–308. https://doi.org/10.1006/jssc.1996.0241

40. Manolikas C. New results on the phase transformations of In_2Se_3. *Journal of Solid State Chemistry*. 1988;74: 319–328. https://doi.org/10.1016/0022-4596(88)90361-1

41. Landuyt J., Tendeloo G., Amelinckx S. Phase transitions in In_2Se_3 as studied by electron microscopy and electron diffraction. *Physica Status Solidi (a)*. 1975;30: 299–302. https://doi.org/10.1002/pssa.2210300131

42. Ye J., Yoshida T, Nakamura Y.; Nittono O. Optical activity in the vacancy ordered III_2VI_3 compound semiconductor $(Ga_{0.3}In_{0.7})_2Se_3$. *Applied Physics Letters*. 1995;67(21): 3066–3068. https://doi.org/10.1063/1.114866

43. Kojima N., Morales C., Ohshita T., Yamaguchi M. Ga_2Se_3 and $(InGa)_2Se_3$ as novel buffer layers in the GaAs on Si system. *AIP Conference Proceedings*. 2013;1556(1): 38–40. https://doi.org/10.1063/1.4822194

44. Küpers M., Konze P. M., Meledin A., ... Dronskowski R. Controlled crystal growth of indium selenide, In_2Se_3, and the crystal structures of α-In_2Se_3. *Inorganic Chemistry*. 2018;57(18): 11775–11781. https://doi.org/10.1021/acs.inorgchem.8b01950

45. Popovic S., Celustka B., Bidjin D. X-ray diffraction measurement of lattice parameters of In_2Se_3. *Physica Status Solidi (a)*. 1971;6(1): 301–304. https://doi.org/10.1002/pssa.2210060134

46. Likforman A., Guittard M., Tomas A., Mise en evidence d'une solution de type spinelle dans le diagramme de phase du systeme In – S. *Journal of Solid State Chemistry*. 1980;34(3): 353–359. https://doi.org/10.1016/0022-4596(80)90434-X

47. Kosyakov A. V., Zavrazhnov A. Yu., Naumov A. V. Refinement of the In-S phase diagram using spectrophotometric characterization of equilibria between hydrogen and indium sulfides. *Inorganic Materials*. 2010;46(4): 343–345. https://doi.org/10.1134/s0020168510040035

48. Kosyakov A. V., Zavrazhnov A. Y., Naumov A. V., Sergeyeva A. V. Specification of the phase diagram of system In - S according to spectrophotometric researches of balance between sulfide of indium and hydrogen. *Proceedings of Voronezh State University. Series: Chemistry. Biology. Pharmacy". Series: Chemistry. Biology. Pharmacy*. 2009;2: 28–39. (In Russ., abstract in Eng.). Available at: https://elibrary.ru/item.asp?id=12992199

49. Zavrazhnov A. Y., Naumov A. V., Anorov P. V., ... Pervov V. S. *T-x* phase diagram of the In-S system. *Inorganic Materials*. 2006:42: 1294–1298. https://doi.org/10.1134/S0020168506120028

50. Naumov A. V., Sergeeva A. V., Semenov V. N. Structure and reflection spectra of $In_{3-x}S_4$(111)/mono-Si and $In_{3-x}S_4$(111)/SiO_2/mono-Si films. *Inorganic Materials*. 2015;51(12): 1205–1212. https://doi.org/10.1134/S0020168515110060

51. Naumov A. V., Sergeeva A. V., Semenov V. N. Oriented $In_{3-x}S_4$ films on the (100) surface of Si, GaAs, and InP single crystals. *Inorganic Materials*. 2017;53(6): 560–567. https://doi.org/10.1134/S0020168517060127

52. Pistor P., Alvarez J. M., Leon M., di Michiel M. Structure reinvestigation of α-, β- and γ-In_2S_3. *Acta Crystallographica Section B Structural Science, Crystal Engineering and Materials*. 2016;72(3): 410–415. https://doi.org/10.1107/S2052520616007058

53. Bartzokas D., Manolikas C. Spyridelis J. Electron microscopic study of the destabilization of stabilized γ-phase of indium sesquisulphide. *Physica Status Solidi (a)*. 1978;47(2): 459–467. https://doi.org/10.1002/pssa.2210470216

54. Diehl R., Carpentier C. D., Nitsche R. The crystal structure of γ-In_2S_3 stabilized by As or Sb. *Acta Crystallographica Section B Structural Crystallography and Crystal Chemistry*. 1976;32(4): 1257–1260. https://doi.org/10.1107/s0567740876005062

55. Liu K., Dai L., Li H., Hu H, ... Hong M. Evidences for phase transition and metallization in β–In_2S_3 at high pressure. *Chemical Physics*. 2019;524: 63–69. https://doi.org/10.1016/j.chemphys.2019.04.025

56. Jebasty R. M., Sjastad A. O., Vidya R. Prediction of intermediate band in Ti/V doped γ-In_2S_3. *RSC Advances*. 2022;12(3): 1331–1340. https://doi.org/10.1039/d0ra08132a

57. Berezin S. S., Berezina M. V., Zavrazhnov A. Yu., Kosyakov A. V., Sergeeva A. V., Sidei V. I. Phase transformations of indium mono- and sesquisulfides studied by a novel static thermal analysis technique. *Inorganic Materials*. 2013;49(6): 555–563. https://doi.org/10.1134/S0020168513060010

58. Zavrazhnov A. Y., Kosyakov A. V., Naumov A. V., Sergeeva A. V., Berezin S. S. Study of the In-S phase diagram using spectrophotometric characterization of equilibria between hydrogen and indium sulfides. *Thermochimica Acta*. 2013;566(20): 169–174. https://doi.org/10.1016/j.tca.2013.05.031

59. Depeursinge Y., Electronic properties of the layer III–VI semiconductors. A comparative study. *Il Nuovo*

Cimento B Series 11. 1981;64: 111–150. https://doi.org/10.1007/BF02721299

60. Jie W., Hao J. Two-dimensional layered gallium selenide: preparation, properties and applications. In: *Advanced 2D Materials*. Tiwari A., Syväjärvi M. (eds.). New York: Wiley; 2016: 1–36. 514 p. https://doi.org/10.1002/9781119242635.ch1

61. Schluter M., Camassel J., Kohn S., ... Cohen M. L. Optical properties of GaSe and GaS_xSe_{1-x} mixed crystals. *Physical Review B*. 1976;13(8): 3534–3547. https://doi.org/10.1103/PhysRevB.13.3534

62. Liu F., Shimotani H., Shang H., ... Drummond N. High-sensitivity photodetectors based on multilayer GaTe flakes. *ACS Nano*. 2014;8(1): 752–760. https://doi.org/10.1021/nn4054039

63. Edwards D. F. Gallium telluride (GaTe). In: *Handbook of Optical Constants of Solids*. Palik E. D. (ed.). Amsterdam: Elsevier; 1997. p. 489–505. https://doi.org/10.1016/b978-012544415-6/50114-x

64. Grygorchak I., Voitovych S., Stasyuk I., Velychko O., Menchyshyn O. Electret effect in intercalated crystals of the $A^{III}B^{VI}$ group. *Condensed Matter Physics*. 2007;10(1): 51–60. https://doi.org/10.5488/CMP.10.1.51

65. Rajapakse M., Karki B., Abu U. O., ...Yu M. Intercalation as a versatile tool for fabrication, property tuning, and phase transitions in 2D materials. *Npj 2D Materials and Applications*. 2021;5: Article-30. https://doi.org/10.1038/s41699-021-00211-6

66. Nekrasov O. V., Zavrazhnov A. Yu., Semenov, V. N. Dolgopolova E. A., Averbakh E. M. Incorporation of HNO_3 into GaSe and InSe*. *Inorganic Materials* 1994;30(6): 737–740. (In Russ.). Available at: https://elibrary.ru/item.asp?id=28934301

67. Zavrazhnov A. Yu., Turchen D. N., Semenov V. N. Zlomanov V. P, Pervov V. S. Oxidizing intercalation of layered structures. *Materials Technology*. 2000;15(2): 155–160. https://doi.org/10.1080/10667857.2000.11752872

68. Zavrazhnov A. Yu., Nekrasov O. V., Averbakh E. M. Falkengof A. T. On the possibility of insertion of some organic molecules into GaSe and InSe*. *Inorganic Materials*. 1994;30(6): 1030–1032. (In Russ.). Available at: https://elibrary.ru/item.asp?id=29831583

69. Vela Y. G., Juan D., Dicorato S., Losurdo M. Layered gallium sulfide optical properties from monolayer to CVD crystalline thin films. *Optics Express*, 2022;30: 15. https://doi.org/10.1364/OE.459815

70. Zavrazhnov A. Yu., Turchen D. N. Oxidative insertion into GaSe-type structures*. *Condensed Matter and Interphase*. 1999;1(2): 190–196. (In Russ.). Available at: https://www.elibrary.ru/item.asp?id=24120596

71. Motter J. P., Koski K. J. Cui Y. General strategy for zero-valent intercalation into two-dimensional layered nanomaterials. *Chemistry of Materials*. 2014;26: 2313–2317. https://doi.org/10.1021/cm500242h

72. Turchen D. N., Zavrazhnov A. Yu., Goncharov E. G., Suvorov A.V . Nonstoichiometry research for the low-volatilaty phases. Homogeneity region of GaSe*. *Russian Journal of General Chemistry*. 1998;68(6): 920–925. (In Russ.). Available at: https://elibrary.ru/ynceoh

73. Turchen D. N., Zavrazhnov A. Yu., Prigorodova T. V. Scanning of *T-x*-projections of phase microdiagrams based on the gas solubility in melts*. *Russian Journal of General Chemistry*. 1999;69(5): 1–8. (In Russ.).

74. Ikram R., Jan B. M., Ahmad W. An overview of industrial scalable production of graphene oxide and analytical approaches for synthesis and characterization. *Journal of Materials Research and Technology*. 2020;9(5): 11587–11610. https://doi.org/10.1016/j.jmrt.2020.08.050

75. Julien C., Nazri G. A. Intercalation compounds for advanced lithium batteries. Chapter 3. In: *Handbook of Advanced Electronic and Photonic Materials and Devices*. H. S. Nalwa (ed.). USA. Academic Press; 2001;10: 99–181. https://doi.org/10.1016/b978-012513745-4/50083-4

76. Ng B., Wong C., Niu W., ... Tsang S. Molecular layer-by-layer re-stacking of MoS_2–In_2Se_3 by electrostatic means: assembly of a new layered photocatalyst. *Materials Chemistry Frontiers*. 2023;7(5): 937–945. https://doi.org/10.1039/D2QM01095J

77. Karpov V. V., Bandura A. V., Evarestov R. A. Nonempirical calculations of the structure and stability of nanotubes based on gallium monochalcogenides. *Physics of the Solid State*. 2020;62(6): 1017–1023. https://doi.org/10.1134/S1063783420060116

78. Xu K., Yin L., Huang Y. Synthesis, properties and applications of 2D layered $M^{III}X^{VI}$ (M = Ga, In; X = S, Se, Te) materials. *Nanoscale*. 2016;8(38): 16802-16818. https://doi.org/10.1039/C6NR05976G

79. Abd-Elkader O. H., Abdelsalam H., Sakr M. A., Teleb N. H., Zhang Q. Electronic and optical properties of finite gallium sulfide nano ribbons: a first-principles study. *Crystals*. 2023;1215: 13. https://doi.org/10.3390/cryst13081215

80. Ren D., Merdrignac-Conanec O., Dorcet V., ... Zhang X. *In situ* synthesis and improved photoelectric performances of a Sb_2Se_3/β-In_2Se_3 heterojunction composite with potential photocatalytic activity for methyl orange degradation. *Ceramics International*. 2020;46(16): 25503–25511. https://doi.org/10.1016/j.ceramint.2020.07.021

81. Ambrosi A., Pumera A. Exfoliation of layered materials using electrochemistry. *Chemical Society Reviews*. 2018;47: 7213–7224. https://doi.org/10.1039/c7cs00811b

82. Wang T., Wang J., Wu J., Ma P., Su R., Zhou P. Near-infrared optical modulation for ultrashort pulse generation employing indium monosulfide (InS) two-dimensional semiconductor nanocrystals. *Nanomaterials*. 2019;9: 865. https://doi.org/10.3390/nano9060865

83. Shao M., Bie T., Yang L., ... He L. Over 21% efficiency stable 2D perovskite solar cells *Advanced Materials*. 2022;34: 2107211. https://doi.org/10.1002/adma.202107211

84. Harvey A., Backes C., Gholamvand Z., Hanlon D., McAteer D. Preparation of gallium sulfide nanosheets by liquid exfoliation and their application as hydrogen evolution catalysts. *Chemistry of Materials*. 2015;27: 3483–3493. https://doi.org/10.1021/acs.chemmater.5b00910

85. Zhang C., Park S. H., Ronan O. ... Nicolosi V. Enabling flexible heterostructures for Li-ion battery an-odes based on nanotube and liquid-phase exfoliated 2D gallium chalcogenide nanosheet colloidal solutions. *Small*, 2017;13(34): 1701677. https://doi.org/10.1002/smll.2017016

86. Ahmed S., Cheng P.K., Qiao J. Nonlinear optical activities in two-dimensional gallium sulfide: a comprehensive study. *ACS Nano*. 2022;16(8): 12390–12402 https://doi.org/10.1021/acsnano.2c03566

87. Zappia M. I., Bianca G., Bellani S., Curreli N. Two-dimensional gallium sulfide nanoflakes for UV-selective photoelectrochemical-type photodetectors. *The Journal of Physical Chemistry C.* 2021;125(22):11857–11866. https://doi.org/10.1021/acs.jpcc.1c03597

88. Opoku F., Akoto O., Asare-Donkor N. K., Adimado A. A. Defect-engineered two-dimensional layered gallium sulphide molecular gas sensors with ultrahigh selectivity and sensitivity. *Applied Surface Science.* 2021;562: 150188. https://doi.org/10.1016/j.apsusc.2021.150188

89. Lu Y., Warner J. H. Synthesis and applications of wide bandgap 2D layered semiconductors reaching the green and blue wavelengths. *ACS Applied Electronic Materials*. 2020;7(2): 1777–1814. https://doi.org/10.1021/acsaelm.0c00105

90. Côté M., Cohen M. L., Chadi J. D. GaSe nanotubes. *Physical Review B.* 1998;58: R4277. https://doi.org/10.1103/PhysRevB.58.R4277

91. Seral-Ascaso A., Metel S., Pokle A. Long-chain amine-templated synthesis of gallium sulfide and gallium selenide nanotubes. *Nanoscale*. 2016;8: 11698–11706. https://doi.org/10.1039/C6NR01663D

92. Petroni E., Lago E., Bellani S. Liquid-phase exfoliated indium-selenide flakes and their application in hydrogen evolution reaction. *Small*. 2018;26(14): e1800749. https://doi.org/10.1002/smll.201800749

93. Shi G., Kioupakis E. Anisotropic spin transport and strong visible-light absorbance in few-layer SnSe and GeSe. *Nano Letters*. 2015;15:6926. https://pubs.acs.org/doi/10.1021/acs.nanolett.5b02861

94. Wasala M., Sirikumara H. I., Raj Sapkota Y., ... Talapatra S. Recent advances in investigations of the electronic and optoelectronic properties of group III, IV, and V selenide based binary layered compounds. *Journal of Materials Chemistry C.* 2017;43(5): 11214–11225. https://pubs.acs.org/10.1039/c7tc02866k

95. Yüksek M., Elmali A., Karabulut M. Nonlinear absorption in undoped and Ge doped layered GaSe semiconductor crystals. *Applied Physics B*. 2010;98: 77–81. https://doi.org/10.1007/s00340-009-3665-y

96. Zhou X., Cheng J., Zhou Y., ... Yu D. Strong second-harmonic generation in atomic layered GaSe. *American Chemical Society.* 2015;137(25): 7994–7997. https://doi.org/10.1021/jacs.5b04305

97. Hu L., Huang X., Wei D. Layer-independent and layer-dependent nonlinear optical properties of two-dimensional GaX (X = S, Se, Te) nanosheets. *Physical Chemistry Chemical Physics*. 2017;19(18): 11131–11141. https://doi.org/10.1039/c7cp00578d

98. Gan X. T., Zhao C., Hu S. Microwatts continuous-wave pumped second harmonic generation in few- and mono-layer GaSe. *Light: Science and Applications.* 2018;7: 17126. https://doi.org/10.1038/lsa.2017.126

99. Karatay A., Yuksek M., Ertap H., Elmali A., Karabulut M. Enhancing the blue shift of SHG signal in GaSe:B/Ce crystal. *Optics and Laser Technology*. 2018;99: 392–395. https://doi.org/10.1016/j.optlastec.2017.09.027

100. Yuan Q., Fang L., Fang H., ... Gan X. Second harmonic and sum-frequency generations from a silicon metasurface integrated with a two-dimensional material. *ACS Photonics*. 2019;6: 2252–2259. https://doi.org/10.1021/acsphotonics.9b00553

101. Fernelius N. Properties of gallium selenide single crystal. *Progress in Crystal Growth and Characterization of Materials.* 1994;28(4): 275–353. https://doi.org/10.1016/0960-8974(94)90010-8

102. Sarkisov S. Yu., Mikhailov T. A., Bereznaya S. A., Korotchenko Z. V., Redkin R. A. *Nonlinear optical element based on a GaSe single crystal with a double-sided antireflection coating for generating terahertz radiation*[*]. Patent RF: No. 193143U1. Publ. 15.10.2019, bull. No. 29. (In Russ.) Available at: https://patents.google.com/patent/RU193143U1/ru

103. Lubenko D. M., Ezhov D. M., Losev V. F., Andreev Yu. M., Lanskii G. V. IR-to-THz down conversion in nonlinear GaSe:Al crystals. *Bulletin of the Russian Academy of Sciences: Physics*. 2020;84(7): 780–782. https://doi.org/10.3103/s1062873820070163

104. Kul'chitskii N. A., Naumov A. V. Modern state of markets of selenium and selenium-based compounds. *Izvestiya Vuzov. Tsvetnaya Metallurgiya (Proceedings of Higher Schools. Nonferrous Metallurgy).* 2015;3: 40–48. https://doi.org/10.17073/0021-3438-2015-3-40-48

105. Gershenzon E. G. Submillimeter spectroscopy[*]. *Sorosovskij obrazovatel'nyj zhurnal. Serija Fizika. Physics Series*. 1998;4: 78–85. (In Russ.). Avalable at: https://www.pereplet.ru/obrazovanie/stsoros/533.html

106. Song M., An N., Zou Y. Epitaxial growth of 2D gallium selenide flakes for strong nonlinear optical response and visible-light photodetection. *Frontiers of Physics*. 2023;18: 52302. https://doi.org/10.1007/s11467-023-1277-3

107. Yan D., Xu D., Wang Y., Zhong K., Tunable J. High-repetition-rate, tunable and coherent mid-infrared source based on difference frequency generation from a dual-wavelength 2 μm laser and GaSe crystal. *Laser Physics.* 2018;28(12): 126205. https://doi.org/10.1088/1555-6611/aae060

108. Rao Z., Wang X., Lu Y. Tunable terahertz generation from one CO_2 laser in a GaSe crystal. *Optics Communications.* 2011;23(284): 5472–5474. https://doi.org/10.1016/j.optcom.2011.08.009

109. Gamal G. A., Azad M. A. Photoelectric studies of gallium monosulfide single crystals. *Journal of Physics and Chemistry of Solids*. 2005;66(1): 5–10. https://doi.org/10.1016/j.jpcs.2004.06.011

110. Qasrawi A. F., Gasanly N. M. Carrier transport properties of InS single crystals. *Crystal Research and Technology.* 2002;37: 1104. https://doi.org/10.1002/1521-4079(200210)37:10<1104::AID-CRAT1104>3.0.CO;2-A

111. Ayddinli A., Gasanly N. M., Uka A. Anharmonicity in GaTe layered crystals. *Crystal Research and Technology.* 2002;37(12): 1303–1309. https://doi.org/10.1002/crat.200290006

112. Ahmad H., Azali N., Yusoff N. Layered gallium telluride for inducing mode-locked pulse laser in thulium/

holmium-doped fiber. *Luminescence*, 2022;248: 119002. https://doi.org/10.1016/j.jlumin.2022.119002

* *Translated by author of the article*

Information about the authors

Alexander Y. Zavrazhnov, Dr. Sci. (Chem.), Professor at the Department of General and Inorganic Chemistry, Voronezh State University (Voronezh, Russian Federation).
https://orcid.org/0000-0003-0241-834X
alexander.zavrazhnov@gmail.com

Nikolay Y. Brezhnev, Junior Researcher at the Department of Chemistry, Voronezh State Agricultural University (Voronezh, Russian Federation).
https://orcid.org/0000-0002-3287-8614
brezhnevnick@gmail.com

Ivan N. Nekrylov, Department Assistant at the Department of General and Inorganic Chemistry, Voronezh State University (Voronezh, Russian Federation).
https://orcid.org/0000-0003-4491-4739
Icq492164858@gmail.com

Andrew V. Kosyakov, Cand. Sci. (Chem.), Assistant Professor, Department of General and Inorganic Chemistry, Voronezh State University (Voronezh, Russian Federation).
https://orcid.org/0000-0001-9662-7091.
lavchukb@mail.ru

Viktor F. Kostryukov, Dr. Sci. (Chem.), Associate Professor, Associate Professor at the Department of Materials Science and the Industry of Nanosystems, Voronezh State University (Voronezh, Russian Federation).
https://orcid.org/0000-0001-5753-5653
vc@chem.vsu.ru

Received 28.07.2024; approved after reviewing 18.08.2024; accepted for publication 16.09.2024; published online 25.12.2024.

Translated by Valentina Mittova

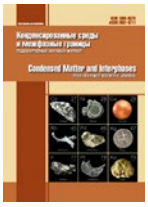

ISSN 1606-867X (Print)
ISSN 2687-0711 (Online)
Condensed Matter and Interphases
Kondensirovannye Sredy i Mezhfaznye Granitsy
https://journals.vsu.ru/kcmf/

Review

Review article
https://doi.org/10.17308/kcmf.2024.26/12397

Phase transformations in systems formed by titanium, silicon, aluminum, and zirconium oxides: Phase diagrams prediction and modeling. Review

V. I. Lutsyk, A. E. Zelenaya✉, V. P. Vorob'eva

Institute of Physical Materials Science, Siberian Branch of the Russian Academy of Sciences, 6 Sakhyanova st., Ulan-Ude 670047, Russian Federation

Abstract

This paper provides a review of variants of phase diagrams of binary and ternary systems constituting the TiO_2-Al_2O_3-SiO_2-ZrO_2 four-component system.

The study involved building spatial (three-dimensional (3D)) computer models of the isobaric phase diagrams for four ternary oxide systems (and their variants, in case of contradicting initial data obtained by different researchers) constituting this quaternary system. The geometric structure of its phase diagram was also predicted. For this purpose, phase diagram models were constructed as geometric objects in three-dimensional (3D) or four-dimensional (4D) space in the "concentration-temperature" coordinates by assembling (hyper)surfaces (unruled and ruled) and/or phase regions.

As a result:

– For the TiO_2-Al_2O_3-SiO_2 system, it was considered possible variants of the structure of liquidus surfaces. These variations were due to availability of different theories describing the formation of compounds in the TiO_2-Al_2O_3 binary system (Al_2TiO_5 can melt congruently or incongruently and either possesses or does not possess the property of polymorphism).

– For the TiO_2-Al_2O_3-ZrO_2 and TiO_2-SiO_2-ZrO_2 systems, 3D-models of phase diagrams were developed at temperatures above 1,280 and 1,400 °C, respectively. The temperature limits were due to the lack of definitive description of the structure of subsolidus regions in the TiO_2-ZrO_2 binary boundaring system.

– Since the main contradictions in the ZrO_2-SiO_2-Al_2O_3 system are associated with the type of phase reaction related to zircon formation (peritectic or peritectoid), the 3D model of the phase diagram was built according to the second variant, which involved the formation of the internal field of liquidus corresponding to the primary crystallization of $ZrSiO_4$.

The structure of the phase diagrams in the subsolidus was deduced for all four systems. It was also shown that in these systems at decreasing of temperature triangulation had a place twice.

For the TiO_2-Al_2O_3-SiO_2-ZrO_2 quaternary system, a scheme of phase reactions with the participation of the melt was deduced. This scheme includes six five-phase invariant reactions: two peritectic, two eutectic, and two quasi-peritectic reactions.

Keywords: Phase diagrams, Computer modeling, Four-dimensional visualization, Titanium, aluminum, Silicon, and Zirconium oxides

Funding: This work was performed under the program of fundamental research of the Institute of Physical Materials Science of the Siberian Branch of the Russian Academy of Sciences, project No. 0270-2024-0013.

For citation: Lutsyk V. I., Zelenaya A. E., Vorob'eva V. P. Phase transformations in systems formed by titanium, silicon, aluminum, and zirconium oxides: Phase diagrams prediction and modeling. Review. *Condensed Matter and Interphases*. 2024;25(3): 666–686. https://doi.org/10.17308/kcmf.2024.26/12397

Для цитирования: Луцык В. И., Зеленая А. Э., Воробьева В. П. Фазовые превращения в системах, образованных оксидами титана, кремния, алюминия, циркония: прогноз и моделирование фазовых диаграмм. Обзор. *Конденсированные среды и межфазные границы*. 2024;25(3): 666–686. https://doi.org/10.17308/kcmf.2024.26/12397

✉ Anna E. Zelenaya, e-mail: zel_ann@mail.ru

1. Introduction

Innovative ceramics based on ZTA, a combination of zirconium, titanium, and aluminum oxides, have a wide range of practical applications. Therefore, there is a need to provide a precise and experiment-consistent description of isobaric phase diagrams for both the ternary systems formed by ZTA and SiO_2 and the TiO_2-Al_2O_3-SiO_2-ZrO_2 quaternary system. Phase diagrams of its binary systems are very contradictory, which is associated with disagreements on the properties of the compounds formed within these systems (the presence or absence of polymorphism, the nature of the formation, and the type of melting).

2. Literature review

It is known that silicon and zirconium oxides, which together with titanium and aluminum oxides form the TiO_2-Al_2O_3-SiO_2-ZrO_2 system, have several polymorphic modifications. Zirconium (IV) oxide has three modifications: cubic (*c*-ZrO_2), tetragonal (*t*-ZrO_2), and monoclinic (*m*-ZrO_2) [1–3]. Silicon (IV) oxide has four modifications: cristobalite (*cr*-SiO_2), tridymite (*tr*-SiO_2), high-temperature quartz (HQ-SiO_2), and low-temperature quartz (LQ-SiO_2) [1].

2.1. Binary systems in the TiO_2-Al_2O_3-SiO_2-ZrO_2 four-component system

The Al_2O_3-ZrO_2 system has the simplest geometric structure of the six considered binary systems constituting TiO_2-Al_2O_3-SiO_2-ZrO_2 (Fig. 1a). Experimental [2-5] and thermodynamically calculated [6, 7] data indicate that there is an eutectic reaction between Al_2O_3 and the tetragonal form of zirconium oxide (*t*-ZrO_2), the *c*-ZrO_2 → *t*-ZrO_2 + L metatectic polymorphic transition, and the eutectoid transition from the tetragonal *t*-ZrO_2 to the monoclinic *m*-ZrO_2 [2].

In the TiO_2-SiO_2 eutectic system (Fig. 1b), in addition to liquid immiscibility, there are three polymorphic transitions from cristobalite (*cr*-SiO_2) to tridymite (*tr*-SiO_2) and further to high and low-temperature quartzes (HQ-SiO_2 and LQ-SiO). This system has been studied in many papers [8–21]. All researchers agree that the system is characterized by liquid immiscibility and the eutectic reaction. Their opinions only differ with regard to the values of the coordinates of the eutectic reaction and the dimensions of the liquid immiscibility region, both in terms of its composition and temperature.

The SiO_2-ZrO_2 system (Fig. 1c) has an immiscibility region of two liquids and the $ZrSiO_4$ compound (zircon) [22–26]. The main differences in publications devoted to this system relate to the type of phase reaction by which this compound is formed: peritectic [22] or peritectoid. More recent studies confirm the peritectoid nature of the reaction [25]: *tr*-SiO_2 + *t*-ZrO_2 → $ZrSiO_4$ with the participation of tridymite and tetragonal form of zirconium oxide. In the subsolidus, zircon participates in low-temperature polymorphic transitions, in which polymorphic forms of SiO_2 and ZrO_2 also take part. The "liquidus" part of the phase diagram is characterized by a high-temperature metatectic transition from *c*-ZrO_2 to *t*-ZrO_2, liquid immiscibility, and the eutectic reaction. An overview of opinions on the structure of the ZrO_2-SiO_2 phase diagram is presented in [23–26].

The descriptions of the Al_2O_3-SiO_2 system provide different interpretations of the nature of mullite melting (mainly with the $Al_6Si_2O_{13}$ stoichiometry). In [27–48], it is defined either as congruent (then the mullite divides the system into two eutectic subsystems (Fig. 1d)), or as incongruent (then the mullite is formed by a peritectic reaction).

The TiO_2-ZrO_2 system has been extensively researched with the main differences in its description relating to the presence of zirconium titanate (Fig. 1e). The phase diagrams presented in [49] and [50] have a similar structure, but differ in the presence of the ordered and disordered phase of $ZrTiO_4$. Importantly, since there is no definitive description of phase transformations in this system, in this work we limited the modeling of the TiO_2-Al_2O_3-ZrO_2 and TiO_2-SiO_2-ZrO_2 ternary systems formed by them to the temperatures of 1,280 and 1,400 °C, respectively.

There are four main versions of phase transformations in the TiO_2-Al_2O_3 system. What they have in common is the recognition of the existence of aluminum titanate, however, they differ in the interpretations of the type of its melting (incongruent [51] (Fig. 1f) or congruent), the presence or absence of its second polymorphic modification, and/or the formation of one more compound $Al_6Ti_2O_{13}$ [52-63].

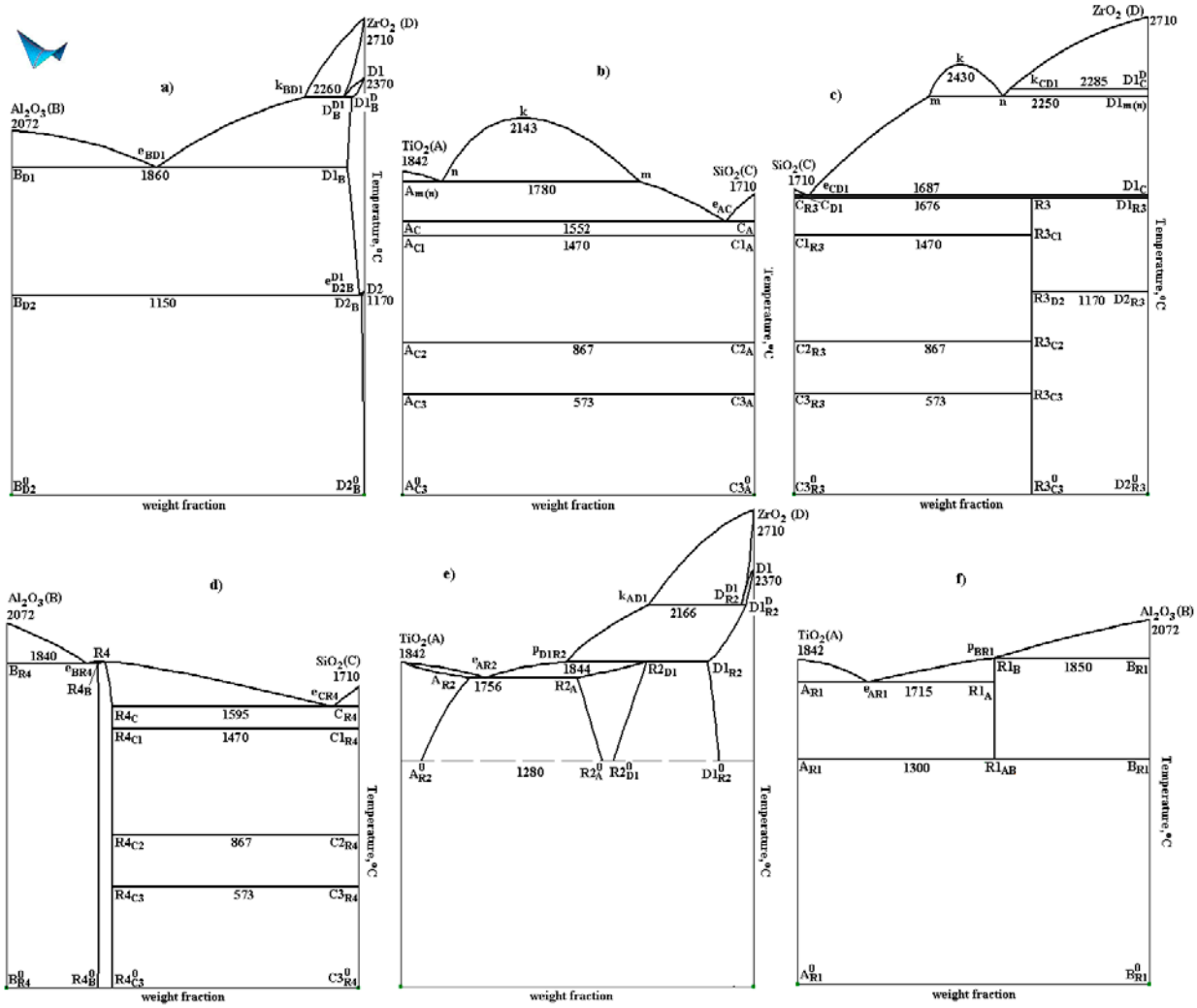

Fig. 1. Phase diagrams of binary systems: Al_2O_3-ZrO_2 (B-D) (a) [2, 7], TiO_2-SiO_2 (A-C) (b) [19], SiO_2-ZrO_2 (C-D) (c) [1], Al_2O_3-SiO_2 (B-C) (d) [30, 35], TiO_2-ZrO_2 (A-D) (e) [49], TiO_2-Al_2O_3 (A-B) (f) [51] with the formation of: titanates of aluminum Al_2TiO_5 (R1) and zirconium $ZrTiO_4$ (R2), zircon $ZrSiO_4$ (R3), mullite $Al_6Si_2O_{13}$ (R4) (C – cristobalite cr-SiO_2, C1 – tridymite *tr*-SiO_2, C2 – high-temperature HQ-SiO_2 and S3 – low-temperature LQ-SiO_2 quartz; D – cubic *c*-ZrO_2 , D1 – tetragonal *t*-ZrO_2, D2 - monoclinic *m*-ZrO_2 polymorphic modifications of ZrO_2)

2.2. Ternary systems in the TiO_2-Al_2O_3-SiO_2-ZrO_2 four-component system

The authors of the work [64] (cited from [65]) studied the phase diagram of the TiO_2-Al_2O_3-SiO_2 ternary system, rich in alumina, and established the presence of two invariant reactions, eutectic and quasi-peritectic (Fig. 2a):

E_1: $L \rightarrow TiO_2 + SiO_2 + Al_2TiO_5$ and
Q_2: $L + Al_6Si_2O_{13} \rightarrow SiO_2 + Al_2TiO_5$.

Later, a third invariant reaction was recorded, corresponding to another quasi-peritectic transformation [66]:

Q_1: $L + Al_2O_3 \rightarrow Al_6Si_2O_{13} + Al_2TiO_5$.

Studies [67] in the subsolidus region showed the presence of two phase regions: $TiO_2 + SiO_2 + Al_6Si_2O_{13}$ and $TiO_2 + Al_2TiO_5 + Al_6Si_2O_{13}$.

The authors of [68] experimentally recorded the same invariant reactions but with different melt compositions. They also established the presence of a quasi-peritectoid reaction in the solid-phase region: $SiO_2 + Al_2TiO_5 \rightarrow TiO_2 + Al_6Si_2O_{13}$.

Since there are four main variants of the structure of the phase diagram of the TiO_2-Al_2O_3 binary system, it is also possible to obtain four variants of the structure of the ternary systems constituted by this binary system together with silicon or zirconium oxides.

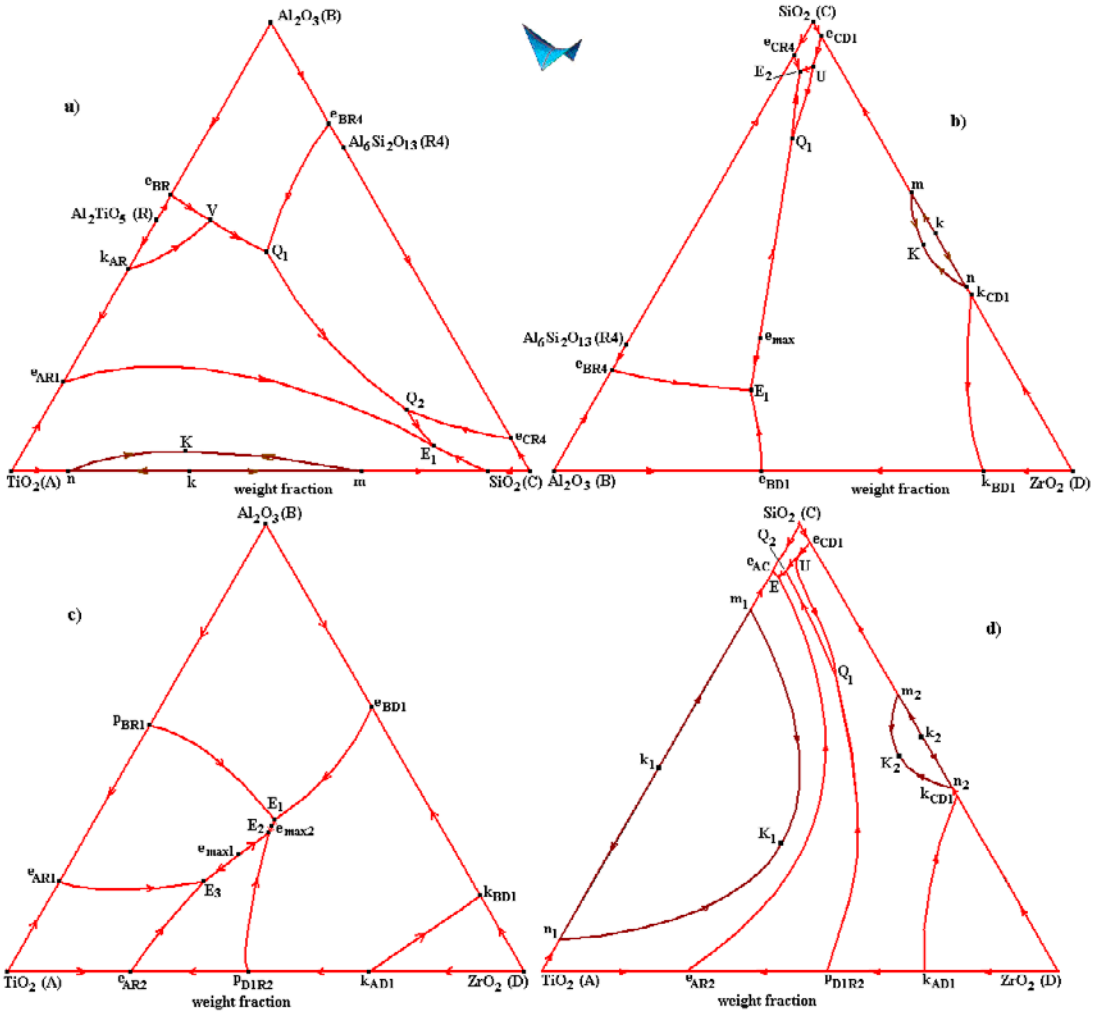

Fig. 2. Liquidus surfaces projections of the TiO_2-Al_2O_3-SiO_2 (A-B-C) (a), Al_2O_3-SiO_2-ZrO_2 (B-C-D) (b), TiO_2-Al_2O_3-ZrO_2 (A-B-D) (c), TiO_2-SiO_2-ZrO_2 (A-C-D) (d) systems with compounds Al_2TiO_5 (R1), $ZrTiO_4$ (R1), $ZrSiO_4$ (R3), $Al_6Si_2O_{13}$ (R4)

The liquidus of the TiO_2-Al_2O_3-SiO_2 ternary system consists of a region of liquid immiscibility and five surfaces of onset primary crystallization: three initial oxides and two binary compounds with aluminum titanate melting either incongruently or congruently. If we accept the version about the existence of two polymorphic modifications of aluminum titanate, according to which the low-temperature modification of aluminum titanate on the phase diagram of the TiO_2-Al_2O_3 binary system has the corresponding liquidus line (interestingly, it is only present in one subsystem with TiO_2, while in the other subsystem it can only be found in the subsolidus), then two fields of primary crystallization of aluminum titanate for both its polymorphic modifications appear in the ternary system (Fig. 2a). However, there is no information about liquidus surfaces corresponding to the onset crystallization of a low-temperature modification in any of the studies devoted to this ternary system. Data are only available for a high-temperature modification [17, 21, 64–68].

According to another version, in addition to the congruently melting aluminum titanate Al_2TiO_5, an incongruently melting compound $Al_6Ti_2O_{13}$ is formed. This means that a sixth field is present in the system corresponding to the primary crystallization of the compound.

To take into account the polymorphism of aluminum titanate (its two modifications), the listed Q_1, Q_2, and E_1 reactions must be preceded by an invariant four-phase polymorphic transition between the high-temperature and

low-temperature modifications of Al_2TiO_5 in the presence of Al_2O_3 and the melt in the temperature range of T_{eBR}-T_{Q1}. This transition corresponds to point V on the $e_{BR}Q_1$ line, where the liquidus field of the high-temperature modification of aluminum titanate closes (Fig. 2a). As a result, the surface of its liquidus consists of two fragments: $k_{AR}Re_{BR}V$ (primary crystallization of the high-temperature modification of Al_2TiO_5) and $e_{AR1}k_{AR}VQ_1Q_2E_1$ (separation of primary crystals of its low-temperature modification).

Thus, a large amount of contradictory data significantly complicates the task of constructing a quality model of the phase diagram. The lack of definitive experimental data about the structure of the TiO_2-Al_2O_3 binary system makes it difficult to obtain a single, unified, thermodynamically justified model of the phase diagram. A more effective solution in this case is building a geometric spatial model of the phase diagram, which will be discussed below.

Papers [69-71] present the results of studies, according to which, the liquidus of the Al_2O_3-SiO_2-ZrO_2 ternary system is characterized by six surfaces corresponding to the initial components (including two polymorphic forms of zirconium oxide), mullite, and zircon, and by quasi-peritectic and two eutectic reactions (Fig. 2b):

Q_1: L + *t*-ZrO_2 → $Al_6Si_2O_{13}$ + $ZrSiO_4$,
E_1: L → Al_2O_3 + *t*-ZrO_2 + $Al_6Si_2O_{13}$, E_2: L →
→ SiO_2 + $Al_6Si_2O_{13}$ + $ZrSiO_4$.

The main contradictions in this ternary system are associated with the structure of the liquidus and, in particular, the surface corresponding to the onset primary crystallization of the $ZrSiO_4$ zircon. The works [72-75] indicate the formation of five primary crystallization surfaces, including an internal field corresponding to $ZrSiO_4$, and four invariant reactions. Earlier, following the logic of the scheme of phase transformations, two phase reaction schemes were deduced corresponding to two variants of zircon formation [76]. The formation of zircon by the peritectoid reaction (Fig. 1c) results in the formation of the internal liquidus field of $ZrSiO_4$ and another invariant peritectic reaction (Fig. 2b):

L + *t*-ZrO_2 + SiO_2 → $ZrSiO_4$.

The description of the liquidus surfaces of the TiO_2-Al_2O_3-ZrO_2 system are contradictory. The structure of the diagram of TiO_2-ZrO_2 in the subsolidus can be interpreted in many ways. What is more, the discrepancies in the interpretation of the data related to the TiO_2-Al_2O_3 binary system also complicate the experimental study of the ternary system constituded by this binary system and aluminum oxide. According to [77], there are three eutectic transformations in this ternary system (Fig. 2c). Work [78, p. 107] presents the projection of the liquidus surfaces with three invariant points marked: two eutectic and one quasi-peritectic. The univariant liquidus line connecting the eutectic and quasi-peritectic points contains the maximum point located on the quasi-binary section of ZrO_2-Al_2TiO_5. Importantly, the point characterized as quasi-peritectic is located inside the ZrO_2-Al_2TiO_5-$ZrTiO_4$ simplex. However, such position of the point means that the phase reaction can only be eutectic in nature. Otherwise, in order to preserve the quasi-peritectic nature of the reaction corresponding to this point, it must be shifted to the TiO_2-Al_2TiO_5-$ZrTiO_4$ simplex. The projection of the liquidus surfaces obtained by thermodynamic calculations [79] has 4 invariant points.

Contradictory information about the TiO_2-ZrO_2 binary system [80, 81] (Fig. 2d) also significantly complicates the study of the phase diagram of the TiO_2-SiO_2-ZrO_2 system over the entire range of temperatures from the liquidus to subsolidus. The structure of the liquidus surfaces is shown in [82].

3. 3D modeling of isobaric phase diagrams of ternary systems

Currently, thermodynamic databases are widely used to describe phase equilibria in multicomponent systems, which make it possible to use the CALPHAD technology to produce precise calculations of phase diagrams [83, 84]. This approach allows calculating phase equilibria in multicomponent systems at high temperatures, for example, by using the NUCLEA database designed to simulate emergency situations at nuclear power plants [85, 86].

However, the limitations of using the results of the description of phase equilibria in the studied systems obtained by using the NUCLEA database include the representation of a significant number of phases as stoichiometric [86]. This also concerns mullite, the phase diagrams of which usually show the formation of a solid solution. Another limitation of the potential of the

NUCLEA database is a simplified understanding of the metatectic reactions associated with polymorphic transformations [87, Fig. 8].

Earlier [88], a thermodynamic database for the corresponding binary and ternary systems containing ZrO_2 was created to use the CALPHAD approach for calculations of phase diagrams. This allowed to avoid distortions in the image of metatectic reactions and to calculate the surface of the liquidus and fourteen polythermal sections of the Al_2O_3-SiO_2-ZrO_2 phase diagram.

One of the complications related to the construction of phase diagrams of multicomponent systems is the presence of polymorphic modifications of initial components and compounds formed in the system. This is especially true in cases of limited solubility of the polymorphic modifications of compounds within the studied system, which should also be taken into account.

3.1. Key provisions related to the construction of phase diagrams of ternary systems from the surfaces/phase regions

Good results related to the modeling of isobaric phase diagrams have been shown by an approach that allows assembling phase diagrams from the surfaces and/or phase regions. These diagrams can be further used to develop their spatial computer models. According to [89–94], such approach allows:

– Considering in detail the features of the physicochemical characteristics of the studied system, for example, negligibly small mutual solubility of the phases and the peculiarities of the solidus structure in a three-component system with immiscibility present in the melt.

– Freely operating with phase diagrams, including visualization of various isothermal and polythermal sections.

– Taking into account all surfaces and phase regions of the phase diagram.

– Correctly interpreting various experimental and calculated data on phase equilibria displayed on the isothermal and polythermal sections.

To build computer models of phase diagrams, the PD Designer and Neditor programs are used to assemble phase diagrams from the surfaces and/or phase regions [92, 95–98].

The initial data used to build a computer model include both experimental and matching thermodynamic data on binary boundaring systems and the surfaces of primary crystallization with due account of the nature of the melting (decomposition) of the binary and ternary compounds present in the system.

The assembly of the phase diagram from the surfaces and phase regions for spatial (3D) computer model involves several steps: 1) scheme of mono- and invariant states presented in a tabulated (Table 1) and graphical (Fig. 3) forms; 2) prototype of the phase diagram; 3) computer 3D model of the phase diagram of the real system.

The scheme of mono- and invariant states presented in a tabulated form is similar to Scheil's scheme of phase reactions; however, it includes attributed trajectories of changes in phase compositions during three-phase transformations. This allowes to directly obtain from the scheme detailed information about the geometrical structure of the phase diagram, i.e. about the number and type of all surfaces and phase regions. Such a table is very helpful since it is very convenient to track (or predict) the sequence of phase transformations not only with the participation of the melt, but also in the subsolidus.

Further, the two-dimensional (tabulated) scheme is transformed into the spacial scheme with due account of the location of points by temperature. In other words, the tabulated form is converted into geometric in the "concentration-temperature" coordinates. First, all the planes corresponding to the invariant transformations in the ternary system are constructed. Then, segments the ends of which are indicated in the scheme and which correspond to the changes in the compositions of the phases (participating in three-phase transformations) are brought to these planes [90]. Thus, the template of the phase diagram is formed.

The template is then completed with the surfaces imitating the surfaces of liquidus, solidus, solvus, and transus and phase regions are formed. The resulting prototype of a computer 3D model gives a deep understanding of the structure of the phase diagram.

The ruled surfaces are formed by the generating segment and two directing curves and comprised the boundaries of the corresponding three-phase transformation. All other surfaces (liquidus, solidus, solvus, transus, etc) are unruled. It is obvious that kinematic method is used to generate the ruled surface. In many cases, this method also

Table 1. Scheme of uni- and invariant states of the Al_2O_3-SiO_2-ZrO_2 (B-C-D) system with compounds $ZrSiO_4$ (R3) и $Si_2Al_6O_{13}$ (R4), D>k>D1(k_{CD1})>k_{BD1}>m(n)>B>e_{BD1}>R4>e_{BR4}> >e_{max}>E_1>C>e_{CD1}>R3>U>Q_1>e_{CR4}> E_2>C1(e^{C}_{C1R3},e^{C}_{C1R4},E_4)>P>D2(e^{D1}_{D2R3}>E_3)>e^{D1}_{BD2}>Q_2> >C2(e^{C1}_{C2R3},e^{C1}_{C2R4},E_5)>C3(e^{C2}_{C3R3},e^{C2}_{C3R4},E_6)

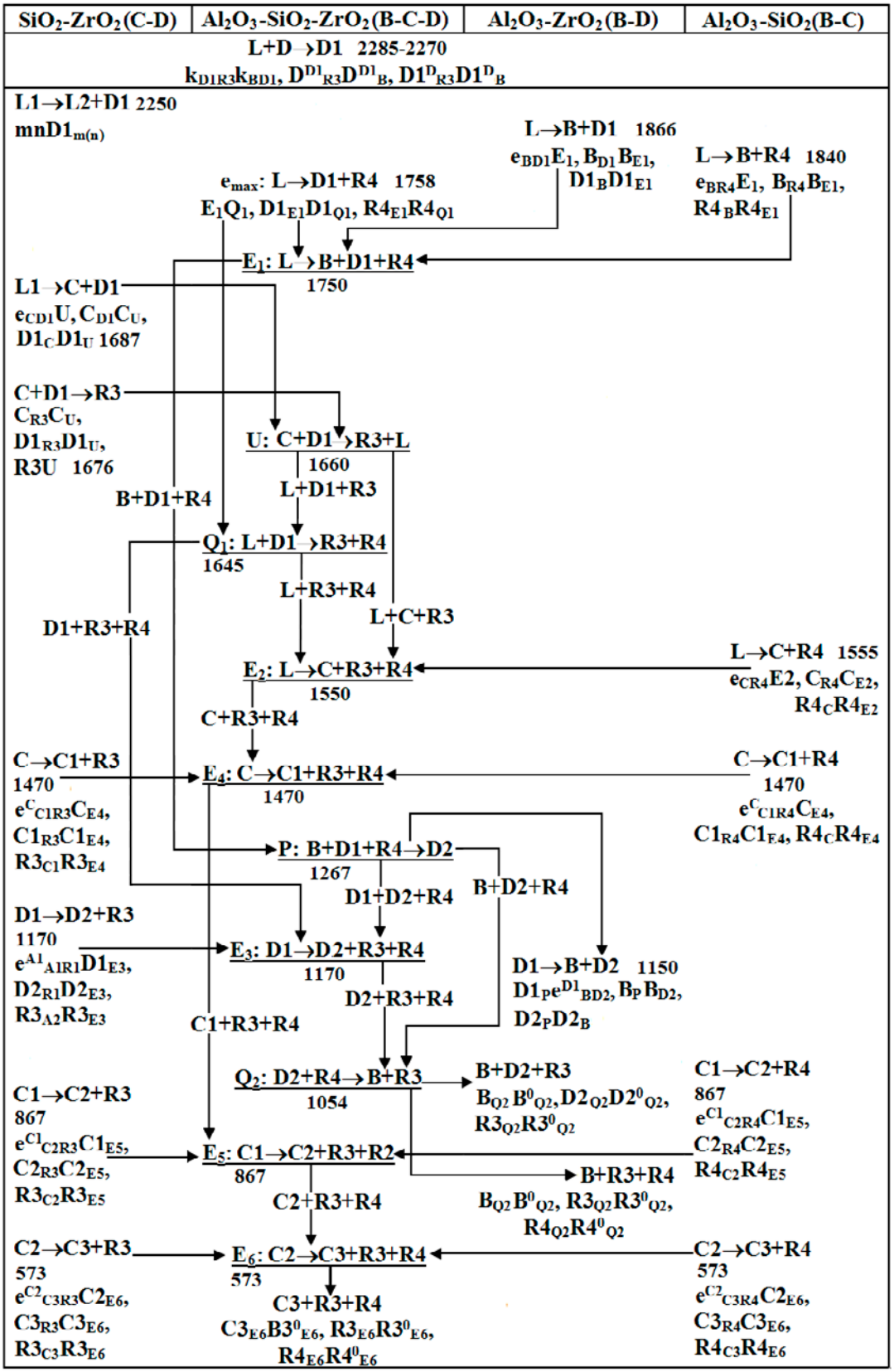

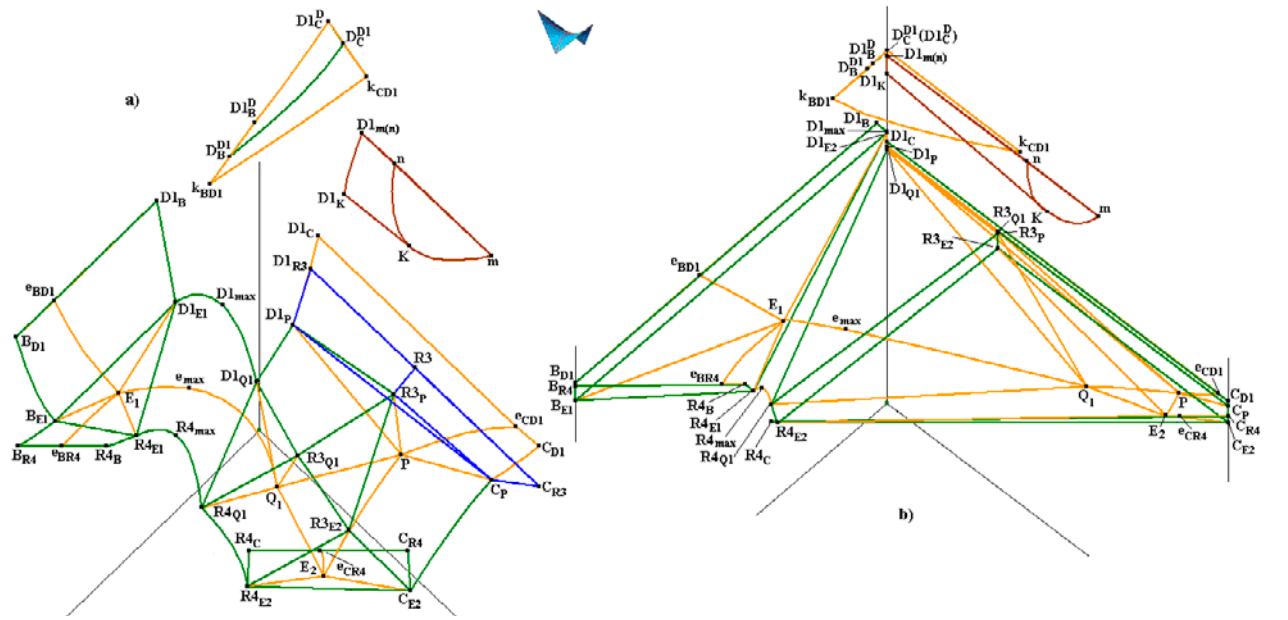

Fig. 3. Fragment of a 3D scheme of uni- and invariant states with a melt participation: a prototype (a), a real Al_2O_3-SiO_2-ZrO_2 (B-C-D) system with the formation of zircon Zr_3SiO_4 (R3) and mullite $Al_6Si_2O_{13}$ (R4) (b)

allows properly representing unruled surfaces as the movement of the generating element along the directing curves. Then, the surface is determined using directing and generating curves specified by Lagrange interpolation polynomials of *m* degree. This approach allows taking into account the presence of Van Rijn points, the curvature of the curves on the contour of the surfaces, the convexity of the surfaces, and the complex contour of the surfaces.

If the kinematic method cannot "cover" the entire surface (for example, when there is a fold, i.e. immiscibility region), it is divided into fragments. Then, the problem of proper representation of the surface is reduced to "merging" the surface from the fragments with mandatory control of equalizing derivatives at the points of their connection.

It should be noted that an important stage in phase diagram modeling is the construction of its prototype. A prototype is an ideal design of a phase diagram: i.e. a hypothetical phase diagram that completely reproduces the structure of the real phase diagram; it is its topological analogue comprising surfaces degenerated in a real system.

Moreover, the surfaces must be constructed in such a way as to give the best idea of both the surfaces themselves and the phase regions, for which these surfaces serve as the boundaries. To achieve this, the base points coordinates (concentrations and temperatures) are given so that the surfaces are not degenerated into the faces or verticals of the prism within which they are constructed.

To convert the prototype into a 3D model of the phase diagram of a real system, the real coordinates of all base points are first given and those surfaces that merge with the facets of the phase diagram (i.e. edges and faces of the prism) are "degenerated". The next stage deal with providing accurate and sound representation of the available experimental data (or information obtained from various sources, including thermodynamic calculations). To do this, the curvatures of lines and surfaces are specified and, as a result, a spatial computer model of a particular phase diagram is obtained. The process of obtaining a perfect model can be long; it may require additional clarifying experiments. However, it can be sure that the computer model of the phase diagram constructed in such a way has no methodological errors caused by an incorrect interpretation of the experiment that can occur when constructing phase diagrams using conventional methods [93, 94].

It is important to highlight that despite the fact that the limited solubility of some oxides and compounds is negligibly low, the 3D model makes it possible to take into account all surfaces and phase regions, and thus the phase diagram is protected

from errors. The obtained models can be used as the basis for further planning of experiments, while the approach to building spatial computer models of phase diagrams of ternary and more complex systems by assembling them from the surfaces and phase regions opens new opportunities in the digitalization of materials science.

The model of the phase diagram, which includes all its topological elements, is a tool for its comprehensive study. It can be used to build iso- and polythermal sections, to calculate crystallization paths and vertical and horizontal mass balances, which allow obtaining complete data on the crystallization stages, the phase and microstructural composition of the sample (without taking into account diffusion processes for each crystallization field), to visualize the results of phase interactions at all crystallization stages, and even to predict the microstructural compositions [99–102] (Fig. 6).

Before constructing a computer 3D model of the phase diagram with the help of the PD Designer program, all components of the system and formed in it compounds were redesignated.

In the case of the TiO_2-Al_2O_3-SiO_2-ZrO_2 quaternary system, the initial oxides were assigned the following letters: A - TiO_2, B - Al_2O_3, C - SiO_2, D - ZrO_2; and their polymorphic modifications were assigned the same letters but with numbers, namely: C – cristobalite (*cr*-SiO_2), C1 – tridymite (*tr*-SiO_2), C2 – high-temperature quartz (HQ-SiO_2) and C3 – low-temperature quartz (LQ-SiO_2); D – cubic (c-ZrO_2) polymorphic modification , D1 – tetragonal (*t*-ZrO_2) polymorphic modification, and D2 – monoclinic (*m*-ZrO_2) polymorphic modification; compounds were indicated with letters R: R1 – Al_2TiO_5, R2 – $ZrTiO_4$, R3 – $ZrSiO_4$, and R4 – $Al_6Si_2O_{13}$.

3.2. A 3D model of the phase diagram of Al_2O_3-SiO_2-ZrO_2

All known information on the Al_2O_3-SiO_2-ZrO_2 (B-C-D) ternary system only concerns the liquidus [69–75], which corresponds to the formation of the $ZrSiO_4$ (R3) zircon by peritectoid reaction (Fig. 2b). This contributes to the determination of the shape of its liquidus surface [69, 70] with the following transformation of its internal field [72–74] (indicated in Fig. 2b as UQ_1E_2).

In addition to the eutectic (E_1, E_2) and quasi-peritectic (Q_1) invariant reactions (Table 1), which we have already mentioned, there is another reaction in the system, described in papers [72-74] as a peritectic or class III reaction [103]. If to consider only the temperature ratios of the invariant points on the liquidus, then this reaction is, indeed, peritectic one:

(1,660 °C): L + SiO_2 + *t*-ZrO_2 → $ZrSiO_4$ ((L+C+D1→R3).

However, it should be taken into account that in the SiO_2-ZrO_2 (C-D) binary system, the eutectic reaction of L → *t*-ZrO_2 + SiO_2 (L→C+D1) at a temperature of 1,687 °C is preceded by the zircon formation in the reaction SiO_2 + *t*-ZrO_2 → $ZrSiO_4$ (C+D1→R3) at 1,676 °C.

Hence, the reaction in a three-component system at a temperature of 1,660 °C cannot be considered peritectic (P) and should be attributed to class II. However, this is a four-phase transformation U: SiO_2 + ZrO_2 → $ZrSiO_4$ + L (C+D→R3+L) and it is not quasi-peritectic (Q). It corresponds to the coexistence of zircon with the melt; therefore, when constructing the 3D model, the corresponding invariant point shall be indicated with the letter U, rather than Q, as was mentioned above.

Despite the fact that the melts formed in the Al_2O_3-SiO_2-ZrO_2 (B-C-D) system at high temperatures are of the greatest practical importance, it is equally important to get an idea of the processes occurring in the solid-phase regions of the system, which is impossible to do without taking into account all polymorphic transitions.

Thus, five more invariant reactions could be expected to occur in the subsolidus, including four eutectoid ones [76].

After the completion of crystallization, three-phase subsolidus regions are formed: Al_2O_3 - *m*-ZrO_2 - $Si_2Al_6O_{13}$ (B-D2-R4), *m*-ZrO_2 - $ZrSiO_4$ - $Si_2Al_6O_{13}$ (D2-R3-R4), and LQ-SiO_2 - $ZrSiO_4$ - $Si_2Al_6O_{13}$ (C3-R3-R4). However, calculations using the NUCLEA database at temperatures above and below 1,054 °C showed that such triangulation is only possible at high temperatures [104]. At lower temperatures (below 1,054°C), triangulation in the subsolidus results in the formation of three other subsystems: Al_2O_3 - *m*-ZrO_2 - $ZrSiO_4$ (B-D2-R3), Al_2O_3 - $ZrSiO_4$ - $Si_2Al_6O_{13}$ (B-R3-R4), and LQ-SiO_2 - $ZrSiO_4$ - $Si_2Al_6O_{13}$ (C3-R3-R4).

Therefore, according to the data on binary systems and the liquidus surfaces of the ternary

system, it should expect six more invariant reactions in the subsolidus, including four eutectoid (E_3-E_6), a quasi-peritectoid (Q_2), and a peritectoid (P) reactions, as shown in the scheme of mono- and invariant states (Table 1) [76, 105, 106].

The tabulated scheme of mono- and invariant states can be converted into a three-dimensional scheme with the help of the PD Designer program [92] (Fig. 3). First, all isothermal planes (simplices) corresponding to invariant reactions are constructed: triangles for E_1-E_6 and P, then, quadrangles for Q_1, Q_2, and U. The directing curves of all ruled surfaces are brought to them (first with straight lines), which results in a 3D scheme of mono- and invariant states, a fragment of which is shown in Fig. 3a. If the surfaces imitating liquidus, solidus, solvus, and transus are constructed on the obtained frame, this gives a prototype of the phase diagram. It consists of 195 surfaces and 72 phase regions. Next, to move to the 3D model of the phase diagram of the real system (Fig. 4b), the base points are moved to the positions specified

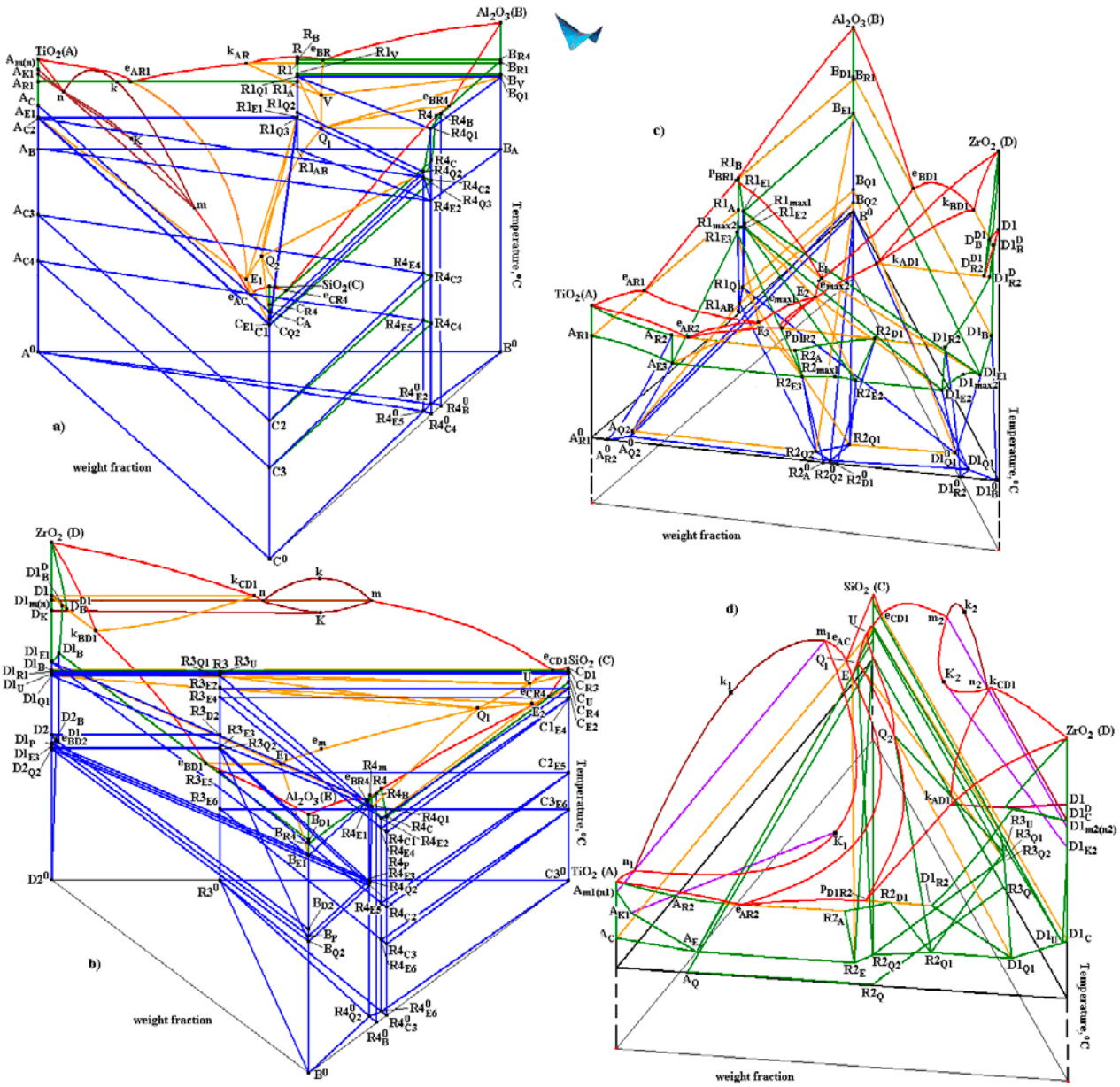

Fig. 4. Computer 3D models of phase diagrams: TiO_2-Al_2O_3-SiO_2 (A-B-C) (a), Al_2O_3-SiO_2-ZrO_2 (B-C-D) (b), TiO_2-Al_2O_3-ZrO_2 (A-B-D) (c) and TiO_2-SiO_2-ZrO_2 (A-C-D) (d), constructed above 1280 °C (c) and 1400 °C (d), correspondingly, with binary compounds Al_2TiO_5 (R1), $ZrTiO_4$ (R2), $ZrSiO_4$ (R3), $Si_2Al_6O_{13}$ (R4)

by real coordinates, and then the curvatures of the lines and surfaces are corrected.

The polythermal sections presented in [88] can be used to assess the quality of the calculations performed with the help of the computer 3D model. However, it should be taken into consideration that they were built at temperatures above 1,500 °C and do not allow evaluating the results of subsolidus modeling.

A comparison of the sections obtained by the 3D model with 14 polythermal sections shown in [88] did not reveal any fundamental discrepancies. However, it be noticed that the shape of the lines that form as a result of the intersection of the vertical plane with the ruled boundaries of three-phase regions (for example, at the boundaries of the L1+L2+D1 region indicated in Fig. 5b as 2L+Tss) is unacceptable for the sections of ruled surfaces. In addition, the regions of limited solubility of the components and zircon (R3) in the polymorphic modifications of ZrO_2 are so small in the 3D model that, unlike [88], they are not visible in the polythermal section S(0, 0.9, 0.1)-ZrO_2 (Fig. 5a). However, in contrast to [88], two-phase regions of mullite (R4) with all four modifications of SiO_2 (C) appear in this section.

The 3D model of the phase diagram of the ZrO_2-SiO_2-Al_2O_3 system was used to calculate the vertical diagrams of material balances for a given center of mass in the entire range of temperatures (Fig. 6a, Table 2).

For example, the crystallization of the G(0.34, 0.46, 0.20) melt proceeded through the following stages:

– Separation of primary crystals of *t*-ZrO_2 (D1) in the range from 1,896.9 to 1,677 °C.

– Eutectic crystallization of *t*-ZrO_2 and $Al_6Si_2O_{13}$ (R4) mullite within the range of 1,677-1,645 °C.

– Quasi-peritectic invariant reaction Q_1 at 1,645 °C: L+D1→R3+R4.

– Eutectic separation of mullite and zircon in the range of 1,645-1,550 °C, transitioning to the eutectic invariant transformation E_2 at 1,550 °C together with SiO_2 (C). This was followed by three polymorphic eutectoid transformations between SiO_2 modifications at temperatures of 1,470, 867, and 573 °C, respectively (Table 2). The same stages of crystallization were confirmed by the calculation of phase trajectories (Fig. 6b), where the crystallization path for the center of mass G is shown by the green line.

3.3. A 3D model of the phase diagram of TiO_2-Al_2O_3-SiO_2

Earlier, a simplified 3D model of the phase diagram of the TiO_2-Al_2O_3-SiO_2 (A-B-C) system was developed with congruently melting aluminum titanate. This model only included the high-temperature part (above 1,470 °C) of the phase diagram [107].

If the version of the TiO_2-Al_2O_3 phase diagram which does not take into account the formation of the $Al_6Ti_2O_{13}$ compound, but does take into account the polymorphism of $AlTiO_5$ is taken as the basis, then its high-temperature polymorphic modification shall be assigned with the designation R, its low-temperature polymorphic modification shall be indicated as R1, and the $Al_6Si_2O_{13}$ mullite as R4 (Fig. 4a).

There are an eutectic reaction between silicon and titanium oxides. The liquid immiscibility

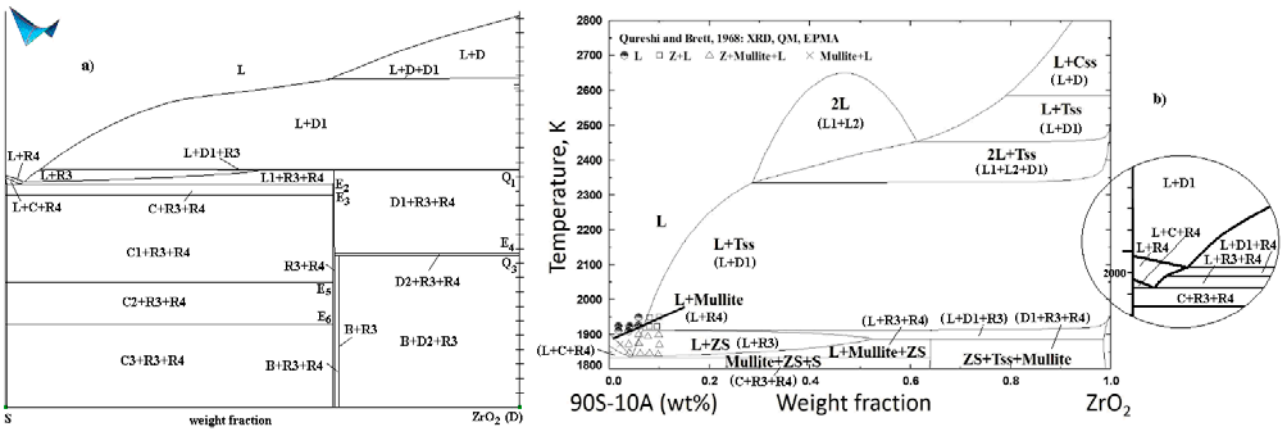

Fig. 5. Polythermal section S(0.1, 0.9, 0)-ZrO_2 (D): of the 3D model (a), calculated by CALPHAD-technology [88] (b)

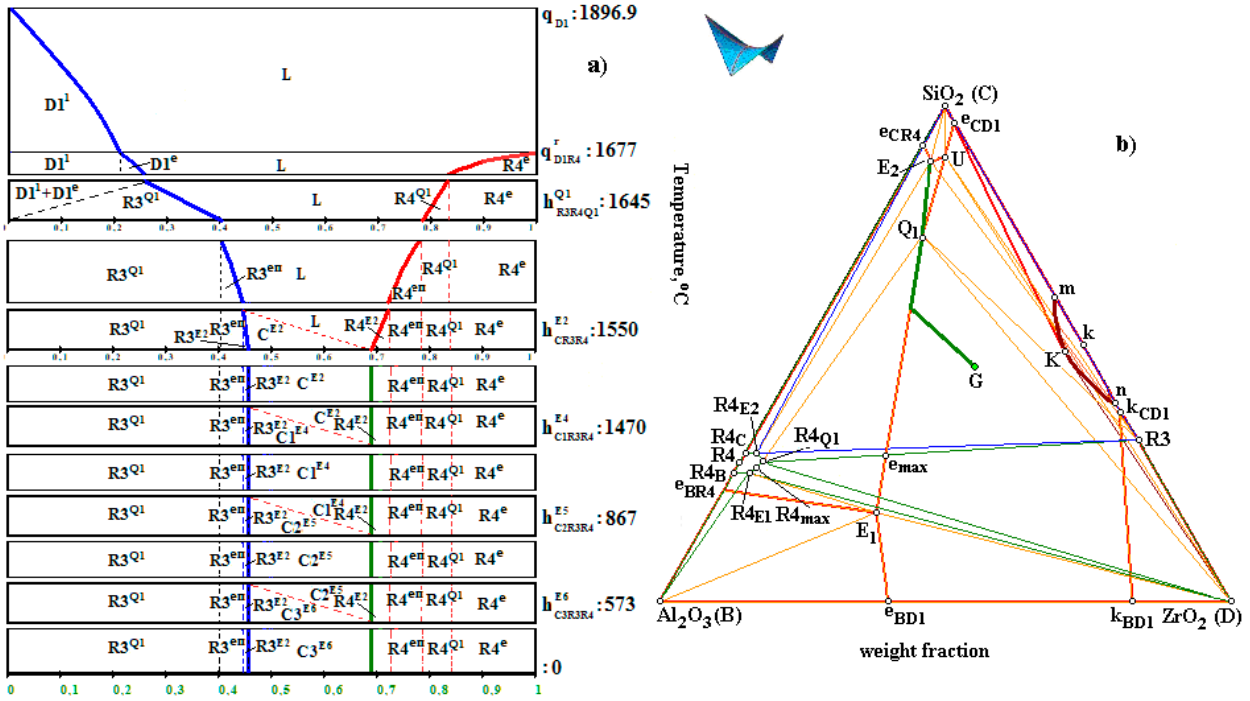

Fig. 6. Mass balance diagram showing the change in the phase composition of the melt G(0.34, 0.46, 0.20) during its crystallization in the Al_2O_3-SiO_2-ZrO_2 (B-C-D) system (a) and the melt path (b) (temperature °C, compositions – wt. fractions)

Table 2. Calculation of mass fractions of phases during crystallization of melt G(0.34, 0.46, 0.20) in the Al_2O_3-SiO_2-ZrO_2 (B-C-D) system (Fig. 6) until the end of the E_2 reaction (temperature °C, compositions - wt. fractions)*

Phase region	*T*, °C	Mass fractions of phases
L+D1 (L→D1[1])	1896.9 1677	L=1, D1=0 L=0.758, D1[1]=0.242
L+D1+R4 (L→D1[e]+R4[e])	1677 1645	L=0.758, D1[1]=0.242, R4=0 L=0.563, D1(D1[1]=0.242, D1[e]=0.042)=0.284, R4[e]=0.153
L+D1→R3[Q1]+R4[Q1]	1645	L=0.563, D1(D1[1]=0.242, D1[e]=0.042)=0.284, R4[e]=0.153, R3=0 L=0.345, D1=0, R3[Q1]=0.447, R4(R4[e]=0.153, R4[Q1]=0.055)=0.208
L+R3+R4 (L→R3[en]+R4[en])	1645 1550	L=0.345, R3[Q1]=0.447, R4(R4[e]=0.153, R4[Q1]=0.055)=0.208; L=0.249, R3(R3[Q1]=0.447, R3[en]=0.039)=0.486; R4(R4[e]=0.153, R4[Q1]=0.055, R4[en]=0.057)=0.265
L→C[E2]+R3[E2]+R4[E2]	1550	L=0.249, R3(R3[Q1]=0.447, R3[en]=0.039)=0.486; R4(R4[e]=0.153, R4[Q1]=0.055, R4[en]=0.057)=0.265; C=0 L=0; R3(R3[Q1]=0.447, R3[en]=0.039, R3[E2]=0.01)=0.496; R4(R4[e]=0.153, R4[Q1]=0.055, R4[en]=0.057, R4[E2]=0.029)=0.294; C[E2]=0.210

[*1] – primary crystallization;
[e] – univariant eutectic crystallization;
[ep] – post-peritectic univariant crystallization;
[Q] – invariant quasi-peritectic mass regrouping;
[E] – invariant eutectic (eutectoid) crystallization

L1 → L2 + TiO_2 (L1→L2+A) in the TiO_2-SiO_2 (A-C) binary system is appeared in the form of a small mknK cupola on the TiO_2 liquidus surface in the TiO_2-Al_2O_3-SiO_2 (A-B-C) ternary system. It only affectes the geometry of the solidus surface of titanium oxide in the form of the $A_{m(n)}A_K$ fold conjugated with the line of the intersection of the immiscibility cupola with this liquidus surface.

Since the congruently melting Al_2TiO_5 (R1) aluminum titanate devides the TiO_2-Al_2O_3 (A-B)

binary system into two subsystems: TiO_2-Al_2TiO_5 (A-R1) and Al_2TiO_5-Al_2O_3 (R1-B), the high-temperature modification R has two liquidus branches extending both into the subsystem with TiO_2 (liquidus cuver Rk_{AR}) and into the subsystem with Al_2O_3 (cuver Re_{BR}) (Fig. 4a).

Importantly, the polymorphism of Al_2TiO_5 manifestes itself differently in the subsystems. In the TiO_2-Al_2TiO_5 (A-R1) subsystem, it has the form of the R→R1+L metatectic reaction, as a result the liquidus in this subsystem consists of three branches corresponding to the onset primary crystallization of TiO_2 (A) (cuver Ae_{AR1}) and of compounds R (cuver Rk_{AR}) and R1 (cuver $k_{AR}e_{AR1}$) (Fig. 4a). In the Al_2TiO_5-Al_2O_3 (R1-B) subsystem, the liquidus has two branches: the onset primary crystallization of Al_2O_3 (B) (cuver Be_{BR}) and of R (cuver Re_{BR}). The polymorphic transition occurres below the liquidus by the R→R1+B eutectoid reaction.

Another feature of aluminum titanate is its decomposition into initial oxides at 1,300 °C [51].

In the Al_2O_3-SiO_2 (B-C) system, the $Al_6Si_2O_{13}$ (R4) mullite devides the system into two eutectic subsystems: Al_2O_3-$Al_6Si_2O_{13}$ (B-R4) and $Al_6Si_2O_{13}$-SiO_2 (R4-C).

Both binary systems with silicon oxide are differed by polymorphic transitions between the four modifications of silicon oxide (C). Polymorphic transitions are degenerated and their type are not clear. The 3D model suggests that eutectoid transformations took place. In the system constituting TiO_2 (A), they occurres with the participation of titanium oxide (A): C→C1+A, C1→C2+A, C2→C3+A, while in the system with Al_2O_3 (B), it occurres with the participation of mullite (R4): C→C1+R4, C1→C2+R4, C2→C3+R4.

To proceed with the 3D model, it are necessary to understand the structure of the phase diagram in the subsolidus. After the Q_1, Q_2, E_1 reactions completed (see section 2.2 and Fig. 2a), there are three ternary subsystems: B-R1-R4 (after Q_1), C-R1-R4 (after Q_2), and A-R1-C (after E_1). However, after completion of the eutectic reaction E_1, further solid-phase transformations takes place. First, there are three polymorphic transitions of silicon oxide. Secondly, in the TiO_2-Al_2O_3 (A-B) binary system, the low-temperature polymorphic modification of aluminum titanate (R1) decomposes into the initial oxides, TiO_2 and Al_2O_3. Naturally, the decomposition of R1 are also expected in the ternary system.

Earlier, the authors of [105] represented the following rearrangement in the Al_2O_3-SiO_2-ZrO_2 (B-C-D) system: in the B-R3-R4-D subsystem, the stable diagonal D-R4 replaced the diagonal B-R3. A similar situation are in the TiO_2-Al_2O_3-SiO_2 (A-B-C) system: after the completion of the Q_2 and E_1 reactions, the A-R1-R4-C subsystem has a stable diagonal C-R1. Therefore, there is a high probability of a rearrangement with stable diagonal A-R4 due to the invariant transformation of the quasiperitectoid type Q_3: C+R1→A+R4. This can be explained by the fact that in all variants of the binary system (Fig. 4), aluminum titanate R1 decomposes into TiO_2 (A) and Al_2O_3 (B). Therefore, if conditions for its decomposition are created in a ternary system, we should expect such a triangulation on the the A-R1-R4 and B-R1-R4 subsystems and the subsequent disappearance of the R1-R4 diagonal. Therefore, after the completion of the Q_3 reaction (rearrangement), the subsolidus should be presented by three subsystems: B-R1-R4 (after Q_1), A-R1-R4, and A-C-R4. Further, the R1-R4 segment separating the A-R1-R4 and B-R1-R4 subsystems should disappear. This should occur after the decomposition of R1 into A and B (in the presence of R4) by the reaction E_2: R1→A+B+R4.

In confirmation of this fact, a reaction was experimentally determed at 1469.85 °C in work [68]:

Q_3: $SiO_2 + Al_2TiO_5 \rightarrow TiO_2 + Al_6Si_2O_{13}$ (C+R1→A+R4),

which indicates rearrangement from the C+R1 diagonal to the A+R4 diagonal. In [67], studies in the subsolidus region showed that at 1,470–1,300°C (i.e. within the interval between the reactions Q_3 and E_2), two phase regions are formed: $TiO_2 + SiO_2 + Al_6Si_2O_{13}$ (A+C+R4) and $TiO_2 + Al_2TiO_5 + Al_6Si_2O_{13}$ (A+R1+R4).

In the TiO_2-Al_2O_3 (A-B) binary system, the decomposition of aluminum titanate (R1) occurs at 1,300 °C and zero mutual solubility of both initial oxides, while in the ternary system, the decomposition E_2: R1→A+B+R4 should occur at the same temperature of 1,300 °C. Therefore, the Q_3 rearrangement can be expected in the temperature range of $T_{E2} < T < T_{E1}$. The

temperature indicated in [68] is 1,470 °C / 1,743 K.

After the R1 decomposition by the E_2 reaction, crystallization in the A-B-R4 subsystem is completed. In the second subsystem A-C-R4, the set of polymorphic transitions E_3: C→C1+A+R4, E_4: C1→C2+A+R4, E_5: C2→C3+A+R4 are followed the after Q_3 rearrangement.

Thus, a 3D model of the TiO_2-Al_2O_3-SiO_2 (A-B-C) phase diagram is formed and consisted of 173 surfaces and 64 phase regions (Fig. 4a).

When constructing the 3D model, the following data on the structure of binary systems were used: the TiO_2-SiO_2 system [18], the TiO_2-Al_2O_3 system [51], and the Al_2O_3-SiO_2 system [29]. For the ternary system, we used liquidus data published in [68]. The choice was due to the fact that these data were obtained experimentally and contained the most complete information about the structure of the phase diagrams of binary systems, liquidus surfaces, and possible transformations in the subsolidus.

Model sections and obtained in [68] are compared for validation of the 3D model. These sections are well matched, which confirmed the correctness of the constructed model.

3.4. 3D models of phase diagrams of TiO_2-Al_2O_3-ZrO_2 and TiO_2-SiO_2-ZrO_2

When constructing 3D models of phase diagrams of ternary systems based on the TiO_2-ZrO_2 (A-D) binary system with the addition of Al_2O_3 (B) (Fig. 4c) and SiO_2 (Fig. 4d), we used the interpretation of the TiO_2-Al_2O_3 (A-B) binary system, according to which aluminum titanate polymorphism was not taken into account and the type of its melting was understood as being incongruent (Fig. 1f). This version was accepted in one of the recent works [51], but experimental work in this area continues. Nevertheless, the missing data are not an obstacle to constructing a 3D model, because the possible future adjustment of the type of aluminum titanate melting will not require significant changes in the geometry of the phase diagram. And even if the polymorphism of Al_2TiO_5 (R1) is confirmed, according to [52], its liquidus field will have to be divided into two fragments, which will not significantly affect the 3D model as a whole and will only affect a few fragments of the "upper" temperature part of the phase diagram.

According to [77], there are three eutectic transformations on the liquidus in the system with aluminum oxide (Fig. 2c):

E_1 (1,705 °C): L → Al_2O_3 + t-ZrO_2 + Al_2TiO_5 (L→B+D1+R1),

E_2 (1654 °C): L → t-ZrO_2 + Al_2TiO_5 + $ZrTiO_4$ (L→D1+R1+R2),

E_3 (1636 °C): L → TiO_2 + Al_2TiO_5 + $ZrTiO_4$ (L→A+R1+R2),

There are also rearrangements in the subsolidus:

Q_1 (1,375 °C): *t*-ZrO_2 + Al_2TiO_5 → Al_2O_3 + $ZrTiO_4$ (D1+R1→B+R2),

Q_2 (1,320 °C): Al_2TiO_5 + $ZrTiO_4$ → TiO_2 + Al_2O_3 (R1+R2→A+B).

After eutectic transformations, the system is triangulated into three subsystems:

TiO_2 - Al_2TiO_5 - $ZrTiO_4$ (A-R1-R2),
t-ZrO_2 - Al_2TiO_5 - $ZrTiO_4$ (D1-R1-R2),
Al_2O_3 - *t*-ZrO_2 - Al_2TiO_5 (B-D1-R1).

At the stage of the first rearrangement, as a result of reaction Q_1, the stable diagonal ZrO_2-Al_2TiO_5 (D1-R1) is replaced by Al_2O_3+$ZrTiO_4$ (B-R2). The second rearrangement result is the decomposition of aluminum titanate (R1) into TiO_2 and Al_2O_3 (A and B) and the system being divided into two subsystems: TiO_2 - Al_2O_3 - $ZrTiO_4$ (or A-B-R2), Al_2O_3 - *t*-ZrO_2 - $ZrTiO_4$ (B-D1-R2).

When constructing a computer 3D model of the phase diagram of the TiO_2-Al_2O_3-ZrO_2 system, we took into account the experimental and calculated data on the structure of binary systems and primary crystallization surfaces published in [2, 6–7, 49, 51, 77].

The coordinates of ternary eutectic reactions (E_1, E_2) were determined experimentally in [77]. The temperatures of the invariant transformations Q_1 and Q_2 in the subsolidus were also presented. (The coordinates of the maximum points on the invariant liquidus lines were only obtained by calculation in [77], and they were set approximately in the 3D model).

As a result, the computer 3D model of the phase diagram fragment limited from below by the temperature of 1,280 °C is formed by 77 surfaces and 27 phase regions.

The 3D model of the TiO_2-SiO_2-ZrO_2 (A-C-D) phase diagram is limited to a temperature of

1,400 °C, since isothermal sections at temperatures of 1,400 and 1,500 °C are described in [82] and only this limited information can be used to assess the quality of the obtained 3D model.

Two regions of liquid immiscibility on the side of binary systems with silicon oxide are two cupolas located on the surfaces of the onset crystallization of TiO_2 and the tetragonal form of ZrO_2, respectively (Fig. 2d). In addition to the primary crystallization fields of the cubic form of ZrO_2, SiO_2, and zirconium titanate ($e_{AR2}EQ_2Q_1p_{D1R2}$), the internal field of zircon (Q_1Q_2U) appeares on the liquidus.

In total, four invariant reactions with the participation of the melt take place in the system, including two quasiperitectic reactions and one eutectic reaction:

Q_1 (1,575 °C): L + *t*-ZrO_2 → $ZrTiO_4$ + $ZrSiO_4$ (L+D1→R2+R3),

Q_2 (1,545 °C): L + $ZrSiO_4$ → SiO_2 + $ZrTiO_4$ (L+R3→C+R2),

E (1,500 °C): L → TiO_2 + SiO_2 + $ZrTiO_4$ (L→A+C+R2).

As mentioned above the 3D model was constructed according to the data provided in [82], in which the temperature of the invariant peritectic reaction P: L + SiO_2 + *t*-ZrO_2 ZrSiO→ $ZrSiO_4$ (L+C+D1→R3) was indicated as 1,670 °C, while the temperature of the SiO_2 + *t*-ZrO_2 → $ZrSiO_4$ (C+D1→R3) zircon formation, according to the data in [1], was 1,676 °C, which was higher than the temperature of the ternary peritectic reaction. Then, one of the following is possible: either the invariant reaction in the ternary system is not peritectic, or zircon decomposes at a temperature lower than 1,670 °C.

When we constructed the 3D model, we assumed that the invariant reaction named in [82] as peritectic was actually not peritectic. Technically, this reaction could be considered as peritectic according to the reduction in temperature on the invariant liquidus lines (Fig. 2d), however, since this reaction was preceded the zircon formation at 1,676 °C, along with binary eutectic reaction e_{CD1}: L → SiO_2 + *t*-ZrO_2 (L→C+D1) at 1,687 °C, this invariant reaction at 1,670 °C can be presents as follows

U: SiO_2 + t-ZrO_2 → $ZrSiO_4$ + L (C+D1→R3+L),

which also corresponds to the formation of zircon, but in the presence of melt L. Since there is no unified terminology for invariant reactions, this reaction is indicated with letter U in the 3D model.

Therefore, a three-phase region ZrO_2 + $ZrTiO_4$ + $ZrSiO_4$ (D1+R2+R3) is formed in the ternary system after the quasi-peritectic reaction Q_1 below 1,575 °C. In the TiO_2-SiO_2-$ZrSiO_4$-$ZrTiO_4$ (A-C-R3-R2) subsystem, initially divided by the diagonal SiO_2-$ZrTiO_4$ (C-R2) [82], the rearrangement SiO_2 + $ZrTiO_4$ → TiO_2 + $ZrSiO_4$ (C+R2→A+R3) is predicted.

Further studies of the TiO_2-ZrO_2 (A-D) binary system in the subsolidus are needed to draw conclusions about phase transformations in the rest of the concentration space of the phase diagram after the rearrangement at temperatures below 1,400 °C.

Hence, the 3D model of a fragment of the phase diagram is assembled from 67 surfaces and 26 phase regions.

The projection of the liquidus surfaces presented in [82] does not take into account an immiscibility region on the side of the ZrO_2-SiO_2 binary system and the liquidus surface corresponding to the cubic modification of c-ZrO_2 either. Therefore, to form the immiscibility surface, we added a binary monotectic line at 2,250 °C in the range of 41–62 wt. % of SiO_2 and the upper critical point at 2,430 °C and 53 wt. % SiO_2 according to [23].

The 3D model of the phase diagram took into account the configuration and curvature of the liquidus surfaces and the immiscibility surface on the side of the TiO_2-SiO_2 binary system. The corresponding immiscibility surface in the crystallization field of TiO_2 occupies a significant area and its projection extendes to the middle of the triangle of compositions. When modeling the liquidus surface corresponding to the primary crystallization of zircon, the *s*-shape of the liquidus line at the boundary of the zircon field and the tetragonal form of ZrO_2 was taken into account. In addition, the 3D model specified the immiscibility surface adjacent to the SiO_2-ZrO_2 binary system and the surface of the primary crystallization of the cubic form of ZrO_2, which were not previously cosiderated in [82].

4. A 4D model of the isobaric phase diagram of the TiO_2-Al_2O_3-SiO_2-ZrO_2 quaternary system and prediction of the geometric structure of its high-temperature part

The data on invariant transformations in the boundaring systems was used to propose the scheme of phase reactions for the TiO_2-Al_2O_3-SiO_2-ZrO_2 quaternary system (Table 3) [108]. The system is symmetrical and consists of two parts, each of which includes a peritectic π, a quasi-peritectic μ, and a eutectic ε reactions. The main difference in these reactions is the participation of either mullite or zirconium titanate. Zircon is formed in both peritectic reactions, while in quasi-peritectic transformations crystallization of either of zirconium titanate (in μ_2) or tetragonal polymorphic modification of zirconium oxide (in μ_1) is completed.

After the completion of eutectic reactions, tetrahedration results in four subsystems (Fig. 7):

TiO_2 - SiO_2 - Al_2TiO_2 - $ZrTiO_4$ (A-C-R1-R2) after ε_2 at T < 1,470 °C,

SiO_2 - t-ZrO_2 - Al_2TiO_2 - $ZrTiO_4$ (C-D1-R1-R2) after μ_2,

SiO_2 - t-ZrO_2 - Al_2TiO_2 - $Al_6Si_2O_{13}$ (C-D1-R1-R4) after μ_1,

Al_2O_3-(t-ZrO_2)-Al_2TiO_2-$Al_6Si_2O_{13}$ (B-D1-R1-R4) after ε_1 at T < 1,480 °C.

This scheme can be used to describe the contours of ten liquidus hypersurfaces and ten solidus hypersurfaces (the zircon liquidus consists of two fragments). Immiscibility of liquid, which takes place in the TiO_2-SiO_2 and SiO_2-ZrO_2 binary systems both within the corresponding ternary and quaternary systems, remains independent and does not affect in any way the overall geometric configuration of the phase diagram of the quaternary system, or the phase transformations in this system. In addition, according to the scheme, 19 three-phase regions with the participation of the melt have been formed in the system (with due account of two regions of liquid immiscibility, L1+L2 + TiO_2 and L1 + L2+Al_2O_3) and 18 similar four-phase regions.

5. Conclusion

For the TiO_2-Al_2O_3-SiO_2 system, a total of eight variants of the liquidus structure are possible. They differ in the type melting (congruent or incongruent) of both mullite and aluminum titanate, the presence or absence of its polymorphism, and the possibility of the formation of one more compound, $Al_6Ti_2O_{13}$.

A three-dimensional computer model for one of the variants, i.e. congruently melting mullite and aluminum titanate with two polymorphic modifications has been designed. This model can be easily transformed into any of the seven

Table 3. The scheme of phase reactions with the melt participation in the TiO_2-Al_2O_3-SiO_2-ZrO_2 system*

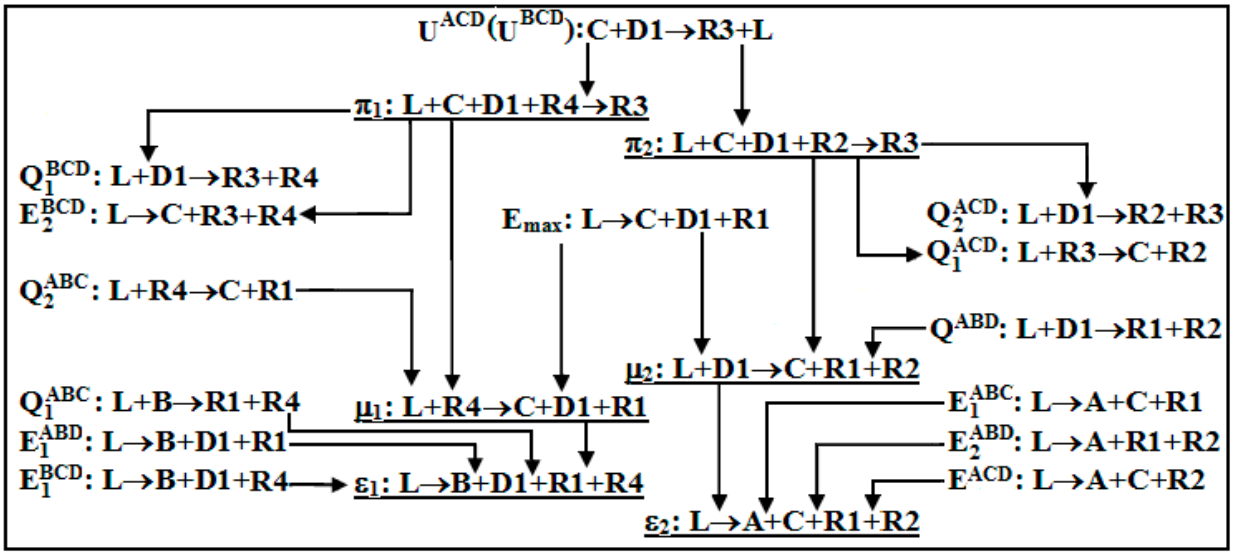

* Initial oxides are designated as: TiO_2 – A, Al_2O_3 – B, SiO_2 – C, c-ZrO_2 – D, t-ZrO_2 – D1, compounds – Al_2TiO_5 – R1, $ZrTiO_4$ – R2, $ZrSiO_4$ – R3, $Al_6Si_2O_{13}$ – R4

The superscripts indicate the invariant points of the corresponding ternary systems

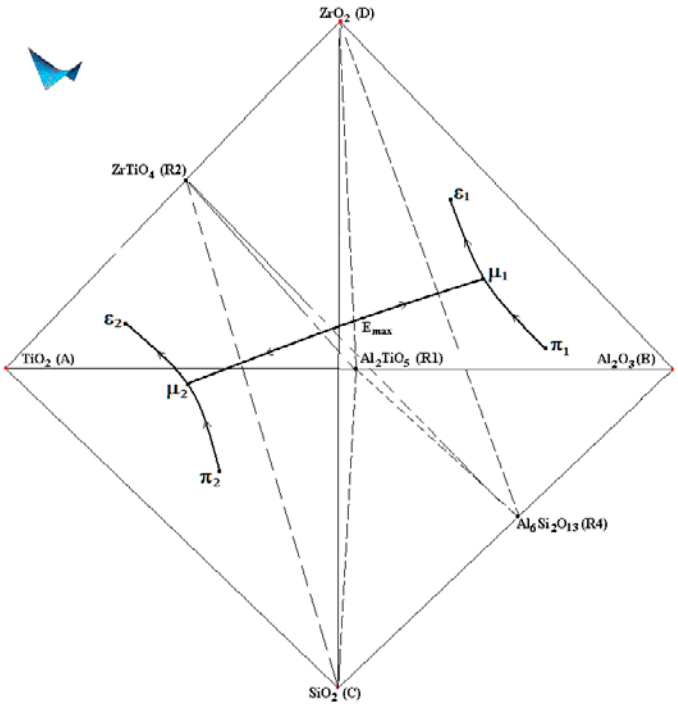

Fig. 7. Tetrahedration scheme of the TiO_2-Al_2O_3-SiO_2-ZrO_2 system with compounds Al_2TiO_5 (R1), $ZrTiO_4$ (R2), $Al_6Si_2O_{13}$ (R4) after eutectic reactions ending and drawing of univariant liquidus lines connecting quaternary invariant points

other variants should new refined experimental data appear.

Since there is no definitive description of the phase transformations in the TiO_2-ZrO_2 system, the modeling of two ternary systems formed on its basis is limited by the temperatures of aluminum titanate decomposition:

– 1,280 °C, which was used to construct four variants of the TiO_2-Al_2O_3-ZrO_2 phase diagram (which is due to the presence of four versions of the TiO_2-Al_2O_3 phase diagram). The quality of the 3D models can be assessed by comparing them with the isothermal sections described in previous studies [77].

– 1,400 °C, which was used for both versions of the 3D model of the TiO_2-SiO_2-ZrO_2 phase diagram (built in the assumption that zircon is formed by either a peritectic or a peritectoid reaction). In this case, it is possible to compare the model sections at 1,400 and 1,500 °C with previously published data [82].

Of the four possible variants of the Al_2O_3-SiO_2-ZrO_2 phase diagrams, which differ in the type melting of mullite and zircon, two variants of 3D models were constructed: when mullite melts congruently, zircon can be formed either by a peritectic or by a peritectoid reaction.

In general, the 3D models of the phase diagrams of the considered ternary systems, after minor adjustments that may be required when new, clarifying information is received, can be used in practice.

For the TiO_2-Al_2O_3-SiO_2-ZrO_2 four-component system, a scheme of phase reactions with the participation of the melt was deduced, which includes six five-phase invariant reactions: two peritectic, two eutectic, and two quasi-peritectic reactions.

It was assumed that its liquidus consists of 12 hypersurfaces, of which two correspond to the regions of immiscibility of liquid, while the remaining ten correspond to the onset primary crystallization of the initial oxides, including two high-temperature polymorphic modifications of zirconium oxide, two congruently melting compounds (aluminum titanate and mullite), incongruently melting zirconium titanate, and two fragments of the liquidus hypersurfaces of zircon.

The resulting prototype of the liquidus of the four-component oxide system will be used for the planning of further experiments, first of all, aimed at determining the coordinates of the estimated six invariant points.

Contribution of the authors

The authors contributed equally to this article.

Conflict of interests

The authors declare that they have no known competing financial interests or personal relationships that could have influenced the work reported in this paper.

References

1. Butterman W. C., Foster W. R. Zircon stability and the ZrO_2-SiO_2 phase diagram. *American Mineralogist*. 1967;52(5-6): 880–885.

2. Lakiza S. M., Lopato L. M. Stable and metastable phase relations in the system alumina-zirconia-yttria. *Journal of the American Ceramic Society*. 1997;80(4): 893–902. https://doi.org/10.1111/j.1151-2916.1997.tb02919.x

3. Fedorov P. P., Yarotskaya E. G. Zirconium dioxide. Review. *Condensed Matter and Interphases*. 2021;23(2): 169–187. https://doi.org/10.17308/kcmf.2021.23/3427

4. Fischer G. R., Manfredo L. J., McNally R. N., Doman R. C. The eutectic and liquidus in the Al_2O_3-ZrO_2 system. *Journal of Materials Science*. 1981;16: 3447–3451. https://doi.org/10.1007/BF00586307

5. Jerebtsov D. A., Mikhailov G. G., Sverdina S. V. Phase diagram of the system: Al_2O_3–ZrO_2. *Ceramics International*. 2000;26: 821. https://doi.org/10.1016/S0272-8842(00)00023-7

6. Lakiza S., Fabrichnayay O., Wang Ch., Zinkevich M., Aldinger F. Phase diagram of the ZrO_2-Gd_2O_3-Al_2O_3 system. *Journal of the American Ceramic Society*. 2006;26: 233–246. https://doi.org/10.1016/j.jeurceramsoc.2004.11.011

7. Fabrichnaya O., Aldinger F. Assessment of thermodynamic parameters in the system ZrO_2-Y_2O_3-Al_2O_3. *International Journal of Materials Research*. 2004;95: 27–39. https://doi.org/10.3139/146.017909

8. Bunting E. N. Phase equilibria in the systems TiO_2, TiO_2-SiO_2 and TiO_2-Al_2O_3. *Bureau of Standards Journal of Research*. 1933;11: 719–725. https://doi.org/10.6028/jres.011.049

9. Toropov N. A., Barzakovskii V. P., Lapin V. V., Kurtseva N. N. *State diagrams of silicate systems. The handbook. Part 1: binary systems**. Leningrad: Nauka Publ.; 1969. 822 p. (In Russ.)

10. Umezu S., Kakiuchi F. Investigations on iron blast. Furnace slags containing titanium. *Nippon Kogyo Kwaishi*. 1930;46: 866–877.

11. DeVries R. C., Roy R., Osborn E. F. The system TiO_2-SiO_2. *Transactions of the British Ceramic Society*. 1954;53 (9): 525–540.

12. Morey G. W. *Data of geochemistry. Chapter L. Phase-equilibrium relations of the common rock-forming oxides except water*. Washington: United States Government Printing Office; 1964. 146 p. https://doi.org/10.3133/pp440l

13. McTaggart G. D., Andrews A. I. Immiscibility area in the system TiO_2-ZrO_2-SiO_2. *Journal of the American Ceramic Society*. 1957;40(5): 167–170. https://doi.org/10.1111/j.1151-2916.1957.tb12596.x

14. Galakhov F. Ya., Areshev M. P., Vavilonova V. T., Aver'yanov V. I. Determination of the boundaries of metastable liquation in the silica part of the TiO_2-SiO_2 system*. *Izvestiia Akademii nauk SSSR: Neorganicheskie materialy*. 1974;10(1): 179–180. (In Russ.)

15. Kamaev D. N., Archugov S. A., Mikhailov G. G. Experimental study and thermodynamic modeling of the TiO_2-SiO_2 system*. In: *Computer modeling of the physicochemical properties of glasses and melts: Proc. VIII Rus. seminar, 16–19 October 2006*. Kurgan: Kurgan State University; 2006. p. 35–36. (In Russ.)

16. DeCapitani C., Kirschen M. A Generalized multicomponent excess function with application to immiscible liquids in the system CaO-SiO_2-TiO_2. *Geochimica et Cosmochimica Acta*. 1998;62 (23/24): 3753–3763. https://doi.org/10.1016/S0016-7037(98)00319-6

17. Kirschen M., DeCapitani C., Millot F., Rifflet J.-C., Coutures J.-P. Immiscible silicate liquids in the system SiO_2-TiO_2-Al_2O_3. *European Journal of Mineralogy*. 1999;11(3): 427–440. https://doi.org/10.1127/ejm/11/3/0427

18. Kirillova S. A., Almjashev V. I., Gusarov V. V. Spinodal decomposition in the SiO_2-TiO_2 system and hierarchically organized nanostructures formation. *Nanosystems: Physics, Chemistry, Mathematics*. 2012;3(2): 100–115. (In Russ.). Available at: https://nanojournal.ifmo.ru/files/volume7/10Almjashev.pdf

19. Kirillova S. A., Almjashev V. I., Gusarov V. V. Phase Relationships in the SiO_2-TiO_2 System. *Russian Journal of Inorganic Chemystry*. 2011;56 (9): 1464–1471. 10.1134/S0036023611090117.

20. Boulay E., Nakano J., Turner S., Idrissi H., Schryvers D., Godet S. Critical assessments and thermodynamic modeling of BaO-SiO_2 and SiO_2-TiO_2 systems and their extensions into liquid immiscibility in the BaO-SiO_2-TiO_2 system. *CALPHAD*. 2014;47: 68–82. https://doi.org/10.1016/j.calphad.2014.06.004

21. Ilatovskaia M., Fabrichnaya O. Liquid immiscibility and thermodynamic assessment of the Al_2O_3-TiO_2-SiO_2 system. *Journal of Phase Equilibria and Diffusion*. 2022;43: 15–31. https://doi.org/10.1007/s11669-021-00935-4

22. Geller R. F., Lang S. M. System SiO_2-ZrO_2. Journal of the American Ceramic Society. 1949;32: 157–159.

23. Toropov N. A., Galakhov F. Ya. Liquation in ZrO_2-SiO_2 system. *Bulletin of the Academy of Sciences of the USSR*. 1956;(2): 153–162. https://doi.org/10.1007/BF01177636

24. Berezhnoi A. S. *Multicomponent systems of oxides*. Kiev: Naukova Dumka Pulb.; 1970. 542 p. (In Russ.)

25. Kwon S. Y., Jung I.-H. Critical evaluation and thermodynamic optimization of the CaO-ZrO_2 and SiO_2-ZrO_2 systems. *Journal of the European* Ceramic *Society*. 2017;37(3): 1105–1116. https://doi.org/10.1016/j.jeurceramsoc.2016.10.008

26. Kamaev D. N., Archugov S. A., Mikhailov G. G. Study and thermodynamic analysis of the ZrO_2-SiO_2 system. *Russian Journal of Applied Chemistry*. 2005;78: 200–203. https://doi.org/10.1007/s11167-005-0259-2

27. Björkvall J., Stolyarova V. L. A mass spectrometric study of Al_2O_3-SiO_2 melts using a Knudsen cell. *Rapid Communications in Mass Spectrometry*. 2001;15: 836–842. https://doi.org/10.1002/rcm.251

28. Bowen N. L., Greig J. W. The system Al_2O_3-SiO_2. *Journal of the American Ceramic Society*. 1924;7(4): 238–254. https://doi.org/10.1111/j.1151-2916.1924.tb18190.x

29. Toropov N. A., Galakhov F. Ya. Solid solutions in the Al_2O_3-SiO_2 system. *Bulletin of the Academy of Sciences of the USSR Division of Chemical Science*. 1958;7(1): 5–9. https://doi.org/10.1007/BF01170853

30. Aramaki S., Roy R. Phase diagram for the system Al_2O_3-SiO_2. *Journal of the American Ceramic Society*. 1962;45(5): 229–242. https://doi.org/10.1111/j.1151-2916.1962.tb11133.x

31. Levin E. M., Robbins C. R., McMurdie H. F. *Phase diagrams for ceramists*. Ohio: American Ceramic Society; 1964. 600 p.

32. *Atlas of slags*®. Ref. book: trans. with him. I. S. Kulikova (ed.). Moscow: Metallurgy Publ.; 1985. 208 p. (In Russ.)

33. Strelov K. K., Kashcheev I. D. Phase diagram of the system Al_2O_3-SiO_2. *Refractories*. 1995;36 (7-8): 244–246. https://doi.org/10.1007/BF02227394

34. Fabrichnaya O., Costa e Silva A., Aldinger F. Assessment of thermodynamic functions in the MgO-Al_2O_3-SiO_2 system. *International Journal of Materials Research*. 2004;95(9): 793–805. https://doi.org/10.3139/146.017909

35. de Noirfontaine M. N., Tusseau-Nenez S., Girod-Labianca C., Pontikis V. CALPHAD formalism for Portland clinker: thermodynamic models and databases. *The Journal of Materials Science*. 2012;47: 1471–1479. https://doi.org/10.1007/s10853-011-5932-7

36. Shepherd E. S., Rankin G. A., Wright F. E. The binary systems of alumina with silica, lime and magnesia. *American Journal of Science*. 1909;(28): 293–333. Available at: https://zenodo.org/records/1633772

37. Klug F. J., Prochazka S. Alumina-silica phase diagram in the mullite region. *Journal of the American Ceramic Society*. 1987;70(10): 750–759. https://doi.org/10.1111/j.1151-2916.1987.tb04875.x

38. Aksay I. A., Pask J. A. Stable and metastable equilibria in the system SiO_2-Al_2O_3. *Journal of the American Ceramic Society*. 1975;58(10-14): 507–512. https://doi.org/10.1111/j.1151-2916.1975.tb18770.x

39. Shornikov S. I., Archakov I. Yu., Chemekova T. U. A mass spectrometry study of evaporation processes and phase equilibria in the Al_2O_3-SiO_2 system. *Russian Journal of Physical Chemistry A*. 2000;74(5): 684–688. Available at: https://elibrary.ru/item.asp?id=13347337

40. Eriksson G., Pelton A. D. Critical evaluation and optimization of the thermodynamic properties and phase diagrams of the CaO-Al_2O_3, Al_2O_3-SiO_2, and CaO-Al_2O_3-SiO_2 systems. *Metallurgical Transactions B*. 1993;24B: 807–816. https://doi.org/10.1007/BF02663141

41. Mao H., Selleby M., Sundman B. Phase equilibria and thermodynamics in the Al_2O_3-SiO_2 system - modeling of mullite and liquid. *Journal of the American Ceramic Society*. 2005;88(9): 2544–2551. https://doi.org/10.1111/j.1551-2916.2005.00440.x.

42. Yazhenskikh E., Hack K., Müller M. Critical thermodynamic evaluation of oxide systems relevant to fuel ashes and slags. Part 3: silica-alumina system. *CALPHAD*. 2008;32: 195–205. https://doi.org/10.1016/j.calphad.2007.05.004

43. Ban T., Hayashi S., Yasumori A., Okada K. Calculation of metastable immiscibility region in the Al_2O_3-SiO_2 system. *Journal of Materials Research*. 1996;11 (6): 1421-1427. https://doi.org/10.1557/jmr.1996.0178

44. Björkvall J., Stolyarova V. L. A mass spectrometric study of Al_2O_3-SiO_2 melts using a Knudsen cell. *Rapid Communications in Mass Spectrometry*. 2001;15(10): 836–842. https://doi.org/10.1002/rcm.251

45. Kwon S. Y., Jung I.-H. Thermodynamic assessment of the Al_2O_3-ZrO_2, CaO-Al_2O_3-ZrO_2, and Al_2O_3-SiO_2-ZrO_2 system. *Ceramics International*. 2022;48: 5413–5427. https://doi.org/10.1016/j.ceramint.2021.11.085

46. Lambotte G., Chartrand P. Thermodynamic evaluation and optimization of the Al_2O_3–SiO_2-AlF_3-SiF_4 reciprocal system using the modified quasichemical model. *Journal of the American Ceramic Society*. 2011;94: 4000–4008. https://doi.org/10.1111/j.1551-2916.2011.04656.x

47. Igami Y., Ohi S., Miyake A. Sillimanite-mullite transformation observed in synchrotron X-ray diffraction experiments. *Journal of the American Ceramic Society*. 2017;100: 4928–4937. https://doi.org/10.1111/jace.15020

48. Yarotskaya E. G., Fedorov P. P. Mullite and its isomorphic substitution. *Condensed Matter and Interphases*. 2018;20(4): 537–544. https://doi.org/10.17308/kcmf.2018.20/626

49. Saenko I., Ilatovskaia M., Savinykh G., Fabrichnaya O. Experimental investigation of phase relations and thermodynamic properties in the ZrO_2-TiO_2 system. *Journal of the American Ceramic Society*. 2018;101: 386–399. https://doi.org/10.1111/jace.15176

50. Troitzsch U., Ellis D. J. The ZrO_2-TiO_2 phase diagram. *Journal of Materials Research*. 2005;40(11): 4571–4577. https://doi.org/10.1007/s10853-005-1116-7

51. Ilatovskaia M., Savinykh G., Fabrichnaya O. Thermodynamic description of the Ti-Al-O system based on experimental data. *Journal of Phase Equilibria and Diffusion*. 2017;38 (3): 175–184. https://doi.org/10.1007/s11669-016-0509-4

52. Lang S., Fillmore C., Maxwell L. The system beryllia-alumina-titania: phase relations and general physical properties of three-component porcelains. *Journal of Research of the National Bureau of Standards*. 1952;48: 301–321. Available at: https://doi.org/10.6028/jres.048.038

53. Freudenberg B. *Etude de la reaction à l'état solide: Al_2O_3+TiO_2-Al_2TiO_5*. Tesis Doctoral. Eĉole Polytécnique, Lausanne. 1987. 262 p. https://doi.org/10.5075/epfl-thesis-709

54. de Arenas I. B. Reactive sintering of aluminum titanate. In: *Sintering of Ceramics-New Emerging Techniques*. Arunachalam Lakshmanan (ed.). InTech; 2012. p. 501–526. https://doi.org/10.5772/34366

55. Norberg S. T., Hoffmann S., Yoshimura M., Ishizawa N. $Al_6Ti_2O_{13}$, a new phase in the Al_2O_3-TiO_2 system. *Acta Crystallographica. Section C*. 2005;C61: i35-i38. https://doi.org/10.1107/s0108270105002532

56. Hoffmann S., Vasylechko L. O., Trots D. M., Yoshimura M. Thermal expansion of $Al_6Ti_2O_{13}$ between 20 K and 1173 K. *Zeitschrift für anorganische und allgemeine Chemie*. 2010;636: 2059–2059. https://doi.org/10.1002/zaac.201009020

57. Hoffmann S., Norberg S. T., Yoshimura M. Melt synthesis of Al_2TiO_5 containing composites and reinvestigation of the phase diagram Al_2O_3-TiO_2 by powder X-ray diffraction. *Journal of Electroceramics*. 2006;16: 327–330. https://doi.org/10.1007/s10832-006-9873-5

58. Berger M. H., Sayir A. Directional solidification of the Al_2O_3-Al_2TiO_5 system. *Journal of the European* Ceramic *Society*. 2008;28: 2411–2419. https://doi.org/10.1016/j.jeurceramsoc.2008.03.005

59. Jung I.-H., Eriksson G., Wu P., Pelton A. Thermodynamic modeling of the Al_2O_3-Ti_2O_3-TiO_2 system and its applications to the Fe-Al-Ti-O inclusion diagram. *ISIJ International*. 2009;49: 1290–1297. https://doi.org/10.2355/isijinternational.49.1290

60. Panda S. K., Jung I.-H. Coupled experimental study and thermodynamic modeling of the Al_2O_3-Ti_2O_3-TiO_2 system. *ISIJ International*. 2020:60: 31–41. https://doi.org/10.2355/isijinternational.ISIJINT-2019-006

61. Azimov S. A., Gulamova D. D. Mel'nik N. N., Sarkisova M. Kh., Suleimanov S. Kh., Tsapenko L. M. An investigation of aluminum titanate produced in the solar furnace*. *Izvestiya Akademii Nauk SSSR. Inorganic Matererials*. 1984;20(3): 469–471. (In Russ.)

62. Guljamova D. D., Sarkisova M. H. Interaction of aluminium and titanium oxides at high temperatures*. *Doklady Akademii Nauk SSSR. Inorganic Materials*. 1989;25(5): 789–794. (In Russ.)

63. Stolyarova V. L., Vorozhtcov V. A., Shemchuk D. V., Lopatin S. I., Bogdanov O. A. High temperature mass spectrometry study of the TiO_2-Al_2O_3 system. *Russian Journal of General Chemistry*. 2021;91(10): 1999–2007. https://doi.org/10.1134/S107036322110011X

64. Agamawi Y. M., White J. The system Al_2O_3-TiO_2-SiO_2. *Transactions of the British Ceramic Society*. 1952;51(5): 293–325.

65. Toropov N. A., Barzakovsky V. P., Lapshin V. V., Kurtseva N. N., Boikova A. I. *State diagrams of silicate systems. Reference book. Issue 3. Ternary silicate systems**. Leningrad, Nauka Publ.; 1972. 448 p. (In Russ.)

66. Galakhov F. Ya. The study of the alumina-rich area of aluminosilicate systems. Report 3. The TiO_2-Al_2O_3-SiO_2 system*. *Izvestiia Akademii Nauk SSSR. Seriia Khimicheskaia*. 1958;(5): 529–534. (In Russ.).

67. Fidancevska E., Vassilev V. Obtaining of powders by controlled hydrolysis and sintering of materials from the TiO_2-Al_2O_3-SiO_2 system. *Journal of Chemical Technology and Metallurgy*. 2010;45(4): 421–430. Available at: https://journal.uctm.edu/node/j2010-4/10_Venci_Vassilev_425-434.pdf

68. Ilatovskaia M., Bärtel F., Fabrichnaya O. Phase relations in the Al_2O_3-TiO_2-SiO_2 system. *Ceramics International*. 2020;46(18): Part B: 29402–29412. https://doi.org/10.1016/j.ceramint.2020.05.103

69. Budnikov P. P., Litvakovsky A. A. To study the Al_2O_3-SiO_2-ZrO_2 system*. *Bulletin of the Russian Academy of Sciences USSR*. 1956;106(2): 267. (In Russ.)

70. Greca M. C., Emiliano J. V., Segadães A. M. Revised phase equilibrium relationships in the system Al_2O_3-ZrO_2-SiO_2. *Journal of the European* Ceramic *Society*. 1992;9(4): 271–283. https://doi.org/10.1016/0955-2219(92)90062-I

71. Ferrari C. R., Rodrigues J. A. Microstructural features of alumina refractories with mullite-zirconia aggregates. *Boletín de la Sociedad Española de Cerámica y Vidrio*. 2003;42: 15–20. https://doi.org/10.3989/cyv.2003.v42.i1.651

72. Quereshi M. H., Brett N. H. Phase equilibria in ternary systems containing zirconia and silica. II. The system $A1_2O_3$-ZrO_2-SiO_2. *Transactions of the British Ceramic Society*. 1968;67(11): 569–579.

73. Pena P., De Aza S. The zircon thermal behavior: effect of impurities. *Journal of Materials Science*. 1984;19: 135–142. https://doi.org/10.1007/bf02403119

74. Pena P. Refractarios para zonas de contacto con el vidrio. *Boletín de la Sociedad Española de Cerámica y Vidrio*. 1989;28: 89–96. Available at: https://boletines.secv.es/upload/198928089.pdf

75. Sánchez Soto P. J., Pérez Rodríguez J. L. Características generales, propiedades, yacimientos y aplicaciones de pirofilita. II. Yacimientos, aplicaciones y utilización como materia prima cerámica. *Boletín de la Sociedad Española de Cerámica y Vidrio*. 1998;37: 359–368. https://doi.org/10.3989/cyv.1998.v37.i5.995

76. Vorob'eva V. P., Zelenaya A. E., Lutsyk V. I. Using a 3D computer model of the *T-x-y* diagram of the ZrO_2-SiO_2-Al_2O_3 system to resolve contradictions in the initial experimental data. *Russian Journal of Inorganic Chemystry*. 2021;66(6): 894–901. https://doi.org/10.1134/S003602362106022X

77. Ilatovskaia M., Savinykh G., Fabrichnaya O. Thermodynamic description of the ZrO_2-TiO_2-Al_2O_3 system based on experimental data. *Journal of the European* Ceramic *Society*. 2017;37(10): 3461–3469. https://doi.org/10.1016/j.jeurceramsoc.2017.03.064

78. Barzakovskii V. P., Lapin, V. V., Bojkova A. I., Kurtseva N. N. *State diagrams of silicate systems. The Handbook. Part 4: Ternary silicate systems**. Leningrad: Nauka Publ.; 1974. 514 p. (In Russ.).

79. http://www.crct.polymtl.ca/fact/phase_diagram.php?file=Al-Ti-Zr-O_Al2O3-TiO2-ZrO2_liquidus-projection.jpg&dir=FToxid

80. Coughanour L. W., Roth R. S., De Prosse V. A. Phase equilibrium relations in the system lime-titania and zirconia-titania. *Journal of Research of the National Bureau of Standards*. 1954;52(1): 37–42. Available at: https://nvlpubs.nist.gov/nistpubs/jres/52/jresv52n1p37_A1b.pdf

81. Shevchenko A. V., Lopato L. M., Meister I. M., Gorbunov O. S. ZrO_2-TiO_2 system*. *Russian Journal of Inorganic Chemystry*. 1980;25(9): 2496–2499. (In Russ.)

82. Pena P., De Aza S. El sistema ZrO_2-SiO_2-TiO_2. *Boletín de la Sociedad Española de Cerámica y Vidrio*. 1976;15(2): 93–95.

83. Belov G. V., Aristova N. M. Databases on the properties of materials and substances for nuclear power*. *Mathematical Models and Computer Simulations*. 2017;29(6): 135–142. Available at: http://mi.mathnet.ru/eng/mm/v29/i6/p135 (In Russ.)

84. Ohnuma I., Ishida K. Phase diagrams as tools for advanced materials design: applications to non-ferrous alloys. *Tecnologia em Metalurgia, Materiais e Mineração*. 2016;13(1): 46. http://dx.doi.org/10.4322/2176-1523.1085

85. Bakardjieva S., Barrachin M., Bechta S., ... Wiss T. Quality improvements of thermodynamic data applied to corium interactions for severe accident modelling in SARNET2. *Annals of Nuclear Energy*. 2014;74: 110–124. https://doi.org/10.1016/j.anucene.2014.06.023

86. Kitagaki T., Yano K., Ogino H., Washiya T. Thermodynamic evaluation of the solidification phase of molten core-concrete under estimated Fukushima daiichi nuclear power plant accident conditions. *Journal of Nuclear Materials*. 2017;486: 206–215. https://doi.org/10.1016/j.jnucmat.2017.01.032

87. Bakardjieva S., Barrachin M., Bechta S., ... Wiss T. Improvement of the european thermodynamic database NUCLEA. *Progress in Nuclear Energy*. 2010;52: 84–96. https://doi.org/10.1016/j.pnucene.2009.09.014

88. Kwon S. Y. *Thermodynamic optimization of ZrO_2-containing systems in the CaO-MgO-SiO_2-Al_2O_3-ZrO_2 system*. Dissertation. Department of mining and materials engineering. McGill University. Montreal, QC. 2015. 113 p. Available at: https://escholarship.mcgill.ca/concern/theses/dz010t00f

89. Lutsyk V. I., Vorob'eva V. P. Computer models of eutectic-type *T-x-y* diagrams with allotropy. Two inner liquidus fields of two low-temperature modifications of the

same component. *Journal of Thermal Analysis and Calorimetry*. 2010;101(1): 25–31. https://doi.org/10.1007/s10973-010-0855-0

90. Lutsyk V. I., Vorob'eva V. P. 3D Model of the *T–x–y* Diagram of the Bi-In-Sn System for designing microstructure of alloys. *Russian Journal of Inorganic Chemystry*. 2016;61(2): 188–207. https://doi.org/10.1134/S0036023616020121

91. Vorob'eva V. P., Zelenaya A. E., Lutsyk V. I., Sineva S. I., Starykh R. V., Novozhilova O. S. High-Temperature area of the Fe-Ni-Co-Cu diagram: experimental study and computer design. *Journal of Phase Equilibria and Diffusion*. 2021;42(2): 175–193. https://doi.org/10.1007/s11669-021-00863-3

92. Lutsyk I. V., Zelenaya A. E., Zyryanov A. M. Multicomponent systems simulation by the software of "Diagrams Designer". *Journal of International Scientific Publications: Materials, Methods and Technologies*. 2008;2(1): 176–184. Available at: https://www.scientific-publications.net/download/materials-methods-and-technologies-2008.pdf

93. Lutsyk V. I., Vorob'eva V. P. Three-dimensional model of phase diagram of Au-Bi-Sb system for clarification of thermodynamic calculations. *Russian Journal of Physical Chemistry*. 2015;89(10): 1715–1722. https://doi.org/10.1134/S0036024415100192

94. Lutsyk V. I., Vorob'eva V. P., Shodorova S. Ya. Verification of the *T–x–y* diagram of the Ag–Au–Bi system using a 3D computer model. *Russian Journal of Inorganic Chemystry*. 2016;61(7): 858–866. https://doi.org/10.1134/S0036023616070123

95. Nasrulin E. R., Lutsyk V. I., Vorobyova V. P. *Visualization of crystallization paths and calculation of material balance in ternary phase diagrams**. Copyright certificate of RF No. 50200601390; ESPD.03524577.01520-01; No. 6632; application 06/29/2006; Publ. 08.08.2006 (In Russ.)

96. Lutsyk V. I., Vorob'eva V. P., Zelenaya A. E. 3D reference book on the oxide systems space diagrams as a tool for data mining. *Solid State Phenomena*. 2015;230: 51–54. https://doi.org/10.4028/www.scientific.net/ssp.230.51

97. Vorob'eva V. P., Zelenaya A. E., Lutsyk V. I. Analysis of the geometric features of *T-x-y* diagrams with melt immiscibility for silicate systems. *Journal of Physics: Conference Series*. 2021;1791(1): 012121. https://doi.org/10.1088/1742-6596/1791/1/012121

98. Vorob'eva V. P., Zelenaya A. E., Lutsyk V. I., Lamueva M. V. A 3D computer model of the CaO-MgO-Al_2O_3 *T-x-y* diagram at temperatures above 1300 °C. *Condensed Matter and Interphases*. 2021;23(3): 380–386. https://doi.org/10.17308/kcmf.2021.23/3529

99. Lutsyk V. I., Zelenaya A. E., Savinov V. V. Phase trajectories in CaO-Al_2O_3-SiO_2 melts. *Crystallography Reports*. 2012;57(7): 943–947. https://doi.org/10.1134/s1063774512070176

100. Lutsyk V., Zelenaya A. Crystallization paths in SiO_2-Al_2O_3-CaO system as a genotype of silicate materials. *IOP Conference Series: Materials Science and Engineering*. 2013;47: 012047. https://doi.org/10.1088/1757-899x/47/1/012047

101. Lutsyk I. V., Zelenaya A. E., Nasrulin E. R., Zyryanov A. M. The NaCl-$CaCl_2$-$MgCl_2$ system: analysis of zero-, one- and two-dimensional concentration fields. *Melts*. 2016;(3): 216–225. Available at: https://www.elibrary.ru/item.asp?id=27184380 (In Russ.)

102. Lutsyk V. I., Zelenaya A. E. *T-x-y* diagram of the MgO-SiO_2-Al_2O_3 system: microstructure design. *Russian Journal of Inorganic Chemistry*. 2018;63(8): 1087–1091. https://doi.org/10.1134/S0036023618080132

103. Connell R. G. A tutorial on flow diagrams: a tool for developing the structure of multicomponent phase diagrams. *Journal of Phase Equilibria and Diffusion*. 1994;15(1): 6–19. https://doi.org/10.1007/BF02667677

104. Vorozhtcov V. A., Yurchenko D. A., Almjashev V. I., Stolyarova V. L. Phase equilibria in the Al_2O_3-SiO_2-ZrO_2 system: calculation and experiment. *Glass Physics and Chemistry*. 2021;47: 417–426. https://doi.org/10.1134/S1087659621050175

105. Vorob'eva V. P., Zelenaya A. E., Lutsyk V. I., Vorozhtcov V. A., Almjashev V. I., Stolyarova V. L. State diagram of the ZrO_2-SiO_2-Al_2O_3 system with visualization by 3D computer model and calculation using the NUCLEA database. *Doklady Physical Chemistry*. 2023;511(1): 107–116. https://doi.org/10.1134/S0012501623600079

106. Vorob'eva V. P., Zelenaya A. E., Lutsyk V. I., Vorozhtcov V. A., Almjashev V. I., Sokolova T. V., Stolyarova V. L. Modeling of the ZrO_2-SiO_2-Al_2O_3 phase diagram using simulation by the 3D computer model and the NUCLEA database. *Materials Science and Engineering B*. 2023;297: 116790. https://doi.org/10.1016/j.mseb.2023.116790

107. Lutsyk V., Zelenaya A., Zyryanov A., Nasrulin E. Computer models of phase diagrams for ceramic systems. TiO_2-SiO_2-Al_2O_3 and ZrO_2-SiO_2-Al_2O_3. *Epitoanyag - Journal of Silicate Based and Composite Materials*. 2016;68(2): 52–55. https://doi.org/10.14382/epitoanyag-jsbcm.2016.9

108. Vorob'eva V. P., Zelenaya A. E., Lutsyk V. I., Almjashev V. I., Vorozhtcov V. A., Stolyarova V. L. Prediction of the liquidus of the quaternary system of titanium, aluminim, silicon, and zirconium oxides. *Glass Physics and Chemistry*. 2021;47(6): 616–621. https://doi.org/10.1134/S1087659621060328

* *Translated by author of the article*

Information about the authors

Vasily I. Lutsyk, Dr. Sci. (Chem.), Head of Sector of Computer Materials Design, Institute of Physical Materials Science of Siberian Branch of Russian Academy of Sciences (Ulan-Ude, Russian Federation).
https://orcid.org/0000-0002-6175-0329
vluts@ipms.bscnet.ru

Anna E. Zelenaya, Cand. Sci. (Phys.-math.), Senior Researcher of Sector of Computer Materials Design, Institute of Physical Materials Science of Siberian Branch of Russian Academy of Sciences (Ulan-Ude, Russian Federation).
https://orcid.org/0000-0001-5232-8567
zel_ann@mail.ru

Vera V. Vorob'eva, Dr. Sci. (Phys.-math.), Leading Researcher of Sector of Computer Materials Design, Institute of Physical Materials Science of Siberian Branch of Russian Academy of Sciences (Ulan-Ude, Russian Federation).
https://orcid.org/0000-0002-2714-3808
vvorobjeva@mail.ru

Received 28.06.2024; approved after reviewing 08.07.2024; accepted for publication 16.09.2024; published online 25.12.2024.

Translated by Irina Charychanskaya

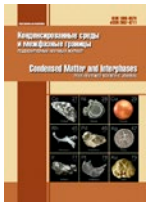

ISSN 1606-867X (Print)
ISSN 2687-0711 (Online)
Condensed Matter and Interphases
Kondensirovannye Sredy i Mezhfaznye Granitsy
https://journals.vsu.ru/kcmf/

Review

Review article
https://doi.org/10.17308/kcmf.2024.26/12415

Sodium fluoride and rare earth trifluorides systems. Review

P. P. Fedorov[1]✉, I. I. Buchinskaya[2]

[1]*Prokhorov General Physics Institute of the Russian Academy of Sciences,*
38 Vavilova st., Moscow 119991, Russian Federation

[2]*Shubnikov Institute of Crystallography, Kurchatov Complex of Crystallography and Photonics,*
National Research Centre "Kurchatov Institute,"
59 Leninskii pr., Moscow 119333, Russian Federation

Abstract

NaF–RF_3 systems, which are composed of sodium fluorides and rare earth trifluorides, are sources of many functional materials. Data on phase formation and phase equilibria in these systems were analyzed. The polymorphism and morphotropy of rare earth fluorides were considered taking into account the influence of pyrohydrolysis. A summary series of NaF–RF_3 phase diagrams are presented and the coordinates of invariant equilibria are tabulated. The data of research by Thoma et al., performed in the sixties of the twentieth century, are now only of historical interest. In these systems, α-$Na_{0.5-x}R_{0.5+x}F_{2+2x}$ (cubic, R = Pr-Lu, Y) and β-$Na_{3x}R_{2-x}F_6$ (hexagonal, R = La–Lu,Y) phases of variable composition with fluorite and gagarinite structures, respectively, are formed. In addition, solid solutions based on rare earth trifluorides with the LaF_3–tysonite (R = La–Gd) structure and the berthollide phase of such a structure in the system with TbF_3 were identified. Data was presented on the concentration dependence of the lattice parameters of fluorite phases. High temperature α-phases with maxima on the melting curves allow growing single crystals from the melt. A complex pattern of ordering of these phases with decreasing temperature was observed. Low-temperature syntheses of intermediate phases in these systems led, in accordance with the Ostwald's step rule, to the initial formation of nonequilibrium phases of a fluorite structure, usually designated as "α-NaRF_4", which were then replaced by equilibrium low-temperature hexagonal phases of "β-NaRF_4". The hexagonal phase in the NaF–YF_3 system, doped with ytterbium and erbium ("β-$NaYF_4$:Yb,Er"), is one of the most well-known, efficient up-conversion phosphors.

Keywords: Sodium fluoride, Rare earth fluorides, Phase diagrams, Fluorite, Gagarinite, Morphotropy

Funding: The work was carried out within the framework of state assignments of the General Physics Institute of the Russian Academy of Sciences and the National Research Centre "Kurchatov Institute".

For citation: Fedorov P. P., Buchinskaya I. I. Sodium fluoride and rare earth trifluorides systems. Review. *Condensed Matter and Interphases*. 2024;26(4): 687–705. https://doi.org/10.17308/kcmf.2024.26/12415

Для цитирования: Федоров П. П., Бучинская И. И. Системы из фторидов натрия и редкоземельных элементов. Обзор. *Конденсированные среды и межфазные границы*. 2024;26(4): 687–705. https://doi.org/10.17308/kcmf.2024.26/12415

✉ Pavel P. Fedorov, e-mail: e-mail: ppfedorov@yandex.ru

1. Introduction

The NaF–RF_3 systems composed of sodium fluorides and rare earth trifluorides are sources of many functional materials. These systems are also of considerable interest from the point of view of non-stoichiometry, isomorphism, morphotropy, order-disorder transition processes, and phase equilibria theory [1].

Recently, the main emphasis has been on studying the processes of synthesis of nanomaterials in these systems for use in nanophotonics and other fields [2]. Nanofluorides are used for the visualization of infrared radiation, marking and protection against counterfeiting, luminescent thermometry and vacuum measurement, increasing the efficiency of solar panels, creating anti-reflective coatings, and 2D/3D monitors [3–10]. Due to the low toxicity of nanofluorides of alkaline and rare earth fluorides, their biomedical applications is very important [10].

Up-conversion phosphors are materials characterized by anti-Stokes luminescence, i.e. the emission of light with a shorter wavelength than the exciting radiation. Among other things, they convert energy from the near infrared spectrum into the visible range using a nonlinear optical process. Operating principles of such luminophores were described in the 1960s by Ovsyankin and Feofilov [14] and Ozel [15]. More often Er^{3+}, Tm^{3+}, and Ho^{3+} are used as up-conversion luminescent ions, and the Yb^{3+}ion is used as an up-conversion sensitizer, since it is characterized by a very simple energy level diagram. The most widely used matrix is the low temperature phase in the NaF–YF_3 system with a hexagonal structure of the gagarinite type [16–18], denoted in the literature as β-$NaYF_4$ [6].

Information on the low-temperature stability of the corresponding phases is essential. Methods used for the synthesis of nano- and micromaterials (co-precipitation from aqueous and non-aqueous solutions, hydrothermal synthesis, synthesis from high-boiling organics, synthesis from salt melts, sol-gel method, glass crystallization, etc.) [2, 20–27], provide limited information on phase formation in the corresponding systems, which can only indirectly be related to the problem of phase equilibria. In this preparative area of chemistry, nonequilibrium processes predominate, during which, in accordance with the Ostwald's step rule [28, 29], nonequilibrium phases are formed first. In particular, the nonequilibrium nature of the $NaYF_4$ cubic phase synthesized by coprecipitation was demonstrated in the study [30].

Since bulk single crystals are still in demand in photonics and laser technologies, growing single crystals from melt remains important. Here, the consideration of solid-liquid equilibria is essential. The main methods for growing single crystals are the Czochralski and Bridgman-Stockbarger methods. Due to the need to obtain thin laser wave guides, the micro-pulling-down (μ-PD) method has been developed [31, 32]. The key factor is the preparation of the starting reagents and the use of a fluorinating atmosphere during the growth process [33–35].

The *M*F-RF_3 systems are model for actinides [36, 66, 121].

The aim of this review is the presentation of a complete series of phase diagrams of NaF–RF_3 systems and characterization of the phases formed in these systems.

2. Polymorphism of rare earth trifluorides

It might appear that the question of polymorphism and morphotropy in the series of rare earth element trifluorides had been finally resolved a long time ago [37–47]. However, misunderstandings arise again and again.

The diagram of phase transitions in the series of rare earth trifluorides is shown in Fig. 1. Lanthanum-neodymium trifluorides, as well as high-temperature modifications of fluorides

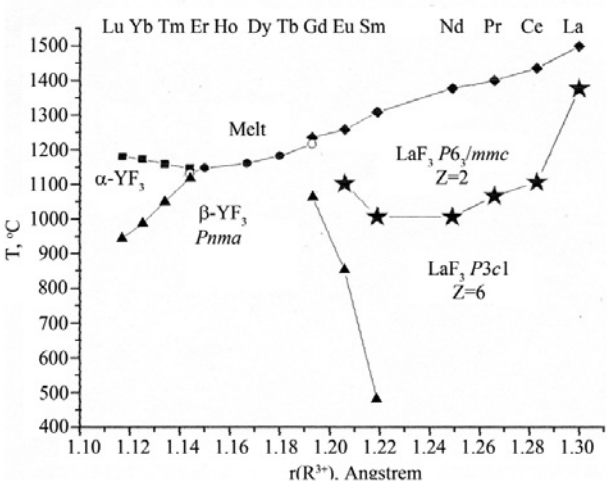

Fig. 1. Phase transitions in RF_3 rare-earth trifluoride series [38]

of samarium, europium, gadolinium, crystallize in the structural type LaF_3 - tysonite. The tysonite structure, characterized by sp. gr. $P\bar{3}c1$, Z = 6, at high temperature undergoes slight anionic disordering and passes into the sp. gr. $P6_3/mmc$, Z = 2 [48, 49]. This transition is not accompanied by jumps in heat capacity and molar volume and has a diffuse nature. The Tb–Ho fluorides, as well as low-temperature modifications of Sm–Gd, Er–Lu, and Y trifluorides crystallize in the orthorhombic crystal system, β-YF_3 type, sp. gr. *Pnma*. Based on powder X-ray diffraction patterns, unquenched high-temperature modifications of Er–Lu trifluorides crystallize in the trigonal crystal system, α-YF_3 structural type. Its structure is related to α-UO_3 and anti-Li_3N [41, 50]. Cubic fluorite-like phases, which can be stable at high pressure, are characteristic of rare earth oxofluorides and arise during intense pyrohydrolysis of rare earth trifluorides.

For example, the data of Sui et al. [51] fit well into this scheme of polymorphism and morphotropy of REE fluorides. Hexagonal modification of EuF_3, which is in a nonequilibrium state at room temperature, overcomes the potential barrier upon heating and transforms into an equilibrium orthorhombic modification of the β-YF_3 type; with further heating and cooling, a reversible phase transition between equilibrium modifications is realized. In the study of Xie et al. [24] equilibrium modifications of trifluorides were obtained in the form of nanoparticles for R = La–Nd (LaF_3 type) and R = Tb–Lu (β-YF_3 type) during the synthesis from high-boiling organic at 300 °C. The nonequilibrium high-temperature modifications of the LaF_3 type were synthesized for R = Sm, Eu, and a mixture of equilibrium orthorhombic and nonequilibrium hexagonal modifications was obtained for Gd. It should be noted that, judging by the presented X-ray diffraction patterns, the hexagonal phase nanopowders obtained in this work are characterized by a high-temperature sp. gr. $P6_3/mmc$.

The main difficulty in studying phase formations and obtaining materials containing rare earth fluorides is the problem of pyrohydrolysis. Hydrolysis, including pyrohydrolysis is the interaction with water vapor or water adsorbed on the surface of fluoride particles, leading to contamination of samples with hydroxyl ions, isomorphically replacing fluorine, and subsequently to the appearance of oxygen impurities, causing the formation of new oxofluoride phases [52–54]. The resistance to hydrolysis of rare earth fluorides decreases with an increase in the atomic number of the element, i.e., when moving from light to heavy lanthanides. An exception is the increased hydrolytic capacity of cerium fluoride [55]. The intensity of hydrolysis processes accelerates sharply at the nanoscale level [52, 56]. Syntheses from high-boiling organic compounds are preferable from the point of view of eliminating hydrolysis.

The partial pyrohydrolysis of rare earth trifluorides leads to an incorrect scheme of the RF_3 phase transformation [57] (lower temperatures of phase transformations in Gd, Er, Tm, Yb, Lu, Y trifluorides; false polymorphic transformations in TbF_3, DyF_3, HoF_3). These results were obtained in high-temperature X-ray diffraction experiments. Under these conditions, it is practically impossible to eliminate pyrohydrolysis, despite all precautions, since the process begins from the surface of the samples. At the same time, the action of X-ray radiation accelerates the process of pyrohydrolysis.

A good marker of the pyrohydrolysis process is the temperature of the polymorphic transformation of gadolinium fluoride GdF_3 [39, 57–59]. There are significant discrepancies in these data in the literature: Thoma and Brunton indicate a lower value of 900 °C [57], Spending and Henderson demonstrated 1074 °C [39]. Temperatures close to the data shown by Spending were obtained in [43,44,46]. Sobolev et al. in the study of phase equilibria in the GdF_3–Gd_2O_3 system [58], demonstrated that the low value of the polymorphic transition temperature is associated with contamination of the samples with oxygen and the formation of a solid solution based on the high-temperature polymorphic modification of α-GdF_3.

Recently, fantastic "cubic modifications" of rare earth trifluorides have appeared in the literature. A number of studies [22, 60, 61] contain statement that REE fluorides, such as YF_3, CeF_3 and others crystallize in the sp. gr. $Fm\bar{3}m$. However, there are no chemical analyses data confirming that these are RF_3 compounds. There are no cubic modifications of RF_3 at normal pressure [45], since they can only be stable at very high pressures [62], or they appear when the preparations are seriously contaminated with

oxygen. Thus, cubic fluorides of both rare earth elements and bismuth trifluoride [60] are fakes.

3. Phase diagrams of NaF–RF_3 systems

For phase diagrams of NaF–RF_3 systems it should be noted that the most widespread and frequently cited is the phase diagram scheme obtained by Thoma et al. during the implementation of the American nuclear energy project, see Fig. 2 [63–65]. The authors have considerable experience with fluoride systems, carefully studied the pyrohydrolysis and the influence of oxygen impurity on the type of phase equilibria, and eliminated this problem (with the exception of high-temperature X-ray data, see above). Thermal analysis (cooling curves) and an original gradient annealing technique were used to construct phase diagrams. According to this method, a capillary filled with powder of the studied composition was annealed in a temperature gradient, and the phase composition of the sintering products was analyzed by X-ray diffraction with reference to a specific temperature. Data on the NaF–CeF_3 system, studied using a similar method were used [66]. The NaF–YF_3 system was carefully studied in advance [63]. The results of this study were rationalized in the following extravagant way: two compounds with the compositions NaF·YF_3 and 5NaF·9YF_3 are formed in the system, each of which has two polymorphic modifications, and the high-temperature polymorphs crystallize in the fluorite structure and form a solid solution

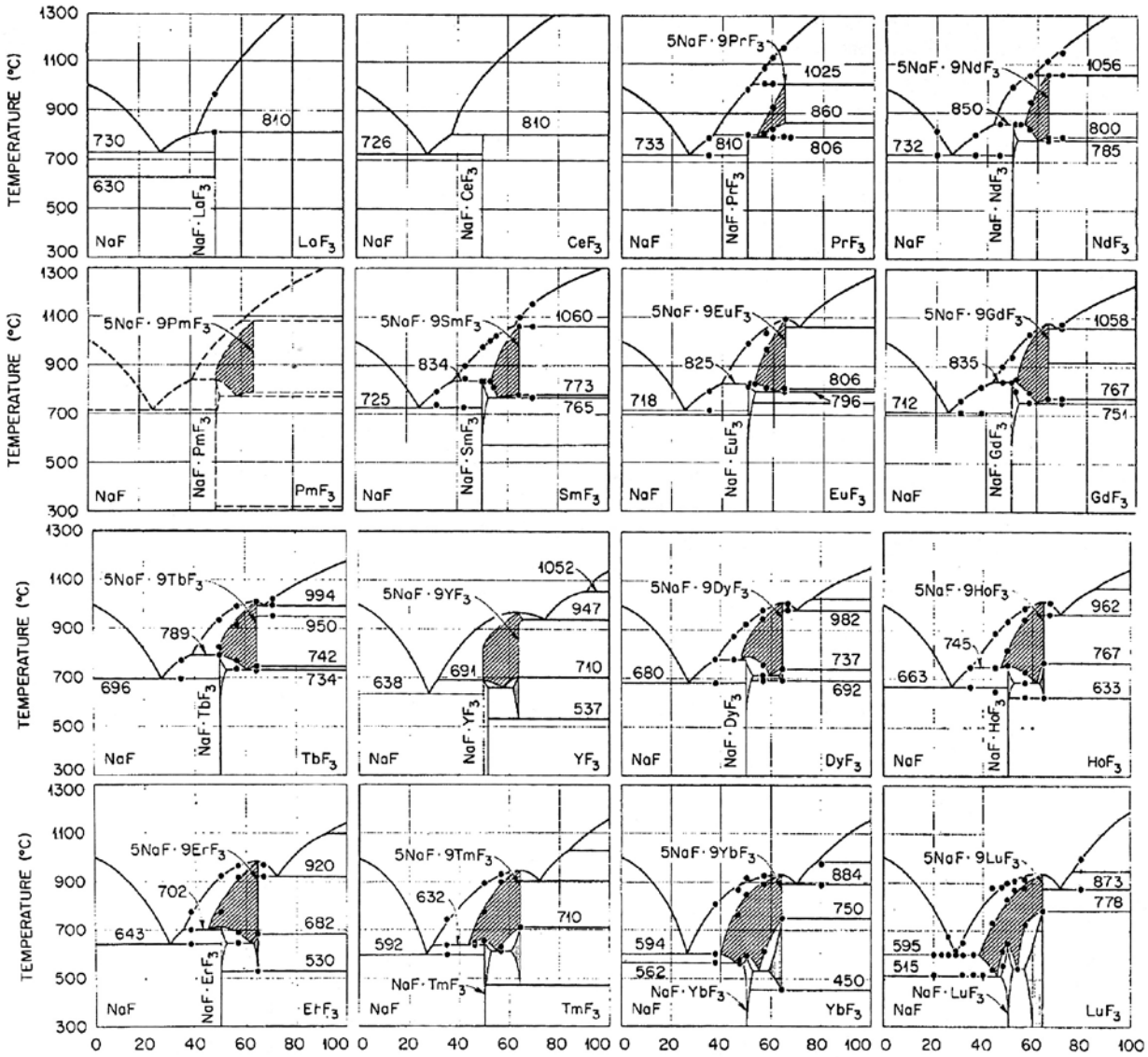

Fig. 2. Phase diagrams of the NaF–RF_3 systems according to Thoma et al. [63, 64]

between themselves. Data on other NaF–RF_3 systems were interpreted in a similar way [64].

It should be emphasized that the studies of Thoma et al. [63, 64] and Roy [67] were good for their time, but now these studies are of only historical interest. The conducted studies of phase equilibria in a series of NaF–RF_3 systems [68–76], including the polymorphism of RF_3, revealed a number of inaccuracies and errors in studies of Thoma.

Disadvantages of the Thoma scheme were as follows: an incorrect scheme of phase transformations of REE fluorides, distorted due to hydrolysis [57]; the small number of studied compositions; arbitrary schematization with postulation of 5:9 compositions and resulting from it incorrect fixation of the maxima compositions on the melting curves of intermediate phases of the fluorite structure; the incorrect determination of the compositions of ordered fluorite-like phases; the absence of solid solutions based on modifications with the tysonite structure; an impairment of the phase rule for a number of systems (R = Pr–Tb). Horizontal segments corresponding to temperatures of 860 °C (R = Pr), 800 °C (R = Nd), 773 °C (R = Sm), 806 °C (R = Eu), 767 °C (R = Gd), 742 °C (R = Tb), have no physical meaning, and their designation on phase diagrams is mistake.

A general schematic sequence of phase diagrams of NaF–RF_3 systems is shown in Fig. 3. The phase diagram of the most important NaF–YF_3 system is shown in Fig. 4a [30, 77], and the phase diagram of NaF–GdF_3 is shown in Fig. 4b [70]. Fig. 3 differs from the scheme shown in the article [1] in two features: the indicated low-temperature stability boundary of the $NaLaF_4$ phase and the nature of melting of the fluorite phase in the NaF–TbF_3 system, adjusted based on the results of growing single crystals (see below).

The methodology for studying systems [68–76] was similar to that previously developed for studying series of MF_2–RF_3 (M = Mg, Ca, Sr, Ba) systems [38, 79–83]. The initial reagents of rare earth fluorides were remelted under a fluorinating atmosphere of Teflon pyrolysis products. Differential thermal analysis was carried out in a static inert atmosphere of high-purity helium using graphite crucibles. Phase diagrams were constructed using heating curves. Phase equilibria in the solid state were studied by the X-ray diffraction of samples annealed in a fluorinating atmosphere and quenched.

In addition to the studies [68–76], correct experimental data were obtained in the studies of Cantor, Ward [84], and van der Meer et al. [36].

Low-temperature hexagonal phases with compositions close to a 1:1 ratio are formed in all NaF–RF_3 systems. High-temperature cubic phases with a fluorite-type structure are formed in systems with R = Pr–Lu, Y.

The coordinates of the nonvariant points are presented in Table 1. The thermal stability of the phases is shown in Fig. 5.

Both the hexagonal and cubic phases are phases of variable composition (non-stoichiometric). The representation of such phases as polymorphic β- and α-modifications of the compounds "NaRF_4", now widely used in the literature, is a very primitive approximation, although it is used in many studies (see, for example, [6, 86, 87]). The compositions of these phases, according to the structural data, can be written as $Na_{0.5-x}R_{0.5+x}F_{2+2x}$ (cubic) and $Na_{3x}R_{2-x}F_6$ (hexagonal), and they generally do not coincide. For example, in the NaF–GdF_3 system the hexagonal phase has a homogeneity region of 52–56 mol. % GdF_3, fluorite 50–70 mol. % GdF_3 [70].

In [88] it was shown that the α→β transformation of "$NaYF_4$", caused by the application of pressure, was accompanied by the release of YF_3 due to the different composition of these phases. In the NaF–YF_3 system (Fig. 4a) the equilibrium regions of the phases were 47–65 and ~50–53 mol. % YF_3, for the cubic and hexagonal phases, respectively. The hexagonal phase is a low-temperature phase, stable up to 695 °C, the cubic phase is a high-temperature phase. The 1:1 composition for the cubic modification has a temperature stability range of 680–850 °C.

The production of cubic single crystals of stoichiometric composition $NaYF_4$ from a melt is almost impossible. The optimal composition for the production of crystals, corresponding to the maximum on the melting curve, is 60 mol. % YF_3, composition $Na_{0.4}Y_{0.6}F_{2.2}$ [89, 90] (established in the study [68], in contrast to the composition of $Na_5Y_9F_{32}$ – 64.3 mol. % YF_3, proposed by Thoma [63]).

In NaF–RF_3 systems with a decrease in the ionic radius of cations, a transition from peritectic

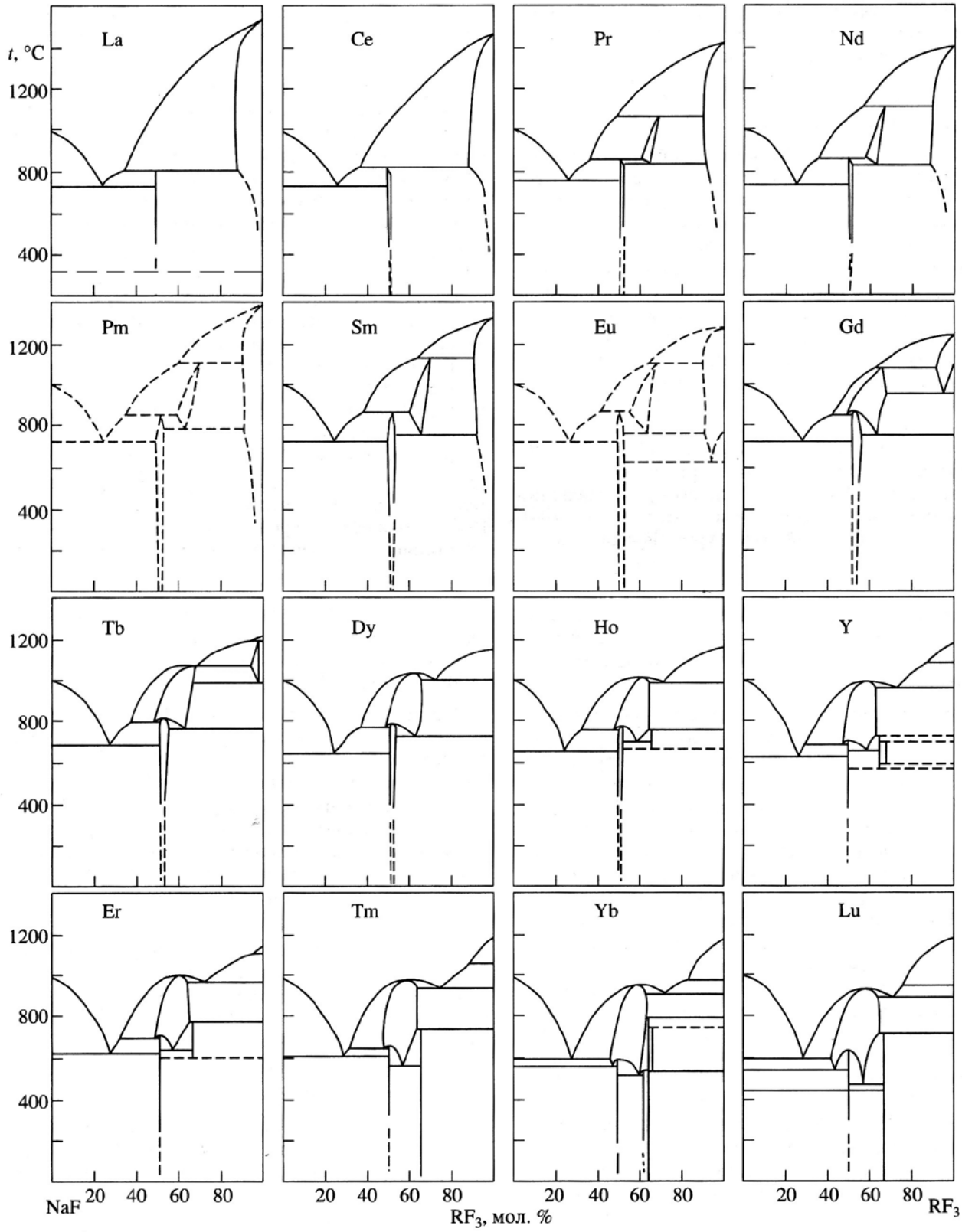

Fig. 3. Phase diagrams of the NaF–RF_3 systems according to [1, 68–77]

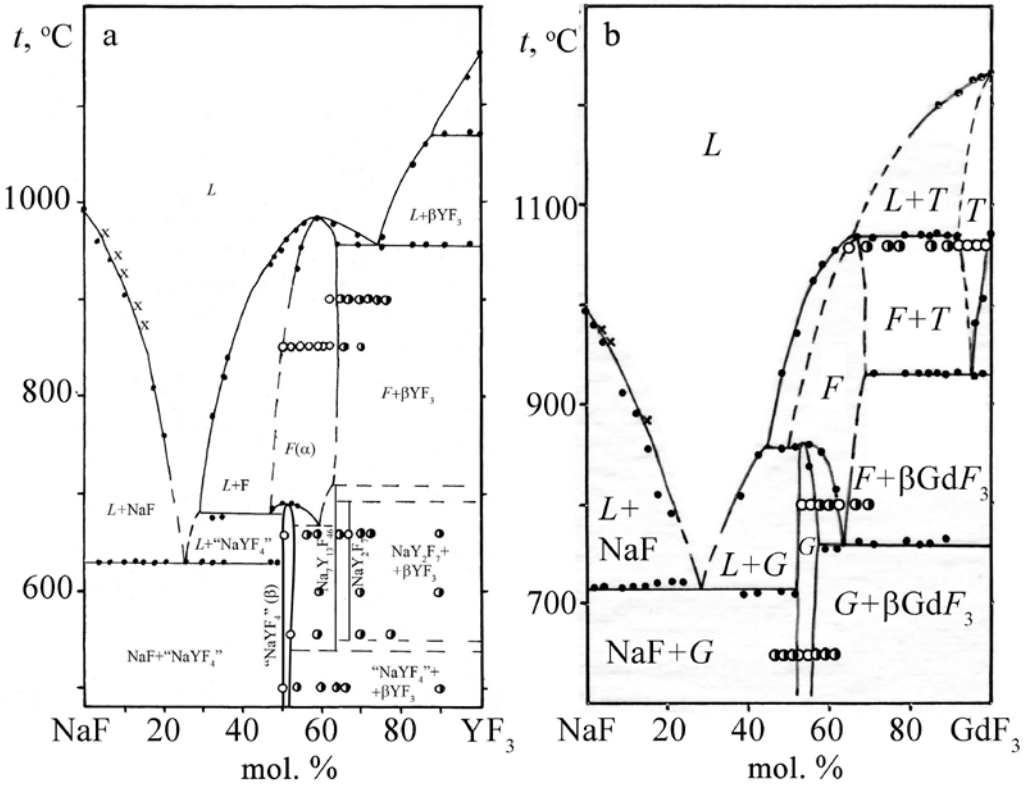

Fig. 4. Phase diagrams of NaF–YF_3[30,78] (a) and NaF–GdF_3 [70](b) systems. Points – thermal analysis data, circles – single phase samples, semi black circles –two-phase samples after annealing and quenching, x – data of [84]. Phase notations: *L* – melt, *F* – $Na_{0.5-x}R_{0.5+x}F_{2+2x}$, *G* – $Na_{3x}R_{2-x}F_6$, α – α-YF_3, β – β-YF_3, *T* – solid solution on the base α-GdF_3

Table 1. Co-ordinates of some non-variant points in NaF–RF_3 systems (*C* ± 2 mol % RF_3, *T* ± 5 °C)

R	Eutectics I		Upper boundary of thermal stability of gagarinite phase		Upper boundary of thermal stability of fluorite phase		Low boundary of thermal stability of fluorite phase		Eutectic II	
	C	*T*	*C*	*T*	*C*	*T*	T_1	T_2	*C*	*T*
La	26	730	36	800*	–	–	–	–	–	–
Ce	27	730	37	825	–	–	–	–	–	–
Pr	27	744	33	840		1050*				
Nd	28	730	35	842		1090*				
Sm	25	731	36	862		1120*		(760)	–	–
(Pm)	26	730	35	852						
Gd	28	718	52	860	67.5	1070*	856**	760***		
Tb	28	685	52	800	65.0	1056****	790**	755***	65	1056
Dy	26	650	52	780 ±10	64.0	1028	770**	730***	72	1005
Ho	25	652	51	753	62.5	1004	750**	715±10***	71	988
Er	28	630	50	700	62.0	1000	696**	640±15***	73	980
Tm	29	608	50	660	60.0	980	640**	560±20***	76	940
Yb	28	598	50	600	60.0	954	561***	520±10***	75	915
Lu	28	602	50	450±40	57.5	940	550±10***	470±30***	72	895
Y	26	632	52	695	60.0	984	680**		75	955

* – peritectic
** – metatectic
*** – eutectoid
**** – transition point between congruent and incongruent melting

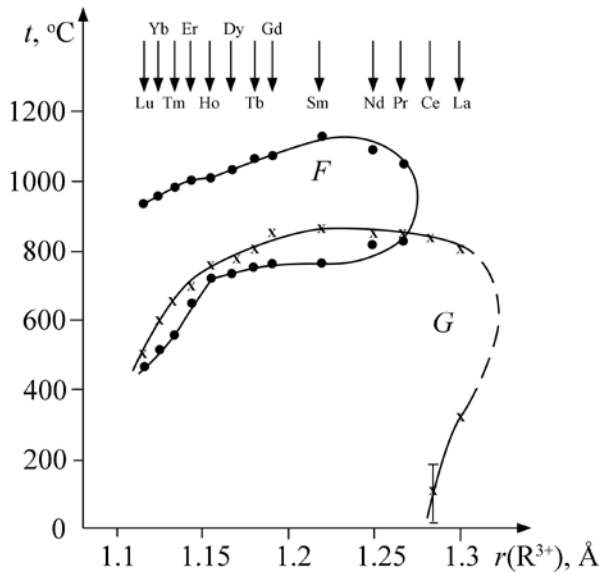

Fig. 5. Thermal stability boundaries of fluorite and gagarinite phases in series of NaF–RF_3 systems. F–$Na_{0.5-x}R_{0.5+x}F_{2+2x}$ phases, G – $Na_{3x}R_{2-x}F_6$ phases. Ionic radii according Shannon [85] for coordination number 8

melting of phases of the fluorite structure (R = Pr–Gd) to their congruent melting with the formation of maxima on the curves (R = Dy–Lu,Y) occurs. Changes in the compositions of the maxima on the melting curves of fluorite phases in the NaF–RF_3 systems (R = Tb–Lu) when moving along the lanthanide series [33] from $Na_{0.37}Tb_{0.63}F_{2.26}$ [91, 92] to $Na_{0.425}Lu_{0.575}F_{2.15}$ [93, 94] was confirmed during the growth of single crystals from the melt. At the same time, as experiments on crystal growth demonstrated [91, 92], the situation in the NaF–TbF_3 system is close to the transition point [95] (bifurcation of the phase diagram of B_1II type according to classification [96]). According to [92], the melting of the $Na_{0.5-x}Tb_{0.5+x}F_{2+2x}$ solid solution of has a transitional "eutectic-peritectic" character. With directional crystallization of the melt of the $Na_{0.37}Tb_{0.63}F_{2.26}$ composition in the initial part of the crystalline boule, an admixture of TbF_3 was sometimes recorded, and the central transparent part corresponds to the fluorite phase with a lattice parameter a = 5.5785(1) Å, which, according to the dependence [76], corresponds to the $Na_{0.36}Tb_{0.64}F_{2.28}$ composition. It should be noted that in the vicinity of the bifurcation point, fluctuations of the phase transformation type occur.

It should be emphasized that the fluorite structural phases in these systems are high-temperature ones, i.e. they are thermodynamically unstable at room temperature. This imposes restrictions on the growth of crystals from the melt, which cannot be annealed at temperatures below the eutectoid decomposition. The technological stability of single crystals in these systems increases with a decrease in the ionic radius of the lanthanide. Nominally pure and doped crystals grown by vertical directional crystallization without signs of decomposition are summarized in Table 2.

Experiments with low-temperature syntheses have shown that the $NaLaF_4$ phase has a lower stability limit, namely, it is stable only above 330±15 °C [77, 103, 104], see Fig. 3. These results are contradicted by the study [105], in which unalloyed $NaLaF_4$ powders were obtained by hydrothermal synthesis at 180 °C. However, the hydroxyl content in these samples is unknown. Calorimetric measurements performed by Yang et al. [106] recorded positive values of the enthalpy of

Table 2. Melt–grown single crystals

Composition	R	Ref.
$Na_{0.5-x}R_{0.5+x}F_{2+2x}$	Y, Dy–Lu	[97, 98]
$Na_{0.4}R_{0.6}F_{2.2}$	Y, Yb, Lu	[90]
$Na_{0.4}(Y,R)_{0.6}F_{2.2}$ (NYF)	Ce, Pr, Nd, Er, Tm, Yb	[90,99]
$Na_{0.4}(Lu,R)_{0.6}F_{2.2}$ (NLF)	Ce, Nd, Er, Tm,	[99]
$Na_{0.4}(Y,R)_{0.6}F_{2.2}$ (NYF)	Er	[89]
$Na_{0.38}Dy_{0.62}F_{2.24}$ (NDF)		[100]
$Na_{0.38}Ho_{0.62}F_{2.24}$		[101]
$Na_{0.4}R_{0.6}F_{2.2}$	Dy, Ho, Er, Tm, Yb	[102]
$Na_{0.35}Dy_{0.65}F_{2.3}$		[102]
$Na_{0.4}(Lu,R)_{0.6}F_{2.2}$ (NLF)*	Nd, Eu	[93,94]

* micro-pulling-down (μ-PD) method

formation of $NaLaF_4$ and $NaCeF_4$ from components. Therefore, the lower stability limit is also probable for $NaCeF_4$ at a temperature of about 100 °C.

The cubic $NaCeF_4$ reported by Virgil et. al. [107] is information noise.

The third type of phases of variable composition in the considered systems are solid solutions with the LaF_3-tysonite structure. Mansmann [48], who solved the structure of lanthanum fluoride, also pointed out that this close-packed structure should be stabilized by anion vacancies. This prediction was perfectly confirmed by studying the phase diagrams of rare earth fluoride systems with a LaF_3-tysonite structure type: La–Nd trifluorides and high-temperature modifications of Sm, Eu, and Gd trifluorides. Solid solutions based on RF_3 with a tysonite structure are formed in all RF_3–MF_2 systems where R = La–Gd, M = Ca, Sr, Ba. In these solutions during heterovalent substitution, anion vacancies are introduced into the lattice according to the equation $R^{3+} + F^- \rightarrow M^{2+} + V_F$ [80–83, 108]. Another way of introducing anion vacancies into the tysonite lattice is the replacement of fluorine with oxygen. Again, in RF_3–R_2O_3 systems with the corresponding rare earth elements, solid solution regions are formed [58]. Therefore, the appearance of solid solutions in NaF–RF_3 systems based on trifluorides of the corresponding structure according to the scheme $R^{3+} + 2F^- \rightarrow Na^+ + 2V_F$ is logical from the point of view of crystal chemistry. Such solid solutions were detected by thermal analysis in systems of NaF with trifluorides of La, Ce, Gd [70, 75]. Moreover, when the modification of the tysonite structure of REE trifluorides becomes unstable due to a decrease in the ionic radius of the cation, the phase of variable composition of the tysonite structure, stabilized by anion vacancies, is retained in the phase diagram of the NaF–TbF_3 system [73].

The structures of α-$Na_{0.5-x}R_{0.5+x}F_{2+2x}$ (cubic) and β-$Na_{3x}R_{2-x}F_6$ (hexagonal) phases are fundamentally different. The structure of the hexagonal modification was determined not only for single crystals obtained from the melt by the Czochralski method [109–113], but also for natural crystals (enriched with calcium), which were formed in nature by a hydrothermal process (the mineral gagarinite) [114, 115]. The hexagonal modification was composed by columns of nine-vertex polyhedra (Fig. 6). The coordination polyhedron of rare earth elements is a hexagonal prism with centered lateral faces. The sodium is located in wells. There is a strong statistical disorder in the distribution of cations over crystallographic positions, typical of non-stoichiometric phases.

For the cubic α-phases, the conducted structural studies [116–118] indicated that the REE do not statistically alternate with sodium in the cationic positions of the fluorite lattice, but are located in clusters of the R_6F_{36} type (Fig. 7). The

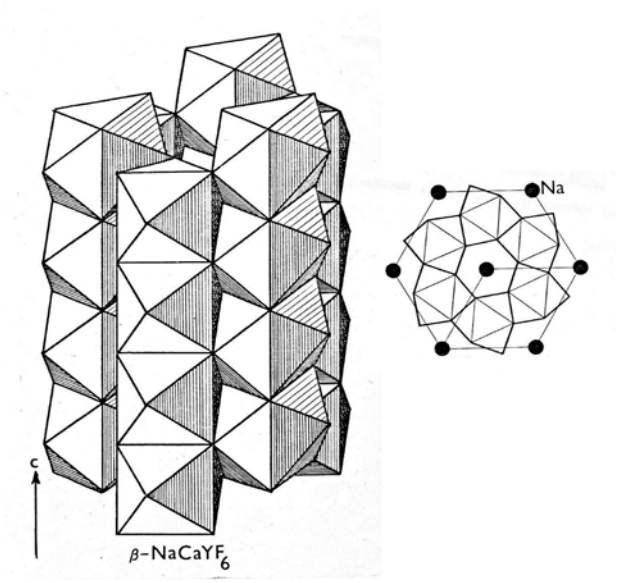

Fig. 6. Crystal structure of "β-NaRF_4" phase (gagarinite) [114]

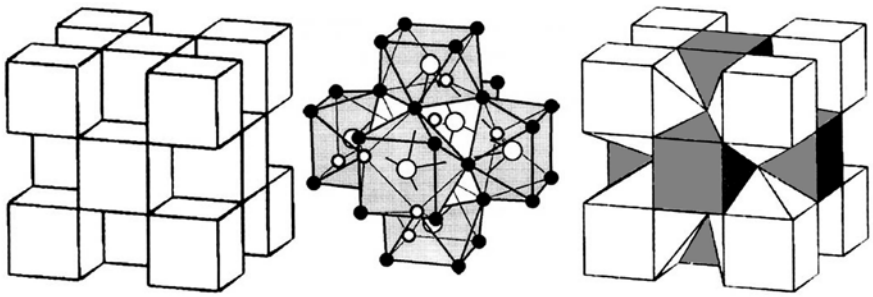

Fig. 7. Embedding of R_6F_{36} clusters into the fluorite lattice according to the Bevan, Greis, and Strahle model [119]

coordination number of REE is 8, coordination polyhedra are Thompson antiprisms. Such clusters are present in $M_{1-x}R_xF_{2+x}$ fluorite solid solutions in MF_2–RF_3 systems, M – alkaline earth element [119, 120]. The compounds of KY_3F_{10} type are composed from such clusters. It should be noted that the performed structural studies cover only cations of the yttrium subgroup, which are characterized by a coordination number of 8. However, it is not typical for large cations of rare earth elements of the cerium subgroup. It is possible that in the fluorite phases formed in NaF–RF_3 systems with large cations that the defect structure of fluorite phases is different. The formation of clusters of the R_4F_{23} type is possible R_4F_{23} with a CN of 9 is possible [33]. The diagram in Fig. 5 suggests this assumption.

The $Na_7Y_{13}F_{46}$ and NaY_2F_7 compounds, present in the NaF–YF_3 phase diagram (Fig. 4a), are fluorite-like phases with an ordered arrangement of clusters of R_6F_{36} type (Thoma quite accurately determined the temperature limits of stability and the lattice parameters of one of the phases, but made a mistake regarding the composition [63]).

Concentration dependences of unit cell parameters a of non-stoichiometric $Na_{0.5-x}R_{0.5+x}F_{2+2x}$ fluorite phases [76], see Fig. 8, are well described by the equation:

$$a = 5.398 + (6.7238r - 7.259)(x + 0.13)\ [Å], \quad (1)$$

where r – ionic radii of REE cations for a CN of 8 according to the Shannon system [65]. These dependencies can be used to clarify the composition of the synthesized phases with a fluorite structure in these systems.

The data of Furuya et al. [93] for R = Lu fit well in the graph in Fig. 8b.

Enthalpies of mixing for a number of the NaF–RF_3 (R = La, Nd, Yb, Y) systems, defined in study [123], are the basis for the thermodynamic modelling of the considered systems. However, thermodynamic modelling is not always successful. The model for the NaF–NdF_3 system, proposed by Ard et al. [124], according to Thoma, is unacceptable. Interpretation of the $Na_{0.5-x}Nd_{0.5+x}F_{2+2x}$ phase of variable composition with the fluorite structure formed in this system as a solid NaF solution in the "$Na_5Nd_9F_{32}$" compound, is extremely unsuccessful. This interpretation, invented by Thoma [63, 64], has no experimental basis. There is no evidence indicating the existence of compounds of such

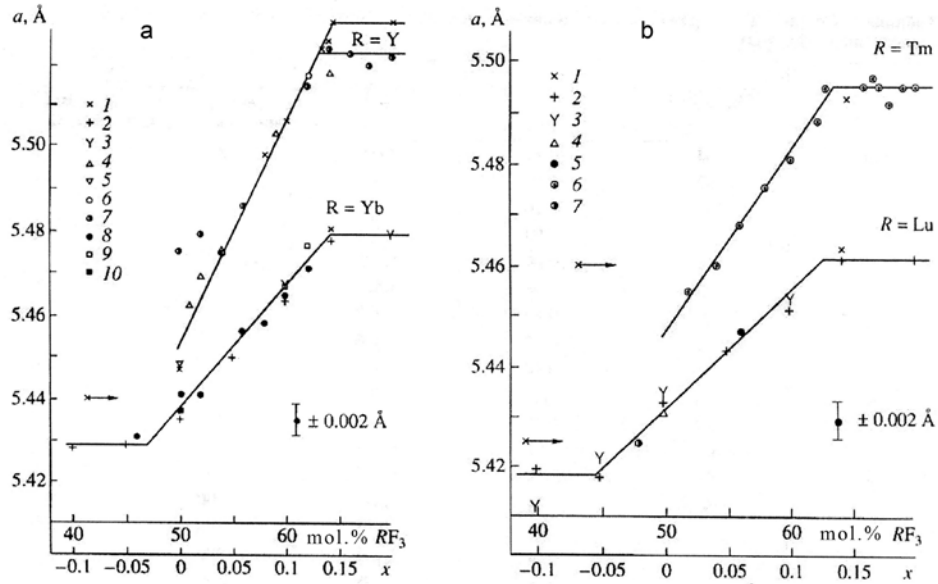

Fig. 8. Concentration dependences of the lattice parameter a of phases $Na_{0.5-x}R_{0.5+x}F_{2+2x}$ [76]. (a): data of Thoma et al. [63, 64]; *2* – data of Schmutz [121], annealing at 700 °C; *3* – the same, annealing at 900 °C; *4* – data of Pontonnie [116]; *5* – data of Hund [122]; *6* – our data, annealing at 900 °C; *7* – the same, annealing at 850 °C; *8* – the same, annealing at 720 °C; *9* – the same, annealing at 550 °C; *10* – the same, remelting under a fluorinating atmosphere after precipitation from an aqueous solution. (b): *1* – data of Thoma et al. [64]; *2* – data of Schmutz [121], annealing at 700 °C; *3* – the same, annealing at 900 °C; *4* – the same, annealing at 550 °C; *5* – our data, annealing at 700 °C; *6* – the same, annealing at 800 °C; *7* – the same, annealing at 550 °C

composition either in this system or in other sodium fluoride systems with rare earth fluorides.

In thermodynamic modelling in studies [36, 124] the lower limit of stability of the $NaLaF_4$ phase is not taken into account and solid solutions based on RF_3 tysonite modifications are not considered.

4. Ordering processes of non-stoichiometric phases

Formation of ordered fluorite-like phases in $NaF–RF_3$ systems was studied in detail in [73, 74, 125].

To obtain a general picture of the ordering in the series of $NaF–RF_3$ systems [125] annealing was carried out on carefully ground samples packed in Ni capillaries and placed in an hermetically sealed Ni container, inside which a fluorinating atmosphere was created by the pyrolysis of Teflon and thermal decomposition of $BaF_2·HF$. The container was quenched in water at a cooling rate of 200°/min. Compositions with 64.3, 67, 75 mol. % RF_3 (R = Dy–Lu), corresponding to $Na_5R_9F_{32}$ compounds (Thoma's phases), NaR_2F_7 and NaR_3F_{10} were selected. Annealing was carried out at 700 °C for 100 hours. In addition, for the $NaF–HoF_3$ system, annealings for up to 720 h were carried out [71]. The indexing of X-ray diffraction patterns of fluorite-like phases was performed using the homology method [126, 127].

The unit cell parameters of the obtained compounds are given in Table 3.

In $NaF–RF_3$ (R = La–Dy) systems ordered fluorite-like phases were not identified. The appearance of ordered phases is caused by a decrease in the ionic radius of R^{3+}.

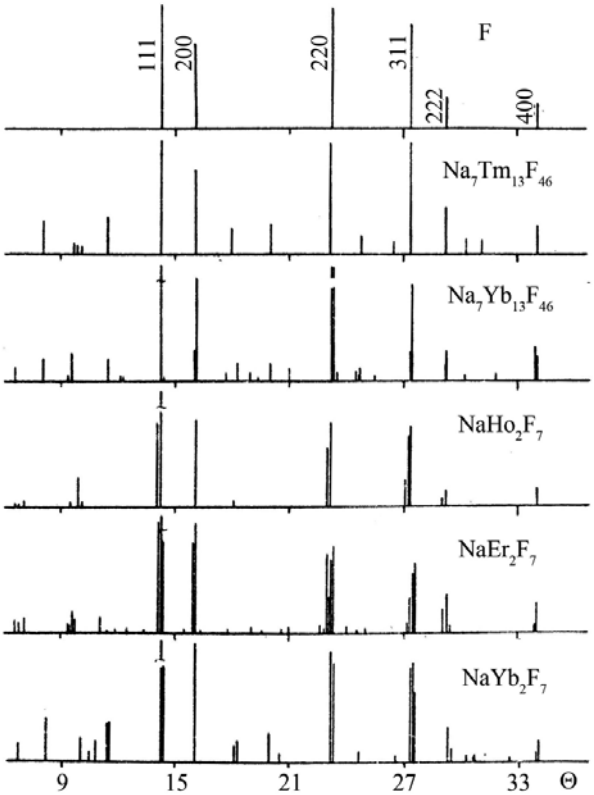

Fig. 9. X-ray patterns of the phases in $NaF–RF_3$ systems. Annealing at 700 °C, 100 h, λ = CuKα [125]

In the system with HoF_3 in the studied composition range, only one phase, containing 67% HoF_3 ($NaHo_2F_7$) was found. At 75% HoF_3 there is an excess of trifluoride, and at 64.3 mol. % HoF_3 admixture of cubic fluorite phase is present.

Samples in the system with ErF_3 have a similar phase composition. The X-ray diffraction pattern of $NaEr_2F_7$ similar to the X-ray diffraction pattern of a holmium compound, it is distinguished by a higher complexity of changes of the main fluorite

Table 3. Lattice parameters of fluorite-related ordered phases in $NaF–RF_3$ systems

Compound	Crystal system	*a*, Å	*b*, Å	*c*, Å	comment
$NaHo_2F_7$	trigonal	3.896		9.732	Sub-cell
$NaEr_2F_7$	trigonal	3.880		9.691	Sub-cell
$Na_7Tm_{13}F_{46}$	tetragonal	3.880		5.512	Sub-cell
$Na_{0.35}Yb_{0.65}F_{2.3}$	tetragonal	3.867		5.491	Melt-grown
$Na_7Yb_{13}F_{46}$	orthorhombic	7.759	38.80	5.524	
$NaYb_2F_7$	orthorhombic	3.90	13.54	28.32	
$Na_7Lu_{13}F_{46}$	orthorhombic	7.744	38.58	5.508	
γ-$NaLuF_4$	hexagonal	13.57		9.38	Medium-temperature polymorph, $KErF_4$ type [72]
$Na_2Y_3F_{11}$	tetragonal	12.29		10.69	Annealing of a $Na_{0.39}Y_{0.61}F_{2.22}$ single crystal at 600 °C*

*A. Golubev, private communication

reflexes with the same superstructure. In the NaF–TmF_3 system the composition containing 64.3% is single-phase and its X-ray pattern corresponds to a weak tetragonal distortion of the fluorite lattice; TmF_3 lines are present on X-ray patterns of samples with a high content of RF_3. In systems with YbF_3 and LuF_3 samples with 64.3 mol. % RF_3 are single-phase, characterized by the same superstructure. The splitting of the main fluorite reflections for the lutetium-containing compound corresponds to the orthorhombic nature of the distortion of the fluorite lattice. For the ytterbium compound, the splitting of the main lines is weaker and, to a first approximation, corresponds to a tetragonal distortion. In the system with LuF_3 samples with its high content are two-phase; the $NaYb_2F_7$ phase was detected in the ytterbium system, the X-ray diffraction pattern of which differs both by the superstructure and the nature of the splitting of the main lines from the $NaYb_2F_7$ (R = Ho, Er) compound.

It should be noted that we observed a very complex ordering pattern in the NaF–LuF_3 system in the range of 64–75 mol. % LuF_3 on samples annealed at 750 ° for 540 hours. In addition, a tetragonal phase, very close to the thulium phase by the X-ray diffraction pattern, was formed during the growth of single crystals from a melt in the NaF–YbF_3 system. The growth of a fluorite solid solution was carried out using the Bridgman method in a fluorinating atmosphere in graphite crucibles with a drawing speed of 10–12 mm/h. The tetragonal phase was observed in the lower part of the crystals with a composition of 58–62 mol. % YbF_3, and its relative quantity increased with increasing concentration of RF_3.

The X-ray diffraction patterns of phases of such composition for R = Ho, Er and R = Yb are very different from each other. This indicates the presence of two structural types and a morphotropic transition in the NaR_2F_7 series. The X-ray diffraction patterns of sodium phases do not correspond to any of the modifications of potassium compounds of such stoichiometry.

Main lines on the X-ray diffraction pattern of $NaYb_2F_7$ were indexed in a trigonal cell by the homology method with parameters a = 3.90 Å ≈ $a_0\sqrt{2}/2$, c = 9.44 Å ≈ $a_0\sqrt{3}$, where a_0 is the parameter of the fluorite subcell. However, superstructural reflections are not indicated in the trigonal cell with different variants of increasing a and c parameters. In addition, subtle additional splittings of the main lines are observed, which indicate a further decrease in symmetry. The simplest option of reducing the symmetry of the trigonal cell to a orthorhombic, base-centered was considered for the interpretation of the X-ray diffraction pattern. It is assumed that equality $b = a\sqrt{3}$, strictly valid for trigonal symmetry, becomes approximate. This variant is omitted in the summary homology tables of splittings. The transition from trigonal to orthorhombic crystal system according to this scheme allows immediately index most of the reflections of the $NaYb_2F_7$ superstructure. Full indexing is achieved by increasing the b parameter twice and the c parameter by three times.

The X-ray diffraction pattern of $NaHo_2F_7$, obtained by sintering at 700 °C for 100 hours, is well indicated in the trigonal crystal system with parameters a = 3.887 Å ≈ $a_0\sqrt{2}/2$, c = 9.732 Å ≈ $a_0\sqrt{3}$. However, with an increase in the annealing time to 700 hours, further ordering occurs, which is manifested in additional splitting of the main peaks and in the appearance of superstructural reflections (Fig. 10). The X-ray diffraction pattern of the $NaEr_2F_7$ compound, obtained at 700 °C for

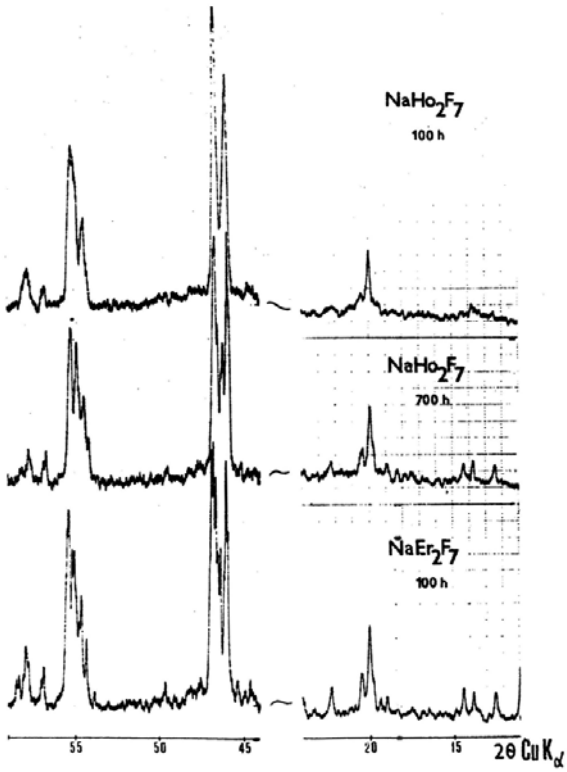

Fig. 10. Kinetics of ordering in NaR_2F_7 phases. Annealing at 700 °C [125]

100 hours has the same complex character. The general character of the splittings corresponds to triclinic crystal system. Based on these data, it is not possible to calculate the lattice parameters. It should be noted that trigonal cells, which are the prototype of NaR_2F_7 (R = Ho, Er) and $NaYb_2F_7$ phases (R = Ho, Er), formed by the deformation of the initial cubic cell with the opposite sign: for Ho and Er there is an extended rhombohedron (c/a = 2.50 in hexagonal packing), and for Yb – a compressed rhombohedron (c/a = 2.42). For a cubic cell in a hexagonal packing $c/a \approx \sqrt{6} = 2.45$.

The X-ray diffraction pattern of $NaEr_2F_7$ similar to the X-ray diffraction pattern of a holmium compound, but differs by the greater complexity of the splitting of the main reflections with the same superstructure.

Compositions of ordered phases proposed by Thoma for the NaF–RF_3system correspond to single-phase (with the accuracy of X-ray phase analysis) samples in systems with LuF_3, YbF_3, and TmF_3. The X-ray diffraction patterns of the lutetium and ytterbium phases were indexed [74, 125] with the parameters provided by Thoma et al. [63, 64] $a \approx a_0\sqrt{2}$, $b \approx a_0\, 5\sqrt{2}$, $c \approx a_0$. For ytterbium compound a = 7.770 Å, b = 38.71 Å, c = 5.524 Å; for the lutetium phase a = 7.744 Å, b = 38.57 Å, c = 5.508 Å. It should be noted that the unit cell proposed by Thoma contains 40 cations, which does not correspond to the formula $Na_5R_9F_{32}$, proposed in [63, 64], since with this choice Z is a fractional value. The simplest formula corresponding to this cell is $Na_7R_{13}F_{46}$, providing Z = 2 and a composition of 65 mol. % RF_3. A slight deviation from the 5:9 composition (64.3 mol. % RF_3) may be within the sensitivity of X-ray phase analysis, especially since the second fluorite-like phase, which may be present in samples with 64.3% RF_3, produces lines on X-ray diffraction patterns that overlap the reflections of ordered phases. The possibility of the existence of small areas of homogeneity based on these phases also cannot be excluded. It should be noted that in the system with HoF_3 we did not detect any orthorhombic ordering in the composition of 64.3 mol. % HoF_3, corresponding R = Yb–Lu, although according to Thoma at this temperature it should take place. On the other hand, the temperature range indicated by Thoma for the existence of an ordered phase in the holmium system agrees well with the temperature range determined by us for the $NaHo_2F_7$ compound. Thus, it can be assumed that in [64] a simple distortion of the fluorite lattice was recorded without detailing its nature.

In the study [69] the $Na_7Yb_{13}F_{46}$ compound was omitted due to the fact that a significant part of the superstructural reflections of this phase and $NaYb_2F_7$ match.

The tetragonal $Na_2Y_3F_{11}$ phase prepared by long-time annealing of melt-grown single crystal (see Table 3), is apparently metastable.

The $Na_{3x}R_{2-x}F_6$ hexagonal phases with the structure of gagarinite represent the second family of phases of variable composition in NaF–RF_3 systems. Accordingly, we can expect an ordering of these phases with decreasing temperature, especially since they demonstrate a contraction of compositions to stoichiometric $NaRF_4$. The appearance of superstructural reflections on X-ray diffraction patterns of samples of the corresponding phases synthesized from nitrate melts was demonstrated in [87]. However, overall, further investigation of this issue is required.

5. Transformations of alpha-beta phases in NaF–RF_3 systems

In the process of low-temperature syntheses of samples of the "$NaRF_4$" phases by various methods a phase formation sequence is systematically observed in NaF–RF_3 systems, in which cubic fluorite nanoparticles of α-phase are first formed, which then transforms into the β-phase [86, 128-136]. This was also observed *in situ* with a sharp increase in luminescence brightness during the formation of the β-phase [127]. Increasing temperatures and/or increasing the duration of synthesis promote the transition α→β.

In these cases, at the synthesis temperature, the hexagonal β-phase is in equilibrium. As shown in [30, 137], nanoparticles of the cubic phase of sodium yttrium fluoride synthesized from an aqueous solution during heating transform into a hexagonal phase with a large exothermic effect. The observed phase sequence during the crystallization of sodium yttrium fluoride represents the implementation of the Ostwald step rule [28, 29].

It is obvious that in low-temperature syntheses of sodium-yttrium fluoride, a mechanism of oriented growth of nanoparticles takes place [138,

139]. However, it does not exhaust the process. Considering the different crystal structures of the two polymorphs, it is obvious that beta phase fragments cannot be formed from alpha phase fragments. The change in the coordination number of rare earth cations during the transition from their alpha to beta phase inevitably requires complete recrystallization of the particles. In other words, in this process, there is a complete disappearance of one phase and the growth of another phase.

It should be noted that the formation of ordered fluorite-like phases in NaF–RF_3 systems was not observed in low-temperature syntheses.

Currently, there are a number of chemical methods for the synthesis of nanosized particles such as $NaYF_4$ (high-temperature co-precipitation, hydro- and solvothermal synthesis, thermolysis, etc.), see, for example, [140–142]. However, there is a problem with the reproducibility of product properties.

6. Conclusions

Among the unresolved problems of phase equilibria and phase formation in systems of sodium fluoride with fluorides of rare earth elements, the following can be listed.

– Structure of ordered fluorite-like phases. It is obvious that in these phases there is an ordered arrangement of R_6F_{36}-type clusters, but the specific pathways of their arrangement are unknown.

– Identification of the ordering of gagarinite phases. Obviously, the ordering must take place, since these phases are non-stoichiometric. Similar systems with bismuth fluoride demonstrate a rich set of compounds of this type.

– Intriguing cooperative transformation of ensembles of fluorite nanoparticles into the hexagonal structure of gagarinite, which is beyond the problems relating to phase equilibria.

– Possible pyrohydrolysis of samples and its influence on the functional characteristics of materials. Heat treatment in the presence of water results in the replacement of the fluoride ion by an hydroxyl ion, which is very similar in size [143]. The hydroxyl concentration should increase with increasing crystallization time and increases sharply with increasing temperature of the process. Both $Y(OH)_3$ and $La(OH)_3$ have a hexagonal structure and is isostructural with the β-phase [144]. The hydrolysis process may be the driving force behind the transition of α→β phases in "$NaRF_4$".

– A critical drawback of many studies devoted to the synthesis of sodium fluoride samples with rare earth elements, despite the use of modern research methods such as TEM, STEM, XRD, APT, EXAFS, is the complete disregard for monitoring the actual chemical composition of the synthesized samples and tracking their changes during the synthesis process. The composition of cubic phases can be estimated based on the lattice parameter (equation (1)), however, surprisingly, in many studies these crystallographic data are not shown and only a primitive comparison of X-ray diffraction patterns with a reference database is provided.

Contribution of the authors

The authors contributed equally to this article.

Conflict of interests

The authors declare that they have no known competing financial interests or personal relationships that could have influenced the work reported in this paper.

References

1. Fedorov P. P. Systems of alcali and rare-earth metal fluorides. *Russian Journal of Inorganic Chemistry*. 1999;44(11): 1703–1727. Available at: https://elibrary.ru/item.asp?id=13323144

2. Fedorov P. P., Luginina A. A., Kuznetsov S. V., Osiko V. V. Nanofluorides. *Journal of Fluorine Chemistry* 2011;132(12): 1012-1039. https://doi.org/10.1016/j.jfluchem.2011.06.025

3. Li J., Xia D., Gao M., Jiang L., Zhao S., Li G. Invisible luminescent inks and luminescent films based on lanthanides for anti-counterfeiting. *Inorganica Chimica Acta*. 2021;526: 120541. https://doi.org/10.1016/j.ica.2021.120541

4. Karimov D. N., Demina P. A., Koshelev A. V., ... Panchenko V. Ya. Upconversion nanoparticles: synthesis, photoluminescence properties, and applications. *Nanotechnologies in Russia*. 2020;15: 655–678. https://doi.org/10.1134/s1995078020060117

5. Richards B. S., Hudry D., Busko D., Turshatov A., Howard I. A. Photon upconversion for photovoltaics and photocatalysis: a critical review. *Chemical Reviews*. 2021;121: 9165–9195. https://doi.org/10.1021/acs.chemrev.1c00034

6. Joseph R. E., Hudry D., Busko D., ... Howard I. A. Bright constant color upconversion based on dual 980 and 1550 nm excitation of SrF_2:Yb^{3+}, Er^{3+} and β-$NaYF_4$:Yb^{3+}, Er^{3+} micropowders – considerations for persistence of vision displays. *Optical Materials*. 2021;111: 110598. https://doi.org/10.1016/j.optmat.2020.110598

7. Ansari A. A., Parchur A. K., Nazeeruddin M., Tavakoli M. M. Luminescent lanthanide nanocomposites in thermometry: Chemistry of dopant ions and host matrices.

Coordination chemistry reviews. 2021;444: 214040. https://doi.org/10.1016/j.ccr.2021.214040

8. Singh R., Madirov E., Busko D., ... Turshatov A. Harvesting sub-bandgap photons via up-conversion for perovskite solar cells. *ACS Appl. Mater. Interfaces*. 2021;13: 54874–54883. https://doi.org/10.1021/acsami.1c13477

9. Woidasky J., Sander I., Schau A., ... Lang-Koetz C. Inorganic fluorescent marker materials for identification of post-consumer plastic packaging. *Resources, Conservation and Recycling*. 2020;161: 104976. https://doi.org/10.1016/j.resconrec.2020.104976

10. Wolfbeis O. S. An overview of nanoparticles commonly used in fluorescent bioimaging. *Chemical Society Reviews*. 2015;44: 4743–4768. https://doi.org/10.1039/c4cs00392f

11. Ansari A. A., Parchur A. K., Thora N. D., Chen G. New advances in pre-clinical diagnostic imaging perspectives of functionalized upconversion nanoparticle-based nanomedicine. *Coordination Chemistry Reviews*. 2021;440: 213971. https://doi.org/10.1016/j.ccr.2021.213971

12. Li H., Wang X., Ohulchanskyy T. Y., Chen G. Lanthanide-doped near-infrared nanoparticles for biophotonics. *Advanced Materials*. 2021;33(6): 2000678. https://doi.org/10.1002/adma.202000678

13. Jaque D., Vetrone F. Luminescence nanothermometry. *Nanoscale*. 2012;4: 4301–4326. https://doi.org/10.1039/C2NR30764B

14. Ovsyankin V. V., Feofilov P. P. Mechanism of summation of electronic excitation in activated crystals. *JETP Letters*. 1966;3: 494–497. Available at: http://jetpletters.ru/ps/1621/article_24809.shtml

15. Auzel F. Upconversion and anti-stokes process with f and d ions in solids. *Chemical Reviews*. 2004;104(1): 139–174. https://doi.org/10.1021/cr020357g

16. Menyuk N., Dwight K., Pierce J.W. $NaYF_4$:Yb, Er – an efficient upconversion phosphor. *Applied Physics Letters*. 1972;21(4): 159–161. https://doi.org/10.1063/1.1654325

17. Kano T., Yamamoto H., Otomo Y. $NaLnF_4$:Yb^{3+},Er^{3+} (Ln: Y, Gd, La): efficient green-emitting infrared-excited phosphors. *J. Electrochemical Society*. 1972;119(11): 1561–1564.

18. Li Z., Zhang Y., Jiang S. Multicolor core/shell-structured upconversion fluorescent nanoparticles. *Advanced Materials*. 2008;20(24): 4765–4769. https://doi.org/10.1002/adma.200801056

19. Kaiser M., Würth C., Kraft M., Hyppänen I., Soukka T., Resch-Genger U. Power-dependent upconversion quantum yield of $NaYF_4$:Yb^{3+}, Er^{3+} nano- and micrometer-sized particles – measurements and simulations. *Nanoscale*. 2017;9(28): 10051–10058. https://doi.org/10.1039/C7NR02449E

20. Fedorov P. P., Kuznetsov S. V., Mayakova M. N., ... Osiko V.V. Coprecipitation from aqueous solutions to prepare binary fluorides. *Russian Journal of Inorganic Chemistry*. 2011;56(10): 1525–1531. https://doi.org/10.1134/S003602361110007X.

21. Fedorov P. P., Alexandrov A. A. Synthesis of inorganic fluorides in molten salt fluxes and ionic liquid mediums. *Journal of Fluorine Chemistry*. 2019;227: 109374. https://doi.org/10.1016/j.jfluchem.2019.109374

22. Guricova M., Pinc J., Malincik J., Rak J., Kuchar M., Bartunek V. Rare earth nanofluorides: synthesis using ionic liquids. *Reviews in Inorganic Chemistry*. 2019;39(2): 77–90. https://doi.org/10.1515/revic-2018-0016

23. Fedorov P. P., Luginina A. A., Popov A. I. Transparent oxyfluoride glass ceramics. *Journal of Fluorine Chemistry*. 2015;172: 22–50. https://doi.org/10.1016/j.jfluchem.2015.01.009

24. Xie J., Gao Z., Zhou E., ... Huang W. Insighs into the growth principles of REF (RE = La-Lu, Y) nanocrystals: hexagonal and/or orthorhombic. *Nanoscale*. 2017;9: 15974–15981. https://doi.org/10.1039/C7NR06210A

25. You F., Huang S., Shi Q. Hydrothermal synthesis of mixed rare earth-alkali metal or ammonium fluorides. *Journal of Rare Earths*. 2010;28(5): 676–679. https://doi.org/10.1016/s1002-0721(09)60177-0

26. Kemnitz E., Mahn S., Krahl T. Nano metal fluorides: small particles with great properties. *ChemTexts*. 2020;6: 19 (27 pp.). https://doi.org/10.1007/s40828-020-00115-w

27. Gulina L. B., Tolstoy V. P., Murin I. V. Crystallization of new inorganic fluoride nanomaterials at soft chemistry conditions and their application prospects. *Russian Journal of Inorganic Chemistry*. 2024;69(3): 1–12. https://doi.org/10.1134/S0036023623603070

28. Ostwald, W. Studien über die Bildung und Umwandlung fester Körper. *Zeitschrift für Physikalische Chemie*. 1897;22: 289–330. https://doi.org/10.1515/zpch-1897-2233

29. Threlfall T. Structural and thermodynamics explanation of Ostwald's rule. *Organic Process Research and Development*. 2003;7: 1017–1027. https://doi.org/10.1021/op030026l

30. Fedorov P. P., Kuznetsov S. V., Voronov V. V., Yarotskaya I. V., Arbenina V. V. Soft chemical synthesis of $NaYF_4$ nanopowders. *Russian Journal of Inorganic Chemistry*. 2008;53(11): 1681–1685. https://doi.org/10.1134/s0036023608110028

31. Yoshikawa A., Chani V. Growth of optical crystals by the micro-pulling-down method. *MRS Bulletin*. 2009;34: 266–270. https://doi.org/10.1557/mrs2009.77

32. Shu J., Damiano E., Sottile A., Zhang Z., Tonelli M. Growth by the μ-PD method and visible laser operation of a single-crystal fiber of Pr^{3+}:KY_3F_{10}. *Crystals*. 2017;(7): 200. https://doi.org/10.3390/cryst7070200

33. Sobolev B. P. *The rare earth trifluorides. P.2. Introduction to materials science of multicomponent metal fluoride crystals*. Barcelona: Institut d'estudis Catalans; 2001. 460 p.

34. Fedorov P. P., Osiko V. V. Crystal growth of fluorides. In: *Bulk crystal growth of electronic, optical and optoelectronic materials*. P. Capper (ed.). John Wiley & Son, Ltd. Chichester, UK; 2005. 339–356. https://doi.org/10.1002/9780470012086.ch11

35. Moncorge R., Braud A., Camy P., Doualan J. L. Fluoride laser crystals. In: *Handbook on solid-state lasers: materials, systems and applications. Book Series: Woodhead publishing series in electronic and optical materials*. B. Denker and E. Shklovsky (eds.). Oxford Cambridge Philadelphia New Delhi: Woodhead Publishing Limited, UK; 2013. 82–109.

36. Van der Meer J. P. M., Konings R. J. M., Jacobs M. H. G., Oonk H. A. G. Modeling and calculation of the LiF-NaF-MF_3 (M = La, Ce, Pu) phase diagrams. *Chemistry of Materials*. 2006;18: 510–517. https://doi.org/10.1021/cm051531v

37. Bergmann H. *Gmelin handbuch der anorganischen chemie. B. 39. Seltenerdelemente C.3. Fluoride, oxifluoride und zugehogige alkalidoppelverbindunge*. Springer; 1976. 439 p.

38. Sobolev B. P. *The rare earth trifluorides. Part I. The high temperature chemistry of the rare earth trifluorides*. Barcelona: Institut d'Estudis Catalans; 2000. 520 p.

39. Spedding F. H., Henderson D. C. High-temperature heat contents and related thermodynamic functions of seven trifluorides of the rare earths: Y, La, Pr, Nd, Gd, Ho, and Lu. *The Journal of Chemical Physics*. 1971;54: 2476–2483. https://doi.org/10.1063/1.1675202

40. Spedding F. H., Beaudry B. J., Henderson D. C., Moorman J. High-temperature enthalpies and related thermodynamic functions of the trifluorides of Sc, Ce, Sm, Eu, Gd, Tb, Dy, Er, Tm, and Yb. *The Journal of Chemical Physics*. 1974;60(4): 1578–1588. https://doi.org/10.1063/1.1681233

41. Sobolev B. P., Fedorov P. P. Hexagonal YF_3 structure type and high-temperature modifications of rare-earth trifluorides isostructural with YF_3. *Soviet Physics. Crystallography*. 1973;18(3): 392. (1 p.)

42. Sobolev B. P., Garashina L. S., Fedorov P. P., Tkachenko N. L., Seiranyan K. B. Polymorphism and crystallographic properties of yttrium and rare-earth trifluorides. *Soviet Physics. Crystallography*. 1973:18(4): 473–476.

43. Sobolev B. P., Fedorov P. P., Seiranyan K. B., Tkachenko N. L. On the problem of polymorphism and fusion of lanthanide trifluorides. II. Interaction of LnF_3 with MF_2 (M=Ca,Sr,Ba). Change in structural type in the LnF_3 series and thermal characteristics. *Journal of Solid State Chemistry*. 1976;17(1/2): 201–212. https://doi.org/10.1016/0022-4596(76)90221-8

44. Greis O., Cader M. S. R. Polymorphism of high purity rare earth trifluorides. *Thermochimica Acta*. 1985;87(1): 145–150. https://doi.org/10.1016/0040-6031(85)85329-6

45. Fedorov P. P., Sobolev B. P. Morphotropic transitions in the rare-earth trifluoride series. *Crystallography Reports*. 1995;40(2): 284–290.

46. Stankus S. S., Khairulin R. A., Tyagel'sky P. V. Thermal properties of rare-earth fluorides in solid and liquid states. *High Temperatures-High Pressures*. 1995/1996; 27/28(5): 493–498. https://doi.org/10.1068/htrt04

47. Sobolev B. P. High-temperature chemistry of Y, La and lanthanide trifluorides in RF_3-$R'F_3$ systems. Part 2. Phase diagrams of the studied systems. *Journal of Solid State Chemistry*. 2021;298: 122078. https://doi.org/10.1016/j.jssc.2021.122078

48. Mansmann M. Die Kristallstruktur von lanthantrifluorid. *Zeitschrift für Kristallographie*. 1965;122: 375–398. https://doi.org/10.1524/zkri.1965.122.5-6.375

49. Bolotina N. B., Chernaya T. S., Verin I. A., Khrykina O. N., Sobolev B. P. Dimorphism of RF_3 (R = La-Nd) crystals based on the data of X-ray diffraction studies. *Crystallography Reports*. 2016;61: 29–34. https://doi.org/10.1134/s1063774516010041

50. Fedorov P. P., Sorokin N. I. Stabilization of the α-YF_3 structure type by isomorphous substitutions. *Inorganic Materials*. 2017;53(12): 1307–1311. https://doi.org/10.1134/S0020168517120044

51. Sui Z., Wu J., Wang X., ... Zhang Z. Cyclic phase transition from hexagonal to orthorhombic then back to hexagonal of EuF_3 while loading uniaxial pressure and under high temperature. *The Journal of Physical Chemistry C*. 2016;120: 18780–18787. https://doi.org/10.1021/acs.jpcc.6b05907

52. Kuznetzov S. V., Osiko V. V., Tkatchenko E. A., Fedorov P. P. Inorganic nanofluorides and related nanocomposites. *Russian Chemical Reviews*. 2006;75(12): 1065–1082. https://doi.org/10.1070/RC2006v075n12ABEH003637

53. Banks C. V., Burke K. E., O'Laughlin J. W. The determination of fluorine in rare earth fluorides by high temperature hydrolysis. *Analytica Chimica Acta*. 1958;19: 239–243. https://doi.org/10.1016/S0003-2670(00)88149-0

54. Warf J. C., Cline W. C., Tevebaugh R. D. Pyrohydrolysis in the determination of fluorides and other halides. *Analytical Chemistry*. 1954;26: 342–346. https://doi.org/10.1021/ac60086a019

55. Yonezawa S., Jae-Ho K., Takashima M. Pyrohydrolysis of rare-earth trifluorides in moist air. *Solid State Sciences*. 2002;4: 1481–1485. https://doi.org/10.1016/s1293-2558(02)00039-0

56. Fedorov P. P., Mayakova M. N., Kuznetsov S. V., ... Iskhakova L. D. Coprecipitation of barium–bismuth fluorides from aqueous solutions: nanochemical effects. *Nanotechnologies in Russia*. 2011;6(3-4): 203–210. https://doi.org/10.1134/S1995078011020078

57. Thoma R. E., Brunton G. D. Equilibrium dimorphism of the lanthanide trifluorides. *Inorganic Chemistry*. 1966;5: 1937–1939. https://doi.org/10.1021/ic50045a022

58. Sobolev B. P., Fedorov P. P., Steynberg D. B., Sinitsyn B. V., Shakhkalanian G. S On the problem of polymorphism and fusion of lanthanide trifluorides. I. Influence of oxygen on phase transition temperatures. *Journal of Solid State Chemistry*. 1976;17(1/2): 191–199. https://doi.org/10.1016/0022-4596(76)90220-6

59. Fedorov P. P. Comment on the paper «The phase diagram YF_3 - GdF_3» by D. Klimm, I. M. Ranieri, R. Bertram, and S. L. Baldochi. *Materials Research Bulletin*. 2012;47(9): 2700–2701. https://doi.org/10.1016/j.materresbull.2012.05.059

60. Fedorov P. P., Mayakova M. N. Comment on the article "BiF_3:Ho^{3+} system for upconversion of 2-mcm laser radiation into visible emission" of authors A. P. Savikin, A. S. Egorov, A. V. Budruev, and I. A. Grishin, Russ. J. Appl. Chem. 89 (2), 337–340 (2016). *Russian Journal of Applied Chemistry*. 2018;91(10): 1729-1731. https://doi.org/10.1134/S1070427218100221

61. Martínez-Esaín J., Ros J., Faraudo J., Ricart S., Yáñez R. Tailoring the synthesis of LnF_3 (Ln= La-Lu and Y) nanocrystals via mechanistic study of the coprecipitation method. *Langmuir*. 2018;34(22): 6443–6453. https://doi.org/10.1021/acs.langmuir.7b03454

62. Bendeliani N. A. Phase transitions of transition metal trifluorides at high pressure*. *Inorganic Materials*. 1984;20(10): 1726–1729. (In Russ.)

63. Thoma R. E.; Hebert G. M., Insley H., Weaver C. F. Phase equilibria in the system sodium fluoride-yttrium fluoride. *Inorganic Chemistry*. 1963;2: 1005–1012. https://doi.org/10.1021/ic50009a030

64. Thoma R. E., Insley H., Hebert G. M. The sodium fluoride-lanthanide trifluoride systems. *Inorganic Chemistry*. 1966;5: 1222–1229. https://doi.org/10.1021/ic50041a032

65. Thoma R. E. Binary systems of the lanthanide trifluoorides with the alkali fluorides. *Revie de Chimie Minerale*. 1975;10(1-2): 363–381.

66. Barton C. J., Redman J. D., Strehlow R. A. Phase equilibria in the systems NaF-PuF_3 and NaF-CeF_3. *Journal of Inorganic and Nuclear Chemistry*. 1961;20: 45–52. https://doi.org/10.1016/0022-1902(61)80456-9

67. Roy D. M., Roy R. Controlled massively defective crystalline solutions with the fluorite structure. *Journal of The Electrochemical Society.* 1964;111(4): 421–429. https://doi.org/10.1149/1.2426145

68. Fedorov P. P., Sobolev B. P., Belov S. F. Fusibility diagram of the system NaF-YF_3, and the cross-section $Na_{0.4}Y_{0.6}F_{2.2}$-YOF. *Inorganic Materials*. 1979;15: 640–643.

69. Fedorov P. P., Rappo A. V., Spiridonov F. M., Sobolev B. P. NaF-YbF_3 system*. *Russian Journal of Inorganic Chemistry.* 1983;28(3): 744–748. (In Russ.)

70. Pavlova L. N., Fedorov P. P., Ol'khovaya L. A., Ikrami D. D., Alexsandrov V. B., Sobolev B. P. The NaF- GdF_3 system*. *Russian Journal of Inorganic Chemistry.* 1989;34(7): 1234–1235. (In Russ.)

71. Fedorov P. P., Pavlova L. N., Ol'khovaya L. A., Ikrami D. D., Sobolev B. P. The NaF - HoF_3 system*. *Russian Journal of Inorganic Chemistry.* 1990;35(11): 1676–1677. (In Russ.)

72. Fedorov P. P., Bondareva O. S., Buchinskaya I. I., Vistin'L. L., Sobolev B. P. A new form of sodium tetrafluorolutetate $NaLuF_4$*. *Russian Journal of Inorganic Chemistry.* 1992;37(2): 125–126. (In Russ.)

73. Fedorov P. P., Buchinskaya I. I., Bondareva O. S., Vistin'L. L., Bystrova A. A., Sobolev B. P. Phase diagrams of the NaF-RF_3 (R = Tb, Dy, Er) systems*. *Russian Journal of Inorganic Chemistry*. 1996;41(10): 1715–1719. (In Russ.)

74. Fedorov P. P., Buchinskaya I. I., Bondareva O. S., Vistin L. L., Sobolev B. P. Phase diagrams of the NaF-RF_3 (R = Tm, Yb, Lu) systems*. *Russian Journal of Inorganic Chemistry*. 1996;41(11): 1920–1924. (In Russ.)

75. Fedorov P. P., Buchinskaya I. I., Bondareva O. S. ... Sobolev B.P. Phase diagrams of the NaF-RF_3 (R = La, Ce, Pr, Nd, Sm) systems. *Russian Journal of Inorganic Chemistry*. 2000;45(6): 949–952.

76. Fedorov P. P., Alexandrov V. B., Bondareva O. S., Buchinskaya I. I., Val'covskii M. D., Sobolev B. P. Concentration dependences of the unit-cell parameters of nonstoichiometric fluorite-type phases $Na_{0.5-x}R_{0.5+x}F_{2+2x}$ (*R* = rare-earth elements). *Crystallography Reports.* 2001;46: 239–245. http://doi.org/10.1134/1.1358401

77. Fedorov P. P., Kuznetsov S. V., Osiko V. V. Elaboration of nanofluorides and ceramics for optical and laser applications. In: *Photonic & Electronic Properties of Fluoride Materials.* Tressaud A., Poeppelmeier K. (eds.). Elsevier; 2016:7-31. 513 p. http://doi.org/10.1016/B978-0-12-801639-8.00002-7

78. Fedorov P. P. Comment on "A Mechanistic Understanding of NonClassical Crystal Growth in Hydrothermally Synthezied Sodium Yttrium Fluoride Nanowires". *Chemistry of Materials*. 2021;33(10): 3859–3861. https://doi.org/10.1021/acs.chemmater.0c01515

79. Olkhovaya L. A., Fedorov P. P., Ikrami D. D., Sobolev B. P. Phase diagrams of MgF_2–(Y,Ln)F_3 systems. *Journal of Thermal Analysis*. 1979;15: 355–360. https://doi.org/10.1007/BF01903660

80. Sobolev B. P., Fedorov P. P. Phase diagramms of the CaF_2–(Y,Ln)F_3 systems. I. Experimental. *Journal of the Less Common Metals*. 1978;60: 33–46. https://doi.org/10.1016/0022-5088(78)90087-5

81. Sobolev B. P., Seiranian K. B., Garashina L. S., Fedorov P. P. Phase diagrams of the SrF_2–(Y,Ln)F_3 systems part I.—X-ray characteristics of phases. *Journal of Solid State Chemistry*. 1979;28(1): 51–58. https://doi.org/10.1016/0022-4596(79)90057-4

82. Sobolev B. P., Seiranian K. B., Phase diagrams of the SrF_2– (Y,Ln)F_3 systems. II. Fusibility of systems and thermal behavior of phases. *Journal of Solid State Chemistry*. 1981;39(2): 337–344. https://doi.org/10.1016/0022-4596(81)90268-1

83. Sobolev B. P., Tkachenko N. L. Phase Diagrams of BaF_2–(Y,Ln)F_3 Systems. *Journal of the Less Common Metals*. 1982;85: 155. https://doi.org/10.1016/0022-5088(82)90067-4

84. Cantor S., Ward W.T. Freezing point depression in sodium fluoride. 4. Effect of trivalent fluorides. *The Journal of Physical Chemistry.* 1963;67(12): 2766–2769. https://doi.org/10.1021/j100806a061

85. Shannon R. D. Revised effective ionic radii and systematic studies of interatomic distances in halides and chalcogenides. *Acta Crystallographica Section A*. 1976;32: 751–767. https://doi.org/10.1107/s0567739476001551

86. Bard A. B., Zue X., Xia X., ... Pauzauskie P. J. A mechanistic understanding of nonclassical crystal growth in hydrothermally synthesized sodium yttrium fluoride nanowires. *Chemistry of Materials* 2020;32: 2753–2763. https://doi.org/10.1021/acs.chemmater.9b04076

87. Fedorov P. P., Mayakova M. N., Voronov V. V., Baranchikov A. E., Ivanov V. K. Preparation of "$NaRF_4$" phases from the sodium nitrate melt. *Journal of Fluorine Chemistry*. 2019;218: 69–75. https://doi.org/10.1016/j.jfluchem.2018.11.018

88. Grzechnik A., Bouvier P., Crichton W.A., Farina L., Kohler J. Metastable $NaYF_4$ fluorite at high pressures and high temperatures. *Solid State Sciences*. 2002;4: 895–899. https://doi.org/10.1016/s1293-2558(02)01353-5

89. Tkachuk A. M., Ivanova S. E., Joubert M. F., Guyot Y. Spectroscopic study of double sodium-yttrium fluoride crystals doped with erbium $Na_{0.4}Y_{0.6}F_{2.2}$:Er^{3+}. *Optics and Spectroscopy*. 2005;99: 932–949. https://doi.org/10.1134/1.2149418

90. Bezhanov V. A., Mikhailin V. V., Chernov S. P., Karimov D. N. UV and VUV spectroscopic study of $Na_{0.4}Y_{0.6}F_{2.2}$ crystals doped with rare-earth ions. *Optics and Spectroscopy*. 2006;101: 571–581. https://doi.org/10.1134/S0030400X06100122

91. Karimov D. N., Sobolev B. P., Ivanov I. A., Kanorsky S. I., Masalov A. V. Growth and magneto-optical properties of $Na_{0.37}Tb_{0.63}F_{2.26}$ cubic single crystal. *Crystallography Reports*. 2014;59: 718–723. https://doi.org/10.1134/S1063774514050083

92. Sorokin N. I., Karimov D. N., Volchkov I. S., Grigor'ev Yu. V., Sobolev B. P. Fluorine-ionic conductivity of superionic conductor crystals $Na_{0.37}Tb_{0.63}F_{2.26}$. *Crystallography Reports*. 2019;64(4): 626–630. https://doi.org/10.1134/S1063774519040229

93. Furuya Y., Tanaka H., Fukuda K., ... Yoshikawa A. Growth and luminescence properties of Eu-doped $(Na_{0.425-x}Lu_{0.575x})F_{2.15-2x}$ single crystals. *Journal of Crystal Growth*. 2011;318: 549–552. https://doi.org/10.1016/j.jcrysgro.2010.10.037

94. Furuya Y., Tanaka H., Fukuda K., ...Yoshikawa A. Crystal growth, Nd distribution and luminescence properties of $(Na_{0.425-x}Lu_{0.575x})F_{2.15-2x}$ single crystals. *Journal of Crystal Growth*. 2011;318: 791–795. https://doi.org/10.1016/j.jcrysgro.2010.11.048

95. Novikov I. I. Two types of phase diagrams with congruently melting chemical compounds*. *Doklady Akademii nauk SSSR*. 1955;100(6): 1119–1121. (In Russ.)

96. Fedorov P. P. Transformations of *T-x* phase diagrams of binary systems in the condensed state: II. Phase equilibria under constraints. *Russian Journal of Physical Chemistry A*. 1999;73(9): 1387–1392. Available at: https://elibrary.ru/item.asp?id=13311944

97. Vistin L. L., Bondareva O. S., Fedorov P. P., Buchinskaya I. I., Sobolev B. P. Fluorite-like phases in the NaF-RF_3 systems for rare earths from Tb to Lu. *Butll. Soc.Cat. Sien*. 1991;13(1): 285–291. Available at: https://www.researchgate.net/publication/266870490_FLUORITE-LIKE_PHASES_IN_THE_NaF-RF3_SYSTEMS_FOR_RARE_EARTHS_FROM_Tb_TO_Lu

98. Krivandina E. A., Bystrova A. A., Sobolev B. P., ... Shtyrkova A. P. Growth and some properties of $Na_{0.5-x}R_{0.5+x}F_{2+2x}$ (R = Y, Dy-Lu; *x* = 0.1 and 0.15) single crystals with fluorite structure. *Soviet Phusics Crystallography.* 1992;37(6): 1523–1534.

99. Blistanov A. A., Chernov S. P., Karimov D. N., Ouvarova T. V. Peculiarities of the growth of disordered Na,*R*-fluorite (*R* = Y, Ce–Lu) single crystals. *Journal of Crystal Growth.* 2002; 237–239: 899–903. https://doi.org/10.1016/S0022-0248(01)02076-0

100. Vojna D., Karimov D. N., Ivanova A. G, ... Mocek T. Growth and characterization of the KDy_3F_{10} and $Na_{0.38}Dy_{0.62}F_{2.24}$ fluoride crystals for the Faraday devices. *Optical Materials*. 2023;142: 114016. https://doi.org/10.1016/j.optmat.2023.114016

101. Starobor A. V., Mironov E. A, Volkov M. R., ... Palashov O. V. Thermal lens investigation in $EuF_{2.11}$, PrF_3, and $Na_{0.38}Ho_{0.62}F_{2.24}$ crystals for magnetooptical applications. *Optical Materials*. 2020;99: 109542. https://doi.org/10.1016/j.optmat.2019.109542

102. Bohigas X., Lluma J., Tejada J., Krivandina E. A., Sobolev B. P. Magnetic susceptibility of sodium rare-earth fluorites $Na_{0.5-x}R_{0.5+x}F_{2+2x}$ (R = Dy, Ho, Er, Tm, Yb) and some ordered phases. *Crystallography Reports*. 2001;46(3): 483–487. https://doi.org/10.1134/1.1376482

103. Yi G. S., Lee W. B., Chow G. M. Synthesis of $LiYF_4$, $BaYF_5$, and $NaLaF_4$ optical nanocrystals. *Journal of Nanoscience and Nanotechnology*. 2007;7(8): 2790–2794. https://doi.org/10.1166/jnn.2007.638

104. Kuznetsov S. V., Ovsyannikova A. A., Tupitsyna E. A., ... Osiko V. V. Phase formation in LaF_3-$NaGdF_4$, $NaGdF_4$-$NaLuF_4$, $NaYF_4$-$NaLuF_4$ systems: synthesis of powders by co-precipitation from aqueous solutions. *Journal of Fluorine Chemistry*. 2014;161: 95–101. https://doi.org/10.1016/j.jfluchem.2014.02.011

105. Ladol J., Khajuria H., Khajuria S., Sheikh H. N. Hydrothermal synthesis, characterization and luminescent properties of lanthanide-doped $NaLaF_4$ nanoparticles. *Bulletin of Materials Science.* 2016;39(4): 943–952. https://doi.org/10.1007/s12034-016-1225-8

106. Yang S., Anderko A., Riman R. E., Navrotsky A. Thermochemistry of sodium rare earth ternary fluorides, $NaREF_4$. *Acta Materialia*. 2021;220: 117289. https://doi.org/10.1016/j.actamat.2021.117289

107. Constantin V., Popescu A.-M. Structure and heat capacity of the $NaCeF_4$ compound. *Journal of Rare Earths*. 2013;31: 911–915. https://doi.org/10.1016/s1002-0721(12)60378-0

108. Sobolev B. P., Aleksandrov V. B., Fedorov P. P., Seiranyan K. B., Tkachenko N. L. Variable-composition phases with the LaF_3 structure in the systems MF_2-$(Y,Ln)F_3$. IV. X-ray characteristics, heterovalent isomorphic substitutions. *Soviet Physics – Crystallography*. 1976;21(1): 49–54.

109. Burns J. H. Crystal structure of hexagonal sodium neodymium fluoride and related compounds. *Inorganic Chemistry.* 1965;4: 881–886. https://doi.org/10.1021/ic50028a025

110. Krämer K., Biner W., Frei D. G., Gudel H. U., Heblen M. P., Luthi S. R. Hexagonal sodium yttrium fluoride based green and blue emitting upconversion phosphors. *Chemistry of Materials*. 2004;16: 1244–1251. https://doi.org/10.1021/cm031124o

111. Lage M. M., Moreira R. L., Matinaga F. M., Gesland J.-Y. Raman and infrared reflectivity getermination of phonon modes and crystal structure of Czochralski-grown $NaLnF_4$ (Ln = La,Ce,Pr,Sm,Eu, and Gd) single crystals. *Chemistry of Materials*. 2005;17: 4523–4529. https://doi.org/10.1021/cm050860k

112. Aebischer A., Hostettler M., Hauser J., ... Burgi H.-B. Structural and spectroscopic characterization of active sites in a family of light-emitting sodium lanthanide tatrafluorides. *Angewandte Chemie International Edition*. 2006;45: 2802–2806. https://doi.org/10.1002/anie.200503966

113. Shi R., Brites C. D. S., Carlos L. D. Hexagonal-phasse $NaREEF_4$ upconversion nanocrystals the matter of crystal structure. *Nanoscale*. 2021;13: 19771–19782. https://doi.org/10.1039/d1nr04209b

114. Voronkov A. A., Shumyatskaya N. G., Pyatenko Yu. A. Crystal structure of gagarinite. *Journal of Structural Chemistry.* 1962;3: 665–669. https://doi.org/10.1007/bf00744128

115. Frank-Kamenetskaya O. V., Fundamanskii V. S., Tsytsenko A. K., Frank-Kamenetskii V. A. Crystal structure of gagarinite from precision X-ray data: structural changes in the $NaCaTRF_6$-$Na_{1.5}TR_{1.5}F_6$ series. *Crystallography Reports.* 1994;39: 923–928.

116. Pontonnier L., Patrat G., Aleonard S., Capponi J.-J., Brunel M., de Bergevin F. An approach to the local arrangement of the fluorine atoms in the anionic conductors with the fluorite structure $Na_{0.5-x}Y_{0.5+x}F_{2+2x}$. *Solid State Ionics.* 1983;9-10: 549–554. https://doi.org/10.1016/0167-2738(83)90293-x

117. Zhurova E. A., Maksimov B. A., Sobolev B. P., Simonov V. I., Hull S., Wilson S. S. Defect structure of $Na_{0.39}Y_{0.61}F_{2.22}$ crystals. *Crystallography Reports*. 1997;42: 238–242.

118. Otroshchenko L.P., Fekin L.E., ,Bystrova A.A., Sobolev B.P. Defect structure of $Na_{0.5-x}R_{0.5+x}F_{2+2x}$ (R = Ho,Yb) solid solutions (fluorite type). *Crystallography Reports*. 2000;45(6): 926–929.

119. Bevan D. J., Greis O., Strahle J. A new structural principle in anion-excess fluorite-related superlattices. *Acta Crystallographica A*. 1980;36: 889–890. https://doi.org/10.1107/s0567739480001878

120. Greis O., Haschke J. M. Rare earth fluorides. In: *Handbook on the Physics and Chemistry of Rare Earth*. Gscheidner K. A. & Eyring L. (eds.) Amsterdam, New York, Oxford: 1982;5(45): 387–460. https://doi.org/10.1016/s0168-1273(82)05008-9

121. Schmutz H. *Untersuchungen in den Systemen Alkalifluorid-Lanthaniden/Actinidenfluorid (Li, Na, K, Rb-La, S.E.,Y/Np,Pu,Am)*. Thesis. Institute fur Radiochemie. Karsruhe. 1966. 71 p.

122. Hund F. Das ternäre Fluorid $NaYF_4$. *Zeitschrift für anorganische Chemie*. 1950;261: 106–115. https://doi.org/10.1002/zaac.19502610110

123. Gaune-Escard M., Hoch M. Analysis of the enthalpy of mixing data of binary and ternary [rare earth (Nd,La, Y,Yb), Al-alkali metal] – fluoride systems. *Journal of Alloys and Compounds*. 2001;321: 267–275. https://doi.org/10.1016/s0925-8388(01)00962-8

124. Ard J. C., Schorne-Pinto J., Aziziha M., ... Besmann Th. M. Thermodynamic assessmants or reassessmants of 30 pseudo-binary and – ternary systems. *The Journal of Chemical Thermodynamics*. 2023;177: 106931. https://doi.org/10.1016/j.jct.2022.106931

125. Fedorov P. P., Pavlova L. N., Bondareva O. S., ... Sobolev B. P. *Phases with a structure derived from fluorite in the NaF–RF_3 and NaF–RF_3–BaF_2 systems**. Preprint No. 11. Moscow: A. V. Shubnikov Institute of Crystallography. 1990. 33 p. (In Russ.)

126. Mikheev V. I. *X-ray determinant of minerals**. Moscow: Nedra Publ. 1957. (In Russ.)

127. Kovba L. M., Trunov V. K. *X-ray phase analysis**. Moscow: Moscow State University Publ. 1978. (In Russ.)

128. Mai H.-X., Zhang Y.-W., Sun L.-D., Yan C.-H. Size- and phase-controlled synthesis of monodisperse $NaYF_4$:Yb,Er nanocrystals from a unique delayed nucleation pathway monitored with upconversion spectroscopy. *The Journal of Physical Chemistry C*. 2007;111: 13730–13739. https://doi.org/10.1021/jp073919e

129. Li C., Yang J., Yang P., Zhang X., Lian H., Lin J. Two-dimensional β-$NaLuF_4$ hexagonal microplates. *Crystal Growth and Design*. 2008;8: 923–928. https://doi.org/10.1021/cg7007528

130. Zhang F., Li J., Shan J., Xu L., Zhao D. Shape, size, and phase-controlled rare-earth fluoride nanocrystals with optical up-conversion properties. *Chemistry – A European Journal*. 2009;15: 11010–11019. https://doi.org/:10.1002/chem.200900861

131. Yang L. V., Han H. L., Zhang Y. Y., Zhong J. X. White emission by frequency up-conversion in Yb^{3+}-Ho^{3+}-Tm^{3+} triply doped hexagonal $NaYF_4$ nanorods. *The Journal of Physical Chemistry C*. 2009;113: 18995–18999. https://doi.org/10.1021/jp9021689

132. Zhang F., Deng Y., Shi Y., Zhang R., Zhao D. Photoluminescence modification in upconversion rare-earth fluoride nanocrystal array conducted photonic crystals. *Journal of Materials Chemistry*. 2010;20: 3895–3900. https://doi.org/10.1039/c000379d

133. Liu Q., Sun Y., Yang T., Feng W., Li C., Li F. Sub-10nm hexagonal lanthanide-doped $NaLuF_4$ upconversion nanocrystals for sensitive bioimaging in vivo. *Journal American Chemical Society*. 2011;133: 17122–17125. https://doi.org/10.1021/ja207078s

134. Nordmann J., Voss B., Komban R., ... Haase M. Synthasis of β-phase $NaYF_4$:Yb,Er upconversion nanocrystals and nanorods by hot-injection of small particles of the α-phase. *Zeitschrift für Physikalische Chemie*. 2015;229: 247–262. https://doi.org/10.1515/zpch-2014-0616

135. Naccache R., Yu Q., Capobianco A. The fluride host: nucleartion, growth, and upconversion of lanthanide-doped nanoparticles. *Advanced Optical Materials*. 2015;3: 482–509. https://doi.org/10.1002/adom.201400628

136. Shen J.-W., Wang Z., Wei X., Liu J., Wei Y. Facile ex situ NaF size/morphology tuning strategy for highly monodisperse sub-5 nm β-$NaGdF_4$:Yb/Er. *CrystEngComm*. 2018;20: 1185–1188. https://doi.org/10.1039/C7CE02141K

137. Laihinen T., Lastusaari M., Pihlgren L., ... Hölsä J.. Thermal behaviour of the $NaYF_4$:Yb^{3+},R^{3+} materials. *Journal of Thermal Analysis and Calorimetry*. 2015;121: 37–43. https://doi.org/10.1007/s10973-015-4609-x

138. Ivanov V. K., Fedorov P. P., Baranchikov A. Y., Osiko V. V. Oriented aggregation of particles: 100 years of investigations of non-classical crystal growth. *Russian Chemical Review*. 2014;83: 1204–1222. https://doi.org/10.1070/RCR4453

139. De Yoreo J. J., Gilbert P. U. P. A., Sommerdijk N. A. J. M., ... Dove P. M. Crystallization by particle attachment in synthetic, biogenic, and geologic environments. *Science*. 2015;349: 6247. https://doi.org/10.1126/science.aaa6760

140. Du P., Luo L., Yu J. S. Controlled synthesis and upconversion luminescence of Tm^{3+}-doped $NaYbF_4$ nanoparticles for non-invasion optical thermometry. *Journal of Alloys and Compounds*. 2018;739: 926–933. https://doi.org/10.1016/j.jallcom.2017.12.260

141. Vuković M., Dinić I., Jardim P., ... Mančić L. The low-temperature sonochemical synthesis of up-converting β $NaYF_4$: Yb, Er mesocrystals. *Advanced Powder Technology*. 2022;33(2): 103403. https://doi.org/10.1016/j.apt.2021.103403

142. Koshelev A. V., Grebenev V. V., Arkharova N. A., Shiryaev A. A., Karimov D. N. Preparation of rare-earth doped $NaYF_4$ luminescent nanoparticles by a high-energy ball milling process. *CrystEngComm*. 2023;25(33): 4745–4754. https://doi.org/10.1039/d3ce00642e

143. Yang S., Jayanthi K., Anderko A., Riman R. E., Navrotsky A. Thermochemical investigatiion of the stability and conversion of nanocrystalline and high-temperature phases in sodium neodymium fluorides. *Chemistry of Materials*. 2021;33: 9571–9579. https://doi.org/10.1021/acs.chemmater.1c02829

144. Buznik V. M., Komissarova L. N., Moskvich Yu. N., Pushkina G. Ya. Study of anion mobility in lanthanum hydroxyfluorides*. *Russian Journal of Inorganic Chemistry*. 1980;425(6): 1488. (In Russ.). Available at: https://elibrary.ru/item.asp?id=29176401

* *Translated by author of the article*

Information about the authors

Pavel P. Fedorov, Dr. Sci. (Chem.), Full Professor, Chief Researcher at the Prokhorov General Physics Institute of the Russian Academy of Sciences (Moscow, Russian Federation).
https://orcid.org/0000-0002-2918-3926
ppfedorov@yandex.ru

Irina I. Buchinskaya, Cand. Sci. (Chem.), Senior Researcher, Shubnikov Institute of Crystallography, Kurchatov Complex of Crystallography and Photonics, National Research Centre "Kurchatov Institute," (Moscow, Russian Federation).
https://orcid.org/0000-0002-4658-5695
buchinskayaii@gmail.com

Received 28.07.2024; approved after reviewing 03.09.2024; accepted for publication 16.09.2024; published online 25.12.2024.

Translated by Valentina Mittova

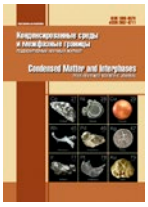

ISSN 1606-867X (Print)
ISSN 2687-0711 (Online)
Condensed Matter and Interphases
Kondensirovannye Sredy i Mezhfaznye Granitsy
https://journals.vsu.ru/kcmf/

Original articles

Research article
https://doi.org/10.17308/kcmf.2024.26/12428

Phase transformations of ternary copper iron sulfide $Cu_{1.1}Fe_{1.9}S_{3.0}$ under temperature variations: thermodynamic and kinetic aspects

I. G. Vasilyeva[1]✉, E. F. Sinyakova[2], S. A. Gromilov[1]

[1]*Nikolaev Institute of Inorganic Chemistry of Siberian Branch Russian Academy of Sciences*
3 Lavrent'ev ave., Novosibirsk 630090, Russian Federation

[2]*VS Sobolev Institute of Geology and Mineralogy Siberian Branch Russian Academy of Sciences*
pr. Akademika Koptyuga 3, Novosibirsk, 630090, Russian Federation

Abstract

The article considers ternary sulfide $Cu_{1.1}Fe_{1.9}S_3$ with a metal/sulfur ratio corresponding to the complete stoichiometry of cubanite $CuFe_2S_3$ as an intermediate phase of a solid solution with chemically disordered Cu and Fe cations in the ordered anionic framework. A new approach to determining the nature of the solid solution, its stability and behavior during cooled over a wide temperature and time range is suggested. To synthesize the sample, we used controlled directional solidification of a homogeneous melt with the $Cu_{1.1}Fe_{1.9}S_3$ composition under quasi-equilibrium conditions and obtained a solidified zoned ingot, where the distribution of Cu, Fe, and S elements along its length was quantitatively determined. To detect small-scale structural and chemical changes, we used optical and electron microscopy methods, electron-probe X-ray spectral microanalysis, full-profile X-ray diffraction analysis, and the differential dissolution method, which allowed to determine the phase and chemical states of the samples both at the macro level and with a high spatial resolution. With this approach, we established the following: $Cu_{1.1}Fe_{1.9}S_3$ is an intermediate phase of a system with end-members of cubanite $CuFe_2S_3$ and chalcopyrite $CuFeS_2$; a homogeneous solid solution of chalcopyrite with 5 mol. % of cubanite exists near 930 °C with a chaotic distribution of Cu and Fe between the existing crystallographic positions; a solid solution of chalcopyrite with 6 mol. % of cubanite at 900 °C facilitates lattice strain relaxation through the formation of a block nanostructure; there is a solid solution of cubanite with 30 mol. % of chalcopyrite at 900–720 °C, with small-size clusters with a chalcopyrite stoichiometry evenly distributed inside the $Cu_{0.94}Fe_2S_3$ matrix. The factors determining the evolution and stability of solid solutions are discussed taking into account the polymorphism of chalcopyrite phase. The newly obtained data is important for the synthesis of magnetic nanosized Cu-Fe sulfide materials and can also be used in the processing of sulfide ores rich in copper.

Keywords: System Cu-Fe-S, Directional Crystallization, Solid Solutions, Ordering

Funding: The research was carried out with the financial support of the Ministry of Science and Higher Education of the Russian Federation under the Government Order by Nikolaev Institute of Inorganic Chemistry of the Siberian Branch of the Russian Academy of Sciences (agreement No. 121031700315-2) and V.S. Sobolev Institute of Geology and Mineralogy of the Siberian Branch of the Russian Academy of Sciences (agreement No. 122041400237-8).

Acknowledgements: Scanning electron microscopy and energy-dispersive spectrometry (SEM/EDS) studies were performed at the Centre for Collective Use of Multielement and Isotope Studies of the Siberian Branch of the Russian Academy of Sciences.

For citation: Vasilyeva I. G., Sinyakova E. F., Gromilov S. A. Phase transformations of ternary copper iron sulfide $Cu_{1.1}Fe_{1.9}S_{3.0}$ under temperature variations: thermodynamic and kinetic aspects *Condensed Matter and Interphases*. 2024;26(4): 706–715. https://doi.org/10.17308/kcmf.2024.26/12428

Для цитирования: Васильева И. Г., Синякова Е. Ф., Громилов С. А. Фазовые превращения тройного сульфида железа-меди $Cu_{1.1}Fe_{1.9}S_{3.0}$ при варьировании температуры: некоторые термодинамические и кинетические аспекты. *Конденсированные среды и межфазные границы*. 2024;26(4): 706–715. https://doi.org/10.17308/kcmf.2024.26/12428

✉ Inga G. Vasilyeva, e-mail: kamars@niic.nsc.ru

1. Introduction

Ternary sulfides $CuFe_2S_3$ and $CuFeS_2$, especially nanosized, have recently attracted a lot of attention due to their magnetic and semiconductor properties, which make them promising materials for the development of information technologies [1-3]. Being the main minerals of sulfide ores rich in copper, they are also the main source of non-ferrous metals [4–6]. Both sulfides are formed in a similar way, namely by means of melt crystallization followed by solid-phase transformations of the crystallized product during the cooling process. In this regard, cubanite $CuFe_2S_3$ and chalcopyrite $CuFeS_2$ are unique compounds that besides stable polymorphic phases they have a large number of metastable structural forms with the Cu and Fe cations distribution depending on the cooling kinetics [4–6]. Such a diversity of structures ensures as well the variability of the properties of ternary sulfides. Therefore, an understanding of the evolution of solid-phase processes is very important both for the purposeful synthesis of new materials and for the development of efficient technologies for the processing of mineral associations.

The existing knowledge about cubanite and chalcopyrite transformations is mainly based on the results of numerous studies of natural minerals, which are final products of crystallization, whereas synthetic analogues are used to determine their intermediate states through annealing- quenching procedure. At the moment, there is plenty of data regarding the transformation of low-temperature orthorhombic cubanite $CuFe_2S_3$ (*Pcmn* a = 6.46 Å, b = 11.12 Å, c = 6.23 Å) into a high-temperature cubic polymorph ($F\bar{4}3m$ a = 5.29 Å). It is known that the reverse transition is kinetically inhibited and cannot be implemented in laboratory experiments. Under nature conditions, on the contrary, the association of orthorhombic cubanite – chalcopyrite is stable with reaching equilibrium at 300–400 ºC during 1–10 years [4, 5]. An alternative to polymorphic transition, a metastable process of the tetragonal chalcopyrite exsolution from cubanite was found [4, 7-10] or tetragonal chalcopyrite with iron monosulfide according to the following reaction: $CuFe_2S_3 \rightarrow CuFeS_2 + FeS$ [11]. These processes are usually studied using electron probe microanalysis (EPM) and X-ray diffraction analysis of the microstructures of the minerals and their analogues. Nevertheless, according to references [1, 4, 9–10], serious limitations of these diagnostic methods, and long-term isothermal annealing of tetragonal chalcopyrite at temperature close to the equilibrium 300–400 ºC, makes practically impossible studying of high-temperature small-scale order-disorder transformations with participation of high-temperature cubic chalcopyrite. A high-temperature chalcopyrite polymorph with a completely cation-disordered cubic structure ($F\bar{4}3m$ a = 5.29 Å) was discovered during an *in situ* experiment with transmission electron microscopy (TEM) [12, 13]. The critical temperature 557 °C was determined for the phase transition of the tetragonal $CuFeS_2 \rightarrow$ cubic $CuFeS_2$ using a combination of methods, including neutron powder and X-ray diffraction, thermal analysis, and magnetic and electron transport measurements. It is important that this temperature is characteristic only for the strictly stoichiometric composition of both these phases [11, 14]. Since phase transformations of cubic chalcopyrite – cubic cubanite at high temperatures depend on the stoichiometry of the interacting phases, these experiments aimed should be carefully designed. When the symmetry and the lattice parameters of both these phases are identical, efficient methods should be used to identify chalcopyrite in cubanite mixtures, especially when it occurs in a dispersed state in the cubic cubanite matrix. So, cubanite, cooled from high temperatures in *the in-situ* TEM experiment, contained lamellae with isolated finely dispersed particles, but its diffraction picture was absolutely identical to the initial one [15]. Unfortunately, for study of the order-disorder transformations of ternary Cu-Fe sulfides, abilities of TEM experiments are hindered both the difficulty in preparing the samples and even more so by the radiation causing a loss of sulfur and therefore changes in the characteristics of themselves transformations. Therefore, to study high-temperature transformations of a solidified $Cu_{1.1}Fe_{1.9}S_3$ melt, a new synthesis and new diagnostic methods of small-scale structural changes were used. A sample was obtained in the form of an ingot during conservative directional

crystallization and the solidified melt passed across zones with lowered temperatures over various periods of time. The calculation of the qualitative distribution of Cu, Fe, and S along the ingot length gave data regarding the Cu/Fe ratio in the each moment of crystallization and the bulk compositions varying along the length. The crystallization method is described in [16, 17], its efficiency for the study of exsolution process of stoichiometric cubanite $CuFe_2S_3$ is demonstrated in [20]. Fragments of equilibrium *T*-*x* diagrams in the range adjacent to $CuFe_2S_3$ and $Cu_{1.1}Fe_2S_3$ compositions were shown in [18, 19]. To study fine structure transformations, the reference-free differential dissolution method (DD) was used along with traditional methods. It reliably identified phases having identical structures but different compositions and internal arranging, based on differences in their chemical activity. The principles of the DD method is given in [21, 22] with its abilities to identify unknown, amorphous, or low-dimensional phases based on their composition without referring to the phase standards. And it is an advantage over the X-ray diffraction method (XRD), especially when the analyzed samples have a complex spatial arrangement. Scanning composition with a resolution of 5Å/cm^2, DD method determines the spatial chemical inhomogeneity of the phase, caused difference of its internal arrange, and like this practically substitutes for TEM, which registers this arrange structurally.

2. Experimental

Directional crystallization of the melt with a composition Fe 32.5, Cu 18.5, S 49.0 at. % was performed using the Bridgman-Stockbarger method with moving the ampoule with the homogeneous melt from the hot area to the cold area at $2.3 \cdot 10^{-8}$ m/s and its quenching in air at ~ 100 deg/min, when the temperature at its end reached 720 °C. As known, this cooling procedure practically corresponds to the natural equilibrium crystallization of minerals [5]. The ingot, 70 mm long and 7 mm in diameter, was cut into 14 wafers. Based on the results of the analysis of these wafers, we practically obtained a kinetic time-temperature-transformation diagram. Changes in the morphology, phase and chemical states of the polished wafers were registered by means of step-wise scanning of the surface using optical and electron microscopy. The average (scanning area of ~2 mm^2) and local chemical compositions of components with different morphology and geometry were measured using the methodology developed at the Centre for Collective Use of Multielement and Isotope Studies of the Siberian Branch of the Russian Academy of Sciences by means of energy-dispersive spectrometry (SEM-EDS) on a MIRA 3 LMU high-resolution microscope (Tescan Orsay Holding) equipped with INCA Energy 450+ X-Max 80 and INCA Wave 500 (Oxford Instruments Nanoanalysis Ltd) microanalysis systems. The error in determining the main components was 0.1–0.3 wt.%. The compositions of ~ 5 μm particles of different phases were determined based on single measurements with a relative error of 1-2%.

The XRD was performed using a Shimadzu XRD-7000 powder diffractometer at 20 ºC, Cu*K*α-radiation, range 20–75° 2θ, scan rate of 0.1 °/min, standards Si and LaB_6. After abrasion, thin layers of the sample were put on the polished side of a standard cuvette. The phases were identified using ICSD No. 42105 for $CuFe_2S_3$, No. 28894 for $CuFeS_2$, and No. 42487 for FeS [23]; a full-profile analysis of the X-ray diffraction patterns was performed using the Powder Cell program [24].

In the DD experiment (Fig. 1a), the consequent dissolution of phases was realized in a solvent flow with the concentration gradually increasing from 3N HNO_3 at 40 °C to 6N HNO_3 at 85 °C. Phases with different chemical potentials dissolve consequently once their potentials equal the potential of the solvent. The solvent was fed to the reactor in portions at a constant speed. Each portion with a dissolved 5Å surface layer of the sample then came to an ICP-AES spectrometer, which simultaneously determined amounts of Cu, Fe, and S. Kinetic curves of dissolution of the components and their stoichiograms, presented as pairwise atomic ratios of the components of this sample, were obtained based on the analysis of 50–200 portions of the solution. The computer-processed primary data was used to determine the number of phases, their compositions, quantities, and spatial homogeneity, and it was demonstrated by dissolving a model phase mixture $A_2B_3 + AB_3$ (Fig. 1b).

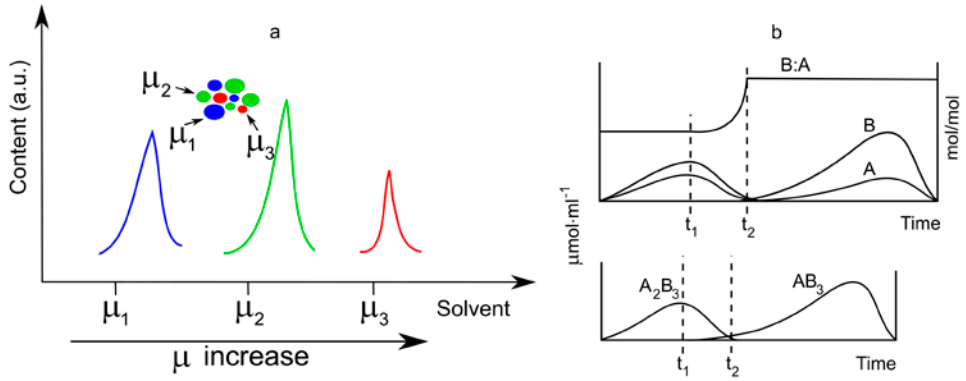

Fig. 1. Principles of DD: consecutive dissolution of phases according to chemical potentials μ (a); dissolution of the model phase mixture A_2B_3 + AB_3(b): A, B – kinetic curves of A and B elements dissolution and stoichiogram line B:A (top); kinetic curves of dissolution of the A_2B_3 и AB_3 phases (bottom)

3. Results and discussion

In [6], the fragmentary equilibrium *T-x* diagram $Cu_{0.19}Fe_{0.33}S_{0.48}$ - $Cu_{0.31}Fe_{0.23}S_{0.46}$ of the Cu-Fe-S system is shown (Fig. 2) where the phase of a constant composition $Cu_{1.1}Fe_{1.9}S_{3.0}$ was considered as a nonstoichiometric cubanite (*icb**) being in equilibrium with the melt. However, there are two facts indicating a different nature of this sulfide. The first is a partial cationic substitution of iron with copper, without deviation of the metal/sulfur ratio from generally 2/3 stoichiometry. The second, known from [5, 6], is the ability of the high-temperature cubic solid solution *iss* of the Cu-Fe-S ternary system to interact with chalcopyrite of the same structure. A reconstruction of elementary composition of $Cu_{1.1}Fe_{1.9}S_{3.0}$ to crystallochemical composition $CuFe_{1.73}S_{2.73}$ reflects a novel nature of the phase where the cationic substitution happens in the anionic framework of cubanite remaining unchanged. The chemical disorder results in the formation of substitutional solid solutions with variable contents of Cu and Fe. From the point of view of crystal chemistry, the composition $CuFe_{1.73}S_{2.73}$ is defined as an intermediate solid solution with the $0.73CuFe_2S_3 \cdot O.27CuFeS_2$ composition, where the end-members are cubanite and chalcopyrite. The purpose of our study was to gather evidence of the nature of the solid solution and determine its stability and behavior over a wide temperature during cooling.

Fig. 3 demonstrates the cooling regime of the ingot, i.e. a kinetic diagram of high-temperature subsolidus transformations of the solidified $Cu_{1.1}Fe_{1.9}S_{3.0}$ melt. According to macrostructure, the ingot has three obviously differ zones. We focused on zones II and III, where the numbers in the figure correspond to the wafers cut from the ingot. It is easy to see the duration of stay of the samples in each temperature field. Micrographs of the surface of the polished wafers in an optical and electron microscopes are given in Fig. 4. The microstructure of the 0.56 sample was typical for all the samples in zone II, microstructures of samples 0.96 and 1.0 in zone III were different from each other and from the samples in zone II. Optical microscopy demonstrated that all the samples, except for 0.96, are single-phase at the macro level according to the uniformity of their color and reflectivity. Sample 0.96 includes light and dark domains of various size,

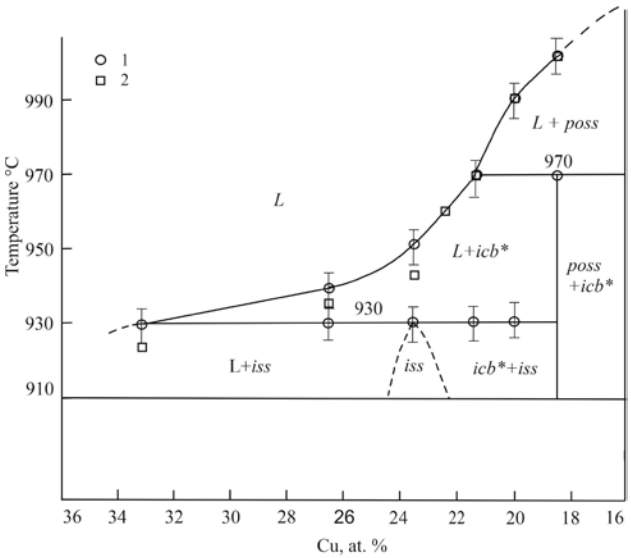

Fig. 2. Polythermal section along the $Cu_{0.19}Fe_{0.33}S_{0.48}$ - $Cu_{0.31}Fe_{0.23}S_{0.46}$ direction [19]. *L* – sulfide melt, *poss* – $(Fe,Cu)S_{1.04}$, *icb** – $Cu_{1.1}Fe_{2.0}S_{3.0}$, and *iss* – $Cu_{1.0}Fe_{1.2}S_{2.0}$

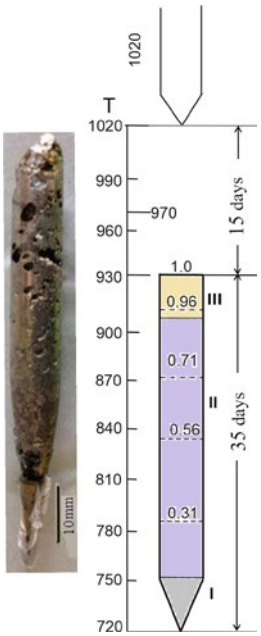

Fig. 3. View of ingot (left) and kinetic diagram (right)

and the difference in color is explained by the difference in their compositions and internal arranges (Fig. 4b, c). Microstructure of all the samples from SEM observation did not shown diffraction contrast as well as lamellae, rims, or microinclusions being visible signs of exsolution process (Fig. 4e-i). The high accuracy of the average composition of wafers due to a large wealth of EDX data obtained by EDS, and the sum of the determined concentrations of the components practically equal to 100 %, make it possible to reconstruct the bulk composition into a corresponding crystallochemical formula.

Table 1 presents bulk and crystallochemical compositions of the samples. It shows that compositions of the samples in zone II are kept constant but different from 0.96 and 1.0 samples in zone III. There is only a slight difference between the latter two compositions. According to crystallochemical formulas, in zone II a cubanite-based solid solution with 30 mol. % of chalcopyrite is realized; in zone III a solid solution of chalcopyrite with 5 or 6 mol. % of cubanite is formed. What formation of these solid solutions is realistic fact is supported by their homogeneous microstructures.

The single-phase state of the representative specimens 0.31–0.71, 0.96, and 1 was emerged

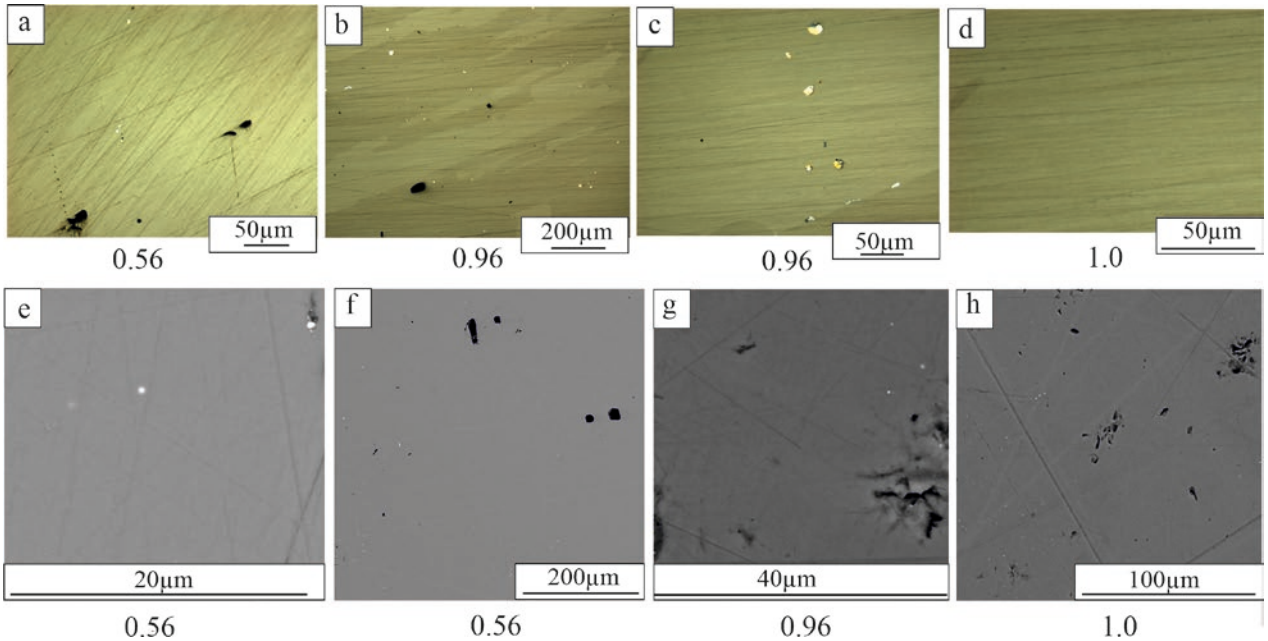

Fig. 4. Microstructure of samples 0.56, 0.96 and 1.0 in reflected light (a-d) and in BSE (e-h)

Table 1. Variation of average composition along the ingot length in zones II and III

Samples	0.31	0.56	0.71	0.83	0.95	0.96	1.0
Состав	$CuFe_{1.73}S_{2.6}$	$CuFe_{1.73}S_{2.6}$	$CuFe_{1.73}S_{2.6}$	$CuFe_{1.73}S_{2.6}$	$CuFe_{1.73}S_{2.6}$	$CuFe_{1.20}S_{2.08}$	$CuFe_{1.18}S_{2.05}$
Solid solutions	$0.7CuFe_2S_3 \cdot 0.3CuFeS_2$					$0.95CuFeS_2 \cdot 0.05CuFe_2S_3$	

also from a diffraction experiment (Table 2). Quite reproducible diffraction patterns, taking from various parts of the samples 0.56, 0.96, and 1.0, with full-profile analysis showed the same type of cubic structure $F\bar{4}3m$ (Fig. 5). The only difference was observed in the lattice parameter and a specific change in the relative intensity of the diffraction peak (220). The largest lattice parameter was observed for sample 1.0. For samples 0.96 and 0.56, it decreased, becoming the lowest in the part of the 0.96 sample that adjacent to the boundary of zone III. Changes in the lattice parameter of cubic cubanite are usually associated with the presence of microdistortions deforming the lattice [8–10, 25, 26]. In our experiment, changes in the lattice parameters caused significant changes in the Cu:Fe ratio and therefore changes in the manner of their distribution between corresponding crystallographic positions. A peculiar profile of the peak (220), namely broadening of the pedestal, is typical of samples in zone II with the boundary part of the 0.96 sample. Since this peculiarity can be caused by various local structure distortions, reliability of X-ray diffraction data was ensured by the results of the DD method, which performs also the phase analysis through differential dissolution of the representative specimens. Kinetic curves of the Cu, Fe, and S elements dissolution of the 1.0 sample shows only one peak and the Cu:Fe

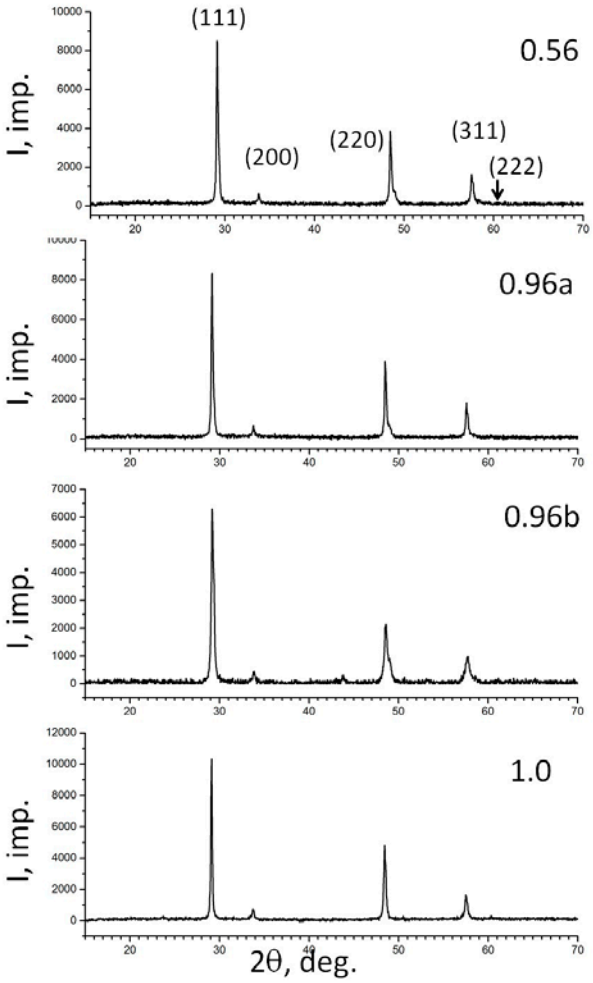

Fig. 5. Difractograms of powder samples 0.56, 0.96a, 0.96b and 1.0

Table 2. Structural parameters of samples 0.56, 0.96 and 1.0

	111	200	220	311*
Sample 0.56 (a = 5.307 Å)				
2q	29.126	33.757	$48.470_{дв}$**	57,549
d_{exp}, Å	3.063	2.653	1.877	1.600
FWHM, °	0.18	0.19	0.19	0.21
Sample 1.0 (a = 5.312 Å)				
2q	29.089	33.719	48.422	57.498
d_{exp}, Å	3.067	2.656	1.878	1.602
FWHM, °	0.13	0.20	0.20	0.24
Sample 0.96a (a = 5.307 Å)				
2q	29.121	33.738	$48.478_{дв}$**	57.555
d_{exp}, Å	3.064	2.655	1.876	1.600
FWHM, °	0.17	0.19	0.17	0.18
Sample 0.96б (a = 5.298 Å)				
2q	29.197	33.802	$48.570_{дв}$**	57.659
d_{exp}, Å	3.056	2.649	1.873	1.597
FWHM, °	0.29	0.29	0.44	0.54

* Line used for determination of the unit cell parameter. ** Double line.

stoichiogram is linear, equals 0.84 and remains constant during the full dissolution of the sample. The quantities of Cu and Fe together with the S quantity, gives a chemical formula $CuFe_{1.19}S_2$ of this spatially homogeneous phase with the content of 94±4 wt. % (Fig. 6b). The 0.96 sample dissolves also as a single phase with the content of 92±4 wt. %. However, the kinetic curve of the elements dissolution demonstrates three peaks, and a linear Cu:Fe stoichiogram gradually changes the initial value 0.85 to 0.81 at the end of the dissolution process (Fig. 6a). The deduced composition as $CuFe_{1.20\text{-}1.23}S_2$ reflects the chemical inhomogeneity of this phase caused by blocks of various compositions. Sample 0.56 has another bulk composition ($CuFe_{1.78}S_{2.7}$) and dissolves in a different manner. Its kinetic curves have several peaks, and Cu:Fe stoichiogram involves two linear fragments of various length: the first fragment, plotted on 30 experimental points, was $Cu_{0.8\pm0.1}Fe_1$, the second, $Cu_{0.47\pm0.04}Fe_1$ was plotted on 114 points (Fig. 7a). Both fragments, recalculated into chemical formula, indicate the presence of the stoichiometric cubanite as main phase (83 wt. %) and stoichiometric chalcopyrite as impurity nanoparticles (13 wt. %), i.e. an ordered structure. Here, composition is a reliable dignostic sign of the phase for the chalcopyrite nanoparticles, but the DD method cannot determine the size, shape, and the particle–matrix interface. However, location of the chalcopyrite peak inside the cubanite peak on the kinetic curves and the observed chemical variability of each portion of the solution, dissolving thin surface layer of the sample, mean that chalcopyrite particles are uniformly dispersed in the cubanite matrix.

Summarized diagnostic data of the samples 0.56, 0.96, and 1 allowed to present the sequence of the solidified melt transformations under cooling conditions. Sample 1.0 with a bulk composition $CuFe_{1.19}S_{2.04}$ crystallized from the melt with a ratio Cu/Fe = 0.71 and rather quickly cooled down at temperatures close to 930 °C; according to the spatial resolution of the used diagnostic methods, it is a uniform, chemically and structurally homogeneous phase based on $CuFeS_2$ with composition moved towards $CuFe_2S_3$ by 5 mol. % within the homogeneity range. At a higher resolution, a quasi-homogeneous state with associations can be found. Earlier, when the cubic chalcopyrite had not yet been identified, the homogeneous state of $0.7{\cdot}CuFeS_2 + 0.3{\cdot}CuFe_2S_3$ at high temperatures was identified as a tetragonal chalcopyrite phase enriched with iron [25]. This means that studying the mechanisms of solid-phase transformations of Cu-Fe sulfide phases presents severe problems caused by the lack of key data for correctly interpret thin phase and chemical changes.

Sample 0.96 of the bulk composition $CuFe_{1.21}S_{2.07}$ with chemically different domains that are not registered on diffraction patterns, demonstrates the initial stage of the ordering process with Cu and Fe cations, occupying topologically inequivalent positions in the cubic structure. According to the kinetic diagram

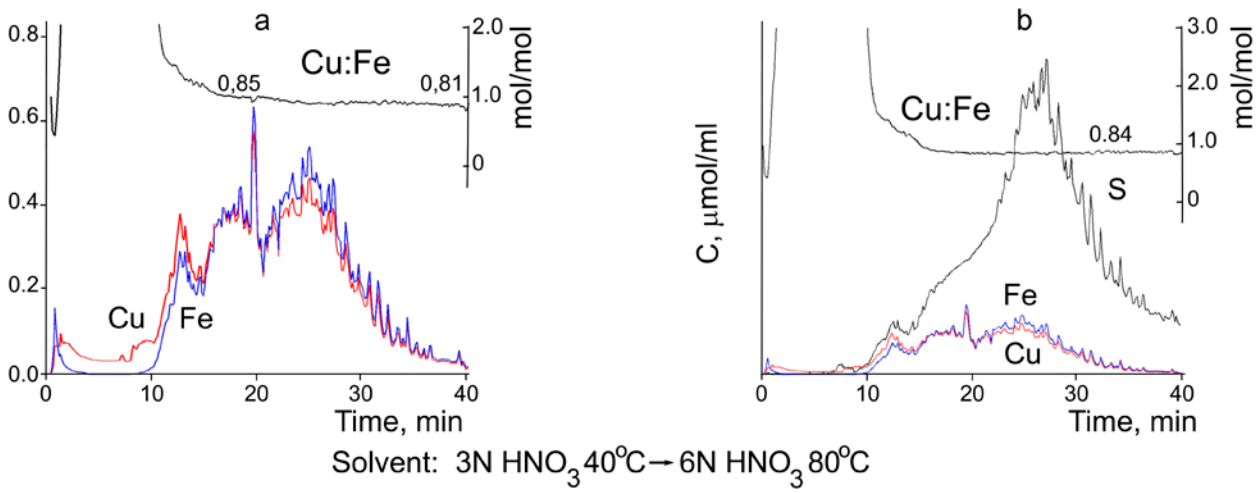

Fig. 6. Kinetic curves of Cu, Fe, S elements dissolution for samples 0.96 (a) and 1.0 (b)

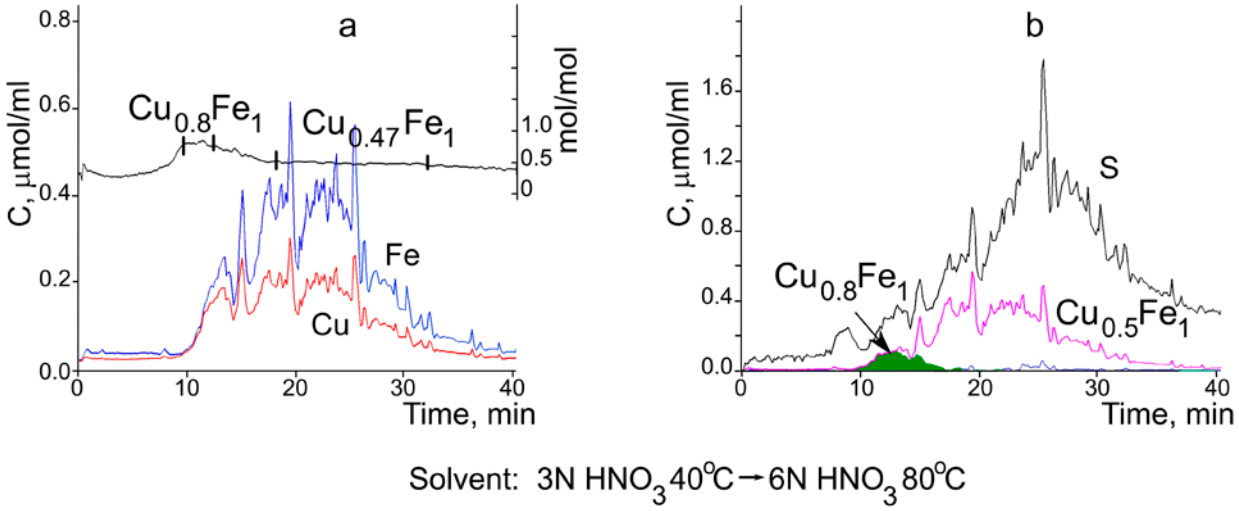

Fig. 7. Kinetic curves of Cu, Fe, S elements dissolution and linear dashes fragments of stoichiograms Cu:Fe (a); kinetic curves of chalcopyrite and cubanite dissolution (b)

(Fig. 3), formation of this state took a long period of time required for the migration of cations through the sulfide lattice. This is the early stage of decomposition of the solid solution, which is usually allusive and cannot be detected due to small-scale changes of this homogeneous solid solution. This stage is associated with the ordering of cations without changing the structure, but with altering the bonds length depending on the distribution of multi-charge cations with similar radii (Cu_4^{+1} = 0.74Å, Fe_4^{+3} = 0.77Å). The changes in the lattice parameter of sample 0.96 relative the parameter of sample 1.0 are demonstrated in Table 2. Finding the early ordering stage is of crucial importance, because a new internal structural arrange of the ordered state forms also other physico-chemical properties and thus other characteristics of the polymorphic transition from cubic chalcopyrite to tetragonal.

Sample 0.56, homogeneous in its reflectivity and diffraction properties, is heterogeneous at micro level according to the DD results: the cubanite matrix contains low-dimensional chalcopyrite clusters occurring in specific lattice centers. According to a TEM experiment, the size of such dispersed formations exsoluted from cubanite during its cooling from the highest temperatures is several nm [3, 15]. In our experiment, the small size of the clusters indicated the inhibition of the nucleation and growth processes. That is why the SEM experiment did not reveal any signs of decomposition of the solid solution in all the samples of the II zone, even those that were cooled for a long time at lower temperatures, Fig. 4. These clusters escape detection by X-ray diffraction, but their appearance caused changes in the interplanar distances resulting in a broadening of the peak (220). The nature of the peak broadening was discussed in [8, 9, 14, 26, 27]. Most authors agree that this phenomenon is associated with the formation of intergrowth structures of cubanite with chalcopyrite: the peak with d = 1.862, which is characteristic for pure cubanite, is laid over a peak with d = 1.878, corresponding to the intergrowth structure. We believe that clusters of cubic chalcopyrite form tense microstructures with the cubic matrix, thus increasing the unit cell volume. This metastable state remains even after long-term annealing at 400 °C, i.e. in the field of stability of tetragonal chalcopyrite, Fig. 4f. The stability of this solid solution is also confirmed by two other well-known facts: adding cubanite to chalcopyrite reduces the temperature of its polymorphic transition from 570 to 400 °C [26]; kinetic inhibition of the reconstructive polymorphic transition of chalcopyrite proceeds very slowly and gradually following the ordering of the cubic structure and desymmetrization of type $F\bar{4}3m \rightarrow P\bar{4}3m \rightarrow I\bar{4}3m \rightarrow P\bar{4}2m$ [12].

As a result, we obtained justified and agreed data regarding the early decomposition stages of

the $Cu_{1.1}Fe_{1.9}S_{3.0}$ solid solution. The decomposition is initiated by cationic ordering with the formation of domains with various compositions and internal structural arrange without interrupting the interface surface. This is followed by the decomposition and formation of a nanostructure of two coexisting cubic phases of chalcopyrite and cubanite, which is stable over a wide temperature range, metastable, and apparently coherent.

4. Conclusions

In this article, we suggested a new methodological approach for solving a complex task of determining nature of the initial stages of transformations of the intermediate phase $Cu_{1.1}Fe_{1.9}S_{3.0}$ of cubic solid solution during cooling. In our experiment, we focused on the development of diagnostic methods that can determine the texture changes, composition, and structure of the samples with a high spatial resolution in function of thermodynamic and kinetic cooling conditions. This allowed us to understand the process, which includes stages of cationic ordering followed by the formation of a metastable solid solution of nanosized clusters of cubic chalcopyrite in the cubic cubanite matrix. The identification of the two phases with different compositions determining the properties of the solid solution is an important result, which can facilitate the development of new magnetic sulfide nanomaterials and can be used for the processing of Cu-Fe sulfide ores.

Author contributions

I. G. Vasilyeva – methodology development, research concept, conducting research, text writing and editing, final conclusions. E. F. Sinyakova – methodology development, conducting experiments, results description, text editing. S. A. Gromilov – conducting X-ray diffraction analysis and interpreting the results, text writing.

Conflict of interests

The authors declare that they have no known competing financial interests or personal relationships that could have influenced the work reported in this paper.

References

1. Lyubutin I. S., Lin C.-R., Starchikov S. S., ... Wang S.-C. Synthesis, structural and magnetic properties of self-organized single-crystalline nanobricks of chalcopyrite $CuFeS_2$. *Acta Materialia*. 2013;61(11): 3956–3962. https://doi.org/10.1016/j.actamat.2013.03.009

2. Lyubutin I. S., Lin C.-R., Starchikov S. S., Siao Y.-J., Tseng Y.-T. Synthesis, structural and electronic properties of monodispersed self-organized single crystalline nanobricks of isocubanite $CuFe_2S_3$. *Journal of Solid State Chemistry*. 2015;221: 184–190. https://doi.org/10.1016/j.jssc.2014.10.006

3. Starchikov S. S. *Magnetic, structural and electronic properties of nanoparticles of iron sulfides and oxides with different crystal structure*[*]. Cand. of (phys.–math.) sci. diss. Abstr. Moscow: Nauka Publ.; 2015. 18 p. (In Russ.). Available at: https://www.crys.ras.ru/dissertations/Starchikov/Starchikov_avtoref.pdf

4. Putnis A., McConnel J. D. C. *Principle of mineral behavior*. Oxford-London-Edinburg-Boston-Melbourne: Blackwell Scientific Publications; 1980, 272 p.

5. Vaughan D. J., Craig J. R. *Mineral chemistry of metal sulfides*. Cambridge, UK: Cambridge Earth Science Series; Cambridge University Press: 1978, 493 p.

6. Sulfide mineralogy and geochemistry. D. J. Vaughan (ed.), Volume 61 in the series *Reviews in Mineralogy & Geochemistry*. https://doi.org/10.1515/9781501509490

7. Berger E. L., Keller L. P., Lauretta D. S. An experimental study of the formation of cubanite ($CuFe_2S_3$) in primitive meteorites. *Meteoritics and Planetary Science*. 2015;50: 1–14. https://doi.org/10.1111/maps.12399

8. Cabri L. J., Hall S. R., Szymanski J. T., Stewart J. M. On the transformation of cubanite. *Canadian Mineralogist*. 1973;12: 33–38.

9. René C., Cervelle B., Cesbron F., Oudin E., Picot P., Pillard F. Isocubanite, a new definition of the cubic polymorph of cubanite $CuFe_2S_3$. *Mineralogical Magazine*. 1988;52: 509–514. https://doi.org/10.1180/minmag.1988.052.367.10

10. Yund R. A., Kullerud G. Thermal stability of assemblages in the Cu-Fe-S system. *Journal of Petrology*. 1966;7: 454 – 488. https://doi.org/10.1093/petrology/7.3.454

11. Pruseth K. L., Mishra B., Bernhardt H. J. An experimental study on cubanite irreversibility: implications for natural chalcopyrite–cubanite intergrowths. *European Journal of Mineralogy*. 1999;11(3): 471–476. https://doi.org/10.1127/ejm/11/3/0471

12. Putnis A., McConnel J. D. C. The transformation behavior of metal-enriched chalcopyrite. *Contributions of Mineralogy and Petrology*. 1976;58: 127–136. https://doi.org/10.1007/bf00382181

13. Putnis A. Talnakhite and Mooihoekite: the accessibility of ordered structures in the metal-rich region around chalcopyrite. *Canadian Mineralogist*. 1978;16: 23–30.

14. Engin T. E., Powel A. B, Hull S. A high temperature diffraction-resistance study of chalcopyrite $CuFeS_2$. *Journal of Solid State Chemistry*. 2011;184: 2272–2277. https://doi.org/10.1016/j.jssc.2011.06.036

15. Putnis A. Electron microscope study of phase transformations in cubanite. *Physics and Chemistry of Minerals*. 1977;1: 335–349. https://doi.org/10.1007/bf00308844

16. Kosyakov V. I. Possible usage of directional crystallization for solving petrological problems. *Russian Geology and Geophysics*. 1998;39(9): 1245–1256.

17. Kosyakov V. I, Sinyakova E. F. Directional crystallization of Fe–Ni sulfide melts within the crystallization field of monosulfide solid solution. *Geochemistry International*. 2005;43(4): 372–85.

18. Kosyakov V. I., Sinyakova E.F. Melt crystallization of $CuFe_2S_3$ in the Cu–Fe–S system. *Journal of Thermal Analysis and Calorimetry*.2014;115: 511-516. https://doi.org/10.1007/s10973-013-3206-0

19. Kosyakov V. I., Sinyakova E. F. A. Study of crystallization of nonstoichiometric isocubanite $Cu_{1.1}Fe_{2.0}S_{3.0}$ from melt in the system Cu–Fe–S. *Journal of Thermal Analysis and Calorimetry*. 2017;129(2): 623–628. https://doi.org/10.1007/s10973-017-6215-6

20. Vasilyeva I. G., Sinyakova E. F., Gromilov S. A. Structural and chemical transformations of isocubanite $CuFe_2S_3$ at cooling from melt*. *Journal of Structural Chemistry = Zhurnal Strukturnoi Khimii*. 2024;65: 127132. (In Russ.). https://doi.org/10.26902/jsc_id127132

21. Malakhov V. V., Vasilyeva I. G. Stoichiography and chemical methods of phase analysis of multielement multiphase substances and materials. *Russian Chemical Reviews*. 2008;77(4): 351–372. https://doi.org/10.1070/RC2008v077n04ABEH003737

22. Malakhov V. V., Vasilyeva I. G. Stoichiography: evolution of solid-phase reactions. New principles of research, preparation and characterization of functional materials*. Novosibirsk: Siberian Branch of Russian Academy of Sciences Publ.; 2023. 251 c. (In Russ.)

23. Inorganic crystal structure database. D–1754. Eggenstein–Leopoldshafen: Germany. 2022.

24. Kraus W., Nolze G. POWDER CELL – a program for the representation and manipulation of crystal structures and calculation of the resulting X-ray powder patterns. *Journal of Applied Crystallography*. 1996;29: 301–303. https://doi.org/10.1107/s0021889895014920

25. Cabri L. J., Hall S. R., Szymanski J. T., Stewart J. M. On the transformation of cubanite. *Canadian Minerologist*. 1973;12: 33–38.

26. Dutrizac J. E. Reactions in cubanite and chalcopyrite. *Canadian Minerologist*. 1976; 14, 172–18

** Translated by author of the article*

Information about the authors

Inga G. Vasilyeva, Dr. Sci. (Chem.), Leading Research Fellow of Nikolaev Institute of Inorganic Chemistry Siberian Branch of RAS (NIIC SB RAS) (Novosibirsk, Russian Federation).
https://orcid.org/0000-0003-4045-9820
kamars@niic.nsc.ru

Elena F. Sinyakova, Dr. Sci. (Geol.–Min.), Leading Research Fellow of Sobolev Institute of Geology and Mineralogy of SB RAS (Novosibirsk, Russian Federation).
https://orcid.org/0000-0001-6288-3425
efsin@igm.nsc.ru

Sergey A. Gromilov, Dr. Sci. (Phys.–Math.), Leading Research Fellow, Nikolaev Institute of Inorganic Chemistry Siberian Branch of RAS (Novosibirsk, Russian Federation).
https://orcid.org/0000-0003-1993-5159
grom@niic.nsc.ru

Received 21.06.2024; approved after reviewing 31.07.2024; accepted for publication 16.09.2024; published online 25.12.2024.

Translated Yulia Dymant

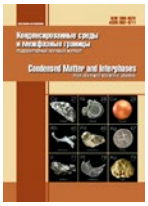

ISSN 1606-867X (Print)
ISSN 2687-0711 (Online)
Condensed Matter and Interphases
Kondensirovannye Sredy i Mezhfaznye Granitsy
https://journals.vsu.ru/kcmf/

Original articles

Research article
https://doi.org/10.17308/kcmf.2024.26/12435

Physicochemical study of the processes of β-cyclodextrin hydrates dehydration

L. N. Zelenina[1, 2]✉, T. V. Rodionova[1], T. P. Chusova[1], A. V. Sartakova[1,2], A. Yu. Manakov[1]

[1]*Nikolaev Institute of Inorganic Chemistry of the Siberian Branch of the Russian Academy of Sciences, 3 Lavrent'ev ave., Novosibirs 630090, Russian Federation*

[2]*Novosibirsk State University, 2 Pirogova st., Novosibirsk 630090, Russian Federation*

Abstract

The research involved synthesizing β-cyclodextrin hydrates of the β-CD·nH$_2$O (n = 11.9–0.9) composition.

The obtained compounds were studied by powder X-ray diffraction (XRD), which revealed the transition from a monoclinic unit cell to an orthorhombic one with a decrease in the water content in the samples. The pressure of saturated vapor of the water in the β-CD·nH$_2$O (n = 10.6–7.0) hydrates was measured by static tensimetry with membrane null-manometer over a wide temperature range (293–384 K) under conditions of a quasi-constant hydrate composition. The measured vapor pressure increases in proportion to the increase in the water content of the hydrate samples.

The experimental data reduced to a single composition of β-CD·1H$_2$O were approximated by the ln$p$(1/T) equation, from which the thermodynamic parameters ($\Delta_{pr}H^\circ_T$ and $\Delta_{pr}S^\circ_T$) of the process of β-cyclodextrin hydrate dehydration were calculated. This information was used to estimate the binding energies of the water molecules to the β-CD framework.

Keywords: β-cyclodextrin hydrates, PXRD, Static tensimetry, Saturated vapor pressure, Dehydration enthalpy and entropy

***Funding*:** The study was supported by the grant of the Russian Science Foundation (project No. 24-23-00237).

For citation: Zelenina L. N., Rodionova T. V., Chusova T. P., Sartakova A. V., Manakov A. Yu. Physicochemical study of the processes of β-cyclodextrin hydrates dehydration. *Condensed Matter and Interphases*. 2024;26(4): 716–724. https://doi.org/10.17308/kcmf.2024.26/12435

Для цитирования: Зеленина Л. Н., Родионова Т. В., Чусова Т. П., Сартакова А. В., Манаков А. Ю. Физико-химическое исследование процессов дегидратации гидратов β-циклодекстринов. *Конденсированные среды и межфазные границы*. 2024;26(4): 716–724. https://doi.org/10.17308/kcmf.2024.26/12435

✉ Lyudmila N. Zelenina, e-mail: zelenina@niic.nsc.ru

1. Introduction

The macromolecules of cyclodextrins (CDs) consist of glucopyranose units interconnected by α-1,4-glycosidic bonds. Among the most studied and widely used cyclodextrins are α-, β-, and γ-cyclodextrins consisting of 6, 7, and 8 glucopyranose units. The shape of the resulting macromolecule is described as a truncated cone with a hydrophobic interior cavity and a hydrophilic outer surface. Due to their structure, cyclodextrins form inclusion compounds (complexes) with numerous guest molecules that can be fully or partially incorporated into the cyclodextrin cavity. Due to the ability of cyclodextrins to change the physicochemical properties of the incorporated guest molecules, i.e. thermal stability, volatility, solubility, resistance to oxidation, visible and UV radiation, and, most importantly, due to their non-toxicity, these compounds are widely used in pharmaceutics [1–3], food [4, 5] and cosmetic [6, 7] industries, analytical chemistry [8], catalysis [9–12], separation of mixtures [13-15], agrochemistry [16], etc. The history, structures, properties, and various application areas of cyclodextrins and their inclusion complexes are described in several recent reviews [17–19].

Since cyclodextrins in the solid state always contain water molecules (inside their cavity and in the intermolecular space), the process of forming cyclodextrin complexes consists in the partial or complete substitution of water molecules with other guest molecules. Therefore, it is important to know the thermodynamic characteristics of the processes of cyclodextrin dehydration. β-cyclodextrin is one of the most popular cyclodextrins. Its overall production exceeds all other cyclodextrins, and, judging by the number of published articles, this cyclodextrin is the most studied. Despite a huge number of studies, there is hardly any information on thermodynamic characteristics that allow estimating the binding energy of water in β-cyclodextrin hydrates. It is known that in the structures of cyclodextrin hydrates, one part of the water molecules fills the cavity of the macromolecule, and the other part connects the macromolecules to each other with hydrogen bonds. First X-ray diffraction studies determined the structures of two β-cyclodextrin hydrates crystallizing from aqueous solutions: β-CD (β-CD·12H_2O) dodecahydrate [20] and β-CD (β-CD·11H_2O) undecahydrate [21]. Both are cell type structures, the differences are mainly in the distribution of water molecules between the cavity and the intermolecular space: in the β-CD·12H_2O, there are 6.5 H_2O molecules in the cavity and 5.5 H_2O in the intermolecular space, while in β-CD·11H_2O, this distribution is 6.13 H_2O and 4.88 H_2O, respectively. Later, another isomorphic structure of the β-CD·7.5H_2O hydrate was found [22], in which one H_2O molecule is incorporated in the cavity, and the remaining 6.5 are distributed in the intermolecular space. The β-CD hydrate in contact with the mother solution has a composition of ~ β-CD·12H_2O, however, at room temperature and ~ 50% humidity, its composition changes to β-CD·10.5H_2O and the process is reversible [23]. The study of the structures of β-CD hydrates [24] at different humidity levels showed that with a decrease in humidity from 100 to 15%, the process of the hydrate dehydration from the composition of β-CD 12.3H_2O to β-CD·9.4H_2O is fast (it takes minutes), continuous, reversible, and proceeds mainly due to the loss of water from the inner cavity of the β-CD macromolecule. The structure is preserved up to a moisture content of 15%, however, there is a slight decrease in the volume of the unit cell. NMR spectroscopy data [25] also indicated the non-stoichiometric nature of β-CD hydrates in the β-CD 10.5H_2O – β-CD·12H_2O interval. The study of dehydration by powder diffraction (PXRD), thermogravimetric analysis (TGA), and differential scanning calorimetry (DSC) showed [26] that the hydrated phase of β-CD remains thermodynamically stable up to about β-CD·2H_2O at room temperature and higher. Dehydration of β-CD·11H_2O hydrates is described as a single-stage process in the temperature range of 50–110 °C [27] and 64–100 °C [28]. It takes one stage for β-CD hydrates with β-CD·11.3H_2O, β-CD·10.5H_2O, β-CD·10H_2O (commercial sample) compositions to lose water in the range of 40–80 °C [29]. The thermal behavior of the β-CD·11H_2O commercial sample studied by the TGA and DSC methods (from –150 to 300 °C) indicates a two-stage dehydration process: 7 moles of H_2O are lost during the first stage and 4 moles during the second stage [30]. In the same study, the enthalpy of the β-CD·11H_2O hydration was determined

by the method of dissolution calorimetry at 25 °C, which was −102.8 ± 1.1 kJ/mol for the process of β-CD(s) + $11H_2O$(l) = β-CD·$11H_2O$(s). The specific enthalpy of the dehydration of the β-CD·$11H_2O$ calculated from the experimental curves obtained by the method of simultaneous thermogravimetric and differential analysis in [31] for the β-CD·$11H_2O$(s) = β-CD(s) + $11H_2O$(l) process was 40±2 kJ/ mol at T = 100 °C. As can be seen from the above review, the data obtained in previous studies can be contradictory and the available thermodynamic characteristics are not enough for quantitative estimation of the dehydration processes of β-cyclodextrin hydrates.

In this paper, the dehydration processes of β-CD hydrates were studied by powder X-ray diffraction (PXRD) and by static tensimetry with membrane null-manometer over a wide temperature range (293–384 K). As shown in our previous work on the study of α-cyclodextrin hydrates [32], measuring vapor pressure during dehydration by static tensimetry allows characterizing this process and obtaining its quantitative thermodynamic characteristics.

2. Experimental

2.1. Materials

The experiments were conducted on β-cyclodextrin (Wacker Fine Chemicals, β-CD Cavamax WG7 Pharma, mass fraction of the dry main substance ⩾ 0.98). The hydrate with the highest water content (β-CD 11.9H_2O) was obtained by recrystallization from distilled water (⩾ 0.9999). Samples with a lower water content were obtained by drying the resulting hydrate in a desiccator over P_2O_5. The composition of the sample was controlled by weight. After the samples reached the required composition, they were kept for several days in a hermetically sealed container to achieve equilibrium.

2.2. Diffraction experiments

Diffraction experiments were performed on a Bruker D8 Advance diffractometer (Cu$K\alpha$ radiation, λ = 1.5418 Å). Samples were mixed with ~ 10 vol. % of finely ground silicon powder, which was used as the internal standard. Powder diffraction patterns were recorded at 20 °C. The parameters of the unit cell of the hydrate were refined for all clearly visible reflexes in the range of angles 3–28°. The CHEKCELL software was used for the refinement of cell parameters [33]. Powder patterns were indexed using the WinPLOTR package [34].

2.3. Static tensimetry

The temperature dependence of the pressure of the water vapor of the β-CD·nH_2O (n = 10.9; 9.6; 7.0) hydrates was measured by static tensimetry using a Novikov-Suvorov glass (pyrex) null manometers [35]. The experimental unit was described in detail in our previous works [36–38]. The pressure was measured to a precision of 0.4 Torr with due account of the error compensation, the cathetometer measurement error, and the inaccuracies associated with the irreversible temperature drift of the null position. The temperature accuracy estimated from the results of the thermocouple (Pt-Pt10Rh) calibration by mercury and naphthalene was 0.3 °C. The error of maintaining a constant temperature in the 3-zone furnace of the unit was 0.1 °C, the radial and linear temperature gradients in the working cell of the manometer did not exceed 0.5 °C. The volume of the working cell of the manometer was determined with an accuracy of 10^{-1} cm^3 by weighing an empty manometer and a manometer filled with water. A weighed hydrate sample (±10^{-4} g) was put into the chamber of the null-manometer and pumped out for 1–2 min at room temperature under dynamic vacuum (10^{-2} Torr); the gauge was then disconnected from the vacuum system by a gas burner and placed into the furnace of the unit. The pressure values were recorded after the coincidence of two or three measurements with an interval of 15 to 20 minutes at a fixed temperature. Experimental pressures measured at the same temperature during both heating and cooling of the manometer were consistent within the reduced measurement errors, which is the criterion for obtaining equilibrium data.

The conditions of the experiments are given in Table 1. The ratio of the mass of the sample to the volume of the working cell (m_{water}/V) was chosen so that the composition of the condensed phase could be considered as quasi-constant: the loss of water in the β-CD·nH_2O samples at the maximum temperature of the experiment varied from 0.97 to 3.64% of the total amount of water (Table 1).

Table 1. Conditions for tensimetric experiments with β-CD·nH_2O: n is the number of moles of water per mole of β-CD, m is the mass of the weighed portion of the sample, m_{water} is the mass of the water in the sample, V is the volume of the manometer

Experiment number	n	m, г	m_{water}, g	m_{water}/V, g/l	Water loss at T_{max}, %
1	10.9	1.0156	0.1498	16.53	2.28
2	9.6	1.3995	0.1846	13.54	3.64
3	7.0	2.7021	0.2700	44.26	0.97

Table 2. Parameters of unit cells and volumes of unit cells for the main samples of β-CD hydrate with different compositions

Samples	sp. gr.	a, Å	b, Å	c, Å	b, deg.	V, Å^3
β-CD·11.9H_2O (1)	$P2_1$	20.874(16)	10.176(4)	15.147(17)	111.04(7)	3003(4)
β-CD·11.9H_2O (2)	$P2_1$	21.286(60)	10.256(16)	15.048(46)	112.33(28)	3039(15)
β-CD·10.0H_2O (1)	$P2_1$	20.845(25)	10.201(5)	15.141(17)	110.75(12)	3011(7)
β-CD·10.0H_2O (2)	$P2_1$	21.185(63)	10.200(12)	15.158(45)	112.19(29)	3033(15)
β-CD·0.9H_2O	орт.*	26.422(5)	16.082(5)	12.521(3)	–	5318

* orthorhombic unit

3. Results and discussion

3.1. XRD experiments

Powder diffraction patterns of seven β-CD·nH_2O hydrate samples with different water content (n = 11.9-0.9) were recorded. The obtained powder diffraction patterns are shown in Fig. 1.

Powder diffraction patterns of β-CD·11.9H_2O and β-CD·10.0H_2O samples were indexed in a monoclinic unit cell (variant (1) in Table 2).

The obtained parameters of the cells were close to those described in [24] for compositions synthesized at a humidity of ⩾ 50%. Nevertheless, the unit cell parameter a and the monoclinic angle obtained during indexing were respectively 2% and 1° less than those reported in the cited work. Using the values given in [24] as the starting parameters resulted in slightly large errors in the refined parameters of the cell (variant (2) in Table 2). Overall, the coincidence between the obtained powder diffraction patterns and those obtained during previous research [24] can be considered satisfactory. For the β-CD·7.9H_2O and β-CD·6.1H_2O samples, the general view of the powder patterns differed little from those discussed above. The main difference was the appearance of several weak additional reflexes, most likely related to the dehydrated phase. Overall, it can be stated that for β-CD·nH_2O in the

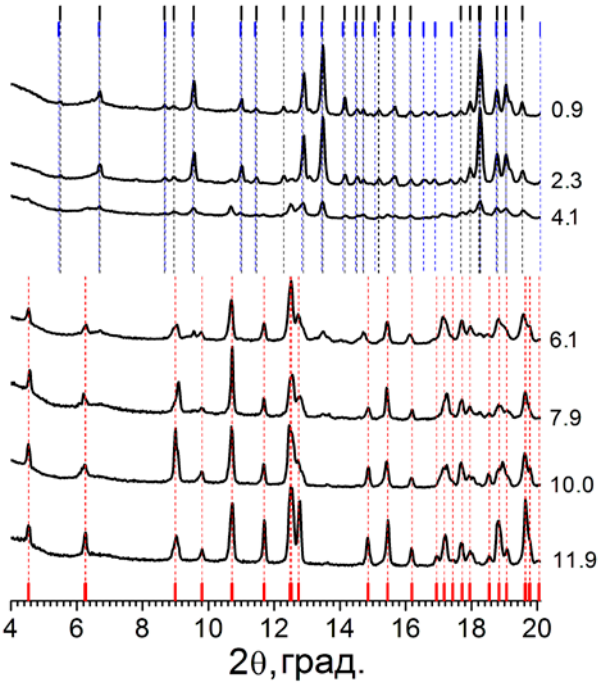

Fig. 1. Powder diffraction patterns of β-CD·nH_2O hydrate samples. The values of n for the corresponding samples are given to the right of the curves. The red strokes and lines correspond to the expected positions of the reflexes calculated for the β-CD·11.9H_2O sample (variant (1) in Table 2). The blue strokes and lines correspond to the positions of the dehydrated β-CD, according to data in [39]. Black strokes and lines correspond to the positions of the reflexes calculated for the β-CD·0.9H_2O sample

range of compositions of n = 11.9-6.1, the hydrate structure changed insignificantly. It was slightly wider than the homogeneity range n = 10.5–12.0 previously reported in [25].

It is known [20, 24] that inside the cavity of β-CD·12H_2O there are about 6.5 water molecules. It can be assumed that the change in compositions in the range of n = 11.9–6.1 occurred due to the removal of intracavitary water, which did not lead to a change in the packing of cyclodextrin molecules. With the further removal of water, the intensity of the peaks on the powder patterns dropped sharply and the peaks expanded. The quality of the powder patterns deteriorated sharply (powder pattern of the β-CD·4.1H_2O sample in Fig. 1). The changes can be attributed to hydrate amorphization. Two samples with a minimum water content, β-CD·2.3H_2O and β-CD·0.9H_2O, had almost identical powder patterns (Fig. 1), which were indexed in the orthorhombic crystal system (Table 2). We failed to find detailed crystallographic data for anhydrous β-CD in previous publications. However, [39] provides an unprocessed powder pattern for an anhydrous sample. We found that the position of the main peaks in this powder pattern was well matched to our data (Fig. 1). Thus, the study of powder diffraction patterns of samples of β-CD·$n$$H_2O$ hydrates showed that the loss of water from the inner cavity of the cyclodextrin molecule to a composition with n = 6.1 did not lead to a change in the appearance of the powder diffraction pattern, i.e. there were no significant changes in the structure of the hydrate. Further loss of water led first to partial amorphization of the hydrate, and then to the formation of a new crystalline phase, with a structure which, apparently, corresponded to the anhydrous β-CD. Indexing of the powder pattern of this phase showed that it most likely belonged to the orthorhombic crystal system.

3.2. Measuring the vapor pressure of water

Three experiments were conducted to measure the temperature dependence of the saturated vapor pressure of water in the studied hydrates by static tensimetry with membrane null-manometers. The obtained data are shown in Fig. 2a in the lg p–1000/T coordinates.

It can be seen from the figure that the experimental data for different compositions of β-CD·$n$$H_2O$ lie parallel to each other. When reduced to a single composition of β-CD·1H_2O ($p_n = p/n$), the experimental data coincided (Fig. 2b), as was observed in our study of α-CD hydrates [32]. Such a coincidence is possible only if the water-β-CD bond is the same in terms of energy for different compositions.

The data reduced to the β-CD·1H_2O composition (38 experimental points) were processed by the method of least squares using the criterion function described in detail in our papers [40–41]:

$$\psi = \sum_{i=1}^{N}\sum_{j=1}^{ni}\left[p_{\mathrm{e}}^{(ij)} - p_{\mathrm{p}}^{(ij)}\right]^2 / W_{ij},$$
$$W_{ij} = \Delta p_{ij}^2 + \left(\frac{dp}{dT}\right)_{ij}^2 \Delta T_{ij}^2, \quad (1)$$

where N is the number of experiments; n_i is the number of experimental points in the jth expe-

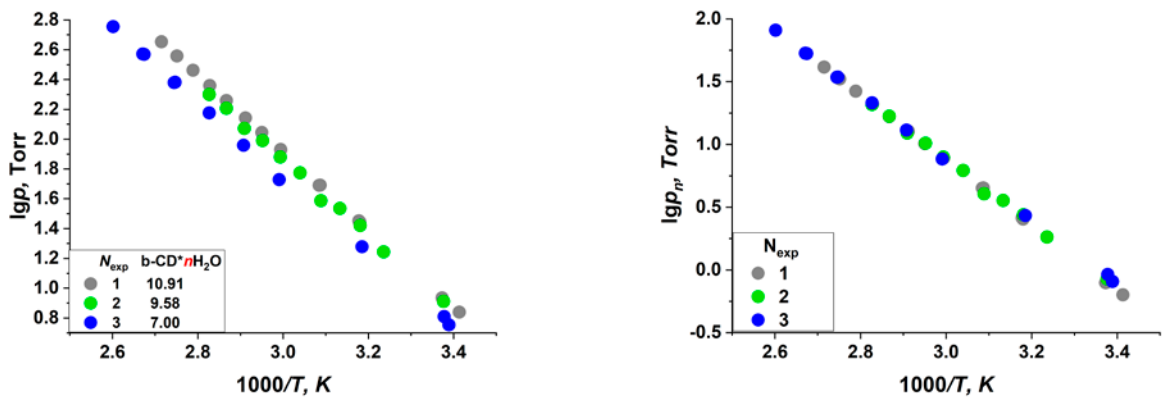

a b

Fig. 2. (a) Experimental data in the lg p – 1000/T coordinates for β-CD·$n$$H_2O$, where n = 7.0; 9.6; 10.9. (b) Temperature dependence of saturated vapor pressure for β-CD·1H_2O, where $p_n = p/n$

riment; $p_e^{(ij)}$ is the experimentally measured pressure; $p_p^{(ij)}$ is the pressure calculated using the isotherm equation; and W_{ij} is the weight function taking into account the pressure and temperature errors. The criterion function ψ uses the principle of maximum likelihood in the method of least squares to estimate the thermodynamic parameters of the process.

The parameters sought were the enthalpy and entropy of the dehydration process at an average temperature since there were no data on the β-CD·1H_2O heat capacity. The minimization of the criterion function (1) in the sought parameters space was carried out using a program that applied the algorithm of the modified Newton-Gauss method allowing for the choice of the step size and the direction.

The results of processed data are shown in Table 3. The uncertainties in the obtained values of $\Delta_{pr}H^\circ_{Tav}$ and $\Delta_{pr}S^\circ_{Tav}$ corresponded to a 95% confidence interval. The temperature dependence of the calculated pressure dispersion was described by the equation $\sigma^2 = a/T^2 - b/T + c$.

Deviations of experimental pressure values (p_n(exp.)) from those calculated by the equation from Table 3 (p_n(calc.)) did not exceed the errors of pressure and temperature measurements. The points were randomly scattered (Fig. 3), which indicated the absence of systematic errors in our study.

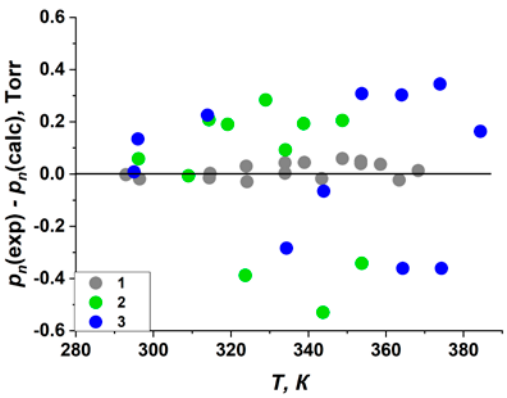

Fig. 3. The difference between the values of the experimental pressure (p_n(exp)) and the pressure calculated from the equation from Table 3 (p_n(calc)) for the process of β-CDH_2O dehydration

The obtained equation of temperature dependence of pressure (ln($p/p°$), Table 3) allowed calculating the vapor pressure of water over β-CD nH_2O at a given temperature T for any n from 7.0 to 10.9 by multiplying the vapor pressure value ($p/p°$) for $n = 1$ by the number of n moles of water in the β-CD·nH_2O hydrate:

$$p/p° = n \exp(A - B/T) \quad (2)$$

Fig. 4 shows the data obtained in this work and the data obtained earlier for α-CD·H_2O [32] in comparison with the process of water evaporation [42]. The saturated vapor pressure of pure water during the evaporation process was much higher

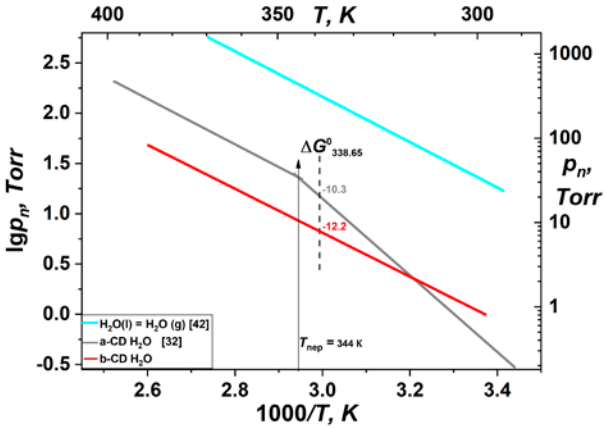

Fig. 4. Temperature dependences of the saturated vapor pressure of water in the processes of β-CD·H_2O, α-CD·H_2O dehydration [32], and the evaporation of pure water [42]. The values of the changes in the Gibbs energy ($\Delta G^\circ_{348.85}$/kJ·mol^{-1}) during the binding of 1 mole of gaseous water to 1 mole of solid α- or β-cyclodextrin are presented at the average temperature of the interval (T_{av} = 338.65 K) investigated in this work. The black arrow marks the temperature of solid-phase transition in α-CD hydrates

Table 3. Thermodynamic characteristics of the process of β-CD 1H_2O dehydration: temperature dependence of the saturated vapor pressure ln (p/p^o) ± 2σ = A – B/T, where p^o is the standard pressure of 1 atm; $\sigma^2 = f(T)$ is the dispersion of the calculated pressure; the enthalpy ($\Delta_{pr}H^o_{Tav}$) and entropy ($\Delta_{pr}S^o_{Tav}$) of the process at the average temperature of the studied interval (T_{av} = 338.65 K)

ΔT, K	ln ($p/p°$) = A – B/T; $\sigma^2 = a/T^2 - b/T + c$	$\Delta_{pr}H^o_{Tav}$ kJ/mol	$\Delta_{pr}S^o_{Tav}$ J K^{-1}·mol^{-1}
292.95–384.35	ln($p/p°$) ± 2σ =13.31 -5976/T; σ^2 = 396.3/T^2 - 2.200/T+0.0031	49.7±0.3	110.7±0.9

than the water pressure over the β-CD and α-CD hydrates. On the α-CD·H_2O dehydration line, there was a break that corresponded to a solid-phase transition in α-CD·H_2O hydrates [43]. In the β-CD·nH_2O hydrates, such a transition was not detected in the studied ΔT and Δn intervals.

The binding energy of water-β-cyclodextrin can be characterized by a change of Gibbs energy during the process of binding of 1 mole of gaseous water and 1 mole of solid β-CD:

$$\beta\text{-CD(s)} + H_2O(g) = \beta\text{-CD}\cdot H_2O(s),$$
$$\Delta G^\circ_T = -RT\ln(p/p^\circ). \quad (3)$$

The obtained thermodynamic data (Table 3) was used to estimate quantitatively the binding energy of the molecules of water and β-CD: $\Delta G^\circ_{338.65} = -12.2\pm0.3$ kJ/mol. In the case of α-CD H_2O [32], $\Delta G^\circ_{338.65} = -10.3\pm0.5$ kJ/mol (Fig. 4).

4. Conclusions

The method of X-ray diffraction was used to show that the monoclinic structure characteristic of β-CD·11.9H_2O hydrate is maintained over the range n = 6–11.9. When n < ~2, the powder diffraction patterns of the samples were indexed in the orthorhombic crystal system. For intermediate n, the samples were mixtures of the hydrates discussed above. The static tensimetry with membrane null-manometers was used to measure temperature dependences of the vapor pressure of water over β-CD·nH_2O (n = 10.9; 9.6; 7.0) under conditions of a quasi-constant hydrate composition. An analysis of the obtained dependences showed that the vapor pressure increases proportionally with increasing water content in the initial hydrate samples. The experimental data were used to calculate the thermodynamic parameters of the dehydration process. The equation for the $\ln p - 1/T$ dependence found in this work allows calculating the vapor pressure over β-CD-nH_2O hydrates in the studied temperature range for any value of n from 7.0 to 10.9. In addition, the results of the study can be used to quantitatively estimate the binding energy of water to β-CD molecules. Thermodynamic characteristics of dehydration processes were obtained for the first time and are valuable data not only for fundamental science, but also for the practical application of β-cyclodextrin hydrates.

Contribution of the authors

The authors contributed equally to this article.

Conflict of interests

The authors declare that they have no known competing financial interests or personal relationships that could have influenced the work reported in this paper.

References

1. Jambhekar S. S., Breen P. Cyclodextrins in pharmaceutical formulations I: structure and physicochemical properties, formation of complexes, and types of complex. *Drug Discovery Today*. 2016;21(2): 356–362. https://doi.org/10.1016/j.drudis.2015.11.017

2. Jansook P., Ogawa N, Loftsson T. Cyclodextrins: structure, physicochemical properties and pharmaceutical applications. *International Journal of Pharmaceutics*. 2018;535: 272–284. https://doi.org/10.1016/j.ijpharm.2017.11.018

3. Lachowicz M., Stańczak A., Kołodziejczyk M. Characteristic of cyclodextrins: their role and use in the pharmaceutical technology. *Current Drug Targets*. 2020;21: 1495–1510. https://doi.org/10.2174/1389450121666200615150039

4. Matencio A., Navarro-Orcajada S., García-Carmona F., Lopez-Nicolas J. M. Applications of cyclodextrins in food science. A review. *Trends in Food Science & Technology*. 2020;104: 132–143. https://doi.org/10.1016/j.tifs.2020.08.009

5. Gonzalez Pereira A., Carpena M., García Oliveira P., Mejuto J. C., Prieto M. A., Simal J. Gandara main applications of cyclodextrins in the food industry as the compounds of choice to form host-guest complexes. *International Journal of Molecular Sciences*. 2021;22(3): 1339. https://doi.org/10.3390/ijms22031339

6. Adeoye O., Figueiredo A., Cabral Marques H. Cyclodextrins and skin disorders: therapeutic and cosmetic applications. Chapter 13 In: *Carrier-mediated dermal delivery*. Ascenso A, Ribeiro H, Simões S (eds.). New York: Jenny Stanford Publishing; 2017. 586 p. https://doi.org/10.4324/9781315364476

7. Jicsinszky L., Cravotto G. Cyclodextrins in skin formulations and transdermal delivery. *Journal of Skin and Stem Cell*. 2019;6(4): e102561. https://doi.org/10.5812/jssc.102561

8. Szente L., Szeman J. Cyclodextrins in analytical chemistry: host–guest type molecular recognition. *Analytical Chemistry*. 2013;85(17): 8024–8030. https://doi.org/10.1021/ac400639y

9. Rousseau J., Menuel S., Rousseau C., Hapiot F., Monflier E. Chapter 2 - Cyclodextrins as porous material for catalysis. In: *Organic nanoreactors*. Elsevier Inc.; 2016. 582 p. https://doi.org/10.1016/B978-0-12-801713-5.00002-1

10. Bai C. C., Tian B. R., Zhao T., Huang Q., Wang Z. Z. Cyclodextrin-catalyzed organic synthesis: reactions, mechanisms, and applications. *Molecules*. 2017;22(9): 1475. https://doi.org/10.3390/molecules22091475

11. Dalal D. S., Patil D. R., Tayade Y. A. β-cyclodextrin: a green and efficient supramolecular catalyst for organic transformations. *The Chemical Record*. 2018;18(11): 1560–1582. https://doi.org/10.1002/tcr.201800016

12. Mitra B., Pariyar G. Ch., Ghosh P. β-cyclodextrin: a supramolecular catalyst for metal-free approach towards the synthesis of 2-amino-4,6-diphenylnicotinonitriles and 2,3-dihydroquinazolin-4(1*H*)-one. *RSC Advances*. 2021;11: 1271–1281. https://doi.org/10.1039/d0ra09562a

13. Wren S., Berger T. A., Boos K.-S., ... Stock R. The use of cyclodextrins as chiral selectors. In: Berger T. A., et al. *The separation of enantiomers by capillary electrophoresis*. *Chromatographia CE Series*. Wiesbaden: Vieweg+Teubner Verlag; 2001;6: 59–77. https://doi.org/10.1007/978-3-322-83141-5_5

14. Wang Y., Sun Y., Bian H., Zhu L., Xia D., Wang H. Cyclodextrin porous liquid materials for efficient chiral recognition and separation of nucleosides. *ACS Applied Materials & Interfaces*. 2020;12(41): 45916–45928. https://doi.org/10.1021/acsami.0c15836

15. Yu R. B., Quirino J. P. Chiral separation using cyclodextrins as mobile phase additives in open-tubular liquid chromatography with a pseudophase coating. *Journal of Separation Science*. 2022;45(6): 1142–1291. https://doi.org/10.1002/jssc.202100835

16. Decool G., Kfoury M., Paitel L., Sardo A., Fourmentin S. Cyclodextrins as molecular carriers for biopesticides: a review. *Environmental Chemistry Letters*. 2024;22: 321–353. https://doi.org/10.1007/s10311-023-01658-3

17. Morin-Crini N., Fourmentin S., Fenyvesi É., ... Crini G. 130 years of cyclodextrin discovery for health, food, agriculture, and the industry: a review. *Environmental Chemistry Letters*. 2021;19: 2581–2617. https://doi.org/10.1007/s10311-020-01156-w

18. Poulson B. G., Alsulami Q. A., Sharfalddin A., ... Jaremko M. Cyclodextrins: structural, chemical, and physical properties, and applications. *Polysaccharides*. 2022;3(1): 1–31. https://doi.org/10.3390/polysaccharides3010001

19. Amiri S., Amiri S. *Cyclodextrins: properties and industrial applications*. First Editio: JohnWiley & Sons Ltd. Published by JohnWiley & Sons Ltd.; 2017. 320 p. https://doi.org/10.1002/9781119247609

20. Lindner K., Saenger W. Crystal and molecular structure of cyclohepta-amylose dodecahydrate. *Carbohydrate Research*. 1982;99: 103–115. https://doi.org/10.1016/s0008-6215(00)81901-1

21. Betzel C., Saenger W., Hingerty B. E., Brown G. M. Circular and flip-flop hydrogen bonding in β-cyclodextrin undecahydrate: a neutron diffraction study. *Journal of the American Chemical Society*. 1984;106: 7545–7557. https://doi.org/10.1021/ja00336a039

22. Li J-Y., Sun D-F., Hao A-Y., Sun H-Y., Shen J. Crystal structure of a new cyclomaltoheptaose hydrate: β-cyclodextrin·7.5H_2O. *Carbohydrate Research*. 2010;345: 685–688. https://doi.org/10.1016/j.carres.2009.12.016

23. Steiner T., Koellner G., Ali S., Zakim D., Saenger W. Crystalline β-cyclodextrin·12 H_2O reversibly dehydrates to β-cyclodextrin·10.5 H_2O under ambient conditions. *Biochemical and Biophysical Researc*. 1992;188(3): 1060-1066. https://doi.org/10.1016/0006-291x(92)91339-r

24. Steiner T., Koellner G. Crystalline β-cyclodextrin hydrate at various humidities: fast, continuous, and reversible dehydration studied by X-ray diffraction. *Journal of the American Chemical Society*. 1994;116: 5112–5128. https://doi.org/10.1021/ja00091a014

25. Ripmeester J. A. Crystalline β-cyclodextrin hydrate is non-stoichiometric with 10.5-12 waters per cyclodextrin molecule. *Supramolecular Chemistry*. 1993;2: 89–91. https://doi.org/10.1080/10610279308038301

26. Marini A., Berbenni V., Bruni G., Massarotti V., Mustarelli P., Villa M. Dehydration of the cyclodextrins: a model system for the interactions of biomolecules with water. *The Journal of Chemical Physics*. 1995;103(17): 7532–7540. https://doi.org/10.1063/1.470321

27. Szafranek A. Kinetic parameters of thermal decomposition of complex of β-cyclodextrin with water. *Journal of Thermal Analysis*. 1988;34: 917-926. https://doi.org/10.1007/BF01913497

28. Kohata S., Jyodoi K., Ohyoshi A. Thermal decomposition of cyclodextrins (α-, β-, γ-, and modified β-CyD) and of metal—(β-CyD) complexes in the solid phase. *Thermochimica Acta*. 1993;217: 187–198. https://doi.org/10.1016/0040-6031(93)85107-K

29. Specogna E., Li K., Djabourov M., Carn F., Bouchemal K. Dehydration, Dissolution, and melting of cyclodextrin crystals. *The Journal of Physical Chemistry B*. 2015;119: 1433–1442. https://doi.org/10.1021/jp511631e

30. Claudy P., Germain P., Letoffe J. M., Bayol A., Gonzalez B. Étude thermodynamique de la éation d'hydratation de la β-cyclodextrine. *Thermochimica Acta*. 1990;161: 75–84. https://doi.org/10.1016/0040-6031(90)80288-A

31. Bettinetti G., Novák C. S., Sorrenti M. Thermal and structural characterization of commercial α-, β-, and γ-cyclodextrins. *Journal of Thermal Analysis and Calorimetry*. 2002;68: 517–529. https://doi.org/10.1023/a:1016043920156

32. Zelenina L. N., Chusova T. P., Isakov A. V., Rodionova T. V., Villevald G. V., Manakov A. Yu. Thermodynamic investigation of water evaporation process from a-cyclodextrin hydrate. *The Journal of Chemical Thermodynamics*. 2021;158: 106424. https://doi.org/10.1016/j.jct.2021.106424

33. CHEKCELL program. Available at: http://www.cristal.org/SDPD-list/2000/msg00084.html

34. Roisnel T., Rodriguez-Carvajal J. WinPLOTR: a windows tool for powder diffraction patterns analysis. *Materials Science Forum*. 2001;378-381: 118–123. https://doi.org/10.4028/www.scientific.net/msf.378-381.118

35. Suvorov A. V. *Thermodynamic chemistry of the vapor state**. Leningrad: Khimiya Publ.; 1970. 208 p. (In Russ.)

36. Zelenina L. N, Chusova T. P, Vasilyeva I. G. Thermodynamic investigation of phase formation processes in the systems $LnSe_2$–$LnSe_{1.5}$ (Ln = La, Ce, Pr, Nd). *The Journal of Chemical Thermodynamics*. 2013;57: 101–107. https://doi.org/10.1016/j.jct.2012.08.005

37. Zelenina L. N., Chusova T. P., Sapchenko S. A., Ukraintseva E. A., Samsonenko D. G., Fedin V. P. Thermodynamic study of sorption processes of gaseous benzene and water on metal–organic framework [Zn_4(dmf)(ur)$_2$(ndc)$_4$]. *The Journal of Chemical Thermodynamics*. 2013;67: 128–133. https://doi.org/10.1016/j.jct.2013.07.021

38. Zelenina L. N., Chusova T. P., Isakov A. V., Adonin S. A., Sokolov M. N., Thermodynamic study of bromine evaporation from solid Bi(III) polybromides. *The Journal of Chemical*

Thermodynamics. 2020;141: 105958. https://doi.org/10.1016/j.jct.2019.105958

39. Wongmekiat A., Tozuka Y., Oguchi T., Yamamoto K. Formation of fine drug particles by cogrinding with cyclodextrins. I. The use of β-cyclodextrin anhydrate and hydrate. *Pharmaceutical Research*. 2002;19(12): 1867–1872. https://doi.org/10.1023/a:1021401826554

40. Titov V. A., Kokovin G. A. in coll. *Mathematical methods and chemical thermodynamics**. Novosibirsk: Nauka Publ.; 1980. 205 p. (In Russ.)

41. Zelenina L. N., Chusova T. P. Tensimetric study of the tris(2,2,6,6-tetramethylheptan-3,5-dionato)yttrium(III) dissociation in a gas phase. *Russian Journal of General Chemistry*. 2021;91(10): 1541–1547. https://doi.org/10.1134/s1070363221100091

42. Gurvich L. V. IVTANTERMO, automated system of data on thermodynamic properties of substances*. *Vest. AN SSSR = Proceedings of the Academy of Sciences of the USSR*. 1983;3: 54. (In Russ.)

43. Manakov A. Yu., Rodionova T. V., Aladko L. S., ... Karpova T. D. α-cyclodextrin – water binary system. New data on dehydration of α-cyclodextrin hexahydrate. *The Journal of Chemical Thermodynamics*. 2016;101: 251–259. https://doi.org/10.1016/j.jct.2016.06.008

* *Translated by author of the article*

Information about the authors

Lyudmila N. Zelenina, Cand. Sci. (Chem.), Research Fellow at the Institute of Inorganic Chemistry of the Siberian Branch of the Russian Academy of Sciences; Senior Lecturer, Novosibirsk State University (Novosibirsk, Russian Federation).

zelenina@niic.nsc.ru
https://orcid.org/0000-0002-5027-5278

Tatyana V. Rodionova, Cand. Sci. (Chem.), Research Fellow at the Nikolaev Institute of Inorganic Chemistry of the Siberian Branch of the Russian Academy of Sciences (Novosibirsk, Russian Federation).

tvr@niic.nsc.ru
https://orcid.org/0000-0001-8989-1900

Tamara P. Chusova, Cand. Sci. (Chem.), Research Fellow at the Nikolaev Institute of Inorganic Chemistry of the Siberian Branch of the Russian Academy of Sciences (Novosibirsk, Russian Federation).

chu@niic.nsc.ru
https://orcid.org/0000-0001-5246-0138

Anastasia V. Sartakova, 5th year student of the Faculty of Natural Sciences, Novosibirsk State University (Novosibirsk, Russian Federation).

a.sartakova@g.nsu.ru

Andrey Yu. Manakov, Dr. Sci. (Chem.), Chief Researcher at the Nikolaev Institute of Inorganic Chemistry of the Siberian Branch of the Russian Academy of Sciences (Novosibirsk, Russian Federation).

manakov@niic.nsc.ru
https://orcid.org/0000-0003-0214-8714

Received 26.06.2024; approved after reviewing 08.07.2024; accepted for publication 16.09.2024; published online 25.12.2024.

Translated by Irina Charychanskaya

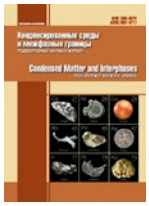

ISSN 1606-867X (Print)
ISSN 2687-0711 (Online)
Condensed Matter and Interphases
Kondensirovannye Sredy i Mezhfaznye Granitsy
https://journals.vsu.ru/kcmf/

Original articles

Research article
https://doi.org/10.17308/kcmf.2024.26/12446

The solid-phase equilibria in the $GeBi_2Te_4$-$SnBi_2Te_4$-Bi_2Te_3 system at 300 K and the characterization of tetradymite-type layered solid solutions

E. R. Nabiyev[1], E. N. Orujlu[2]✉, A. I. Aghazade[3], A. A. Hasanov[4], M. B. Babanly[3,4]

[1]*Ganja State University,*
429 Heydar Aliyev ave., Ganja AZ-2001, Azerbaijan

[2]*Azerbaijan State Oil and Industry University,*
6/2,1 Azadlıq ave., Baku AZ-1010, Azerbaijan

[3]*Institute of Catalysis and Inorganic Chemistry,*
113 H. Javid ave., Baku, AZ-1143, Azerbaijan

[4]*Baku State University,*
23 Z. Khalilov, Baku Az-1048, Azerbaijan

Abstract

The GeTe-SnTe-Bi_2Te_3 system is of great interest due to the potential formation of a series of cation-substituted solid solutions based on ternary layered compounds with a tetradymite-type structure, which have significant potential as valuable thermoelectric materials and topological insulators. This study presents the results of investigating this system in the composition range of $GeBi_2Te_4$-$SnBi_2Te_4$-Bi_2Te_3 using powder X-ray diffraction analysis. Particular attention is given to obtaining equilibrium alloys.

An isothermal section of the phase diagram at 300 K has been constructed, consisting of four single-phase regions separated by three two-phase regions. The X-ray diffraction patterns of the equilibrium alloys were refined using the Rietveld method. The obtained diffraction results clearly indicate the presence of continuous series of solid solutions along the sections $GeBi_2Te_4$-$SnBi_2Te_4$, $GeBi_4Te_7$-$SnBi_4Te_7$, and $GeBi_6Te_{10}$-$SnBi_6Te_{10}$. The lattice parameters for all the solid solution series were determined, showing a linear increase with the rise in Sn concentration.

Keywords: Solid solutions, Germanium bismuth tellurides, Tin bismuth tellurides, Topological insulators, Isothermal section, XRD

Funding: The work was partially supported by the Azerbaijan Science Foundation - Grant № AEF-MCG-2022-1(42)-12/10/4-M-10.

For citation: Nabiyev E. R., Orujlu E. N., Aghazade A. I., Hasanov A. A., Babanly M. B. The solid-phase equilibria in the $GeBi_2Te_4$-$SnBi_2Te_4$-Bi_2Te_3 system at 300 K and characterization of tetradymite-type layered solid solutions. *Condensed Matter and Interphases*. 2024;26(4): 725–731. https://doi.org/10.17308/kcmf.2024.26/12446

Для цитирования: Набиев Э. Р., Оруджлу Э. Н., Агазаде А. И., Гасанов А. А., Бабанлы М. Б. Твердофазные равновесия в системе $GeBi_2Te_4$-$SnBi_2Te_4$-Bi_2Te_3 при 300 К и характеристики тетрадимитоподобных слоистых твердых растворов. *Конденсированные среды и межфазные границы*. 2024;26(4): 725–731. https://doi.org/10.17308/kcmf.2024.26/12446

✉ Elnur N. Orujlu, e-mail: elnur.oruclu@yahoo.com

1. Introduction

The quest for advanced materials with enhanced properties has led to extensive research in the field of multi-component chalcogenides, particularly those based on *M*-Bi-Te (*M* – Ge, Sn, Pb, and Mn) systems [1–8]. These materials, which have attracted great interest due to their thermoelectric properties, have been intensively studied in recent years again as materials exhibiting properties of a new quantum state of matter – topological insulators [9–14]. Topological insulators (TIs) are a class of materials that have garnered significant interest due to their ability to conduct electricity on their surfaces while remaining insulating in their bulk [15–18].

Recently, a homologues series of layered ternary compounds with a general formula of $nA^{IV}Te{\cdot}mBi_2Te_3$ have gained great attention for their unique electronic structures. Systhematic investigations into ternary compounds in these chalcogenides systems show that these tetradymite-type layered van der Waals phases are 3D Tls and hold potential for revolutionary applications in spintronics, quantum computing, and low-power electronics [19–24]. All these compounds share a structural similarity as they belong to the tetradymite-type layered structure which is composed of repeating units of quintuple or septuple layers, typically consisting of alternating atomic layers such as chalcogenides (e.g., Se or Te) and metals (e.g., Bi or Sb with *M* – Ge, Sn, Pb, and Mn) [1–4; 14]. Research on existing layered topological insulator phases indicates that addressing the limitations of their applicability across various fields necessitates the precise tuning of their bulk band structure. An effective approach to promoting electron transport dominated by topologically protected states is through targeted chemical substitution, whereby specific atomic sites in the material's crystal lattice are replaced to modify its electronic structure and enhance the prevalence of these states. This type of topological engineering has been previously studied in numerous works and has demonstrated significant potential for tuning material properties and improving performance for application prospects [25–30].

In this study, by means of differential thermal analysis (DTA) and powder X-ray diffraction (XRD) methods, we studied solid-phase equilibria diagram in the $GeBi_2Te_4$-$SnBi_2Te_4$-Bi_2Te_3 system at 300 K and characterized the $Ge_{1-x}Sn_xBi_2Te_4$, $Ge_{1-x}Sn_xBi_4Te_7$, and $Ge_{1-x}Sn_xBi_6Te_{10}$ continuous series of solid solutions with examining compositional effects on the material's crystalline behaviours. Our findings provide insights into the phase diagrams of the GeTe-SnTe-Bi_2Te_3 pseudoternary system and contribute to understanding the influence of Ge↔Sn substitution on the thermodynamic and structural properties of these topological insulator compounds. Data on phase equilibria in the boundary systems GeTe-Bi_2Te_3 and SnTe-Bi_2Te_3 are taken from [2, 5].

2. Experimental

The starting materials for the preparation of alloys were high-purity germanium pieces (Alfa Aesar, CAS 7440-56-4), tin lump (Alfa Aesar, CAS 7440-31-5), bismuth shots (Alfa Aesar, CAS 7440-69-9), and tellurium lump (Alfa Aesar, CAS 13494-80-9). During the first stage, GeTe, SnTe, and Bi_2Te_3 binary compounds were synthesized. The phase purity of the synthesized binary compounds was checked via DTA and powder XRD methods. Alloys of the studied systems with different compositions were prepared using presynthesized binary compounds. The weighed three components were sealed in quartz ampoules, then melted at 1050 K for 6 h, followed by rapid quenching in ice water. All the ampoules were then placed in a muffle furnace at a temperature of 770 K for 720 hours to achieve a state close to equilibrium. After heat treatment, the alloys were cooled in a switched off furnace.

Powder XRD and DTA techniques were used to characterize the products. The temperatures of the phase transformations were determined by DTA using the LINSEIS HDSC PT1600 system (heating rate of 10 °C/min) and a multichannel DTA device based on a TC-08 Thermocouple Data Logger. Powder X-ray diffraction (XRD) was examined on Bruker D2 PHASER diffractometer using Cu$K\alpha_1$ radiation within a scanning range of $2\theta = 5 \div 75$. COD and PDF-2 databases were used for the interpretation of the powder diffraction patterns. Both qualitative and quantitative assessments of the XRD patterns were carried out using Rietveld analysis with FullProf and HighScore Plus software package.

3. Results and discussion

The powder XRD patterns of annealed alloys of $Ge_{1-x}Sn_xBi_2Te_4$ systems are shown in Fig. 1. The observed peaks of the XRD patterns indicate a trigonal symmetry with the *R*-3*m* space group. As can be seen, the diffraction peaks exhibit a systematic shift towards lower 2θ angles as the Sn content increases, indicating an expansion of the lattice due to the larger atomic radius of Sn compared to Ge. Additionally, the absence of any new peaks or the splitting of existing peaks suggests that no phase separation occurs, confirming the formation of a continuous solid solution. The broadening of peaks with increasing Sn content may also be attributed to microstrains or slight variations in crystallite size as the alloy composition changes. Overall, these patterns confirm the successful incorporation of Sn into the Ge-Bi-Te matrix, leading to a tunable modification of the crystal structure without disrupting the overall phase stability.

Similarly, the XRD patterns of $Ge_{1-x}Sn_xBi_4Te_7$ exhibit a comparable trend (see Fig. 2) with a systematic shift of diffraction peaks towards lower 2θ angles as the Sn concentration increases. This shift, like in the $Ge_{1-x}Sn_xBi_2Te_4$ system, indicates an expansion of the lattice due to the substitution of Sn for Ge. The consistency of this shift across the entire compositional range supports the formation of a continuous solid solution along the $GeBi_4Te_7$-$SnBi_4Te_7$ section.

The XRD patterns of alloys of the $GeBi_6Te_{10}$-$SnBi_6Te_{10}$ section also show a similar shift towards lower 2θ angles with increasing Sn content, indicating lattice expansion and the formation of a continuous solid solution without

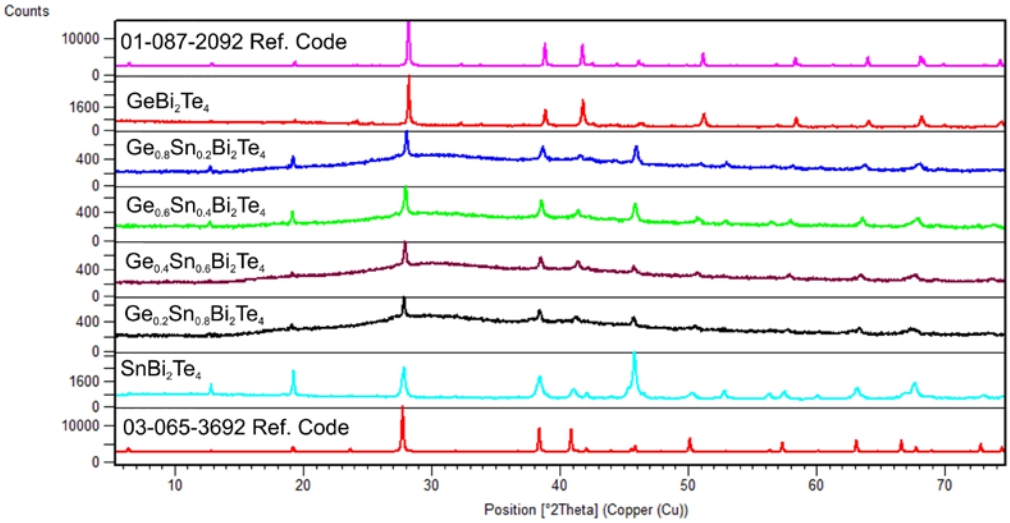

Fig. 1. Powder XRD patterns of $Ge_{1-x}Sn_xBi_2Te_4$ alloys

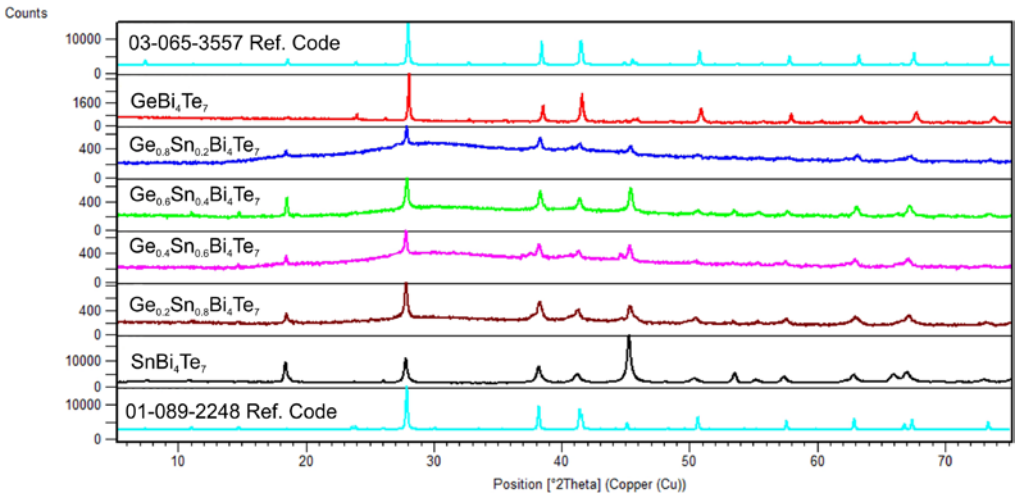

Fig. 2. Powder XRD patterns of $Ge_{1-x}Sn_xBi_4Te_7$ alloys

phase separation, as seen in Fig. 3. Thus, based on the obtained results, it can be stated that the $GeBi_2Te_4$-$SnBi_2Te_4$, $GeBi_4Te_7$-$SnBi_4Te_7$, and $GeBi_6Te_{10}$-$SnBi_6Te_{10}$ sections of the GeTe-SnTe-Bi_2Te_3 system are characterized by the formation of continuous series of solid solutions below the subsolidus temperature.

The structural parameters of all the alloys were refined by the Rietveld technique. Powder XRD-based Rietveld refinements yield the final lattice parameter values by showing good agreement between the experimental and calculated profiles across all compositions. Calculated lattice parameters for the $Ge_{1-x}Sn_xBi_2Te_4$, $Ge_{1-x}Sn_xBi_4Te_7$, and $Ge_{1-x}Sn_xBi_6Te_{10}$ solid solutions were listed in Table 1. It can been seen that the values obtained by our refinements for all ternary end-member compounds are in good agreement with the values of the literature [2, 5]. Results for intermediate compositions are consistent with Vegard's law, which describes the linear relationship between lattice parameters and composition in solid solutions. The variation of lattice parameters *a*, and *c* with the Sn content is presented in Fig. 4 (a), (b), and (c). As expected,

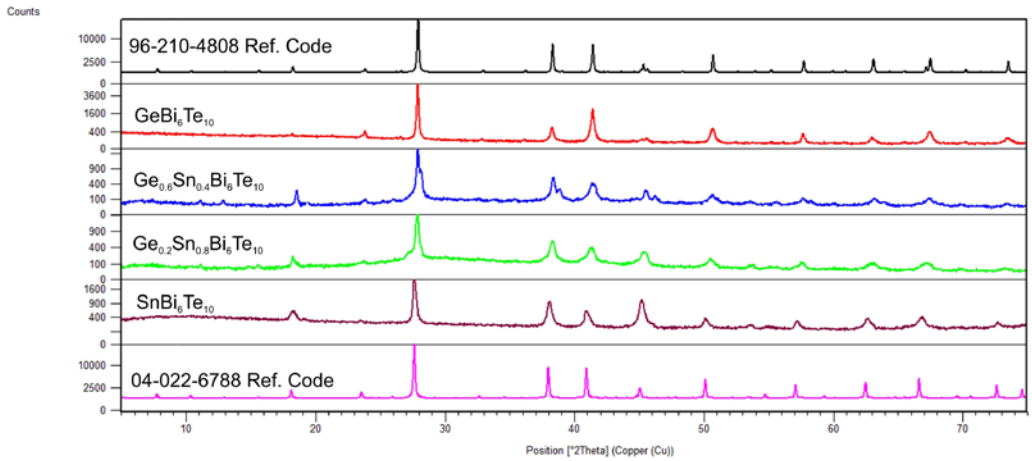

Fig. 3. Powder XRD patterns of $Ge_{1-x}Sn_xBi_6Te_{10}$ alloys

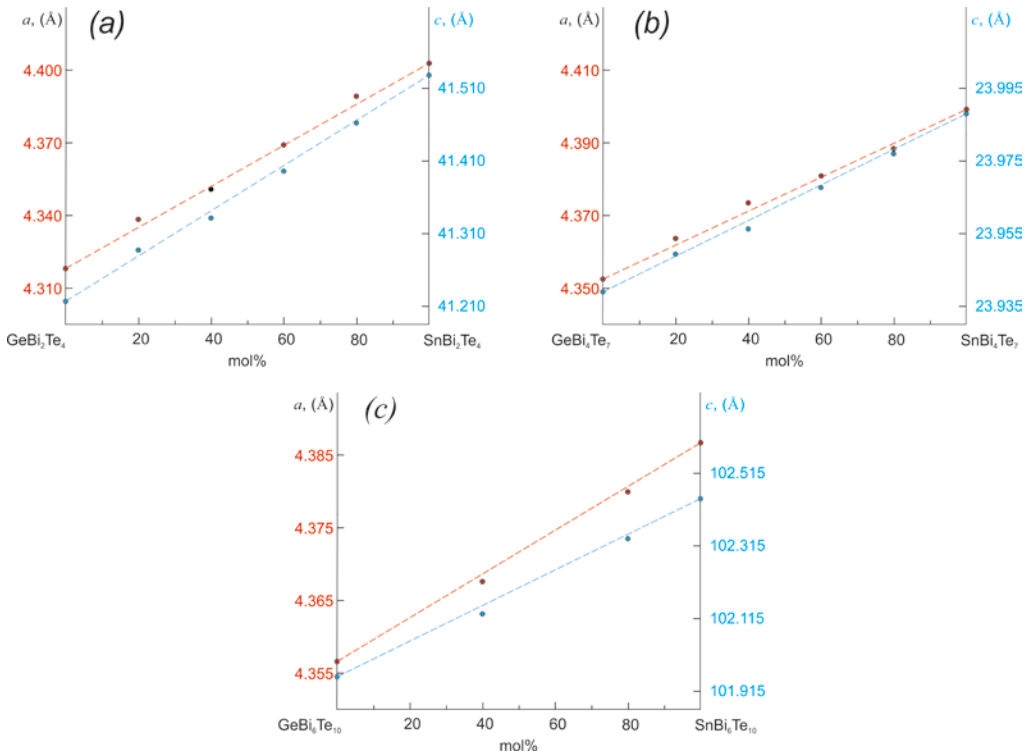

Fig. 4. Dependence of lattice parameters *a* and *c* for alloys of $Ge_{1-x}Sn_xBi_2Te_4$ (a), $Ge_{1-x}Sn_xBi_4Te_7$ (b), and $Ge_{1-x}Sn_x$-Bi_6Te_{10} (a) systems versus Sn content

Table 1. Crystal structure parameters of some phases

Composition, mol%	Lattice parameters, Å		Ref.
	a	*c*	
$Ge_{1-x}Sn_xBi_2Te_4$			
x = 0.0	4.3176(3)	41.259(5)	[5]
	4.3181(4)	41.217(5)	This work
x = 0.2	4.3384(2)	41.288(3)	This work
x = 0.4	4.3508(7)	41.332(5)	This work
x = 0.6	4.3691(4)	41.396(4)	This work
x = 0.8	4.3892(3)	41.462(5)	This work
x = 1.0	4.4035(3)	41.511(2)	[25]
	4.4029(3)	41.528(5)	This work
$Ge_{1-x}Sn_xBi_4Te_7$			
x = 0.0	4.3556(2)	23.928(4)	[5]
	4.3525(4)	23.939(2)	This work
x = 0.2	4.3637(2)	23.949(4)	This work
x = 0.4	4.3735(5)	23.956(3)	This work
x = 0.6	4.3809(7)	23.967(7)	This work
x = 0.8	4.3884(1)	23.977(1)	This work
x = 1.0	4.3998(2)	23.981(3)	[31]
	4.3992(5)	23.988(6)	This work
$Ge_{1-x}Sn_xBi_6Te_{10}$			
x = 0.0	4.3572(3)	101.911(2)	[5]
	4.3566(1)	101.918(4)	This work
x = 0.4	4.3676(8)	102.128(3)	This work
x = 0.8	4.3799(5)	102.335(1)	This work
x = 1.0	4.3873(8)	102.431(1)	[32]
	4.3867(2)	102.438(4)	This work

both lattice parameters increase with increasing concentration of Sn content due to the larger ionic radius of Sn^{2+} compared to Ge^{2+}.

Fig. 5 shows the solid-phase equilibrium diagram of the $GeBi_2Te_4$-$SnBi_2Te_4$-Bi_2Te_3 system at 300 K constructed using the above experimental results and literature data. The isothermal section consists of four monophasic and three two-phase regions. As mentioned above, three out of four single-phase regions belong to a continuous series of solid solutions which are the ε-, φ-, and χ-phases. The β-phase corresponds to the homogeneity region of Bi_2Te_3, which we delimited taking into account the data from [2, 5]. The formation of biphasic areas is confirmed with XRD. Alloy #1 clearly demonstrated that the ε-phase is in equilibrium with the φ-phase, as shown in Fig. 6 (a). Similarly, alloy #2 (Fig. 2(b)) had two equilibrium phases, which were identified as the φ- and χ- phases. Since both alloy compositions located on the Ge-rich side of the diagram (see Fig. 5), reference XRD lines shown in Fig. 6 (a) and (b) were chosen for comparison from germanium ternary compounds.

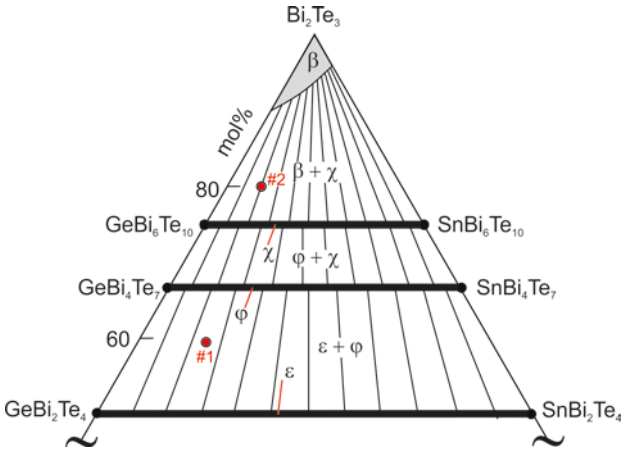

Fig. 5. The solid-phase equilibrium diagram of the $GeBi_2Te_4$-$SnBi_2Te_4$-Bi_2Te_3 system at 300 K. Red circles show alloy compositions for XRD in Fig. 6

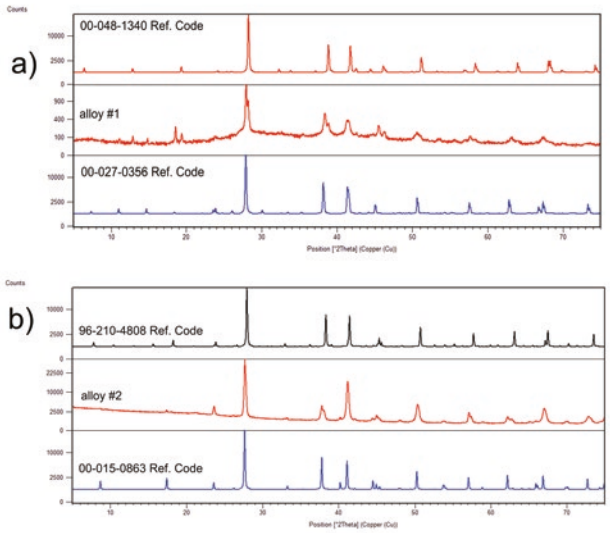

Fig. 6. Powder XRD patterns of alloys #1 and #2 in Fig. 5

4. Conclusions

In this work, based on the results of XRD of equilibrium alloys, a solid-phase equilibrium diagram of the GeTe-SnTe-Bi_2Te_3 system in the composition range of $GeBi_2Te_4$-$SnBi_2Te_4$-Bi_2Te_3 at 300 K was constructed. It was established that this subsystem is characterized by the formation of continuous series of substitution solid solutions with the general formula $Ge_{1-x}Sn_xBi_2Te_4$, $Ge_{1-x}Sn_xBi_4Te_7$ and $Ge_{1-x}Sn_xBi_6Te_{10}$ with a layered tetradymite-type structure and a wide homogeneity region based on Bi_2Te_3. The lattice parameters of the above-mentioned series of solid solutions were refined based on powder diffraction patterns using the Rietveld method. It is shown that their concentration dependences are in good agreement with Vegard's law. The solid solutions obtained in this work are of practical interest from the point of view of developing new topological insulators and thermoelectric materials with adjustable properties.

Conflict of interests

The authors declare that they have no known competing financial interests or personal relationships that could have influenced the work reported in this paper.

Contribution of the authors

The authors contributed equally to this article.

References

1. Aliev Z. S., Amiraslanov I. R., Nasonova D. I., ... Chulkov E. V. Novel ternary layered manganese bismuth tellurides of the MnTe-Bi_2Te_3 system: synthesis and crystal structure. *Journal of Alloys and Compounds*. 2019;789: 443–450. https://doi.org/10.1016/j.jallcom.2019.03.030

2. Orujlu E. N., Seidzade A .E., Babanly D. M., Amiraslanov I. R., Babanly M. B. New insights into phase equilibria of the SnTe–Bi_2Te_3 pseudo-binary system: synthesis and crystal structure of new tetradymite-type compound $Sn_3Bi_2Te_6$. *Journal of Solid State Chemistry*. 2024;330: 124494. https://doi.org/10.1016/j.jssc.2023.124494

3. Seidzade A. E., Orujlu E. N., Doert T., Amiraslanov I. R., Aliev Z. S., Babanly M. B. An updated phase diagram of the SnTe-Sb_2Te_3 system and the crystal structure of the new compound $SnSb_4Te_7$. *Journal of Phase Equilibria and Diffusion*. 2021;42: 373–8. https://doi.org/10.1007/s11669-021-00888-8

4. Alakbarova T. M., Meyer H.-J., Orujlu E. N., Amiraslanov I. R., Babanly M. B. Phase equilibria of the GeTe–Bi_2Te_3 quasi-binary system in the range 0–50 mol% Bi_2Te_3. *Phase Transitions*. 2021;94: 366–75. https://doi.org/10.1080/01411594.2021.1937625

5. Alakbarova T. M., Meyer H.-J., Orujlu E. N., Babanly M. B. A refined phase diagram of the GeTe-Bi_2Te_3 system. *Kondensirovannye Sredy I Mezhfaznye Granitsy = Condensed Matter and Interphases*. 2022;24: 11–18. https://doi.org/10.17308/kcmf.2022.24/9050

6. Huang D., Xia D., Ye T., Fujita T. New experimental studies on the phase relationship of the Bi–Pb–Te system. *Materials & Design*. 2022;224: 111384. https://doi.org/10.1016/j.matdes.2022.111384

7. Omoto T., Kanaya H., Ishibashi H., Kubota Y., Kifune K., Kosuga A. Formation phases and electrical properties of Ge-Bi-Te compounds with homologous structures. *Journal of Electronic Materials*. 2015;45: 1478–83. https://doi.org/10.1007/s11664-015-4083-z

8. Gojayeva I. M., Babanly V. I., Aghazade A. I., Orujlu E. N. Experimental reinvestigation of the PbTe–Bi_2Te_3 pseudo-binary system. *Azerbaijan Chemical Journal*. 2022;0: 47–53. https://doi.org/10.32737/0005-2531-2022-2-47-53

9. Heremans J. P., Cava R. J., Samarth N. Tetradymites as thermoelectrics and topological insulators. *Nature Review Materials*. 2017;2: 17049. https://doi.org/10.1038/natrevmats.2017.49

10. Banik A., Roychowdhury S., Biswas K. The journey of tin chalcogenides towards high-performance thermoelectrics and topological materials. *Chemical Communications*. 2018;54: 6573–6590. https://doi.org/10.1039/c8cc02230e

11. Lukyanova L. N., Usov O. A., Volkov M. P., Makarenko I. V. Topological thermoelectric materials based on bismuth telluride. *Nanotechnologly Reports*. 2021;16: 282–293. https://doi.org/10.1134/s2635167621030125

12. Xu N., Xu Y., Zhu J. Topological insulators for thermoelectrics. *Npj Quantum Materials*. 2017;2(1). https://doi.org/10.1038/s41535-017-0054-3

13. Yang T., Yang Y., Wang X., Zhang G., Cheng Z. Topological thermoelectrics: new opportunities and challenges. *Materials Today Chemistry*. 2023;30: 101488. https://doi.org/10.1016/j.mtchem.2023.101488

14. Babanly M. B., Chulkov E. V., Aliev Z. S., Shevelkov A. V., Amiraslanov I. R. Phase diagrams in materials science of topological insulators based on metal chalcogenides. *Russian Journal of Inorganic Chemistry*. 2017;62: 1703–1729. https://doi.org/10.1134/S0036023617130034

15. Hasan M. Z., Kane C. L. Colloquium: topological insulators. *Review of Modern Physics*. 2010;82: 3045–3067. https://doi.org/10.1103/revmodphys.82.3045

16. Qi X.-L., Zhang S.-C. Topological insulators and superconductors. *Review of Modern Physics*. 2011;83: 1057–1110. https://doi.org/10.1103/revmodphys.83.1057

17. Zhang H., Liu C.-X., Qi X.-L., Dai X., Fang Z., Zhang S.-C. Topological insulators in $BiSe_3$, Bi_2Te_3 and Sb_2Te_3 with a single Dirac cone on the surface. *Nature Physics*. 2009;5: 438–442. https://doi.org/10.1038/nphys1270

18. Rachel S. Interacting topological insulators: a review. *Reports on Progress in Physics*. 2018;81: 116501. https://doi.org/10.1088/1361-6633/aad6a6

19. McGuire M. A., Zhang H., May A. F., ... Yan J. Superconductivity by alloying the topological insulator $SnBi_2Te_4$. *Physical Review Materials*. 2023;7. https://doi.org/10.1103/physrevmaterials.7.034802

20. Saxena A., Karn N. K., Sharma M. M., Awana V. P. S. Detailed structural and topological analysis of $SnBi_2Te_4$ single crystal. *Journal of Physics and Chemistry of Solids*. 2023;174: 111169. https://doi.org/10.1016/j.jpcs.2022.111169

21. Wang L-L. Highly tunable band inversion in AB_2X_4 (A=Ge, Sn, Pb; B=As, Sb, Bi; X=Se, Te) compounds. *Physical Review Materials*. 2022;6. https://doi.org/10.1103/physrevmaterials.6.094201

22. Marcinkova A., Wang J. K., Slavonic C., ... Morosan E. Topological metal behavior in $GeBi_2Te_4$ single crystals. *Physical Review B*. 2013;88. https://doi.org/10.1103/physrevb.88.165128

23. Klimovskikh I. I., Otrokov M. M., Estyunin D., ... Chulkov E. V. Tunable 3D/2D magnetism in the $(MnBi_2Te_4)(Bi_2Te_3)m$ topological insulators family. *Npj Quantum Materials*. 2020;5. https://doi.org/10.1038/s41535-020-00255-9

24. Kuroda K., Miyahara H., Ye M., ... Kimura A. Experimental verification as a 3D topological insulator. *Physical Review Letters*. 2012;108. https://doi.org/10.1103/physrevlett.108.206803

25. Orujlu E. Phase equilibria in the $SnBi_2Te_4$–$MnBi_2Te_4$ system and characterization of the $Sn_{1-x}Mn_xBi_2Te_4$ solid solutions. *Physics and Chemistry of Solid State*. 2020;21: 113–116. https://doi.org/10.15330/pcss.21.1.113-116

26. Pan L., Li J., Berardan D., Dragoe N. Transport properties of the $SnBi_2Te_4$–$PbBi_2Te_4$ solid solution. *Journal of Solid State Chemistry*. 2015;225: 168–173. https://doi.org/10.1016/j.jssc.2014.12.016

27. Frolov A. S., Usachov D. Yu., Tarasov A. V., ... Yashina L. V. Magnetic Dirac semimetal state of $(Mn,Ge)Bi_2Te_4$. *Communications Physics*. 2024;7. https://doi.org/10.1038/s42005-024-01675-w

28. Wang S., Xing T., Hu P., ... Chen, L. Optimized carrier concentration and enhanced thermoelectric properties in $GeSb_{4-x}Bi_xTe_7$ materials. *Applied Physics Letters*. 2022;121. https://doi.org/10.1063/5.0123298

29. Qian T., Yao Y.-T., Hu C., ... Ni N. Magnetic dilution effect and topological phase transitions in $(Mn_{1-x}Pb_x)Bi_2Te_4$. *Physical Review B*. 2022;106. https://doi.org/10.1103/physrevb.106.045121

30. Tokumoto Y., Sugimoto K., Hattori Y., Edagawa K. Electronic transport properties of $Pb(Bi_{1-x}Sb_x)_2(Te_{1-y}Se_y)_4$ topological insulator. *Journal of Applied Physics*. 2022;131. https://doi.org/10.1063/5.0077002

31. Aghazade A. I. Phase relations and characterization of solid solutions in the $SnBi_2Te_4$–$PbBi_2Te_4$ and $SnBi_4Te_7$–$PbBi_4Te_7$ systems. *Azerbaijan Chemical Journal*. 2022;0(3): 75–80. https://doi.org/10.32737/0005-2531-2022-3-75-80

32. Aghazade A. I., Orujlu E. N., Salimov Z. E., Mammadov A. N., Babanly M. B. Experimental investigation of the solid phase equilibria at 300 K in the $SnBi_2Te_4$-$PbBi_2Te_4$-Bi_2Te_3 system. *Physics and Chemistry of Solid State*. 2023;24: 453–459. https://doi.org/10.15330/pcss.24.3.453-459

Information about the authors

Elnur R. Nabiyev, PhD student, Ganja State University (Ganja, Azerbaijan).
https://orcid.org/0009-0006-1907-3957
azechemist@gmail.com

Elnur N. Orujlu, PhD in Chemistry, Head of "Nanomaterials and nanotechnologies" science-research laboratory, Azerbajan State Oil and Industry University (Baku, Azerbaijan).
https://orcid.org/0000-0001-8955-7910
elnur.oruclu@yahoo.com

Aytan I. Aghazade, PhD student, Researcher at the Institute of Catalysis and Inorganic Chemistry (Baku, Azerbaijan).
https://orcid.org/0000-0002-6072-1075
aytenagazade94@gmail.com

Alakbar A. Hasanov, Dr. Sci. (Tech.), Professor, Azerbajan State Oil and Industry University (Baku, Azerbaijan).
https://orcid.org/0000-0001-7505-4925
alakbar48-48@mail.ru

Mahammad B. Babanly, Dr. Sci. (Chem.), Professor, Associate Member of the Azerbaijan National Academy of Sciences, Deputy-director of the Institute of Catalysis and Inorganic Chemistry (Baku, Azerbaijan).
https://orcid.org/0000-0001-5962-3710
babanlymb@gmail.com

Received 19.08.2024; approved after reviewing 10.09.2024; accepted for publication 16.09.2024; published online 25.12.2024.

Translated by the author

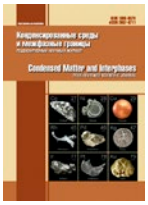

ISSN 1606-867X (Print)
ISSN 2687-0711 (Online)
Condensed Matter and Interphases
Kondensirovannye Sredy i Mezhfaznye Granitsy
https://journals.vsu.ru/kcmf/

Original articles

Research article
https://doi.org/10.17308/kcmf.2024.26/12447

The effect of the aging time of the $ZrO_2 \cdot nH_{2\,O}$ coagel: features of its phase formation and the evolution of its adsorption properties

Sh. O. Omarov[1]✉, N. A. Pakhomov[2]

[1]*Ioffe Institute,*
26 ul. Politechnicheskaya, Saint Petersbutg 194021, Russian Federation

[2]*St. Petersburg State Technological Institute (Technical University),*
26 Moskovskiy pr., Saint Petersbutg 190013, Russian Federation

Abstract

To date, researchers have failed to provide a physicochemical explanation of the crystallization of low-soluble X-ray amorphous $ZrO_2 \cdot nH_2O$ caused by its aging in contact with the mother liquor. Data obtained in previous studies may be erroneous due to the unpredictable effect of Si^{4+}, Na^+ and K^+ impurity ions. This study is aimed at establishing the regularities and features of the phase formation, as well as changes in the adsorption properties of $ZrO_2 \cdot nH_2O$ and the functional composition of the ZrO_2 surface depending on the aging time of the $ZrO_2 \cdot nH_2O$ coagel in contact with the mother solution and in absence of impurity ions. The research was carried out on $ZrO_2 \cdot nH_2O$ obtained by direct precipitation at pH = 10 followed by aging for 6–406 h in a fluoroplastic reactor and on ZrO_2 obtained by heat treatment of the corresponding $ZrO_2 \cdot nH_2O$ at 500 °C.

The properties of $ZrO_2 \cdot nH_2O$ and ZrO_2 were studied by methods of synchronous thermal analysis, X-ray diffraction, scanning electron microscopy, low-temperature N_2 sorption, vacuum infrared spectroscopy, infrared spectroscopy, and temperature programmed desorption of molecular probes. It was shown that there is an extremum of the phase composition and adsorption properties of $ZrO_2 \cdot nH_2O$ and ZrO_2 after 24–96 h of aging.

It was established for the first time that the process of decomposition of dense aggregates of primary particles and submicron and micron aggregates and agglomerates of X-ray amorphous $ZrO_2 \cdot nH_2O$ accompanied by the appearance of edge OH-groups precedes its crystallization in contact with the mother solution (6–48 h). Further aging (96–406 h) revealed a gradual crystallization of $ZrO_2 \cdot nH_2O$ in the form of a mixture of the tetragonal and monoclinic phases of ZrO_2 in a 1:1 ratio as a result of the attachment of primary particles of $ZrO_2 \cdot nH_2O$ with the participation of edge and bridging OH groups. Acid-base properties of the ZrO_2 surface are in extreme dependence on the aging time. With prolonged aging (more than 213 hours), the acid function of the ZrO_2 surface begins to prevail due to the participation of the basic edge OH groups in the attachment of the $ZrO_2 \cdot nH_2O$ primary particles. The observed changes are discussed from the perspective of the theory of oriented attachment of nanocrystals.

Keywords: Zirconium, Dioxide, Hydrated, Phase, Porosity, Morphology, Attachment, Surface, Acidity, Basicity

Funding: The study was supported by the Ministry of Science and Higher Education of the Russian Federation within the framework of state order to Ioffe Institute of the Russian Academy of Sciences, project No. FFUG-2024-0036

Acknowledgments: The authors thank Tenevich M. I. for the study using the scanning electron microscopy method on the equipment of the Engineering Center of St. Petersburg State Technological Institute, as well as Fedorov S. P. and Serazhim M. S. for the study using the low-temperature nitrogen sorption method on the equipment of the Laboratory of Catalytic Technologies of St. Petersburg State Technological Institute.

For citation: Omarov Sh. O., Pakhomov N. A. The effect of the aging time of the $ZrO_2 \cdot nH_2O$ coagel: features of its phase formation and the evolution of its adsorption properties. *Condensed Matter and Interphases*. 2024;26(4): 732–744. https://doi.org/10.17308/kcmf.2024.26/12447

✉ Shamil O. Omarov, e-mail: somarov@mail.ioffe.ru

Для цитирования: Омаров Ш. О., Пахомов Н. А. Влияние длительности старения коагеля $ZrO_2 \cdot nH_2O$: особенности фазообразования и эволюции адсорбционных свойств. *Конденсированные среды и межфазные границы*. 2024;26(4): 732–744. https://doi.org/10.17308/kcmf.2024.26/12447

1. Introduction

Zirconium dioxide has been widely used in industry as the main component of ceramic, refractory, composite, and other materials [1]. The constant need in new catalysts with improved or unique properties explains increased attention to zirconium dioxide as a promising material for the production of domestic catalysts for refining and petrochemistry, the importance of which has increased in the context of import substitution [2].

The main obstacle to a wider use of ZrO_2 in this field is the difficulty of regulating its phase composition, poorly developed porosity, and acid-base surface properties. These characteristics can be improved either by changing the synthesis method and conditions [3, 4] in order to change the texture or by controlled introduction of promoters to stabilize the phase composition and adjust the surface properties. In the case of zirconium dioxide, the most popular has been the method of aging the hydrated precursor of $ZrO_2 \cdot nH_2O$ in contact with the mother solution under mild conditions ($T \leqslant 100$ °C, atmospheric pressure) [5–14]. The following synthesis parameters have been studied: aging time and temperature, suspension pH, the type of precipitant, the method of precipitation, etc. However, these studies share one disadvantage, they do not consider or control the effect of impurities on the phase formation, texture, and adsorption properties of ZrO_2. They are also characterised by insufficient aging time and fragmentary information about the crystallization of $ZrO_2 \cdot nH_2O$ in contact with the mother solution. Impurities can originate from alkaline precipitants (NaOH, KOH), and leached silicon from the reactor in an alkaline environment. Their effect is enhanced as they are accumulated during a prolonged aging. This problem can be solved by eliminating the factors that cause the presence of impurities, i.e. precipitation with an ammonia solution followed by the $ZrO_2 \cdot nH_2O$ aging in a reactor made from a chemically inert material. The study of the phase composition is complicated by the fact that zirconium dioxide can normally exist in two metastable modifications: a tetragonal t-ZrO_2 (space group $P4_2/nmc$) or cubic c-ZrO_2 (space group Fm-$3m$) [15, 16]. They are formed under the influence of various factors (size effect, oxygen vacancies, anionic and cationic impurities, OH-groups), which are also inherent in the modification which is thermodynamically stable monoclinic modification (space group $P2_1/c$) in normal conditions [14–17].

The influence of the conditions of the $ZrO_2 \cdot nH_2O$ aging on the changes in the porosity and phase composition of $ZrO_2 \cdot nH_2O$ and ZrO_2 can be explained, in particular, by repeated dissolution and repeated precipitation [6, 7, 9, 10]. These processes take place at pH = 13.7, at which crystallization of $ZrO_2 \cdot nH_2O$ to t-ZrO_2 was observed in [6] within 24 hours. However, the low solubility product of $ZrO_2 \cdot nH_2O$ ($K_{sp} = 10^{-57}$–10^{-62}) in a wide range of pHs [18, 19], nanoparticle sizes [20], and temperatures [21] does not allow considering repeated dissolution as the main cause of changes in the porosity and crystallization of $ZrO_2 \cdot nH_2O$ under the most common conditions of aging: pH = 4–10 and $T \leqslant 100$ °C. As a result, it is necessary to study alternative approaches to explaining the processes occurring during the aging of $ZrO_2 \cdot nH_2O$ and the phase formation of ZrO_2. One such approach is the oriented attachment theory (OAT) [22–26], the concepts of which have been used to explain the formation of anisotropic ZrO_2 particles with complex morphology under hydrothermal conditions [27–34].

The dependence of the acid-base properties of the ZrO_2 surface on the aging time of $ZrO_2 \cdot nH_2O$ remains unclear. The little available data [35] do not take into account the above-mentioned effect of impurities, which can unpredictably affect the adsorption properties of ZrO_2. This problem might be solved by using a set of methods to study the surface. In particular, temperature programmed desorption (TPD) of molecular probes is used to determine integral indicators of acidity and basicity. IR spectroscopy of adsorbed molecular probes allows qualitatively and quantitatively determining the type of Brønsted acid sites and Lewis acid sites.

The purpose of this study is to establish the regularities and features of the phase formation, as well as the changes in the adsorption properties of $ZrO_2 \cdot nH_2O$ and the functional composition of the ZrO_2 surface depending on the aging time of the $ZrO_2 \cdot nH_2O$ coagel in contact with the mother solution and in the absence of Si^{4+}, Na^+, and K^+ impurity ions. For this, the aging of $ZrO_2 \cdot nH_2O$ precipitated with ammonia solution was carried out in a polychlorotrifluoroethylene (PTFE) reactor for 406 hours, which was twice the time used in all previous studies carried out in this area. A set of methods was chosen to study the adsorption properties, i.e. low-temperature N_2 sorption, TPD, and IR spectroscopy of molecular probes, which allow for a comprehensive study of various aspects of the surface formation, as well as the changes in the texture of X-ray amorphous $ZrO_2 \cdot nH_2O$.

2. Experimental

$ZrO_2 \cdot nH_2O$ was synthesized by direct precipitation from a 0.62 M solution of $ZrOCl_2$ (ρ = 1.096 g/cm^3 at 20 °C) with a 13M ammonia solution (ρ = 0.913 g/cm^3 at 20 °C) in a 0.5 L glass beaker at 20 °C and pH = 10.0 ± 0.1. The flow rate of the ammonia solution was 0.7 ml/min, the draining time was 20 min. The rotation speed of the stirring shaft was within 400–500 rpm. Further continuous aging of $ZrO_2 \cdot nH_2O$ was carried out in a 500 mL PTFE beaker at 90±1 °C for 6, 24, 48, 96, 213, 334, and 406 h. NH_3 solution was added regularly to maintain the suspension pH within 9.9–10.1 (measured at (20±2) °C). The precipitate was washed off Cl^- and NH_4^+ with distilled water at the rate of 0.2–0.25 L of H_2O per 1 g (control of 0.1 n with an $AgNO_3$ solution). After washing, the precipitate was dried at 70 °C for 4 h and at 90 °C for 1 h. The heat treatment of $ZrO_2 \cdot nH_2O$ was carried out in a muffle furnace in a stepwise mode: 170 °C – 0.5 h; 250 °C – 0.5 h; 350 °C – 0.5 h; 430 °C – 0.5 h; 500 °C – 2 h (the rate of temperature increase was 4 °/min), followed by cooling in the furnace.

Weight loss, the temperature limits of the main thermal transformations, and the values of thermal effects were determined on a DTG-60A synchronous thermal analyzer (Shimadzu, Japan). The samples (15–20 mg) were heated at 10 °C/min to 800 °C in static air.

The phase composition was determined on an XRD–6100 diffractometer (Shimadzu, Japan) with a Cu anode, Ni filter, with slits D:S:R = 0.5°: 0.5°:0.15 mm. The imaging was performed at 0.02° interval and the exposure time at each point of 1.2 or 3 s. To calculate the volume content of t-ZrO_2 V_t (vol %), we used the technique described in [36]. The Selyakov-Scherrer formula (K = 0.94; $\lambda(CuK\alpha_1)$ = 0.15406 nm) was used to calculate the coherent scattering regions (CSR) of the t-ZrO_2 (d_t, nm) and m-ZrO_2 (d_m, nm) phases.

The amount of the amorphous phase in the non-thermal treated samples was determined by absolute background calibration at 26° (2θ). For calibration, we used mixtures (10% : 90%, 50% : 50%, and 90% : 10% wt. ZrO_2) of the initial non-aged $ZrO_2 \cdot nH_2O$; t-ZrO_2, which had been obtained by heat treatment of the specified $ZrO_2 \cdot nH_2O$ at 500 °C; and reactive m-ZrO_2 with CSR = 20–25 nm.

The morphology of $ZrO_2 \cdot nH_2O$ powder particles was studied on a VEGA 3 SBH scanning electron microscope (Tescan, Czech Republic) in the backscattered electron mode.

The texture characteristics were studied by the method of low-temperature N_2 sorption on an Autosorb 6iSA unit (Quantachrome, USA) at –196 °C. The samples (0.04–0.2 g) were degassed under vacuum at 100 °C (for $ZrO_2 \cdot nH_2O$) or 250 °C (for the heat-treated samples) for 1 h. The value of the specific surface area (SSA, m^2/g) was calculated by the multipoint BET method; the total pore volume (V_Σ, cm^3/g) was calculated by the limit value of absorbed N_2 at p/p_0 = 0.99; the average pore size (d_{pore}, nm) relative to $4V_\Sigma/SSA$ and the pore size distribution were calculated by the density functional method using a nucleus for slit pores (QSDFT, equilibrium mode) for $ZrO_2 \cdot nH_2O$ or cylindrical pores (NLDFT, adsorption branch) for ZrO_2.

The hydroxyl cover of $ZrO_2 \cdot nH_2O$ was studied on an IrTracer-100 IR-Fourier spectrometer (Shimadzu, Japan) with an HTC-3-S12 vacuum attachment (Harrick, USA). For this, 10–15 mg of powder was compressed at a pressure of 1–2 t into a tablet with a diameter of 13 mm. Then, the tablet was placed in a cuvette, heated in a vacuum to 350 °C at a rate of 10° C/min, and kept for 10 minutes. After that, the IR spectrum of the sample was taken.

To study the acid-base properties of the ZrO_2 surface by IR spectroscopy of molecular probes, 15–25 mg of the ground catalyst sample was

compressed at a pressure of 3–4 t into a tablet with a diameter of 13 mm. The cuvette with the tablet was heated in vacuum to 360 °C and kept for 20 min. The time of the pyridine or CO_2 adsorption was 20 min after the cuvette cooled down to 150 °C. Spectra of the sorbed pyridine or CO_2 were taken at 150, 250, and 350 °C after exposure at each of the temperatures for 20 minutes. The concentration of the sorbed pyridine at BAS and LAS was calculated according to [37].

The total acidity and basicity of the surface and the distribution of the centers by the adsorption strength were determined by the method of temperature programmed desorption of NH_3 and CO_2 on a Khemosorb chemisorption analyzer (*SOLO*, Russia). The thermal desorption products were analyzed using an MC7-200D quadrupole mass spectrometer (Institute for Analytical Instrumentation of the Russian Academy of Sciences). The sample was heated in the He flow (99.9995% vol.) to 500 °C at a rate of 20 °C/min, kept for 20–30 min, and then cooled to 110 °C/min. A mixture of 10% NH_3 or CO_2 in He (20 mL/min) was then passed, followed by pure carrier gas (20 mL/min) until the mass spectrometer signal stabilized at m/z = 16 or m/z = 44. Desorption curves were recorded when the sample was heated in He (20 ml/min) at a rate of 10 °C/min. The calibration of the mass spectrometer by the selected mass numbers was carried out using gas mixtures with a known concentration of NH_3 or CO_2 with a total flow rate at the outlet of the chemisorption analyzer of 20 ml/min.

3. Results and discussion

3.1. Characteristics of $ZrO_2 \cdot nH_2O$

The morphology of freshly precipitated $ZrO_2 \cdot nH_2O$ was represented mainly by arbitrary-shaped dense agglomerates with a size of 10–100 μm consisting of plate-like agglomerates of a smaller size (Fig. 1A). Aging at 90 °C/min for 6 h led to partial destruction of agglomerates, the appearance of cracks of about 2 μm in size, and a decrease in the bulk density of the powder from 1.2 to 0.6 g/ml (Fig. 1B). The plates that made up loose agglomerates became more distinguishable, and their sizes reached 20–40 μm with a thickness of 2 μm (Fig. 1B). A further increase in the aging time to 48 hours resulted in a deeper decomposition of loose agglomerates to spheroid aggregates of about 100–300 nm (Fig. 1C, D). The latter became compacted again after 334 h of aging (Fig. 1E, F).

The described change in the morphology was also accompanied by a significant restructuring of the $ZrO_2 \cdot nH_2O$ porosity. According to the N_2 sorption data, the initial $ZrO_2 \cdot nH_2O$ (0 h of aging) was characterized by a type Ib isotherm, which corresponded to the microporous structure (Fig. 2A) with a small number of small mesopores of 2–4 nm (Fig. 2B). $ZrO_2 \cdot nH_2O$, which had been

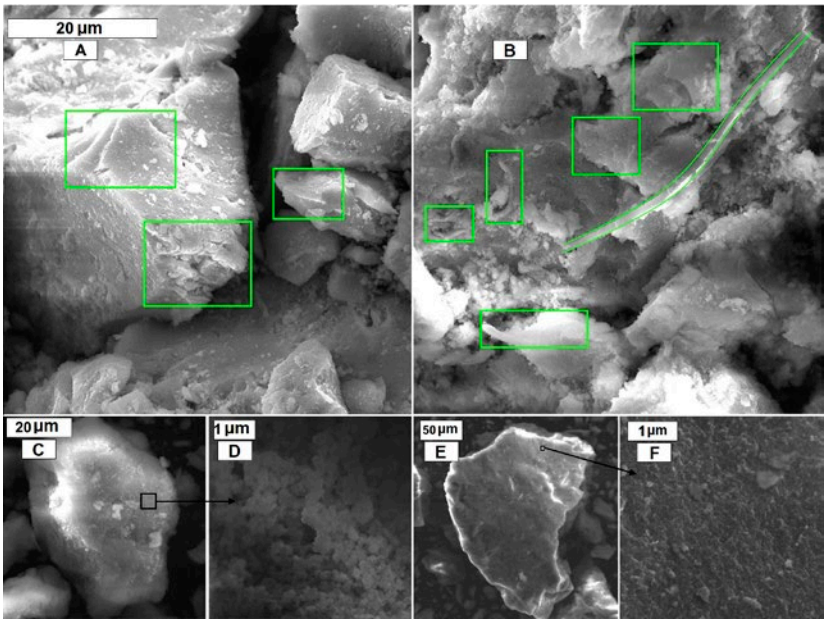

Fig. 1. SEM images of the $ZrO_2 \cdot nH_2O$ non-aged and aged under the mother liquor for 6 h (A, B), 48 h (C, D), and 334 h (E, F)

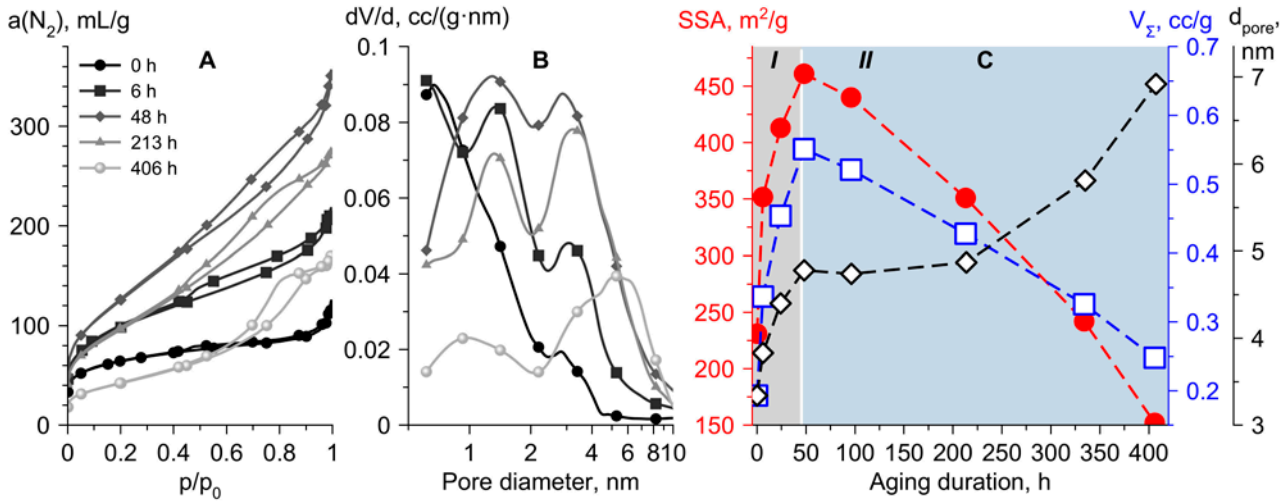

Fig. 2. Isotherms of N_2 sorption (A), pore size distribution (B), and dependence of textural characteristics (C) of $ZrO_2 \cdot nH_2O$ on the aging duration

aged for 6–48 hours, had an increased N_2 sorption at $p/p_0 > 0.4$ due to an increase in the contribution of a type IVA isotherm. This was also confirmed by an increase in the size of micropores from that close to ultramicropores to supermicropores of 1–2 nm and by the appearance of mesopores of 2–10 nm. The shape of the hysteresis loop changed from H4 (0 h) to H3 (6–48 h). Such changes indicate the decomposition of the initial dense microporous $ZrO_2 \cdot nH_2O$ aggregates to non-rigid aggregates of plate-like particles of the micro-mesoporous $ZrO_2 \cdot nH_2O$. Integral indicators of porosity (*SSA* and V_Σ) increased and reached their maximum (461 m^2/g and 0.55 cm^3/g) at 48 h.

Further aging for 96–406 h led to a decrease in the contribution of a type I isotrem and, accordingly, micropores, and a general decrease in the porosity indicators (*SSA* and V_Σ). The hysteresis loop of the 96 h sample corresponded to the H5 type (formation of open and partially closed mesopores), and of the 213–406 h samples to the H2a type (blind mesopores with narrow mouths), which was most distinct in the 406 h sample.

The results of the synchronous thermal analysis of $ZrO_2 \cdot nH_2O$ are shown in Fig. 3. The initial thermograms had several regions corresponding to the successive transformations of $ZrO_2 \cdot nH_2O$: stepwise dehydration at 30–125 and 125–300 °C, which resulted in the formation of a-ZrO_2 and were accompanied by removal of physically adsorbed water and a hydrated surface cover in the form of bridging and terminal OH groups (thermal decomposition of hydroxyoxide); and crystallization of a-ZrO_2 at 370–520 °C. An

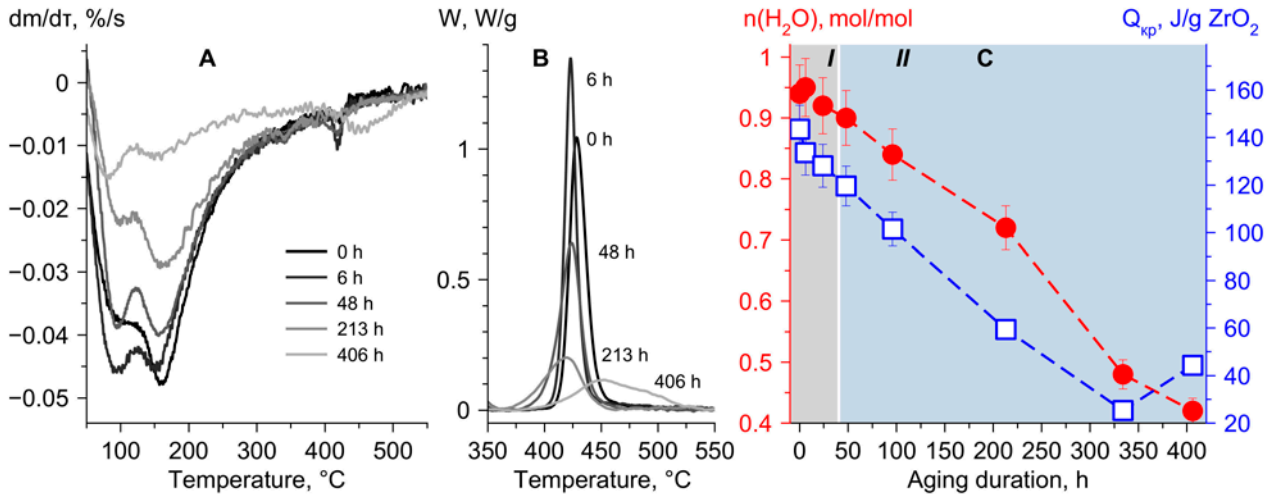

Fig. 3. DTG curves of $ZrO_2 \cdot nH_2O$ (A), the region of DTG curves of crystallization of a-ZrO_2 (B) and the dependence of hydration and crystallization heat of a-ZrO_2 (C) on the aging duration of $ZrO_2 \cdot nH_2O$

increase in the aging time to 48 h led to a slight decrease in the hydration of $ZrO_2 \cdot nH_2O$ and Q_{cr}, while further aging up to 406 h led to the deep dehydration and crystallization of $ZrO_2 \cdot nH_2O$. The dehydration of $ZrO_2 \cdot nH_2O$ during aging manifested itself mainly by a decrease in weight loss at the second stage of 125–300 °C.

X-ray phase analysis provided more information about the crystallization of $ZrO_2 \cdot nH_2O$ (Fig. 4). The X-ray amorphous state of the initial $ZrO_2 \cdot nH_2O$ (halo in the range of 20–40° 2θ) was maintained up to 48 h. The corresponding diffraction pattern had a slight increase in the intensity of approximately 30° 2θ. At 96 h, there were visible reflexes of t-ZrO_2 (111) and m-ZrO_2 (-111) (insert in Fig. 4A). Further aging resulted in the gradual crystallization of $ZrO_2 \cdot nH_2O$ and the formation of a mixture of t- and m-ZrO_2 and a phase ratio close to 1:1 (Fig. 4B). By 406 hours, the residual amount of a-ZrO_2 was 18% wt. The size of the t-ZrO_2 crystallites (CSR) was smaller than that of m-ZrO_2, but both tended to increase in size from 7.7 to 10.3 nm and from 14 to 18.1 nm, respectively (Fig. 4B).

3.2. Characteristics of ZrO_2

Heat treatment at 430 and 500 °C of freshly precipitated $ZrO_2 \cdot nH_2O$ led to the crystallization of the t-ZrO_2 phase (Fig. 5A) and the formation of large crystallites of 22–25 nm (Fig. 5B). As a

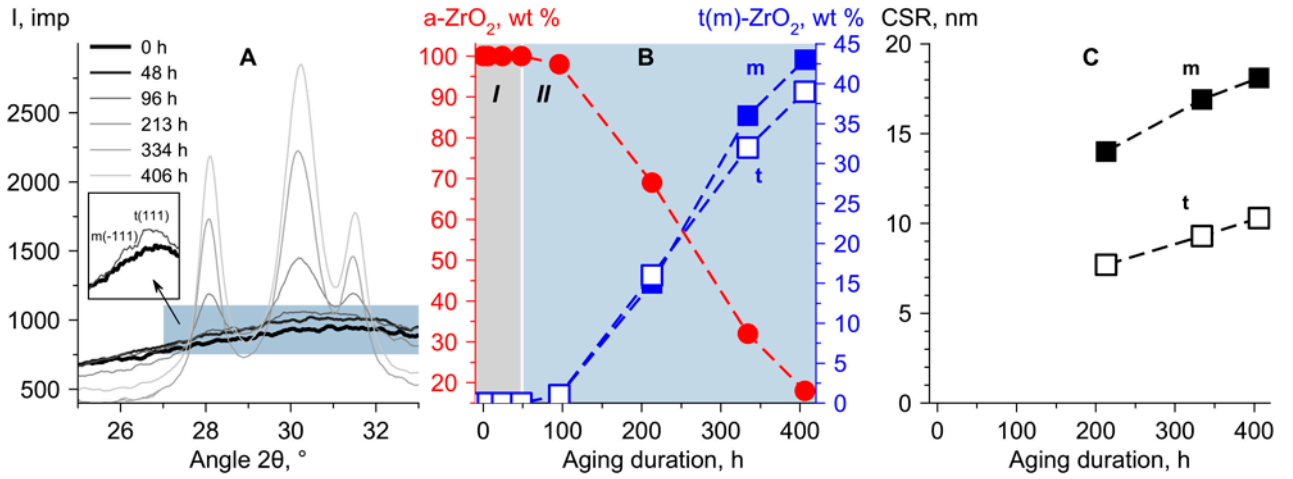

Fig. 4. Diffractograms of $ZrO_2 \cdot nH_2O$ (A), the dependence of the phase composition (B) and the CSR size of ZrO_2 phases (C) on the aging duration of $ZrO_2 \cdot nH_2O$

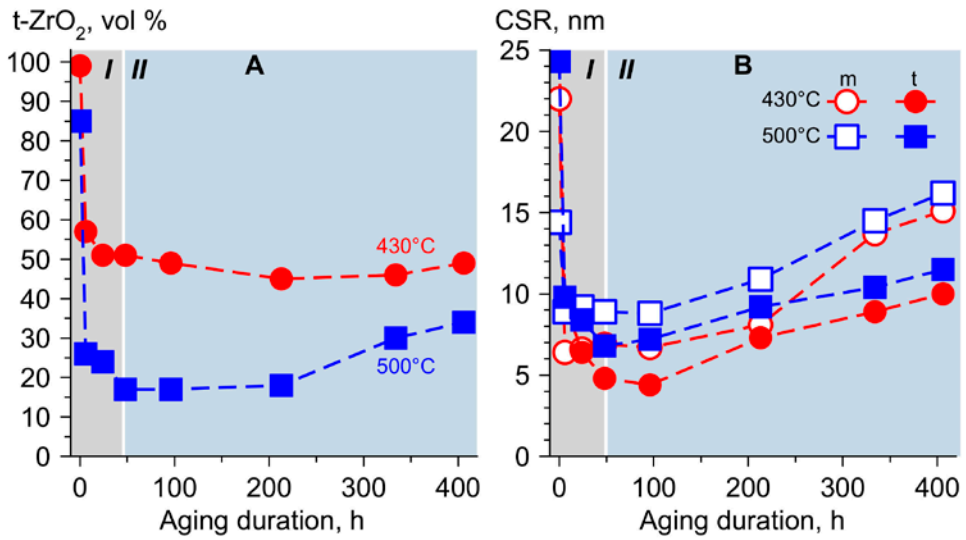

Fig. 5. The dependence of the phase composition (A) and the CSR size of ZrO_2 phases (430 and 500 °C) on the aging duration of $ZrO_2 \cdot nH_2O$ (B)

result of the $ZrO_2 \cdot nH_2O$ aging for 6 h, the *m*-ZrO_2 phase content increased significantly to 43% and the size of the crystallites decreased to 6 (10) nm at 430 °C (500 °C). With increasing aging time, the phase ratio remained close to 1 (430 °C). The minimum size of phase crystallites was achieved at 48–96 h of aging. Aging for 213–406 h led to a slight increase in the amount of *t*-ZrO_2 and an increase in the size of the CSR of the phases. The latter was in line with the trend in Fig. 4B and the size of ZrO_2 (430 °C) crystallites did not differ from the CSR of the phases for the corresponding $ZrO_2 \cdot nH_2O$.

The isotherms of N_2 sorption of all ZrO_2 samples after heat treatment at 500 °C (Fig. 6A) corresponded to type IVA, which was confirmed by the corresponding pore size distribution (Fig. 6B). The type of hysteresis loops varied: H3 (non-rigid aggregates of plate-like particles) for the ZrO_2 sample, whose $ZrO_2 \cdot nH_2O$ had not undergone aging; 6 h – H5; 24–213 (96) h – H2a (blind mesopores with narrow mouths) with signs of H3 or H5 (partially blocked ordered mesopores); 406 h – H1 (materials with blind pores with a close distribution over the width of the pore mouth and cavity or a narrow range of uniform open mesopores). The latter was further confirmed by a narrow pore size distribution (5.5–20.5 nm for 213 h and 7.3–24.6 nm for 406 h) (Fig. 6B).

The dependences of the porosity indicators, *SSA*, V_Σ, and d_{por}, of ZrO_2 on the aging time of the corresponding $ZrO_2 \cdot nH_2O$ were similar to those in Fig. 4. The maximum *SSA* (91 m^2/g) and V_Σ (0.32 cm^3/g) were achieved during aging for 48 h and heat treatment at 500 °C.

Since $ZrO_2 \cdot nH_2O$ has several types of OH groups (terminal, single- and triple-bridging, hydrogen bond between OH groups) [38–41], IR spectroscopy was used to study the change in the ratio between them depending on the aging time when $ZrO_2 \cdot nH_2O$ was heated to 350 °C in vacuum (Fig. 7). The absorption band corresponding to the terminal (edge) OH groups with a maximum of 3,760±5 cm^{-1} overlapped with the absorption band of the double-bridging OH groups with a maximum of 3,735±5 cm^{-1}. With an increase in the aging time, there was an extreme dependence of the ratio of the area of the terminal band to the sum of the areas of all bridging OH groups with a maximum at 48 hours of aging.

3.3. Acid-base properties of the ZrO_2 surface

Aging of $ZrO_2 \cdot nH_2O$ affects the acid-base properties of the surface of calcined ZrO_2 (500 °C). According to the data of TPD-NH_3 and TPD-CO_2 (Fig. 8), an increase in the aging time to 6–24 hours led to an increase in the specific acidity and basicity of the surface (Fig. 8A), especially of the basic sites. This result was apparently associated with the decomposition of the aggregates. On the one hand, it led to the appearance of Zr edge atoms dehydrated during heat treatment accompanied by the formation of LAS. On the other hand, the decomposition of aggregates contributed to an increase in the share of terminal OH groups (Fig. 7B), which had

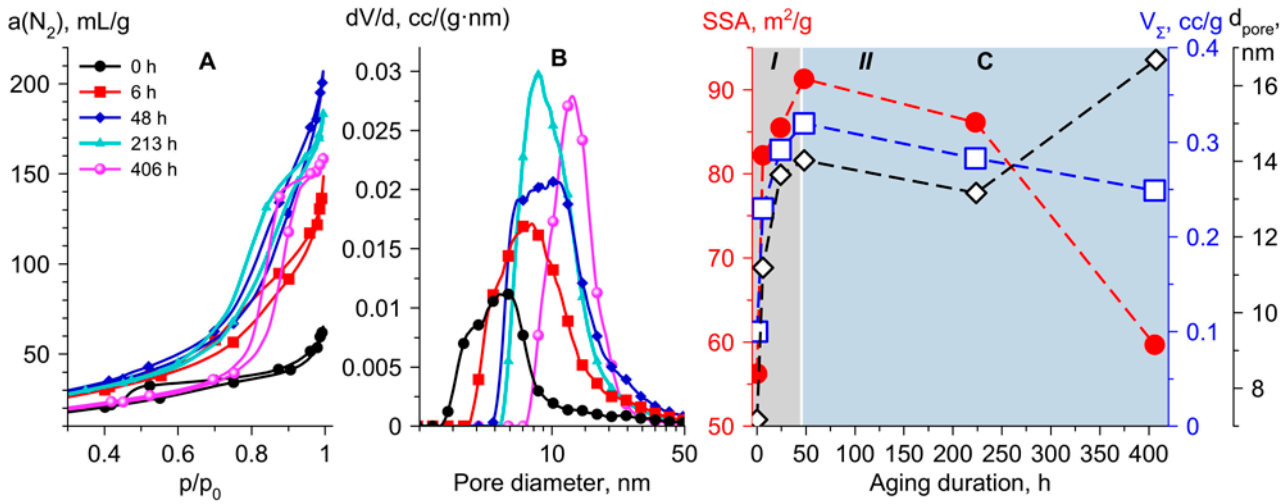

Fig. 6. Isotherms of N_2 sorption (A), pore size distribution, and dependence of textural characteristics (B) of ZrO_2 (500 °C) on the aging duration of $ZrO_2 \cdot nH_2O$

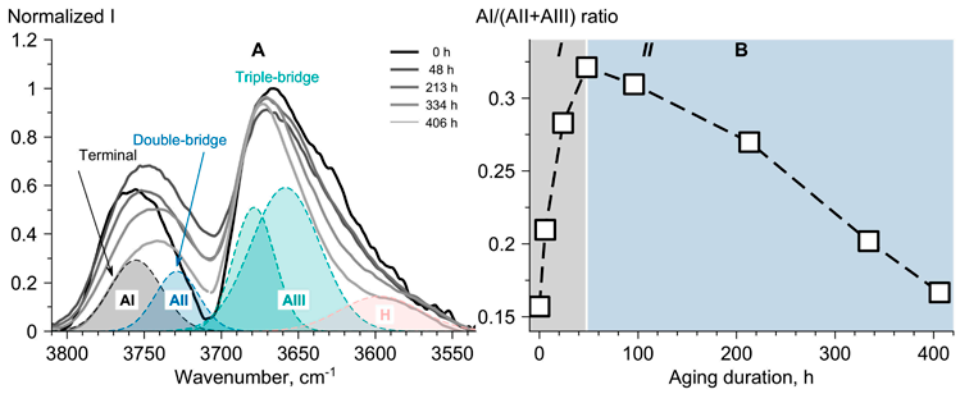

Fig. 7. IR spectra of $ZrO_2 \cdot nH_2O$ OH groups (A) and the dependence of the ratio of the absorption band area of terminal OH-groups and bridge OH-groups on the aging duration of (B)

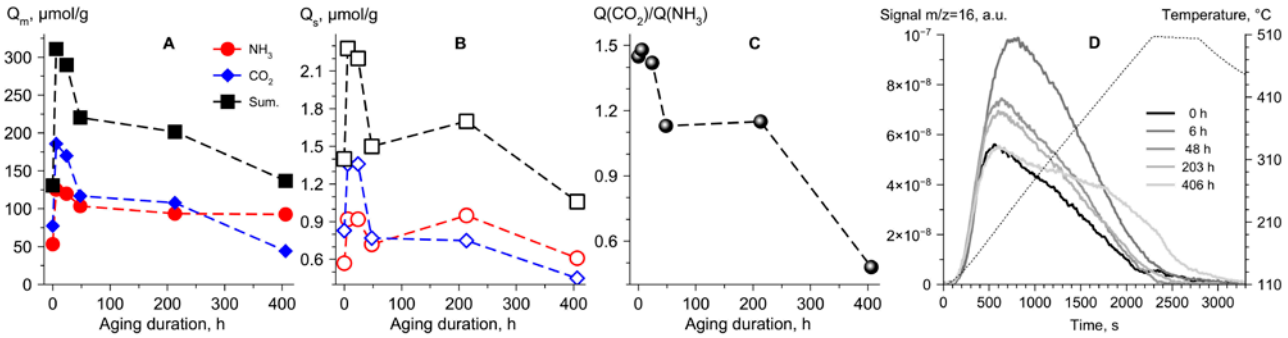

Fig. 8. The dependence of the acidity and basicity of the ZrO_2 surface on the aging duration of $ZrO_2 \cdot nH_2O$

basic properties [42-44]. Further aging led to a decrease in the acidity and basicity of the ZrO_2 surface. What is more, the basicity decreased more than the acidity (Fig. 8B). This effect can be also explained by the participation of terminal OH groups in the attachment of the $ZrO_2 \cdot nH_2O$ PPs and the corresponding decrease in their number relative to the bridging OH groups.

The adsorption strength of the molecular probes, which is directly proportional to the temperature (Fig. 8G), also varied depending on the aging time. An increase in the latter from 0 to 6 h led to a shift in the maximum NH_3desorption peak from 197 to 237 °C; while an increase from 213 to 406 h resulted in an increase in the relative amount of NH_3 desorbed above 400 °C and a decrease in the amount of CO_2 desorbed above 300 °C.

Fourier IR spectroscopy of sorbed pyridine at 150°C (Fig. 9A) and CO_2 at 110°C (Fig. 9B) on ZrO_2 obtained from $ZrO_2 \cdot nH_2O$ with different aging times confirmed the TPD results. An increase in the surface acidity was due to an increase in the number of LAS (1,444 cm^{-1} – 19b, 1,489 cm^{-1} – 19a, 1,574 cm^{-1} – 8b, and 1,604 cm^{-1} – 8a). The number of LAS varied extremely depending on the $ZrO_2 \cdot nH_2O$ aging time, 20 – 78 – 41 μmol/g. Aging also led to the formation of a small number of BAS (1,540 cm^{-1} – 19b and 1,636 cm^{-1} – 8a) (0 – 15 – 10 μmol/g, respectively). CO_2 was sorbed on the surface in the form of mono- (1,680–1,650 cm^{-1}) and bidentate (1,605, 1,470–1,440, and 1,223 cm^{-1}) hydrocarbonates, bidentate carbonates (1,555 and 1,331 cm^{-1}), and bridging (polydentate) carbonates (1,680–1,650 and 1,470–1,440 cm^{-1}). Surface hydrocarbonates were formed with the participation of the ZrO_2 basic (edge) OH-groups, while surface carbonates were formed with the participation of the Zr^{4+}–O^{2-} acid-base pair [42, 45, 46].

3.4. Results and discussion

The described results allow distinguishing two time regions in which different transformations of $ZrO_2 \cdot nH_2O$ occurred during its aging at pH = 10, T = 90 °C:

I. *Region of 0–48 h.* This interval is characterized by the decomposition of $ZrO_2 \cdot nH_2O$ aggregates and agglomerates at all levels: aggregates of nanometer

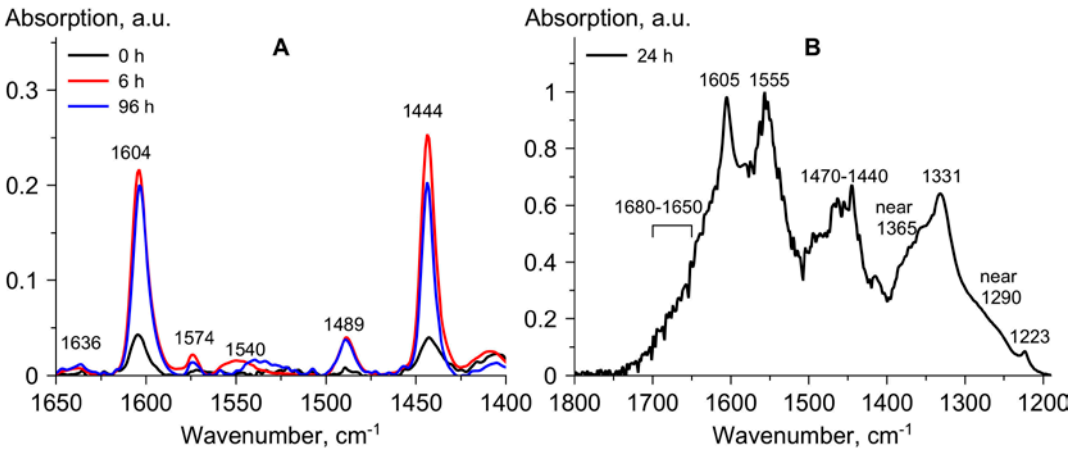

Fig. 9. IR spectra of pyridine (A) and CO_2 sorbed on ZrO_2 obtained by heat treatment at 500 °C $ZrO_2 \cdot nH_2O$ with different aging duration

primary particles (PP), which constituted the walls of micro - and mesopores; and secondary aggregates with the size of hundreds of nm, which constituted large micrometer dense and loose agglomerates. The results of low-temperature N_2 sorption were used to determine the particle size for adsorption, d_{ads}, under the assumption that they can be of different shapes, and to determine the wall thickness of cylindrical pores, 2δ, [9] according to the following formulas:

$$d_{ads} = \frac{A}{\rho \cdot S_{sp}}, \text{ [nm]}, \quad (1)$$

$$2\delta = 2\sqrt{\frac{d_{por}^2}{4} + \frac{d_{por}^2}{4 \cdot \rho \cdot V_{\Sigma}}} - \frac{d_{por}}{2}, \text{ [nm]}, \quad (2)$$

where A is the particle shape coefficient: 6 – spherical, 4 – rod-like, 2 – plate-like; and $\rho = 4.86$ g/cm³ is the density of X-ray amorphous $ZrO_2 \cdot nH_2O$ [47]. Since $ZrO_2 \cdot nH_2O$ exists in the form of particles rather than a single long cylinder, the thickness of the walls between the pores is 2δ [9]. Assuming that the shape of PPs and their aggregates is plate-like (A = 2), the values of d_{ads} are close to the value of the thickness of pore walls, 2δ (Fig. 10A). This is consistent with the general ideas about the shape of $ZrO_2 \cdot nH_2O$ nanoparticles [48-51] and the estimates based on previous research (Fig. 10B). Therefore, during an aging time of up to 48 h, the PP aggregates in the initial $ZrO_2 \cdot nH_2O$ broke up into their constituent PPs 2 times smaller in size.

Interaction between PPs accompanied by the formation of aggregates occurred through the Zr-O (H)-Zr bridging group, the decomposition of which (Zr-O bond breakage) led to the release of

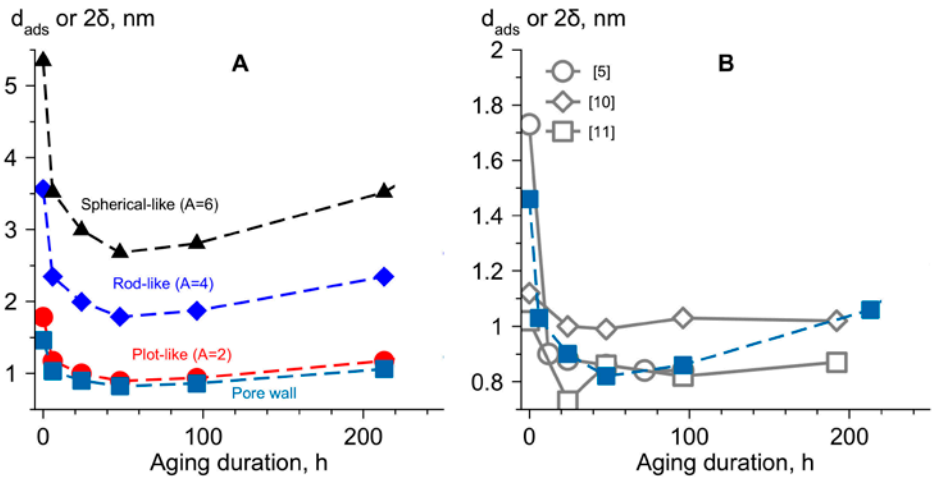

Fig. 10. Changes in the adsorption size of $ZrO_2 \cdot nH_2O$ particles and the thickness of the pore walls depending on the aging duration of $ZrO_2 \cdot nH_2O$ (A) and comparison with the literature data (B)

Zr-OH and an increase in the ratio of terminal OH groups to bridging OH groups. On the other hand, the formation of aggregates can be explained by a combination of hydrogen bonds and dispersion interactions (adhesion) [40]. Then the formation and decomposition of aggregates is of a physical rather than chemical nature. The latter is supported by the fact that the greatest increase in *SSA* was observed during the first 6 hours of aging, during which there was no significant dehydration of $ZrO_2 \cdot nH_2O$ and no change in the ratio between terminal OH groups and bridging OH groups. However, as a result of these processes, some of the additional water molecules and/or OH groups located between the aggregates were removed. This was also confirmed by a 10–12% decrease in the $ZrO_2 \cdot nH_2O$ hydration and decrease in Q_{cr} of aZrO_2 by 16% after 48 h of aging. A change in the type of N_2 sorption isotherms and the hysteresis loop revealed a change in the packing or ordering degree of the PPs and their aggregates: from dense microporous aggregates through loose aggregates of plate-like particles with PP microporosity and mesopores between them, to partially blocked mesopores with narrow mouths or $ZrO_2 \cdot nH_2O$ with an ordered mesoporous grid-like structure.

The presence of PP aggregates in $ZrO_2 \cdot nH_2O$ is a key condition for the formation of *t*-ZrO_2 after heat treatment at 430 and 500 °C, whereas their decomposition to primary particles is a key condition for the formation of *m*-ZrO_2. In terms of factors explaining the stabilization of *t*-ZrO_2 [15, 16], aggregation increased the contribution of interfacial energy, which reached the value necessary for the formation of *t*-ZrO_2. However, the aggregation of $ZrO_2 \cdot nH_2O$ PPs apparently contributed to the formation of nuclei of the necessary local structure, spatial orientation, and ordering [14], while oriented attachment explained the high rate of their formation during thermal crystallization [34]. The decomposition of the $ZrO_2 \cdot nH_2O$ aggregates reduced the role of the initial spatial orientation, local structure and/or ordering of the $ZrO_2 \cdot nH_2O$ PPs and reduced the role of the thermodynamic and kinetic factors of the *t*-ZrO_2 formation. According to the Buyanov-Krivoruchko oriented attachment theory [25], such behavior is characteristic of precipitation consisting of tightly packed (ordered) aggregates. According to this theory, the decomposition of aggregates to PPs is followed by the formation from them of partially crystallized particles, and from those of well-crystallized particles, crystallization centers, which does not lead to a change in the value of *SSA*.

II. *Region of 96–406 h*. In this time region, the primary particles of the X-ray amorphous $ZrO_2 \cdot nH_2O$ formed as a result of the decomposition of aggregates crystallized and formed a mixture of *t*- and *m*-ZrO_2, which was accompanied by intensive dehydration. The ratio of terminal OH groups to bridging OH groups decreased, which indicated the reaction of terminal groups with each other or bridging OH groups resulting in the formation of Zr-O-Zr oxygen bridges (oxolation). This resulted in a decrease in *SSA* and V_{Σ}, an increase in the diameter and wall thickness of the $ZrO_2 \cdot nH_2O$ and ZrO_2 pores (500 °C), and a denser texture of secondary aggregates and agglomerates.

The fact that as a result of heat treatment at 430 °C, the ratio of crystalline phases was still at about 0.9–1 and was not accompanied by the growth of the crystallites formed at the aging stage indicates the following. The crystallization centers of phases "oriented" the nearest $ZrO_2 \cdot nH_2O$ PPs and the nuclei to get attached and crystallize into secondary crystals exactly with them. The crystallization centers which were formed during 96–213 h of aging also grew by attachment mechanism during further aging for 213–406 h. Apparently, the disordering of the PPs which were formed during 48 h of aging contributed to the possibility of their orientation relative to each other in different spatial configurations, for example, a rod and a "sandwich" [14], with further binding through terminal OH-groups to form nuclei and then crystallization centers. What is more, the probability of such configurations was equal. Apparently, this also required an excess of OH groups in the mother solution and alkaline pH, which contributed to the deformation of nanoparticles [40]. The Buyanov-Krivoruchko oriented attachment theory explains the bimodal distribution of $ZrO_2 \cdot nH_2O$ pore sizes by a higher rate of the formation of secondary crystals during the attachment of nuclei to crystallization centers as compared to the rate of the formation of crystallization centers from nuclei.

4. Conclusions

This paper presents the results of the study of the changes in the phase composition, porosity, and acid-base properties of the $ZrO_2 \cdot nH_2O$ surface and the ZrO_2 nanocrystallites which are formed from it and their dependence on the aging time of $ZrO_2 \cdot nH_2O$ in contact with the mother solution at 90 °C and pH = 10 and in the absence of the influence of impurities (Si^{4+}, Na^+, and K^+). It was established for the first time that in the absence of impurities during aging, the above properties of $ZrO_2 \cdot nH_2O$ and ZrO_2 are extremely dependent on the aging time with an extremum at 24–96 h. It was established that the decomposition of dense aggregates of the primary particles and submicron and micron aggregates and agglomerates of X-ray amorphous $ZrO_2 \cdot nH_2O$ precedes its crystallization into a mixture of *t*- and *m*-ZrO_2 phases, which is described by the Buyanov-Krivoruchko oriented attachment theory. During the decomposition of PP aggregates, $ZrO_2 \cdot nH_2O$ is characterized by the formation of edge OH groups, which participate in the further PP attachment and crystallization. It was assumed that another peculiarity identified during the research, i.e. the ratio of *t*- and *m*-ZrO_2 phases close to 1, which does not change after heat treatment, can be explained by the spatial orientation of PPs during their attachment. The orientation of PPs in dense aggregates of the initial $ZrO_2 \cdot nH_2O$ is a key factor in the formation of nanocrystallites of the *t*-ZrO_2 metastable phase during the heat treatment of $ZrO_2 \cdot nH_2O$.

The revealed features allow expanding the applications of the concepts of the oriented attachment theory to the mild conditions of $ZrO_2 \cdot nH_2O$ aging. From a practical perspective, we determined the aging time of $ZrO_2 \cdot nH_2O$ which makes it possible to achieve the best porosity and acid-base properties of the surface, which are important for the production of ZrO_2-based catalyst supports.

Author contributions

Sh. O. Omarov, research concept, methodology development, text writing, final conclusions, conducting research, review writing, and text editing. M. B. Pakhomov, scientific supervision of research, research concept, and methodology development.

Conflict of interests

The authors declare that they have no known competing financial interests or personal relationships that could have influenced the work reported in this paper.

References

1. Fedorov P. P., Yarotskaya E. G. Zirconium dioxide. Review. *Condensed Matter and Interphases*. 2021;23(2): 169–187. https://doi.org/10.17308/kcmf.2021.23/3427

2. Noskov A. S. Scientific and technical aspects of research and prospects for import substitution in the area of industrial catalysts*. *Vestnik rossiiskoi akademii nauk = Herald of the Russian Academy of Sciences*. 2022;92(10): 940–949. (In Russ). https://doi.org/10.31857/S0869587322100085

3. Gao L., Zhi H., Zhang S., Liu S. Template-free hydrothermal synthesis of octahedron-, diamond-, and plate-like ZrO_2 mono-dispersions. *Nanomaterials*. 2022;12(19): 3405. https://doi.org/10.3390/nano12193405

4. Omarov Sh. O., Pakhomov N. A. Variation of conditions of $ZrO_2 \cdot nH_2O$ precipitation and aging as a method for controlling the phase composition and texture of ZrO_2. *Kataliz v promyshlennosti*. 2020;20(5): 335–43. https://doi.org/10.18412/1816-0387-2020-5-335-343

5. Deshmane V. G., Adewuyi Y. G. Synthesis of thermally stable, high surface area, nanocrystalline mesoporous tetragonal zirconium dioxide (ZrO_2): effects of different process parameters. *Microporous and Mesoporous Materials*. 2012;148(1). https://doi.org/10.1016/j.micromeso.2011.07.012

6. Chuah G. K. An investigation into the preparation of high surface area zirconia. *Catalysis Today*. 1999;49(1–3). https://doi.org/10.1016/s0920-5861(98)00417-9

7. Chuah G. K., Jaenicke S. The preparation of high surface area zirconia - Influence of precipitating agent and digestion. *Applied Catalysis A: General*. 1997;163(1–2). https://doi.org/10.1016/s0926-860x(97)00103-8

8. Chan K. S., Chuah G. K., Jaenicke S. Preparation of stable, high surface area zirconia. *Journal of Materials Science Letters*. 1994;13(21). https://doi.org/10.1007/bf00626515

9. Chuah G. K., Jaenicke S., Pong B. K. The preparation of high-surface-area zirconia: II. Influence of precipitating agent and digestion on the morphology and microstructure of hydrous zirconia. *Journal of Catalysis*. 1998;175(1). https://doi.org/10.1006/jcat.1998.1980

10. Jaenicke S., Chuah G. K., Raju V., Nie Y. T. Structural and morphological control in the preparation of high surface area zirconia. *Catalysis Surveys from Asia*. 2008;12(3). https://doi.org/10.1007/s10563-008-9048-2

11. Chuah G. K., Jaenicke S., Cheong S. A., Chan K. S. The influence of preparation conditions on the surface area of zirconia. *Applied Catalysis A: General*. 1996;145(1–2). https://doi.org/10.1016/0926-860x(96)00152-4

12. Hong E., Baek S. W., Shin M., Suh Y. W., Shin C. H. Effect of aging temperature during refluxing on the textural and surface acidic properties of zirconia catalysts. *Journal of Industrial and Engineering Chemistry*. 2017;54. https://doi.org/10.1016/j.jiec.2017.05.026

13. Sato S., Takahashi R., Sodesawa T., Tanaka S., Oguma K., Ogura K. High-surface-area SiO_2-ZrO_2 prepared by depositing silica on zirconia in aqueous ammonia solution. *Journal of Catalysis*. 2000;196(1). https://doi.org/10.1006/jcat.2000.3027

14. Kuznetsova T. G., Sadykov V. A. Specific features of the defect structure of metastable nanodisperse ceria, zirconia, and related materials. *Kinetics and Catalysis*. 2008;49(6): 840–858. https://doi.org/10.1134/s0023158408060098

15. Shukla S., Seal S. Mechanisms of room temperature metastable tetragonal phase stabilisation in zirconia. *International Materials Reviews*. 2005;50(1). https://doi.org/10.1179/174328005x14267

16. Esposito V., Castelli I. E. Metastability at defective metal oxide interfaces and nanoconfined structures. *Advanced Materials Interfaces*. 2020;7(13). https://doi.org/10.1002/admi.201902090

17. Strekalovsky V. N., Polezhaev Yu. M., Palyguev S. F. *Oxides with impurity disordering: composition, structure, and phase transformations*. Moscow: Nauka Publ.; 1987. 160 p. (In Russ).

18. Brown P. *Chemical thermodynamics of zirconium*. Amsterdam: Elsevier; 2005. 542 p.

19. Sasaki T., Kobayashi T., Takagi I., Moriyama H. Hydrolysis constant and coordination geometry of zirconium(IV). *Journal of Nuclear Science and Technology*. 2008;45(8): 735–739. https://doi.org/10.1080/18811248.2008.9711474

20. Kobayashi T., Bach D., Altmaier M., Sasaki T., Moriyama H. Effect of temperature on the solubility and solid phase stability of zirconium hydroxide. *Radiochimica Acta*. 2013;101(10). https://doi.org/10.1524/ract.2013.2074

21. Denkewicz R. P., TenHuisen K. S., Adair J. H. Hydrothermal crystallization kinetics of m-ZrO_2 and *t*-ZrO_2. *Journal of Materials Research*. 1990;5(11). https://doi.org/10.1557/jmr.1990.2698

22. Ivanov V. K., Fedorov P. P., Baranchikov A. Y., Osiko V. V. Oriented attachment of particles: 100 years of investigations of non-classical crystal growth. *Russian Chemical Reviews*. 2014;83(12): 1204–1222. https://doi.org/10.1070/rcr4453

23. Pathiraja G., Obare S., Rathnayake H. Oriented attachment crystal growth dynamics of anisotropic one-dimensional metal/metal oxide nanostructures: mechanism, evidence, and challenges. In: *Crystal Growth and Chirality - Technologies and Applications*. 2023. https://doi.org/10.5772/intechopen.107463

24. He W., Wen K., Niu Y. Introduction to oriented-attachment growth mechanism. In: *Springer Briefs in Energy*. Switzerland: Springer; 2018. 84 p. https://doi.org/10.1007/978-3-319-72432-4_1

25. Buyanov R. A., Krivoruchko O. P. Development of the theory of crystallization of low-soluble metal hydroxides and scientific foundations for the preparation of catalysts from substances of this class*. *Kinetics and Catalysis*. 1976;17(3): 765–75. (In Russ). Available at: https://www.elibrary.ru/item.asp?id=22694458

26. Zi W., Hu Z., Jiang X., ... Liu, F. Morphology regulation of zeolite MWW via classical/nonclassical crystallization pathways. *Molecules*. 2023;29(1): 170. https://doi.org/10.3390/molecules29010170

27. Xia Y., Shi J., Sun Q., ... Chen J.-F. Controllable synthesis and evolution mechanism of monodispersed Sub-10 nm ZrO_2 nanocrystals. *Chemical Engineering Journal*. 2020;394. 124843. https://doi.org/10.1016/j.cej.2020.124843

28. Xu X., Wang X. Fine tuning of the sizes and phases of ZrO_2 nanocrystals. *Nano Research*. 2009;2(11). https://doi.org/10.1007/s12274-009-9092-x

29. Pokratath R., Lermusiaux L., Checchia S., ... De Roo J. An amorphous phase precedes crystallization: unraveling the colloidal synthesis of zirconium oxide nanocrystals. *ACS Nano*. 2023;17(9): 8796–8806. https://doi.org/10.1021/acsnano.3c02149

30. Stolzenburg P., Freytag A., Bigall N. C., Garnweitner G. Fractal growth of ZrO_2 nanoparticles induced by synthesis conditions. *CrystEngComm*. 2016;18(43). https://doi.org/10.1039/c6ce01916a

31. Yan H., Di J., Li J., Liu Z., Liu J., Ding X. Synthesis of zirconia micro-nanoflakes with highly exposed (001) facets and their crystal growth. *Crystals*. 2021;11(8). https://doi.org/10.3390/cryst11080871

32. Qin W., Zhu L. Anisotropic morphology, formation mechanisms, and fluorescence properties of zirconia nanocrystals. *Scientific Reports*. 2020;10(1). https://doi.org/10.1038/s41598-020-70570-5

33. Ribeiro C., Vila C., De Matos J. M. E., Bettini J., Longo E., Leite E. R. Role of the oriented attachment mechanism in the phase transformation of oxide nanocrystals. *Chemistry – A European Journal*. 2007;13(20). https://doi.org/10.1002/chem.200700034

34. Almyasheva O. V. *Formation of oxide nanocrystals and nanocomposites in hydrothermal conditions and the structure and properties of materials based on them**. Dr. Sci. (Chem.) diss. Saint-Petersburg: 2017. 363 c. Available at: https://www.dissercat.com/content/formirovanie-oksidnykh-nanokristallov-i-nanokompozitov-v-gidrotermalnykh-usloviyakh-stroenie (In Russ).

35. Chuah G. K., Jaenicke S., Xu T. H. Acidity of high-surface-area zirconia prepared from different precipitants. *Surface and Interface Analysis*. 1999;28(1): 131–134. https://doi.org/10.1002/(sici)1096-9918(199908)28:1<131::aid-sia634>3.0.co;2-5

36. Toraya H., Yoshimura M., Somiya S. Calibration curve for quantitative analysis of the monoclinic-tetragonal ZrO_2 system by X-ray diffraction. *Journal of American Ceramic Society*. 1984;67: C119–121. https://doi.org/10.1111/j.1151-2916.1984.tb19715.x

37. Emeis C. A. Determination of integrated molar extinction coefficients for infrared absorption bands of pyridine adsorbed on solid acid catalysts. *Journal of Catalysis*. 1993;141(2): 347–354. https://doi.org/10.1006/jcat.1993.1145

38. King G., Soliz J. R., Gordon W. O. Local structure of $Zr(OH)_4$ and the effect of calcination temperature from X-ray pair distribution function Analysis. *Inorganic Chemistry*. 2018;57(5). https://doi.org/10.1021/acs.inorgchem.7b03137

39. Mogilevsky G., Karwacki C. J., Peterson G. W., Wagner G.W . Surface hydroxyl concentration on $Zr(OH)_4$ quantified by 1H MAS NMR. *Chemical Physics Letters*. 2011;511(4–6): 384–388. https://doi.org/10.1016/j.cplett.2011.06.072

40. Iordanov I. O., Bermudez V. M., Knox C. K. Computational modeling of the structure and properties of

$Zr(OH)_4$. *Journal of Physical Chemistry C.* 2018;122(10). https://doi.org/10.1021/acs.jpcc.7b11107

41. Li J., Chen J., Song W., Liu J., Shen W. Influence of zirconia crystal phase on the catalytic performance of Au/ZrO_2 catalysts for low-temperature water gas shift reaction. *Applied Catalysis A: General.* 2008;334(1–2). https://doi.org/10.1016/j.apcata.2007.10.020

42. Wan E., Travert A., Quignard F., Tichit D., Tanchoux N., Petitjean H. Modulating properties of pure ZrO_2 for structure–activity relationships in acid-base catalysis: contribution of the alginate preparation route. *ChemCatChem.* 2017;9(12): 2358–2365. https://doi.org/10.1002/cctc.201700171

43. Ouyang F., Nakayama A., Tabada K., Suzuki E. Infrared study of a novel acid–base site on ZrO_2 by adsorbed probe molecules. I. pyridine, carbon dioxide, and formic acid adsorption. *The Journal of Physical Chemistry B.* 2000;104(9): 2012–2018. https://doi.org/10.1021/jp992970i

44. Ma Z. Y., Yang C., Wei W., Li W. H., Sun Y. H. Surface properties and CO adsorption on zirconia polymorphs. *Journal of Molecular Catalysis A: Chemical.* 2005;227(1–2). https://doi.org/10.1016/j.molcata.2004.10.017

45. Ouyang H., Li C., Li K., Li H., Zhang Y. Effect of pH on crystallization of nanocrystalline zirconia in a microwave-hydrothermal process. *Journal Wuhan University of Technology, Materials Science Edition.* 2016;31(1). https://doi.org/10.1007/s11595-016-1332-9

46. Köck E. M., Kogler M., Götsch T., ... Penner S. Surface chemistry of pure tetragonal ZrO_2 and gas-phase dependence of the tetragonal-to-monoclinic ZrO_2 transformation. *Dalton Transactions.* 2017;46(14): 4554–4570. https://doi.org/10.1039/c6dt04847a

47. Ceresoli D., Vanderbilt D. Structural and dielectric properties of amorphous ZrO_2 and HfO_2. *Physical Review B.* 2006;74(12): 125108. https://doi.org/10.1103/physrevb.74.125108

48. Livage J., Doi K., Mazieres C. Nature and thermal evolution of amorphous hvdrated zirconium oxide. *Journal of the American Ceramic Society.* 1968;51(6): 349–353. https://doi.org/10.1111/j.1151-2916.1968.tb15952.x

49. Azarova L. A., Kopitsa G. P., Yashina E. G., Garamus V. M., Grigoriev S. V. The model of fractal particle of hydrated zirconium dioxide based on small-angle neutron scattering data. *Journal of Surface Investigation: X-Ray, Synchrotron and Neutron Techniques.* 2019;(10): 23–29. (In Russ, abstract in Eng.). https://doi.org/10.1134/S0207352819100044

50. Ivanov V. K., Kopitsa G. P., Baranchikov A. E., Grigoriev S. V., Garamus V. M. Regularities of changes in composition and fractal structure of hydrated zirconium dioxide xerogels during thermal annealing*. *Russian Journal of Inorganic Chemistry.* 2010;55(2): 190–196. (In Russ). Available at: https://www.elibrary.ru/item.asp?id=13725937

51. Tiseanu C., Parvulescu V. I., Sanchez-Dominguez M., Boutonnet M. Spectrally and temporarily resolved luminescence study of short-range order in nanostructured amorphous ZrO_2. *Journal of Applied Physics.* 2011;110(10). https://doi.org/10.1063/1.3662117

* *Translated by author of the article*

Information about the authors

Shamil O. Omarov, postgraduate student, Research Fellow, Ioffe Institute (Saint-Petersburg, Russian Federation).
https://orcid.org/0000-0002-6862-128X
somarov@mail.ioffe.ru

Nikolay A. Pakhomov, Cand. Sci (Chem.), Research Fellow, St. Petersburg State Technological Institute (Technical University) (Saint-Petersburg, Russian Federation).
https://orcid.org/0009-0001-8414-2561
npakhomov@technolog.edu.ru

Received 05.08.2024; approved after reviewing 20.08.2024; accepted for publication 16.09.2024; published online 25.12.2024.

Translated by Irina Charychanskaya

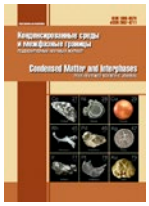

ISSN 1606-867X (Print)
ISSN 2687-0711 (Online)
Condensed Matter and Interphases
Kondensirovannye Sredy i Mezhfaznye Granitsy
https://journals.vsu.ru/kcmf/

Original articles

Research article
https://doi.org/10.17308/kcmf.2024.26/12450

Phase subsolidus separation of the Ge–P–Sn ternary system

G. V. Semenova✉, T. P. Sushkova, A. N. Golentsova

Voronezh State University,
1 Universitetskaya pl., Voronezh 394018, Russian Federation

Abstract

2D materials are becoming increasingly attractive for use in modern electronic devices due to new properties that can arise from reduced dimensionality and the quantum confinement of charge carriers. Many studies are aimed at the search for materials characterized by a layered structure, which allows obtaining chemically stable atomic layers without surface broken bonds. Binary compounds of elements of IV (Si, Ge, Sn) and V (P, As) groups form layered structures in which two-dimensional layers with covalent bonds are bound by weak van der Waals forces, and from this point of view they can be considered as being promising 2D materials. However, it should be noted, that obtaining crystals of compounds of this class is associated with significant difficulties due to the high vapor pressure of phosphorus. Attempts have been made to obtain the GeP samples from tin melt solutions, which can significantly soften the synthesis conditions. The study of phase equilibria and the construction of a phase diagram of the Ge–P–Sn ternary system would allow approaching the production of both bulk and two-dimensional samples of germanium phosphide, as well as determining the possibility of alloying them with tin.

In this study, based on the investigation of several alloys of the Ge–P–Sn ternary system using the X-ray phase analysis, it was established that the phase subsolidus separation of the state diagram is carried out by the Sn_4P_3–Ge, Sn_4P_3–GeP, Sn_3P_4–GeP and SnP_3–GeP sections. The composition of the alloys corresponded to the figurative points of the intersecting sections. A scheme of phase equilibria in the Ge–P–Sn system was proposed. This scheme assumes the existence of a nonvariant peritectic equilibrium L+Ge ↔ Sn_4P_3+GeP and eutectic processes L ↔ Ge+Sn+Sn_4P_3 and L ↔ Sn_4P_3+GeP+SnP_3.

The study of alloys using the differential thermal analysis method allowed determining the temperatures of these processes, equal to 795 K, 504 K, and 790 K, respectively. The *T-x* diagram of the Sn–GeP polythermal cross section, which experimentally confirms the proposed scheme, was constructed.

Keywords: Phase diagrams, Germanium phosphide, Tin phosphides, Ge–P–Sn system, Subsolidus phase separation

Acknowledgements: X-ray powder diffraction studies were performed using the equipment of the VSU Centre for Collective Use of Scientific Equipment.

For citation: Semenova G. V., Sushkova T. P., Golentsova A. N. Phase subsolidus separation of the Ge–P–Sn ternary system. *Condensed Matter and Interphases*. 2024;26(4): 745–754. https://doi.org/10.17308/kcmf.2024.26/12450

Для цитирования: Семенова Г. В., Сушкова Т. П., Голенцова А. Н. Фазовое субсолидусное разграничение системы Ge–P–Sn. *Конденсированные среды и межфазные границы*. 2024;26(4): 745–754. https://doi.org/10.17308/kcmf.2024.26/12450

✉ Galina V. Semenova, e-mail: semen157@chem.vsu.ru

1. Introduction

The $A^{IV}B^{V}$ compounds have been known for a long time and have been quite well studied [1, 2]. However, their wide application was extremely limited due to the complex conditions of their synthesis. Recently, interest in these compounds has significantly increased due to the possibility of obtaining 2D materials based on them. Along with research into graphene, black phosphorus, and arsenic subgroup elements [3–9], an active search for binary compounds that can be used as 2D materials is being carried out. $A^{IV}B^{V}$ compounds are characterized by a layered structure with unequal bonds, which allow to obtain these phases in the form of atomically thin layers [10–14]. GeP samples in the form of two-dimensional layers were obtained in [10], however, the harsh synthesis conditions significantly limit widespread use of this material, therefore attempts to obtain this phase from a melt solution in tin are being made. The authors [10] believed that the addition of a low-melting component such as tin, should soften the conditions for the production of germanium phosphide, lowering the synthesis temperature and the vapor pressure of phosphorus in the system. However, in addition to germanium phosphide, the presence of tin phosphide was detected in the samples. In order to predict the composition of the obtained samples, it is necessary to know the nature of the phase diagram of the ternary Ge-P-Sn system. The process, as well as the optimal conditions for obtaining materials with the required composition and the characteristics can be selected based on the nature of phase equilibria.

At the same time, information about the phase diagram in the literature is very limited. The following circumstances make the analysis of the Ge–P–Sn ternary system quite difficult. If the Ge–Sn binary system is characterized by a eutectic type of phase diagram [15], then in the other two Ge–P and Sn–P binary systems there are intermediate phases. The Ge–P system has been studied quite well; germanium monophosphide GeP is the only compound and melts by a peritectic reaction at a temperature of 998 K and a pressure of about 4.6 MPa [16]. The nature of the equilibria in the Sn–P binary system has not yet been definitively established, especially in the region of high phosphorus content. The system contains three intermediate phases with a similar rhombohedral structure and space group $R\bar{3}m$: Sn_4P_3, Sn_3P_4 and SnP_3 [17]. There is also information about the existence of high-pressure phases, in particular, SnP with tetragonal and cubic structures [18]. The existence of tin monophosphide at normal pressures was first reported in [19], and $P321$, $P3m1$, $R\bar{3}m1$ were indicated as the possible space groups. On the other hand, in a metallographic study of the Sn–P system for an equimolar composition Vivian [20] demonstrated a eutectic mixture of Sn_4P_3 and Sn_3P_4. The author [21] thinks that the contradictory results may be related to the metastability of the SnP phase.

The authors of this study previously [22] detected the SnP phase using X-ray phase analysis (XRD) and X-ray electron microscopy in alloys with equimolar composition, but after prolonged annealing the phase decomposed. A conclusion about the fairly high kinetic stability of SnP below 773 K was made, but the question of thermodynamic stability remained open. In [23], the phase composition of samples obtained for establishing equilibrium between tin and phosphorus at given values of temperature and phosphorus vapor pressure was determined. Moreover, the tin monophosphide phase was not recorded under any conditions, which may also indicate the metastability of this phase.

In [24,25], based on the study of samples of the Sn–P system using differential thermal analysis (DTA), X-ray phase analysis and local X-ray structural microanalysis, the existence of a eutectic equilibrium $L \leftrightarrow Sn_4P_3 + SnP_3$ at 824 K was established. The Sn_3P_4 intermediate phase was formed in the solid state according to the peritectoid scheme at a temperature of less than 673 K. The coordinates of the points of four-phase equilibrium were established by studying the temperature dependence of the saturated vapor pressure using the optical-tensimetric method: synthetic equilibrium ($Sn_4P_3 + V + L_1 + L_2$) was realized at 836 K and 0.6 atm; the eutectic equilibrium point ($L + V + Sn_4P_3 + SnP_3$) existed at 820 K and 2.8 atm. However, the SnP phase was not detected, which confirms the version about its metastability. Tin triphosphide, according to [20], decomposes into two liquids of different compositions, but the temperature of this synthetic equilibrium has not been established.

In [26], we studied the alloys of the Ge–Sn_4P_3 polythermal secttion of Ge–P–Sn ternary system using differential thermal and X-ray phase analysis methods. The samples were shown to be a heterogeneous mixture of two phases: germanium and tin phosphide with a Sn_4P_3 composition. Neither tin lines nor germanium phosphide reflexes were detected on X-ray diffraction patterns. Two endothermic effects, with the low-temperature effect occurring at the same temperature (800 K) were revealed on the thermograms of the samples. Thus, it was concluded that this section is partially quasi-binary (due to the synthetic transformation in the tin-phosphorus system, since the stratification of the liquid phase characteristic of a binary system can affect the nature of the liquidus surface of the ternary diagram in general, and, in particular, on the appearance of the considered section). However, in the study [26], when considering the division of the diagram into partial systems below the solidus, the appearance of the Sn_3P_4 by the peritectoid reaction was not taken into account, which requires additional experimental research.

The aim of this study was the identification of the nature of the phase subsolidus separation and the presentation of a possible scheme of phase equilibria in the Ge–P–Sn ternary system.

2. Experimental

The samples were obtained using a single-zone furnace SNOL 4/1100 ALSCO1220. The synthesis was carried out in quartz ampoules, which were pre-graphitized to prevent any possible interaction of the phosphorus with the walls of the ampoule. The OSCH-9-5 red phosphorus, OVCH-000 tin, and polycrystalline zone-purified germanium GOST 16154-80 were used to obtain the samples. The weighing was performed on AR2140 scales with an error of ± 1 10^{-3} g. The ampoules with the weighed portions of the starting substances were evacuated to a residual pressure of $5{\cdot}10^{-2}$ Pa and sealed.

The furnace heating mode was as follows: heating for 1 h to 693 K, then holding for two h at the specified temperature, and then heating for 7 h to 1233 K and holding for 1.5 h. The samples were then annealed for 150 h at a temperature below the expected solidus. The annealing temperature was selected based on the nature of equilibria in binary systems. For majority of the studied alloys it was 623 K.

The samples were studied using differential thermal analysis (DTA) in a programmable furnace heating system at a heating rate of 3.5 K/min, using calcined aluminum oxide as a standard. The samples and standards were kept in Stepanov quartz evacuated vessels. The signal from the chromel-alumel thermocouples was digitized and processed using the "MasterSCADA" computer program.

The X-ray diffraction was performed using an ARL X'TRA diffractometer with Bragg–Brentano Θ–Θ focusing geometry; the source of radiation was an X-ray tube with a copper anode: λ(Cu-Kα1) = 0.1541 nm; λ(Cu-Kα2) = 0.1544 nm; a step size of 0.04° and a counting time of 3 seconds. The diffraction patterns were interpreted using the ICDD PDF2 database.

3. Results and discussion

It should be noted that all binary compounds in the analyzed system do not melt congruently, as is assumed in the classical version of singular triangulation. Thus, germanium phosphide melts by a peritectic reaction [16], Sn_4P_3 and SnP_3 decompose into two liquids of different composition (synthetic equilibrium) [20], and Sn_3P_4 is formed in the solid state according to the peritectoid scheme [24, 25]. Therefore, only phase subsolidus separation is characteristic of the studied triple system [27].

Possible variants for separation in the Ge–P–Sn ternary system are shown in Fig. 1. The position of the secant cuts may vary, therefore experimental research is required for the determination of the correct separation pattern in the solid state.

To determine the subsolidus separation scheme of the phase diagram, alloys with compositions corresponding to the intersection points of the sections (Fig. 2) were prepared, and their phase analysis was carried out.

The $Ge_{0.30}P_{0.30}Sn_{0.40}$ (No. 1) sample corresponds to the intersection of Sn_4P_3–Ge and Sn–GeP sections. As shown in [26], it is a heterophase mixture of germanium and tin phosphide Sn_4P_3, which confirms the conclusions presented earlier. The Sn_4P_3–Ge section separates the secondary Sn_4P_3–Ge–Sn system, in which L↔Sn_4P_3+Ge+Sn

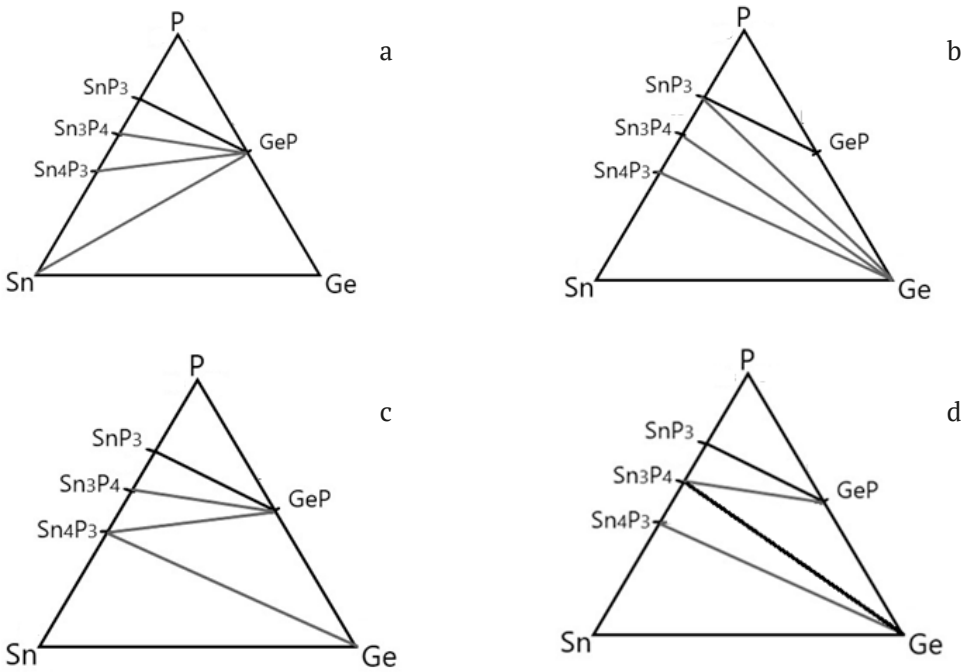

Fig. 1. Possible separation schemes in the Ge–P–Sn ternary system

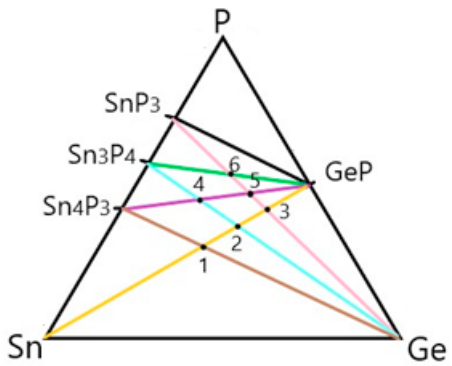

Fig. 2. Alloy compositions corresponding to the intersection of sections in the Ge–P–Sn system

equilibrium will be realized. This suggests that the diagram partitioning presented in Fig. 1a is incorrect. This conclusion was also confirmed by the results of X-ray phase analysis of $Ge_{0.36}Sn_{0.28}P_{0.36}$ (No. 2) and $Ge_{0.41}Sn_{0.15}P_{0.44}$ (No. 3) alloys, the diffraction patterns of which are shown in Fig. 3a, b. The alloys did not contain a tin-based phase, and the samples were a mixture of three phases: germanium, germanium phosphide, and Sn_4P_3. Since the figurative points of these alloys are the intersection points of the Sn_3P_4–Ge and SnP_3–Ge sections with the Sn–GeP section, it can be concluded that the indicated cuts will not be secant cuts as the presence of neither Sn_3P_4 nor SnP_3 were recorded in the samples.

From this point of view, out of the variants of the diagram division presented in Fig. 1, the correct variant is 1c. In this case, the compositions of the $Ge_{0.36}Sn_{0.28}P_{0.36}$ (No. 2) and $Ge_{0.41}Sn_{0.15}P_{0.44}$ (No. 3) samples belong to the triangle formed by the figurative points of the germanium, germanium phosphide and Sn_4P_3 phases, which also indicates that the Sn_4P_3–Ge and Sn_4P_3–GeP sections are secant sections below the solidus.

If the division of the state diagram of the considered system is performed by the Sn_4P_3–GeP section, then for $Ge_{0.17}Sn_{0.35}P_{0.48}$ (No. 4) and $Ge_{0.35}Sn_{0.16}P_{0.49}$ (No. 5) alloys we should observe the coexistence of two phases, germanium phosphide and Sn_4P_3. This is demonstrated by the diffraction pattern of the $Ge_{0.17}Sn_{0.35}P_{0.48}$ (No. 4) sample, shown in Fig. 3c. The diffraction pattern of the $Ge_{0.29}Sn_{0.18}P_{0.53}$ (No. 6) alloy, the figurative point of which represents the intersection of two sections: SnP_3–Ge and Sn_3P_4–GeP is shown in Fig. 3d. In the sample, GeP and Sn_3P_4 are the main phases.

Summarizing all the results obtained by the X-ray phase analysis, we can propose a scheme of phase subsolidus separation in the Ge–P–Sn system, performed by Sn_4P_3–Ge, Sn_4P_3–GeP, Sn_3P_4–GeP, and SnP_3–GeP sections.

Alloys of the Ge–P–Sn system were also studied using differential thermal analysis. Since the samples belong to different polythermal sections,

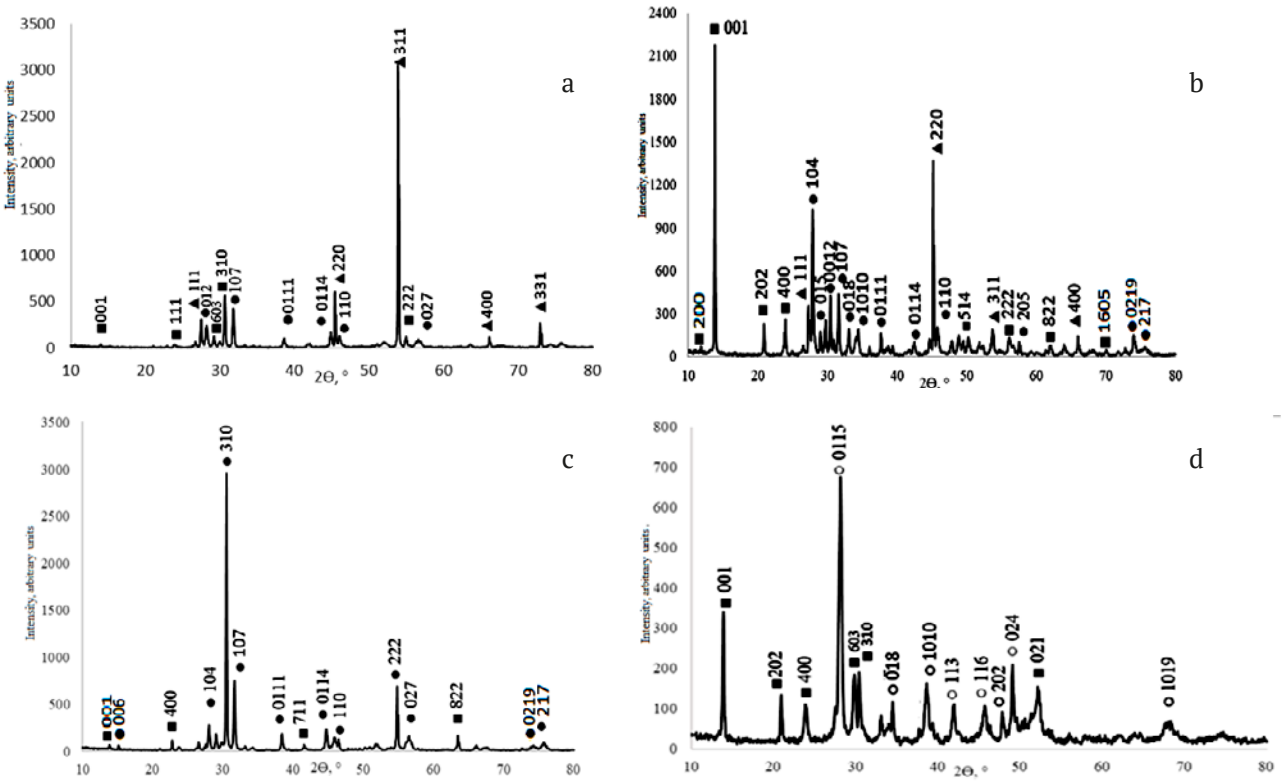

Fig. 3. Diffraction patterns of samples of the Ge–P–Sn system: a – $Ge_{0.36}P_{0.36}Sn_{0.28}$; b – $Ge_{0.41}P_{0.44}Sn_{0.15}$; V - $Ge_{0.17}P_{0.48}Sn_{0.35}$; g – $Ge_{0.29}P_{0.53}Sn_{0.18}$. ▲ – Ge; ● – Sn_4P_3; ■ – GeP; ○ – Sn_3P_4

information can only be obtained by comparing the lowest temperature effects on the heating curves. Such effects correspond to invariant equilibria involving a melt and three crystalline phases. At the same time, even lower temperature transformations in the solid state are possible (with the participation of Sn_3P_4), but they are usually rarely recorded by the DTA method. The temperatures of the onset of the first effects for the studied alloys are shown in Table, and thermograms of $Ge_{0.41}Sn_{0.15}P_{0.44}$ (No. 3) and $Ge_{0.29}Sn_{0.18}P_{0.53}$ (No. 6) samples are shown as the example in Fig. 4.

Alloys of the compositions $Ge_{0.36}Sn_{0.28}P_{0.36}$ (No. 2) and $Ge_{0.41}Sn_{0.15}P_{0.44}$ (No. 3) are characterized by the same temperature of the onset of the first effect (795±1 K). Because their figurative points belong to the Ge–GeP–Sn_4P_3 triangle, it can be stated that at this temperature a four-phase invariant process is carried out in the system with the participation of the melt and these three solid phases. Germanium phosphide is formed according to the peritectic scheme, then in the ternary system the L + Ge ↔ GeP monovariant process should occur, and the four-phase transformation should also be peritectic. Accordingly, the following diagram of phase equilibria in the germanium – phosphorus – tin system can be proposed (Fig. 5).

The pU_1 line corresponds to the L + Ge ↔ GeP monovariant process and along the e_6U_1 curve the L ↔ Ge + Sn_4P_3 process takes place, which is also monovariant. At the U_1 point, a four-phase L + Ge ↔ GeP + Sn_4P_3 transformation takes place.

The triangle formed by the figurative points of tin, germanium and tin phosphide Sn_4P_3, also has a four-phase transformation point (E_1), at a temperature probably very close to the melting point of tin:

Table. Temperatures of the onset of the first effect for alloys of the Ge–P–Sn system

	Alloy composition	*T*, K		Alloy composition	*T*, K
№ 1	$Ge_{0.30}P_{0.30}Sn_{0.40}$	800 ± 1	№ 4	$Ge_{0.17}P_{0.48}Sn_{0.35}$	794 ± 1
№ 2	$Ge_{0.36}P_{0.36}Sn_{0.28}$	795 ± 1	№ 5	$Ge_{0.35}P_{0.49}S_{n0.1}6$	795 ± 1
№ 3	$Ge_{0.41}P_{0.44}Sn_{0.15}$	796 ± 1	№ 6	$Ge_{0.29}P_{0.53}Sn_{0.18}$	789 ± 1

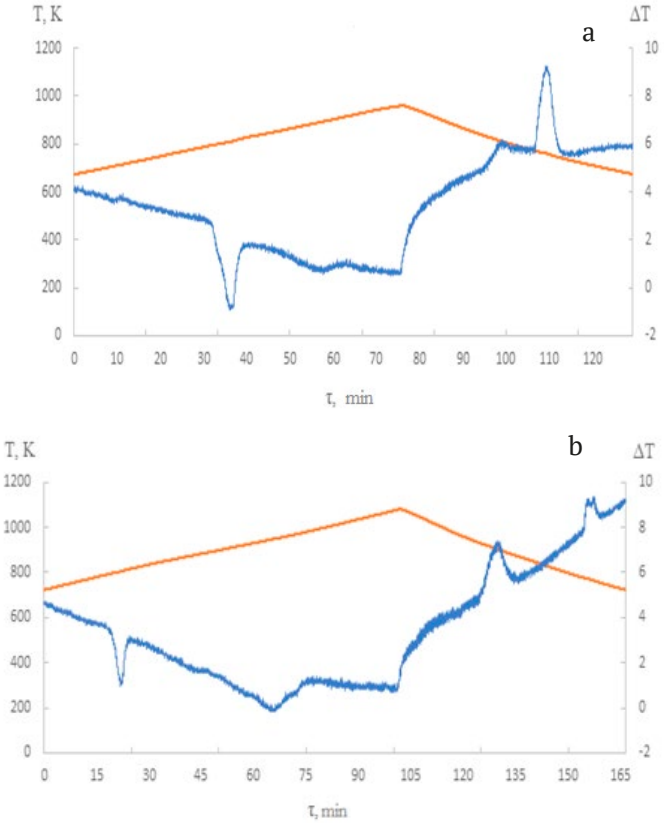

Fig. 4. Thermograms of alloys of the Ge–P–Sn system: a – $Ge_{0.41}P_{0.44}Sn_{0.15;}$ b – $Ge_{0.29}P_{0.53}Sn_{0.18}$

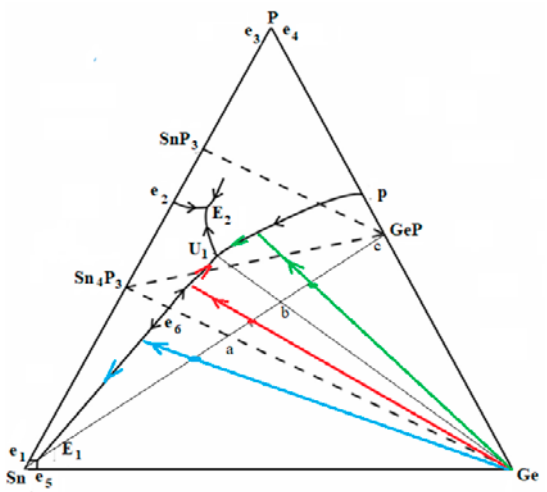

Fig. 5. Scheme of phase equilibria in the Ge–P–Sn system and crystallization processes of the alloy of the Sn–GeP cross section

e_1E_1	$L \leftrightarrow Sn + Sn_4P_3$
e_5E_1	$L \leftrightarrow Sn + Ge$
e_6E_1	$L \leftrightarrow Ge + Sn_4P_3$
E_1	$L \leftrightarrow Ge + Sn + Sn_4P_3$

It should be noted that the phase diagram of the Sn_4P_3–Ge section constructed in [21] based on differential thermal analysis data is a eutectic type diagram with coordinates of the eutectic point e_6 800 K, 15 mol. % Ge. Thus, in e_6 point, the $L \leftrightarrow Ge + Sn_4P_3$ process is non-variant, carried out at constant temperature and composition of the melt.

Since the thermogram of the $Ge_{0.29}Sn_{0.18}P_{0.53}$ (No. 6) sample, shown in Fig. 5c, demonstrates a lower temperature than the other alloys, it can be assumed that the crystallization of this alloy ends at the point of four-phase equilibrium, located inside the triangle formed by the figurative points of the solid phases: Sn_4P_3, SnP_3, and GeP. Accordingly, the following processes occur:

U_1E_2	$L \leftrightarrow Sn_4P_3 + GeP$
e_2E_2	$L \leftrightarrow SnP_3 + Sn_4P_3$
E_2	$L \leftrightarrow Sn_4P_3 + SnP_3 + GeP$

The processes occurring in areas with high phosphorus content and characterized by high saturated vapor pressure require additional research. Nevertheless, based on the data presented in this study, it can be concluded that in the Ge–P–Sn ternary system, the invariant peritectic equilibrium $L + Ge \leftrightarrow Sn_4P_3 + GeP$ and the eutectic process $L \leftrightarrow Sn_4P_3 + GeP + SnP_3$ are realized.

This diagram does not contradict the *T-x* diagram of the Sn–GeP polythermal section (Fig. 6), constructed in this work. The investigation of this section was interesting from a practical point of view to explain the possibility of using tin as a solvent, which was proposed by the authors [10].

For alloys with a tin content of more than 40 mol. % , lines of germanium, tin, and tin phosphide of the Sn_4P_3 composition were recorded on the diffraction patterns. The X-ray diffraction data for the $Ge_{0.20}P_{0.20}Sn_{0.60}$ sample are shown as an example in Fig. 7a. In the thermograms of samples in this concentration range, the first endothermic effect is realized at a temperature close to the melt point of tin (Fig. 8a). This confirms the presence of a four-phase equilibrium L ↔ Ge + Sn + Sn_4P_3 (E_1 point), and since double eutectics in binary systems are degenerate, then the E_1 point of the triple eutectic also exists in the region of very high tin concentrations.

With a lower tin content in alloys, GeP lines appeared in alloys along with Ge and Sn_4P_3 reflexes, which can be seen in the spectrum

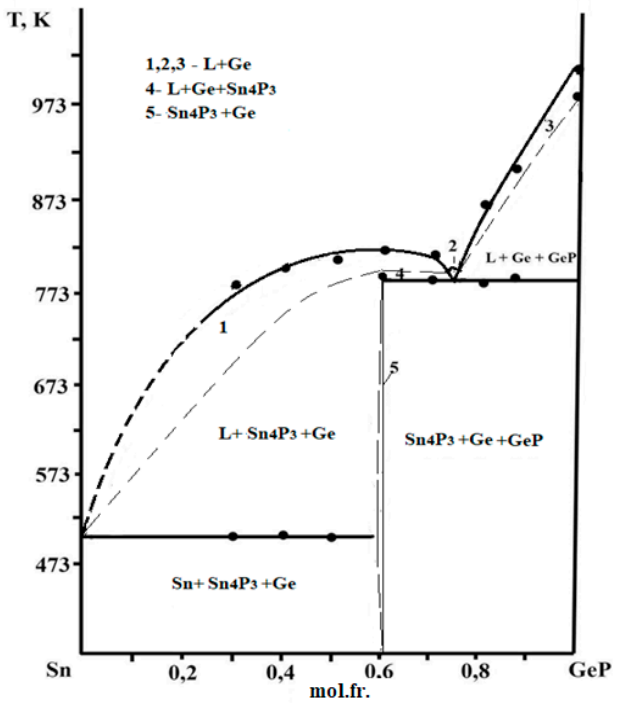

Fig. 6. The *T-x* diagram of the Sn–GeP polythermal cross section

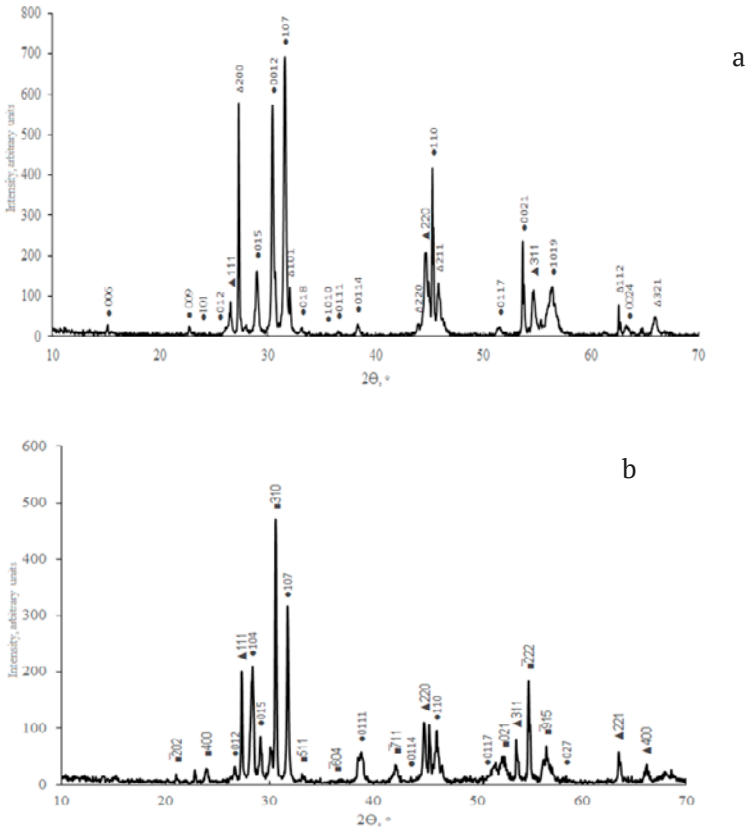

Fig. 7. Diffraction patterns of samples of the Sn–GeP polythermal cross section: a – $Ge_{0.2}P_{0.2}Sn_{0.6}$; b – $Ge_{0.35}P_{0.35}Sn_{0.3}$. ▲ – Ge; ● – Sn_4P_3; ■ – GeP; Δ – Sn

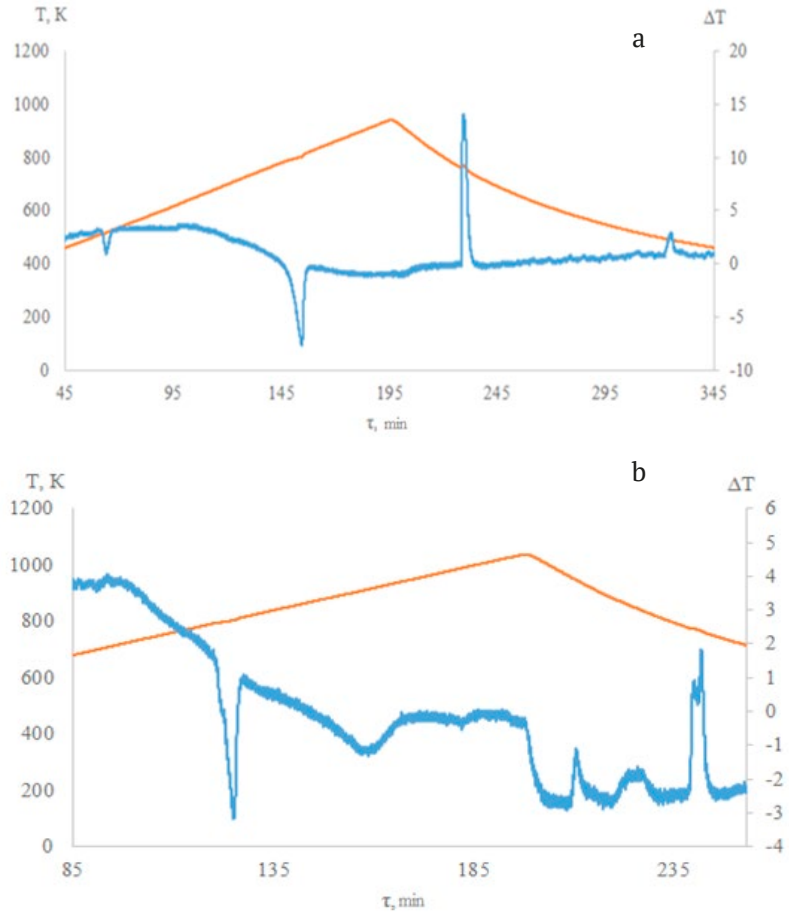

Fig. 8. Thermograms of alloys of the Ge–P–Sn system: a –$Ge_{0.20}P_{0.20}Sn_{0.60}$; b –$Ge_{0.35}P_{0.35}Sn_{0.30}$

shown in Fig. 7b. The alloy, corresponding to the intersection of the studied section with the Sn_4P_3–Ge section, was a two-phase mixture of germanium and tin phosphide, which confirms the partially quasi-binary nature of the Sn_4P_3–Ge section. A study of alloys with a tin content of less than 40 mol. % by differential thermal analysis showed that the lowest endothermic effect in temperature was recorded at a temperature of 795 K. When cooling samples whose composition lies in the ab range, after the primary precipitation of germanium L ↔ Ge, the melting point falls on the curve of the monovariant equilibrium e6U1. For alloys with even lower tin content (*bc* segment) after the primary crystallization follows the L + Ge ↔ GeP secondary process (the pU_1 monovariant equilibrium line). However, after, in any case, for all alloys a four-phase process L + Ge ↔ GeP + Sn_4P_3, occurred, which corresponded to a temperature of 795 K. This is demonstrated by the thermogram of the $Ge_{0.35}P_{0.35}Sn_{0.30}$ alloy shown in Fig. 8b.

4. Conclusions

Based on the study of a number of alloys of the Ge–P–Sn ternary system using the X-ray phase analysis method, it was established that the phase subsolidus separation of the state diagram is performed by the Sn_4P_3–Ge, Sn_4P_3–GeP, Sn_3P_4–GeP and SnP_3–GeP sections. Taking into account the type of phase diagrams of binary systems and the established phase partition of the state diagram of a ternary system, a scheme of phase equilibria in the Ge–P–Sn system was proposed, which assumes the existence of a nonvariant peritectic equilibrium L + Ge ↔ Sn_4P_3 + GeP and the eutectic processes L ↔ Ge + Sn + Sn_4P_3 and L ↔ Sn_4P_3 + GeP + SnP_3. The study of alloys using the DTA method allowed determining the temperatures of these processes, equal to 795 K, 504 K, and 790 K, respectively. The *T*-x diagram of the Sn–GeP polythermal cross section, experimentally confirming the proposed scheme, was constructed.

Contribution of the authors

The authors contributed equally to this article.

Conflict of interests

The authors declare that they have no known competing financial interests or personal relationships that could have influenced the work reported in this paper.

References

1. Goncharov E. G. *Semiconductor phosphides and arsenides of silicon and germanium*[*]. Voronezh: VSU Publ.; 1989. 208 p. (In Russ.)

2. Semenova G. V., Goncharov E. G. *Solid solutions with the participation of elements of the fifth group*[*]. Moscow: MFTI Publ.; 2000. 160 p. (In Russ.). Available at: https://www.elibrary.ru/item.asp?id=25882424

3. Khan K., Tareen A. K., Khan Q. U., Iqbal M., Zhang H. and Guo Z. Novel synthesis, properties and applications of emerging group VA two-dimensional monoelemental materials (2D-Xenes). *Materials Chemistry Frontiers*. 2021;5: 6333-6391. https://doi.org/10.1039/D1QM00629K

4. Yu X., Liang W., Xing Ch., ... Zhang H. Emerging 2D pnictogens for catalytic applications: status and challenges. *Journal of Materials Chemistry A*. 2020;8: 12887–12927. https://doi.org/10.1039/D0TA04068A

5. Tao W., Kong N., Ji X., ... Kim J. S. Emerging two-dimensional monoelemental materials (Xenes) for biomedical applications. *Chemical Society Reviews*. 2019;48: 2891-2912. https://doi.org/10.1039/C8CS00823J

6. Carrasco J. A., Congost-Escoin P., Assebban M., Abellán G. Antimonene: a tuneable post-graphene material for advanced applications in optoelectronics, catalysis, energy and biomedicine. *Chemical Society Reviews*. 2023;52: 1288–1330. https://doi.org/10.1039/D2CS00570K

7. Pang J., Bachmatiuk A., Yin Y., ... Rümmeli M. H. Applications of phosphorene and black phosphorus in energy conversion and storage devices. *Advanced Energy Materials*. 2018;8(8): 1702093. https://doi.org/10.1002/aenm.201702093

8. Niu T. New properties with old materials: layered black phosphorous. *Nano Today*. 2017;12: 7–9. https://doi.org/10.1016/j.nantod.2016.08.013

9. Goswami A., Gawande M. B. Phosphorene: current status, challenges and opportunities. *Frontiers of Chemical Science and Engineering*. 2019;13(2): 296–309. https://doi.org/10.1007/s11705-018-1783-y

10. Lee K., Synnestvedt S., Bellard M., Kovnir K. GeP and $(Ge_{1-x}Sn_x)(P_{1-y}Ge_y)$ (x~0.12, y~0.05): synthesis, structure, and properties of two-dimensional layered tetrel phosphides. *Journal of Solid State Chemistry*. 2015;224: 62–70. https://doi.org/10.1016/j.jssc.2014.04.021

11. Barreteau C., Michon B., Besnard C., Giannini E. High-pressure melt growth and transport properties of SiP, SiAs, GeP, and GeAs 2D layered semiconductors. *Journal of Crystal Growth*. 2016;443(1): 75–80. https://doi.org/10.1016/j.jcrysgro.2016.03.019

12. Cheng A-Q., He Z., Zhao J., Zeng H., Chen R-Sh. Monolayered silicon and germanium monopnictide semiconductors: excellent stability, high absorbance, and strain engineering of electronic properties. *ACS Applied Materials & Interfaces*. 2018;10(6): 5133–5139. https://doi.org/10.1021/acsami.7b17560

13. Zhou L., Guo Y., Zhao J. GeAs and SiAs monolayers: novel 2D semiconductors with suitable band structures. *Physica E: Low-dimensional Systems and Nanostructures*. 2018;95: 149–153. https://doi.org/10.1016/j.physe.2017.08.016

14. Ramzan M. S., Bacic V., Jing Y., Kuc A. Electronic properties of a new family of layered materials from groups 14 and 15: first-principles simulations. *The Journal of Physical Chemistry C*. 2019;123(41): 25470–25476. https://doi.org/10.1021/acs.jpcc.9b07068

15. Olesinski R. W., Abbaschian G. J. The Ge–Sn (Germanium–Tin) system. *Bulletin of Alloy Phase Diagrams*. 1984;5(3): 265–271. https://doi.org/10.1007/bf02868550

16. Ugai Ya. A., Sokolov L. I., Goncharov E. G., Pshestanchik V. R. *P-T-x* diagram of the state of the Ge-P system and the thermodynamics of the interaction of the components. *Russian Journal of Inorganic Chemistry*. 1978;23(7): 1907–1911. (In Russ.). Available at: https://www.elibrary.ru/item.asp?id=29096578

17. Olofsson O. X-ray investigation of the tin-phosphorus system. *Acta Chemica Scandinavica*. 1970;24: 1153 -1162. https://doi.org/10.3891/acta.chem.scand.24-1153

18. Donohue P. C. The synthesis, structure and superconducting properties of new high-pressure forms of tin phosphide. *Inorganic Chemistry*. 1970;9(2): 335–348. https://doi.org/10.1021/ic50084a032

19. Katz G., Kohn Y. A., Broder Y. D. Crystallographic data for tin monophosphide. *Acta Crystallographica*. 1957;9: 607–609. https://doi.org/10.1107/s0365110x57002170

20. Vivian A. C. The tin-arsenic system. *Journal of the Institute of Metals*. 1920;23: 325–336.

21. Gullman J. The crystal structure of SnP. *Journal of Solid State Chemistry*. 1990;87: 202–207. https://doi.org/10.1016/0022-4596(90)90083-a

22. Sushkova T. P., Kononova E. U., Savinova Y. A., Dorokhina E. S., Semenova G. V. Intermediate phases in Sn-P system. *Condensed Matter and Interphases*. 2014;16(2): 210–214. Available at: https://www.elibrary.ru/item.asp?edn=sitfep

23. Ritcher A. Pressure dependence of the tin-phosphorus phase diagram. *Monatshefte für Chemie – Chemical Monthly*. 2012;143(12): 1593–1602. https://doi.org/10.1007/s00706-012-0861-y

24. Proskurina E. Yu., Semenova G. V., Zavrazhnov A. Yu., Kosyakov A. V. *P-T-x* diagram of Sn - P system. *Condensed Matter and Interphases*. 2015;17(4): 498–509. (In Russ., abstract in Eng.). Available at: https://www.elibrary.ru/item.asp?id=25946590

25. Zavrazhnov A. Yu., Semenova G. V., Proskurina E. Yu., Sushkova T. P. Phase diagram of the Sn - P system. *Journal of Thermal Analysis and Calorimetry*. 2018;134(1): 475–481. https://doi.org/10.1007/s10973-018-7123-0

26. Semenova G. V., Leont'eva T. A., Sushkova T. P. Analysis of phase equilibria in the Ge–P–Sn ternary system. *Condensed Matter and Interphases*. 2019;21(2): 249–261. (In Russ., abstract in Eng.). https://doi.org/10.17308/kcmf.2019.21/763

27. Khaldoyanidi K. A. *Phase diagrams of heterogeneous systems with transformations*[*]. F. A. Kuznetsov (ed.). Novosibirsk: INKh RAN Publ.; 2004. 382 c. (In Russ.)

Information about the authors

Galina V. Semenova, Dr. Sci. (Chem.), Full Professor, Department of General and Inorganic Chemistry, Voronezh State University (Voronezh, Russian Federation).
https://orcid.org/0000-0003-3877-985X
semen157@chem.vsu.ru

Tatiana P. Sushkova, Cand. Sci. (Chem.), Associate Professor, Department of General and Inorganic Chemistry, Voronezh State University (Voronezh, Russian Federation).
https://orcid.org/0000-0003-1969-7082
sushtp@yandex.ru

Angelina N. Golentsova, Engineer of 1 category, Department of General and Inorganic Chemistry, Voronezh State University (Voronezh, Russian Federation).
https://orcid.org/0009-0002-0824-8062
An.golentsovaa@mail.ru

Received 11.07.2024; approved after reviewing 03.09.2024; accepted for publication 16.09.2024; published online 25.12.2024.
Translated by Valentina Mittova

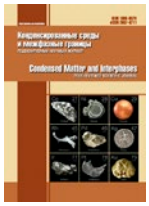

ISSN 1606-867X (Print)
ISSN 2687-0711 (Online)
Condensed Matter and Interphases
Kondensirovannye Sredy i Mezhfaznye Granitsy
https://journals.vsu.ru/kcmf/

Original articles

Research article
https://doi.org/10.17308/kcmf.2024.26/12449

Behavior of major and minor elements during directional crystallization of Fe-Ni-Cu-S-(Rh, Ru, Ir, Pt, Pd, Ag, Au) melt

E. F. Sinyakova✉, **K. A. Kokh**

V. S. Sobolev Institute of Geology and Mineralogy Siberian Branch Russian Academy of Sciences
pr. Akademika Koptyuga 3, Novosibirsk, 630090, Russian Federation

Abstract

The Cu-Fe-Ni-S system is unique in terms of the number of crystalline phases with a variety of combinations of properties, which makes it relevant for prospective material studies. The phases of this system compose typical associations of massive zonal sulfide Cu-Ni ores, and their copper-rich zones are characterized by a high content of noble metals. Therefore, this system is among the most important of those used for the geochemistry of sulfides and for the metallurgy of copper and nickel. There is insufficient quantitative information on the equilibrium distribution coefficients of macrocomponents and the behavior of impurities upon crystallization of solid solutions in the region of the solid-melting diagram corresponding to natural ores or intermediate products of metallurgical production. Therefore, the goal of the work was to obtain new data on the phase diagram of the Cu-Fe-Ni-S system and corresponding phases of noble metals (Rh, Ru, Ir, Pt, Pd, Ag, Au) during the process of fractional crystallization of the melt simulating zonal copper-rich ores of platinum-copper-nickel sulfide deposits.

We conducted quasi-equilibrium directional crystallization of the melt with a composition of (at. %): Fe 29.20, Ni 5.85, Cu 17.60, S 47 with addition of 0.05% of Rh, Ru, Ir, Pt, Pd, Ag, and Au. The obtained sample was studied using optical and scanning electron microscopy, energy-dispersive spectrometry (SEM/EDS), and X-ray phase analysis. Differential thermal analysis (DTA) was used to determine the liquidus temperatures along the crystallization path.

The distribution of macrocomponents along the cylindrical ingot showed that it consisted of five primary zones. Primary phases and phase associations crystallized from the melt in the following sequence: mss / mss + iss / iss / iss + bnss / bnss + pnss, where mss is monosulfide solid solution $(Fe_xNi_{1-x})S_{1\pm y}$, iss is intermediate solid solution $(Cu,Fe)S_{1-x}$, bnss is bornite solid solution $Cu_{5\pm x}Fe_{1\pm x}S_{4\pm y}$, and pnss is pentlandite solid solution $(Fe_xNi_{1-x})_{9\pm y}S_8$. This indicated a complex structure of the solid-melting diagram in the studied region. We determined the crystallization temperatures of mss and iss. A new type of secondary (phase) zoning was identified, formed as a result of subsolidus transformations of primary phases, which can be present in Cu-Ni sulfide ores. It was found that impurities can dissolve in the main sulfide phases, form individual microphases in the sulfide matrix, or be present in these microphases in the form of solid solutions. The main concentrators of Pd were pn and sug. Ir, Rh, and Ru were distributed between mss and pn, and Ag preferred bnss. Most impurities of noble metals formed inclusions as independent microphases: RuS_2, Pt_3Fe, Au* gold-based alloy, Pt-Fe-Au alloy, $CuIr_2S_4$, and native Ag. The results of the work showed that the behavior of macrocomponents could be described using distribution coefficients, and the behavior of microcomponents did not strictly correspond to the classical theory of fractional crystallization of multicomponent melts with impurities.

Keywords: Cu-Fe-Ni-S system, Phase equilibria, Noble metals, Directional crystallization, DTA

Funding: The research was carried out with the financial support of the Ministry of Science and Higher Education of the Russian Federation under the state assignment of the Sobolev Institute of Geology and Mineralogy of the Siberian Branch of the Russian Academy of Sciences No. 122041400237-8 and No. 122041400031-2.

Acknowledgements: Powder X-ray diffraction, scanning electron microscopy, energy-dispersive spectrometry (SEM/EDS) studies were performed at the Centre for Collective Use of multi-element and isotope studies of the Siberian Branch of the Russian Academy of Sciences.

✉ Elena F. Sinyakova, e-mail: efsin@igm.nsc.ru

For citation: Sinyakova E. F., Kokh K. A. Behavior of major and minor elements during directional crystallization of Fe-Ni-Cu-S-(Rh, Ru, Ir, Pt, Pd, Ag, Au) melt. *Condensed Matter and Interphases*. 2024;26(4): 755–771. https://doi.org/10.17308/kcmf.2024.26/12449

Для цитирования: Синякова Е. Ф., Кох К. А. Поведение основных элементов и примесей при направленной кристаллизации расплава Fe-Ni-Cu-S-(Rh, Ru, Ir, Pt, Pd, Ag, Au). *Конденсированные среды и межфазные границы*. 2024;26(4): 755–771. https://doi.org/10.17308/kcmf.2024.26/12449

1. Introduction

The Cu-Fe-Ni-S system is unique in terms of the number of crystalline phases with a variety of combinations of properties, which makes it relevant for prospective material studies. Therefore, this system is among the most important of those used for the geochemistry of sulfides and for the metallurgy of copper and nickel [1-10]. From a geochemical point of view, the most interesting region of this system is located in the vicinity of the iron monosulfide (Fe,Ni) $S_{1\pm\delta}$ (mss) composition. There is only one paper dedicated to the construction of a quantitative model of a fragment of the phase diagram of the Cu-Fe-Ni-S system [3]. The authors obtained equations for the liquidus and solidus surfaces in the iron-rich mss crystallization region with an S content of 50 to 52.5 at. % and also approximated the data for the distribution coefficients of nickel, iron, and copper during its crystallization from the melt. It is obvious that this region should be expanded and a similar description should be obtained for other solid solutions, as well as for regions of multiphase crystallization.

So far, many fragments of the phase diagram of this system and its subsystems Cu-Fe-S and Fe-Ni-S have been characterized by discrepancies between the results of studies by different authors, and these differences were found not only in quantitative data, but also in the fundamental features of the structure of the phase diagrams. The problems of immiscibility of the quaternary melt of the Cu-Fe-Ni-S system [5, 6], mechanisms of formation of the intermediate solid solution $(Cu,Fe)S_{1-x}$, $CuFe_2S_3$ cubanite, $(Fe,Ni)_9S_8$ pentlandite, $CuFeS_2$ chalcopyrite and the boundaries of their regions of existence in the temperature-composition coordinates [11–16] are still a matter of debate. For example, in [3] the existence of two intermediate solid solutions was assumed: $Cu_{1+x}Fe_{1+x}S_2$, iss, stable up to 900-950 °C in nickel-poor compositions, and a new (Fe,Cu,Ni)S quaternary solid solution between iss and mss that exists at temperatures below 850 °C. There is not enough quantitative information on the positions of the conodes (i.e. on the equilibrium distribution coefficients of the components) upon crystallization of solid solutions in a wide range of temperature and melt composition variations in the middle part of the melting diagram near 50 at. % S.

This system has been widely used to model the formation of magmatic platinum-bearing copper-nickel deposits. Massive ore bodies of these deposits are characterized by highly expressed chemical and mineral zoning. Copper-poor zones are enriched in Ir, Os, Ru, and Rh, while copper-rich zones are enriched in Pd, Pt, Au, Ag, and chalcophile elements (Te, As, Bi, Sb and Sn) [5, 7, 17–22]. Zoning is associated with the hypothesis of the origin of ore bodies as a result of fractional crystallization of sulfide melt [5, 7, 17, 20, 21, 23–26]. For experimental modeling of this process we carried out the quasi-equilibrium directional crystallization of melts simulating natural sulfide melts [27–30]. The prospects for using directional crystallization in the study of phase diagrams of sulfide systems are mainly related to the possibility of determining the equilibrium compositions of the melt and solid phases at an arbitrary moment of crystallization. Theoretical analysis and experiments on directional crystallization of sulfide melt showed the possibility of the existence of several types of zoning, which are determined by the composition of the initial melt and the structure of the phase diagram of the Cu-Fe-Ni-S system and its boundary systems: Cu-Fe-S and Fe-Ni-S [31]. Due to the complexity of the analysis of fractional crystallization of natural Cu-Ni sulfide melts and the lack of information for theoretical modeling, direct experimental studies of the Cu-Fe-Ni-S-(noble metals) model system are of interest for sulfide copper-nickel ores and intermediate products of metallurgical production. Therefore, the goal of the work was to obtain new data on the phase diagram of the Cu-Fe-Ni-S system and on the types of formation of noble metals during the process of fractional crystallization of the melt simulating copper-rich zonal sulfide platinum-copper-nickel ores.

2. Experimental

A sample of the initial composition (at. %): Fe – 29.20, Ni – 5.85, Cu – 17.16, S – 47.00, Rh, Ru, Ir, Pt, Pd, Au, Ag, 0.05 of each was obtained from pure metals (99.99%) and analytically pure sulfur (99.99%) by heating the mixture of elements in a quartz ampoule evacuated to a residual pressure of $1.5\cdot10^{-2}$ mm Hg to 1000 °C. It was held at this temperature for 24 hours and then cooled in air. The synthesized sample with a weight of about 11 g was placed in a quartz ampoule with a conical bottom, which was evacuated to $1.5\cdot10^{-2}$ mm Hg. Crystallization was performed by the Bridgman-Stockbarger method in a two-zone furnace with a diaphragm. The container with the sample was placed in the upper zone of the furnace, heated until the sample melted, and held for two days. Then it was lowered into the cold zone at a speed of $2.25\cdot10^{-8}$ m/s. This regime provided quasi-equilibrium conditions for directional crystallization. In this case, the obtained results can be attributed to the phase diagram of the Cu–Fe–Ni–S system. The temperature at the lower end of the quartz ampoule was 890 and 601 °C at the beginning and end of crystallization, respectively. Once crystallization was complete, the ampoule was cooled in the switched-off furnace.

The resulting ingot, approximately 120 mm long and 8 mm in diameter, was cut perpendicular to the longitudinal axis into 25 pieces. They were weighed and the fraction of crystallized melt g was determined. Fifteen fragments were used to prepare and study the polished sections. We identified a list of phases and their chemical composition in each fragment. The average chemical composition of the ingot, as well as the average composition of inclusions and local composition of phases were measured at the Analytical Center for Multielement and Isotope research, Siberian Branch of the Russian Academy of Sciences (using energy-dispersive spectrometry (SEM-EDS) on a MIRA 3 LMU high-resolution microscope (Tescan Orsay Holding) equipped with INCA Energy 450+ X-Max 80 and INCA Wave 500 (Oxford Instruments Nanoanalysis Ltd) microanalysis systems. The K series (S, Fe, Cu, Ni) and L series (Rh, Ru, Ir, Pt, Pd, Au, Ag) of X-ray radiation were used for the analysis. FeS_2 (on S) and pure Fe, Ni, Cu, Rh, Ru, Ir, Pt, Pd, Au, Ag were used as references. The measurements were performed at an accelerating voltage of 20 kV, an electron beam current of 1.5 nA, and a live spectra accumulation time of 30 s. With these analytical conditions, the lower limit of the detectable concentrations was 0.4–0.5 wt. % for Pt, Au, and Ir and 0.1–0.2 wt. % for the remaining elements. The error did not exceed 1–1.5 rel. % in determining the main components and 2–5 rel. % for impurities. To estimate the average composition of multiphase sections, we used the total spectrum obtained by scanning sections with an area of up to 1.5 mm^2. To reduce the lower limit of detectable concentrations by approximately twice, we increased the the accumulation time of spectra up to 120 s. The average composition of phase mixtures was calculated from 3–5 analyses from different sections of each cross-section along the ingot. The error in determining the main components was 1–2 rel. %.

The melt composition at an arbitrary moment of crystallization was calculated from the average chemical composition of the solid phases using the material balance equation [32]:

$$c_i^L = \frac{c_{i0} - \int_0^g c_i^S dg}{1-g}.$$

Here g is the mole fraction of the crystallized melt ($g = 0$ corresponds to the melted sample, while $g = 1$ corresponds to the solidified sample), c_{i0} is the concentration of the i-th component in the initial ingot, c_i^s is the average concentration of the i-th component in the ingot layer of thickness dg adjacent to the crystallization front, c_i^L is the average concentration of the i-th component in the melt.

The phases were diagnosed by powder X-ray diffraction on a DRON-4 automated powder diffractometer using CuK_α radiation with a graphite monochromator. The diffraction patterns were scanned in the range of 2θ to 8° up to 90° with a step of 0.05°, and the scanning time per point was 4 s, with a slit of 0.5 mm. The obtained diffraction patterns were decoded using the ASTM database. The parameters were calculated using the UnitCell program. The sample from the initial zone was recorded with an external standard of Si.

Differential thermal analysis (DTA) was performed for three specially synthesized samples with compositions located along the

crystallization path. To perform DTA, we placed a sample weighing ~ 50 mg in a thermoanalytical cell in the form of an evacuated quartz ampoule with a concave bottom, which was installed on the thermocouple junction. The melting temperatures of the samples were determined by the reference-free DTA method with heating at a rate of 10 deg/min. The thermocouple was tested using the melting point of gold (1063 °C). The error in recording the temperature was ± 5 °C.

Table 1 contains a list of the phases obtained during the experiment and their designations.

3. Results and discussion

3.1. Behavior of macrocomponents

Based on the data on the change in the chemical composition of the substance along the ingot (Table 2), we plotted the distribution curves of the components up to g = 0.86 (Fig. 1). The trajectory of the melt composition upon crystallization is also presented, and the values of the average distribution coefficients of components between the solid ingot and the melt are provided. The average chemical composition of the substance of the ingot zones and the average distribution coefficients of macrocomponents changed abruptly when moving from one zone to an adjacent one. These data indicated that the resulting ingot consisted of five primary zones. Fig. 1 shows the process in a simplified way, although it clearly demonstrates the general patterns of crystallization of a zonal sample.

In zone I ($0 \leqslant g \leqslant 0.28$), the average chemical composition of the ingot changes from $Fe_{40.19}Ni_{6.16}Cu_{2.08}S_{50.86}Ru_{0.38}Rh_{0.15}Ir_{0.20}$ to $Fe_{38.85}Ni_{7.76}Cu_{2.17}S_{51.07}Ru_{0.08}Rh_{0.01}Ir_{0.07}$. It can be seen that upon crystallization Fe and Ni generally transited into solid solutions (κ_{Fe} = 1.4–1.5,

Table 1. Phases obtained in the present work in the Cu-Fe-Ni-S-(Pt, Pd, Rh, Ru, Ir, Au,Ag) system Intermediate solid solution

Phase	Designation	Formula
Primary solid solutions (ss) crystallizing from the melt		
Monosulfide ss	mss	$(Fe_xNi_{1-x})S_{1\pm y}$
Intermediate ss	iss	$(Cu,Fe)S_{1-x}$
Bornite ss	bnss	$Cu_{5\pm x}Fe_{1\pm x}S_{4\pm y}$
Pentlandite ss	pnss	$(Fe_xNi_{1-x})_{9\pm y}S_8$
Secondary phases formed as a result of Subsolidus transformations during cooling of the sample		
Monosulfide ss	mss’	$(Fe_xNi_{1-x})S_{1\pm y}$ (Ni from 6 to 10 at.%)
Ni-rich Monosulfide ss	Ni-mss	$(Fe_xNi_{1-x})S_{1\pm y}$ (Ni ~19 at. %)
Low-temperature intermediate ss of haycockite composition	iss’	$(Cu,Fe)S_{1-x}$ (Fe > Cu) $Cu_4Fe_5S_8$
Low-temperature intermediate ss of mooihoekite composition	iss’	$(Cu,Fe)S_{1-x}$ (Fe = Cu) Cu9Fe9S16
Pentlandite	pn	$(Fe, Ni)_9S_8$ (at. ratio Fe/Ni = 1)
Fe-rich Pentlandite	Fe-pn	$(Ni, Fe)_9S_8$ (at. ratio Fe/Ni = 1.1-1.3)
Ni-rich Pentlandite	Ni-pn	$(Ni, Fe)_9S_8$ (at. ratio Fe/Ni = 0.90-0.96)
Sugakiite	sug	$Cu(Fe,Ni)_8S_8$ (Fe/Ni ~ 1-1.5), Cu to 7 ат.%)
Bornite	bnss’	$Cu_{5\pm x}Fe_{1\pm x}S_{4\pm y}$
Native copper	Cu	Cu
Фазы благородных металлов		
Laurite	RuS_2	RuS_2
Isoferroplatinum	Pt_3Fe	Pt_3Fe
Gold-based alloy	Au*	Au from 52 to 69 at. %, impurities Ag, Cu, Pd
Alloy of Pt-Fe-Au system	Pt-Fe-Au	Pt-Fe-Au
Native silver	Ag	Ag
Cuproiridsite	$CuIr_2S_4$	$(Cu,Fe)(Ir,Rh,Pt)_2S_4$

Table 2. Average concentrations of elements in the ingot and in the melt

g	Average solid composition, at. %					Melt composition, at. %				
	Fe	Ni	Cu	S	Rh	Fe	Ni	Cu	S	Rh
Zone I (0 ⩽ g ⩽ 0.28)										
0.04	40.19	6.16	2.08	50.86	0.15	28.74	5.84	18.25	46.84	0.05
0.09	40.13	6.38	2.15	50.79	0.14	28.09	5.81	19.17	46.61	0.04
0.25	38.85	7.76	2.17	51.07	0.01	25.79	5.39	22.80	45.66	0.05
Zone II (0.28 ⩽ g ⩽ 0.40)										
0.28	36.71	8.5	4.35	50.45	<mdl	25.35	5.26	23.55	45.47	0.05
0.33	34.47	8.17	7.82	49.54	<mdl	24.56	5.01	24.90	45.12	0.05
Zone III (0.40⩽ g ⩽ 0.68)										
0.40	26.64	4.59	22.39	46.37	<mdl	24.34	5.06	25.17	44.98	0.06
0.49	25.87	4.98	23.02	46.13	<mdl	24.08	5.07	25.54	44.78	0.07
0.57	24.78	5.17	24.51	45.54	<mdl	23.94	5.05	25.74	44.64	0.08
Zone IV (0.68 ⩽ g ⩽ 0.89)										
0.68	19.56	4.27	33.05	43.05	0.07	25.55	5.34	23.05	45.21	0.11
0.79	19.37	4.34	33.07	43.12	0.10	28.61	5.83	18.07	46.22	0.17
0.86	19.04	4.46	33.24	43.07	0.10	33.82	6.57	9.77	47.91	0.26
Zone V (0.89 ⩽ g ⩽ 1)										
0.89	19.86	9.49	25.55	44.06	0.11	–				
0.92	20.07	9.66	24.29	44.67	0.12	–				
0.94	20.08	9.70	24.22	44.66	0.12	–				

Note. mdl – minimum level of elements determination by SEM/EDS method.
In zone I the content of Ru in solid 0.08–0.38 at. %, in melt 0.01–0.04 at. %.
Ir in solid 0.07–0.20 at. %, in melt 0.03–0.04 at. %, in zones II–IV the content of these elements <mdl.
In zone V the content of Au about 0.15 at. %, Pt about 0.37 at. %, Pd up to 0.40 at. %, Ag about 0.30 at. %; in zones I–IV the content of these elements <mdl.

κ_{Ni} = 1.0-1.4), while Cu was rejected to melt (κ_{Cu} = 0.1). Sulfur has a weak tendency to concentrate in the solid ingot (κS = 1.1).

In zone II (0.28 ⩽ g ⩽ 0.40), the composition of the ingot is $Fe_{36.7\text{-}34.5}Ni_{8.5\text{-}8.2}Cu_{4.4\text{-}7.8}S_{50.4\text{-}49.5}$. Since the distribution coefficients were κ > 1 for Fe and Ni, these components generally transited into the solid phase. Copper accumulated in the melt during crystallization (κ_{Cu} = 0.2–0.3). The sulfur distribution coefficient was κ_S = 1.1.

In zone III (0.40 ⩽ g ⩽ 0.68), the composition of the ingot is $Fe_{26.6\text{-}24.8}Ni_{4.6\text{-}5.2}Cu_{22.4\text{-}24.5}S_{46.4\text{-}45.5}$. The distribution coefficients of the components between the solid phase and the sulfide melt were close to 1. This signifies a minor modification to the composition of the solid phase that was released from the melt. Since κ_{Fe} = 1.09–1.02 and κ_S = 1.03, it was slightly enriched with these components, and since κ_{Cu} = 0.9, it indicated that the sulfide melt was slightly enriched with Cu. The distribution coefficient of nickel (κ_{Ni}) changed from 0.9 at the beginning of this zone to 1 at its end.

In zone IV (0.68 ⩽ *g* ⩽ 0.86), the average composition $Fe_{19.31\pm0.25}Ni_{4.35\pm0.10}Cu_{33.11\pm0.12}S_{43.07\pm0.06}$ solidified from the melt. Upon crystallization, the solid phase was enriched with copper (κ_{Cu} = 1.4–3.4), while the sulfide melt was enriched with the remaining components (κ_{Ni} = 0.7–0.8, κ_{Fe} = 0.6–0.8, κ_S ~ 0.9).

As for zone V (0.86 ⩽ *g* ⩽ ~1), Fig. 1 shows only the average composition of the ingot. Its abrupt change in relation to zone IV and the differences in microstructure and association of secondary phases (Fig. 2) allowed assuming the existence of a new zone at the end of the ingot.

Fig. 2 shows a scheme of a directionally crystallized sample and the microstructure of its cross sections. Studies of the polished sections also showed that the ingot consisted of five zones. When passing from one zone to another, the microstructure of the samples changed abruptly. Structural elements in the form of large grains and lamellae consisting of one or several phases can be identified in the micrographs of the samples. It can be assumed that some

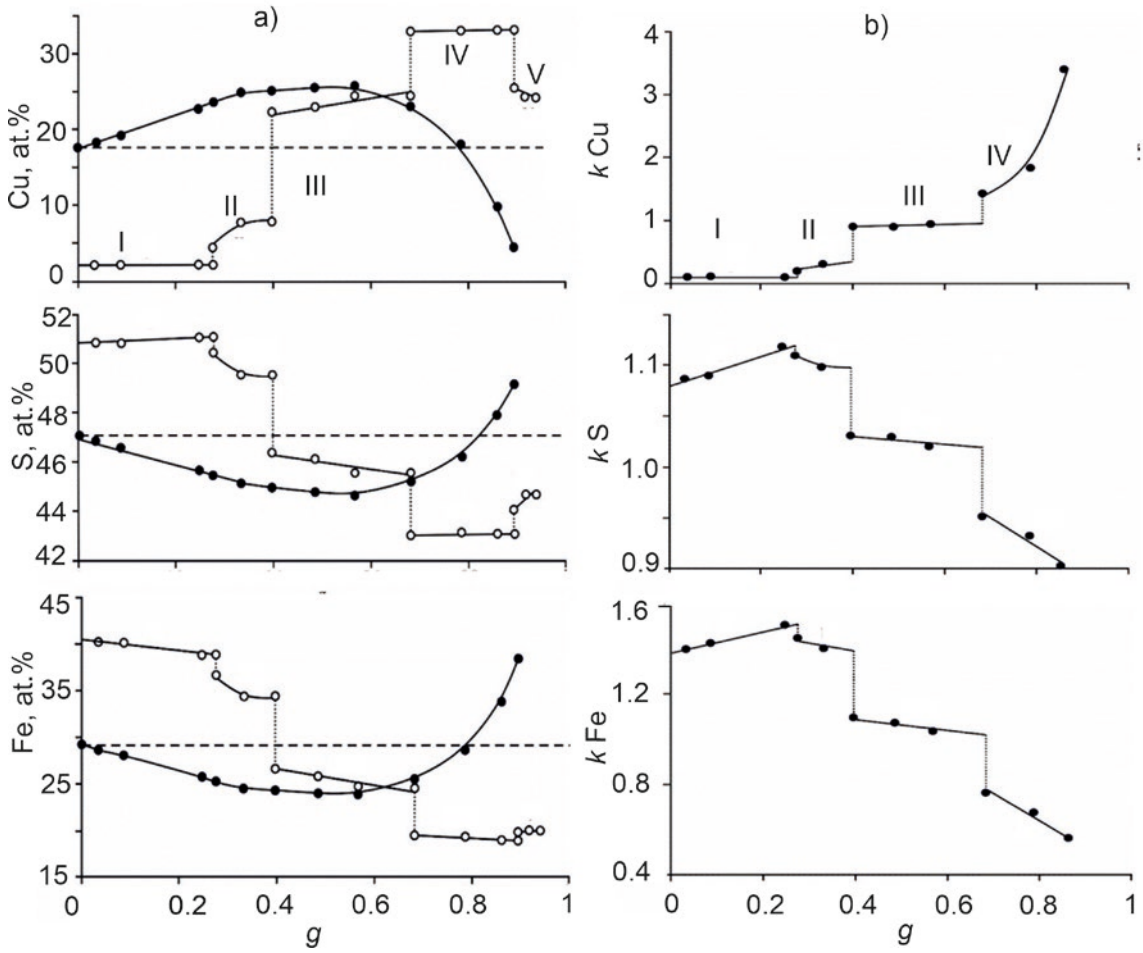

Fig. 1. Change in the average concentration of Cu, S, and Fe in the sulfide melt (closed circles) and solid ingot (open circles) up to *g* 0.85 (a) and the dependence of the average distribution coefficients of these components between solid ingot and melt on *g* (b). The dashed horizontal line shows the concentration of the component in the initial melt, the dashed vertical lines separate the zones

multiphase formations appeared as a result of the solid solution decay initially formed from the melt. Determination of their average chemical composition taking into account the existing data on high-temperature phases in the Cu-Fe-Ni-S system and its boundaries Cu-Fe-S and Fe-Ni-S systems allowed identifying these primary phases and reconstructing the primary phase zoning of the sample (Table 3). Local analysis allowed recording the phase composition of the sample corresponding to the temperature range in which phase reactions ceased upon cooling. The expected temperatures are ~ 300–400 °C. The results of the study of the phase composition of the ingot related to ~ "isothermal" sections of the phase diagram in this temperature range (Table 4).

During the first stage, an iron-rich solid solution containing about 2 at. % Cu and 6–8 at. % Ni, which is usually called monosulfide (mss), crystallized from the melt. In the Fe-Ni-S system, there is a wide mss region between high-temperature FeS_{1+x} and NiS_{1+x} [1, 4]. It is known that up to 8 at. % of copper can be dissolved in it [33]. The initial section of the trajectory of the change in the melt composition was in the region of primary crystallization of this solid solution. According to DTA, the liquidus temperature was 956 °C at the beginning of mss crystallization and 902 °C at the point of the end of its crystallization.

The microstructure of the sample cooled to room temperature consisted of a matrix of low-temperature monosulfide solid solution mss' and rare inclusions of intermediate solid solution iss' of a composition close to haycockite ($Cu_4Fe_5S_8$, hc) (Table 4, Fig. 2c, *g* = 0.09). It was found that mss' had a hexagonal unit cell with parameters *a* = 6.8890±0.0070 Å, *c* = 40.0995±0.0872 Å, unit with

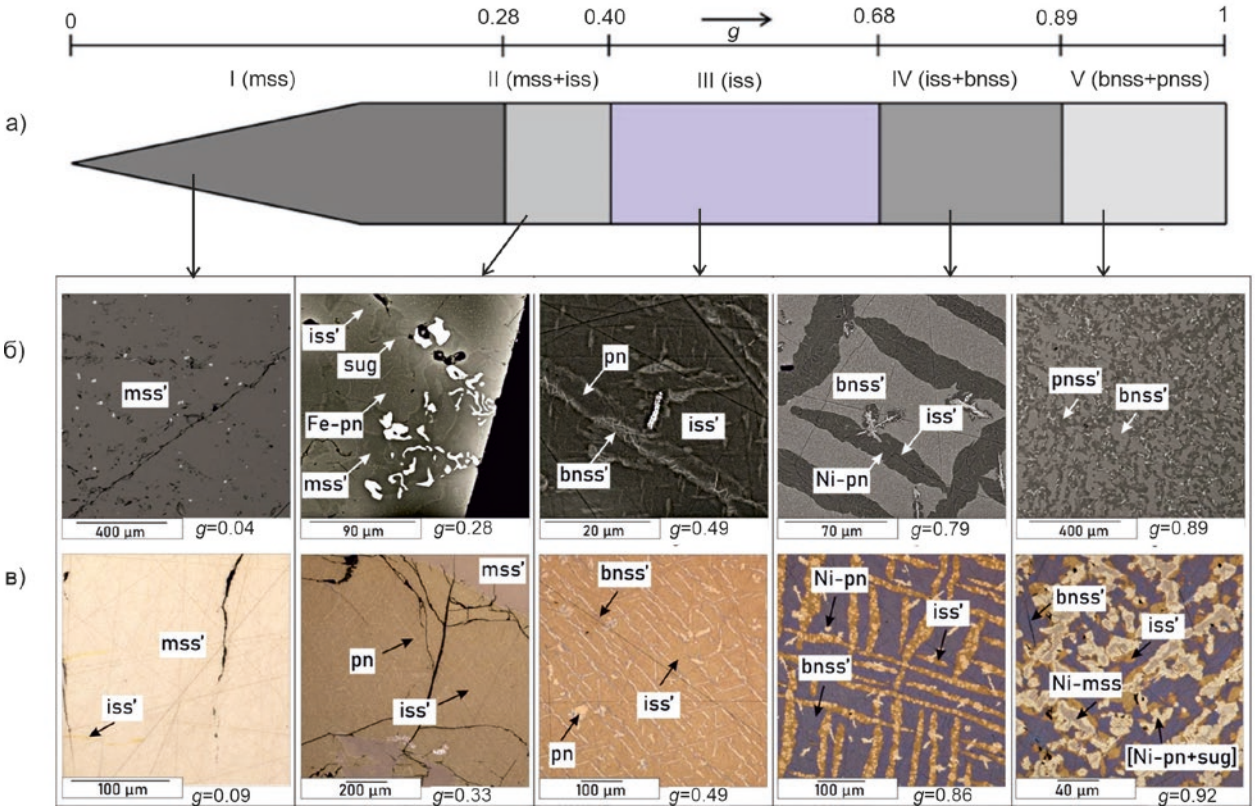

Fig. 2. Schematic of the directionally crystallized sample showing the primary zones (I-V) (a) and the characteristic microstructure of secondary phases in reflected electrons (b) and reflected light (c). See text for comments and phase designations

cell volume 1648.0809 ± 3.1008 Å^3. The release of hc was associated with a decreased copper solubility in mss when the sample was cooled to room temperature.

Upon transitioning from zone I to zone II, the sample underwent an abrupt enrichment with copper and depletion of sulfur (Fig. 1). The micrographs (Fig. 2b, c, g = 0.28, 0.33) showed large inclusions in the mss' matrix, representing a finely dispersed decomposition structures, with average composition $Fe_{28.78\pm0.11}Ni_{4.44\pm0.11}Cu_{19.22\pm0.18}S_{47.58\pm0.39}$, corresponding to the intermediate solid solution iss (Table 3). The amount of iss gradually increased along zone II. These data allowed us to conclude that the change in the composition of the sample was mainly caused by the appearance of iss. The Ni-containing intermediate solid solution is known to coexist with the melt in the Cu-Fe-Ni-S system [29, 30]. This allowed us to assume that the Ni-containing solution in our experiment was also formed in the process of crystallization from a sulfide melt at a temperature of 902 °C of a two-phase cotectic (mss + iss). Upon further cooling, iss decomposed into several phases that formed a characteristic decomposition structure of iron-rich iss' (atomic ratio Fe/Cu ~ 1.5), iron-rich pentlandite Fe-pn (atomic ratio Fe/Ni ~ 1.2) in the form of grains and rims at the boundary of mss' and iss', and Cu(Fe,Ni)8S8 sugakiite (Table 4, Fig. 2b, c, g = 0.28, 0.33). It should be noted that the iss matrix also contained finely dispersed inclusions sized < 1 μm that could not be identified.

In zone III, the average chemical composition $Fe_{25.76\pm0.93}Ni_{4.1\pm0.30}Cu_{23.31\pm1.09}S_{46.01\pm0.43}$ corresponded to an intermediate iss solid solution. This means that the trajectory of the melt composition from the cotectic surface proceeded into the field of primary crystallization of iss. The crystallization path associated with such a transition was described in [31]. The microstructure of zone III consisted of iss' (hc), bornite solid solution (bnss'), and iron-rich pentlandite (Fe-pn) (Fig. 2b, c, g = 0.49, Table 4).

The transition from zone III to zone IV led to an abrupt increase in the copper content

Table 3: Average composition of primary phases along the ingot and partition coefficients of components between these phases and the sulfide melt

g	Phase	Composition of phases, at. %									*k* (Solid/L)			
		Fe	Ni	Cu	S	Ru	Rh	Pd	Ag	Ir	Fe	Ni	Cu	S
Zone I mss (0 ⩽ g ⩽ 0.28)														
0.04	mss	40.19	6.16	2.08	50.86	0.38	0.15	< mdl	< mdl	0.2	1.40	1.05	0.11	1.09
0.09	mss	40.13	6.38	2.15	50.79	0.28	0.14	< mdl	< mdl	0.13	1.43	1.10	0.11	1.09
0.25	mss	38.85	7.76	2.17	51.07	0.08	<0.01	< mdl	< mdl	0.07	1.51	1.44	0.10	1.12
Zone II mss + iss (0.28 ⩽ g ⩽ 0.40)														
0.28	mss	38.1	8.99	2.19	50.73	< mdl	< mdl	< mdl	< mdl	< mdl	1.50	1.71	0.09	1.12
	iss	28.85	4.52	19.34	47.3	< mdl	< mdl	< mdl	< mdl	< mdl	1.14	0.86	0.82	1.04
0.33	mss	37.61	9.51	1.98	50.90	< mdl	< mdl	< mdl	< mdl	< mdl	1.53	1.90	0.08	1.13
	iss	28.7	4.36	19.09	47.85	< mdl	< mdl	< mdl	< mdl	< mdl	1.17	0.87	0.77	1.06
Zone III iss (0.40 ⩽ g ⩽ 0.68)														
0.40	iss	26.64	4.59	22.39	46.37	< mdl	< mdl	< mdl	< mdl	< mdl	1.09	0.91	0.89	1.03
0.49	iss	25.87	4.98	23.02	46.13	< mdl	< mdl	< mdl	< mdl	< mdl	1.07	0.98	0.90	1.03
0.57	iss	24.78	5.17	24.51	45.54	< mdl	< mdl	< mdl	< mdl	< mdl	1.02	1.02	0.95	1.02
Zone IV iss + bnss (0.68⩽ g ⩽ 0.89)														
0.68	iss	28.43	1.47	23.86	46.24	< mdl	< mdl	< mdl	< mdl	< mdl	1.11	0.28	1.03	1.02
	bnss	13.72	0.27	45.37	40.63	< mdl	< mdl	< mdl	< mdl	< mdl	0.54	0.05	1.97	0.90
0.79	iss	28.03	1.81	23.62	46.54	< mdl	< mdl	< mdl	< mdl	< mdl	0.49	0.07	2.48	0.88
	bnss	14.02	0.42	44.75	40.82	< mdl	< mdl	< mdl	< mdl	< mdl	0.98	0.31	1.31	1.01
0.86	iss	27.63	4.81	20.78	46.78	< mdl	< mdl	< mdl	< mdl	< mdl	0.82	0.73	2.13	0.98
	bnss	13.78	0.22	45.71	40.29	< mdl	< mdl	< mdl	< mdl	< mdl	0.41	0.03	4.68	0.84
Zone V bnss + pnss (0.89⩽ g ⩽ 1)														
0.89	bnss	13.99	0.30	44.13	41.25	< mdl	< mdl	< mdl	0.33	< mdl	–	–	–	–
	pnss	24.02	24.94	3.47	46.55	< mdl	0.24	0.78	< mdl	< mdl	–	–	–	–
0.92	bnss	14.04	0.23	44.36	41.21	< mdl	< mdl	< mdl	0.16	< mdl	–	–	–	–
	pnss	24.25	23.69	2.79	47.79	< mdl	0.58	0.53	< mdl	0.36	–	–	–	–
0.94	bnss	13.96	0.41	43.18	41.63	< mdl	< mdl	< mdl	0.82	< mdl	–	–	–	–
	pnss	23.28	25.67	2.36	46.92	< mdl	0.45	1.06	< mdl	0.27	–	–	–	–

Note. mdl – minimum level of element determination by SEM/EDS method. In zone I partition coefficients (mss/L): *k* Ru =10.48, 12.56 and 6.92, *k* Ir = 4.57, 3.35, 1.96 at *g* = 0.04, 0.09 and 0.25, respectively; *k* Rh = 3.27 and 3.46 at *g* = 0.04 and 0.09, respectively

Table 4. Composition of secondary phases in zones along the ingot

g	Phase	Sum, wt. %	Composition, at. %								
			Fe	Ni	Cu	S	Ru	Rh	Pd	Ag	Ir
1	2	3	4	5	6	7	8	9	10	11	12
Zone I (0 ⩽ g ⩽ 0.28) mss' + iss'(hc)											
0.04	mss'	99.45	40.19	6.16	2.08	50.86	0.38	0.15	< mdl	< mdl	0.20
	iss' (hc)	98.45	28.80	0.87	20.11	50.23	< mdl	< mdl	< mdl	< mdl	< mdl
0.09	mss'	99.67	40.13	6.38	2.15	50.79	0.28	0.14	< mdl	< mdl	0.13
	iss' (hc)	99.16	30.00	1.85	20.01	48.14	< mdl	< mdl	< mdl	< mdl	< mdl
0.25	mss'	99.93	38.85	7.76	2.17	51.07	0.08	0.01	< mdl	< mdl	0.07
	iss' (hc)	Not defined									
Zone II (0.28 ⩽ g ⩽ 0.40) mss' + iss'(hc) + Fe-pn +sug											
0.28	mss'	101.04	37.3	10.08	2.07	50.46	< mdl	< mdl	< mdl	< mdl	< mdl
	iss' (hc)	100.76	30.30	1.26	19.69	48.76	< mdl	< mdl	< mdl	< mdl	< mdl
	Fe-pn	100.81	28.55	22.73	1.57	47.01	< mdl	< mdl	0.15	< mdl	< mdl
	sug	101.08	28.35	19.27	4.84	47.39	< mdl	< mdl	0.14	< mdl	< mdl

Eng of Table 4

1	2	3	4	5	6	7	8	9	10	11	12
0.33	mss'	99.06	37.81	9.60	2.33	50.25	< mdl	< mdl	< mdl	< mdl	< mdl
	iss' (hc)	98.89	28.57	0.84	23.26	47.33	< mdl	< mdl	< mdl	< mdl	< mdl
	Fe-pn	99.08	26.05	25.18	1.44	46.89	< mdl	< mdl	0.44	< mdl	< mdl
	sug	Not defined									
0.40	mss'	98.52	36.47	10.22	3.64	49.50	< mdl	0.15	< mdl	< mdl	< mdl
	iss' (hc)	98.01	27.76	1.82	23.82	46.59	< mdl	< mdl	< mdl	< mdl	< mdl
	Fe-pn	97.77	27.40	22.87	2.37	47.0	< mdl	< mdl	0.36	< mdl	< mdl
	sug	98.47	26.75	19.28	7.44	46.28	< mdl	< mdl	0.13	< mdl	< mdl
Zone III (0.40 ⩽ g ⩽ 0.69) iss' (hc) + pn + bnss'											
0.48	iss' (hc)	99.08	27.54	0.79	25.21	46.46	< mdl	< mdl	< mdl	< mdl	< mdl
	pn	99.07	25.24	25.88	1.74	46.81	< mdl	< mdl	0.33	< mdl	< mdl
	bnss'	101.97	15.59	0.4	43.26	40.75	< mdl	< mdl	< mdl	< mdl	< mdl
0.57	iss' (hc)	98.95	27.17	3.11	23.41	46.31	< mdl	< mdl	< mdl	< mdl	< mdl
	pn	Not defined									
	bnss'	101.26	13.75	0.30	45.95	40.00	< mdl	< mdl	< mdl	< mdl	< mdl
Zone IV (0.68⩽ g ⩽ 0.89) iss'(hc) + Ni-pn + bnss' +Cu											
0.68	iss' (hc)	99.36	27.86	0.83	24.71	46.61	< mdl	< mdl	< mdl	< mdl	< mdl
	Ni-pn	99.95	25.2	25.68	1.78	46.88	< mdl	< mdl	0.46	< mdl	< mdl
	bnss'	100.22	13.72	0.27	45.37	40.63	< mdl	< mdl	< mdl	< mdl	< mdl
	Cu	97.75	1.06	0.28	98.34	0.32	< mdl	< mdl	< mdl	< mdl	< mdl
0.79	iss' (hc)	98.67	28.17	1.21	23.78	46.84	< mdl	< mdl	< mdl	< mdl	< mdl
	Ni-pn	100.27	24.78	25.82	1.88	47.06	< mdl	< mdl	0.45	< mdl	< mdl
	bnss'	100.67	14.02	0.42	44.75	40.82	< mdl	< mdl	< mdl	< mdl	< mdl
	Cu	99.18	2.34	0.39	96.91	0.36	< mdl	< mdl	< mdl	< mdl	< mdl
0.86	iss' (hc)	100.98	28.82	1.34	21.72	48.12	< mdl	< mdl	< mdl	< mdl	< mdl
	Ni-pn	101.18	24.71	26.29	1.84	46.69	< mdl	< mdl	0.47	< mdl	< mdl
	bnss'	100.79	13.78	0.22	45.71	40.29	< mdl	< mdl	< mdl	< mdl	< mdl
	Cu	Not defined									
Zone V (0.89 ⩽ g ⩽ 1) iss' (mh) + Ni-pn + sug + Ni-mss + bnss'											
0.89	iss' (mh)	101.12	26.33	0.9	25.75	47.03	< mdl	< mdl	< mdl	< mdl	< mdl
	Ni-pn	102.07	23.02	25.84	2.78	46.57	< mdl	0.22	1.56	< mdl	< mdl
	sug	101.47	24.49	22.75	4.76	47.09	< mdl	0.14	0.77	< mdl	< mdl
	Ni-mss	101.57	28.26	18.35	1.79	50.03	< mdl	0.71	< mdl	< mdl	0.58
	bnss'	101.82	13.57	0.28	44.68	40.89	< mdl	< mdl	< mdl	0.59	< mdl
0.92	iss'(mh)	98.12	25.14	1.02	26.40	47.44	< mdl	< mdl	< mdl	< mdl	< mdl
	Ni-pn	100.08	23.33	25.77	1.93	46.97	< mdl	< mdl	2.0	< mdl	< mdl
	sug	100.3	25.43	20.15	5.06	48.68	< mdl	0.36	< mdl	< mdl	0.32
	Ni-mss	99.73	27.40	18.64	1.81	50.82	< mdl	0.75	< mdl	< mdl	0.57
	bnss'	100.44	14.04	0.23	44.36	41.21	< mdl	< mdl	< mdl	0.16	< mdl
0.94	iss'(mh)	Not defined									
	Ni-pn	103.93	23.28	25.67	2.36	46.92	< mdl	0.45	1.06	< mdl	0.27
	sug	103.23	24.93	21.33	4.54	48.16	< mdl	0.48	0.19	< mdl	0.38
	Ni-mss	Not defined									
	bnss'	102.60	13.67	0.32	44.6	41.13	< mdl	< mdl	< mdl	< mdl	< mdl

Note. Au and Pt content in all phases < mdl. mss' – low-temperature monosulfide solid solution (Ni 6-10 at. %), Ni-mss – nickel monosulfide solid solution (Ni~19 at. %), iss' – low-temperature intermediate solid solution, bnss' – low-temperature boronitic solid solution (Ni 6-10 at. %), iss' – low-temperature intermediate solid solution, bnss' – low-temperature bornite solid solution, Fe-pn – pentlandite with Fe/Ni = 1.1-1.3, pn – pentlandite with Fe/Ni=1, Ni-pn – pentlandite with Fe/Ni=0.90-0.96, sug – sugakiite $Cu(Fe,Ni)_8S_8$, Cu – native copper.

and a decrease in the iron and sulfur content in the sample (Fig. 1). Large lamellar inclusions, representing a finely dispersed decay structure, were visible in the micrographs (Fig. 2b, c, g = 0.79, 0.86). They have an average composition of $Fe_{27.6-28.4}Ni_{1.5-4.8}Cu_{20.8-23.9}S_{46.2-46.8}$, so they should be attributed to the intermediate solid solution (iss). These inclusions were present in the matrix of the bornite solid solution $Fe_{13.7}Cu_{45.4}Ni_{0.3}S_{40.6}$ (bnss) (Table 3). The obtained data allowed stating that the change in the sample composition was mainly caused by the appearance of bnss in it. In [34, 35] it was shown that in the middle part of the phase diagram of the Cu-Fe-S system, the liquidus surface consisted of the fields of primary crystallization of the pyrrhotite solid solution (poss), the digenite-bornite solid solution Cu_2S–Cu_5FeS_4 (bnss), and the intermediate solid solution $CuFeS_2$–$Cu_3Fe_4S_6$ (iss). The ternary eutectic poss + bnss + iss, as well as quasi-binary eutectics (poss + bnss), (poss + iss), and (iss + bnss) were present on the liquidus surface. Bnss is also known to coexist with the melt in the Cu-Fe-Ni-S system [28]. Thus, in our experiment, the melt trajectory can also correspond to the crystallization of the cotectic (iss + bnss). We found that iss decomposed upon cooling to form low-temperature iss' of the $Fe_{27.6-28.2}Ni_{1.21-4.8}Cu_{20.8-24.7}S_{46.6-46.8}$ composition, Ni-pn with an atomic ratio of Fe/Ni = 0.96-1, while bnss decomposed into low-temperature bnss' and native copper (Fig. 2b, c, g = 0.79, 0.86, Table 4).

It was difficult to determine the exact set of primary phases released from the melt in zone V due to its complex structure. The decomposition was complicated by the formation of intergrowths of sulfide minerals with impurity phases, the amount of which took up a noticeable fraction of this section of the sample (Fig. 2b, c, g = 0.89, 0.92). It is possible that during the transition from zone IV to zone V, the trajectory of the melt composition entered the crystallization region of the bivariant cotectic of pnss ($Fe_{23.3-24.2}Ni_{23.4-25.7}Cu_{2.4-3.5}S_{46.6-47.8}$) + bnss ($Fe_{14.0}Ni_{0.2-0.4}Cu_{43.2-44.4}S_{41.2-41.6}$) (Table 3, Fig. 2b, g = 0.89, 0.92). It should be noted that previously we obtained the bivariant cotectic (bnss + pnss) in [28]. The following low-temperature phases were present in zone V: iss' of mooihoekite composition (mh), Ni-pn, Ni-mss, sug and bnss' (Table 4, Fig. 2c, g = 0.92) and, possibly, other unidentified phases of basic sulfides.

3.2. Behavior of microcomponents

Over the course of the directional crystallization of the sulfide melt, impurities can pass into the solid ingot either in the main phases as solid solutions or form inclusions as independent phases (e.g., [16, 28]). Let us study the behavior of noble metals in the experiment.

3.2.1. Solid solution in base metal sulfides

Noble elements in primary sulfide solid solutions. The results on the mss composition in zone I presented in Table 3 showed that Ir, Ru, and Rh were concentrated in this phase at the initial moment of melt crystallization. Their distribution coefficients mss/L > 1, which was consistent with the data in [6, 22, 36–38]. The content of Pt, Pd, Ag, and Au in mss was less than the minimum level of their detection by SEM/EDS. However, their content measured by the precision laser ablation method allowed calculating the distribution coefficients mss/L: k Pt 0.02-0.2, k Pd <0.03-0.2, k Au 0.01-0.09 [6, 14, 36–39]. According to the data in [22], the values of k for Pd, Pt, Au, and Ag ranged from ~ 0.1 to ~ $1\cdot10^{-3}$, so these elements should be mainly expelled into the melt.

The content of noble metals in primary mss, iss, and bnss in zones II-IV was below the limit of their detection by SEM/EDS (Table 3). Therefore, these crystallization stages were accompanied by a more intense accumulation of impurities in the melt. According to [22], the distribution coefficients of Pt, Pd, Ag, and Au had low values, which led to the enrichment of the sulfide liquid with these elements. Pt and Au were not found in iss [14, 40], Rh dissolved in sulfur-rich iss [41], while Pd (up to 0.4 at.%) could enter into iss with Cu > Fe and into Ni-rich iss (up to 1 at.%) [14]. Data on the directional crystallization of sulfide melts showed that 0.13-0.15 at. % Au could dissolve in iss with Cu > Fe [42]. Bornite solid solution associated with Ni-rich iss could dissolve 0.1 at. % Pd [14].

Measurement of the average composition of the ingot in zone V showed that the bnss + pnss cotectic crystallized in it. According to the data in Table 3, Pd and Rh were concentrated in pnss (0.8 and 0.2 at. %, respectively), and Ag expelled into bnss (0.3 at. %), which corresponded to the results obtained earlier in [28].

Noble elements in secondary sulfide solid solutions. In zone I, up to 0.15 at. % Rh can be dissolved in low-temperature mss' (Table 4). In zone II, the content of impurities of all noble metals in mss' was less than the analytical error. Upon cooling, iss decomposed into a mixture of iss', Fe-pn, and sug. The Pd was distributed between Fe-pn and sug. Obviously, Pd was initially present in iss, which was crystallized from the melt in this zone. In zone III, up to 0.3 at. % Pd could be dissolved in pn with the atomic ratio Ni / Fe = 1. The main concentrator of Pd in zone IV was Ni-pn. In zone V, Pd and Rh were distributed between Ni-pn and sug. Rh can also be present in Ni-mss.

3.2.2. Phases of micro-elements

The sample contained phases that were synthetic analogues of the following minerals: RuS_2 laurite, $Pt_{3-x}Fe$ isoferroplatinum, $CuIr_2S_4$ cuproiridsite, as well as an alloy based on native gold Au*, native silver Ag, and a solid solution of the composition Pt-Fe-Au.

RuS_2. At the beginning of the crystallization process (*g* ~ 0.04), a mass formation of laurite RuS_2 was observed (Fig. 3a). Laurite was present in the mss' matrix as single faceted crystals sized about 15 μm^2 and plates sized about 3 x 30 μm or their fragments (Fig. 3 a-c). It may contain the following impurities (at.%): 0.9-4.7 Ir, about 0.5 Rh, 0.4 Pd, 0.2 Ag, up to 1.7 Fe, and 0.4 Ni (Table 5). The heterogeneity of the chemical composition of the laurite crystals should be noted: their central zone was richer in ruthenium, and the edge zone was doped with iridium, which was consistent with the data in [43].

Ruthenium remaining in the melt was released in zones IV and V as large rare single crystals of RuS_2 sized up to 130 μm^2 (Fig. 3 n, j, k) and in intergrowths with $CuIr_2S_4$ cuproiridsite (Fig. 3 k, n). The Ir impurity in laurite varied from ~5 to ~8 at. %, and RuS_2 may also contain Rh, Pd, Ag, Ni, Fe, and Cu (up to 0.5-1 at. %).

$CuIr_2S_4$. Iridium formed its own phase, similar in composition to the natural mineral of the thiospinel group – $CuIr_2S_4$ cuproiridsite. $CuIr_2S_4$ was present in zones IV and V in the form of isolated inclusions of irregular shape sized about 20 μm^2 and in intergrowths with RuS_2 sized up to 150 μm^2 (Fig. 3 k, l, m). Cuproiridsite contained up to 2 at. % of Pt and Rh, about 5 at. % Fe and ~4 at. % Ni (Table 5).

Pt_3Fe. Platinum formed a phase similar to the mineral isoferroplatinum Pt_3Fe. It was detected in the mss' matrix in zones I and II as dendritic structures of inclusions ranging in size from ≤ 1 μm to about 7 x 15 μm (Fig. 3g, zone I; Fig. 3e, zone II). Isoferroplatinum contained about 1 at. % Au, about 3 at. % Cu and Ni (Table 5).

For the analysis of gold-based alloy Au*, solid solution of Pt-Fe-Au composition, and native Ag, we selected the largest inclusions, but they are usually smaller in size than the value of the X-ray generation zone, i.e. up to about 1 μm. Therefore, the results of the analysis of the composition of these phases were contaminated with components of the host phase.

Au*. Gold formed an independent phase containing (at.%): from ~ 53 to ~ 69 Au and impurities of Pd (up to 10 at.%), Ag (up to 6 at.%) and Pt (up to 1.5 at.%) (Table 5). These impurities formed solid solutions with Au, which was consistent with the structure of the solid-melting diagrams of binary Au-Ag, Au-Cu, Au-Pd and ternary systems Au-Ag-Cu and Au-Ag-Pd [44, 45]. Au* inclusions were localized in zone II in the iss' matrix and in zone V at the mh / Ni-pn interphase boundaries as elongated inclusions about 1 μm wide and 10–30 μm long (Fig. 3e, 3p)

Pt-Fe-Au solid solutions. The Pt-Fe-Au microphase was established in zones II–V. In zones II and III, the results of the analysis of the composition of this solid solution were strongly contaminated with the components of the pentlandite matrix. In zones IV and V, its composition varied within the following range (at. %): Pt from 43.2 to 49.0, Fe from 21.7 to 23.7, Au from 7.4 to 14.9 (Table 5). This phase was present in the form of isolated inclusions or colonies of inclusions of a maximum size of up to 5 μm long and up to 1–2 μm wide in the matrix Fe-pn in zone II (Fig. 3g), pn in zone III (Fig. 3h), Ni-pn in zone IV (Fig. 3k, m) and Ni-mss in zone V (Fig. 3n, o, p). The high content of Pt, Fe, and Au and the nature of decomposition similar to that in similar inclusions in [28] allowed attributing the discovered inclusions to a Pt-Fe-Au solid solution. The authors of [28] found that in case of cooling, inclusions of such a solid solution decomposed into a mixture of $Pt_{3-x}Fe$ and an alloy based on Au*.

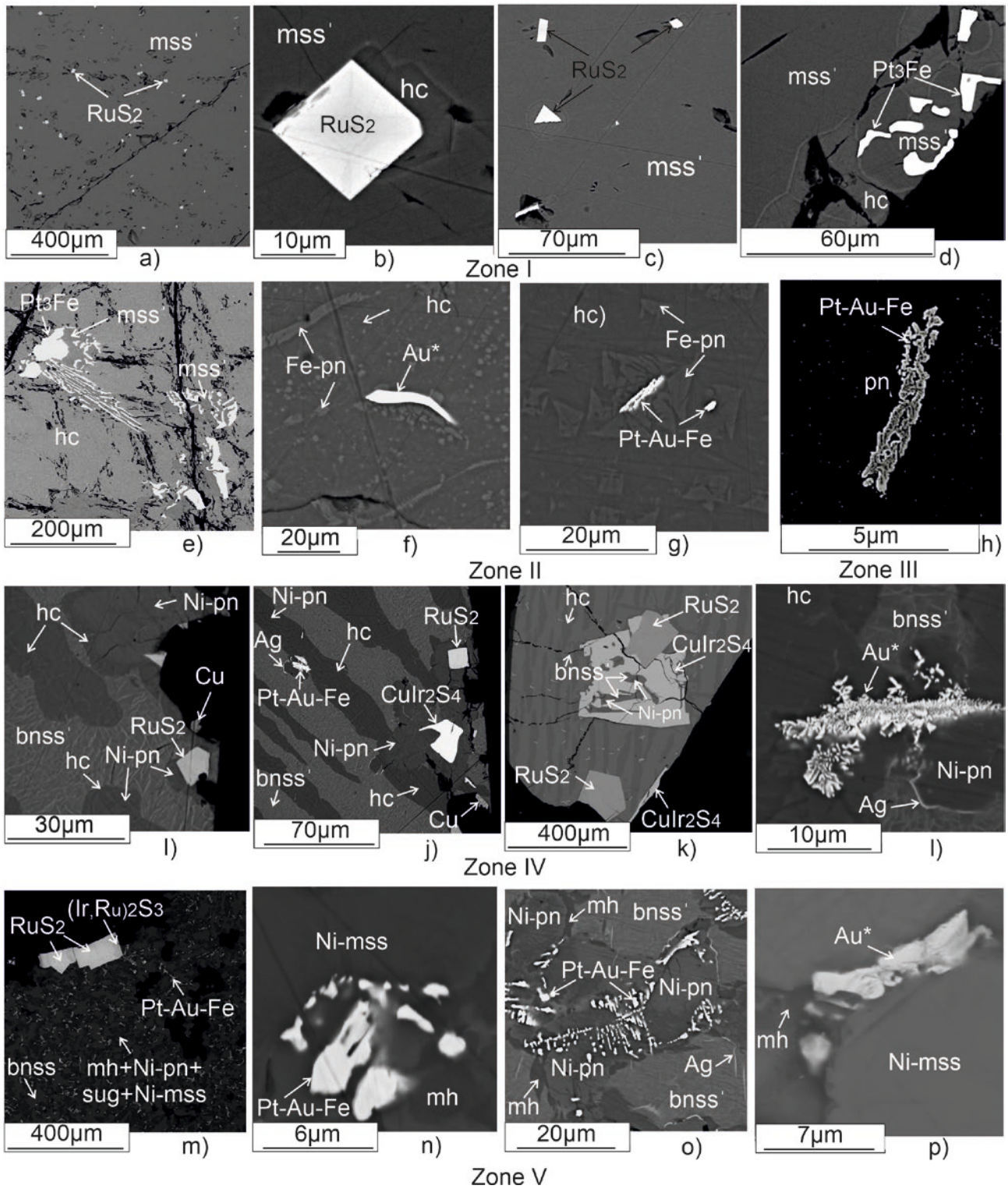

Fig. 3. Forms of noble metal microphase separation in sulfide matrices in zones I–V. Microphotographs were obtained in reflected electrons. RuS_2 crystals in the mss' matrix at g 0.04 (a, b, c); Pt_3Fe inclusions in the mss' matrix at g 0.09 (d) and 0.33 (e); Au* inclusions in the hc' matrix at *g* 0.28 (f) and in the Ni-mss' matrix at *g* 0. 92 (p); single RuS_2 and $CuIr_2S_4$ inclusions in Ni-pn matrix at *g* 0.68 (i, j); RuS_2 and $CuIr_2S_4$ intergrowths at *g* 0.86 (l) and 0.92 (n); Pt-Fe-Au alloy inclusions in pn at *g* =0.57 (h), in Ni-pn at *g* 0.68 (k), 0.86 (m) and 0.92 (n, o, p)

Table 5. Chemical composition of selected grains of characteristic microphases of noble metals in the sample

Phase	Ideal formula	Fe	Ni	Cu	Au	Ag	Pt	Pd	Ru	Ir	Rh	S	Сумма
Zone I (mss)													
Laurite	RuS_2	1.23	0.27	–	–	0.46	–	–	56.04	3.1	0.82	36.13	98.05
		1.27	0.26	–	–	0.25	–	–	31.93	0.93	0.46	64.9	
		1.19	0.29	–	–	0.44	–	0.77	54.79	6.98	–	37	101.46
		1.2	0.28	–	–	0.23	–	0.41	30.63	2.05	–	65.2	
		1.63	0.42	–	–	–	–	–	46.77	15.37	–	35.47	99.65
		1.73	0.42	–	–	–	–	–	27.46	4.74	–	65.64	
Isoferroplatinum	Pt_3Fe	11.01	1.02	1.08	1.48	–	81.32	–	–	–	–	0.42	96.33
		29.47	2.6	2.54	1.12	–	62.31	–	–	–	–	1.96	
Zone II (mss+iss)													
Isoferroplatinum	Pt_3Fe	11.8	1.35	1.36	–	–	84.09	–	–	–	–	0.45	99.06
		30.15	3.28	3.05	–	–	61.51	–	–	–	–	2	
Gold-based alloy	Au*[1]	2.33	0.85	5.36	85.82	0.86	–	2.51	–	–	–	0.76	98.48
		6.61	2.29	13.36	68.99	1.26	–	3.74	–	–	–	3.75	
Alloy of Pt-Fe-Au system	Pt-Fe-Au[1]	11.76	7.35	6.83	42.42	1.85	17.07	4.01	–	–	–	10.96	102.26
		18.43	10.96	9.4	18.84	1.5	7.66	3.3	–	–	–	29.91	
Zone III (iss)													
Alloy of Pt-Fe-Au system	Pt-Fe-Au[1]	13.29	9.51	8.28	36.65	1.88	17.49	3.81	–	–	–	13.2	104.11
		18.72	12.75	10.25	14.64	1.37	7.05	2.82	–	–	–	32.39	
Zone IV (iss+bnss)													
Native silver	Ag[1]	18.78	15.65	6.15	–	38.72	–	0.74	–	–	–	19.5	99.55
		20.09	15.93	5.78	–	21.45	–	0.42	–	–	–	36.34	
Alloy of Pt-Fe-Au system	Pt-Fe-Au[1]	10.28	1.59	5.19	12.45	–	71.18	1.64	–	–	–	1.3	103.62
		23.69	3.49	10.51	8.14	–	46.97	1.98	–	–	–	5.22	
Laurite	RuS_2	1.04	0.66	1.26	–	–	–	0.59	44.51	16.77	0.88	34.54	100.26
		1.12	0.67	1.19	–	–	–	0.33	26.39	5.23	0.51	64.56	
		0.33	0.33	–	–	–	–	–	42.06	24.37	–	35.36	102.45
		0.36	0.34	–	–	–	–	–	25.11	7.65	–	66.55	
Cuproiridsite	CuIr2S4	3.58	2.98	8.01	–	–	3.26	–	–	56.44	2.40	24.09	100.75
		4.83	3.83	9.51	–	–	1.26	–	–	22.15	1.76	56.67	
Zone V (bnss+pnss)													
Cuproiridsite	CuIr2S4	3.57	2.84	7.99	–	–	4.71	–	–	54.87	2.73	23.63	100.35
		4.88	3.69	9.59	–	–	1.84	–	–	21.77	2.02	56.21	
Laurite	RuS2	0.34	0.37	–	–	0.21	–	0.14	45.13	18.85	0.46	35.40	100.88
		0.37	0.38	–	–	0.12	–	0.08	26.76	5.88	0.27	66.17	
		0.39	0.24	–	–	–	–	–	46.88	18.22	0.86	36.2	102.8
		0.41	0.24	–	–	–	–	–	27.17	5.55	0.49	66.14	
		0.28	0.39	–	–	–	–	–	42.93	22.4	1.19	35.5	102.69
		0.3	0.4	–	–	–	–	–	25.41	6.97	0.69	66.23	
		0.45	0.39	–	–	0.41	–	–	43.86	20.25	1.11	35.5	101.96
		0.48	0.4	–	–	0.23	–	–	25.89	6.29	0.64	66.07	
Native silver	Ag[1]	13.18	4.23	28.04	–	33.61	–	0.51	–	–	–	18.44	98.02
		14.38	4.39	26.89	–	18.99	–	0.29	–	–	–	35.05	
Gold-based alloy	Au*[1]	2.17	1.02	7.42	74.55	4.49	2.10	7.79	–	–	–	1.40	100.94
		5.39	2.41	16.20	52.51	5.78	1.49	10.16	–	–	–	6.06	
Pt-Fe-Au-ss	Pt-Fe-Au[1]	9.64	2.22	4.06	10.67	0.57	70.38	1.03	–	–	–	1.04	99.61
		23.43	5.13	8.67	7.35	0.72	48.97	1.31	–	–	–	4.4	
		9.22	2	4.09	13.1	0.39	70.13	1.41	–	–	–	1.18	101.53
		22.21	4.58	8.66	8.95	0.49	48.37	1.78	–	–	–	4.95	
		8.63	1.91	4.36	20.91	0.38	59.98	1.01	0	0	0	0.94	98.11
		21.72	4.57	9.64	14.92	0.5	43.2	1.33	0	0	0	4.12	
		Fe	Ni	Cu	Au	Ag	Pt	Pd	Ru	Ir	Rh	S	

Note. For each phase the composition expressed in wt. % is in the upper row, in at. % – in the lower row. ss- solid solution.

[1] – high content of major components indicates the entrapment of sulfide phases in the analyzed area of the matrix.

Ag. Native Ag was released in the form of rims less than 1 μm wide around bnss' and Ni-pn grains in zones IV and V of the sample. Elongated inclusions of Ag in the bnss' matrix were also observed there (Fig. 3k, m, p) (Table 5).

As can be seen from the above-described experimental results, micro-elements can be present as solid solutions in the primary and secondary main phases of the Fe–Ni–Cu–S system, as independent phases crystallized from the melt, or as a result of partial decomposition of sulfide solid solutions during their cooling, and also in the form of impurities dissolved in other microphases. Impurities of noble metals soluble in the main phases of this system distributed during crystallization in accordance with the classical theory, similar to macrocomponents. Thus, Ir and Ru dissolved well in the matrix of high-temperature mss, and upon cooling they transited into the low-temperature modification of mss'. Rhodium's behavior was more complex. It was present at the beginning of crystallization in mss, while the remaining Rh noticeably accumulated in the melt only in zone V, where it was present in pnss, upon decomposition of which in case of cooling it transited into Ni-mss. Palladium and silver were concentrated in the final products of melt crystallization, pentlandite and bornite solid solutions, respectively. The main low-temperature concentrator of Pd was pentlandite. A recent work [46] proved its inclusion in the pentlandite crystal lattice, and in [47] a discovery of pentlandite containing 11.26 wt. % Pd in Norilsk ores was reported.

Impurities that did not transit into sulfide solid solutions can form independent phases: primary ones directly in the process of fractional crystallization of the melt and secondary ones as a result of solid-phase reactions. It is likely that the compounds with a melting point significantly exceeding the crystallization temperature of this melt were formed from the melt. Crystallization of Pt_3Fe and mass formation of RuS_2 were associated with the initial stage of the directional crystallization process. Refractory RuS_2 (melting point ~ 1600 °C) was formed in the Ru-S binary system [44]. The Pt-Fe phase diagram contained a non-stoichiometric Pt_3Fe compound with a wide homogeneity region, formed as a result of the decomposition of a continuous solid solution at a temperature of 1350 °C ([48] and references from it).

It should be noted that Pt_3Fe inclusions were observed in the mss' matrix of zone I, while RuS_2 was found not only in this matrix, but also in the decomposition products of the eutectic alloys iss + bnss and bnss + pnss in zones IV and V, respectively, as an independent phase and in intergrowths with $CuIr_2S_4$. The formation of these phases directly from the melt was confirmed by the large sizes and expressed faceting of the inclusions. In accordance with the theory of quasi-equilibrium directional crystallization of multicomponent melts with impurities, the process of zoning formation made up by primary sulfide solid solutions should be accompanied by the formation of primary impurity zoning [49]. The impurity phases should appear in the ingot in a sequence, one after another. Each impurity zone was distinguished by its own set of microphases. The transition from one zone to another meant rather the disappearance or the emergence than the emergence of a new microphase. As a result, a regular change in the distribution of microphases should occur along the sample. In our experiment, this pattern was not observed. Thus, RuS_2 crystals were formed in zones I, IV, and V, which meant that there was no fractionation. It should be noted that the processes of formation of new phases upon directional crystallization were determined only by the processes of their incorporation at the crystallization front. Upon crystallization of phases composed of macrocomponents, a continuous crystallization front was formed. Upon crystallization of microphases, a continuous crystallization front could not be formed, and thus the main limiting stage was the formation of nuclei. The formation of nuclei occurred under strongly nonequilibrium conditions, and thus it was natural to expect that the theory of quasi-equilibrium directional crystallization would not work in this case.

Silver rims around secondary inclusions bnss' and Ni-pn were most likely formed as a result of solid-phase processes. Primary bnss partially captured Ag in the process of crystallization from the melt. In case of cooling, inclusions of Ag appeared due to a decrease in its solubility in bnss'. Secondary formations included Pt-Fe-Au solid solutions, which were observed to occur

within grains of secondary Ni-pn and Ni-mss, and this indicated their formation as a result of solid-phase reactions. They were represented by the structure of decomposition of Pt_3Fe and Au*. Au* inclusions were associated with iss' (hc) or with mh/Ni-mss boundaries. This suggested that their formation was a consequence of subsolidus iss decay. The processes of microphase separation during solid-phase reactions, as well as during crystallization from a melt, proceeded as nonequilibrium through the stage of nucleation and their subsequent growth.

4. Conclusions

In this work we obtained new data on the behavior of the main elements and impurities upon fractional crystallization of a multicomponent melt of the Cu-Fe-Ni-S-(PGE, Au, Ag) system with its own special type of zoning.

It was shown that during fractional crystallization the macrocomponents were distributed in accordance with the classical theory. Their behavior can be described using distribution coefficients. It was established that during melt crystallization, the sequence of primary phase formation had the following form: mss / mss + iss / iss / iss + bnss / bnss + pnss. These results indicated a more complex structure of the melting diagram in the studied region of the Fe-Ni-Cu-S system than was known before from classical experiments using samples obtained by long-term annealing and subsequent quenching.

The results of chemical analysis and the ingot microstructure study allowed determining a list of low-temperature secondary phases and their associations that must be taken into account when constructing subsolidus sections. A new type of secondary (phase) zonality may be present in Cu-Ni sulfide ores.

In the first approximation, the behavior of noble metal impurities upon fractional crystallization can be described using distribution coefficients. The processes of microphase separation from the melt or during solid-phase reactions proceeded as non-equilibrium through the stage of formation of nuclei and their subsequent growth. Therefore, the process of formation of impurity zonality did not strictly correspond to the theory of quasi-equilibrium directional crystallization of multicomponent melts with impurities.

Author contributions

E. F. Sinyakova: scientific supervision, methodology and concept development, research, writing of text, final conclusions. K. A. Kokh: methodology development, conducting experiments, research, text editing.

Conflict of interests

The authors declare that they have no known competing financial interests or personal relationships that could have influenced the work reported in this paper.

References

1. Craig J. R., Kullerud G. Phase relations in the Cu–Fe–Ni–S system and their application to magmatic ore deposits. *Economic Geology Monograph* / Ed. H.D.B. Wilson. 1969;4: 344–358. https://doi.org/10.5382/Mono.04.25

2. Fleet M. E., Chryssoulis S. L., Stone W. E., Weisener C. G. Partitioning of platinum-group elements and Au in the Fe–Ni–Cu–S system: experiments on the fractional crystallization of sulfide melt. *Contributions of Mineralogy and Petrology*. 1993;115: 36–44. https://doi.org/10.1007/BF00712976

3. Fleet M. E., Pan Y. Fractional crystallization of anhydrous sulfide liquid in the system Fe–Ni–Cu–S, with application to magmatic sulfide deposits. *Geochimica et Cosmochimica Acta*. 1994;58: 3369–3377. https://doi.org/10.1016/0016-7037(94)90092-2

4. Ebel D. S., Naldrett A. J. Crystallization of sulfide liquids and interpretation of ore composition. *Canadian Journal of Earth Sciences*. 1977;34: 352–356. https://doi.org/10.1139/e17-031

5. Дистлер В. В., Гроховская Т. Л., Евстигнеева Т. Л. и др. *Петрология сульфидного магматического рудообразования*. М.: Наука; 1988, 230 с.

6. Ballhaus C., Tredoux M., Spath A. Phase relations in the Fe-Ni-Cu-PGE-S system at magmatic temperature and application to massive sulphide ores of the Sudbery igneous complex. *Journal of Petrolology*. 2001;42(10): 1911–1926. https://doi.org/10.1093/petrology/42.10.1911

7. Naldrett A. J. *Magmatic sulfide deposits. Geology, geochemistry and exploration*. Springer-Verlag, Heidelberg, Germany; 2004, 727 p.

8. Fleet M. E. Phase equilibria at high temperature. *Reviews in Mineralogy and Geochemistry*. 2006;61: 365–419. https://doi.org/10.2138/rmg.2006.61.7

9. Cafagna F., Jugo P. J. An experimental study on the geochemical behavior of highly siderophile elements (HSE) and metalloids (As, Se, Sb, Te, Bi) in a mss-iss-pyrite system at 650 °C: a possible magmatic origin for Co-HSE-bearing pyrite and the role of metalloid-rich phases in the fractionation of HSE. *Geochimica et Cosmochimica Acta*. 2016;178: 233–258. https://doi.org/10.1016/j.gca.2015.12.035

10. Helmy H. M., Botcharnikov R., Ballhaus C., ... Hager T. Evolution of magmatic sulfide liquids: how and when base metal sulfides crystallize? *Contributions of Mineralogy and Petrology*. 2021;176: 1–15. https://doi.org/10.1007/s00410-021-01868-4

11. Kullerud G., Yund R. A., Moh G. H. Phase relations in the Cu–Fe–S, Cu–Ni–S, and Fe–Ni–S systems. *Economic Geology Monograph*. 1969;4: 323–343.

12. Sugaki A., Kitakaze A. High form of pentlandite and its thermal stability. *American Mineralogist.* 1998;83(1–2): 133–140. https://doi.org/10.2138/am-1998-1-213

13. Cabri L. J. New phase relations in the Cu-Fe-S system. *Economic Geology*. 1973;68(4): 443–454. https://doi.org/10.2113/gsecongeo.68.4.443

14. Peregoedova A., Ohnenstetter M. Collectors of Pt, Pd and Rh in a S-poor Fe–Ni–Cu sulfide system at 760°C: experimental data and application to ore deposits. *The Canadian Mineralogist*. 2002;40: 527–561. https://doi.org/10.2113/gscanmin.40.2.527

15. Kosyakov V. I., Sinyakova E. F. Melt crystallization of $CuFe_2S_3$ in the Cu–Fe–S system. *Journal of Thermal Analysis and Calorimetry*. 2014;115(1): 511–516. https://doi.org/10.1007/s10973-013-3206-0

16. Sinyakova E. F., Vasilyeva I. G., Oreshonkov A. S., Goryainov S. V., Karmanov N. S. Formation of noble metal phases (Pt, Pd, Rh, Ru, Ir, Au, Ag) in the process of fractional crystallization of the $CuFeS_2$ melt. *Minerals.* 2022;12(9): 1136. https://doi.org/10.3390/min12091136

17. Tolstykh N., Brovchenko V., Rad'ko V., Shapovalova M., Abramova V., Garcia J. Rh, Ir and Ru partitioning in the Cu-poor IPGE massive ores, Talnakh intrusion, Skalisty mine, Russia. *Minerals*. 2022;11:18. https://doi.org/10.3390/min12010018

18. Mungall J. E. Crystallization of magmatic sulfides: an empirical model and application to Sudbury ores. *Geochimica et Cosmochimica Acta*. 2007;71(11): 2809–2819. https://doi.org/10.1016/j.gca.2007.03.026

19. Dare S. A. S., Barnes S.-J., Prichard H. M., Fisher P. C. Mineralogy and geochemistry of Cu-Rich ores from the McCreedy East Ni-Cu-PGE deposit (Sudbury, Canada): implications for the behavior of platinum group and chalcophile elements at the end of crystallization of a sulfide liquid. *Economic Geology.* 2014;109(2): 343–366. https://doi.org/10.2113/econgeo.109.2.343

20. Barnes S.-J., Ripley E. M. Highly siderophile and strongly chalcophile elements in magmatic ore deposits. *Reviews in Mineralogy and Geochemistry*. 2016;81: 725–774. https://doi.org/10.2138/rmg.2016.81.12

21. Duran, C. J., Barnes S. J., Plese P., Kudrna Prašek M., Zientek M. L., Pagé P. Fractional crystallization-induced variations in sulfides from the Noril'sk-Talnakh mining district (Polar Siberia, Russia). *Ore Geology Review*. 2017;90: 326–351. https://doi.org/10.1016/j.oregeorev.2017.05.016

22. Liu, Y., Brenan J., Partitioning of platinum-group elements (PGE) and chalcogens (Se, Te, As, Sb, Bi) between monosulfide-solid solution (MSS), intermediate solid solution (ISS) and sulfide liquid at controlled conditions. *Geochimica et Cosmochimica Acta*. 2015;159: 139–161. https://doi.org/10.1016/j.gca.2015.03.021

23. Hawley J. E. The Sudbury ores: their mineralogy and origin. *The Canadian Mineralogist*. 1962;7(1): 1–207.

24. Naldrett A. J., Ebel D. S., Asif M., Morrison G., Moore C. M. Fractional crystallization of sulfide melts as illustrated at Noril'sk and Sudbury. *European Journal of Mineralogy*. 1997;9: 365–377. https://doi.org/10.1127/ejm/9/2/0365

25. Barnes S-J., Cox R. A., Zientek M. L. Platinum-group element, gold, silver and base metal distribution in compositionally zoned sulfide droplets from the Medvezky Creek mine, Noril'sk, Russia. *Contributions of Mineralogy and Petrology.* 2006;152: 187–200. https://doi.org/10.1007/s00410-006-0100-9

26. Holwell D. A., McDonald I. A review of the behavior of platinum group elements within natural magmatic sulfide ore systems. *Platinum Metals Review*. 2010;54: 26–36. https://doi.org/10.1595/147106709x480913

27. Kosyakov V. I., Sinyakova E. F., Distler V. V. Experimental simulation of phase relationships and zoning of magmatic nickel–copper sulfide ores, Russia. *Geology of Ore Deposits.* 2012;54: 179–208. (In Russ., abstract in Eng.). https://doi.org/10.1134/S1075701512030051

28. Sinyakova E. F., Kosyakov V. I., Borisenko A. S., Karmanov N. S. Behavior of noble metals during fractional crystallization of Cu–Fe–Ni–(Pt, Pd, Rh, Ir, Ru, Ag, Au, Te) sulfide melts. *Russian Geology and Geophysics.* 2019; 60(6): 642–651. https://doi.org/10.15372/RGG2019050

29. Sinyakova E. F., Kosyakov V. I., Kokh K. A., Naumov E. A. Sequential crystallization of pyrrhotite, cubanite and intermediate solid solution from Cu-Fe-(Ni)-S melt. *Russian Geology and Geophysics.* 2019;60(11): 1257–1267. https://doi.org/10.15372/rgg2019091

30. Kosyakov V. I., Sinyakova E. F., Kokh K. A. Sequential crystallization of four phases from melt on the polythermal section of the Cu–Fe–Ni–S system. *Journal of Thermal Analysis and Calorimetry*. 2020;139(6): 3377–3382. https://doi.org/10.1007/s10973-019-08701-y

31. Kosyakov V. I., Sinyakova E. F. Physicochemical prerequisites for the formation of primary orebody zoning at copper-nickel sulfide deposits (by the example of the systemsFe–Ni–SandCu–Fe–S). *Russian Geology and Geophysics*. 2012;53(9): 861–882. https://doi.org/10.1016/j.rgg.2012.07.003

32. Kosyakov V. I. Possible usage of directional crystallization for solving petrological problems. *Russian Geology and Geophysics.* 1998;39(9): 1245–1256.

33. Sinyakova E. F., Kosyakov V. I. Experimental modeling of zonality of copper-rich sulfide ores in copper–nickel deposits. *Doklady Earth Sciences*. 2009;427: 787–792. https://doi.org/10.1134/S1028334X0709019X

34. Schlegel H., Sehüller A. Das Zustandebild Kupfer-Eisen-Schwefel. *Zeitschrift für Metallkunde*. 1952;43(12): 421–428.

35. Greig J. W., Jensen E., Merwin H. E. The system Cu-Fe-S. *Carnegie Institution of Washington Year Book*. 1955;54: 129–134.

36. Fleet M. E., Chryssoulis S. L., Stone W. E., Weisener C. G. Partitioning of platinum-group elements and Au in the Fe–Ni–Cu–S system: experiments on the fractional crystallization of sulfide melt. *Contributions of Mineralogy and Petrology.* 1993;115: 36–44. https://doi.org/10.1007/bf00712976

37. Li C., Barnes S.-J., Makovicky E. et al. Partitioning of nickel, cooper, iridium, rhenium, platinum, and palladium between monosulfide solid solution and sulfide liquid: Effects of composition and temperature. *Geochimica et Cosmochimica Acta.* 1996;60(7): 1231–1238. https://doi.org/10.1016/0016-7037(96)00009-9

38. Barnes S.-J., Makovicky E., Makovicky M., Rose-Hansen J., Karup-Moller S. Partition coefficients for Ni, Cu, Pd, Pt, Rh and Ir between monosulfide solid solution and sulfide liquid and the formation of compositionally zoned Ni-Cu sulphide bodies by fractional crystallization of sulfide liquid. *Canadian Journal of Earth Sciences*. 1997;34: 366–374. https://doi.org/10.1139/e17-032

39. Mungall J. E., Andrews D. R. A., Cabri L. J., Sylvester P. J., Tuberett M. Partitioning of Cu, Ni, Au, and platinum-group elements between monosulfide solid solution and sulfide melt under controlled oxygen and sulfur fugacities. *Geochimica et Cosmochimica Acta.* 2005;64(17): 4349–4360. https://doi.org/10.1016/j.gca.2004.11.025

40. Simon G., Kesler S. E., Essene E. J., Chryssoulis S. L. Gold in porphyry copper deposits: experimental determination of the distribution of gold in the Cu-Fe-S system at 400 to 700 °C. *Economic Geology.* 2000;95: 259–270. https://doi.org/10.2113/gsecongeo.95.2.259

41. Kolonin G. R., Fedorova Zh. N., Kravchenko T. A. Influence of the composition of phase associations of the Cu-Fe-S system on the mineral forms of rhodium (according to experimental data)*. *Doklady of the Academy of Sciences*. 1994;337(1): 104–107. (In Russ.)

42. Sinyakova E. F., Kosyakov V. I. Experimental modeling of zoning in copper-nickel sulfide ores. *Doklady Earth Sciences*. 2007;417A(9): 1380–1385. https://doi.org/10.1194/S1028334X0709019X

43. Sinyakova E. F., Komarov V. Yu, Sopov K. V., Kosyakov V. I., Kokh K. A. Crystallization of pyrrhotite from Fe-Ni-Cu-S-(Rh, Ru) melt. *Journal of Crystal Growth*. 2020;548: 125822. https://doi.org/10.1016/j.jcrysgro.2020.125822

44. Massalski T. B., Okamoto H., Subramanian P. R., Kacprzak L. *Binary Alloy Phase Diagrams. Second Edition*. Ohio, United States: ASM International, Materials Park; 1990. 3589 p.

45. Ternary alloy systems. Noble metal systems. Selected systems from Ag-Al-Zn to Rh-Ru-Sc. In: *Landolf-Börnstein – Group IV. Physical Chemistry.* G. Effenberg & S. Ilyenko (eds.). 2006;11B. https://doi.org/10.1007/b96200

46. Brovchenko V., Merkulova M., Sittner J., … Cnudde V. X-ray absorption spectroscopic study of Pd^{2+} on Ni site in pentlandite. *American Mineralogist*. 2023;108: 2086–2095. https://doi.org/10.2138/am-2022-8704

47. Kalugin V., Gusev V., Tolstykh N., Lavrenchuk A., Nigmatulina E. Origin of the Pd–rich pentlandite in the massive sulfide ores of the Talnakh deposit, Norilsk Region, Russia. *Minerals*. 2021;11(11): 1258. https://doi.org/10.3390/min11111258

48. Makovicky E. Ternary and quaternary phase systems with PGE. In*: The Geology, Geochemistry, Mineralogy and Mineral Beneficiation of Platinum-Group Elements*. L. J. Cabri (ed.) Canadian Institute of Mining. Metallurgy and Petroleum; 2002, Special Vol. 54, pp. 131-175.

49. Kosyakov V. I., Sinyakova E. F. Peculiarities of behavior of trace elements during fractional crystallization of sulfide magmas. *Doklady Earth Sciences*. 2015;460(2): 179–182. https://doi.org/10.1134/S1028334X1502021X

* *Translated by author of the article*

Information about the authors

Elena F. Sinyakova, Dr. Sci. (Geol.-Min.), Leading Research Fellow, V. S. Sobolev Institute of Geology and Mineralogy, Siberian Branch of the Russian Academy of Sciences (Novosibirsk, Russian Federation).

https://orcid.org/0000-0001-6288-3425

efsin@igm.nsc.ru

Konstantin A. Kokh, Dr. Sci. (Geol.-Min.), Leading Research Fellow, V. S. Sobolev Institute of Geology and Mineralogy, Siberian Branch of the Russian Academy of Sciences (Novosibirsk, Russian Federation).

https://orcid.org/0000-0003-1967-9642

kokh@igm.nsc.ru

Received 27.05.2024; approved after reviewing 31.05.2024; accepted for publication 16.09.2024; published online 25.12.2024.

Translated by Marina Strepetova

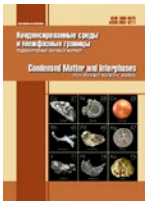

ISSN 1606-867X (Print)
ISSN 2687-0711 (Online)
Condensed Matter and Interphases
Kondensirovannye Sredy i Mezhfaznye Granitsy
https://journals.vsu.ru/kcmf/

Original articles

Research article
https://doi.org/10.17308/kcmf.2024.26/12451

Labile states are the basis of functional materials

P. P. Fedorov✉

Prokhorov General Physics Institute of the Russian Academy of Sciences,
38 Vavilova st., Moscow 119991, Russian Federation

Abstract

The available data refute the widespread postulate of thermodynamics, according to which labile states are physically unrealizable, unobservable and, thus, devoid of practical interest, since the transition to a stable state does not require overcoming a potential barrier, and a random fluctuation leads to an accelerated shift of the system from the initial state. The cases when a system remains in a labile state for an indefinite period of time are well known. The corresponding states are not only observable, but can be used to create functional materials.

The article analyses low-temperature phase equilibria and spinodal behavior in a number of binary systems containing solid solutions with a fluorite structure, such as CaF_2-SrF_2, CaF_2-BaF_2, BaF_2-RF_3 (R = La, Nd), SrF_2-LaF_3, ZrO_2-Y_2O_3. The investigation of low temperature phase formation in the BaF_2-LaF_3 system allowed to reveal the decomposition of the solid solution $Ba_{1-x}La_xF_{2+x}$ with a binodal curve. In the SrF_2-LaF_3 system the equilibrium solubility curve of lanthanum fluoride in strontium fluoride is expressed at the inflection point on the solvus curve with a practically horizontal tangent, which corresponds to the bifurcation point – the practical coincidence of the critical point of the nonequilibrium binodal/spinodal with the solvus curve. The $Ba_{1-x}Ca_xF_2$ continuous solid solution obtained by the mechanochemical method and possessing high fluorine-ion conductivity, remains in a labile state for an indefinitely long period of time. Upon heating, it disintegrates with an exothermic effect at 420-450 °C. In all other fluoride systems, single crystals grown from the melt retain the functional characteristics of photonics materials for years and have no signs of degradation.

Obviously, the technological stability of crystalline samples of the listed solid solutions is determined by the extremely low values of the cation diffusion coefficients. The systems are “falling”, but too slowly to detect it. The fine architecture of materials in a labile state is of considerable interest.

Keywords: Phase diagrams, Stability, Spinodal, Architecture of spinodal decomposition

Funding: The study was funded by a grant Russian Science Foundation No. 22- 13- 00167, https://rscf.ru/project/22-13-00167

Acknowledgements: The author is grateful to A. V. Naumov, A. I. Popov, V. V. Gusarov for discussing the problem, A. A. Alexandrov and A. A. Luginina for conducting the experiments.

For citation: Fedorov P. P. Labile states are the basis of functional materials. *Condensed Matter and Interphases*. 2024;26(4): 772–781. https://doi.org/10.17308/kcmf.2024.26/12451

Для цитирования: Федоров П. П. Лабильные состояния – основа функциональных материалов. *Конденсированные среды и межфазные границы*. 2024;26(4): 772–781. https://doi.org/10.17308/kcmf.2024.26/12451

✉ Pavel P. Fedorov, e-mail: ppfedorov@yandex.ru

1. Introduction

It is known that a system is in equilibrium if it has a minimum of free energy and a maximum of entropy. A stable thermodynamic equilibrium should comply with following inequalities according to thermodynamics [1-3]:

$$C_P > C_V > 0 \quad (1)$$

(thermal stability),

$$\chi_T > \chi_S > 0 \quad (2)$$

(mechanical stability),

$$(\partial^2 G/\partial x^2)_{P,T} = (\partial \mu/\partial x)_{P,T} > 0 \quad (3)$$

(resistance to diffusion).

In these inequalities P – pressure, T – temperature, V – volume, C – heat capacity, S – entropy, G – isobaric-isothermal potential, $\chi = (\partial P/\partial V)$ - compressibility, μ – chemical potential, x - concentration.

Thermodynamics distinguishes three types of equilibria: stable, metastable, and labile. Metastable equilibria are locally stable (satisfy inequalities 1–3), but may be unstable with respect to the appearance of other phases. For the transition into the stable state, the system must overcome a potential barrier. Labile states are locally unstable (one of the inequalities 1–3 is impaired), and the transition to a stable (or metastable) state does not require overcoming a potential barrier.

As for labile equilibria, the thermodynamic literature accepts as a postulate that labile states are not physically realizable, at least not observable, and thus are devoid of practical interest, since the transition to a stable state does not require overcoming a potential barrier, and a random fluctuation leads to an accelerated shift of the system from the initial state.

"If within a certain interval of parameter values any of the inequalities (*stability criteria*) is not satisfied, then this interval cannot be associated with any really existing states. ...Such states... are completely unstable (labile) and, therefore, physically impossible (in any case, unobservable)." [4, p. 74].

"Unstable states are practically unrealizable, since the slightest fluctuations shift the system out of the equilibrium state. Therefore, the use of stability conditions allows to identify real systems and exclude systems that are devoid of practical interest." [5, p. 44].

"Unstable equilibrium is not physically realizable. This statement is often questioned based on phenomenological reasoning, but it can be proven by statistical thermodynamics methods." [6, p. 83].

"We obtain a curve on which thermodynamic inequalities are impaired (for a homogeneous body); it limits the region in which the body under no circumstances can exist as homogeneous." [7, p. 285].

It should be noted that J. W. Gibbs, who actually formulated these stability criteria, expressed them much more cautiously: "A phase which is unstable with respect to continuous changes is evidently incapable of permanent existence on a large scale except in consequence of passive resistances to change" [1, p. 109].

The purpose of this study is the demonstration of the fallaciousness of these statements [4–7]. Systems in labile states are not only observable but also very useful from a practical point of view in materials science.

2. Problem statement

The set of points at which the stability conditions are impaired is called spinodal. The spinodal dimension (point, line or surface) can be different depending on the dimension of the corresponding phase diagram.

In general, determination of the position of spinodals requires the consideration of the thermodynamic model of the system. We will limit ourselves to considering the chemical spinodal, namely, considering the decomposition of solid solutions, i.e., the impairment of the stability of the system in relation to diffusion. According to the third law of thermodynamics, as the temperature decreases, phases of variable composition must undergo decomposition or ordering. We will limit ourselves to binary systems, which does not affect the generality of the conclusions.

At the same time, the position of the binodal, which is determined quite simply, allows to estimate the position of the spinodal with a high degree of reliability. In the immiscibility of solid solutions, the critical point, the binodal dome point K also belong to the spinodal, see Fig. 1. At

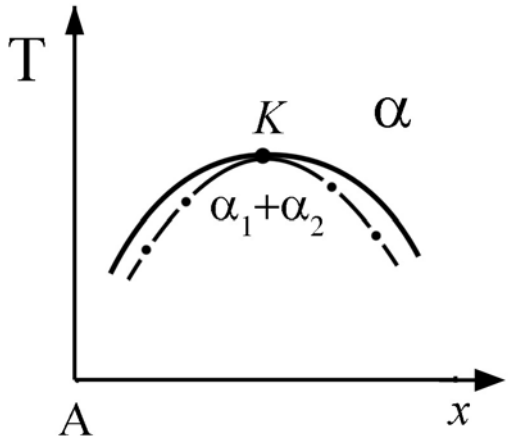

Fig. 1. Binodal and spinodal (dash-dotted line) during immiscibility of a solid solution in a binary system in the vicinity of the critical immiscibility point *K*

this point, both the binodal and the spinodal have a common horizontal tangent, i.e. $(\partial T/\partial x)_P = 0$.

There is a simple thermodynamic model, namely the regular solution model, applicable only to systems with isostructural components, but allows to qualitatively navigate in more complex cases. In the regular solution model for a binary system, the spinodal equation is written as follows [3]:

$$T = 4T_c x(1 - x), \quad (4),$$

where T_c – the absolute temperature of the critical point, which is realized at a composition containing 50 mol. % of components (Fig. 2a). At $T \to 0$ K, the spinodal curve goes to the origin of coordinates, but, unlike the binodal, does not have a vertical tangent at this point (Fig. 2). It should be noted that in the monograph by Prigogine and Defey the position of the spinodal is depicted with an error [3, Fig. 16.16]. Taking into account elastic stresses during the decomposition of solid solutions leads to a shift in the position of binodals and spinodals in the composition-temperature coordinates [8–10].

The immiscibility, i.e. the appearance of both the binodal and the spinodal associated with it, in the metastable region of existence of a solid solution or glass is of great interest [11, 12].

Experimental methods for determination of the position of spinodals are limited and generally effective only for relatively fast kinetics of phase transformations [13, 14]. The change in the microstructure of alloys can be used as a method for determining the spinodal [12]. The study [15] also deserves attention (the experimentally obtained region of solid solution immiscibility exactly corresponds to the spinodal equation).

3. Examples

The **CaF_2-SrF_2** system. The phase diagram is presented in Fig. 3 [16]. There is a continuous series of solid solution between isostructural components. The position of the critical point of decomposition of the solid solution is outlined based on the data of the study of the CaF_2-SrF_2-MnF_2 ternary system [17]. At room temperature,

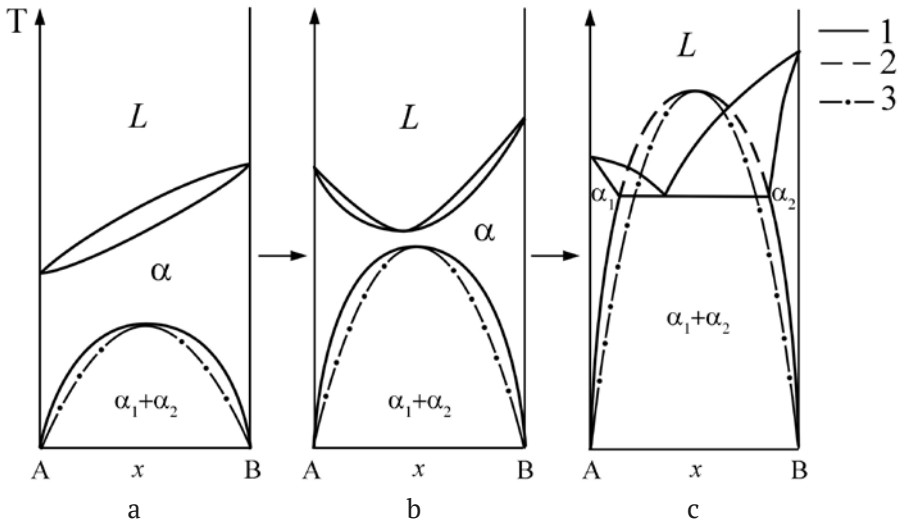

Fig. 2. Position of binodals and spinodals (dash-dotted line) in binary systems in the regular solution model. *L* – melt, α – stratifying solid solution

only solid solutions containing up to 10 mol. % of the second component, while intermediate compositions containing 10-90% CaF_2, are in a labile state.

Nevertheless, the corresponding compositions can be grown in the form of single crystals and are recommended as optical materials, transparent in a wide range of the spectrum from UV to IR [18, 19], as well as matrices for doping with active rare earth ions [20-24]. There are no questions about the technological stability of the relevant materials. Continuous solid solutions of $Ca_{1-x}Sr_xF_2$ is obtained even when using low-temperature synthesis methods, including co-precipitation from aqueous solutions [25].

Another example is the **CaF_2 - BaF_2** system.

Preliminary studies have shown that the picture of phase equilibria in the system is more complex than described in [26]. The system contains intermediate phases stable within a narrow temperature range.

Limited solid solutions based on the components are formed in the system. Both the growth of single crystals from the melt [27] and low-temperature co-precipitation [25] allow the synthesis of only limited solid solutions. However, the $Ba_{1-x}Ca_xF_2$ continuous solid solution was obtained by mechanochemical synthesis [28]. The corresponding samples can exist for an indefinitely long period of time. However, after heating, the system transformed into an equilibrium state. The decomposition of the solid solution accompanied by the release of heat and an exothermic effect on thermograms at 420–450 °C occurs [29].

In general, the behavior of spinodals in complex cases remains unclear. Each specific case requires careful analysis.

The phase diagram of the **BaF_2-LaF_3** system is shown in Fig. 4. At the phase diagram, using a special technique focused on the use of low-temperature phase formation, the immiscibility region of the $Ba_{1-x}La_xF_{2+x}$ heterovalent solid solution was identified (phase *F*) [30]. The indicated position of the spinodal (Fig. 4b) shows that at room temperature the $Ba_{1-x}La_xF_{2\ x}$ solid solution is in a labile state in the approximate concentration range of 0.03 < x < 0.45. This

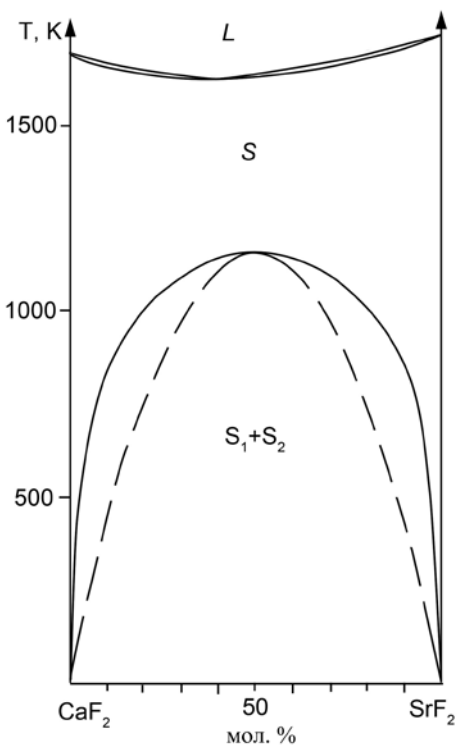

Fig. 3. Phase diagram of the CaF_2-SrF_2 system [16]

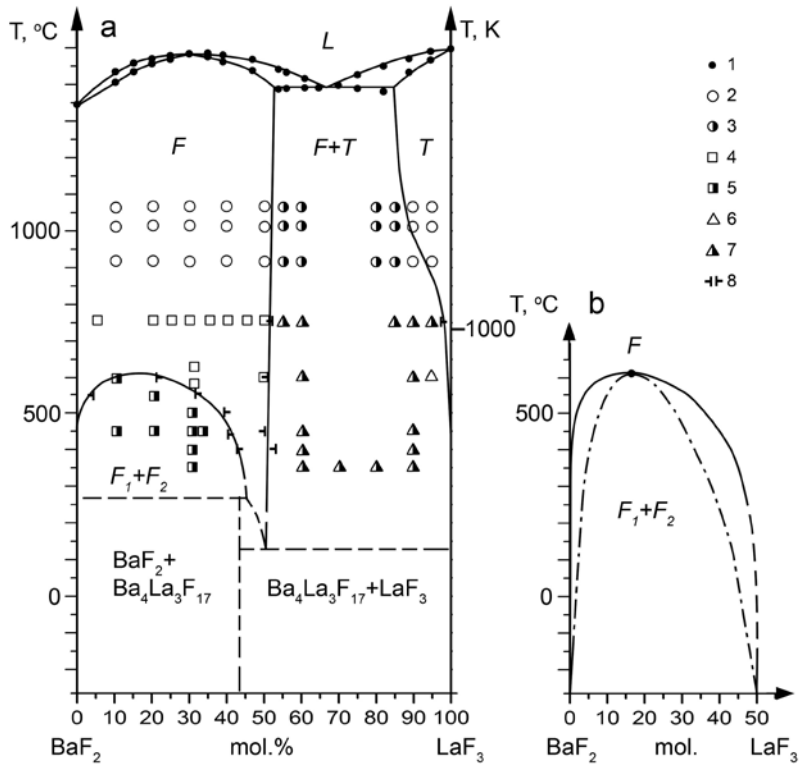

Fig. 4. Phase diagram of the BaF_2-LaF_3 system [30] (a), and the proposed region of spinodal decomposition of the solid solution (dash-dotted line, b). 1-3 – data from Sobolev and Tkachenko [30]

qualitatively corresponds to the results of the synthesis of solid solutions by co-precipitation of fluorides from aqueous solutions [32]. However, the practical stability of the $Ba_{1-x}La_xF_{2+x}$ single crystals, grown from the melt is obvious. In particular, a composition containing 30 mol. % LaF_3 is a promising multifunctional material [33].

The next example is the **SrF_2–LaF_3** system (Fig. 5) [34]. The low-temperature studies have shown that the homogeneity region of the $Sr_{1-x}R_xF_{2+x}$ fluorite solid solution below 400 °C rapidly decreases and almost reaches zero, which corresponds to the requirements of the third law of thermodynamics [35, 36] (Fig. 5). How can the spinodal be located for such a decomposition of the $Sr_{1-x}La_xF_{2+x}$ solid solution?

In this case, the solvus curve has an inflection point with a practically horizontal tangent. According to the van der Waals equation for coexisting phases in a binary system at constant pressure [35, 37]:

$$(\partial T/\partial x)_P = \Delta x(\partial^2 G/\partial x^2)_{P,T}/[\Delta x(\partial S/\partial x)_{P,T} - \Delta S]. \quad (5)$$

In this equation, the derivatives of the isobaric-isothermal potential G and entropy S for the concentration x of any component in the considered solid solution are used. The Δx and ΔS values are equal to the difference in concentrations and entropies of coexisting phases. From this equation it follows that the horizontal tangent to the equilibrium curve of two phases $(\partial T/\partial x)_P = 0$ can occur if $\Delta x = 0$ or $(\partial^2 G/\partial x^2)_{P,T} = 0$. The first condition corresponds to the equality of the compositions of two phases that are in equilibrium and does not correspond to the considered case. The second variant remains.

Thus, the presence of a horizontal tangent to the solvus curve corresponds to the boundary condition of stability with respect to diffusion. In [34], the approach of a diffuse phase transition in the $Sr_{1-x}La_xF_{2+x}$ solid solution from above to the solvus curve was proposed. However, this was not confirmed by the recording of DSC curves. Thus, the approach from below the binodal curve of metastable immiscibility of the $Sr_{1-x}La_xF_{2+x}$ solid solution in a way that the critical point practically coincides with the solvus curve, presented in Fig. 6c, remains. Such a critical state of phase equilibria, changing the topology of the phase

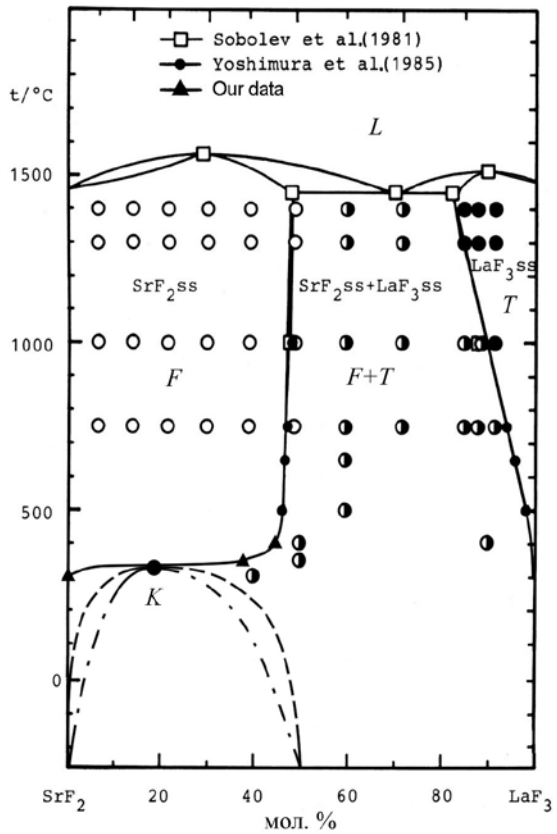

Fig. 5. Phase diagram of the SrF_2-LaF_3 system [34] and the probable position of the binodal (dotted line) and spinodal (dash-dotted line) in the region of metastable stability of the $Sr_{1-x}La_xF_{2+x}$ solid solution

diagram, is a bifurcation of the phase diagram [38, 39]. At the K critical point three lines with a horizontal tangent exist, namely: the solvus curve of the solid solution, the binodal of the metastable decomposition of this solid solution, and the spinodal corresponding to this binodal converge (Fig. 5).

Position of the SrF_2-LaF_3 system in the series shown in Fig. 6, practically corresponds to the bifurcation point (Fig. 6c). while the position of the BaF_2-LaF_3 system corresponds to Fig. 6d. Since the nature of phase equilibria in the vicinity of bifurcation points is subject to fluctuations [40], it is possible that variant (6d) is also implemented for the SrF_2-LaF_3 system with a slight excess of the critical immiscibility point of the solid solution over the solvus curve.

Approximate position of the spinodal in the SrF_2-LaF_3 system is shown in Fig. 5. Again, there are no problems with the stability of $Sr_{1-x}La_xF_{2+x}$ single crystals, grown from the melt. This also applies to a single crystal of the $Sr_{0.70}La_{0.30}F_{2.30}$ composition, the

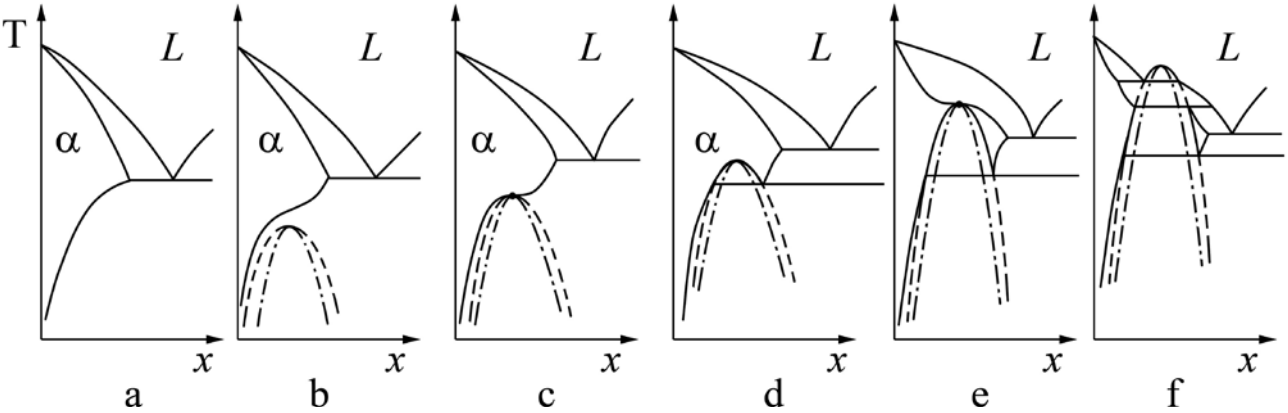

Fig. 6. Change in the phase diagram of a binary system due to an increase in the critical temperature of solid solution immiscibility ("sunrise-sunset" bifurcation) [38]. Dotted line – metastable equilibria, dash-dotted line – spinodals

most refractory inorganic fluoride with a melting temperature of 1570 °C [33].

The BaF_2-RF_3 (R = Pr, Nd) systems studied in the low-temperature region [41] are characterized by inflection points on the solvus curves. This indicates the presence of metastable low-temperature immiscibility of solid solutions. Probably, the corresponding phase diagrams occupy position (b) in the sequence diagram shown in Fig. 6, with metastable immiscibility of the fluorite solid solution (and the corresponding spinodal) at a lower temperature. The assumption of the presence of low-temperature spinodal decomposition of the $Ba_{1-x}R_xF_{2+x}$ solid solutions is confirmed by the results of attempts to synthesize the corresponding solid solutions by co-precipitation from aqueous solutions [32]: as a result of the synthesis, a mixture of practically pure barium fluoride and a fluorite phase containing about 40 mol. % RF_3 was formed.

Finally, we will discuss systems of zirconium dioxide with oxides of rare earth elements, which are sources of optical materials – cubic zirconia (fianite) [42, 43]. Continuation of the curves of the limiting solubility of solid solutions based on the high-temperature ZrO_2 modification into the region of low temperatures [44], taking into account the requirement of the presence of a vertical tangent at a temperature approaching absolute zero [45], inevitably requires the presence of an inflection point on the metastable solvus curve, see Fig. 8. Based on the above description, this also indicates metastable immiscibility of the $Zr_{1-x}R_xO_{2-0.5x}$ solid solutions,

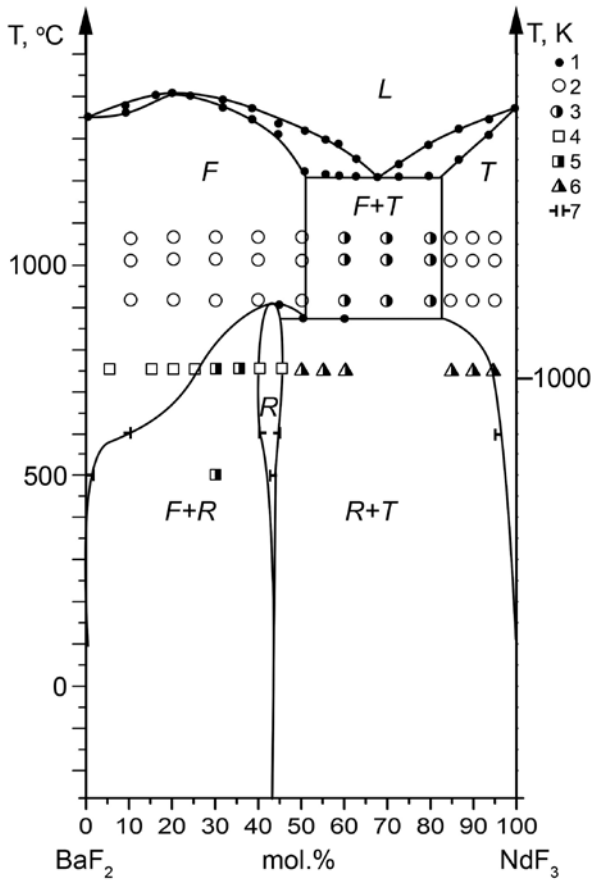

Fig. 7. Phase diagram of the BaF_2-NdF_3 system [41]. 1–3 – data [31]

which, however, occurs at very low temperatures, possibly below room temperature.

4. Architecture of spinodal decomposition

Single-phase materials located in the spinodal decomposition zone must undergo a directed evolution, consisting of decomposition into

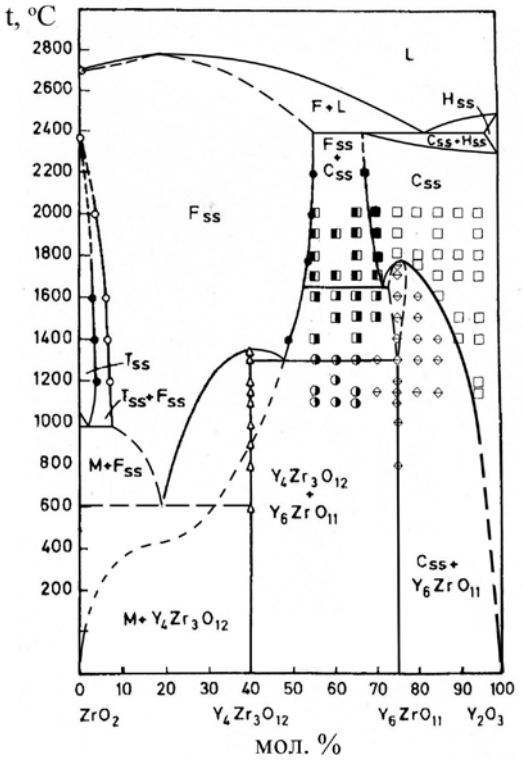

Fig. 8. Phase diagram of the ZrO_2-Y_2O_3 system [42]

two phases, and this process must occur with acceleration. The differences in the coexisting phases and the characteristic size of each of them continuously increase. The structure of the resulting aggregate has a complex topology and is the subject of numerous computational and experimental studies, see, for example, [12, 46-51]. In mathematical modelling, the Cahn-Hilliard equation is usually used. The corresponding materials have a set of topological, mechanical and physicochemical properties that determine the interest in such objects. Such terms as two-framework structures [12], spinodoid metamaterials [49, 50], spinodal architected materials [51], multifunctional spinodal nanoarchitectures [45], self-assembled nanolabyrinthine materials [48], cellular materials with spinodal topologies [47] are used for these materials. These materials are stressed nanocomposites. Surprisingly, the topology of spinodal decomposition resembles the architecture of chalcedons [52].

However, we are primarily interested in single-phase materials in the spinodal decomposition zone. It should be noted that the answer to the question: is the material homogeneous? – mainly depends on the used research methods. In optically transparent single crystals of the $Ba_{1-x}R_xF_{2+x}$ solid solutions, discussed above, heterogeneities of the order of ~20 nm in size were revealed by electron microscopy [33, 53]. However, the quality of single crystals allows laser generation to be obtained even after long-term storage. An example of an optical quality single crystal after storage for about 40 years is shown in Fig. 9. It should be noted that the expected size of the inhomogeneity is approximately an order of magnitude smaller than the wavelength of light. In this case, according to the X-ray diffraction method, such samples are single-phase, with well-defined unit cell parameters, linearly dependent on the composition. At the same time, when these crystals were studied using the Raman light scattering method, they look more like two-phase systems. This issue requires further investigation.

Fig. 9. Single crystal of $Ba_{0.71}Nd_{0.29}F_{2.29}$. – optical filter for a wavelength of 2.5 μm. The faceting is artificial. Grown by T. Turkina [54]. Photographed January 22, 2024

Electron microscopy did not reveal inhomogeneities similar to those described for single crystals of the $Ba_{1-x}R_xF_{2+x}$ solid solutions in single crystals of cubic zirconia with a concentration of about 10 mol. % Y_2O_3.

5. Conclusions

Thus, the conducted analysis of phase diagrams shows that solid solutions with a fluorite structure, such as $M_{1-x}R_xF_{2\,x}$ (M = Ca, Sr, or Ba) fluorides and $Zr_{1-x}R_xO_{2-0.5x}$ (R = rare earth), are labile at normal temperature and pressure, but they do not show degradation corresponding to spinodal decomposition. The same applies to functional materials created on their basis:

their technological stability is much higher than thermodynamic stability [55]. Obviously, this is determined by the extremely low values of the diffusion coefficients of cations. The systems are "falling", but too slowly to be noticed.

Fig. 9, which records the preservation of functional material in a labile state for approximately 40 years, convincingly refutes Gukhman's assertion [4]. Obsidian (volcanic glass), existing in a thermodynamically non-equilibrium state, was a functional material of Paleolithic cultures for thousands of years. Some manifestations of volcanic glass retain its original amorphous (apparently labile) form for 200 million years [56].

Conflict of interests

The author declares that he has no known financial conflicts of interest or personal relationships that could have influenced the work presented in this article.

References

1. Gibbs J. V. *Thermodynamic works**. Moscow; Leningrad: GITTL Publ., 1950. 492 p. (In Russ.)

2. Storonkin A. V. *Thermodynamics of heterogeneous systems**. Leningrad: Leningrad State University Publ., 1967. 447 p. (In Russ.)

3. Prigogin I., Defay R. D. *Chemical themodynamics*. Longman Green and Co. London et al., 1954. 533 p.

4. Gukhman A. A. *On the foundations of thermodynamics**. Moscow: URSS Publ., 2010. 384 p. (In Russ.)

5. Rusanov A. I. *Phase equilibria and surface phenomena**. Leningrad: Khimiya Publ., 1967. 388 p. (In Russ.)

6. Műnster A. *Chemische thermodynamik*. Berlin: Akademie Verlag; 1969.

7. Landau L. D., Lifshitz E. M. *Statistical physics**. Vol. 1. Moscow: Nauka Publ., 586 p. (In Russ.)

8. Cahn J. W. *Spinodal decomposition. The 1967 Institute of Metals Lecture*. TMS AIME 1968;242; 166–180. https://doi.org/10.1002/9781118788295.ch10

9. Cahn J. W., Charles R. J. The initial stages of phase separation in glasses. *Physics and Chemistry of Glasses*. 1965;6(5): 181–191.

10. Carpenter M. A. A "conditional spinodal" within the peristerite miscibility gap of plagioclase feldspars. *American Mineralogist*. 1981;66: 553–560. Available at: http://www.minsocam.org/ammin/AM66/AM66_553.pdf

11. Uhlmann D. R., Kolbeck A. G. Phase separation and the revolution in concepts of glass structure. *Physics and Chemistry of Glasses*. 1976;17(5): 146–158.

12. Mazurin O. V., Roskova G. P., Averyanov V. I., Antropova T. V. *Two-phase glasses: structure, properties, application**. Leningrad: Nauka Publ.; 1991. 276 p. (In Russ.)

13. Bhardwaj M. C., Roy R. Effect of high pressure on crystalline solubility in the system NaCl-KCl. *Journal of Physics and Chemistry of Solids*. 1971;32: 1693–1607. https://doi.org/10.1016/s0022-3697(71)80053-7

14. Schiraldi A., Pezzati E., Chiodelli G. Phase diagram and point defect parameters of the system CsBr-TlBr. *Zeitschrift für Physikalische Chemie*. 1978;110: 1–16. https://doi.org/10.1524/zpch.1978.110.1.001

15. Eliseev A. A., Lukashin A. V., Vertigel A. A. Cryosol synthesis of $Al_{2-x}Cr_xO_3$ solid solutions. *Chemistry of Materials*. 1999;11: 241–246. https://doi.org/10.1021/cm980721l

16. Fedorov P. P., Mayakova M. N., Alexandrov A. A., ... Ivanov V..K. The melt of sodium nitrate as a medium for synthesis of fluorides. *Inorganics*. 2018;6(2): 38–55. https://doi.org/10.3390/inorganics6020038

17. Ol'khovaya L. A., Karpenko G. A., Ikrami D. D., Fedorov P. P. The CaF_2-SrF_2-MnF_2 ternary system. *Russian Journal of Inorganic Chemistry*. 1991;36(11): 1639–1642.

18. Popov P. A., Moiseev N. V., Karimov D. N., ... Fedorov P. P. Thermophysical characteristics of $Ca_{1-x}Sr_xF_2$ solid-solution crystals ($0 \leqslant x \leqslant 1$). *Crystallography Reports*. 2015;60(1): 116–122.

19. Takahashi K., Cadatal-Raduban M., Sarukura N., Kawamata T., Sugiyama K., Fukuda T. Crystal growth and characterization of large $Ca_{0.582}Sr_{0.418}F_2$ single crystal by Czochralski method using cone die. *Journal of Crystal Growth*. 2024;628: 127541. https://doi.org/10.1016/j.jcrysgro.2023.127541

20. Basiev T. T., Vasil'ev S. V., Doroshenko M. E., ... Fedorov P. P. Efficient lasing in diode-pumped Yb^{3+}:CaF_2-SrF_2 solid-solution single crystals. *Quantum Electronics*. 2007;37(10): 934–937. https://doi.org/10.1070/qe2007v037n10abeh013662

21. Ushakov S. N., Uslamina M. A., Nishchev K. N., ... Osiko V.V. Study of Yb^{3+} optical centers in fluoride solid solution crystals CaF_2–SrF_2–YbF_3. *Optics and Spectroscopy*. 2020;128(5): 600–604. https://doi.org/10.1134/S0030400X20050185

22. Kuznetsov S. V., Konyushkin V. A., Nakladov A. N., ... Fedorov P. P. Thermophysical properties of single crystals of CaF_2-SrF_2-RF_3 (R = Ho, Pr) fluorite solid solutions. *Inorganic Materials*. 2020;56(9): 975–981. https://doi.org/10.1134/s0020168520090113

23. Normani S., Loiko P., Basyrova L., ... Camy P. Mid-infrared emission properties of erbium-doped fluorite-type crystals. *Optical Materials Express*. 2023;13(7): 1836–1850. https://doi.org/10.1364/ome.482402

24. Zhu C., Song J., Mei B., Li W., Liu Z. Fabrication and optical characterizations of CaF_2–SrF_2–NdF_3 transparent ceramics. *Materials Letters* 2016;167(10): 115–117. https://doi.org/10.1016/j.matlet.2015.12.083

25. Fedorov P. P., Kuznetsov S. V., Mayakova M. N., ... Osiko V. V. Coprecipitation from aqueous solutions to prepare binary fluorides. *Russian Journal of Inorganic Chemistry*. 2011;56(10): 1525–1531). https://doi.org/10.1134/S003602361110007X

26. Fedorov P. P., Buchinskaya I. I., Ivanovskaya N. A., Konovalova V. V., Lavrishchev S. V., Sobolev B. P. CaF_2-BaF_2 phase diagram. *Doklady Physical Chemistry*. 2005;401(2): 53–55. https://doi.org/10.1007/s10634-005-0024-5

27. Wrubel G. P., Hubbard B. E., Agladge N. I., ... Campbell G. A. Glasslike two-level systems in minimally disordered mixed crystals. *Physical Review Letters*. 2006;96: 235503. https://doi.org/10.1103/PhysRevLett.96.235503

28. Heise M., Scholz G., Düvel A., Heitjans P., Kemnitz E. Mechanochemical synthesis, structure, and properties of solid solutions of alkaline earth metal fluorides: $M^a_{1-x}M^b_xF_2$ (*M*: Ca, Sr, Ba). *Solid State Sciences*. 2016;60: 65–74. https://doi.org/10.1016/j.solidstatesciences.2016.08.004

29. Düvel A., Heitjans P., Fedorov P. P., Voronov V. V., Pynenkov A. A., Nishchev K. N. Thermal stability of $Ca_{1-x}Ba_xF_2$ solid solution. *Solid State Science*. 2018;83: 188–191. https://doi.org/10.1016/j.solidstatesciences.2018.05.011

30. Aleksandrov A. A., Shevchenko A. G., Sorokin N. I., ... Fedorov P. P. Phase equilibria in the BaF-LaF_3 system*. In: *Abstracts of the scientific and practical conference "Fluoride materials and technologies", April 15–19, Moscow, 2024*. Moscow: FSRC "Crystallography and photonics" of NRC «Kurchatov Institute» RAS; 2024. pp. 111–112. Available at: https://fluorchem.ru/

31. Sobolev B. P., Tkachenko N. L. Phase diagrams of BaF_2-(Y,Ln)F_3 systems. *Journal of Less-Common Metals*. 1982;85: 155. https://doi.org/10.1016/0022-5088(82)90067-4

32. Kuznetsov S. V., Fedorov P. P., Voronov V. V., Samarina K. S., Ermakov R. P., Osiko V. V. Synthesis of $Ba_4R_3F_{17}$ (R stands for rare-earth elements) powders and transparent compacts on their base. *Russian Journal of Inorganic Chemistry*. 2010;55(4): 484–493. https://doi.org/10.1134/s0036023610040029

33. Sobolev B. P. *The rare earth trifluorides. Part 2*. Introduction to materials science of multicomponent metal fluoride crystals. Barcelona: Institut d'Estudis Catalans; 2001.

34. Fedorov P. P., Alexandrov A. A., Voronov V. V., Mayakova M. N., Baranchikov A. E., Ivanov V. K. Low-temperature phase formation in the SrF_2–LaF_3 system. *Journal of the American Ceramic Society*. 2021;104(6): 2836–2848. https://doi.org/10.1111/jace.17666

35. Fedorov P. P. Third law of thermodynamics as applied to phase diagrams. *Russian Journal of Inorganic Chemistry*. 2010;55(11): 1722–1739. https://doi.org/10.1134/S0036023610110100

36. Laughlin D. E., Soffa W. A. The third law of thermodynamics: phase equilibria and phase diagrams at low temperatures. *Acta Materialia*. 2018;45: 49–61. https://doi.org/10.1016/j.actamat.2017.11.037

37. van der Waals J. D., Konstamm PH. *Lehrbuch der thermostatic*. Leipzig: verlag von Johann Ambrosius Bath; 1927.

38. Fedorov P. P. Factors responsible for the appearance of inflections in solid-solution demixing curves. *Russian Journal of Inorganic Chemistry*. 2001;46(10): 1567–1570.

39. Fedorov P. P. Transformations of *T-x* phase diagrams of binary systems in the condensed state: II. Phase equilibria under constraints. *Russian journal of Physical Chemistry A*. 1999;73(9): 1387–1392. Available at: https://elibrary.ru/item.asp?id=13311944

40. Fedorov P. P., Medvedeva L. V., Sobolev B. P. Bifurcations in the *T-x* phase diagrams of binary systems in the condsensed state. Fluctuations of the phase transition type in the LiF-YF_3 system. *Russian journal of Physical Chemistry A*. 2002;76(3): 337–342. Available at: https://elibrary.ru/item.asp?id=13407836

41. Fedorov P. P., Alexandrov A. A., Luginina A. A., Voronov V. V., Kuznetsov S. V., Chernova E. V. Phase diagrams of the BaF_2 – NdF_3 and BaF_2 – PrF_3 systems. *Journal of the American Ceramic Society*. 2024. https://doi.org/10.1111/jace.20152

42. Fedorov P. P.,* Yarotskaya E. G. Zirconium dioxide. Review. *Condensed Matter and Interphases*. 2021;23(2): 169–187. https://doi.org/10.17308/kcmf.2021.23/3427

43. Fedorov P.P. Phase equilibria in low-temperature regions of phase diagrams. *Journal of Phase Equilibria and Diffusion*. 2024;45(3): 475–488. https://doi.org/10.1007/s11669-024-01099-7-

44. P. P. Fedorov, E. V. Chernova. Phase diagrams of zirconia systems with yttria and scandia. *Condensed Matter and Interphases*. 2023;25(2): 257–267. https://doi.org/10.17308/kcmf.2023.25/11106

45. Laughlin D. E., Massalski T. B. Construction of equilibrium phase diagrams: Some errors to be avoided. *Progress in Materials Science*. 2020;120: 100715. http://doi.org/10.1016/j.pmatsci.2020.100715

46. Guell Izard A., Bauer J., Crook C., Turlo V., Valdevit L. Ultrahigh energy absorption multifunctional spinodal nanoarchitectures. *Small*. 2019;15(45): 1903834. https://doi.org/10.1002/smll.201903834

47. Hsieh M.-T., Endo B., Zhang Y., Bauer J., Valdevit L. The mechanical response of cellular materials with spinodal topologies. *Journal of the Mechanics and Physics of Solids*. 2019;125: 401–419. http://doi.org/10.1016/j.jmps.2019.01.002

48. Portela C. M., Vidyasagar A., Krödel S., ... Kochmann D. M. Extreme mechanical resilience of self-assembled nanolabyrinthine materials. *Proceedings of the National Academy of Sciences*. 2020;117(11): 5686–5693. http://doi.org/10.1073/pnas.1916817117

49. Zheng L., Kumar S., Kochmann D. M. Data-driven topology optimization of spinodoid metamaterials with seamlessly tunable anisotropy. *Computer Methods in Applied Mechanics and Engineering*. 2021;383: 113894. http://doi.org/10.1016/j.cma.2021.113894

50. Kumar S., Tan S., Zheng L., Kochmann D. M. Inverse-designed spinodoid metamaterials. *npj Computational Materials*. 2020;6(1): 73. http://doi.org/10.1038/s41524-020-0341-6

51. Senhora F. V., Sanders E. D., Paulino G. H. Optimally-tailored spinodal architected materials for multiscale design and manufacturing. *Advanced Materials*. 2022;34(26): 2109304. https://doi.org/10.1002/adma.202109304

52. Gaynutdinov R., Voronov V. V., Chernova E. V., ... Fedorov P. P. Flints as nanostructured chalcedons. *Journal of Surface Investigation: X-ray, Synchrotron and Neutron Techniques*. 2020;14(4): 762–770. https://doi.org/10.1134/S1027451020040084

53. Nikolaichik V. I., Sobolev B. P., Sorokin N. I., Avilov A. S. Electron diffraction study and ionic conductivity of fluorite $Ba_{1-x}La_xF_{2+x}$ and tysonite $La_{1-y}Ba_yF_{3-y}$ phases in the BaF2-LaF3 system. *Solid State Ionics*. 2022;386: 116052. https://doi.org/10.1016/j.ssi.2022.116052

54. Turkina T. *Morphological stability of the crystallization front of solid $M_{1-x}R_xF_{2+x}$ solutions (where M = Ca, Sr, Ba, R - REM)**. Cand. Sci. (Phys.-Math.) thesis. Moscow: Institute of

Crystallography, USSR Academy of Sciences. 1990. Available at: https://search.rsl.ru/ru/record/01000054976

55. Fedorov P. P. Nanotechnology and material science. *Nanosystems: Physics, Chemistry, Mathematics.* 2020;11(3): 314–315, https://doi.org/10.17586/2220-8054-2020-11-3-314–315

56. Lebedinsky V. I. *Volcanic crown of the great plain**. Moscow: Nauka Publ.; 1973. 192 p.

** Translated by author of the article*

Information about the author

Pavel P. Fedorov, Dr. Sci. (Chem.), Full Professor, Chief Researcher at the Prokhorov General Physics Institute of the Russian Academy of Sciences (Moscow, Russian Federation).

https://orcid.org/0000-0002-2918-3926

ppfedorov@yandex.ru

Received 24.07.2024; approved after reviewing 24.09.2024; accepted for publication 16.09.2024; published online 25.12.2024.

Translated by Valentina Mittova

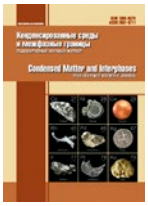

ISSN 1606-867X (Print)
ISSN 2687-0711 (Online)
Condensed Matter and Interphases
Kondensirovannye Sredy i Mezhfaznye Granitsy
https://journals.vsu.ru/kcmf/

Short communications

Short communication
https://doi.org/10.17308/kcmf.2024.26/12453

Evaluation of the thermodynamic stability of $REMgAl_{11}O_{19}$ (RE = La, Pr, Nd, Sm) hexaaluminates with a magnetoplumbite structure in the high temperature region

K. S. Gavrichev✉, **V. N. Guskov, P. G. Gagarin, A. V. Guskov**

Kurnakov Institute of General and Inorganic Chemistry of the Russian Academy of Sciences, 31 Leninsky pr., Moscow 119991, Russian Federation

Abstract

This study is important due to the lack of reliable data about the properties of high temperature materials for energy production and aerospace engineering. The purpose of this article was to evaluate the thermodynamic stability of RE magnesium hexaaluminates $REMgAl_{11}O_{19}$ (RE = La, Pr, Nd, Sm) with a magnetoplumbite structure, which are promising components for thermal barrier coatings. For this, we calculated the values of the Gibbs energy of the decomposition reactions of RE magnesium hexaaluminates into simple oxides and aluminum-magnesium spinel $MgAl_2O_4$ and $REAlO_3$ phases in the temperature range of 298–1,800 K. For calculations, we used data on the thermodynamic properties of hexaaluminates calculated from the values of heat capacity measured by differential scanning calorimetry in the range of 300-1,800 K and from values of thermodynamic properties of simple oxides, $MgAl_2O_4$, and $REAlO_3$ provided in previous research. There is hardly any information about the thermodynamic properties of RE magnesium hexaaluminates, which are promising thermal barrier materials. The purpose of the article is to provide a thermodynamic evaluation of the probability of decomposition reactions of hexaaluminates in the high temperature region.

Previously published data on the high temperature heat capacity of compounds with the composition of $REMgAl_{11}O_{19}$ (RE = La, Pr, Nd, Sm) were used to calculate temperature dependences of entropy and changes in enthalpy, which were used to evaluate the Gibbs energy of the decomposition reactions of hexaaluminates into constituent oxides.

The temperature dependences of the Gibbs energy of the four possible decomposition reactions of hexaaluminates allowed drawing conclusions about thermodynamic stability in the high temperature region.

Keywords: Hexaaluminates, Magnetoplumbite, RE, Thermodynamics, Thermal barrier coatings

***Funding*:** The study was supported by the Russian Science Foundation (grant No. 23-13-00051).

For citation: Gavrichev K. S., Guskov V. N., Gagarin P. G., Guskov A. V. Evaluation of the thermodynamic stability of $REMgAl_{11}O_{19}$ (RE=La, Pr, Nd, Sm) hexaaluminates with a magnetoplumbite structure in the high temperature region. *Condensed Matter and Interphases*. 2024;26(4): 782–788. https://doi.org/10.17308/kcmf.2024.26/12453

Для цитирования: Гавричев К. С., Гуськов В. Н., Гагарин П. Г., Гуськов А. В. Оценка термодинамической стабильности гексаалюминатов $REMgAl_{11}O_{19}$ (RE = La, Pr, Nd, Sm) со структурой магнетоплюмбита в области высоких температур. *Конденсированные среды и межфазные границы*. 2024;26(4): 782–788. https://doi.org/10.17308/kcmf.2024.26/12453

✉ Konstantin S Gavrichev, e-mail: gavrich@igic.ras.ru

1. Introduction

The improved efficiency of modern power turbine plants and aircraft engines largely depends on the development of new materials that allow significantly increasing the temperature of gases in the working area. Parts from nickel-cobalt alloys used for the manufacture of critical parts (for example, turbine blades) can be effectively operated, even with cooling, at temperatures that do not exceed 1,000–1,200 °C [1]. Oxide coatings of metal parts in combination with the cooling of inner surfaces allow increasing the temperature of working gases by hundreds of degrees due to a large temperature gradient in the oxide layer [2, 3]. Coatings designed to protect against the effects of high temperature are known as thermal barrier coatings. Another important function of oxide coatings is protection against chemical exposure to substances in gaseous and condensed states, which are formed during fuel combustion and in the form of suspended particles enter the turbine together with pumping-in air [4].

Until recently, thermal barrier coatings were mainly made of yttria stabilized zirconia, YSZ [5]. This substance has some disadvantages, i.e. temperature restrictions for its application (about 1,200 °C) associated with the presence of a phase transition [6] and a significant diffusion of oxygen at high temperatures leading to the oxidation of the surfaces of metal parts. Therefore, a number of high-temperature complex RE oxides have been proposed for application: zirconates $RE_2Zr_2O_7$ [7], hafnates $RE_2Hf_2O_7$ and RE_2O_3 $2HfO_2$ [8], tantalates $RETaO_4$ and RE_3TaO_7 [9, 10], niobates RE_3NbO_7 [11], etc. These materials meet the key requirements for thermal barrier coatings: they have high melting temperatures, no phase transitions in a wide range of temperatures, have low thermal conductivity, a specified coefficient of thermal expansion, and mechanical properties. Currently, there has been a lot of interest in RE magnesium hexaaluminates [12] due to their lower thermal conductivity and potential chemical resistance to CMAS oxides (CaO, MgO, Al_2O_3, and SiO_2) at high temperatures [13].

One of the ways to evaluate if a particular oxide of thermal barrier coatings can be used under the conditions of high temperatures and the corrosive effect of gases and substances in the condensed state (in particular, melts) is the thermodynamic evaluation of the probability of decomposition reactions of complex oxides into more simple oxides, as well as reactions of interaction with the substances in the environment in the high temperature region. For this, it is necessary to determine the Gibbs energy of these reactions.

The triple phase diagram of RE_2O_3-MgO-Al_2O_3 published in [14] is characterized by the presence of 4 eutectics and a number of phases (La_2O_3, MgO, Al_2O_3, MgO·Al_2O_3, La_2O_3·Al_2O_3, $2La_2O_3$·$11Al_2O_3$) (Fig. 1). It can be noted that it does not have the $LaMgAl_{11}O_{19}$ phase with a magnetoblumbite structure. It can be assumed that in addition to $REAlO_3$ perovskites, the quasibinary diagram of RE_2O_3-Al_2O_3 for other rare-earth elements, starting with terbium, will have other compounds: aluminum garnets $RE_3Al_5O_{12}$ and $RE_4Al_2O_9$ with a monoclinic structure.

There is little information about the experimental determination of the thermodynamic properties of hexaaluminates with a magnetoplumbite structure. For example, such data are only available for heat capacity. In [15], the heat capacity of $LaMgAl_{11}O_{19}$ was determined by means of thermoanalytical analysis. The resulting data was presented in the form of a small graph. In [16], to determine the thermal conductivity of $REMgAl_{11}O_{19}$ (RE = La, Pr, Nd, Sm, Eu, Gd), the authors used the values of specific heat capacity which were calculated by the Neumann–Kopp

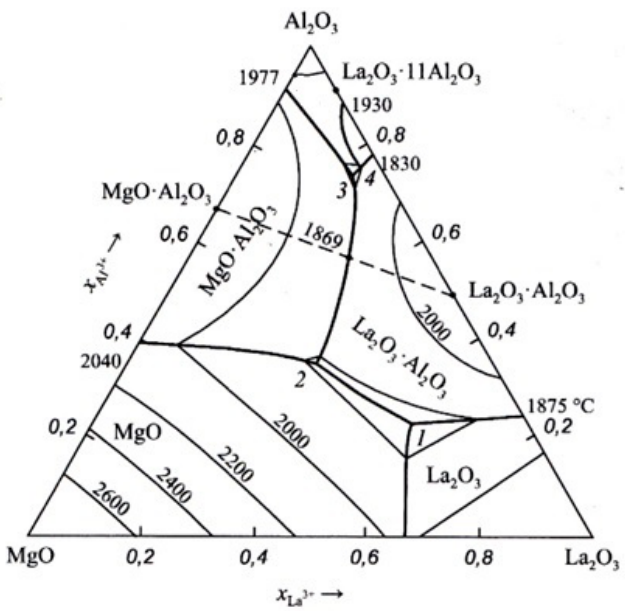

Fig. 1. Phase diagram of La_2O_3-MgO-Al_2O_3 from [14]

rule. The resulting data was also presented graphically. The most reliable data were obtained by measuring the heat capacity of $LaMgAl_{11}O_{19}$ and $SmMgAl_{11}O_{19}$ by differential scanning calorimetry in the high temperature range [17, 18, 19, 20]. These data were presented as the Maier-Kelley equation $C_p(T) = A + B\times T - C/T^2$.

The values of entropy and the changes in enthalpy can be calculated from the known ratios of the heat capacity data:

$$S°(T-298.15) = \int_{298.15}^{T} \frac{C_p}{T} dT \quad (1)$$

and

$$H°(T) - H°(298.15) = \int_{298.15}^{T} C_p dT. \quad (2)$$

2. Evaluation of the Gibbs energy

To evaluate the thermodynamic stability of hexaaluminates $REMgAl_{11}O_{19}$ (RE = La, Pr, Nd, Sm) in the high temperature region, it is necessary to calculate the Gibbs energy of possible reactions for oxides, for which there is data on enthalpies of formation at 298.15 K and on changes in enthalpy and entropy in the high temperature region:

$REMgAl_{11}O_{19} = 0.5\ RE_2O_3 + MgO + 5.5\ Al_2O_3$ (I),

$REMgAl_{11}O_{19} = 0.5\ RE_2O_3 + MgAl_2O_4 + 4.5\ Al_2O_3$ (II),

$REMgAl_{11}O_{19} = REAlO_3 + MgO + 5\ Al_2O_3$ (III),

$REMgAl_{11}O_{19} = REAlO_3 + MgAl_2O_4 + 4\ Al_2O_3$ (IV).

We chose the decomposition reactions into simple oxides, aluminum-magnesium spinel, and $REAlO_3$ aluminates with a perovskite structure because they are present in the triple phase diagram given in [14]. Evaluation by reaction:

$REMgAl_{11}O_{19} = REAl_{11}O_{18} + MgO$ (V)

was impossible due to insufficient data for $REAl_{11}O_{18}$.

For the four above listed reactions, the temperature dependences of the Gibbs energy, which were calculated as the difference between the values for the reaction products and the starting substances, can be presented as follows:

Reaction (I):

$$\Delta_{r(I)}G°(T) = [0.5\Delta_f G°(RE_2O_3, T) + \Delta_f G°(MgO, T) + 5.5\Delta_f G°(Al_2O_3, T)] - \Delta_f G°(REMgAl_{11}O_{19}, T). \quad (3)$$

Reaction (II):

$$\Delta_{r(II)}G°(T) = [0.5\Delta_f G°(RE_2O_3, T) + \Delta_f G°(MgAl_2O_4, T) + 4.5\Delta_f G°(Al_2O_3, T)] - \Delta_f G°(REMgAl_{11}O_{19}, T). \quad (4)$$

Reaction (III):

$$\Delta_{r(III)}G°(T) = [\Delta_f G°(REAlO_3, T) + \Delta_f G°(MgO, T) + 5\times\Delta_f G°(Al_2O_3, T)] - \Delta_f G°(REMgAl_{11}O_{19}, T). \quad (5)$$

Reaction (IV):

$$\Delta_{r(IV)}G°(T) = [\Delta_f G°(REAlO_3, T) + \Delta_f G°(MgAl_2O_4, T) + 4\Delta_f G°(Al_2O_3, T)] - \Delta_f G°(REMgAl_{11}O_{19}, T). \quad (6)$$

The Gibbs energy of reactions (I-IV) can be expressed as the sum of two components: enthalpy and entropy.

Reaction (I):

$$\Delta_{r(I)}G°(T) = \{[0.5\Delta_f H°(RE_2O_3, T) + \Delta_f H°(MgO, T) + 5.5\Delta_f H°(Al_2O_3, T)] - \Delta_f H°(REMgAl_{11}O_{19}, T)\} - T\{[0.5S°(RE_2O_3, T) + S°(MgO, T) + 5.5S°(Al_2O_3, T)] - S°(REMgAl_{11}O_{19}, T)\}. \quad (7)$$

Reaction (II):

$$\Delta_{r(II)}G°(T) = \{[0.5\Delta_f H°(RE_2O_3, T) + \Delta_f H°(MgAl_2O_4, T) + 4.5\Delta_f H°(Al_2O_3, T)] - \Delta_f H°(REMgAl_{11}O_{19}, T)\} - T\{[0.5S°(RE_2O_3, T) + S°(MgAl_2O_4, T) + 4.5S°(Al_2O_3, T)] - S°(REMgAl_{11}O_{19}, T)\}. \quad (8)$$

Reaction (III):

$$\Delta_{r(III)}G°(T) = \{[\Delta_f H°(REAlO_3, T) + \Delta_f H°(MgO, T) + 5\Delta_f H°(Al_2O_3, T)] - \Delta_f H°(REMgAl_{11}O_{19}, T)\} - T\{[S°(REAlO_3, T) + S°(MgO, T) + 5S°(Al_2O_3, T)] - S°(REMgAl_{11}O_{19}, T)\}. \quad (9)$$

Reaction (IV):

$$\Delta_{r(IV)}G°(T) = \{[\Delta_f H°(REAlO_3, T) + \Delta_f H°(MgAl_2O_4, T) + 4\Delta_f H°(Al_2O_3, T)] - \Delta_f H°(REMgAl_{11}O_{19}, T)\} - T\{[S°(REAlO_3, T) + S°(MgAl_2O_4, T) + 4S°(Al_2O_3, T)] - S°(REMgAl_{11}O_{19}, T)\}. \quad (10)$$

To calculate the enthalpy component over a wide range of temperatures, we needed data on the enthalpies of the corresponding reactions at 298.15 K and the temperature dependences of the changes in enthalpy and entropy for each participant in the reaction.

The thermodynamic values necessary for the calculation were taken from the original articles [17–24] and reference books [25–27]. We found values of enthalpy of formation for $LaAlO_3$ and $PrAlO_3$ perovskites in [28], however, we failed to find data on the temperature dependence of heat capacity. Therefore, calculations were only made for neodymium and samarium compounds. We obtained the estimated enthalpies of formation

of hexaaluminates $REMgAl_{11}O_{19}$ (RE = La, Pr, Nd, Sm) with a magnetoplumbite structure by drop calorimetry [29]. The results of calculations of enthalpies and Gibbs energies of type (I–IV) reactions in the temperature range of 298.15–1,800 K are shown in Fig. 2–5.

From Fig. 2, it follows that the values of the Gibbs energy of a type (I) reaction for the lanthanum, praseodymium, and neodymium compounds had positive values in the studied temperature range, while in the case of the samarium compound the sign changed to negative, which may indicate its thermodynamic instability in the region below 1,400 K. However, it should be noted that taking into account the error of determination (about ± 10 kJ/mol), this value can shift to the region of lower temperatures (up to 800 K). There was a general downward trend in thermodynamic stability from lanthanum to samarium.

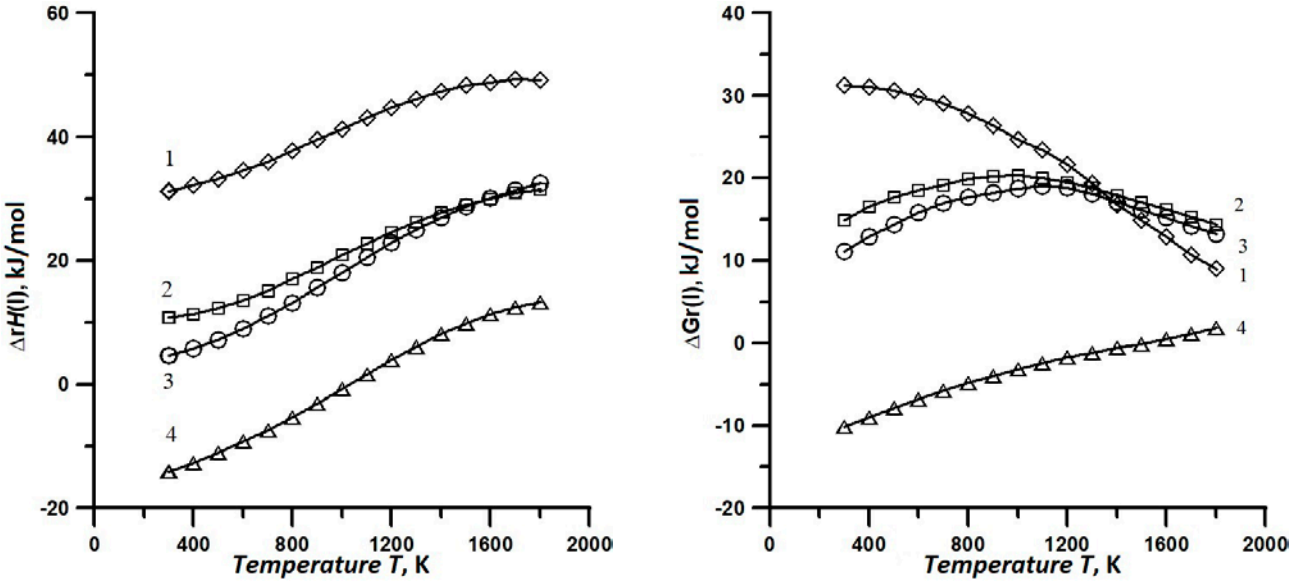

a b

Fig. 2. Temperature dependences of enthalpy (a) and Gibbs energy (b) of reaction (I) for: *1* – $LaMgAl_{11}O_{19}$, *2* – $PrMgAl_{11}O_{19}$, *3* – $NdMgAl_{11}O_{19}$, *4* – $SmMgAl_{11}O_{19}$

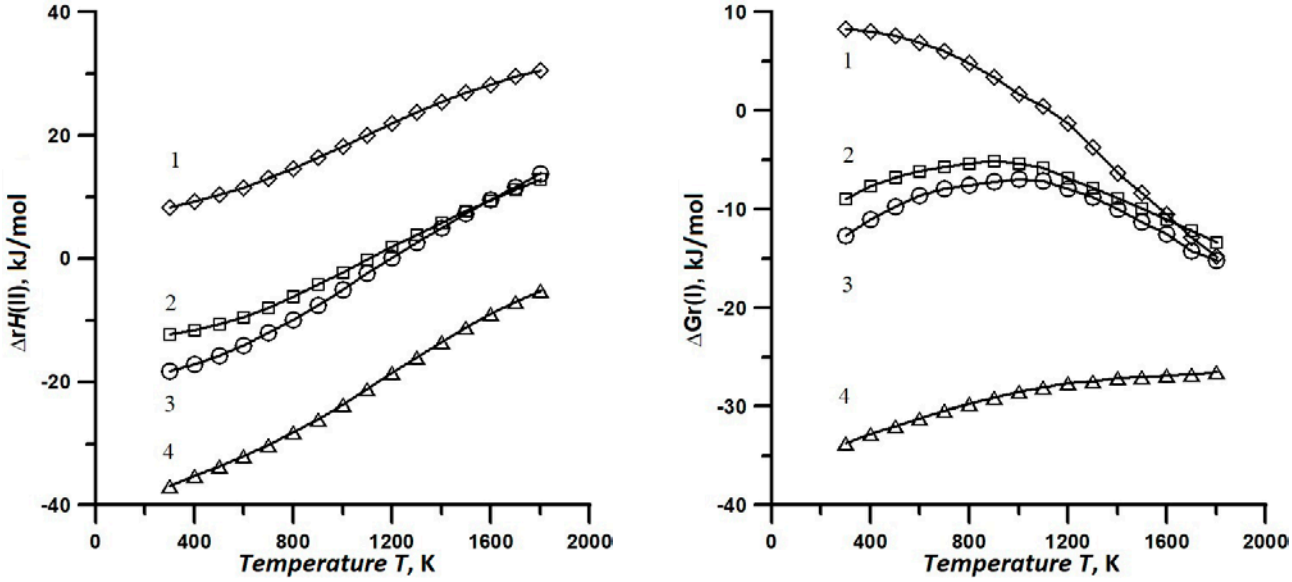

a b

Fig. 3. Temperature dependences of enthalpy (a) and Gibbs energy (b) of reaction (I) for: *1* – $LaMgAl_{11}O_{19}$, *2* – $PrMgAl_{11}O_{19}$, *3* – $NdMgAl_{11}O_{19}$, *4* – $SmMgAl_{11}O_{19}$

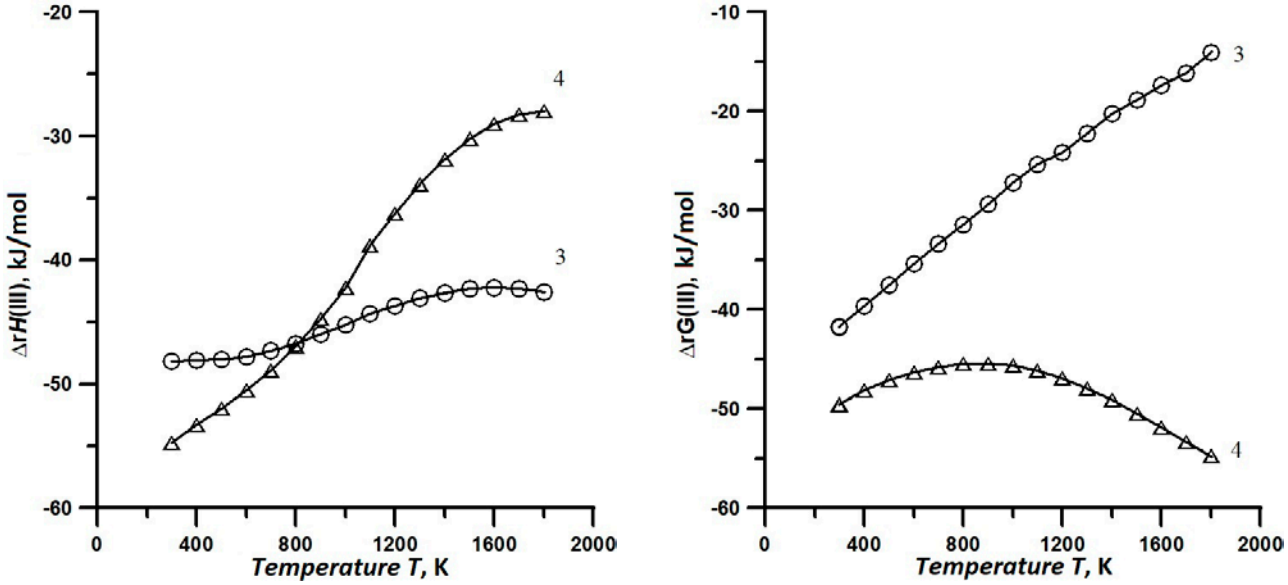

a b

Fig. 4. Temperature dependences of enthalpy (a) and Gibbs energy (b) of reaction (III) for: *3* – $NdMgAl_{11}O_{19}$, *4* – $SmMgAl_{11}O_{19}$

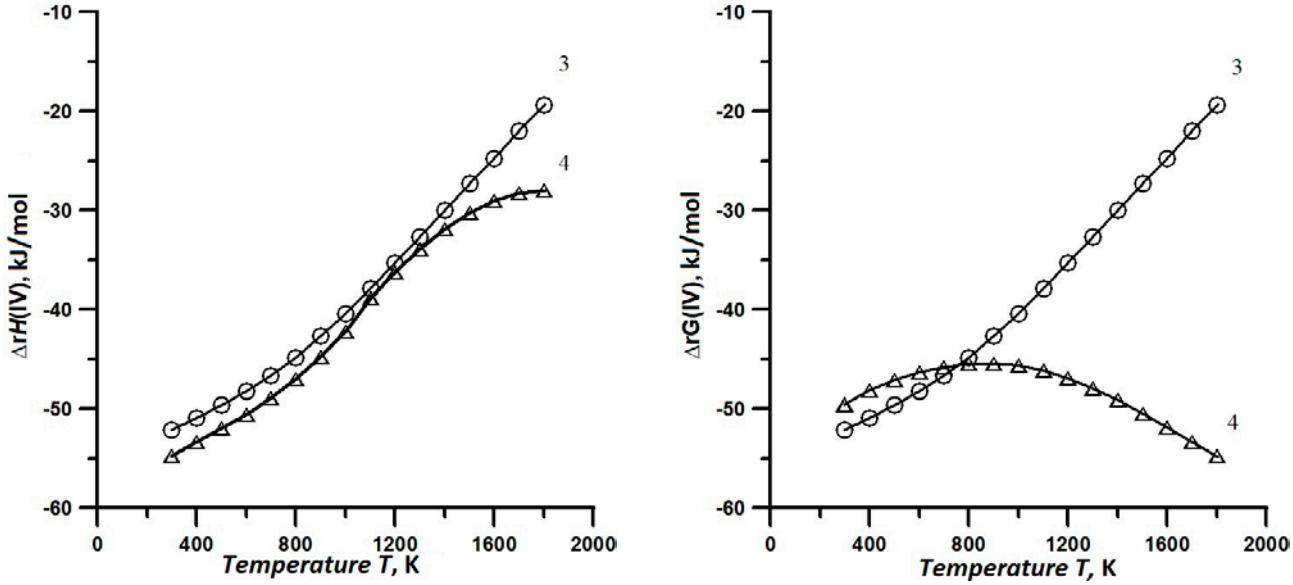

a b

Fig. 5. Temperature dependences of enthalpy (a) and Gibbs energy (b) (IV) for: *3* – $NdMgAl_{11}O_{19}$, *4* – $SmMgAl_{11}O_{19}$

The values of the Gibbs energy of a type (II) reaction for $LaMgAl_{11}O_{19}$ became negative when the temperature exceeded 1,100 K, which indicates the probability of the reaction. Judging by the temperature dependences of the Gibbs energy for $PrMgAl_{11}O_{19}$, $NdMgAl_{11}O_{19}$, and $SmMgAl_{11}O_{19}$ shown in Fig. 3 and their negative values, a type (II) reaction for these compounds is possible over the entire range of high temperatures.

Judging by the sign of the Gibbs energy of the reaction which involved a decomposition into magnesium and aluminum oxides and $REAlO_3$ perovskites (RE = Nd, Sm), this process is very probable.

Very negative values of the Gibbs energy indicated that a type (IV) reaction for obtaining magnesium-neodymium and magnesium-samarium hexaaluminates from perovskites,

spinel, and aluminum oxide should not occur. A significant difference in the type of the Gibbs energy and enthalpy dependencies of type (III) and (IV) reactions can be explained by the influence of the entropy factor.

3. Conclusions

Analysis of the thermodynamic stability of RE magnesium hexaaluminates $REMgAl_{11}O_{19}$ based on the calculation of the Gibbs energy of the decomposition reactions into simple oxides, aluminum-magnesium spinel, and $REAlO_3$ perovskites allowed determining the probability of these reactions over a wide range of temperatures. It was shown that there is influence of enthalpy and entropy factors on the type of temperature dependence of the Gibbs energy of decomposition reactions of hexaaluminates into simpler oxides.

Contribution of the authors

The authors contributed equally to this article.

Conflict of interests

The authors declare that they have no known competing financial interests or personal relationships that could have influenced the work reported in this paper.

References

1. Huang E-W., Tung C., Liaw P. K. High-temperature materials for structural applications: New perspectives on high-entropy alloys, bulk metallic glasses, and nanomaterials. *MRS Bulletin*. 2019;44: 847–853. https://doi.org/10.1557/mrs.2019.257

2. Lakiza S. M., Grechanyuk M. I., Ruban O. K., … Prokhorenko S. V. Thermal barrier coatings: current status, search, and analysis. *Powder Metallurgy and Metal Ceramics*. 2018;57(1-2): 82–113. https://doi.org/10.1007/s11106-018-9958-0

3. Stiger M. J., Yanar M. M., Topping M. G., Pettit F. S., Meier G. H. Thermal barrier coatings for the 21st century. *International Journal of Materials Research*.1999;90(12): 1069–1078. https://doi.org/10.1515/ijmr-1999-901218

4. Tejero-Martin D., Bennett C., T. Hussain T. A review on environmental barrier coatings: History, current state of the art and future developments. *Journal of European Ceramic Society*. 2021;41(3): 1747–1768. https://doi.org/10.1016/j.jeurceramsoc.2020.10.057

5. Poliarus O., Morgiel J., Żórawski W., … Cherniushok O. Microstructure, mechanical and thermal properties of YSZ thermal barrier coatings deposited by axial suspension plasma spraying. *Archives of Civil and Mechanical Engineering*. 2023;23: 89(1-11). https://doi.org/10.1007/s43452-023-00616-8

6. Gorelov V. P., Belyakov S., Abdurakhimova R. K. Phase transitions in monoclinic ZrO_2. *Physics of Solid State*. 2023;65(3): 461–466. https://doi.org/10.21883/pss.2023.03.55589.541

7. Frommherz M., Scholz A., Oechsner M., Bakan E., Vaßen R. Gadolinium zirconate/YSZ thermal barrier coatings: Mixed-mode interfacial fracture toughness and sintering behavior. *Surface and Coating Technologies*. 2016;286: 119–128. https://doi.org/10.1016/j.surfcoat.2015.12.012

8. Kablov E. N., Doronin O. N., Artemenko N. I., Stekhov P. A., Marakhovskii P. S., Stolyarova V. L. Investigation of the physicochemical properties of ceramics in the Sm_2O_3–Y_2O_3–HfO_2 system for developing promising thermal barrier coatings. *Russian Journal of Inorganic Chemistry*. 2020;65(6): 914–923. https://doi.org/10.1134/s0036023620060078

9. Chen L., Hu M., Guo J., Chong X., Feng J. Mechanical and thermal properties of $RETaO_4$ (RE = Yb, Lu, Sc) ceramics with monoclinic-prime phase. *Journal of Materials Science and Technology*. 2020;52: 20–28. https://doi.org/10.1016/j.jmst.2020.02.051

10. Chen L., Song P., Feng J. Influence of ZrO_2 alloying effect on the thermophysical properties of fluorite-type Eu_3TaO_7 ceramics. *Scripta Materialia*. 2018;152: 117–121. https://doi.org/10.1016/j.scriptamat.2018.03.042

11. Chen L., Guo J., Zhu Y., Hu M., Feng J. Features of crystal structures and thermo-mechanical properties of weberites RE_3NbO_7 (RE = La, Nd, Sm, Eu, Gd) ceramics. *Journal of American Ceramic Society*. 2021;104: 404–412. https://doi.org/10.1111/jace.17437

12. Gadow R., Lischka M. Lanthanum hexaaluminate – novel thermal barrier coatings for gas turbine applications – materials and process development. *Surface and Coating Technologies*. 2002;151-152: 392–399. https://doi.org/10.1016/S0257-8972(01)01642-5

13. Pitek F. M., Levi C. G. Opportunities for TBCs in the ZrO_2-$YO_{1.5}$-$TaO_{2.5}$ system. *Surface and Coating Technologies*. 2007;201: 6044–6050. https://doi.org/10.1016/j.surfcoat.2006.11.011

14. Mikhailov G. G., Makrovets L. A., Smirnov L. A. Thermodynamics of the processes of interaction of liquid metal components in Fe – Mg – Al – La – O system. *Izvestiya Visshikh Uchebnykh Zavedenii. Chernaya Metallurgiya = Izvestiya. Ferrous Metallurgy*. 2018;61(6): 460–465. https://doi.org/10.17073/0368-0797-2018-6-460-465

15. Friedrich C., Gadow R., Schirmer T. Lanthanum hexaaluminate – a new material for atmospheric plasma spraying of advanced thermal barrier coatings. *Journal of Thermal Spray Technology*. 2001;10(4): 592–598. https://doi.org/10.1361/105996301770349105

16. Lu H., Wang C.-An, Zhang C., Tong S. Thermophysical properties of rare-earth hexaaluminates $LnMgAl_{11}O_{19}$ (Ln: La, Pr, Nd, Sm, Eu and Gd) magnetoplumbite for advanced thermal barrier coatings. *Journal of the European Ceramic Society*. 2015;35: 1297–1306. https://doi.org/10.1016/j.jeurceramsoc.2014.10.030

17. Gagarin P. G., Guskov A. V., Guskov V. N., Khoroshilov A. V., Ryumin M. A., Gavrichev K. S. Synthesis and high-temperature heat capacity of $LaMgAl_{11}O_{19}$ and $SmMgAl_{11}O_{19}$ hexaaluminates. *Russian Journal of Inorganic Chemistry*. 2023;68(11): 1599–1605. https://doi.org/10.1134/s0036023623602064

18. Gagarin P. G., Guskov A. V., Guskov V. N., Nikiforova G. E., Gavrichev K. S. Heat capacity and thermal expansion of $LaMgAl_{11}O_{19}$*. *Russian Journal of Inorganic Chemistry*. 2024;69(6): accepted for publication. (In Russ.)

19. Gagarin P. G., Guskov A. V., Guskov V. N., Khoroshilov A. V., Efimov N. N., Gavrichev K. S. Heat capacity and magnetic properties of $PrMgAl_{11}O_{19}$*. *Russian Journal of Physical Chemistry A*. 2024; accepted for publication. (In Russ.)

20. Gagarin P. G., Guskov A. V., Guskov V. N., Ryumin M. A., Nikiforova G. E., Gavrichev K. S. Heat capacity of magnesium-neodymium hexaaluminate $NdMgAl_{11}O_{19}$*. *Russian Journal of Physical Chemistry A*. 2024; accepted for publication. (In Russ.)

21. van der Laan R. R., Konings R. J. M., van Genderen A. C. G., van Miltenburg J. C. The heat capacity of $NdAlO_3$ from 0 to 900 K. *Thermochimica Acta*. 1999;329: 1–6. https://doi.org/10.1016/S0040-6031(99)00006-4

22. Kopan A. R., Gorbachuk M. P., Lakiza S. M., Tishchenko Ya. S. Thermodynamic characteristics of $SmAlO_3$ in the range 55–300 K. *Powder Metallurgy and Metal Ceramics*. 2012;51(3-4): 209–216. https://doi.org/10.1007/s11106-012-9419-0

23. Konings R. J. M., Beneš O., Kovács A., … Osina E. The thermodynamic properties of the *f*-elements and their compounds. Part 2. The lanthanide and actinide oxides. *Journal of Physical and Chemical Reference Data*. 2014;4: 013101-1–013101-95. https://doi.org/10.1063/1.4825256

24. Zinkevich M. Thermodynamics of rare earth sesquioxides. *Progress in Materials Science*. 2007;52: 597–647. https://doi.org/10.1016/j.pmatsci.2006.09.002

25. Chase M. W. Jr. *NIST-JANAF thermochemical tables*. *Journal of Physical and Chemical Reference Data Monographs*. Washington DC: American Inst. of Physics; 1998, 1951 p.

26. Barin I. *Thermochemical Data of Pure Substances*. 3rd Edition. Published jointly by G. Platzki. VCH – Weinheim; New York; Base1; Cambridge; Tokyo: VCH. 2003 p.

27. Glushko V. P. *Thermal constants of substances**. Reference book. Moscow: 1965-1982. (In Russ.)

28. Zhang Y., Navrotsky A. Thermochemistry of rare-earth aluminate and aluminosilicate glasses. *Journal of Non-Crystalline Solids*. 2004;341: 141–151. https://doi.org/10.1016/j.jnoncrysol.2004.04.027

29. Gavrichev K. S., Guskov V. N., Gagarin P. G., Guskov A. V., Khoroshilov A. V. Heat capacity and thermodynamic properties of $REMgAl_{11}O_{19}$ (RE = La, Pr, Nd, Sm) hexaaluminates with magnetoplumbite structure. In: *XXIV International Conference on Chemical Thermodynamics in Russia RCCT-2024, July 1–5, 2024, Ivanovo, Russia RCCT-2024. Book of abstracts*. Ivanovo: JSC "Ivanovo Publishing House" Publ.; 2024. p. 318. Available at: https://rcct.isc-ras.ru/sites/default/files/collectionabstracts/56/rcct-2024.pdf

** Translated by author of the article*

Информация об авторах

Konstantin S. Gavrichev, Dr. Sci. (Chem.), Chief Researcher, Head of Laboratory of Thermal Analysis and Calorimetry, Kurnakov Institute of General and Inorganic Chemistry of the Russian Academy of Sciences (Moscow, Russian Federation).
https://orcid.org/0000-0001-5304-3555
gavrich@igic.ras.ru

Vladimir N. Guskov, Dr. Sci. (Chem.), Leading Researcher of Laboratory of Thermal Analysis and Calorimetry, Kurnakov Institute of General and Inorganic Chemistry of the Russian Academy of Sciences (Moscow, Russian Federation).
https://orcid.org/0000-0003-0425-8618
guskov@igic.ras.ru

Pavel G. Gagarin, Cand. Sci. (Chem.), Senior Researcher of Laboratory of Thermal Analysis and Calorimetry, Kurnakov Institute of General and Inorganic Chemistry of the Russian Academy of Sciences (Moscow, Russian Federation).
https://orcid.org/0000-0001-6450-3959
gagarin@igic.ras.ru

Anton V. Guskov, Cand. Sci. (Chem.), Researcher of Laboratory of Thermal Analysis and Calorimetry, Kurnakov Institute of General and Inorganic Chemistry of the Russian Academy of Sciences (Moscow, Russian Federation).
https://orcid.org/0000-0003-0826-5495
a.gus@igic.ras.ru

Received 18.07.2024; approved after reviewing 30.07.2024; accepted for publication 16.09.2024; published online 25.12.2024.

Translated by Irina Charychanskaya